

A Harvard astrophysicist's
controversial UFO hunt p. 372

Sign problem points to
quantum criticality p. 418

A magnetic stop signal
for migratory birds p. 446

Science

\$15
28 JANUARY 2022
science.org

 AAAS

MAIZE POLLEN

Handoff to the next generation p. 424

THE 2021 MICHELSON PRIZES

The Michelson Medical Research Foundation and the Human Vaccines Project congratulate the recipients of the 2021 Michelson Prizes – Next Generation Grants.

These \$150,000 research grants are awarded each year to support promising early career scientists who are applying disruptive research concepts to advance human immunology, vaccine discovery, and immunotherapy across major global diseases.

Dr. Camila Consiglio, Dr. Rong Ma, and Dr. Nicholas Wu were selected via a rigorous global competition and represent the next generation of innovators in human immunology and vaccine research. They will be honored at a virtual ceremony on March 10, 2022, conducted as part of the Human Vaccines Project's Global Lab Meeting: www.humanvaccinesproject.org/webinars

COULD YOU BE THE NEXT MICHELSON PRIZE WINNER?

Applications open April 2022.

For more information visit:

www.humanvaccinesproject.org/michelson-prizes

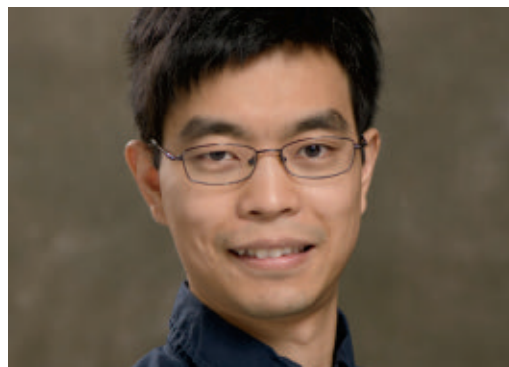
#MichelsonPrizes



Camila Consiglio, Ph.D., postdoctoral researcher, Karolinska Institutet. *"Investigating the Effects of Testosterone on the Human Immune System."*



Rong Ma, Ph.D., postdoctoral fellow, Emory University. *"Harnessing Receptor Mechanics as a Marker for Immunogenicity to Isolate and Identify Potent T-cell Receptors and Recognized Antigens."*



Nicholas Wu, Ph.D., assistant professor, University of Illinois. *"Systematic Identification of Antibody Sequence Signatures for Epitope Prediction."*

CALL FOR PAPERS



OLAR

Ocean-Land-Atmosphere Research (OLAR) is an online-only, Open Access journal published in affiliation with **Southern Marine Science and Engineering Guangdong Laboratory (Zhuhai) (SML-ZHUHAI)** and distributed by the **American Association for the Advancement of Science (AAAS)**. With an emphasis on ocean-related sciences, *OLAR* provides an international platform for researchers engaged in marine, terrestrial, and atmospheric studies and the interactions among them. The journal welcomes relevant fundamental research in physics, chemistry, biology and geology as well as emerging applied research in ocean observation, environment protection, and resources utilization. Manuscripts featuring cutting-edge science, innovative technology, and interdisciplinary studies within the journal's scope are particularly welcome.

Submit your research to OLAR today!

Learn more at spj.sciencemag.org/OLAR

The Science Partner Journal (SPJ) program was established by the American Association for the Advancement of Science (AAAS), the nonprofit publisher of the Science family of journals. The SPJ program features high-quality, online-only, Open Access publications produced in collaboration with international research institutions, foundations, funders, and societies. Through these collaborations, AAAS furthers its mission to communicate science broadly and for the benefit of all people by providing top-tier international research organizations with the technology, visibility, and publishing expertise that AAAS is uniquely positioned to offer as the world's largest general science membership society. Visit us at spj.sciencemag.org



@SPJournals



@SPJournals

 OPEN ACCESS

ARTICLE PROCESSING CHARGES WAIVED UNTIL 2025



The POSTECH campus

POSTECH leads the way toward a greener future

Established in 1986, the Pohang University of Science and Technology in South Korea, commonly called POSTECH, has quickly built a reputation for research excellence. The leadership team of POSTECH, one of the world's most innovative universities, has supported its faculty to focus their attention on the most pressing matters facing the globe today: climate change and global warming.

According to POSTECH climate scientist Jong-Seong Kug, there has never been a more important time for academics to step up and demonstrate the imminent threats posed to the planet by climate change. "I think some members of the public still believe climate change is a story of the distant future and are not aware of its seriousness," he says.

Kug has spent his career researching the effects of adverse climate conditions. His work has advanced the academic community's understanding of what triggers the warming of sea surface temperatures every few years—an effect known as "El Niño." His research has widened the field's understanding of climate dynamics and led to improved modeling systems for predicting climate patterns. "I developed an El Niño prediction model that has been used by the Korea Meteorological Administration," he says.

Now is the time to ensure that these greater understandings are carefully disseminated to the wider community and can facilitate real-life changes that will help mitigate the threats posed by global warming, says Kug. "Pure scientific research on climate change is important, but I think it's also critical to change our society's perception of climate change," he says.

A place of action

Since its establishment as the first research-oriented university in Korea, POSTECH has aimed to set new standards for change and innovation. In 1995, it established the Division of Environmental Science and Engineering (DESE) to dive

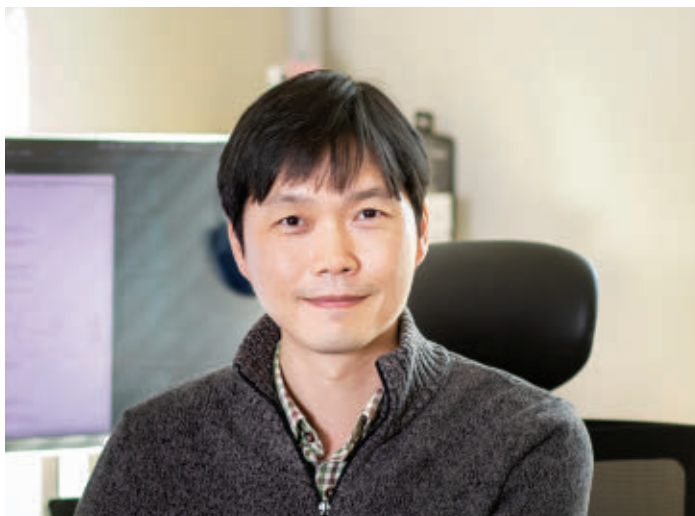
deeper into solving environmental issues. The creation of DESE was in recognition of the vital part that environmental research plays in achieving a sustainable future for humanity, says Kug. "While we are not a large university, POSTECH constantly strives to solve global challenges facing humanity, and to conduct research that will enable the sustainable growth of communities and the nation."

Thanks to its world-class research facilities, such as the university's two synchrotron radiation accelerators, POSTECH was ranked third in the World's Best Small Universities list published by *Times Higher Education* (THE) in 2021, marking its third year on that list.

Now the POSTECH community is striving to lead action on climate change by example, as well as through its academic contributions. The leadership team is reducing the institute's overall energy use by implementing energy savings techniques and greenhouse gas reductions projects across the board. For example, older technical equipment is being replaced with higher-efficiency devices in laboratories and classrooms.

Kug explains that POSTECH provides academics with a supportive environment to manage and solve the practical challenges that come with climate change research. "Our team requires a lot of computing power as we're dealing with huge numerical models to simulate the Earth's climate, and we have well-equipped facilities to manage large and high-speed computers," he says.

For example, in recent years Kug has been working on how biological, physical, and chemical processes across the Earth's ecosystems operate self-correcting feedback loops to help modulate climate variability and negate the effects of climate change. His research has revealed that changes to Arctic phytoplankton and vegetation could play a role in amplifying the warming of the earth's surface and must be considered in future modeling of the effects of climate change (1, 2). "It is well known that increases in carbon dioxide contribute to increased surface



Left, Jong-Seong Kug; **Right**, Seung-Ki Min

temperature, but our study on the physiological feedback of vegetation suggests this can happen even without the greenhouse effect,” explains Kug.

Focusing on the future

POSTECH's academic heart lies in forward-thinking research that will enable citizens across the world to live sustainably. Areas such as artificial intelligence, battery technology, health care, and smart cities are firmly on their radar, for example.

From 2016 to 2021, a fifth of the papers published by POSTECH related to the United Nations Sustainable Development Goals, a clear demonstration of their commitment to pursuing research that will underpin future policies aligned to environmentally sustainable living.

Climate scientist Seung-Ki Min explains that he has been researching how humans have influenced the climate for two decades, particularly regarding how the increase in human-made greenhouse gases has and will affect extreme weather conditions, such as heat waves, heavy rainfall, and tropical cyclones.

His current research focus is on ways to prepare for the imminent effects of the climate change crisis. “If we can improve the predictability of extreme climate disasters under different emission scenarios, this will better inform the policy makers who are preparing climate change adaptation measures,” says Min. “In this way, the work of climate scientists will affect peoples’ lives more and more in the future.”

Min's climate research is challenging. Data from weather and climate systems are inherently noisy, and identifying the signals that indicate the influence of human activity is no easy task. In particular, oceans introduce considerable variability, and understanding their role in climate is imperative. Using advanced climate-modeling approaches, Min demonstrated that the Indo-Pacific warm pool has been expanding in recent decades due to greenhouse gas increases (3). He also quantified the causes of diverse responses of global hydrology to volcanic eruptions.

“Climate models show different degrees of land precipitation reduction after volcanic eruptions, but the causes remain uncertain. Through systematic comparisons of many climate models, we found that various El Niño behaviors following volcanic eruptions could explain a large portion of the uncertainties. This has important implications for so-called climate engineering that mimics volcanic influences by blocking out sunlight,” Min explains (4).



Moving forward, POSTECH is dedicating its academic efforts to further strengthen its role as a leader in climate change research, not only by improving the faculty's capability to predict climate disasters, but also by better quantifying the impacts of global warming on important natural resources, such as water, food, and energy.

To make this goal a reality, POSTECH is encouraging multidisciplinary research collaborations across fields, and has recently established the School of Convergence Science and Technology and the Graduate School of Artificial Intelligence.

Next steps

Climate researchers are playing an ever-increasing role in mitigating the effects of global warming. At POSTECH, Min says, climate research groups are actively expanding their ability to create research impact by fostering the next generation of talented scientists. Faculty members from other fields, such as energy and materials, are conducting related research, such as developing zero-carbon technologies that will help countries meet their carbon-neutrality goals and translating research outcomes into real-world applications through close collaboration with industry. The whole is more than the sum of its parts, and in the case of climate change, a holistic view is essential to solving this crisis.

References

1. J.-Y. Park, J.-S. Kug, J. Bader, R. Rolph, M. Kwon, *Proc. Natl. Acad. Sci. U.S.A.* **112**, 5921–5926 (2015).
2. S.-W. Park, J.-S. Kim, J.-S. Kug, *Nat. Commun.* **11**, 2098 (2020).
3. E. Weller *et al.*, *Sci. Adv.* **2**, e1501719 (2016).
4. S. Paik, S.-K. Min, C. E. Iles, E. M. Fischer, A. P. Schurer, *Sci. Adv.* **6**, eaba1212 (2020).

Sponsored by

POSTECH
POHANG UNIVERSITY OF SCIENCE AND TECHNOLOGY

CONTENTS

28 JANUARY 2022
VOLUME 375 • ISSUE 6579

376
& 460

NEWS

IN BRIEF

362 News at a glance

IN DEPTH

364 Vaccines may cause rare, Long Covid-like symptoms

Researchers probe reports of brain fog, headaches, and blood pressure swings *By J. Couzin-Frankel and G. Vogel*

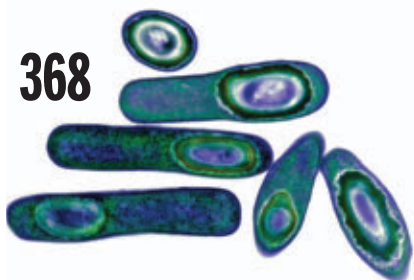
366 After Omicron, some scientists foresee ‘a period of quiet’

The variant's modest toll in many countries has led to a sense of optimism. But new surprises are likely *By K. Kupferschmidt*

367 NASA's Webb telescope reaches deep space home

Operators begin to fine-tune mirror segments after parking scope in L2 orbit *By D. Clery*

368



368 Alternatives to fecal transplants near approval

Trial shows spore-filled pill derived from human stool treats tough gut infections *By K. Servick*

PODCAST

370 Psychedelics without hallucinations?

Chemical relatives of LSD appear to treat depression in mice *By R. F. Service*
RESEARCH ARTICLE p. 403

371 Why a high-profile China Initiative case collapsed

U.S. government drops all charges against MIT engineering professor Gang Chen *By J. Mervis*

FEATURES

372 Paranormal activity

Why is Harvard University astrophysicist Avi Loeb working with ardent UFO believers? *By K. Kloor*

INSIGHTS

PERSPECTIVES

376 Staying strong during hibernation

The microbiota of hibernating squirrels salvages urea to replenish amino acids *By F. Sommer and F. Bäckhed*
REPORT p. 460

377 Intensifying existing urban wastewater

Aerobic granular sludge offers improvements to treatment processes *By M.-K. H. Winkler and M. C. M. van Loosdrecht*

379 How pH affects electrochemical processes

Three mechanisms underlie the impact of pH on the activity of electrochemical reactions *By N. Govindarajan et al.*

380 The African trees that conquered Asia

Fossil pollen from dipterocarps show shared floristic heritage between Asia and Africa *By C. Hoorn and J. Ying Lim*
REPORT p. 455

382 Modeling tuberous sclerosis with organoids

Single-cell profiling reveals a different path for the development of brain lesions *By R.A. Ihrle and E. P. Henske*
RESEARCH ARTICLE p. 401

383 Human cortical interneuron development unraveled

New understanding of principles of neurogenesis widens the use of preclinical models *By N. Kessaris*
RESEARCH ARTICLE p. 402

385 Edward O. Wilson (1929–2021)

Pioneering naturalist with far-reaching insights *By S. Pimm*

EDITORIAL p. 361

POLICY FORUM

386 China's seafood imports— Not for domestic consumption?

An estimated 74.9% of China's seafood imports are reexported *By F. Asche et al.*

BOOKS ET AL.

389 The tech workforce you don't see

From fulfillment centers to social media sites, human labor is essential to digital success *By J. Berg*

390 Biology versus bias

A pair of scholars confront the pernicious role played by racism in shaping our understanding of human difference *By A. Fuentes*

LETTERS

391 Turkish postfire action overlooks biodiversity

By Ç. Tavsanoğlu and J. G. Pausas

391 A sea of possibilities for marine megafauna

By F. Alves et al.

392 Savannas are vital but overlooked carbon sinks

By A. Dobson et al.



RESEARCH

IN BRIEF

398 From *Science* and other journals

RESEARCH ARTICLES

401 Brain development

Amplification of human interneuron progenitors promotes brain tumors and neurological defects *O. L. Eichmüller et al.*

RESEARCH ARTICLE SUMMARY; FOR FULL TEXT: DOI.ORG/10.1126/SCIENCE.ABF5546
PERSPECTIVE p. 382

402 Neurodevelopment

Nests of dividing neuroblasts sustain interneuron production for the developing human brain *M. F. Paredes et al.*

RESEARCH ARTICLE SUMMARY; FOR FULL TEXT: DOI.ORG/10.1126/SCIENCE.ABK2346
PERSPECTIVE p. 383

403 Structural biology

Structure-based discovery of nonhallucinogenic psychedelic analogs *D. Cao et al.*

NEWS STORY p. 370

411 Proteomics

The Blood Proteoform Atlas: A reference map of proteoforms in human hematopoietic cells *R. D. Melani et al.*

418 Quantum criticality

Quantum critical points and the sign problem *R. Mondaini et al.*

424 Plant science

Gametophyte genome activation occurs at pollen mitosis I in maize *B. Nelms et al.*

REPORTS

430 2D materials

Out-of-equilibrium criticalities in graphene superlattices *A. I. Berdyugin et al.*

434 Solar cells

Constructing heterojunctions by surface sulfidation for efficient inverted perovskite solar cells *X. Li et al.*

437 2D materials

Spin-orbit–driven ferromagnetism at half moiré filling in magic-angle twisted bilayer graphene *J.-X. Lin et al.*

442 Molecular biology

Sequence specificity in DNA binding is mainly governed by association *E. Marklund et al.*

446 Animal migration

Magnetic stop signs signal a European songbird's arrival at the breeding site after migration *J. Wynn et al.*

449 Coronavirus

Antibody-mediated broad sarbecovirus neutralization through ACE2 molecular mimicry *Y.-J. Park et al.*

455 Paleobotany

Southeast Asian Dipterocarp origin and diversification driven by Africa-India floristic interchange *M. Bansal et al.*

PERSPECTIVE p. 380

460 Hibernation

Nitrogen recycling via gut symbionts increases in ground squirrels over the hibernation season *M. D. Regan et al.*

PERSPECTIVE p. 376; PODCAST

DEPARTMENTS

361 Editorial

Seeing the big picture *By H. Holden Thorp*

PERSPECTIVE p. 385

466 Working Life

Paying it forward *By Kathleen Hupfeld*

ON THE COVER

Fluorescence microscopy image of pollen (bright objects) on maize silks (long strands). Pollen is the haploid generation of higher plants that is sandwiched between diploid generations. Each pollen grain is a multicellular organism with



distinct cell types and active gene expression. New RNA sequencing results identify when this generation “comes of age” and begins its independent gene expression program. See page 424. Image: Brad Nelms/University of Georgia

AAAS News & Notes393
Science Careers 464

SCIENCE (ISSN 0036-8075) is published weekly on Friday, except last week in December, by the American Association for the Advancement of Science, 1200 New York Avenue, NW, Washington, DC 20005. Periodicals mail postage (publication No. 484460) paid at Washington, DC, and additional mailing offices. Copyright © 2022 by the American Association for the Advancement of Science. The title SCIENCE is a registered trademark of the AAAS. Domestic individual membership, including subscription (12 months): \$165 (\$74 allocated to subscription). Domestic institutional subscription (51 issues): \$2212; Foreign postage extra: Air assist delivery: \$98. First class, airmail, student, and emeritus rates on request. Canadian rates with GST available upon request. GST #125488122. Publications Mail Agreement Number 1069624. Printed in the U.S.A.

Change of address: Allow 4 weeks, giving old and new addresses and 8-digit account number. Postmaster: Send change of address to AAAS, P.O. Box 96178, Washington, DC 20090-6178. Single-copy sales: \$15 each plus shipping and handling available from backissues.science.org; bulk rate on request. Authorization to reproduce material for internal or personal use under circumstances not falling within the fair use provisions of the Copyright Act can be obtained through the Copyright Clearance Center (CCC), www.copyright.com. The identification code for Science is 0036-8075. Science is indexed in the Reader's Guide to Periodical Literature and in several specialized indexes.



**The 2022 (38th)
International Prize for
Biology**

Calling for Nominations

The 2022's research field:
Biology of Fishes

Please access to:
<http://www.jsps.go.jp/english/e-biol>

Deadline: April 8, 2022

- The International Prize for Biology was established in 1985 to commemorate the 60-year reign of Emperor Showa and his longtime devotion to biological research.
- The Prize is awarded each year to an individual who has made an outstanding contribution to the advancement of basic research in a field of biology.
- The Prize shall consist of a medal and a prize of 10 million yen.
- The award ceremony will be held in Tokyo in November or December in the presence of their Imperial Highnesses Crown Prince and Crown Princess Akishino.

Recent Years Prize Winners



2021
Dr. Timothy D. White
(Biology of Human Evolution)



2020
Dr. SHINOZAKI Kazuo
(Biology of Environmental Responses)



2019
Dr. Naomi E. Pierce
(Biology of Insects)



JAPAN SOCIETY FOR THE PROMOTION OF SCIENCE
日本学術振興会

Share Your Robotics Research with the World.

*Shaping the future of robotics with high
impact research!*

As a multidisciplinary online-only journal, *Science Robotics* publishes original, peer-reviewed, research articles that advance the field of robotics. The journal provides a central forum for communication of new ideas, general principles, and original developments in research and applications of robotics for all environments.

Submit your research today.

Learn more at: science.org/journal/scirobotics

Twitter: @SciRobotics

Facebook: @ScienceRobotics

Science Robotics
AAAS

Seeing the big picture

I had the good fortune of spending a lot of time with E. O. Wilson, who recently passed away at the age of 92. Wilson was a towering figure who proposed grand ideas about biology and conservation, not just in scientific papers but in numerous books, some winning Pulitzer Prizes, that stood out for their outstanding writing. I began interacting with Ed Wilson when I was running the Morehead Planetarium and Science Center at the University of North Carolina (UNC) at Chapel Hill, and we worked together on a number of education projects. I had the privilege when I was the UNC chancellor of awarding an honorary degree to Wilson when he spoke at a commencement. Wilson's life is worth examining not just for his extraordinary accomplishments, but also for how debates about his ideas drove science forward.

Wilson was an outstanding researcher, as described in this week's Retrospective by Stuart Pimm. His work on the role of pheromones in the social behavior of ants was published in *Science*, and in 1967 he was recognized with the Newcomb Cleveland Prize of the American Association for the Advancement of Science (AAAS, the publisher of *Science*). From there, he began assembling ideas from across science to make grand proposals that sought to bring biology together with human behavior and even the humanities. His sociobiology hypothesis was

criticized by a number of biologists who felt that he overemphasized the role of genetics in human behavior. He was famously doused with water at a meeting of the AAAS by a critic who felt that his deterministic ideas were discriminatory. Many others, however, believed that Wilson was simply acknowledging the fact that genetics was a contributor to social phenomena.

In understanding the thread of Wilson's career, it is important to recognize that—like any high-profile research—his work was debated and sometimes criticized by other scientists. It's an oversimplification to say that Wilson was suddenly attacked because of the political implications of sociobiology. The controversy was part of the larger scientific debate that extends to

behavioral genetics to this day. Biologist Anne Fausto-Sterling—who was often a critic of Wilson's—believed that even the legendary early work on ant pheromones relied too heavily on the role of genetics. “His ant research had alternate interpretations and there are legitimate criticisms of his methods and conclusions,” she told me, “and they were there all along.” I had many chances to ask Ed about the debates and the famous water throwing, and he was never reticent to discuss it. It was many years later, so maybe he had mellowed, but he seemed to see it all as a passionate argument about something very important, nature versus nurture, which of course it was.

Ed's discipline as a writer always amazed me. I once asked him how he got the determination to crank out so much fantastic prose. “I guess I've always been a writer,” he said. “Southerners are storytellers, and I've always looked on scientific discoveries as stories. I mean, they're factual, but what happens to lead up to them, what ideas are embodied when you make them, what the consequences are—those are stories, and I've always had a great pleasure in telling the stories of science.” I recently asked ecologist Jonathan Losos, who was Wilson's colleague at Harvard, what he made of this. “As for where this talent came from, I don't know,” he said. “I do think that part of it was an incredible knack to see the big picture, to

be able to gather great amounts of information from disparate fields and to put them together in novel and creative ways.” That ability may have led him at times into territory where he wasn't always an expert, but it sparked discussion and experimentation that brought our understanding to new and interesting places.

In the weeks following Wilson's death, many of these debates have been rekindled. That's what he would have wanted. He loved science and battling around big ideas—he lit up when he got to do so.

The human drama, positive and negative, of a life like Ed Wilson's is an asset to science and something to celebrate. Let's not lose our sense of wonder about that.

—H. Holden Thorp



H. Holden Thorp
Editor-in-Chief,
Science journals.
hthorp@aaas.org;
@hholdenthorp

“The human drama, positive and negative, of a life like Ed Wilson's is an asset to science and something to celebrate.”

NEWS

IN BRIEF

Edited by Jeffrey Brainard

GEOSCIENCE

Orbiting radar mapper goes dark

Sentinel sensors recorded ice and snow loss (red and yellow, in false color) from Kangerlussuaq Glacier in Greenland during passes in June 2021.

The head of the European Space Agency said last week the agency may accelerate the launch of its next Earth-observing radar satellite, after a power supply anomaly caused one of its two orbiting radar satellites, Sentinel-1B, to go dark for more than 1 month. Since its launch in 2016, Sentinel-1B—along with its twin, Sentinel-1A—has peered through clouds and mapped displacements of

the planet's surface caused by earthquakes, volcanoes, and melting ice. The duo surveys much of the globe every 6 days and can detect ground motions as small as a few millimeters. Sentinel-1A, which launched in 2014, continues to operate normally, although it has exceeded its design life. If Sentinel-1B cannot be revived, the agency is likely to speed up work to launch Sentinel-1C by the end of this year, instead of in mid-2023.

U.S. beckons STEM students

IMMIGRATION | President Joe Biden's administration has announced new rules designed to make the United States more attractive to international students seeking science, technology, engineering, and math (STEM) degrees. Higher education lobbyists say the changes, unveiled last week, send an encouraging message to foreign students and mark a 180° turn from former President Donald Trump's administration's efforts to restrict visas for students from certain countries. One major change expands by 22 the number of STEM fields

whose foreign students can remain in the United States for up to 3 years of additional training after graduation. Another allows those with "exceptional ability" to seek an employment-based visa even without a job offer. A significant fraction of U.S. technical workers in several areas was born abroad.

Brazil's science budget rebounds

FUNDING | Brazil's federal research budget will rise this year, a turnaround after several years of steep cuts—unless the increase is derailed by a political dispute. The Ministry of Science, Technology, and

Innovations will have \$1.3 billion for discretionary spending this year, a 135% hike from 2021, according to an analysis by the Brazilian Society for the Progress of Science. The final budget, sanctioned by President Jair Bolsonaro on 21 January, will support construction of Brazil's first biosafety level four laboratory—for research on deadly pathogens—and the expansion of Sirius, a synchrotron light source. But scientists say it's too early to celebrate. Most of the new money is allocated to a fund that several ministries control and that can be used for purposes other than basic research. And last year,

PHOTO: CONTAINS MODIFIED COPERNICUS SENTINEL DATA (2021) / PROCESSED BY ESA/CC BY-SA 3.0 IGO

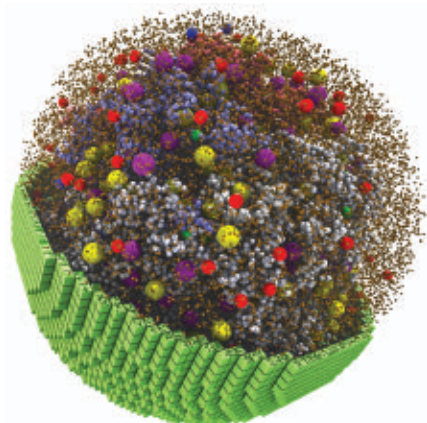
Bolsonaro's administration withheld these funds despite a new law designed to block him from doing so. Meanwhile, this year's budget gives much less research money, only about \$6.5 million, to the National Council for Scientific and Technological Development, a leading grantmaker.

Mexico's COVID-19 chief probed

COVID-19 | A federal judge has ordered Mexico's attorney general to open a homicide investigation of the leader of the country's pandemic response for allegedly failing to avert preventable deaths from COVID-19. In November 2020, relatives of two people who died from the disease filed a complaint accusing health undersecretary Hugo López-Gatell Ramírez of criminally negligent homicide. They blamed the deaths on his controversial advice against closing borders, wearing masks, and conducting widespread testing for the coronavirus. The attorney general's office had declined to investigate, citing lack of evidence. But after appeals from the plaintiffs, a federal judge on 19 January ordered the office to examine possible omissions by López-Gatell Ramírez and any other officials that resulted in pandemic deaths. More than 300,000 deaths in Mexico have been reported from COVID-19, the world's fifth highest total.

Computer mimics 'minimal' cell

MICROBIOLOGY | For years, researchers have pared down the genes in microbes to create "minimal" cells, with the minimum number of components needed to survive and thrive. Now, researchers have created the most complex computer simulation of such a streamlined cell. The model, reported last week in *Cell*, maps out the precise location and chemical characteristics of thousands of cellular components in



Membrane proteins and protein complexes are shown in a computer simulation of a stripped-down cell.

3D space at an atomic scale. It tracks these molecules as they diffuse through the simple cell, their chemical reactions, and how much energy is required for each step. Among the findings: The cell, engineered from a mycoplasma bacterium, uses most of its energy to import essential ions and molecules across its cell membrane. The researchers hope this and future simulations will help them predict how changing a cell's genome will alter its metabolism, an advance that could help optimize the design of cells to make chemicals including medicines and fuels.

China sets rules for edited crops

BIOTECHNOLOGY | China's agriculture ministry this week unveiled safety evaluation guidelines for gene-edited crops as the country moves toward approving their sale. The guidelines, being implemented on a trial basis, are simpler and call for less field testing than is required for genetically modified (GM) crops, in which genes from other species are inserted. Consumer resistance and bureaucratic caution have left China far behind other countries in adopting GM crops, with only a single variety of GM papaya in domestic production. Now, Chinese researchers are well along in developing gene-edited varieties of corn, rice, soybeans, wheat, and other crops, which they hope will be more acceptable to the public and reduce dependence on food imports. China is also revising its regulations for GM crops, and transgenic corn and soybeans might be commercialized this year. Both kinds of genetic engineering give crops useful traits, such as resistance to herbicides sprayed in fields.

Epidemic prevention gets big gifts

PHILANTHROPY | Two of the world's largest foundations last week pledged \$150 million each to the nonprofit Coalition for Epidemic Preparedness Innovations (CEPI), a global partnership working to prevent, prepare for, and equitably respond to future epidemics and pandemics. Leaders of the Bill & Melinda Gates Foundation and the Wellcome Trust called on nations to pony up at a CEPI "replenishment" conference scheduled for March to help it raise \$3.5 billion for the next 5 years. CEPI has financed development of the University of Oxford–AstraZeneca and Novavax vaccines. Its 5-year plan starting this year aims to shorten vaccine development time to less than 100 days after a new pathogen is sequenced, far shorter than the 11 months it took for the first COVID-19 vaccine.

STAR-STUDDED STARTUP A Silicon Valley firm that aims to combat the effects of aging by reprogramming human cells formally announced its start last week with a whopping \$3 billion in private funding. In addition to former U.S. National Cancer Institute head Richard Klausner as chief scientist, Altos Labs boasts several Nobel laureates as board members or advisers—enzyme specialist Frances Arnold, virus expert David Baltimore, gene editing pioneer Jennifer Doudna, and stem cell investigator Shinya Yamanaka.

AI DREAM FAILS IBM has inked a deal to sell off key data sets and software from its Watson Health subsidiary, a much-touted effort to use artificial intelligence (AI) to transform medical research and care. Started in 2015, the unit hadn't earned a profit, *STAT* reported. Critics said its supercomputer-aided analysis of health data merely compiled existing knowledge without producing new insights. IBM said on 21 January that the sale to private equity firm Francisco Partners would help the parent company focus on cloud computing and AI services in other types of industries.

NEW U.K. MEGATRIALS A nonprofit modeled on the United Kingdom's Recovery clinical trial, a leader in the global effort to test treatments for COVID-19, aims to conduct low-cost studies of better treatments for other common, life-threatening diseases such as heart disease and cancer. Like Recovery, Protas plans to cooperate with the U.K. National Health Service to streamline the recruitment of large, inclusive populations.

ANTIBIOTIC RESISTANCE Nearly 1.3 million people died in 2019 from antimicrobial-resistant infections, according to a comprehensive global estimate. Such infections are a leading killer, causing more deaths than AIDS and malaria, according to the study, published on 19 January in *The Lancet*.

GALÁPAGOS RESERVE Ecuador has approved a new marine reserve near the Galápagos Islands that increases an existing protected ocean area by 43%, a boon for the region's endangered marine species. Scientists with the MigraMar marine research network had collected data to justify creating the 60,000-square-kilometer Hermandad Marine Reserve.



A Long Covid patient at a hospital in Poland plays a virtual reality game to test reaction skills.

work continues behind the scenes. Now, some other researchers worldwide are beginning to study whether the biology of Long Covid, still poorly understood, overlaps with the mysterious mechanisms that may drive certain postvaccine side effects.

Other, better defined complications connected to the vaccines have been recognized, including a rare but severe clotting disorder that occurs after the AstraZeneca and Johnson & Johnson vaccines, and heart inflammation documented after the messenger RNA (mRNA) vaccines manufactured by Pfizer and Moderna. Probing possible side effects presents a dilemma to researchers: They risk fomenting rejection of vaccines that are generally safe, effective, and crucial to saving lives. “You have to be very careful” before tying COVID-19 vaccines to complications, Nath cautions. “You can make the wrong conclusion. ... The implications are huge.” Complex and lingering symptoms such as Dressen’s are even more difficult to study because patients can lack a clear diagnosis.

At the same time, understanding these problems could help those currently suffering and, if a link is nailed down, help guide the design of the next generation of vaccines and perhaps identify those at high risk for serious side effects. “We shouldn’t be averse to adverse events,” says William Murphy, an immunologist at the University of California, Davis, who has proposed that an autoimmune mechanism triggered by the SARS-CoV-2 spike protein might explain both Long Covid symptoms and some rare vaccine side effects. “Reassuring the public that everything is being done, researchwise, to understand the vaccines is more important than just saying everything is safe,” he says. Like others, he continues to urge vaccination.

HOW FREQUENTLY side effects like Dressen’s occur is unclear. Some online communities include many thousands of participants, but no one is publicly tracking these cases, which are variable and difficult to diagnose or even categorize. The symptoms also include fatigue, severe headaches, nerve pain, blood pressure swings, and short-term memory problems. Nath is convinced they are “extremely rare.”

Long Covid, in contrast, affects anywhere from about 5% to more than 30% of those infected by SARS-CoV-2. Researchers are making tentative progress in untangling the underlying biology. Some studies suggest the virus may linger in tissues and cause ongoing problems. Other evidence indicates after-

COVID-19

Vaccines may cause rare, Long Covid-like symptoms

Researchers probe reports of brain fog, headaches, and blood pressure swings

By **Jennifer Couzin-Frankel** and **Gretchen Vogel**

In late 2020, Brianne Dressen began to spend hours in online communities for people with Long Covid, a chronic, disabling syndrome that can follow a bout with the virus. “For months, I just lurked there,” says Dressen, a former preschool teacher in Saratoga Springs, Utah, “reviewing post after post of symptoms that were just like my own.”

Dressen had never had COVID-19. But that November, she’d received a dose of AstraZeneca’s vaccine as a volunteer in a clinical trial. By that evening, her vision blurred and sound became distorted—“I felt like I had two seashells on my ears,” she says. Her symptoms rapidly worsened and multiplied, ultimately including heart rate fluctuations, severe muscle weakness, and what she describes as debilitating internal electric shocks.

A doctor diagnosed her with anxiety. Her husband began to comb the scientific literature, desperate to help his wife, a former rock climber who now spent most of her time in

a darkened room, unable to brush her teeth or tolerate her young children’s touch. As time passed, the Dressens found other people who had experienced serious, long-lasting health problems after a COVID-19 vaccine, regardless of the manufacturer. By January 2021, researchers at the National Institutes of Health (NIH) began to hear about such reports and sought to learn more, bringing Dressen and other affected people to the agency’s headquarters for testing and sometimes treatment.

The research drew no conclusions about whether or how vaccines may have caused rare, lasting health problems. The patients had “temporal associations” between vaccination and their faltering health, says Avindra Nath, clinical director at the National Institute of Neurological Disorders and Stroke (NINDS), who has been leading the NIH efforts. But “an etiological association? I don’t know.” In other words, he can’t say whether vaccination directly caused the subsequent health problems.

NIH’s communications with patients faded by late 2021, though Nath says the

effects of the initial infection might play a role.

For example, evidence from animal studies supports the idea that antibodies targeting the SARS-CoV-2 spike protein—the same protein that many vaccines use to trigger a protective immune response—might cause collateral damage, notes Harald Prüss, a neurologist at the German Center for Neurodegenerative Diseases (DZNE) and the Charité University Hospital in Berlin.

Early clinical data point in a similar direction. Research groups have detected unusually high levels of autoantibodies, which can attack the body's own cells and tissues, in people during and after a SARS-CoV-2 infection. In part to understand whether these autoantibodies harm people, DZNE is checking the cerebrospinal fluid of Long Covid patients for antibodies that react to mouse brain tissue—if they do react, they might attack human neural tissues as well. In a paper Prüss and his colleagues are about to submit, they describe finding autoantibodies that attack mouse neurons and other brain cells in at least one-third of those patients.

Some researchers are looking at another possible culprit for Long Covid: tiny clots in the blood. Resia Pretorius, a physiologist at Stellenbosch University in South Africa, and her colleagues published preliminary evidence in August that microscopic clots can linger after a SARS-CoV-2 infection clears. They might interfere with oxygen delivery, which could explain some Long Covid symptoms such as brain fog.

Pretorius suspects COVID-19 vaccines might also sometimes trigger subtle clotting issues. She says she has preliminary evidence that vaccination can lead to microclots, although in most cases they go unnoticed and quickly disappear—an effect she and a colleague saw in their own blood, which they sampled as part of a larger study.

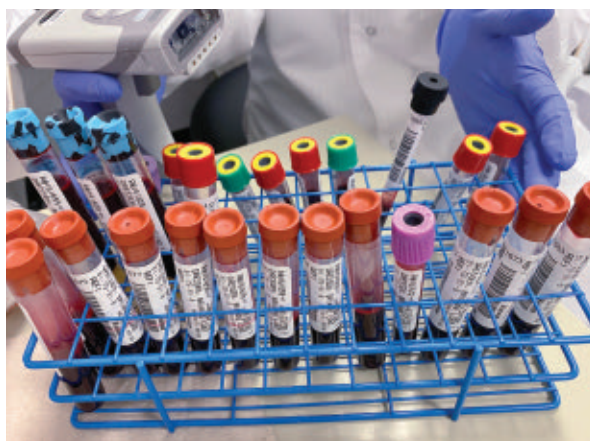
IN JANUARY 2021, the Dressens sought out Nath, who had been studying Long Covid. Nath responded quickly and asked Brianne Dressen to join an ongoing study he leads on the natural history of inflammatory diseases of the nervous system.

Dozens more patients describing post-vaccine complications found their way to Nath and Farinaz Safavi, an NINDS neurologist. “I promise you we will report your issue and other cases we are reviewing now,” Safavi wrote to Danice Hertz in March 2021. Hertz, a retired gastroenterologist who lives in Southern California, had developed debili-

tating symptoms after one dose of the Pfizer vaccine. Senior officials at the U.S. Food and Drug Administration (FDA), the Centers for Disease Control and Prevention, and Pfizer, among others, were copied on the email, which Hertz shared with *Science*.

Over the first half of 2021, Nath and Safavi invited Dressen and others to NIH for testing and, in some cases, short-term treatment, for example with high-dose steroids or intravenous immunoglobulin, which can quell or modulate immune responses. The patients underwent neurological, cardiac, and other tests, including lumbar punctures and skin biopsies.

The NIH researchers were “trying to help people,” says a health care worker whose symptoms began after the Pfizer vaccine, one of four people in the study who spoke to *Science*. Nath says 34 people were enrolled in the protocol, 14 of whom spent time at NIH; the other 20 shipped their blood samples and in some cases cerebrospinal fluid.



Blood drawn from Brianne Dressen, who suffered complications after a coronavirus vaccine, is part of a National Institutes of Health study.

As time passed, however, the patients say the NIH scientists pulled back. A September visit Dressen had scheduled for neurologic testing was converted to a telemedicine appointment. In December, Nath asked her to stop sending other patients his way. “It is best for such patients to receive care from their local physicians,” he wrote to her.

For patients, the silence from NIH was distressing, especially as they struggled to find support and care elsewhere. The scientists “took the data and left us hanging,” says a person who traveled to NIH in the spring of 2021. “I have no treatment, I have no idea what’s happening to my body.”

Nath told *Science* that NIH facilities are not equipped to treat large numbers of patients long-term. Says the health care worker of the effort: “It’s too much for two people at the NIH to do.”

Two top medical journals declined to pub-

lish an NIH case series of about 30 people, which Nath says he first submitted in March 2021. He understands the rejections. The data weren’t “cut and dried; it was observational studies.” This month, the scientists submitted a case series of 23 people to a third publication, and Nath says his group has proposed expanding a Long Covid study to include patients with postvaccine side effects.

Regarding persistent effects after vaccination, a Pfizer spokesperson wrote to *Science*: “We can confirm that it’s something we’re monitoring.” Other vaccinemakers said they take side effects seriously and report them to regulators. FDA and the European Medicines Agency told *Science* they continue to monitor the vaccines’ safety.

Researchers note that the scientific community is uneasy about studying such effects. “Everyone is tiptoeing around it,” Pretorius says. “I’ve talked to a lot of clinicians and researchers at various universities, and they don’t want to touch it.”

Still, her group and others are pushing ahead. Prüss has detected autoantibodies in some patients with postvaccine symptoms, although not in others. Susan Cheng, a cardiologist at Cedars-Sinai Medical Center, and her colleagues are planning to use sophisticated imaging and diagnostic tests to study both Long Covid patients and those with postvaccine symptoms. And Pretorius and her colleagues are hoping to recruit at least 50 people to study clotting patterns before and after vaccination.

At Yale University, immunologist Akiko Iwasaki, who has been studying Long Covid, is planning to collaborate with Nath and look at any potential link between Long Covid and postvaccine effects, she says. She has spoken with affected patients, and her lab intends to collect samples from them, potentially of blood or saliva. Murphy says more work is needed in animal models to trace the body’s response to vaccination. “We need to look at this in controlled situations,” he says.

Prüss is hunting for autoantibodies following COVID-19 vaccination in mice. And he continues to care for patients, both post-vaccine and postinfection. His clinic hopes to soon start a clinical trial of a treatment that removes most antibodies from a patient’s blood. However, even if it works well, the procedure is expensive and might not be widely available.

PEOPLE WITH LASTING health problems after vaccination welcome any attention to their plight. “You have this ugly stain on you, and you’re marginalized and abandoned,” Dressen says. At first, “I was really afraid of

causing vaccine hesitancy,” she says. However, when it appeared that regulators were not promptly investigating the apparent side effects, her frustration outweighed her reluctance. She took part in a June 2021 press conference about vaccine side effects held by Senator Ron Johnson (R-WI), who has been outspoken against COVID-19 vaccinations. “Talking to politicians was not our plan A ... not even close,” Dressen says. “It was more like plan J.”

Jana Rührländer, too, feels caught. After a single dose of the Moderna vaccine, the microbiology graduate student in Kassel, Germany, developed the sensation of internal electric shocks Dressen experienced, muscle weakness, intense thirst, and wild swings in her heart rate and blood pressure. Doctors dismissed her, saying their tests found nothing wrong. She played detective, realizing her symptoms overlapped with those controlled by a hormonal system called the renin-angiotensin-aldosterone system that regulates blood pressure and fluid balance. She has connected with doctors trying to learn whether auto antibodies targeting that system might be causing her symptoms.

Despite her experience, “I still think the vaccines are great,” Rührländer says. And the mRNA technology “has so much potential.” But these side effects, which for her have improved somewhat but haven’t disappeared, should be acknowledged and understood, she says. “We have to speak openly about it.”

Some patients who spoke with *Science* say medications that tamp down the immune system have offered a measure of relief. Nath hopes results from an NIH clinical trial testing immunoglobulin and steroids in Long Covid patients “will be applicable to the vaccine-related complications.” None of the seven patients with whom *Science* spoke has fully recovered.

Researchers exploring postvaccine effects emphasize that the risk of complications from SARS-CoV-2 infection far outweighs that of any vaccine side effect. “You see 10, 100, 1000 times less risk from the vaccine,” Prüss says. But understanding the cause of postvaccine symptoms—and whether early treatment can help prevent long-term problems—could be crucial for designing even safer and more effective vaccines, Murphy says, as well as potentially providing clues to the biology of Long Covid.

Cheng has heard from dozens of people who describe chronic postvaccine problems, and she finds the overlap between their symptoms and those of Long Covid compelling. Now, she wants to move deliberately and scientifically in a search for answers. “We’ve got to retain rigor,” she says. “There’s just this complete dearth of data.” ■



Hong Kong culled more than 2000 hamsters this month after linking a COVID-19 outbreak to a pet store. Scientists say new variants could enter the human population after evolving in animals.

COVID-19

After Omicron, some scientists foresee ‘a period of quiet’

The variant’s modest toll in many countries has led to a sense of optimism. But new surprises are likely

By Kai Kupferschmidt

Barely 2 months after it began, the Omicron wave is already ebbing in some countries. And although it has sickened huge numbers of people, caused massive disruption, and left many health care workers exhausted, it is also leaving something unusual in its wake: a sense of optimism about the pandemic’s trajectory. In countries where many people have been vaccinated or were infected, scientists say, the worst may finally be over.

“We anticipate that there will be a period of quiet before COVID-19 may come back towards the end of the year, but not necessarily the pandemic coming back,” Hans Kluge, director of the European Region of the World Health Organization (WHO), recently said in an interview. In the United Kingdom, where the Omicron wave crested early, many restrictions were scheduled to be dropped this week, including mandatory masks in public indoor spaces and COVID-19 vaccination passes.

The optimism is shared—although couched in caveats—even by some scientists

and public health experts who have stressed the risks of the pandemic from the start and implored politicians to take stricter action. “We have reached a bit of a turning point,” says Devi Sridhar, a global health expert at the University of Edinburgh and an outspoken critic of the U.K. government’s past COVID-19 policies. Not only has the Omicron wave crested in several countries, but its toll has been smaller than feared. And the wave of infections has likely boosted immunity at the population level, which means future waves may wreak even less havoc.

Still, researchers urge caution. Omicron has shown that even a relatively mild wave can put a tremendous burden on health systems and societies as a whole, and it’s unclear how long Omicron immunity will last, how the virus will evolve from here on, and how often breakthrough infections will lead to long-term health problems. “I remain firmly in the camp of: We’ve made great progress but we still have a ways to go before this is truly over,” says Boghuma Titanji, a virologist at Emory University School of Medicine. Besides, “Wealthy countries moving on I fear will push the issues of

access to vaccines and therapeutics access down the global priority list,” she says.

For now, Omicron is still spreading worldwide, its impact very different from country to country. Early hopes of a much milder wave were dashed in the United States, in part because its vaccination rate is relatively low. It is seeing more than 2000 deaths daily, as many as during the peak of the Delta wave. Although cases are now declining in New York, Florida, and California, the wave is still building elsewhere.

Countries with high vaccination coverage, such as Denmark, have had staggering numbers of infections as well but with far less severe disease and death. “Overall, the health pressure that we have felt until now has been less than what we feared,” says Henrik Ullum, head of the Statens Serum Institute. In fact, Denmark may lift all pandemic restrictions soon in spite of record-high case numbers. Health systems in many other European countries have been spared, as well.

South Africa, where Omicron was first sequenced, saw cases peak in mid-December. Although deaths are still on the rise, the overall impact has been relatively light as well. Omicron is unlikely to account for more than 5% of COVID-19 deaths in the country, says Shabir Madhi, a vaccinologist at the University of the Witwatersrand, Johannesburg, compared with roughly 50% for Delta. Omicron’s impact is difficult to gauge in other parts of the world, where data are often sketchier.

Omicron’s massive spread leaves Madhi optimistic about the future. A serosurvey he led in Gauteng province, home to one-quarter of South Africa’s population, showed close to 70% of unvaccinated people carried SARS-CoV-2 antibodies at the start of the Omicron wave. In the next survey, he expects that number to have gone up to at least 85%, a level that should prepare South Africa for a post-Omicron future. “There will probably be another wave, but it is extremely unlikely to result in a higher death rate or hospitalization rate than what transpired during the course of the Omicron wave,” Madhi says.

Indeed, data so far suggest the human immune response becomes better and broader with every exposure to SARS-CoV-2’s spike protein. But Omicron’s spike is so different from previous variants’ that it’s not yet clear just how much immunity the Omicron wave will add, or how long it will last, says Leif Erik Sander, an immunologist at the Charité University Hospital in Berlin. And immunity could wane, leading to a new rise in the number of people susceptible to infection.

What the virus will do next is another wild card. What WHO has termed “Omicron”

actually comprises several slightly different viruses. BA.1, the lineage that dominated early on, appears to be giving way to a sister lineage named BA.2 in Denmark and some other countries. That suggests BA.2 is a bit more transmissible, says virologist Tom Peacock of Imperial College London. Even if it is, “BA.2 is unlikely to cause a separate wave,” Peacock says, “but it may cause a ripple in the Omicron wave or slow down the decline in countries where the peak has passed.”

Delta might also make a comeback. That depends in part on how much more transmissible Omicron really is than Delta. It’s spreading so fast now because it can evade people’s existing immunity. But as immunity to Omicron builds up, that advantage will fade and the variants may compete on a more equal footing—if Omicron does not wipe out Delta before then. “If there is still some Delta circulating in September, then I think you can have coexistence,” says Trevor Bedford of the Fred Hutchinson Cancer Research Center. “And that would add to your burden of disease and add to complications in vaccination.”

The two variants might also recombine to produce a virus that incorporates both Omicron’s immune evasion tricks and Delta’s severity, says virologist Christian Drosten, also at Charité. “That would be worrying because it could lead to a difficult next winter.” Entirely new variants of concern are likely to appear as well, including ones that hit on new combinations of mutations that elude human immunity. “I think the virus still has a lot of tricks up its proverbial sleeve and we need to approach the future of the pandemic with more humility,” Titanji says.

The proliferation of animal reservoirs is also worrying, scientists say. One theory for the origin of Omicron is that SARS-CoV-2 infected some animal species, racked up a series of mutations, then popped back into the human population as a very different virus. Ferrets, lions, deer, and many other species have been infected with the coronavirus, and could provide such a springboard. Hong Kong culled more than 2000 hamsters earlier this month after 11 hamsters in a pet shop tested positive for SARS-CoV-2. (The animals fell under suspicion after a cluster of human cases was traced to a pet shop worker.)

One scenario in particular could put an end to the newfound optimism: the emergence of a variant able to evade not just human antibodies, but also the T cell response, which protects from severe disease and death. No variant so far has done that. “The likelihood of that happening, I believe, is quite slim,” Madhi says. But if it does happen, he says, “then we are really dealing with another pandemic.” ■

ASTRONOMY

NASA’s Webb telescope reaches deep space home

Operators begin to fine-tune mirror segments after parking scope in L2 orbit

By **Daniel Clery**

NASA’s flagship James Webb Space Telescope arrived at its destination this week. After unfolding the carefully packed observatory during its month-long journey, controllers fired Webb’s thrusters for 5 minutes to put it into a “halo orbit” around L2, a gravitational balance point 1.5 million kilometers from Earth. Far from the heat and hubbub of low-Earth orbit, L2 will be Webb’s home for at least the next decade.

But another 5 months of work remain before Webb is ready to beam down images of its targets in the infrared universe, from the first galaxies that formed after the big bang to the atmospheres of exoplanets, which could hold clues to how friendly they are to life. This week, Webb will continue to cool behind its protective sunshield until its sensors are below -173°C . Then operators will begin the long and intricate process of aligning the 18 hexagonal segments of Webb’s 6.5-meter main mirror so they form a single reflector.

“Everything we’re doing is about getting [Webb] ready to do transformative science,” says Jane Rigby, operations project scientist at NASA’s Goddard Space Flight Center.

For the journey to the launch site in French Guiana and into orbit on an Ariane 5 rocket, the mirror segments were locked in place for safety. Operators have just finished releasing them and easing them forward, says Matt Greenhouse, a Webb project scientist at Goddard. Behind each 1.3-meter mirror segment are seven actuators, tiny motors that can adjust the segments’ position, tilt, and even curvature.

First, operators will point Webb at HD 84406, a bright, isolated star in the constellation Ursa Major, chosen for its stability and the lack of other bright stars nearby. When viewed with one of Webb’s detectors, the Near Infrared Camera (NIRCam), operators are

expecting to see 18 separate dots, one from each segment. “It will be very misaligned,” says Lee Feinberg, Webb telescope manager at Goddard.

Each segment will be wiggled to see which dot it is producing. Then begins the process of adjusting the tilt of each segment until the dots are all stacked on top of each other in the sensor’s view. At the same time, operators will adjust the curvature of the segments to make each spot as small and sharp as possible. “It’s a painstakingly detailed sequence of steps,” Feinberg says.

The last step is “phasing,” ensuring that the light is not only focused, but also in tune, with the peaks and troughs of the waves from all 18 segments coinciding. To ensure the light paths are all the same length, operators will adjust the segments’ distance from the secondary mirror by fractions of a wavelength of light—ten-thousandths of the width of a human hair. Only then will the

ant through to MIRI—one of Webb’s most challenging systems to build. Once MIRI is fully cooled in early April, it, too, will be optically aligned.

By early May, operators expect to be testing all 17 observing modes of the instruments. Commissioning involves viewing a range of reference objects, such as stars with precisely known brightness or star fields with exactly measured positions. Researchers want to understand how a sensor’s output relates to the influx of light and whether the telescope’s internal optics distort the positions of stars. Operators will also point the telescope at starless areas of sky to understand the “dark current” created by thermal noise in the instrument itself. “We don’t want the fingerprints of the instrument on the science,” says Scott Friedman, Webb commissioning scientist at the Space Telescope Science Institute.

He and his colleagues want to be sure the telescope can stay on target, too. “Posi-

BIOMEDICINE

Alternatives to fecal transplants near approval

Trial shows spore-filled pill derived from human stool treats tough gut infections

By Kelly Servick

For tens of thousands of people fighting repeat infections of the diarrhea-causing bacterium *Clostridium difficile* each year, there’s a proven, if unappetizing treatment option: a transplant into their intestines of stool from a healthy donor. The transplant, often delivered via colonoscopy, can restore a balanced community of gut microbes and clear the potentially deadly infection.

But several companies are eager to achieve the same effect with more defined collections of microbes that can be protected with patents and marketed as a drug in the United States. One option, a pill containing bacterial spores isolated from human feces, has now passed the critical test of a phase 3 clinical trial, paving the way for its approval in the United States and elsewhere.

“It’s a step forward for the field, for sure,” says Colleen Kelly, a gastroenterologist at Brown University who was an investigator on an earlier trial of the pill, called SER-109. She and others note that reliable sources of acceptable stool for transplants are dwindling in the United States, increasing the need for alternatives like SER-109. “[For] the majority of patients that we see for recurrent *C. diff* ... it might be able to solve the problem,” she says.

C. difficile is most common in elderly patients with other health problems, and often starts when antibiotics deplete the normal gut microbiome. A fecal microbiota transplant (FMT) can break the cycle of recurrent infections. But the contents of the fecal material for these procedures vary—as do safety screening processes, says Sahil Khanna, a gastroenterologist at the Mayo Clinic who was also involved

The James Webb Space Telescope’s 18 mirror segments must be focused and tuned to work in concert as a single, 6.5-meter-wide mirror.



18 separate segments have the resolution of “a beautiful monolithic primary mirror,” Feinberg says, and “a star will look like a star.” It will be the start of a lifelong process: Operators will continue to check Webb’s optics every 2 days and will tweak the segment positions, as required, every 2 weeks. “If they drift by one-twentieth of a wavelength, we care about it,” Feinberg says.

After tuning the mirror with the help of NIRCam, operators will check that light passes cleanly into two other detectors, the Near Infrared Spectrograph and the Near Infrared Slitless Spectrograph. A fourth sensor, the Mid-Infrared Instrument (MIRI), operates at much lower temperatures than the other three, just 6.4° above absolute zero. It requires a mechanical cryocooler which, because it emits waste heat, must sit on the warm side of the sunshield and pipe its cool-

tioning has to be exquisite,” Friedman says. They will test Webb’s Fine Guidance Sensor, which enables a laserlike lock on moving targets such as the moons of Jupiter, or anything that requires long exposures, such as dim exoplanets or distant galaxies. In the final weeks, operators will test the observatory’s thermal stability when pointed in different directions. Although the sunshield keeps the mirror and instruments in permanent shadow, sunlight heats the spacecraft differently at its pointing extremes, and one-tenth of 1°C can have an effect. “Those sort of temperature changes matter,” Feinberg says.

At the end of all that, 6 months after its Christmas Day launch, science observations can begin, and astronomers will see what Webb is capable of. Friedman says: “This is what we’ve worked for, for years and years.” ■

in previous trials of SER-109. In a few recent cases, inadequately screened donor stool has transmitted other potentially deadly pathogens to *C. difficile* patients. COVID-19 has heightened safety concerns: The possibility that introducing fecal matter might transmit SARS-CoV-2 prompted new donor screening requirements from the U.S. Food and Drug Administration (FDA) in 2020. (The agency classifies the fecal microbiota used in transplants as an investigational drug, but doesn't require that it go through the formal approval process for clinical use.)

"I think we've made it as safe as it can possibly be," Kelly says of traditional FMT. She leads a registry tracking hundreds of people who have received the procedure. "Transmission of infection just doesn't seem to be a very common problem, even in highly immunocompromised patients," she notes.

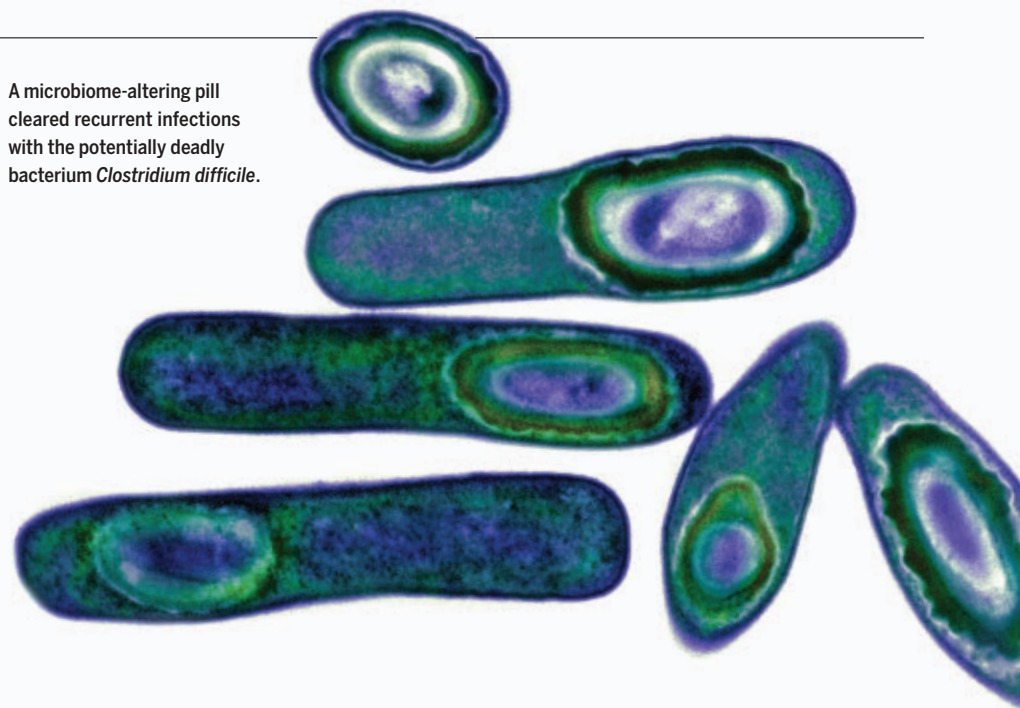
Yet stricter FDA guidelines have made donor screening harder for some medical centers, Kelly says. And the largest U.S. provider of feces for transplant, the nonprofit stool bank OpenBiome, announced in February 2021 it was winding down production, citing financial struggles and the coming approval of FMT alternatives.

Seres Therapeutics hopes its product, SER-109, will be one of those. The pill is made by treating stool from prescreened donors with ethanol, which kills many viruses, fungi, and "vegetative" bacteria—those in a state of growth and reproduction. Left behind are bacteria that can form hearty, thick-walled spores, many of them from the common phylum Firmicutes. Bacteria in this group are valuable because they can compete with *C. difficile* in the gut and discourage its growth by changing the composition of bile acids, says Seres Chief Medical Officer Lisa von Moltke.

Seres's purification process should get rid of most pathogens known to pose safety risks to recipients, says Vincent Young, a microbiologist and infectious disease physician at the University of Michigan, Ann Arbor, who has no connection to the company or the new trial. Although it hasn't been proved yet, he says, "there are reasons to think that [SER-109] is safer than feces."

Seres's phase 3 trial included 182 participants with recurrent *C. difficile* who were randomized to get either SER-109 or a placebo, following a standard course of antibiotics. Of those, 149 completed the study's 8-week follow-up. The infection returned in 40% of the placebo group, but in just 12% of the treatment group, researchers reported last week in *The New Eng-*

A microbiome-altering pill cleared recurrent infections with the potentially deadly bacterium *Clostridium difficile*.



land Journal of Medicine. Those results are comparable to results seen with FMT, Kelly says.

Seres has competitors. The microbiome company Rebiotix Inc. last year announced positive results from a phase 3 trial of its recurrent *C. difficile* treatment, a filtered stool product delivered as an enema, and has filed for FDA approval. Finch Therapeutics, a spinoff of OpenBiome, declared success last year in a phase 2 trial of its product, a pill that contains freeze-dried stool. And Vedanta Biosciences has completed a phase 2 trial of an oral *C. difficile* therapy consisting of eight individually selected bacteria strains grown in cell banks rather than isolated from stool.

Many patients want to avoid the discomfort of colonoscopies, and will opt for a pill if it's available, Kelly says. (Although "full-spectrum" fecal microbiota can also be delivered orally, there are few providers of such pills in the United States, she notes.) How the European Commission will regulate newly developed pills or other fecal microbiota products remains uncertain, says Josbert Keller, a gastroenterologist at Leiden University Medical Center and founder of the Netherlands Donor Feces Bank. But he expects more standardized products are likely to replace whole feces-based products that banks like his currently supply—"and I think that should be the aim," he says.

Other researchers are skeptical that new

microbiome therapies like SER-109 can match the potency of the complete fecal microbiota. "It's a really high standard that nature has established," says Alexander Khoruts, a gastroenterologist at the University of Minnesota, Twin Cities, who developed some of the technology behind Finch's pill.

He notes that components of feces removed during Seres's purification process, including bacteria-killing viruses called phages,

might be important to the success of FMT. "I'm gratified that Firmicutes alone ... is better than placebo," he says, "but I'm not necessarily convinced that the other components are dismissible."

Young, who has consulted for Vedanta, sees SER-109 as "a good bridge" from FMT to more tailored therapies, which he hopes will emerge as researchers get better at determining which microbial species each patient needs.

Kelly stresses that stool banks remain important sources of whole feces for research, as other conditions such as inflammatory bowel disease may require different collections of microbes than those provided by *C. difficile* treatments on the horizon. "I would hate to see the stool bank model disappear completely," she says.

Still, she's eager to see SER-109 rolled out to *C. difficile* patients. "I think everybody is very happy to have something that's safe and readily available," she says. "Let's hope it's not too expensive." ■

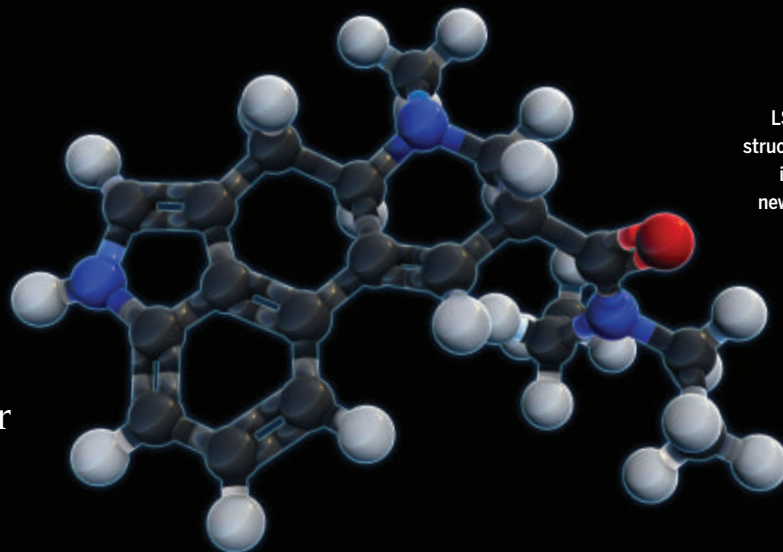
"Everybody is very happy to have something that's safe and readily available. Let's hope it's not too expensive."

Colleen Kelly,
Brown University

Psychedelics without hallucinations?

Chemical relatives of LSD appear to treat depression in mice

By Robert F. Service



LSD's chemical structure provided inspiration for new compounds.

More than 50 years after the Summer of Love, psychedelics are again the rage. This time the love comes from doctors beginning to embrace psychedelics such as LSD and psilocybin to treat depression, substance abuse, and other serious mental health conditions. But because the drugs cause hallucinations, their medical use requires intensive monitoring by clinicians. That drives up treatment costs, making psychedelics impractical for widespread therapeutic use.

In recent years, researchers have begun to tweak psychedelics' chemical structures, aiming to make analogs that retain medical usefulness but don't cause hallucinations. Now, researchers report in *Science* (p. 403) they've teased apart the molecular interactions responsible for psychedelics' antidepressive effects from those that cause hallucinations. They used that knowledge to make new compounds that appear to activate brain cellular circuits that help relieve depression without triggering a closely related pathway involved in hallucinations. So far, the compounds have only been studied in mice. But if such psychedelic analogs work in humans, they could spawn new families of pharmaceuticals.

"This work is going to generate a lot of interest," says Bryan Roth, a pharmacologist at the University of North Carolina School of Medicine, whose lab is also seeking nonhallucinogenic psychedelic analogs.

The need is profound. Mental or neurological disorders are estimated to affect roughly one-quarter of U.S. adults every year, and therapies often don't work. LSD, psilocybin (the main ingredient in magic mushrooms), and other psychedelics might do better. Studies have shown a single dose of psilocybin can offer relief from depression for months at a time, and last year, a clinical trial of 3,4-methylenedioxymethamphetamine, or ecstasy, showed it can alleviate post-

traumatic stress disorder (*Science*, 21 May 2021, p. 774).

How these hallucinogens exert their effects remains something of a mystery. In the brain, LSD, psilocybin, and other psychedelic compounds bind to a class of receptors for the neurotransmitter serotonin, known as 5-HT_{2A}R. The receptors, a type of cell membrane protein called a G-protein coupled receptor (GPCR), trigger two effects: They initiate a host of cellular responses, and they recruit other proteins called beta-arrestins that modulate GPCR activity.

Previous work in people showed hallucinogens strongly activate both the GPCR and beta-arrestin pathways. In 2017, Sheng Wang, then a postdoc in Roth's lab, took first steps toward showing why. He produced an x-ray crystal structure—basically an atomic-scale map—of LSD bound to a serotonin receptor closely related to 5-HT_{2A}R. It revealed that LSD nestles into a pocket within the receptor called the orthosteric binding pocket (OBP).

Now, Wang, at the Shanghai Institute of Biochemistry and Cell Biology, and his colleagues have produced six new crystal structures of compounds including LSD, psilocin (the active metabolite of psilocybin), serotonin, and lisuride, a nonhallucinogenic psychedelic analog, bound to 5-HT_{2A}R itself. Some of the compounds, they found, touched not only OBP, but a neighboring cavity known as the extended binding pocket (EBP).

To make sense of the binding patterns, the researchers turned to behavioral studies with mice injected with the different drugs. The team watched for freezing responses and head twitches, mouse behaviors strongly associated with depression and hallucination in humans, respectively. The results suggested compounds including serotonin that evoke more beta-arrestin activity and less GPCR activity were associated with antidepressive activity without hallucinations.

And those compounds interacted more with the EBP than the OBP.

So, Wang and his colleagues designed structural cousins of LSD they thought would favor binding to the EBP. They then repeated the behavioral tests on mice given these compounds and found that two of them, dubbed IHCH-7079 and IHCH-7806, did not trigger head twitches but did reduce the freezing behavior, much as effective antidepressants do.

IHCH-7079 and -7806 aren't the first compounds to show potential as therapeutic nonhallucinogenic analogs of psychedelics. Lisuride, which is used to treat Parkinson's disease and migraines, was first marketed in the 1970s. But the compound interacts with many receptors in the brain besides 5-HT_{2A}R and, as a result, has side effects including nausea and low blood pressure.

In 2020, researchers led by David Olson, a chemist at the University of California, Davis, reported in *Nature* that a nonhallucinogenic analog of the psychedelic compound ibogaine called tabernanthalog showed antidepressive effects in rodents. Last year in *Cell*, Olson's team reported related nonhallucinogenic compounds that appear more potent than tabernanthalog. Delix Therapeutics, a company Olson co-founded, is working to commercialize his compounds and related nonhallucinogenic experimental drugs as treatments for depression and other conditions. Brigitte Robertson, the company's chief medical officer, says she expects it to begin its first clinical trials later this year.

If any of the new compounds work to improve mental health as effectively and as quickly as psychedelics seem to, "it would change the world of psychiatric care," she says. But even if these first compounds don't pass muster, the new structural insights into how these compounds work give medicinal chemists a road map for taking the hallucinations out of the healing. ■

SCIENCE & SECURITY

Why a high-profile China Initiative case collapsed

U.S. government drops all charges against MIT engineering professor Gang Chen

By Jeffrey Mervis

For the past year, the U.S. government had argued that Massachusetts Institute of Technology (MIT) engineering professor Gang Chen broke the law by failing to disclose his ties to China when applying for a grant from the Department of Energy (DOE). But last week, prosecutors abruptly reversed course and dropped all charges against him, telling a federal court on 20 January that the government “can no longer meet its burden of proof at trial.” How did prosecutors get it so wrong?

Chen’s case was one of the highest profile prosecutions of an academic scientist brought under the China Initiative, a controversial government effort to prevent China from stealing federally funded research that has ensnared some two dozen university researchers. Last month, in another prominent case, a jury convicted Harvard University chemist Charles Lieber of failing to disclose his financial ties to China to federal agencies (*Science*, 7 January, p. 10). But Chen’s case never made it to a jury.

In a motion to dismiss, U.S. Attorney Rachael Rollins informed U.S. District Court Judge Patti Saris that prosecutors had received “additional information bearing on the materiality of the defendant’s alleged omissions.” But observers say the case crumbled because two of its pillars had fatal flaws. In one instance, prosecutors misinterpreted DOE’s disclosure requirements in 2017, when Chen applied for a \$2.7 million grant that loomed large in the case. They also distorted the nature of Chen’s interactions with Chinese institutions and alleged ties that didn’t exist.

“The government’s case often gets stronger after an indictment because it has time to collect additional evidence,” says Chen’s lawyer, Robert Fisher of Nixon Peabody LLP. “But this time their case got progressively worse, until it finally collapsed.”

Chen’s legal nightmare began in January 2020, a year before his arrest, when federal agents questioned him after he returned from a family vacation in China. The government alleged that when Chen applied for his DOE grant in March 2017, he didn’t comply with department rules requiring applicants to list “activities outside the United

States or partnerships with international collaborators” related to his proposed research, which involved studying how polymers conduct heat. But the application form DOE was using at the time—a broad call for proposals that typically results in hundreds of awards across many fields—did not request that information.

Such collaborations, and the potential security concerns, weren’t yet on DOE’s radar, says Chris Fall, who headed DOE’s science office during former President Donald Trump’s administration and worked on research security issues at the White House under former President Barack Obama. Instead, DOE’s disclosure rules were focused on preventing “duplicative grants, where [DOE was] being asked to fund something that another federal

A related flaw in the government’s case, Fisher says, was its assertion that Chen had made seven “material omissions” on his DOE application about relationships with Chinese institutions. But none had anything to do with Chen’s proposed research, Fisher says. And he says five of the seven alleged collaborations didn’t exist; prosecutors might have derived them from erroneous information posted on the internet.

For example, Fisher says Chen’s alleged participation in a foreign talent program run by the city of Wuhan, China, and a nearby industrial park, dubbed Optics Valley, was based on an offer from those entities that Chen rejected. “He was sent a contract describing his potential involvement and he deleted that provision,” Fisher says. “Nothing ever came of the project.”

One relationship that did exist, Fisher says—advising China’s Southern University of Science and Technology (SUSTech)—was part of Chen’s official duties at MIT. In 2018, MIT signed a 5-year agreement with SUSTech in which the Chinese university put up \$19 million to fund a joint engineering center. And Chen had disclosed his work on that deal on the CV he sent to DOE, Fisher notes.

Chen’s colleagues never doubted his innocence. “It was clear that some of what the government was saying was a blatant lie and that there was no criminal intent,” says Yoel Fink, an MIT materials scientist who helped organize a petition signed by hundreds

of academics titled “We are all Gang Chen.” MIT, which placed Chen on leave with pay after his arrest and has paid his legal bills, has welcomed him back. “All of us who know Gang are deeply relieved ... and eager for his full return to our community,” MIT President L. Rafael Reif wrote in a statement.

Chen was back in his lab the day after the case was dropped, and last week he posted a research paper that thanked MIT “for its support during a difficult time.” His DOE grant was renewed in 2020 and is now being led by a colleague in the mechanical engineering department that Chen once chaired. But Chen “wants nothing more to do with [federal funding],” Fisher says. “Gang has been pretty scarred by the whole experience. He doesn’t plan to work on any more government grants.” ■



Gang Cheng has been on MIT’s engineering faculty since 2001.

agency was already supporting,” says Fall, now vice president of applied sciences at the MITRE Corporation, a nonprofit that manages several federal research labs.

It was only in October 2020, more than 3 years after Chen applied for his grant, that DOE began to require applicants to disclose one type of foreign collaboration: “participation in foreign government-sponsored talent recruitment programs.” (The new form has a bold box that says: “WARNING: These instructions have been significantly revised.”) Those talent programs, notably China’s Thousand Talents programs, can provide U.S.-based scientists with generous funding to work in the sponsor nation. Federal officials recently began to worry that U.S. participants could face time and financial conflicts that might jeopardize research integrity.



PARANORMAL ACTIVITY

Why is Harvard University astrophysicist Avi Loeb working with ardent UFO believers?

Abraham “Avi” Loeb got the idea to hunt for aliens from cable TV. In June 2021, Loeb, an astrophysicist at Harvard University, was at home, watching NASA Administrator Bill Nelson on CNN talking about recent UFO incidents involving U.S. Navy pilots. “Do you think we have been contacted by extraterrestrials?” the CNN interviewer asked. Nelson hedged, then said he was “turning to our scientists” to find out what the pilots saw.

UFOs were big news at the time. Outlets from *The New York Times* to *60 Minutes* had

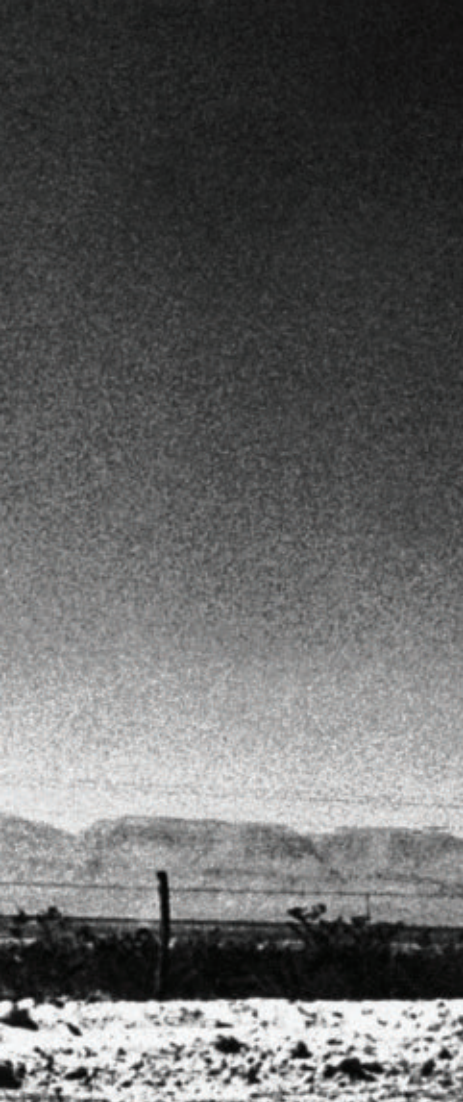
By **Keith Kloor**

run stories on shadowy objects that appear to dart and dance in grainy video clips taken by Navy jet pilots. On 25 June, shortly after Nelson mused about the footage on CNN, the Pentagon issued a report on nearly 2 decades’ worth of the “unidentified aerial phenomena” (UAP)—the government’s preferred new term for UFOs. It said the objects were likely to be drones, weather-related phenomena, or artifacts of sensor glitches. On the other hand, it said that, in some cases, the objects “appeared to exhibit unusual flight charac-

teristics.” Meanwhile, a Pew Research Center poll that month found that half of Americans believed aliens were steering the UFOs.

Loeb, already obsessed with a mysterious interstellar object that whizzed through the Solar System in 2017, sensed an opportunity. Immediately after seeing Nelson on CNN, he emailed NASA science chief Thomas Zurbuchen to propose a government-funded UFO study. Later that day, the two spoke over the phone, and Loeb says Zurbuchen was “supportive” of the idea. But Loeb never heard back after that. He quickly pivoted to private funding. His first

PHOTO: BETTMANN/CONTRIBUTOR/GETTY IMAGES



In 1957, a “flying saucer” was photographed near an Air Force base in New Mexico (left). Avi Loeb (right) wants to gather data on modern UFOs.

lucky strike came when Eugene Jhong, a Silicon Valley entrepreneur and Harvard alum who had heard Loeb talking about aliens on a podcast, offered up \$1 million, no strings attached.

In July, Loeb unveiled the Galileo Project, which he says was designed in the spirit of the revolutionary Italian astronomer Galileo Galilei. (The tagline is “Daring to look through new telescopes.”) The overarching goal of the \$1.8 million project is to search for evidence of extraterrestrial technology, and one branch is traditional: analyzing possible interstellar objects spotted deep in space by mountaintop observatories. More controversial is the construction of a network of rooftop cameras designed to capture any UFOs prowling through Earth’s atmosphere. After enlisting more than three dozen astronomers and engineers in the project—as well as some notorious nonscientists—Loeb hopes to solve the enduring UFO mystery once and for all. “Scientists have to come to the rescue and clear up the fog,” Loeb says.

Some researchers applaud Loeb’s endeavor. “He has mounted a scientific attack

on a problem that is frustratingly fuzzy,” says Gregory Laughlin, an astrophysicist at Yale University. “A project like this would have been unthinkable 10 years ago.” But others say Loeb is tarnishing astronomy and undermining the search for extraterrestrial intelligence (SETI) just as that effort has started to acquire a veneer of respectability (*Science*, 11 September 2020, p. 1288). In particular, they are bothered by the outspoken UFO zealots with no science background whom Loeb has welcomed into the project. “He’s intermingled legitimate scientists with these fringe people,” says Caleb Scharf, an astrobiologist at Columbia University. “I think you lose far more by doing that.”

RAISED ON his family’s farm in Israel, Loeb has demonstrated a lifelong precociousness, as well as a restless and relentless curiosity. After earning a Ph.D. in plasma physics at the Hebrew University of Jerusalem in 1986 at the age of 24, he worked on a project funded by then-President Ronald Reagan’s “Star Wars” missile defense program. While still in his 20s, Loeb rubbed elbows with the luminary

physicist Freeman Dyson at the Institute for Advanced Study, where he switched to theoretical astrophysics, before joining Harvard in 1993. There, he pursued a traditional academic path—until several years ago when he became known as the Harvard professor who talks about aliens.

Loeb considers himself a trendsetter, and maintains a list of his “top 20 confirmed predictions.” Those include theories about how to use gravitational lenses to detect planets; how stars can feed the Milky Way’s central, giant black hole when they stray too close; and what the base of the jet of material that rockets out from the black hole at the center of the M87 galaxy looks like—a prediction confirmed when the black hole’s shadow was captured by the Event Horizon Telescope in 2019. “I worked on imaging black holes before it became fashionable,” he says with matter-of-fact boastfulness. “I worked on the first stars in the universe before it became popular.” He points to that research as an impetus for the James Webb Space Telescope, the just-launched observatory that will probe the early universe.

None of this was controversial or drew a public spotlight. But then, in 2017, a telescope in Hawaii spotted a cigar-shaped rock 400 meters long passing through the Solar System, its immense speed and bizarre trajectory firmly placing it in the category of “not from around here.” ‘Oumuamua, as it ended up being called, was the first documented interstellar object to visit the Solar System, and Loeb leaped at the chance to study something so strange. He noted, as other scientists did, that ‘Oumuamua was brighter than a typical comet—too bright to be natural, he believed. He couldn’t shake the thought: What if it was an alien spaceship? Loeb ended up publishing 20 papers on ‘Oumuamua, and in early 2021, a book on it titled *Extraterrestrial: The First Sign of Intelligent Life Beyond Earth*.

Loeb’s theory that ‘Oumuamua was some kind of technological debris from an otherworldly civilization drew worldwide attention. He became an eager spokesperson, appearing not just in mainstream media outlets, but also UFO podcasts and conferences. But most of Loeb’s colleagues rejected his hypothesis, which he first laid out in a 2018 paper published in *The Astrophysical Journal Letters*. Others mocked it or dismissed it as a publicity stunt. “What’s really irritating is that Avi is a smart guy,” says Karen Meech, a planetary astronomer at the University of Hawaii, Manoa. “He is a good scientist. But he is out for fame here.” The snubs gnawed at Loeb.

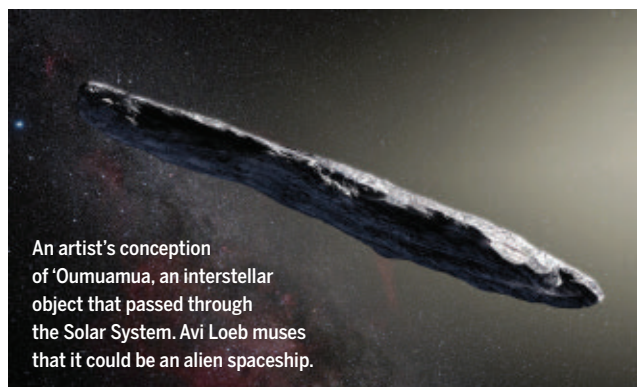
His anger boiled over early last year at an online forum called the Golden Webinar in Astrophysics, where he portrayed himself as the victim of a “close-minded” scientific community unwilling to entertain bold hypotheses. “If we listen to my colleagues we would just forget about [‘Oumuamua],” he said. “We would not put any funds for cameras taking photographs of it. Then we will maintain our ignorance, just like the philosophers in Galileo’s age.”

It was peculiar reasoning, not least because workers at the time were putting the finishing touches on the Vera C. Rubin Observatory, an 8-meter behemoth taking shape in Chile—and designed specifically to look for transient phenomena like ‘Oumuamua when it opens sometime next year. And in 2019, the European Space Agency approved Comet Interceptor, a mission that after launch in 2029 will park itself beyond Earth’s orbit in a position to chase down and inspect fast-moving comets—or even interstellar objects.

One pioneering SETI researcher at the forum could not abide Loeb’s comments. “Some of us have been thinking about and building

instruments to find anomalies for a very long time,” Jill Tarter reminded Loeb during one testy exchange at the forum. (Tarter was the inspiration for the astronomer played by Jodi Foster in the 1997 movie *Contact*.) Tarter said it was important not to make any conjectural leaps about aliens unless there was “extraordinary evidence.” This, she added, was the only way of “differentiating ourselves from the pseudoscience that is so much a part of popular culture with UFOs.”

IN JULY 2021, when Loeb unveiled the Galileo Project, it appeared to be aiming for just this sort of extraordinary evidence. He had recruited a team of scientists from prominent institutions worldwide to design and work on the project. “I was attracted to it because it



An artist's conception of 'Oumuamua, an interstellar object that passed through the Solar System. Avi Loeb muses that it could be an alien spaceship.

is data-driven,” says Kevin Heng, an astrophysicist at the University of Bern.

One part of the project would design software to screen the data coming from telescopes like the Rubin observatory for interstellar objects. But the core of the project would be a worldwide network of sky monitors, hundreds in all. Each dome-shaped unit, roughly the size of an umbrella, will contain infrared and optical cameras arranged like a fly’s eye to capture the full expanse of sky overhead. Audio sensors and radio antennas will listen at other frequencies. Running 24 hours a day, the monitors are meant to record everything that moves through the sky, day and night: from birds and balloons to insects, airliners, and drones. Artificial intelligence (AI) algorithms, trained to discard known objects like birds in favor of fast-moving spherical and lens-shaped objects, will sift through the data, says Richard Cloete, a computer scientist at the University of Cambridge, who is overseeing the system’s software. “We’re basically filtering out all the things that we expect to find in the sky,” he says. “And all these things that are labeled other [by the AI] will be of interest.”

Seth Shostak, an astronomer at the SETI Institute who sits on the Galileo Project’s advisory board, points out that networks of sky

cameras are not new. Since 2010, one SETI Institute network has detected 2 million meteors, and in the past few years, the LaserSETI project has begun to watch the sky for pulses of light from alien technologies. What’s novel about the Galileo Project, Shostak says, is its focus on hunting for aliens in Earth’s atmosphere. Both the Galileo Project and the SETI Institute “are looking for indications of extraterrestrial intelligence,” he adds. “But that’s like saying that studying unknown fauna in the rainforest is similar to those who are hoping to find mermaids or unicorns.”

Loeb says a prototype sky monitor is being built now and will be affixed to the roof of the Harvard College Observatory in the spring. If the instruments work, he plans to make duplicates; if he can raise another \$100 million from private donors, he will place them around the world. He says he won’t utter the UFO word unless they see an object “that looks strange and moves in ways that human technology cannot enable.”

ONE DAY in November, at a virtual meeting for the Galileo Project, the discussion turned to which “high incidence areas” would be best to first deploy the cameras. (Loeb shared Zoom recordings of several team meetings with *Science*.) The widely reported UFOs were spotted during naval training exercises off

the U.S. Pacific and Atlantic coasts—making those the natural places to start the network of UFO detectors. “Do you have the first priority location or recommendation?” Loeb asked Christopher Mellon, who was participating in his first meeting as a “research affiliate,” an unpaid adviser to the project. A former deputy assistant secretary of defense for intelligence, Mellon has publicized the UFO issue in the media for several years, talking up the national security threat he claims they pose.

Before answering, Mellon cleared his throat. “One of the problems is that many of the areas we’re seeing the greatest level of [UFO] activity are restricted military airspace,” he said. “The Defense Department is not going to be real excited about bringing in a lot of instruments to record everything that’s going on.”

The discussion was abruptly tabled, and Loeb has since danced carefully around the issue and deferred to the military concerns raised by Mellon. But they present a quandary for the Galileo Project, says Ed Turner, a Princeton University astrophysicist who is part of the project’s core research team. “The clustering of UAP incidents [in military areas] is a problem,” he says. “I’ve pointed that out to Avi.” Turner, who is more excited by the interstellar component of the project, doesn’t



The Pan-STARRS 1 telescope, atop the island of Maui in Hawaii, discovered 'Oumuamua in 2017.

think the ground-based cameras will pick up any evidence of extraterrestrial visits. “If the aliens don’t want us to know about them, they’ll likely know about the Galileo Project,” he says drily. “They can just avoid our high-resolution cameras.”

In addition to Mellon, Galileo has nearly 50 other research affiliates—many with no background in science but a long interest in UFOs. One is Nick Pope, a former U.K. civil servant-turned-broadcaster who claims to have investigated UFO reports for the U.K. government in the early 1990s. Since then, he has been a regular speaker on the UFO circuit and on *Ancient Aliens*, a long-running TV series that suggests aliens have shaped human history. “We very much look forward to benefitting from your knowledge and wisdom,” Loeb said to Pope after introducing him at a recent weekly Zoom meeting. (Pope says he considers himself a “communicator” and “broadcaster” and rejects being labeled as fringe.)

Another research affiliate is Luis Elizondo, a career military intelligence officer and self-proclaimed UFO whistleblower. In recent years, Elizondo has appeared widely in the media claiming to be the former director of a secretive Pentagon UFO research unit. Although Elizondo is confirmed to have worked

in the Department of Defense until retiring in 2017, Pentagon spokespeople have repeatedly denied that he ever played a role in a UFO research program, much less led one. (In November 2021, however, the Pentagon did establish a UFO office, which it calls the Airborne Object Identification and Management Synchronization Group.)

After word spread on social media of Elizondo’s involvement, Loeb felt compelled to address the matter in one of the project’s weekly Zoom meetings. “I evaluate people based on their intelligence and openness of mind,” he said from the book-lined study of his home in Massachusetts, where Loeb is working on sabbatical this year. “We don’t care so much what other people said in the past. What we want is to collect our data. ... We will not entertain fringe ideas that are outside the boundaries of the standard model of physics.” Elizondo and Mellon declined to comment.

When asked directly about the dangers of involving such outspoken UFO advocates, Loeb points out that he did not recruit them; they all approached him. “We will not rely on anything these people say, just the instruments,” he insists. “I don’t care what people are associated with.” He says he prefers a big tent. “I don’t want to

alienate anyone that cares about the subject, because we could benefit from their knowledge,” he says.

Many on the Galileo Project appreciate Loeb’s open-mindedness. Shostak for one isn’t bothered by the presence of the research affiliates and thinks Loeb’s star power gives a boost to a worthwhile project. “I still don’t think we’re being visited by aliens,” he chuckles. But others on the team are wary. Heng says he has become “uncomfortable” with some of the research affiliates. “This is concerning,” Heng says. “If there comes a day when the influence of the fringe people overrides the influence of people like me and other sober-minded scientists on the team, then I’m gone.”

UFO SIGHTINGS have waxed and waned in the public consciousness since the dawn of the Cold War in the late 1940s, when the term “flying saucers” first appeared. In 1953, during one wave of sightings across the United States, another Harvard astrophysicist tried to calm public jitters. “They are as real as rainbows,” Donald Menzel told *Time* magazine, referring to the saucers. Menzel explained that people were misperceiving distant objects in the skies, such as planes and balloons, or being fooled by optical illusions produced by clouds and celestial phenomena.

Over the years, many public-facing astronomers have investigated UFO claims in a similar spirit. Michael Busch, an astronomer at the SETI Institute, says they do this “in an attempt at debunking and at convincing UFO enthusiasts of their mistake, and sometimes as a way to teach astronomy.” Busch cites Carl Sagan and Neil deGrasse Tyson as others who have taken Menzel’s patient, skeptical approach.

Whether Loeb falls into this category depends on your perspective. Some, like Busch, believe Loeb is cynically riding the UFO zeitgeist to promote himself, his book, and his project. Others, like former National Science Foundation Director and astrophysicist France Córdova, find Loeb to be “imaginative” and “inspiring.” “His views may unsettle some, yet there is no doubt that the goal of finding evidence that we are not alone is an attribute that makes us distinctly human,” she says.

For his part, Loeb can sound a lot like Menzel when he wants to. He says he knows full well that most UFO sightings derive from misperception. He’ll respectfully listen to such accounts, but will put no stock in anecdotal stories, he says. “Humans are subject to hallucinations, optical illusions, all kinds of crazy stuff. You cannot trust people.” What he wants, he says, is data. ■

Keith Kloor is a journalist in New York City.

INSIGHTS

PERSPECTIVES



MICROBIOTA

Staying strong during hibernation

The microbiota of hibernating squirrels salvages urea to replenish amino acids

By **Felix Sommer**¹ and **Fredrik Bäckhed**^{2,3,4}

For mammals, prolonged inactivity and starvation, such as during hibernation, prompt the body to break down muscle proteins to create a source of energy. Known as muscle wasting, this process yields ammonium, which is further converted to urea. Because high concentrations of urea are toxic to neurons in mammals, it is normally excreted with urine. As a result, the body is constantly losing nitrogen in the form of ammonium and needs to replenish it through dietary uptake, because nitrogen is essential for protein and nucleotide synthesis. With the lack of regular food intake, it has been enigmatic how mammals maintain their physiological

functions during hibernation. On page 460 of this issue, Regan *et al.* (1) describe the molecular processes underlying the urea nitrogen salvage mechanism in hibernating squirrels and reveal a functional role of intestinal microorganisms in this adaptive physiological process.

Hibernating animals do not eat or drink over a long period of time, often months, when they are inactive and spend most of their time sleeping. During this torpid state, hibernators can drastically reduce their metabolic rates, allowing them to reduce their energy demands. Despite this combination of fasting and inactivity, hibernating animals keep their lean mass relatively stable, with some even gaining muscle mass by the end of hibernation (2).

To elucidate how squirrels maintain their physiological functions during hibernation, Regan *et al.* used stable isotope labeling to track the flow of nitrogen and carbon in squirrels during the active phase and hibernation. These experiments revealed that urea, which is produced by the host during protein catabolism, is transported from the blood to the gut lumen in addition to being excreted in the urine.

All animals live in close association with a vast diversity of microorganisms—the microbiota—that contributes to various aspects of host physiology (3). Previous research identified that hibernation alters the gut microbiota (4, 5). In bears, the microbiota assists in extracting energy from the diet to facilitate prehibernation fattening (4). In hibernating

Hibernating mammals change between active and inactive phases, which is accompanied by functional alterations in their microbiota that support prehibernation fattening or nitrogen recycling. This discovery may lead to potential targets for microbiota-directed therapies for human muscle-wasting conditions.

frogs, gut microbes encode an increased potential for nitrogen salvage (6). Using metagenomic sequencing, Regan *et al.* found that the gut lumen of squirrels contains microorganisms with urease genes, which enable the microorganisms to produce enzymes (i.e., ureases) that metabolize urea into carbon dioxide and ammonium. The ammonium is then used by the same microbiota as a source of nitrogen to produce amino acids, some of which are then absorbed by the host. As a result of this process, nitrogen loss during protein catabolism and urea formation is compensated, which counteracts muscle wasting. Although the process of urea nitrogen salvaging has been known in ruminants such as cattle, goats, and sheep (7), the identification and molecular delineation of urea nitrogen salvaging in hibernating mammals add another central role for intestinal microorganisms within the coordination of host physiological adaptations.

Muscle wasting is prevalent in humans, for example, during protein malnutrition, which affects millions of people worldwide, especially children in developing countries. The low intake of protein is known to trigger not only muscle wasting but also other health problems, such as various neurological and growth defects, inflammatory episodes, and increased susceptibility for pathogenic infections. Muscle wasting is also prevalent in the elderly owing to age-related muscle loss, which greatly affects quality of life. The exploitation of microbial processes for producing essential amino acids could potentially benefit those whose diets are deficient in protein or those who display impaired food intake or digestion, for example, members of the elderly with sarcopenia (8).

The identification of a microbial contribution to urea nitrogen salvaging in hibernating mammals provides potential targets for developing new treatments for muscle wasting and related conditions. The gut microbiota is plastic in its composition and function and can be shaped by external factors

such as diet (9). Microbiota-directed therapies have already been used successfully for malnutrition (10, 11). These approaches seem promising, especially for treating or preventing muscle wasting, because physiological responses to low-protein conditions similar to those observed in hibernating mammals have been observed in humans, that is, an increase in nitrogen recycling under low-protein conditions (12, 13). The addition of bacteria that produce ureases, for example, from the genus *Alistipes*, which increased in abundance during hibernation in squirrels, could represent potential next-generation probiotics. Successful probiotic supplementation was recently shown when *Lactobacillus plantarum* was administered to malnourished mice, which prevented body weight loss and fostered normal bone development (14). However, it is unclear whether *L. plantarum* increased nitrogen recycling. Another approach would be to develop genetically manipulated bacteria, which colonize the human gut, to express urease, thus providing an alternative avenue to increase nitrogen recycling. The feasibility of this approach was recently demonstrated using engineered *Escherichia coli* Nissle to produce enzymes that enabled phenylalanine degradation in patients with phenylketonuria (15).

The findings of Regan *et al.* add to previous research demonstrating the microbial function in energy harvest of hibernating mammals. Collectively, these studies highlight the importance of the microbiota for nutritional and metabolic adaptations in mammalian hosts. Muscle wasting is prevalent in those suffering from age-related sarcopenia, protein malnutrition, or prolonged inactivity such as during space travel or hospitalizations related to severe diseases. Because mechanisms for nitrogen salvaging from urea seem to be functional in humans, microbiota-directed interventions for urea recycling could be a potential therapy for treating such conditions. ■

REFERENCES AND NOTES

1. M. D. Regan *et al.*, *Science* **375**, 460 (2022).
2. A. G. Hindle *et al.*, *J. Exp. Biol.* **218**, 276 (2015).
3. F. Sommer, J. M. Anderson, R. Bharti, J. Raes, P. Rosenstiel, *Nat. Rev. Microbiol.* **15**, 630 (2017).
4. F. Sommer *et al.*, *Cell Rep.* **14**, 1655 (2016).
5. K. Grond, C. C. Kurtz, J. Hatton, M. M. Sonsalla, K. N. Duddleston, *Anim. Microbiome* **3**, 56 (2021).
6. J. M. Wiebler *et al.*, *Proc. R. Soc. London Ser. B* **285**, 20180241 (2018).
7. H. V. Carey, F. M. Assadi-Porter, *Annu. Rev. Nutr.* **37**, 477 (2017).
8. S. Subramanian *et al.*, *Cell* **161**, 36 (2015).
9. L. Schröder *et al.*, *Nutrients* **12**, 3032 (2020).
10. R. Y. Chen *et al.*, *N. Engl. J. Med.* **384**, 1517 (2021).
11. J. L. Gehrig *et al.*, *Science* **365**, eaau4732 (2019).
12. M. Langran, B. J. Moran, J. L. Murphy, A. A. Jackson, *Clin. Sci. (Lond.)* **82**, 191 (1992).
13. M. I. Smith *et al.*, *Science* **339**, 548 (2013).
14. M. Schwarzer *et al.*, *Science* **351**, 854 (2016).
15. M. K. Puurunen *et al.*, *Nat. Metab.* **3**, 1125 (2021).

¹Institute of Clinical Molecular Biology, University of Kiel, Rosalind-Franklin-Strasse 12, 24105 Kiel, Germany.

²The Wallenberg Laboratory, Department of Molecular and Clinical Medicine, University of Gothenburg, Bruna Stråket 16, 41345 Gothenburg, Sweden. ³Department of Clinical Physiology, Sahlgrenska University Hospital, Gothenburg, Sweden. ⁴Novo Nordisk Foundation Center for Basic Metabolic Research, Faculty of Health and Medical Sciences, University of Copenhagen, Blegdamsvej 3B, 2200 Copenhagen, Denmark. Email: f.sommer@ikmb.uni-kiel.de

WATER TREATMENT

Intensifying existing urban wastewater

Aerobic granular sludge offers improvements to treatment processes

By M.-K. H. Winkler¹
and M. C. M. van Loosdrecht²

As the population continues to grow, increasing engineering challenges are associated with the sustainable life cycle of consumption and production of safe, reusable water. The water industry has identified wastewater as a viable and sustainable source for not only quality water, but also for recovering resources while minimizing footprint and energy demand. A recent innovation that targets all of these key issues is the aerobic granular sludge (AGS) technology, which allows for the simultaneous removal (or recovery) of nitrogen, carbon, and phosphate while reducing the footprint by up to 75%.

Today, 55% of the world's population lives in urban areas, and that number is expected to increase to 68% by 2050, making cosmopolitan square footage more arable. As a result, metropolitan wastewater treatment plants (WWTPs) are constrained in space while having to treat higher flow rates (1). Additionally, recent regulations demand nutrient removal (e.g., in the US) and recovery (e.g., in Europe), but WWTPs were not designed to easily add on functionalities to accommodate treating increased flows with more-stringent discharge limits. This problem is exacerbated by an aging infrastructure. Amid an economic crisis fueled by the coronavirus pandemic, investment in aging water infrastructure has to remain of prime importance for growth (2). The US, for example, was underinvesting in its wastewater systems but has recently passed a massive bill to renew infrastructure (3). This pushes for innovative technologies to offer cost- and space-effective treatment solutions.

Granules are a specific form of biofilm structure (see the figure) because they do not grow on a carrier but are self-aggregating,

¹Civil and Environmental Engineering, University of Washington, Seattle, WA 98165, USA. ²Department of Biotechnology, Delft University of Technology, 2629 HZ Delft, Netherlands. Email: mwinkler@uw.edu

spherical particles with diameters of 0.5 to 2 mm that settle 10 to 15 times as fast as the conventional floc. Flocs can be selectively wasted from the system, enriching for granules and accelerating solid separation substantially. The fast-settling and high-thickening properties of AGS allow integration of the settling process inside only one treatment unit operated at increased solids inventory, thereby bypassing the space-consuming secondary clarifiers and greatly reducing footprint and intensifying reactor operation without energy-intensive recycle flows and mixers (4).

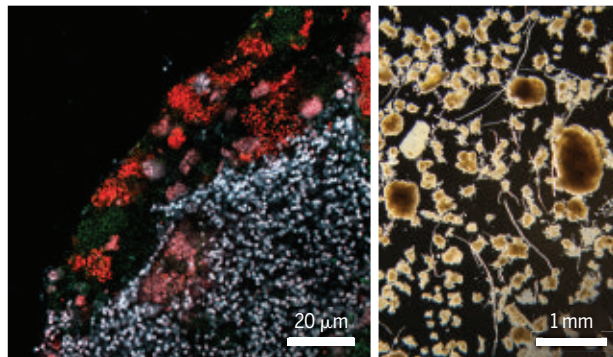
In conventional systems, sludge flocs must be pumped across multiple tanks to allow N, C, and P removal, and they are separated from the water in extremely space-demanding clarifiers. Granules consist of a spatially ordered consortium of nitrifiers, phosphate-accumulating organisms (PAOs), glycogen-accumulating organisms (GAOs), and associated microorganisms (5). The nitrifiers aerobically oxidize ammonium to nitrate and are confined to grow on the oxygenated granule periphery. The PAOs may grow aerobically but preferentially localize to the granule interior, where they reduce nitrate to nitrogen gas and store phosphate. Together, both functional groups (nitrifiers, PAOs and GAOs) are coupling transformations of C, N, and P to allow water purification. Enhanced biological phosphate removal (EBPR) systems form denser and stronger granules than systems based on ordinary heterotrophs (6).

To out-select the fast-growing heterotrophs and promote the growth of slow-growing PAOs and GAOs (that form smoother biofilms), the reactor must be operated with alternating anaerobic and aerobic reactor conditions with influent feeding during the anaerobic period. This task can be accomplished by anaerobically feeding the wastewater directly through the settled granular sludge bed. The concurrent nutrient removal and easy separation of granules allows one to operate the whole process in a single sequencing batch reactor (SBR) at reduced footprint. When three parallel reactors are present, the pre- and posttreatment processes can be operated at continuous flow (CF), as in conventional floc-based processes (4).

Nutrient recovery has similar potential for flocs and granules, but granular sludge is special in that it enables 5 to 10 kg of glycoprotein recovery per person per year, which has good economic value in the chemical and agricultural industry (7). The high-thickening characteristics of AGS may also be used to produce a phosphorus-rich stream by simple anaerobic holding of the

waste granular sludge, offering the promise of P recovery without an anaerobic digester. AGS technology is therefore an attractive alternative for future expansions at many wastewater facilities serving an increasing population with space constraints.

Despite the success story of AGS, which has already reached 70 plants worldwide within the first few years of market introduction, the SBR-based technology does not eas-



A sliced granule of an aerobic granular sludge system (left) includes nitrifiers (red) and denitrifying polyphosphate-accumulating organisms (PAOs) (blue). Granules are shown from a continuous-flow system (right).

ily integrate in existing, mostly shallow CF infrastructure that relies on solid separation in a clarifier. This makes retrofitting an existing plant cumbersome without decommissioning. Recently, a high abundance of PAO-based granules was unexpectedly observed at existing, full-scale CF-EBPR plants, suggesting that widespread adaptation of AGS in existing wastewater facilities might be easier than expected (8). Therefore, the implementation of a granule-floc separator in CF-EBPR systems to enhance granulation by leveraging an anaerobic phase to select for slow-growing bacteria capable of internally storing carbon (such as PAOs and GAOs) may be a way to integrate AGS technology into CF, which is currently considered the crowning glory for sustainable wastewater treatment (9).

A fully aerobic feast-famine regime is sometimes easier to implement in existing infrastructure (10, 11). This strategy can also result in granular sludge, but it needs a stronger selection force for granules than for anaerobic feeding. The main selection pressure used thus far for cultivating granules in CF has been settling velocity based, where fast-settling particles are continuously separated from the slow-settling particles and retained in the system using equipment such as a solids-liquid separator, an external settler, or other designs of similar concept (12). These CF configurations can have varying floc-granule separation methods, but many share the common strategy of favoring the growth of GAOs and PAOs in the granules by recycling

larger particles to the anaerobic zone from the separator.

Challenges remain in uncoupling floc and granule retention time as an essential requirement to establish granules in CF. Additional challenges include the generation of enough biologically available carbon (through hydrolysis and fermentation) and directing it to select efficiently for storage (GAOs and PAOs) (13); sludge aeration and mixing strategies for floc-granular biomass systems; the impact of floc and granule size fractions on diffusive transport (14) and microbial competition to manage nitrification and denitrification (15); and the integration of resource recovery, especially phosphate and biopolymers, in the water treatment process.

Overall, the paradigm of wastewater treatment to protect public health and improve environmental quality has begun to shift—after a century of municipal wastewater treatment—from flocculent to granular sludge, which offers an exciting opportunity for upgrading existing infrastructure while making wastewater treatment more sustainable. SBR-AGS is the best option for plants that require a major infrastructure upgrade, whereas CF-AGS is best suited for plants that are still in good enough shape to allow a retrofit for intensifying existing infrastructure. AGS technology will be of great importance to the water profession to provide high-quality water in constantly growing urban areas combined with efficient resource recovery. ■

REFERENCES AND NOTES

1. United Nations Department of Economic and Social Affairs, "68% of the world population projected to live in urban areas by 2050, says UN" (2018); www.un.org/development/desa/en/news/population/2018-revision-of-world-urbanization-prospects.html.
2. The White House, "Fact Sheet: The Bipartisan Infrastructure Deal" (2021); www.whitehouse.gov/briefing-room/statements-releases/2021/11/06/fact-sheet-the-bipartisan-infrastructure-deal/.
3. The White House, "Fact Sheet: The American Jobs Plan" (2021); www.whitehouse.gov/briefing-room/statements-releases/2021/03/31/fact-sheet-the-american-jobs-plan/.
4. M. Pronk et al., *Water Res.* **84**, 207 (2015).
5. M. K. H. Winkler et al., *Appl. Microbiol. Biotechnol.* **97**, 7447 (2013).
6. M. K. de Kreuk, M. C. M. van Loosdrecht, *Water Sci. Technol.* **49**, 9 (2004).
7. S. Felz et al., *Water Res.* **169**, 115291 (2020).
8. S. P. Wei et al., *Water Res.* **179**, 115865 (2020).
9. C. Roche et al., *Water Environ. Res.* **94**, e1664 (2022).
10. J. J. Beun et al., *Water Res.* **33**, 2283 (1999).
11. Z. An et al., *Environ. Sci. Water Res. Technol.* **7**, 1622 (2021).
12. I. Avila et al., *Water Sci. Technol.* **84**, 302 (2021).
13. M. Leyer et al., *Water Res.* **X** **9**, 100075 (2020).
14. S. P. Wei et al., *Water Res.* **203**, 117514 (2021).
15. B. Nguyen Quoc et al., *Water Res.* **198**, 117119 (2021).

ACKNOWLEDGMENTS

The authors acknowledge support from the National Science Foundation (project nos. 1510665 and 1603707) and the Water Research Foundation (project no. T1RR3C15).

10.1126/science.abm3900

How pH affects electrochemical processes

Three mechanisms underlie the impact of pH on the activity of electrochemical reactions

By Nitish Govindarajan, Aoni Xu, Karen Chan

A promising approach to the sustainable and fossil-free production of fuels and chemicals is the electrochemical conversion of atmospherically available gases such as H_2O , CO_2 , O_2 , and N_2 to fuels and chemicals with renewable electricity (1). Electrocatalysts are essential for practical processes because they increase the reaction rate, efficiency, and selectivity toward desired products. Unfortunately, state-of-the-art electrocatalysts have drawbacks such as the use of precious metals that limit widespread adoption and large overpotentials that lead to very low efficiency. The outstanding challenge is to design and discover active and selective electrocatalysts that are based on earth-abundant materials. It has been understood for decades that the electrolyte pH affects the activity of electrochemical processes. However, the origins of this effect are still under debate.

Interfacial proton-electron transfer reactions are central to electrochemical conversion schemes and include H_2 and O_2 redox reactions and CO reduction (COR), as well as alcohol oxidation reactions (AORs). The reaction thermodynamics of these multistep reactions depend both on pH and the absolute electrode potential, which are captured by the potential U [here, all U values and voltages are versus the reversible hydrogen electrode (RHE)]. However, the reaction kinetics, given by the current density J , do not generally follow the same dependence on U .

We define “pH effects” as such deviations in J from a dependence on U . The relative increase in J with a change in pH (ΔpH) for several proton-electron transfer reactions for a given U (see the figure, top) can be several orders of magnitude. Three possible sources of pH effects in electrochemical systems are changes in the proton donor or acceptor with the electrolyte pH, adsorbate dipole-

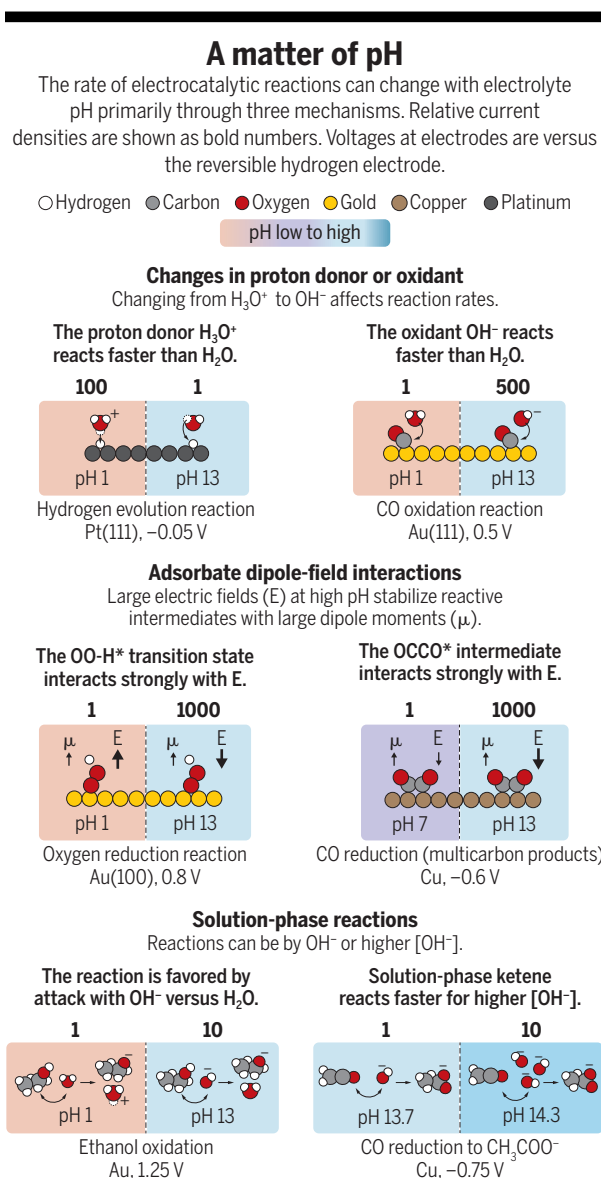
field interactions, and solution-phase reactions. These mechanisms are illustrated in the figure for relevant intermediates in the rate- or selectivity-determining steps of the reactions shown.

The change in the proton donor, such as H_3O^+ to H_2O , or oxidant, such as OH^- to H_2O_2 , with pH can affect the rates of electrochemical reaction steps by orders of magnitude. The magnitude of this effect is analogous to that in the variation in acid (K_a) and base (K_b) dissociation constants for bulk acid-base reactions. The potential impact of changes

in proton donor and oxidant on electrocatalytic activity are exemplified by the hydrogen evolution (HER) and CO-electrooxidation (COOR) reactions, respectively.

In the HER, the proton donor changes from H_3O^+ in acidic solution to H_2O in alkaline solution. The proton-electron transfer barriers for the elementary steps are much lower with H_3O^+ as the proton donor than with H_2O —that is, $K_a(\text{H}_3\text{O}^+) \ll K_a(\text{H}_2\text{O})$ (2). Thus, the activity at pH 1 is about two orders of magnitude higher than at pH 13 at -0.05 V on Pt(111) electrodes (3). Similarly, the strong pH dependence of COOR on Au(111) surfaces has also been proposed to likely originate from a change in the oxidant from OH^- to H_2O_2 with a decrease in electrolyte pH (4). Because OH^- is a more facile oxidant than H_2O as $K_b(\text{OH}^-) \gg K_b(\text{H}_2\text{O})$, there is a ~ 2.5 orders of magnitude increase in the COOR current density at 0.5 V in base versus acid (5).

A second mechanism behind pH effects is the adsorbate dipole-field interaction (see the figure, middle). Electrochemical interfaces are in general highly charged, and these charges give rise to large interfacial electric fields at the electrode-electrolyte interface. These fields drive the electron transfer to and from the adsorbates involved in the reaction. The electric field also interacts strongly with adsorbates that have a large dipole moment (μ), polarizability (α), or both, which results in changes in their adsorption energies. Because the interfacial field strength depends only on the absolute electrode potential, for a given U versus RHE, different pH conditions create different interfacial fields and corresponding stabilizations of the polar adsorbates. This mechanism gives rise to the pH-dependent activity in COR on Cu (6) and oxygen reduction (ORR) on Au(100) (7). In the former process, the critical reaction intermediate $^*\text{OCCO}$ has a large dipole moment (8), and its stabilization by the interfacial field gives rise to more than three orders of magnitude increase in activity toward multicarbon products such as ethylene or ethanol under alkaline conditions



Catalysis Theory Center, Department of Physics, Technical University of Denmark, 2800 Kongens Lyngby, Denmark. Email: kchan@fysik.dtu.dk

compared with neutral conditions at -0.6 V. For ORR on Au(100) electrodes, adsorbate dipole-field interactions result in up to three orders of magnitude increase in activity from acidic to alkaline conditions at 0.8 V (7) through strong-field stabilization of the *OOH transition state (9).

The electrolyte pH can also affect electrocatalytic activity through solution-phase reactions with OH^- without any involvement of the electrode (see the figure, bottom). The pH dependence then arises from the first-order dependence of the corresponding elementary step on OH^- concentration. For several AORs on Au, the first deprotonation step was proposed to be catalyzed by OH^- ions in alkaline solutions, which react with the alcohol to form a reactive alkoxide species that promotes the overall reaction rate (10). For the specific case of ethanol oxidation on Au electrodes, a ~ 10 -fold increase in the peak current density was observed at pH 13 relative to pH 1 (11). More recently, a 10-fold increase in acetate production from COR was observed at -0.75 V on Cu nanosheets with increasing pH (12). This effect was attributed to the solution-phase reaction of a highly reactive ketene intermediate (*CH_2CO) with OH^- ions (13).

Other complex pH effects deserve further attention. Buffering anions used to regulate electrolyte pH can act as proton donors and can promote reactions such as CO_2 electroreduction to methane on Cu electrodes (14). The dependence of interfacial solvent dynamics and reorganization effects on pH may play a role in hydrogen electrocatalysis (15). Together, pH effects provide additional descriptors beyond conventional adsorption energies that can open new avenues for catalyst design and enable large-scale adaptation of electrochemical conversion schemes. ■

REFERENCES AND NOTES

1. Z. W. Seh *et al.*, *Science* **355**, eaad4998 (2017).
2. P. S. Lamoureux, A. R. Singh, K. Chan, *ACS Catal.* **9**, 6194 (2019).
3. D. Strmcnik *et al.*, *Nat. Chem.* **5**, 300 (2013).
4. G. J. Edens, A. Hamelin, M. J. Weaver, *J. Phys. Chem.* **100**, 2322 (1996).
5. P. Rodriguez, N. Garcia-Araez, M. T. M. Koper, *Phys. Chem. Chem. Phys.* **12**, 9373 (2010).
6. X. Liu *et al.*, *Nat. Commun.* **10**, 32 (2019).
7. B. B. Bliznac *et al.*, *J. Phys. Chem. B* **108**, 625 (2004).
8. J. Resasco *et al.*, *J. Am. Chem. Soc.* **139**, 11277 (2017).
9. S. R. Kelly, C. Kirk, K. Chan, J. K. Nørskov, *J. Phys. Chem. C* **124**, 14581 (2020).
10. Y. Kwon, S. C. S. Lai, P. Rodriguez, M. T. M. Koper, *J. Am. Chem. Soc.* **133**, 6914 (2011).
11. S. C. S. Lai *et al.*, *Catal. Today* **154**, 92 (2010).
12. W. Luc *et al.*, *Nat. Catal.* **2**, 423 (2019).
13. H. H. Heenen *et al.*, *ChemRxiv* 10.33774/chemrxiv-2021-p3d4s (2021).
14. J. Resasco, Y. Lum, E. Clark, J. Z. Zeledon, A. T. Bell, *ChemElectroChem* **5**, 1064 (2018).
15. L. Rebollar *et al.*, *ACS Catal.* **10**, 14747 (2020).

ACKNOWLEDGMENTS

This work was supported by research grants (9455 and 29450) from Villum Fonden.

10.1126/science.abj2421



PALEOBOTANY

The African trees that conquered Asia

Fossil pollen from dipterocarps show shared floristic heritage between Asia and Africa

By **Carina Hoorn¹** and **Jun Ying Lim²**

With more than 400 species in the tropical lowlands and hill forests of Asia, dipterocarps are among the most abundant, diverse, and economically important trees on the planet (1). Many Asian dipterocarp species, belonging to the subfamily Dipterocarpoideae, are renowned for their stature and have long been valued for their timber. These trees dominate the canopy of the tropical Asian forests and are among the tallest trees on the planet (2). Yet, the biogeographic origin of Asian dipterocarps has been a puzzle because of the lack of fossils that capture the early history of the group. On page 455 of this issue, Bansal *et al.* (3) report filling this critical gap in dipterocarp evolutionary history by presenting fossil pollen from Sudan and India that is far older than any dipterocarp fossils described previously and by characterizing dipterocarp resin from sediments collected in India.

Using the pollen fossils and published molecular data (4), the authors generated a revised time-calibrated phylogenetic tree of dipterocarps. Along with paleogeographic and climatic reconstructions, they propose that these trees originated

in tropical Africa in the Late Cretaceous, 100 million years ago (Ma), and expanded into India between 72 and 66 Ma, during a window of geographic connectivity that coincided with a warming climate, the rise of the angiosperms (5), and the formation of the Deccan Traps in western India—one of the largest volcanic features in the world. The final stage of the dipterocarp journey took place between 50 and 40 Ma, when India and Asia collided, bringing the stowaway plants and animals closer to the tropical habitats of Asia (see the figure). Among these, dipterocarp lineages expanded and diversified, resulting in the integration of ancestrally African elements into the Asian biota.

The flora of tropical Asia is increasingly recognized by biogeographers as a melting pot that has been shaped by multiple exchanges (6). Scientists have long suspected that Asian dipterocarps originate from India, and the out-of-India pattern of dispersal has been documented for a wide variety of plant and animal groups (7). However, several fundamental questions remain: How and when did the dipterocarps colonize India, and where did they migrate from?

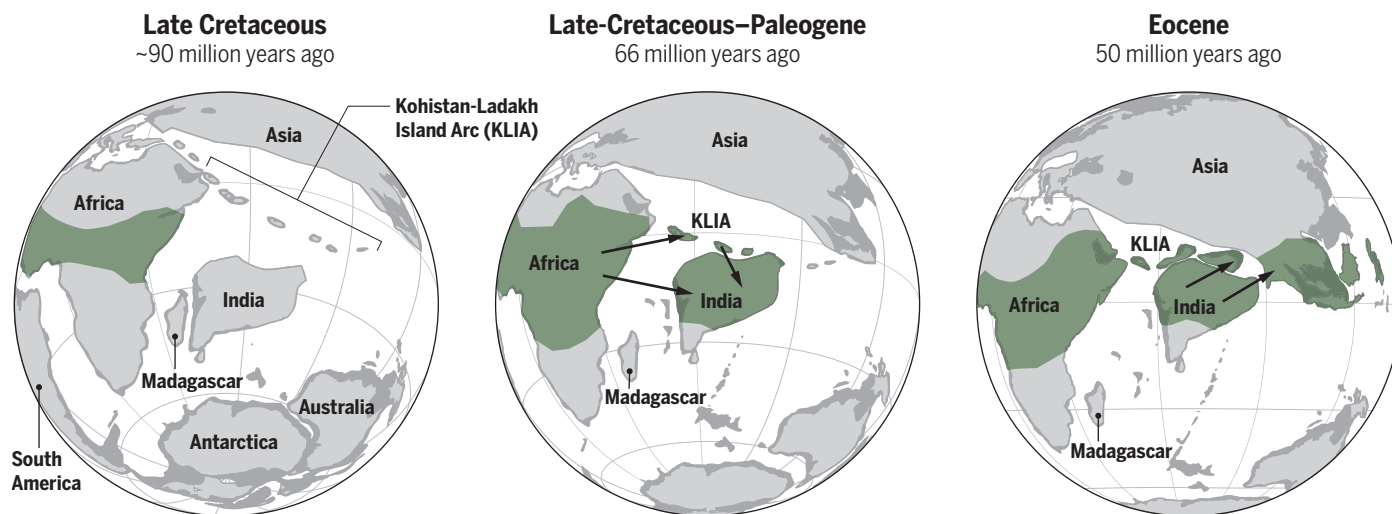
Palynology, the study of pollen and spores, is a powerful tool in paleobiogeography and can provide information not only on past plant composition and diversity, but also on former climatic conditions and topography. When combined with paleobotany, these disciplines provide an even higher accuracy in landscape and vegetation reconstructions.

¹Institute for Biodiversity and Ecosystem Dynamics, University of Amsterdam, Amsterdam, Netherlands.

²Department of Biological Sciences, National University of Singapore, Singapore. Email: m.c.hoorn@uva.nl; junyinglim@gmail.com

The dispersal of dipterocarps

Africa and India were once together as the megacontinent Gondwana. This landmass broke apart well before the origin of the dipterocarps (shown in the photo), with Africa and India drifting apart ~150 million years ago (15). ● Proposed geographic range of dipterocarps



However, one of the greatest challenges in the field of paleobiogeography is the lack of taxonomic resolution—in other words, the precision of the fossil's exact position on the evolutionary tree. Recent developments in optical techniques and machine learning (8) and the wider application of confocal laser scanning microscopes, such as in the study by Bansal *et al.*, are overcoming this problem. With dipterocarps fossils classified into clades, thanks to high-resolution microscopy, the way is paved for more-refined biogeographic models for Dipterocarpaceae at large.

The closest sisters to the Asian dipterocarps are the monotoid dipterocarps, belonging to the subfamily Monotoideae, which are distributed across South America, Africa, and Madagascar. Going back a little more on the family tree, one would find the family Sarcolaenaceae, which is closely related to all dipterocarps and is endemic to Madagascar (4). Because of the apparent shared genetic heritage among these tree species, an African origin of the Asian dipterocarps has been hypothesized before (1, 7), but fossil evidence for dipterocarps from Africa from the Late Cretaceous to early Paleogene has been scant. Most of the global dipterocarp record in India and Africa is comparatively young, but the newly discovered pollen fossils in India and Africa of various Asian dipterocarp clades, together with the recent discovery of *Dipterocarpus* leaves from India (9), push back the age of the dipterocarps in India to the Late Cretaceous.

The spatiotemporal context of these fossils has biogeographic implications. One hundred million years ago—when the dipterocarps originated—India would have been too far south and too dry for dipterocarps.

However, 30 million years later, India advanced far enough north to host a more tropical climate and more suitable conditions for successful dipterocarp colonization. Dispersal to India may have also been promoted by the presence of island arcs created by the subduction of the Indian tectonic plate under the Asian plate, although the size and configuration of these islands is still an open question.

Bansal *et al.* highlight the importance of changes in climatic and geographic connectivities for explaining biogeographic distributions and diversity patterns today. Had such paleogeographical and climatic opportunities not presented themselves, the flora of tropical Asia may well now be quite different. Biotic invasions, such as the Africa-to-Asia connection via India (10) or other continental landmasses, are a recurring phenomenon in life's history on this planet. A similar example of intercontinental dispersal was the Panama Isthmus, which 15 Ma reconnected the Americas after a separation of more than 150 million years. This prompted the Great Biotic Interchange of terrestrial organisms (11). But, like all interchanges between two previously isolated landmasses, such exchanges are usually asymmetric. For example, the intrinsic characteristics of interacting biotas may determine which species successfully invade the other biota and which do not. The ability of dipterocarps to successfully colonize and eventually dominate Asian forests may have depended on their symbiotic relationships with root-associated fungi, which may have offered them a competitive edge over the Asian plants that were there before them (12).

The diaspora of the dipterocarps is not unique and is mirrored in the history of the Mauritiaceae palms, another native of Africa that is now extremely successful in South America (13). It is a strange twist of fate that the African tropics, which contributed to the diversity of both the Asian tropics and the Neotropics, are now depauperate, partly because of the climate-driven extinctions in Africa (14). The legacy of Africa lives on and is a testament to the dynamic biophysical theater in which all life on earth takes place; a legacy that will be lost forever if concerted action is not taken to preserve it. ■

REFERENCES AND NOTES

1. P. S. Ashton, in *Flora Malesiana*, series I, *Spermatophyta*, *Flowering Plants*, vol. 9, part 2 (Leiden, 1982), pp. 237–552.
2. A. Shenkin *et al.*, *Front. For. Glob. Change* **2**, 32 (2019).
3. M. Bansal *et al.*, *Science* **375**, 455 (2022).
4. J. Heckenhauer *et al.*, *Bot. J. Linn. Soc.* **185**, 1 (2017).
5. M. J. Benton, P. Wilf, H. Sauquet, *New Phytol.* **10.1111/nph.17822** (2021).
6. R. M. Kooyman *et al.*, *Annu. Rev. Ecol. Syst.* **50**, 119 (2019).
7. S. Klaus *et al.*, *Nat. Commun.* **7**, 12132 (2016).
8. I. C. Romero *et al.*, *Proc. Natl. Acad. Sci. U.S.A.* **117**, 28496 (2020).
9. M. A. Khan *et al.*, *Plant Syst. Evol.* **306**, 90 (2020).
10. R. M. Morley, *J. Trop. Ecol.* **34**, 209 (2018).
11. J. D. Carrillo *et al.*, *Proc. Natl. Acad. Sci. U.S.A.* **117**, 26281 (2020).
12. P. S. Ashton, *Annu. Rev. Ecol. Syst.* **19**, 347 (1988).
13. J. Y. Lim *et al.*, *Glob. Ecol. Biogeogr.* **10.1111/geb.13436** (2021).
14. T. L. P. Couvreur *et al.*, *Biol. Rev.* **96**, 16 (2021).
15. S. Chatterjee, A. Goswami, C. R. Scotese, *Gondwana Res.* **23**, 238 (2013).

ACKNOWLEDGMENTS

We thank C. Cannon, P. van Welzen, P. Roperch, and G. Dupont-Nivet for discussions on dipterocarps and plate boundaries.

10.1126/science.abn6191

CANCER

Modeling tuberous sclerosis with organoids

Single-cell profiling reveals a different path for the development of brain lesions

By Rebecca A. Ihrie¹ and Elizabeth P. Henske²

Tuberous sclerosis complex (TSC) is a devastating disease characterized by distinctive tumors of the skin (angiofibromas), brain [cortical tubers, subependymal nodules (SENs), and subependymal giant cell astrocytomas (SEGAs)], heart (rhabdomyomas), lungs [lymphangioleiomyomatosis (LAM)], and kidney (angiomyolipomas and renal cell carcinoma) (1). Neurologic manifestations can also include seizures and TSC-associated neuropsychiatric disorder, which encompasses aggressive behaviors, autism

understanding of neurological manifestations of TSC.

The unmet clinical need for patients with TSC is enormous, especially for the complex spectrum of neurologic manifestations. Although many neurological features can present soon after birth, whether these features are due to altered prenatal cellular development versus additional effects on postnatal processes such as synaptic pruning, white matter maturation, and brain circuit connectivity remains unclear. A barrier to progress in this area has been challenges in the development of models that fully recapitulate the brain malformations and neu-

these events are required for pathogenesis is unknown (8).

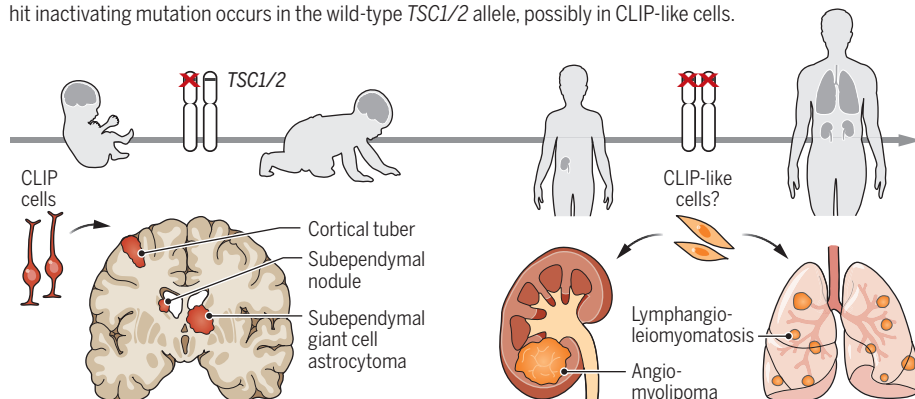
The cell of origin for several manifestations of TSC (including angiomyolipomas, LAM, and brain hamartomas) is not well defined. An additional knowledge gap relates to how TSC is affected by factors such as sex, immune infiltrate, modifying genes, diet, and environmental exposures. Phenotypes and severity are not strictly genotype dependent; individuals with TSC in the same family can have widely different clinical presentation. These knowledge gaps are interrelated with respect to the optimization of disease models for preclinical studies.

Eichmüller *et al.* generate organoids (cell cultures that form three-dimensional masses) using induced pluripotent stem cells (iPSCs) that are derived from TSC patients and then differentiated into neural lineages. These organoids recapitulate two manifestations of TSC: proliferative lesions that resemble SENs or SEGAs and giant cells similar to those in cortical tubers. Using single-cell RNA-sequencing, the authors identify a putative shared cell of origin for both types of lesion, called a caudal late interneuron progenitor (CLIP) cell. CLIP cells express low amounts of TSC2 and thus are hypothesized to be more sensitive to the loss of one *TSC2* allele. CLIP cells are transcriptionally separable from nearby progenitor populations that have been shown to have increased mTORC1 activity and susceptibility to tumor formation (7). The authors argue that brain lesions initially consist of CLIP cells, but other cell types appear during disease progression.

The discovery of CLIP cells, and the hypothesis that they are the precursor of both cortical tubers and subependymal tumors, is potentially a breakthrough in understanding the neurologic manifestations of TSC. These findings contrast with other recent work in human embryonic stem cells cultured into cortical spheroids (9), which showed that loss of both alleles of *TSC1* or *TSC2* was required for altered differentiation and the emergence of dysmorphic cells, supporting a two-hit model of tuber development. This suggests that more than one mechanism can lead to tubers, perhaps depending on the developmental stage. Human iPSC-derived kidney organoids have been found to develop angiomyolipoma-like tumors, but only in the setting of biallelic inactivation of *TSC2*, confirming that two hits are required (10). As or-

Tumorigenesis in tuberous sclerosis complex

Heterozygous germline inactivating mutations in tuberous sclerosis complex 1 (*TSC1*) and *TSC2* result in distinct tumors developing throughout life. Brain lesions present early and likely arise from caudal late interneuron progenitor (CLIP) cells, whereas kidney and pulmonary tumors present later in life when a second-hit inactivating mutation occurs in the wild-type *TSC1/2* allele, possibly in CLIP-like cells.



spectrum disorders, intellectual disability, and psychiatric disorders. TSC is caused by heterozygous germline mutations that inactivate *TSC1* or *TSC2*, which normally inhibit mechanistic target of rapamycin complex 1 (mTORC1). mTORC1 inhibitors are used for the treatment of brain, lung, and kidney tumors and seizures but do not improve all symptoms, and uncertainty persists about how brain tumorigenesis begins. On page 401 of this issue, Eichmüller *et al.* (2) identify a precursor cell that generates cortical tuber-like and subependymal tumor-like cells, increasing the

neuropsychiatric manifestations of TSC. Many animal models diverge from what is seen in patients—for example, requiring loss of additional tumor suppressor genes for tumor development or exhibiting seizures but without evident cortical tubers (3–7).

Uncertainty persists about the mechanisms underlying brain hamartomas, including SEN, SEGA, and tubers. Second-hit genetic events, which cause loss of function in the remaining wild-type copy of *TSC1* or *TSC2*, occur in virtually all TSC-associated renal and lung tumors, which tend to present later in life (see the figure). The second hits lead to unrestrained mTORC1 activity and are believed to be required for tumorigenesis. Second hits in *TSC1* or *TSC2* have been detected in many SENs and SEGAs but not in most cortical tubers; whether

¹Cell & Developmental Biology and Neurological Surgery, Vanderbilt University School of Medicine, Nashville, TN, USA. ²Pulmonary and Critical Care Medicine, Brigham and Women's Hospital, Harvard Medical School, Boston, MA, USA. Email: ehenske@bwh.harvard.edu

ganoid models and studies of patient tissue advance, critical questions will be whether other TSC-associated tumors have CLIP cell-like features, including low amounts of TSC protein, and whether second hits in the *TSC* genes are required for initiation.

It remains unknown what targetable features are distinct to CLIP cells. Although epidermal growth factor receptor (EGFR) is expressed in CLIP cells, and Eichmüller *et al.* find that EGFR inhibition blocks lesion outgrowth in organoids, other progenitor populations in the brain also dynamically express EGFR but appear less susceptible to the effects of *TSC2* mutation (11). The relative prevalence of subcortical tumors in patients raises an additional question: If the CLIP-like state in *TSC2*-heterozygous cells is sufficient to induce formation of all brain hamartomas, why do many TSC patients develop SENs but a minority suffer from the larger SEGA tumors? Immune infiltration, which is not yet captured in TSC organoid studies, may be an important modulator of this and other manifestations (12). Further development of organoid models has the potential to approach these questions to better understand TSC and other rare disorders (13, 14).

It will be essential to determine how the cell types described by Eichmüller *et al.* align with recent single-cell studies of human development. In particular, emerging data from cellular barcoding and lineage tracing suggest that neuronal lineages previously thought to be generated in separate subregions of the developing brain by either cortical progenitors or caudal ganglionic eminence progenitors, which produce CLIP cells, can both emerge from single cortical progenitor cells (15). If a CLIP-like state emerges in parallel in multiple lineages during development, this would again change our understanding of where and how TSC tumors arise. ■

REFERENCES AND NOTES

1. E. P. Henske, S. Jóźwiak, J. C. Kingswood, J. R. Sampson, E. A. Thiele, *Nat. Rev. Dis. Primers* **2**, 16035 (2016).
2. O. L. Eichmüller, *Science* **375**, eaabf5546 (2022).
3. D. M. Feliciano, T. Su, J. Lopez, J. C. Platel, A. Bordey, *J. Clin. Invest.* **121**, 1596 (2011).
4. J. Zou, B. Zhang, D. H. Gutmann, M. Wong, *Epilepsia* **58**, 2053 (2017).
5. J. Zhou *et al.*, *Genes Dev.* **25**, 1595 (2011).
6. P. Zordan *et al.*, *J. Clin. Invest.* **128**, 1688 (2018).
7. G. V. Rushing *et al.*, *Life Sci. Alliance* **2**, e201800218 (2019).
8. A. Bonghaarts *et al.*, *Oncotarget* **8**, 95516 (2017).
9. J. D. Blair, D. Hockemeyer, H. S. Bateup, *Nat. Med.* **24**, 1568 (2018).
10. J. O. R. Hernandez *et al.*, *Nat. Commun.* **12**, 6496 (2021).
11. W. Huang *et al.*, *Cell* **182**, 594 (2020).
12. H. J. Liu *et al.*, *JCI Insight* **3**, e98674 (2018).
13. P. Martin *et al.*, *Mol. Autism* **11**, 2 (2020).
14. K. D. Winden *et al.*, *J. Neurosci.* **39**, 9294 (2019).
15. R. N. Delgado *et al.*, *Nature* **10.1038/s41586-021-04230-7** (2021).

ACKNOWLEDGMENTS

The authors thank S. Bagwe for assistance.

10.1126/science.abn6158

NEUROSCIENCE

Human cortical interneuron development unraveled

New understanding of principles of neurogenesis widens the use of preclinical models

By Nicoletta Kessaris

The cerebral cortex is the most enlarged component of the human brain. It is the seat for higher-order brain functions and the biggest information processing center of the human brain. Interneurons, one of two major classes of neurons in the cortex, have expanded in number in proportion to cortical volume, but their diversity—the number of different subtypes—remains comparable to that of rodents. Shi *et al.* (1) reported conservation of the genetic networks that instruct interneuron identities between human and mouse, explaining how the same set of interneuron subtypes arises across species. On page 402 of this issue, Paredes *et al.* (2) find a distinctive cellular organization of the embryonic brain area where cortical interneurons are born and an extended period of neurogenesis in humans compared with rodents, explaining how interneuron numbers have increased. These studies aid our understanding of human cortical interneuron development and provide a framework for studying human disease.

Improvements in single-cell isolation techniques, large-scale gene expression technologies, and data analysis tools have enabled the characterization and comparison of individual neurons from different species. Between 40 and 60 different subtypes of interneurons have been identified in the adult mouse cortex (3), and homologs of these have been detected in humans, with variation in abundance, distribution, gene expression, and morphology (4, 5). What is the importance of this diversity? Distinct functions have been identified for some of the most abundant populations, but the roles of all the different interneuron populations in cortical function and animal behavior are far from understood. Progress has been hampered by our failure, until recently, to comprehend the full extent of interneuron diversity and

our inability to identify different subtypes in live behaving animals. As genetic tools and technologies for detecting and imaging single neurons and their activities in intact brains improve, so will our insight into the function of interneuron diversity.

The origin of cortical interneurons in the embryonic brain has been extensively studied in mice. Two major sources have been identified in the subcortical brain: the medial and caudal ganglionic eminences (MGE and CGE) (6). Both are found in human embryonic brains, and immature cortical interneurons have been seen migrating out toward the developing cortex in slice cultures (7, 8). How 40 to 60 different types of cortical interneurons arise from two pools of neural stem cells in the embryo remains unknown. Major regulators of gene expression have been identified in neural stem cells and immature cortical interneurons in rodents, but so far, these are insufficient to explain the complexity of the cortical interneuron population (9, 10). The concept of “nature versus nurture” has been invoked: Could some diversity be imposed after cortical interneurons enter the cortex and settle at their final destinations?

To decipher the extent to which interneuron characteristics are determined at the source and to identify genetic pathways that generate diversity, transcriptomic analyses have been performed on single cells isolated from mouse (11, 12) and human (1, 13) embryonic ganglionic eminences. This involved the isolation of neuronal progenitors—neural stem cells—and young neurons from the embryonic brain and the characterization of gene expression in each cell. All four studies demonstrated that immature, but genetically discernible, cortical interneuron subtypes can be identified soon after they are generated in the ganglionic eminences and before they enter the cortex. This argues against major identity characteristics acquired *de novo* when these cells reach their destination. These findings also suggest that the transcriptomic signatures that interneurons exhibit upon maturation are largely defined at the source when these cells are born, through genetic programs

Wolfson Institute for Biomedical Research and Department of Cell and Developmental Biology, University College London, Gower Street, London, UK. Email: n.kessaris@ucl.ac.uk

that unfold gradually as the cells mature. Shi *et al.* also showed conservation between mouse and human gene networks that drive major developmental processes for cortical interneurons, including migration into the cortex, specialization, and acquisition of final characteristics. This provides a clear view of how the repertoire of cortical interneurons has been conserved between the

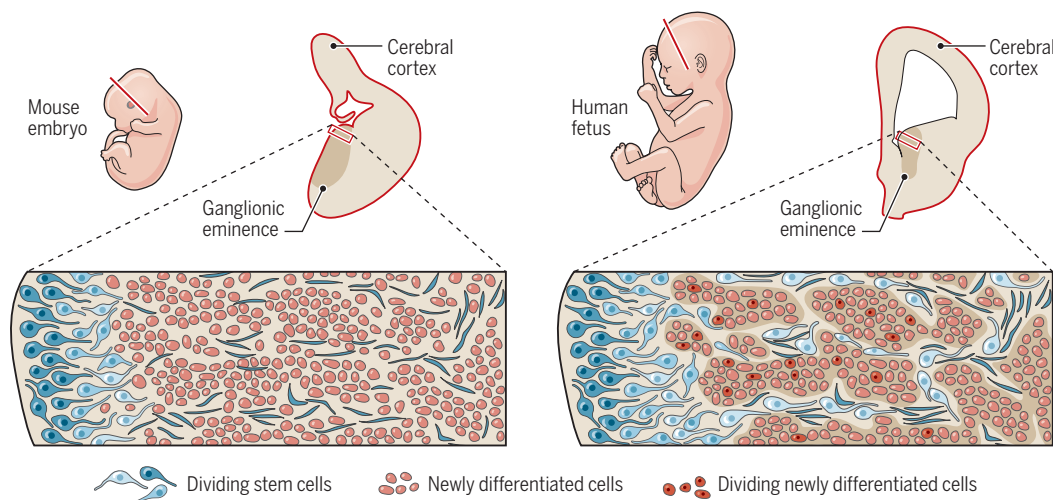
figure). This increase in neuron numbers in humans is thought to underlie the highly evolved human brain (14); with greater numbers come greater brain size and capacity and a greater computational power that is not seen in other species. Embryonic development emerges from these and other studies as one of the most critical and, at the same time, vulnerable periods when

two species but it also provides us with the exciting prospect of transplanting human progenitors or newly differentiated neurons into the rodent cortex to study human interneuron biology, interneuron disease states, and potential drug-based therapies in an *in vivo* setting.

Studies in preclinical models are essential before cortical interneuron transplantation therapies can comfortably move to the clinic. Many questions can be addressed in these models, including identifying the disorders that can be treated with transplantation and which interneuron subtypes are essential in each case. Such models can also be used to study the optimal therapeutic window for each disorder and how cortical interneurons develop, differentiate, integrate, and survive in transplantation settings. They can also help to ascertain how effective these therapies might be. Although such refinements are taking place in preclinical settings, the first-in-human clinical trial for interneuron cell therapy to treat patients with unilateral medial

Building the human cerebral cortical interneuron repertoire

Basic developmental processes and genetic networks underlying the generation of cortical interneurons are similar between mice and humans, allowing the same subtypes of interneurons to arise but with different population sizes. Additions to the stem-cell pool, with differentiated cells being able to divide, allowed the expansion of interneurons in humans.



temporal lobe epilepsy is already being prepared (NCT05135091), spearheading human cortical interneuron transplantation therapy. ■

two species. Major questions remain about how genetic networks and epigenetic modulators translate into distinct transcriptomic identities and how these developmental programs are influenced by external signals, either from neighboring neurons and glia or from outside of the brain. If genetic networks and diversity are conserved, how are interneuron numbers expanded in humans? Paredes *et al.* identified distinctive features in the cellular organization of the MGE in humans. Unlike the mouse MGE, where dividing interneuron progenitor cells reside mainly within a specific compartment of the MGE close to the central lumen, the progenitor zone in humans extends further into the parenchyma and becomes intermingled with newly born neurons (7). In addition, Paredes *et al.* discovered newly differentiated cells that are capable of continued cell division before generating postmitotic neurons. These findings show that not only the territory of the progenitor zone but also the types of neurogenic cells within it and the duration of neurogenesis are expanded, thus allowing for amplification of the number of cortical interneurons that are generated in humans relative to rodents (see the

neuronal diversity and cell numbers are set up. Genetic errors or external insults inflicted during embryogenesis are likely to cause permanent faults in brain development and later functions.

Cortical interneuron defects have been associated with childhood-onset disorders such as autism spectrum disorder and conditions of reduced interneuron function that result in epilepsy. MGE interneuron progenitors have been transplanted into the cerebral cortex of mice to replenish missing or faulty interneurons. Grafted cells were found to disperse long distances, integrate, and mature in the host brain. These experiments in mice have shown great promise for the treatment of interneuron-related deficiencies (15). Breakthrough studies have shown that cortical interneurons can be generated from mouse and human embryonic stem cells or induced pluripotent stem cells (iPSCs), opening up the possibility of developing personalized human therapies. Paredes *et al.* now show that human-derived embryonic MGE cells can fully mature and contribute to neural circuits when grafted into the mouse brain. Not only does this work reinforce the view that cortical interneurons are conserved between the

REFERENCES AND NOTES

1. Y. Shi *et al.*, *Science* **374**, eab6641 (2021).
2. M. F. Paredes *et al.*, *Science* **375**, eabk2346 (2022).
3. B. Tasic *et al.*, *Nature* **563**, 72 (2018).
4. R. D. Hodge *et al.*, *Nature* **573**, 61 (2019).
5. F. M. Krienen *et al.*, *Nature* **586**, 262 (2020).
6. C. P. Wonders, S. A. Anderson, *Nat. Rev. Neurosci.* **7**, 687 (2006).
7. D. V. Hansen *et al.*, *Nat. Neurosci.* **16**, 1576 (2013).
8. T. Ma *et al.*, *Nat. Neurosci.* **16**, 1588 (2013).
9. J. S. Hu, D. Vogt, M. Sandberg, J. L. Rubenstein, *Development* **144**, 3867 (2017).
10. N. Kessaris, L. Magno, A. N. Rubin, M. G. Oliveira, *Curr. Opin. Neurobiol.* **26**, 79 (2014).
11. C. Mayer *et al.*, *Nature* **555**, 457 (2018).
12. D. Mi *et al.*, *Science* **360**, 81 (2018).
13. Y. Yu *et al.*, *Nat. Neurosci.* **24**, 1745 (2021).
14. S. Herculanu-Houzel, *Proc. Natl. Acad. Sci. U.S.A.* **109**, 10661 (2012).
15. R. F. Hunt, S. C. Baraban, *Cold Spring Harb. Perspect. Med.* **5**, a022376 (2015).

ACKNOWLEDGMENTS

I thank W. Richardson, D. Kullmann, and H. Kessaris for comments and discussion. Funding is provided by the UK Biotechnology and Biological Sciences Research Council (BB/N009061/1) and the UK Wellcome Trust (108726/Z/15/Z).

RETROSPECTIVE

Edward O. Wilson (1929–2021)

Pioneering naturalist with far-reaching insights

By **Stuart Pimm**

Edward Osborne Wilson, who wrote extensively on ants and popularized the field of sociobiology, died on 26 December 2021 at age 92. Ed vigorously promoted the idea of biodiversity and understood that the concepts of island biogeography apply to the fragmented habitats pervading much of the world. He titled his autobiography *Naturalist* and proudly considered himself to be one. Ants were his first love, and he used the insights he gained from studying them to understand the living world and the place of humans in it.

Ed was born in Birmingham, Alabama, on 10 June 1929, and he always celebrated his southern heritage. An early fishing accident left him blind in one eye. Because of this deficit, he was at greatest ease when studying small things, and ants quickly became his passion. He earned his BS and MS degrees in 1950, studying biology at the University of Alabama. After that, at the University of Tennessee, his professors recommended he move to Harvard University, which he did. He received his PhD in 1955 in biology. In 1956, he joined the Harvard faculty, and he remained there for the rest of his career.

Ed's earliest papers were on the natural history and taxonomy of ants. His work ranged in geography from Puerto Rico to New Guinea. It covered ant geographical distributions, their social behavior, and how they communicate using pheromones. His prolific subsequent writing includes a taxonomic revision of the genus *Pheidole* in 2003 and his only novel, *Anthill*, in 2010. His last book, *Tales from the Ant World*, published in 2020, was also autobiographical.

In 1963, Ed published his equilibrium theory of island geography with ecologist Robert MacArthur. They observed that smaller oceanic islands and those that are farther from mainland have fewer species. The "equilibrium" refers to the hypothesized processes that explain these patterns—the extinction of small island populations and the recolonization from individuals of species that make it to the island. Ed and his

then-graduate student Dan Simberloff set out to test the theory on small mangrove islands in Florida Bay. Their work not only confirmed their predictions but also initiated an era of ecological experiments.

The influential equilibrium theory extended beyond oceanic islands to "habitat islands"—forest patches left behind by human actions. Ed anticipated, and later large-scale experiments initiated by ecologist Thomas Lovejoy in the Amazon confirmed, that the smaller a habitat fragment, the more species will die out and the more quickly they will do so. Globally, habitat loss



and fragmentation drive biodiversity loss, a term Lovejoy coined and Ed promoted. They both advocated reconnecting habitats with restoration, a practical solution that undoes the habitats' island nature and slows biodiversity loss.

In his 1975 book *Sociobiology: The New Synthesis*, Ed reported a monumental survey of the wide range of animal societies, including our own. That natural selection might shape human behaviors was questioned by some. Many critics made ad hominem attacks, which were short on scientific content. Ed responded vigorously, noting that the adaptive value of animal behaviors was not in dispute, however disturbing this might be to political philosophies. During this time, someone famously threw water

onto Ed at a meeting—the amount involved grows with every telling of the story. When Ed told it, it was with a twinkle and an appreciation of this unique honor.

Ed's accolades were many. He was awarded the US National Medal of Science in 1977 and top environmental prizes in Europe (such as the Crafoord Prize in 1990), North America (the Tyler Prize in 1984), and Asia (the International Cosmos Prize in 2012). *On Human Nature* and *The Ants*, co-written with Bert Hölldobler, both earned him a Pulitzer Prize (in 1979 and 1991, respectively).

I met Ed in the mid-1970s at a scientific meeting, and we talked often thereafter. On one memorable afternoon about a decade ago, he called to talk about ants (of course). He asked me about the evolution within and the natural history of the Hawaiian Islands, where I had worked extensively. They were, originally at least, ant-free. Ed considered ants to be "the little things that rule the world," and he wondered aloud what would happen where they did not rule and how species might have evolved differently. This conversation exemplified his boundless curiosity. Ed was always asking new questions. Not all of them paid off. Those that did changed biology.

"Oh, to be 80 again!" Ed said to me a few years back. But in the past two decades, his energy for writing books was astonishing. Ed was known to many through his popular writings. Who cannot be enchanted by the following declaration: "Anywhere I am in the world I love it when the air is warm and moist, and heat bounces off the sunlit earth, and insects swarm in the air and alight on flowers"? But the book in which this quote appears, *A Window on Eternity* (2014), an account of his first trip to Africa, is no mere travelogue. As he celebrates biodiversity—even the Matabele ant that bites him—he makes a passionate plea for the future of our planet. Current actions, he writes, will lead to a further "slide into extinction [and] will turn the Anthropocene into the Eremocene, the Age of Loneliness."

Ed described his vision for our human future in his 2016 book *Half-Earth*. We must protect biodiversity, celebrate it, be fascinated by it, and protect at least half of nature, giving species a chance to survive and preserving our mental well-being. It is a safe limit, and it is an aspiration for all whom he inspired. And they are legion. Since his death, social media brims with photos of Ed signing books and linking arms with students and younger colleagues and with tales of how much he helped them. He enjoyed those interactions with students above all. ■

Nicholas School of the Environment, Duke University, Durham, NC, USA, and Saving Nature, Durham, NC, USA.
Email: stuartpimm@me.com

10.1126/science.abn9848

POLICY FORUM

SUSTAINABILITY

China's seafood imports— Not for domestic consumption?

An estimated 74.9% of China's seafood imports are reexported

By **Frank Asche**^{1,2}, **Bixuan Yang**³,
Jessica A. Gephart⁴, **Martin D. Smith**⁵,
James L. Anderson³, **Edward V. Camp**¹, **Taryn
M. Garlock**¹, **David C. Love**⁶, **Atle Oglend**²,
Hans-Martin Straume⁷

Global trade in seafood is tightly coupled with environmental, economic, and social sustainability (1–3). Yet, two features of global seafood trade hamper efforts to promote sustainability. First, the recent practice of importing seafood, processing it, and then exporting it (“reexporting”) at a large scale complicates tracing seafood from the water to the plate and enables mislabeling (4). Second, reexports can exacerbate problems stemming from distant-water fishing (DWF), i.e., fish caught in international waters and other countries’ economic zones. DWF obscures the distinction between domestic and imported seafood and is implicated in illegal, unreported, and unregulated (IUU) fishing and other unsustainable practices (5). Both features highlight the critical role of China (5, 6), the world’s largest DWF nation and largest seafood producer, consumer, exporter, and importer (by volume). Contradicting the narrative that Chinese domestic demand is driving imports, we estimate that 74.9% of imports to China are processed and reexported.

Nearly all these imports are from fisheries rather than aquaculture, and for some species, exports are substantially higher than imports plus Chinese production, suggesting mislabeling [see supplementary materials (SM) for all data, methods, and code]. For instance, China is a leading exporter of species like cod for which it does not have domestic catches. Instead, China relies on imported raw materials from multiple species and origins, such as Russian Alaska pollock and Norwegian cod (see SM). Hence, since 2000, China has increasingly become the world’s fish processor.

Traditionally, the majority of seafood, which is the most traded food commodity, was harvested from wild fish populations, processed near fishing grounds, and traded to large population centers. Globally, this structure created an important role for coastal communities where fish were processed and preserved before continuing their journey toward the final consumers, often far away. From the turn of the century, improved preservation technologies, combined with low transportation costs, have increasingly challenged this model: Relatively unprocessed seafood such as whole frozen fish can be shipped over long distances before secondary processing such as filleting is undertaken, and finished products may travel long distances again before reaching final markets (7).

Low wages and an undervalued currency explain the improved competitiveness of Chinese manufacturing in general (8), and because seafood processing is labor-intensive, these factors make China highly competitive in seafood processing. Low transportation costs for frozen seafood augment China’s competitive edge in seafood processing over other coastal nations. The new structure of processing for reexport severs the link between fish stocks and coastal communities and inflates the share of seafood that is traded internationally. With 74.9% of China’s imports being reexported, 11.3% of the global seafood trade is counted first as imports to China and then as imports to the final destination market (see SM). Reexporting can also increase revenue from the same supply of raw product because labor-intensive manual processing gives higher yields than machine processing (9). Secondary processing reinforces competitiveness of the new structure by allowing processing plants to obtain inputs year-round and thus increase capacity utilization relative to processors dependent on local fishery landings in compressed seasons (10). Low wages and the requisite tech-

nologies are not specific to China, suggesting that other countries could adopt the Chinese reexport model and further transform global seafood markets. But at present, most of the world’s largest importers, such as the US and Japan, are primarily consuming seafood and not processing for reexport.

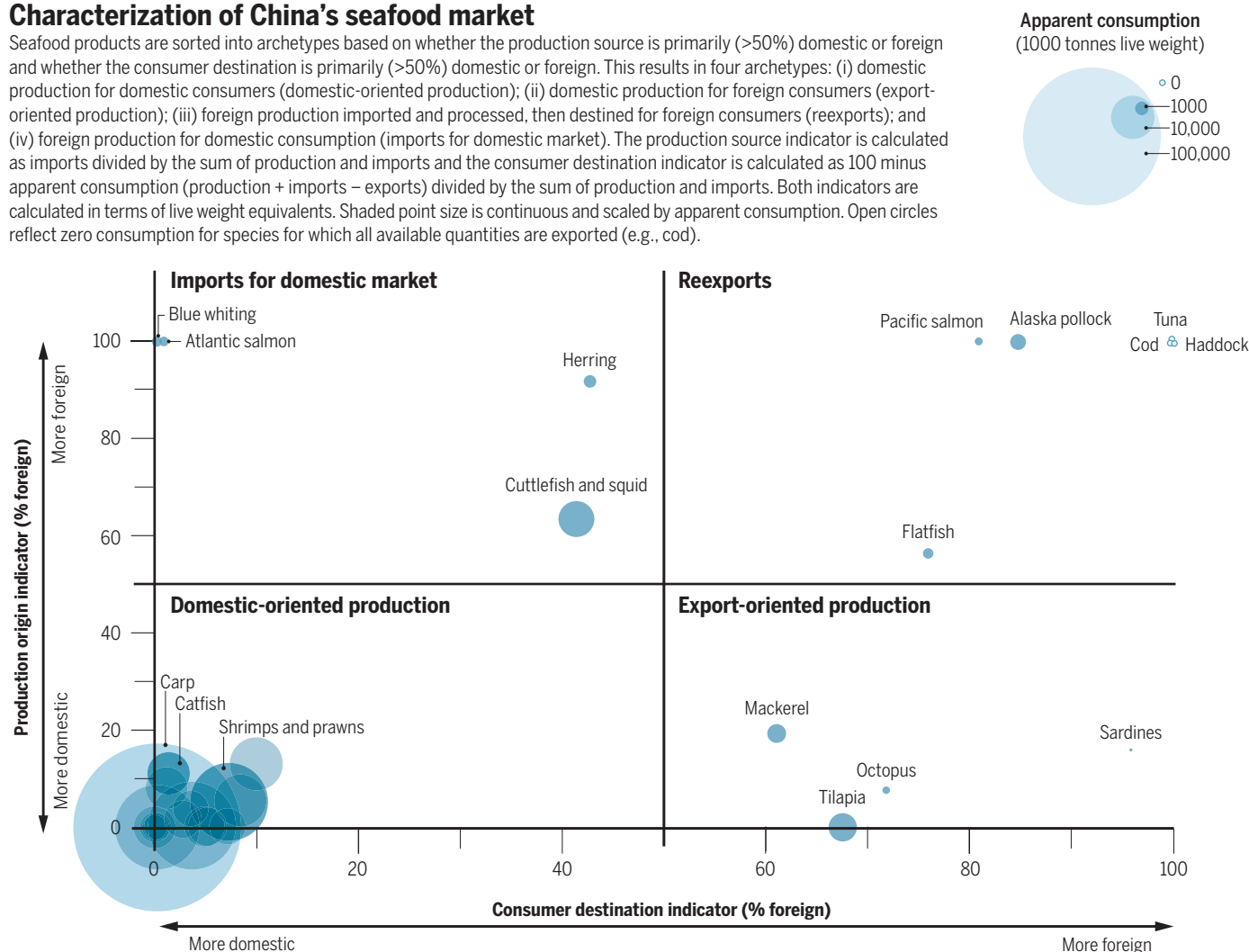
Although high-quality data exist at different levels in the supply chain, data are collected for various purposes, and it is, to our knowledge, never the purpose to compare quantities at different stages in the supply chain. The member countries of the World Trade Organization collect trade data, and they also collect production data, but that is normally done by different organizations. This makes it difficult to reconcile seafood production and trade data because of mismatches in species- versus product-level reporting and weight losses during processing (4). Consequently, species-level data on imports, country of origin, processing, and reexports are scarce. To gain insights about China’s role in the global seafood industry, we convert quantities of different product forms in imports and exports by species group with the same approach used to estimate apparent consumption (4). Conversion factors make the weights of different product forms at different stages in the supply chain comparable (see SM).

The top 15 imported species groups account for 76.5% of China’s total seafood imports and 89.2% of the imports of identified species. Alaska pollock, primarily from Russia, accounts for over 21% of imports (see the table). Cuttlefish and squid, salmon, whitefish (cod, blue whiting, haddock, and hake), and pelagic species (mackerel, herring, and tuna) are also important species groups. Of the top 15 species groups, five are almost exclusively for reexport (reexport share > 75%), and six appear to be primarily imported for domestic consumption. Only three of the species groups—Atlantic salmon, catfish, and shrimp—are primarily produced by aquaculture (11), and these all have small reexport shares. Among all finfish imported into China, 91% are whole frozen fish (see SM), a product category that typically is further processed before the final point of sale. For six species groups, the whitefish, and salmon species, China has no domestic landings. This confirms that exports of these species rely entirely on imports. There are three species groups for which the exports exceed imports plus production. This situation could reflect imprecise conversion factors, short-weighting, and reporting error, includ-

¹School of Forest, Fisheries, and Geomatics Sciences and Food Systems Institute, University of Florida, Gainesville, FL, USA. ²Department of Safety, Economics and Planning, University of Stavanger, Stavanger, Norway. ³Food and Resource Economics Department and Food Systems Institute, University of Florida, Gainesville, FL, USA. ⁴Department of Environmental Science, American University, Washington, DC, USA. ⁵Nicholas School of the Environment and Department of Economics, Duke University, Durham, NC, USA. ⁶Johns Hopkins Center for a Livable Future and Department of Environmental Health and Engineering, Bloomberg School of Public Health, Johns Hopkins University, Baltimore, MD, USA. ⁷Department of Economics, BI Norwegian Business School, Bergen, Norway. Email: frank.asche@ufl.edu

Characterization of China's seafood market

Seafood products are sorted into archetypes based on whether the production source is primarily (>50%) domestic or foreign and whether the consumer destination is primarily (>50%) domestic or foreign. This results in four archetypes: (i) domestic production for domestic consumers (domestic-oriented production); (ii) domestic production for foreign consumers (export-oriented production); (iii) foreign production imported and processed, then destined for foreign consumers (reexports); and (iv) foreign production for domestic consumption (imports for domestic market). The production source indicator is calculated as imports divided by the sum of production and imports and the consumer destination indicator is calculated as 100 minus apparent consumption (production + imports – exports) divided by the sum of production and imports. Both indicators are calculated in terms of live weight equivalents. Shaded point size is continuous and scaled by apparent consumption. Open circles reflect zero consumption for species for which all available quantities are exported (e.g., cod).



ing IUU landings (see SM). For the two high-valued whitefish species—cod and haddock—exports are about 35% higher than imports, suggesting that a cheaper whitefish such as blue whiting, for which there are no recorded exports, is mislabeled. For tuna the reexport share is most likely greater than 100% because DWF landings are recorded not as tuna but instead in the “not specified” category.

Two species groups dominate the long-distance Chinese DWF landings—cuttlefish and squid (71.6%) and tuna (15.3%) (see SM)—and both are important in imports and reexports (see the first table). For both species groups, the exports are larger than the imports but lower than imports plus the landings of the DWF fleet. For groups like shrimp, crab, and hairtail, Chinese production is substantially larger than exports, highlighting the importance of the domestic market despite China being a large exporter of these species groups.

To further explore the Chinese seafood market, we constructed an indicator to ac-

count for origin (where the seafood is produced) and destination (where the seafood is consumed), using the 20 largest species groups by production and the 15 largest species groups by imports and exports. These indicators are sorted into four archetypes based on whether the production source is primarily (>50%) domestic or foreign and whether the consumer destination is primarily (>50%) domestic or foreign: (i) domestic production for domestic consumers, (ii) domestic production for foreign consumers, (iii) reexports, and (iv) imports for the domestic market (see the figure). Most species and those with the largest volumes are in the lower left-hand quadrant of the figure. Hence, domestic production primarily for domestic consumption is by far the dominant archetype. Except for tilapia, all aquaculture species that contribute most of China's seafood production fall within this archetype, and the importance of carp is apparent. However, there is some dispersion toward the right, indicating substantial export quantities for some domestically

produced species groups, e.g., shrimp. Only a few species groups are primarily export-oriented, including sardines, mackerel, octopus, and tilapia, and a few species are primarily imported for domestic consumption, such as Atlantic salmon, or as in the case of blue whiting, most likely exported under a different name. The upper right quadrant contains six major species groups that are primarily imported for reexport, with species in the upper right corner, such as cod, having essentially no domestic production or consumption. We find that most Chinese seafood imports for processing and reexport are wild caught.

These findings largely contradict the narrative that Chinese domestic demand is driving massive Chinese imports because imports are positively correlated with economic and population growth (6, 12), although some imported species like Atlantic salmon primarily go to the domestic market (see the table). Instead, Chinese processing of wild-caught fish for reexport outcompetes processing in other parts of the world in a

way that resembles China's success in manufacturing more broadly, but that is a new development in seafood. Yet, China does not play a comparable role in the global aquaculture industry. Seafood processing thus can be competitive in high-income countries such as Canada and Norway despite favorable conditions of low wages and cost in China.

Our analysis of China's position in global seafood trade has two important policy implications for seafood sustainability. First, work must be done to increase traceability in the global seafood system. Although other products face traceability challenges, features of seafood make traceability especially difficult, including the high degree of international trade (1); the fact that the raw product is processed so that the next step in the supply chain involves smaller pieces of the whole that can be difficult to identify; the sheer number of species of fish and shellfish in seafood markets; and DWF fisheries that are conducted in other countries' waters or entirely outside of any nation's jurisdiction (the high seas). Traceability challenges means that large quantities may be harvested and not reported at all (5).

Narratives that emphasize Chinese domestic demand as driving China's role in the seafood system (6, 12) pay too little attention to the reexport model, which highlights the complexity of tracing seafood sustainability. The same product can be harvested in multiple countries with different management and labor conditions and come in reexport data.

For example, 57% and 39% of Pacific salmon imports originate in the US and Russia, respectively. This is crucial for seafood sustainability because the processing stage is an opportunity for seafood mislabeling with respect to country of origin and species. Consistent with this concern, we find that exports as a share of combined imports and production exceed 100% for some higher-valued species such as cod and haddock, providing evidence of mislabeling. In conjunction with other questionable practices such as IUU fishing directly (5) and providing a market for IUU fish from other countries, mislabeling can be a serious challenge for fish stocks as well as food safety.

Initiatives to limit IUU fishing such as the European Union's red and yellow card system, the US Seafood Import Monitoring

Chinese seafood imports and reexports 2012–2019

Import quantity is in product weight. Import share is imports/(imports + domestic production). Reexport share is exports/(domestic production + imports), where all quantities are converted to live weight equivalents. MT, metric tons.

| SPECIES | IMPORTS (1,000 MT) | IMPORT SHARE BY QUANTITY (%) | DOMESTIC PRODUCTION (1,000 MT) | REEXPORT SHARE (%) |
|----------------------|-----------------------|------------------------------------|--------------------------------------|-----------------------|
| Alaska pollock | 5,148.25 | 21.1 | 0 | 84.8 |
| Cuttlefish and squid | 2,464.69 | 10.1 | 7,870 | 40.9 |
| Shrimp and prawns | 1,512.98 | 6.2 | 31,456 | 7.3 |
| Cod | 1,490.87 | 6.1 | 0 | 136.0 |
| Herring | 1,288.65 | 5.3 | 116 | 42.8 |
| Pacific salmon | 1,281.56 | 5.3 | 0 | 82.1 |
| Flatfish | 1,106.99 | 4.5 | 1,012 | 76.0 |
| Mackerel | 874.26 | 3.6 | 3,728 | 61.1 |
| Tuna | 696.33 | 2.9 | 813 | 155.3 |
| Crab | 525.57 | 2.2 | 14,252 | 8.4 |
| Hairtails | 518.11 | 2.1 | 8,294 | 1.2 |
| Catfish | 490.26 | 2.0 | 8,233 | 1.4 |
| Blue whiting | 449.01 | 1.8 | 0 | 0.2 |
| Atlantic salmon | 413.83 | 1.7 | 0 | 0.9 |
| Haddock | 356.60 | 1.5 | 0 | 135.0 |

Program, and efforts to develop a global seafood traceability system (<https://traceability-dialogue.org/>) are a start, but their reach is still limited. For example, the US program does not even include Alaska pollock and salmon. Systematic use of blockchain technology and international coordination could enable tracing seafood from different territorial waters that are comingled in processing and reexported and thereby reduce incentives for overfishing.

Second, fisheries management systems can inadvertently disadvantage local processing and increase the competitiveness of the reexport model. For example, a total catch limit in a fishery without quotas for individual vessels may hold the fish stock at a sustainable level, but it creates incentives for each vessel to race to catch fish before the catch limit is reached and the fishing season ends. This racing concentrates landings early in the season and leaves processors with minimal fish to process later in the season (10, 13). A consequence is idle or underutilized processing capacity part of the year, effectively increasing the costs of local processing, increasing China's competitiveness as a reexporter. By creating less economic value and fewer jobs locally in the processing sector, fisheries management thus can undermine social sustainability (14). Alternatively, fisheries management that spreads out catches can enhance social sustainability by increasing capacity utilization. Catch shares is one system that empirically has been shown to slow the race to fish (10) and thus

could enhance competitiveness of local processing.

China's limited role as a reexporter of farmed seafood is consistent with this characterization of fisheries management and social sustainability. The vast majority of imports from China's top-15 species groups are not from fisheries managed with catch shares that spread out the catch (table S2), e.g., Russian Alaskan Pollock, Russian cod, and Pacific salmon. So, it is not surprising that China can compete in processing these species groups. Aquaculture processing, by contrast, does not suffer from the same problems of seasonality. By controlling the production process, aquaculture can time the harvest to maintain high-capacity utilization, making local processing more competitive with the reexport model. This feature of aquaculture can explain why China

has limited farmed seafood reexports. Ultimately, maintaining seafood processing locally contributes to social sustainability of fisheries (15), and social sustainability, in turn, mutually reinforces economic and ecological sustainability (14). ■

REFERENCES AND NOTES

1. F. Asche, M. Bellemare, C. Roheim, M. D. Smith, S. Tveterås, *World Dev.* **67**, 151 (2015).
2. J. A. Gephart, M. L. Pace, *Environ. Res. Lett.* **10**, 125014 (2015).
3. U. R. Sumaila *et al.*, *Sci. Adv.* **6**, eaaz3801 (2020).
4. K. Kroetz *et al.*, *Proc. Natl. Acad. Sci. U.S.A.* **117**, 30318 (2020).
5. D. Pauly *et al.*, *Fish Fish.* **15**, 474 (2014).
6. B. Crona *et al.*, *One Earth* **3**, 32 (2020).
7. J. L. Anderson, F. Asche, T. Garlock, *J. Commod. Markets* **12**, 2 (2018).
8. F. G. Adams, B. Gangnes, Y. Shachmurov, *World Econ.* **29**, 95 (2006).
9. J. S. Ng, "Development of China as the world's largest reprocessing centre of frozen fish products and future challenges for the industry" in *Global Trade Conference on Aquaculture* (Food and Agriculture Organization of the United Nations, Rome, 2007), pp. 221–226.
10. A. M. Birkenbach, D. J. Kaczan, M. D. Smith, *Nature* **544**, 223 (2017).
11. T. Garlock *et al.*, *Rev. Fish. Sci. Aquacult.* **28**, 107 (2020).
12. J. K. Abbott, D. Willard, J. Xu, *Mar. Policy* **133**, 104733 (2021).
13. F. R. Homans, J. E. Wilen, *J. Environ. Econ. Manage.* **49**, 381 (2005).
14. F. Asche *et al.*, *Proc. Natl. Acad. Sci. U.S.A.* **115**, 11221 (2018).
15. J. N. Kittinger *et al.*, *Science* **356**, 912 (2017).

ACKNOWLEDGMENTS

Funding was provided by the US Department of Agriculture INFEWS grant 2018-67003-27408 (F.A., B.Y., J.L.A., D.C.L.), Norwegian Research Council grants 324685 and 295114 (F.A., B.Y., A.O., H.-M.S.) and Florida Sea Grant (F.A., J.L.A.). The conclusions are those of the researchers and do not necessarily reflect the views of the funding organizations.

10.1126/science.abl4756



A worker gathers items at an Amazon distribution center in Phoenix, Arizona, in November 2013.

BOOKS *et al.*

LABOR

The tech workforce you don't see

From fulfillment centers to social media sites, human labor is essential to digital success

By Janine Berg

The tech industry has been successful in making us believe that the programs, websites, and apps we rely on work instantly and flawlessly, with information stored in clouds and powered by snack-eating programmers who take breaks to play ping-pong. Yet behind this illusion lies a globe-spanning army, millions in size, of laborers performing tasks that ensure the smooth operation of our digital world.

Moritz Altenried's highly readable and eye-opening book, *The Digital Factory*, demystifies automated technology and describes in persuasive detail the human labor behind the technology that drives the economy and our daily lives. It joins a growing literature that questions the myth, propagated by the tech community, of a future without work.

Altenried surveys the numerous occupations that ensure the smooth functioning of technological systems and industries and highlights the largely precarious work behind an array of services, from search engines and social media sites to gaming and online shopping. Most importantly, he documents how technological systems are used to manage the work process, resulting in what he calls "digital Taylorism." In doing so, he brings to the fore the real challenge facing the world of work: how to ensure good working conditions

and a living wage in a world of unregulated and often cross-border digital labor.

The Digital Factory is organized around the labor process in four areas: logistics, gaming, crowdwork, and social media. Beginning with logistics, Altenried describes how the shipping container and its digitization propelled globalization and reshaped work across the world. While a wide range of new occupations are associated with this transformation, the chapter focuses on distribution and delivery, including workers in Amazon's fulfillment centers and those involved in last-mile delivery. At the Brieselang fulfillment center, just outside of Berlin, we learn that temporary workers outnumber permanent employees by a four-to-one ratio. Every movement in the distribution centers is so highly regulated and standardized that one manager in the UK describes the resulting labor as "human automation."

Similarly precarious working conditions can be found in the gaming industry. Readers learn about the business of gold farming, an industry composed of upwards of 1 million workers employed in gaming workshops throughout China who harvest in-game items in the *World of Warcraft* to sell to Western players who prefer to purchase upgrades that enable them to leapfrog the more tedious parts of the game. Meanwhile in Berlin, Altenried describes the long hours, low pay,

and repetitive work experienced by the city's game testers, many of whom are attracted to the job because of their passion for gaming but who quickly grow tired of clicking their computer mouse "at least seventy thousand times" a day. Pay in the industry is notoriously low, with workers earning five euros an hour prior to the introduction of the national minimum wage in Germany in 2015.

Crowdwork encompasses the millions of outsourced workers (the crowd) behind our digital systems. It includes humans who tag photos for artificial intelligence systems, write descriptions for online retailers, rate the efficacy of Google's search engine, eliminate porn and violence from social media sites (content moderation), and perform freelancing gigs in an array of digital services for clients across the world. While the exact number of crowdworkers is unknown, it easily ranges in the tens of millions, with a presence in most countries in the world. Crowdwork is the quintessential example of how technology both displaces some occupations and creates new ones, and it highlights the challenges posed for these new workers, for whom global competition keeps pay low and insecure.

Altenried compellingly argues that today's digital work is controlled and monitored at every step and that the standardization of such processes "curiously resembl[es] those of Taylorist factories in the early twentieth century even if they look completely different." His analogy is apt, but he stops short of discussing how industrial work, while alienating, was nonetheless a source of good jobs in many Western countries after World War II as a result of collective efforts to organize and regulate work. In Altenried's digital production line, there are hints of collective action at Amazon warehouses, in the gaming industry, and even in crowdwork but scant discussion

of the institutions and efforts needed to turn these precarious jobs into good jobs.

The digital work described in this book is being performed for the richest companies of our times that pay little in taxes and that outsource large swathes of their workforce, despite tremendous profits. Such a world of work is not inevitable.

The Digital Factory is an important contribution to the discussion of digital labor. But it also makes clear that researchers must now address the next task at hand: how to turn these bad jobs into good jobs. ■

10.1126/science.abn1041



The Digital Factory: The Human Labor of Automation
Moritz Altenried
University of Chicago Press, 2022. 216 pp.

RACE AND SCIENCE

Biology versus bias

A pair of scholars confront the pernicious role played by racism in shaping our understanding of human difference

By **Agustín Fuentes**

It is scientifically irrefutable that human “race” (e.g., Asian, Black, white, etc.) is not a valid biological category. It is equally a fact that humans vary biologically on multiple dimensions, patterns, and processes, and some of this variation is meaningful and fundamental to understanding human diversity. Simultaneously, race is real as a lived experience with substantive social and biological outcomes, and race is central in society owing to the systemic and maleficent processes of racism. Unfortunately, being attentive to and comprehending this complex assemblage of facts is not how most people, including many scientists, think about race. Joseph Graves Jr. and Alan Goodman’s unflinching commitment to the integration of biological and social data and processes alongside historical and contemporary assessments of systemic racism in *Racism, Not Race* is therefore powerful and necessary.

The authors achieve this integrative approach effectively, in part because of who they are: an evolutionary biologist and a biological anthropologist, a Black American and a white American. Graves was the first African American to earn a doctorate in evolu-

tionary biology in the United States. He is a prominent scholar of *Drosophila* life history and aging and a pioneer in the study of biological and social concepts of race. Goodman played a foundational role in the development and dissemination of the biocultural approach in anthropology and human biology and is a key figure in anthropology’s public actions around race and racism.

The power of this book comes from its holistic and data-driven insertion of racism into the analyses of race and biology. Framing the discussion in the form of questions, Graves and Goodman guide the reader to a more accurate understanding of racism and race than many similar texts offer. Each chapter contains a set of questions, asked and then answered, that references data, analyses, inference, and consequence. Chapter 1 presents a history of how “race” became biological, and chapters 2 and 3 offer overviews of genetics and race and an examination of racism. Chapters 4 through 10 tackle the intersections of race/racism and disease, life history, aging and mortality, athletics, ancestry testing, and intelligence, as well as the structures and outcomes of systemic racism, the history of race names, and the erroneous notions of “race mixing.” The final chapter lays out the authors’ vision for creating an antiracist society, and the conclusion reviews the 10 key points of the book, ending with a core premise of the

Racism, Not Race: Answers to Frequently Asked Questions

Joseph L. Graves Jr. and Alan H. Goodman
Columbia University Press, 2021. 320 pp.



text: “Antiracism starts with understanding what race is and isn’t.”

The book is outstanding, but I have a few quibbles. To say that someone is 16% European or 67% African is not a biological statement, but it can sound like one. The authors clearly demonstrate that continental labels (e.g., “African,” “Asian,” “European”) are not accurate or effective categorizations of human biological variation, but they nonetheless employ such nomenclature. Such categories are commonly used to represent human groups in much of the biological, psychological, and medical research the authors consider, but we scientists need to stop using them when discussing human biological variation. Also, given how poorly ancestry testing is understood by the public, I would have liked to have seen more detail about what genetic ancestry is from a molecular and/or evolutionary perspective and how it is structured. And finally, the authors missed an opportunity to engage fully with human evolution research. Our current understanding of the dynamics and complexity of the Pleistocene has the potential to add substantially to discussions about human variation, race, and racism.

My minor critiques in no way diminish the importance, and quality, of this text. It will be appealing to the interested public and college students and would be a terrific keystone for biology and anthropology courses. However, I think the book does extra work for scholars, confirming a necessary role for active antiracism on the part of scientists, especially those in the biological and social sciences. In chapter 11, for example, the authors point to a series of actions that are necessary for an antiracist and just society. Here, those who believe that scientists and the practice of science are and can be “neutral” will be made uncomfortable, as the authors illustrate with data and arguments that a main roadblock to the accumulation of scientific knowledge and to the practice of science itself is the abuse and misuse of “science” in support of racism.

Racism and white supremacy are killing people every day, harming society at large, and fostering deep injustice. Graves and Goodman demonstrate why antiracism is not just an ethical and scientifically correct position, but why it is also necessary for the future of science and society. ■

The reviewer is at the Department of Anthropology, Princeton University, Princeton, NJ 08544, USA.
Email: afuentes2@princeton.edu



Medical myths rooted in racism can negatively impact the health outcomes of people of color.

10.1126/science.abn7276



Postfire management in southwest Turkey includes logging, terracing, and planting new pine trees.

Edited by Jennifer Sills

Turkish postfire action overlooks biodiversity

Turkey was hit hard by wildfires in 2021, with a record of about 203,000 ha burnt (1). Most of the area burnt was covered by Mediterranean *Pinus brutia* forests, and the intense fires killed most of the pines (2). However, this species has some closed cones that retain seeds until the heat of a fire releases them (3, 4), allowing regrowth despite the death of the tree (known as post-fire recruitment). A great diversity of other species in the area can also resprout or germinate after fire (4). Given that a high level of postfire regeneration will likely take place naturally (3), postfire management should focus on protecting the forest from aggressive human activities.

Instead, the Turkish General Directorate of Forestry has started postfire management with the salvage logging of dead trees. In many places, heavy machinery is being used and forest roads are being opened (2). Because Turkey's priority is timber production, logging is often followed by seeding or terracing and new tree planting.

These actions limit natural regeneration (4, 5) and disrupt ecosystem function (6). In some cases, they degrade the soil (7) and convert a species-rich ecosystem into artificial afforestation. Given the wide extent of the 2021 fires, these actions may substantially increase the country's land degradation and fail to comply with United Nations objectives (8, 9) and Turkey's commitments in the 2021 United Nations Climate Change Conference (10).

Postfire ecosystem dynamics data suggest that Mediterranean ecosystems are resilient to fire (3). Intense postfire management activities are required in only a few cases (7, 11), such as in areas with fire intervals much shorter than the historical variability or with reduced resilience because of previous land uses. Before aggressive intervention, sustainable postfire management must take into account natural regeneration, biodiversity, and ecosystem function. We urge the Turkish General Directorate of Forestry to stop degrading ecosystems and pursue ecologically sustainable forest management.

Çağatay Tavsanoglu¹ and Juli G. Pausas^{2*}

¹Division of Ecology, Department of Biology, Hacettepe University, 06800 Beytepe, Ankara, Turkey. ²Centro de Investigaciones sobre Desertificación, Consejo Superior de Investigaciones

Científicas (CIDE-CSIC), 46113 Valencia, Spain.

*Corresponding author.

Email: juli.g.pausas@ext.uv.es

REFERENCES AND NOTES

1. European Forest Fire Information System of the European Commission Joint Research Centre, "EFFIS Annual Country Statistics for TR – Turkey" (2022); <https://effis.jrc.ec.europa.eu/apps/effis.statistics/effisestimates>. In the dropdown for zone, select "European non-EU countries," then select Turkey from the country list.
2. H. Ö. Tosun, "Antalya'da yanan ormanlar 100 milyon fidanla yeniden yeşerecek," *AA* (2021); <https://www.aa.com.tr/tr/gundem/antalyada-yanan-ormanlar-100-milyon-fidanla-yeniden-yeserecek-/2354363> [in Turkish].
3. J. E. Keeley *et al.*, *Fire in Mediterranean Ecosystems: Ecology, Evolution and Management* (Cambridge University Press, 2012).
4. Ö. Urker *et al.*, *iForest* **11**, 635 (2018).
5. A. B. Leverkus *et al.*, *J. Environ. Manage.* **133**, 323 (2014).
6. D. B. Lindenmayer *et al.*, *Science* **303**, 1303 (2004).
7. P. Pereira *et al.*, *Curr. Opin. Environ. Sci. Health* **5**, 26 (2018).
8. United Nations Decade on Ecosystem Restoration 2021–2030 (2021); www.decadeonrestoration.org/.
9. United Nations Department of Economic and Social Affairs, "The 17 goals" (2018); <https://sdgs.un.org/goals>.
10. UN Climate Change Conference UK 2021, "Glasgow leaders' declaration on forests and land use" (2021); <https://ukcop26.org/glasgow-leaders-declaration-on-forests-and-land-use/>.
11. A. B. Leverkus *et al.*, *Environ. Res. Lett.* **16**, 021003 (2021).

10.1126/science.abn5645

A sea of possibilities for marine megafauna

Known marine megafauna include more than 300 mammals, fishes, turtles, birds, and cephalopods, which play pivotal roles in ocean ecosystem functions (1). These species increase primary productivity, act as natural carbon reservoirs in climate change mitigation, represent ocean health sentinels and flagship species in conservation issues, and provide food and substantial economic benefits through impacts on the fishing industry and tourism (1, 2). Yet, according to the International Union for Conservation of Nature (3), about one-third of marine megafauna are threatened with extinction (1, 4) as a result of exposure to industrialized human-induced pressures such as direct or indirect catch, marine traffic, climate change, overfishing, and pollution ranging from plastics to noise. Protecting these species is paramount.

Positive steps have been taken toward ocean sustainability, such as whaling moratoria, recovery of populations near extinction, and the creation of marine protected areas worldwide. International agreements such as the Convention on International Trade in Endangered Species of Wild Fauna and Flora, Convention on the Conservation of Migratory Species of Wild Animals, International Convention for the Prevention of Pollution from Ships, and Berne Convention (4) have promoted coordinated actions by multiple nations toward marine species conservation.

In addition, the main threats most of these charismatic species face have been mapped and identified (5). Despite these advantages, many marine megafauna species continue to decline.

Recently, 14 key countries agreed to sustainably manage the totality of the oceans under their national jurisdictions by 2025 (6), and the United Nations proclaimed this as a Decade of Ocean Science for Sustainable Development (7). To meet these goals, we must increase the number and size of highly protected marine protected areas within an integrated ocean management approach (8). Moreover, direct catch (including shark finning but excluding non-endangered bony fishes, cephalopods, and aboriginal subsistence) must be substantially reduced. To reduce bycatch, fishing should be restricted to selective or traditional gear and the use of nets in industrial-based fisheries should be minimized (9, 10). To avoid the generation of marine litter and prevent litter from entering the marine environment, single-use plastics should be prohibited (11). International laws should be revised to promote responsible, inclusive, and community-based tourism and to promote adequate surveillance in the high seas (12). These feasible and efficient mitigation measures are in line with the unprecedented level of commitment and responsibility that the world's leaders have declared.

Filipe Alves^{1*}, Massimiliano Rosso², Songhai Li^{3,4,5}, Douglas P. Nowacek⁶

¹Marine and Environmental Sciences Centre (MARE), Agência Regional para o Desenvolvimento da Investigação, Tecnologia e Inovação, Madeira, Portugal. ²Centro Internazionale in Monitoraggio Ambientale (CIMA) Research Foundation, 17100 Savona, Italy. ³Marine Mammal and Marine Bioacoustics Laboratory, Institute of Deep-sea Science and Engineering, Chinese Academy of Sciences, Sanya 572000, China. ⁴Center for Ocean Mega-Science, Chinese Academy of Sciences, Qingdao 266071, China. ⁵Function Laboratory for Marine Fisheries Science and Food Production Processes, Qingdao National Laboratory for Marine Science and Technology, Qingdao 266237, China. ⁶Nicholas School of the Environment and Pratt School of Engineering, Duke University Marine Laboratory, Beaufort, NC 28516, USA.

*Corresponding author.

Email: filipe.alves@mare-centre.pt

REFERENCES AND NOTES

1. C. Pimiento *et al.*, *Sci. Adv.* **6**, eaay7650 (2020).
2. R. Chami, T. Cosimano, C. Fullenkamp, S. Oztosun, *Finance Dev.* **56**, 34 (2019).
3. IUCN 2021, The IUCN Red List of Threatened Species, Version 2021-1; <https://www.iucnredlist.org>.
4. B. Lascelles *et al.*, *Aquat. Conserv.* **24**, 111 (2014).
5. R. L. Lewison *et al.*, *Proc. Natl. Acad. Sci. U.S.A.* **111**, 5271 (2014).
6. High Level Panel for a Sustainable Ocean Economy, "Towards a sustainable ocean economy" (2020); <https://oceanpanel.org/>.
7. UN Decade of Ocean Science for Sustainable Development, "The ocean decade" (2021); www.oceandecade.org/.
8. E. Sala *et al.*, *Nature* **592**, 397 (2021).
9. J. E. Cinner *et al.*, *Science* **368**, 307 (2020).
10. J. Senko *et al.*, *Anim. Conserv.* **17**, 5 (2014).
11. C. M. Duarte *et al.*, *Nature* **580**, 39 (2020).
12. R. R. Helm *et al.*, *Science* **372**, 1048 (2021).

COMPETING INTERESTS

S.L. receives funding from the National Natural Science Foundation of China (41422604), "One Belt and One Road" Science and Technology Cooperation Special Program of the International Partnership Program of the Chinese Academy of Sciences (183446KYSB20200016).

10.1126/science.abn6022

Savannas are vital but overlooked carbon sinks

On the second day of the 2021 United Nations Climate Change Conference (COP26), 130 nations announced a decision to halt global deforestation by 2030 (1). This is a welcome move and a political success, but ecologically it falls short. The plan needs to be expanded to include savannas, which cover an area of 20 million km²—more than the 17 million km² covered by tropical forests (2)—and are potentially more important carbon sinks than forests.

In the course of a year, each hectare of the Serengeti plains in Tanzania removes between 5000 and 20,000 kg of carbon dioxide (3) from the atmosphere, enough in total to offset every airline flight to East Africa and all the emissions produced in the region (4, 5). The repeated grazing of wildebeests, zebras, and a variety of insects (6) stimulates vegetative growth multiple times within a year (7, 8), which considerably increases the volume of carbon dioxide absorbed from the atmosphere. Wildlife feces and carcasses enrich the store of carbon and nitrogen in the soil.

The Serengeti and other tropical and temperate savannas, which store carbon in the soil rather than in the biomass of trees (4), can capture at least as much carbon as tropical forests if managed correctly (9, 10). They are as threatened as tropical forests by agriculture expansion and land clearing. Like tropical forests, they are crucially in need of protection (11, 12); excessive grazing and fires are diminishing the abundance of wild herbivores and thus their potential to store carbon (8, 10). Substantial amounts of biodiversity, as well as many pastoralist peoples, depend on savannas. They also generate employment and foreign currency through tourism (5).

The parties to United Nations Framework Convention on Climate Change must be bolder in their approach to climate change. Declared goals must include both forests and savannas.

Moreover, target dates should be set as soon as possible. Even 2025 may be too late to save the vulnerable forest and savanna ecosystems that provide the only fully scalable natural solution to remove carbon dioxide from the atmosphere.

Andy Dobson^{1*}, Grant Hopcraft², Simon Mduma³, Joseph O. Ogutu⁴, John Fryxell⁵, T. Michael Anderson⁶, Sally Archibald⁷, Caroline Lehmann^{8,9}, Joyce Poole¹⁰, Tim Caro¹¹, Monique Borgerhoff Mulder¹², Robert D. Holt¹³, Joel Berger¹⁴, Daniel I. Rubenstein¹, Paula Kahumbu¹⁵, Emmanuel N. Chidumayo¹⁶, E. J. Milner-Gulland¹⁷, Dolph Schluter¹⁸, Sarah Otto¹⁹, Andrew Balmford¹⁹, David Wilcove¹, Stuart Pimm²⁰, Joseph Veldma²¹, Han Olff²², Reed Noss²³, Ricardo Holdo²⁴, Colin Beale²⁵, Gareth Hempson⁷, Yustina Kiwango²⁶, David Lindenmayer²⁷, William Bond²⁸, Mark Ritchie²⁹, Anthony R. E. Sinclair¹⁸

¹Department of Ecology and Evolutionary Biology, Princeton University, Princeton, NJ 08544, USA.

²Glasgow University, Glasgow, UK. ³Tanzania Wildlife Research Institute, Arusha, Tanzania.

⁴University of Hohenheim, Stuttgart, Germany.

⁵University of Guelph, Guelph, ON N1G 2W1, Canada. ⁶Wake Forest University, Winston-Salem, NC 27109, USA. ⁷University of the Witwatersrand, Braamfontein, Johannesburg, 2000, South Africa.

⁸Tropical Diversity, Royal Botanical Gardens, Edinburgh EH35LR, UK. ⁹School of GeoSciences, University of Edinburgh, Edinburgh EH93FF, UK.

¹⁰ElephantVoices, San Francisco, CA 94111, USA.

¹¹University of Bristol, Bristol BS8 1TH, UK. ¹²Max Planck Institute for Evolutionary Anthropology, Leipzig, Germany.

¹³University of Florida, Gainesville, FL 32611, USA. ¹⁴Colorado State University, and Wildlife Conservation Society, Fort Collins, CO 80523, USA.

¹⁵Wildlife Direct, Karen 00502, Nairobi, Kenya. ¹⁶Zambian National University, Lusaka, Zambia.

¹⁷Department of Zoology, Oxford University, Oxford OX1 3SZ, UK. ¹⁸University of British Columbia, Vancouver, BC V6T 1Z4, Canada.

¹⁹Cambridge University, Cambridge CB2 3EJ, UK. ²⁰Duke University, Durham, NC 27708, USA.

²¹Department of Ecology and Conservation Biology, Texas A&M University, College Station, TX 77843, USA.

²²University of Groningen, 9712 CP Groningen, Netherlands. ²³Florida Institute for Conservation Science, Oviedo, FL 32766, USA.

²⁴University of Athens, Athens, GA 30602, USA. ²⁵University of York, Heslington, York YO10 5DD, UK.

²⁶Tanzania National Parks, Arusha, Tanzania. ²⁷Australian National University, Canberra, ACT 0200, Australia.

²⁸University of Cape Town, Rondebosch, Cape Town, 7700, South Africa. ²⁹Syracuse University, Syracuse, NY 13244, USA.

*Corresponding author.

Email: dobber@princeton.edu

REFERENCES AND NOTES

1. "Glasgow leaders' declaration on forests and land use" (2021); <https://ukcop26.org/glasgow-leaders-declaration-on-forests-and-land-use/>.
2. P. Elias, C. May-Tobin, in *The Root of the Problem: What's Driving Tropical Deforestation Today*, D. Boucher *et al.*, Eds. (Union of Concerned Scientists, 2011), pp. 1–12.
3. R. M. Holdo *et al.*, *PLOS Biol.* **7**, e1000210 (2009).
4. O. J. Schmitz, *Ecosystems* **17**, 344 (2014).
5. A. Dobson, *Philos. Trans. R. Soc. B Biol. Sci.* **364**, 1665 (2009).
6. S. J. McNaughton, *Ecol. Mono.* **55**, 259 (1985).
7. S. J. McNaughton, *Am. Natural.* **113**, 691 (1979).
8. M. E. Ritchie, J. F. Penner, *Ecol. Evol.* **10**, 5302 (2020).
9. J. Grace *et al.*, *J. Biogeogr.* **33**, 387 (2006).
10. T. H. Tear *et al.*, *One Earth* **12**, 1776 (2021).
11. C. L. Parr, *Trends Ecol. Evol.* **29**, 205 (2014).
12. N. Ramankutty *et al.*, *Glob. Biogeochem. Cyc.* **22**, 10.1029/2007GB002952 (2008).

10.1126/science.abn4482

2021 AAAS Fellows approved by the AAAS Council

In November 2021, the AAAS Council elected 564 members as Fellows of AAAS. Election as a Fellow honors members whose efforts on behalf of the advancement of science or its applications in service to society have distinguished them among their peers and colleagues. Presented by section affiliation, they are:

Section on Agriculture, Food, and Renewable Resources

J. Scott Angle, *Univ. of Florida*

Bruno Basso, *Michigan State Univ.*

William Wesley Bowerman,
Univ. of Maryland, College Park

Gabriela Del Carmen Chavarria,
Burke Museum of Natural History & Culture

Sixue Chen, *Univ. of Florida*

Brad Day,
Univ. of Tennessee, Knoxville

Brian Diers,
Univ. of Illinois Urbana-Champaign

Helene R. Dillard,
Univ. of California, Davis

José R. Dinneny, *Stanford Univ.*

Eunice F. Foster, *Michigan State Univ.*

Niko Geldner, *Univ. of Lausanne*
(Switzerland)

Prasanna H. Gowda, *US Department of Agriculture - Agricultural Research Service*

Linda J. Harris,
Univ. of California, Davis

Julie Jastrow, *Argonne National Laboratory*

Shawn M. Kaeppler,
Univ. of Wisconsin-Madison

Matias Kirst, *Univ. of Florida*

Yuncong Li, *Univ. of Florida*

Junguo Liu, *Southern Univ. of Science and Technology (China)*

Shawn Denton Mansfield,
The Univ. of British Columbia (Canada)

Prabhu Pingali, *Cornell Univ.*

Carl E. Sams,
Univ. of Tennessee, Knoxville

Tai-ping Sun, *Duke Univ.*

Section on Anthropology

Michelle Bezanson, *Santa Clara Univ.*

Nicholas G. Blurton-Jones,
Univ. of California, Los Angeles

Sharon N. DeWitte,
Univ. of South Carolina

Jon M. Erlandson, *Univ. of Oregon*

Michael Gurven, *Univ. of California, Santa Barbara*

Lyle W. Konigsberg, *Univ. of Illinois Urbana-Champaign*

Ripam Singh Malhi, *Univ. of Illinois Urbana-Champaign*

Mary Ann Raghanti, *Kent State Univ.*

Mary K. Shenk, *Pennsylvania State Univ.*

Joan B. Silk, *Arizona State Univ.*

Lynn Stephen, *Univ. of Oregon*

Mark F. Teaford, *Touro Univ.*

Wirt H. Wills, *Univ. of New Mexico*

Section on Astronomy

Reba Bandyopadhyay,
National Science Foundation

Anthony J. Beasley, *National Radio Astronomy Observatory*

Eric Christian, *NASA Goddard Space Flight Center*

Debra Fischer, *Yale Univ.*

David H. Grinspoon,
Planetary Science Institute

Mustapha Ishak-Boushaki,
The Univ. of Texas at Dallas

Angela K. Speck, *The Univ. of Texas San Antonio*

Alan Tokunaga, *Univ. of Hawaii*

Eric M. Wilcots,
Univ. of Wisconsin-Madison

Belinda Jane Wilkes, *Smithsonian Astrophysical Observatory/Univ. of Bristol (United Kingdom)*

Section on Atmospheric and Hydrospheric Science

Wei-Jun Cai, *Univ. of Delaware*

Paolo D'Odorico,
Univ. of California, Berkeley

Alex Guenther,
Univ. of California, Irvine

David G. Hawkins, *Natural Resources Defense Council (NRDC)*

Chuanmin Hu, *Univ. of South Florida*

Witold F. Krajewski, *Univ. of Iowa*

Jeffrey McDonnell,
Univ. of Saskatchewan (Canada)

Murugesu Sivapalan, *Univ. of Illinois Urbana-Champaign*

Owen Brian Toon,
Univ. of Colorado Boulder

Isabella Velicogna,
Univ. of California, Irvine

Enrique R. Vivoni, *Arizona State Univ.*

Paul O. Wennberg, *California Institute of Technology*

Section on Biological Sciences

Spiros N. Agathos, *Université Catholique de Louvain (Belgium)*

Maria-Luisa Alegre,
Univ. of Chicago

Lee-Ann H. Allen, *Univ. of Missouri School of Medicine*

Steven D. Allison,
Univ. of California, Irvine

Rodrigo P. P. Almeida,
Univ. of California, Berkeley

Suzanne H. Alonzo,
Univ. of California, Santa Cruz

Deborah Andrew, *Johns Hopkins Univ. School of Medicine*

A. Elizabeth (Betsy) Arnold,
Univ. of Arizona

Christopher P. Austin,
Flagship Pioneering

Lauren O. Bakaletz,
Nationwide Children's Hospital

Scott E. Baker, *Pacific Northwest National Laboratory*

Lisa T. Ballance, *Oregon State Univ.*

Diane Bassham, *Iowa State Univ.*

Deborah Bell-Pedersen,
Texas A&M Univ.

Joseph A. Berry, *Carnegie Institution for Science*

Madan K. Bhattacharyya,
Iowa State Univ.

Sharon A. Billings, *Univ. of Kansas*

Jeffrey Bluestone, *Univ. of California, San Francisco (Emeritus)/Sonoma Biotherapeutics*

Jeffrey D. Blume, *Univ. of Virginia*

Brendan James Marc Bohannon,
Univ. of Oregon

Michael Boots,
Univ. of California, Berkeley

Santanu Bose, *Washington State Univ.*

James E. Byers, *Univ. of Georgia*

David Cannatella, *The Univ. of Texas at Austin*

Zoe G. Cardon,
Marine Biological Laboratory

Stephen Russell Carpenter,
Univ. of Wisconsin-Madison

Frances Eileen Carr, *Univ. of Vermont Larner College of Medicine*

Emily Carrington, *Univ. of Washington*

Gerardo Ceballos, *Universidad Nacional Autónoma de México (Mexico)*

Janice Elaine Chambers,
Mississippi State Univ.

James Patrick Chambers,
The Univ. of Texas at San Antonio

Sara Cherry, *Univ. of Pennsylvania, Perelman School of Medicine*

Patricia L. Clark, *Univ. of Notre Dame*

Dale Clayton, *Univ. of Utah*

Michael I. Coates, *Univ. of Chicago*

Paula E. Cohen, *Cornell Univ.*

Marty A. Condon, *Cornell College*

Marc Anthony Cubeta,
North Carolina State Univ.

M. Denise Dearing, *Univ. of Utah*

Alan W. Decho, *Univ. of South Carolina*

Janice Edgerly-Rooks,
Santa Clara Univ.

Brandt F. Eichman, *Vanderbilt Univ.*

Berten Ely III, *Univ. of South Carolina*

Donald M. Engelman, *Yale Univ.*

Patricia Fitzgerald-Bocarsly,
Rutgers New Jersey Medical School

Brian C. Freeman, *Univ. of Illinois Urbana-Champaign*

Peter C. Frumhoff,
Union of Concerned Scientists

Aaron John Gassmann,
Iowa State Univ.

Yoav Gilad, *Univ. of Chicago*

Amy S. Gladfelter, *Univ. of North Carolina at Chapel Hill*

David Jonathan Glass,
Regeneron Pharmaceuticals

Carol C. Gregorio, *Univ. of Arizona*

Max M. Häggblom, *Rutgers, The State Univ. of New Jersey*

Candace H. Haigler, *North Carolina State Univ.*

Rasika Harshey, *The Univ. of Texas at Austin*

AAAS NEWS & NOTES

Valerie J. Harwood,
Univ. of South Florida

Elizabeth S. Haswell,
Washington Univ. in St. Louis

Mark E. Hauber, *Univ. of Illinois
Urbana-Champaign*

Katy D. Heath, *Univ. of Illinois
Urbana-Champaign*

Christophe Herman, *Baylor College
of Medicine*

Erik Herzog, *Washington Univ.
in St. Louis*

Michael Edward Hochberg, *Centre
National de la Recherche Scientifique
(CNRS) (France)*

Hopi Elisabeth Hoekstra,
Harvard Univ.

Shuijin Hu, *North Carolina State Univ.*

Kelly Hughes, *Univ. of Utah*

Bruce A. Hungate,
Northern Arizona Univ.

Brian D. Inouye, *Florida State Univ.*

Hanjoong Jo, *Emory Univ./Georgia
Institute of Technology*

A. Daniel Jones, *Michigan State Univ.*

Katalin Karikó, *BioNTech SE/Univ.
of Pennsylvania*

Felicia Keesing, *Bard College*

Mark R. Kelley, *Indiana Univ. School
of Medicine*

Linda J. Kenney, *The Univ. of Texas
Medical Branch*

Jeremy Kerr, *Univ. of Ottawa
(Canada)*

David Louis Kirchman,
Univ. of Delaware

Jessica Carol Kissinger,
Univ. of Georgia

Theresa M. Koehler, *The Univ. of
Texas Health Science Center at Houston*

Bernd Markus Lange,
Washington State Univ.

Ming Li, *Memorial Sloan Kettering
Cancer Center*

Zihai Li, *The Ohio State Univ.
Comprehensive Cancer Center*

Jun (Kelly) Liu, *Cornell Univ.*

Mats Ljungman, *Univ. of Michigan*

Julie L. Lockwood, *Rutgers Univ.,
The State Univ. of New Jersey*

Tara C. Matise, *Rutgers Univ.,
The State Univ. of New Jersey*

Mónica Medina,
Pennsylvania State Univ.

Jens Meiler, *Vanderbilt Univ.*

Xiang-Jin Meng, *Virginia Polytechnic
Institute and State Univ.*

Axel Meyer, *Univ. of Konstanz
(Germany)*

Gary Muehlbauer, *Univ. of Minnesota*

Ronald Mumme, *Allegheny College*

Victor Nizet, *Univ. of California,
San Diego*

Marcelo A. Nóbrega, *Univ. of Chicago*

Eva Nogales, *Univ. of California,
Berkeley*

Charles Ofria, *Michigan State Univ.*

Melanie Diane Ohi, *Univ. of Michigan*

Lydia Olander, *Duke Univ.*

Kim Orth, *The Univ. of Texas
Southwestern Medical Center*

Marc Ostermeier, *Johns Hopkins Univ.*

Brian Palenik, *Scripps Institution of
Oceanography at Univ. of California,
San Diego*

Diane Eve Pataki, *Arizona State Univ.*

Michael Eugene Pfrender,
Univ. of Notre Dame

Leslie Pick, *Univ. of Maryland,
College Park*

Raina Katy Plowright, *Montana
State Univ.*

Mircea Podar, *Oak Ridge
National Laboratory*

Reeta Rao,
Worcester Polytechnic Institute

Rick Relyea, *Rensselaer
Polytechnic Institute*

Phoebe A. Rice,
Univ. of Chicago

Tony Romeo, *Univ. of Florida*

Joel Harry Rothman,
Univ. of California, Santa Barbara

Dustin Rubenstein, *Columbia Univ.*

Olav Rueppell, *Univ. of Alberta
(Canada)*

Stephen H. Safe, *Texas A&M Univ.*

Alejandro Sánchez Alvarado,
Stowers Institute for Medical Research

Crickette Sanz, *Washington Univ.
in St. Louis*

Alexander Schier, *Univ. of Basel
(Switzerland)*

Patrick D. Schloss, *Univ. of Michigan
Medical School*

Ted R. Schultz, *Smithsonian
Institution, National Museum of
Natural History*

Tricia R. Serio, *Univ. of
Massachusetts Amherst*

Scott A. Showalter,
Pennsylvania State Univ.

Kathryn Sieving, *Univ. of Florida*

Andrew Singson, *Rutgers Univ.,
The State Univ. of New Jersey*

Hazel Sive, *Northeastern Univ.*

Vanessa Sperandio, *The Univ. of
Texas Southwestern Medical Center*

Pramod Srivastava,
Univ. of Connecticut School of Medicine

John J. Stachowicz,
Univ. of California, Davis

Jay R. Stauffer,
Pennsylvania State Univ.

Nathan L. Stephenson,
US Geological Survey

Yasuhiro Suzuki, *Univ. of Kentucky*

Ethan J. Temeles, *Amherst College*

Peter Tiffin, *Univ. of Minnesota*

Eva Top, *Univ. of Idaho*

Peter Turchin, *Univ. of Connecticut*

Monica G. Turner, *Univ. of Wisconsin-
Madison*

Nicole Valenzuela, *Iowa State Univ.*

Mary C. Watzin, *North Carolina
State Univ.*

George Weiblen, *Univ. of Minnesota*

Steven W. Wilhelm,
Univ. of Tennessee, Knoxville

Patricia Wittkopp, *Univ. of Michigan*

Patricia L. Yager, *Univ. of Georgia*

Ying E. Zhang, *National Cancer
Institute /NIH*

Renping Zhou, *Rutgers Univ., Ernest
Mario School of Pharmacy*

Section on Chemistry

Penny Beuning, *Northeastern Univ.*

Kristie A. Boering,
Univ. of California, Berkeley

Alexander I. Boldyrev,
Utah State Univ.

Kay M. Brummond,
Univ. of Pittsburgh

Martin D. Burke, *Univ. of Illinois
Urbana-Champaign*

Christopher Cahill, *George
Washington Univ.*

Renée S. Cole, *Univ. of Iowa*

Mircea Dincă, *Massachusetts Institute
of Technology*

Davide Donadio,
Univ. of California, Davis

David P. Goldberg, *Johns Hopkins Univ.*

Joshua E. Goldberger,
The Ohio State Univ.

Alan S. Goldman, *Rutgers Univ.,
The State Univ. of New Jersey*

Mark W. Grinstaff, *Boston Univ.*

Hua Guo, *Univ. of New Mexico*

Sophia E. Hayes, *Washington Univ.
in St. Louis*

Mark R. Hoffmann,
Univ. of North Dakota

De-en Jiang, *Univ. of California, Riverside*

Julia A. Kovacs, *Univ. of Washington*

Randy W. Larsen, *Univ. of South Florida*

Steven Little, *Univ. of Pittsburgh*

Aimin Liu, *The Univ. of Texas
at San Antonio*

Joseph A. Loo, *Univ. of California,
Los Angeles*

Robert E. Maleczka,
Michigan State Univ.

Chérif F. Matta, *Mount Saint Vincent
Univ. (Canada)*

Stephen L. Mayo, *California Institute of
Technology*

Thomas Mark McCleskey,
Los Alamos National Laboratory

Luis Alberto Montero-Cabrera,
Universidad de la Habana (Cuba)

Priyabrata Mukherjee,
Univ. of Oklahoma

Harshini Mukundan, *Los Alamos
National Laboratory*

Gerard Parkin, *Columbia Univ.*

Michael D. Pluth, *Univ. of Oregon*

Jay W. Ponder, *Washington Univ.
in St. Louis*

Kevin D. Raney, *Univ. of Arkansas
for Medical Sciences*

Glenn S. Ruskin,
American Chemical Society

Jennifer Marie Schomaker,
Univ. of Wisconsin-Madison

Roseanne J. Sension,
Univ. of Michigan

Virender K. Sharma, *Texas A&M Univ.*

Mukund P. Sibi, *North Dakota
State Univ.*

Staci L. Simonich, *Oregon State Univ.*

Stefan Stoll, *Univ. of Washington*

Charles Sykes, *Tufts Univ.*

Lynmarie K. Thompson,
Univ. of Massachusetts Amherst

Mark E. Tuckerman, *New York Univ.*

Kathryn Elizabeth Uhrich,
Univ. of California, Riverside

Ming Xian, *Brown Univ.*

Ling Zang, *Univ. of Utah*

Section on Dentistry and Oral Health Sciences

Cecile Arlene Feldman,
Rutgers Univ. School of Dental Medicine

Effie Ioannidou,
Univ. of Connecticut School of Dental Medicine

Anil Misra, *Univ. of Kansas*

Kathy Kay Hartford Svoboda,
Texas A&M Health Science Center

Reginald Wayne Taylor, *Texas A&M Univ. College of Dentistry*

Section on Education

Melissa K. Demetrikopoulos,
Institute for Biomedical Philosophy

Anne E. Egger,
Central Washington Univ.

Noah David Finkelstein,
Univ. of Colorado Boulder

Kenneth D. Gibbs Jr.,
National Institute of General Medical Sciences/NIH

David Hammer, *Tufts Univ.*

Laird Kramer,
Florida International Univ.

Okhee Lee, *New York Univ.*

Edward B. Nuhfer, *Retired*

Margaret Somosi Saha,
College of William and Mary

William A. Sandoval,
Univ. of California, Los Angeles

Ruthmae Sears, *Univ. of South Florida*

Karl A. Smith, *Purdue Univ.*

Mark Urban-Lurain,
Michigan State Univ.

Sandra Urdaneta Hartmann,
Drexel Univ.

Zakiya S. Wilson Kennedy,
Louisiana State Univ.

Section on Engineering

Arvind Agarwal,
Florida International Univ.

Norma Alcantar,
Univ. of South Florida

Ruzena Bajcsy,
Univ. of California, Berkeley

Morton A. Barlaz, *North Carolina State Univ.*

Georges Belfort,
Rensselaer Polytechnic Institute

Pratim Biswas, *Univ. of Miami*

John E. Bowers, *Univ. of California, Santa Barbara*

Gary J. Cheng, *Purdue Univ.*

Giovanni De Micheli, *Swiss Federal Institute of Technology (EPFL) (Switzerland)*

Delcie Rena Durham,
Univ. of South Florida

Rachel S. Goldman, *Univ. of Michigan*

Olivia A. Graeve, *Univ. of California, San Diego*

Dorota A. Grejner-Brzezinska,
The Ohio State Univ.

Susan Hagness,
Univ. of Wisconsin-Madison

Ayman Hawari, *North Carolina State Univ.*

Xiaoping Hu,
Univ. of California, Riverside

Joseph Irudayaraj, *Univ. of Illinois Urbana-Champaign*

Bjorn Ingemar Johansson, *Chalmers Univ. of Technology (Sweden)*

Erick C. Jones Sr., *Univ. of Texas at Arlington*

Ranu Jung, *Florida International Univ. (Emeritus)/Univ. of Arkansas*

Kourosh Kalantar-Zadeh, *Univ. of New South Wales (Australia)*

Leo Charles Kempel,
Michigan State Univ.

Michael R. King, *Vanderbilt Univ.*

Nikhil Ashok Koratkar, *Rensselaer Polytechnic Institute*

Xiuling Li, *The Univ. of Texas at Austin*

Karl G. Linden,
Univ. of Colorado Boulder

Elizabeth G. Lobo,
Southern Methodist Univ.

Judith L. MacManus-Driscoll,
Univ. of Cambridge (United Kingdom)

Lance Manuel, *The Univ. of Texas at Austin*

Ying Shirley Meng,
Univ. of California, San Diego

Karen Ann Panetta, *Tufts Univ.*

Jose C. Principe, *Univ. of Florida*

Chris B. Schaffer, *Cornell Univ.*

David Alan Shifler, *US Office of Naval Research*

John W. Sutherland, *Purdue Univ.*

Madhava Syamlal, *US Department of Energy, National Energy Technology Laboratory*

Evelyn Ning-Yi Wang, *Massachusetts Institute of Technology*

Sharon Weiss, *Vanderbilt Univ.*

Huili Grace Xing, *Cornell Univ.*

Yannis Yortsos,
Univ. of Southern California

Section on General Interest in Science and Engineering

Alan Alda, *Alan Alda Center for Communicating Science, Stony Brook Univ.*

Andrea M. Armani,
Univ. of Southern California

Bradley J. Cardinal,
Oregon State Univ.

Yiu-ming Cheung, *Hong Kong Baptist Univ. (China)*

Erica Goldman, *Federation of American Scientists*

Jeremy S. Hoffman, *Science Museum of Virginia*

Kathleen Hall Jamieson,
Univ. of Pennsylvania

Se Woong Jeong, *Regeneron Pharmaceuticals*

Lee Ann Kahlor,
The Univ. of Texas at Austin

Tiffany Lohwater,
Univ. of California, Berkeley

Kevin J. Niemi,
Univ. of Wisconsin-Madison

Richard M. Preston, *The New Yorker*

Steven L. Richardson, *Howard Univ.*

Section on Geology and Geography

Richard Aster, *Colorado State Univ.*

Paul Arthur Baker, *Duke Univ.*

Samuel J. Bentley Sr.,
Louisiana State Univ.

Marcellus M. Caldas,
Kansas State Univ.

Nicholas Christie-Blick,
Lamont-Doherty Earth Observatory

Kim M. Cobb, *Georgia Institute of Technology*

Kirstin Dow, *Univ. of South Carolina*

Ying Fan Reinfelder, *Rutgers Univ., The State Univ. of New Jersey*

Kip Hodges, *Arizona State Univ.*

Linda Christine Kah,
Univ. of Tennessee, Knoxville

Emily M. Klein, *Duke Univ.*

Zhong Lu, *Southern Methodist Univ.*

Stephen R. McNutt,
Univ. of South Florida

Harvey J. Miller, *The Ohio State Univ.*

Carol Polanskey, *Jet Propulsion Laboratory - NASA*

P. David Polly,
Indiana Univ. - Bloomington

Mary Elizabeth Savina,
Carleton College (Emerita)

Robert J. Stern, *The Univ. of Texas at Dallas*

Shaowen Wang, *Univ. of Illinois Urbana-Champaign*

James Zachos,
Univ. of California, Santa Cruz

Section on History and Philosophy of Science

Gordon Belot, *Univ. of Michigan*

Paul N. Edwards, *Stanford Univ.*

Susan D. Jones, *Univ. of Minnesota*

Michael Kalichman,
Univ. of California, San Diego (Retired)

Wilfried Sieg, *Carnegie Mellon Univ.*

Conevery Bolton Valencius,
Boston College

Section on Industrial Science and Technology

Babu Chalamala,
Sandia National Laboratories

Shaun S. Gleason, *Oak Ridge National Laboratory*

Babetta L. Marrone, *Los Alamos National Laboratory*

Celia Merzbacher, *SRI International*

Eduardo Rosa-Molinar,
The Univ. of Kansas

Krysta Svore, *Microsoft*

Section on Information, Computing, and Communication

Eric Allen Brewer, *Google, Inc.*

Claire Cardie, *Cornell Univ.*

Susan Davidson,
Univ. of Pennsylvania

Rina Dechter,
Univ. of California, Irvine

Paul Dourish, *Univ. of California, Irvine*

Kathleen Fisher, *Tufts Univ.*

Michael Franklin, *Univ. of Chicago*

Juliana Freire, *New York Univ.*

Simson L. Garfinkel, *US Department of Homeland Security*

Mark D. Hill, *Microsoft/Univ. of Wisconsin-Madison*

Ayanna Howard, *The Ohio State Univ.*

Somesh Jha, *Univ. of Wisconsin-Madison*

Ramayya Krishnan,
Carnegie Mellon Univ.

Richard Ladner, *Univ. of Washington*

Yann LeCun, *New York Univ./Meta*

AAAS NEWS & NOTES

Robin R. Murphy, *Texas A&M Univ.*

Elizabeth D. Mynatt,
Northeastern Univ.

Rafail Ostrovsky, *Univ. of California,
Los Angeles*

David A. Padua, *Univ. of Illinois
Urbana-Champaign*

David Parkes, *Harvard Univ.*

Jignesh M. Patel,
Univ. of Wisconsin-Madison

Yong Rui, *Lenovo Group*

Tuomas Sandholm,
Carnegie Mellon Univ.

Michael L. Scott, *Univ. of Rochester*

Padhraic Smyth,
Univ. of California, Irvine

Tandy Warnow, *Univ. of Illinois
Urbana-Champaign*

Section on Linguistics and Language Sciences

Anne Charity Hudley, *Stanford Univ.*

Colleen Fitzgerald, *North Dakota
State Univ.*

Cecile McKee, *Univ. of Arizona*

Section on Mathematics

Dan Abramovich, *Brown Univ.*

Helene Barcelo, *Mathematical
Sciences Research Institute*

Robert Bryant, *Duke Univ.*

Fariba Fahroo, *US Air Force Office
of Scientific Research*

Philip K. Maini, *Univ. of Oxford
(United Kingdom)*

Jill C. Pipher, *Brown Univ.*

Judy Leavitt Walker,
Univ. of Nebraska-Lincoln

Section on Medical Sciences

David Edgar Anderson,
Univ. of Tennessee, Knoxville

David Andes,
Univ. of Wisconsin-Madison

Walter J. Atwood, *Brown Univ.*

Joseph Bonventre,
Harvard Medical School

Jan L. Breslow, *Rockefeller Univ.*

Charles Burant, *Univ. of Michigan*

Lucio H. Castilla,
Univ. of Massachusetts Medical School

Diego H. Castrillon, *The Univ. of
Texas Southwestern Medical Center*

Curt I. Civin,
Univ. of Maryland, Baltimore

David Wade Clapp, *Indiana Univ.
School of Medicine*

Dan G. Duda, *Harvard Medical School*

William G. Dunphy,
California Institute of Technology

Gary S. Firestein, *Univ. of California,
San Diego*

Juan Fueyo, *The Univ. of Texas MD
Anderson Cancer Center*

Sarah L. Gaffen, *Univ. of Pittsburgh*

William C. Gause, *Rutgers Univ.,
New Jersey Medical School*

Douglas R. Green, *St. Jude Children's
Research Hospital*

Neil S. Greenspan, *Case Western
Reserve Univ./Univ. Hospitals
Cleveland Medical Center*

Stephen Craig Hadler, *US Centers
for Disease Control and Prevention
(Retired)*

Johannes Wilhelm Hell,
Univ. of California, Davis

Richard Heller, *Univ. of South Florida*

Dean Ho, *National Univ. of Singapore*

Mark S. Humayun,
Univ. of Southern California

Ian W. Hunter, *Massachusetts
Institute of Technology*

Elizabeth Marion Jaffee,
*Johns Hopkins Univ. School
of Medicine*

Vasanthi Jayaraman, *The Univ.
of Texas at Houston, McGovern
Medical School*

Constance Jeffery,
Univ. of Illinois Chicago

Christine Kreuder Johnson, *Univ. of
California, Davis School of Veterinary
Medicine*

Thomas Kawula,
Washington State Univ.

Sabra L. Klein, *Johns Hopkins Univ.*

Teri E. Klein, *Stanford Univ.*

Bjorn C. Knollmann, *Vanderbilt Univ.
School of Medicine*

Yong Li, *Baylor College of Medicine*

Hui-Kuan Lin, *Wake Forest Univ.
School of Medicine*

Michail S. Lionakis,
*National Institutes of Allergy &
Infectious Diseases/NIH*

Joseph Anthony Lorenzo, *UConn
Health*

David Margolis, *Univ. of North
Carolina at Chapel Hill*

George A. Mashour, *Univ. of Michigan*

Katrina L. Mealey,
Washington State Univ.

Sofia D. Merajver, *Univ. of Michigan*

David Charles Musch,
Univ. of Michigan

Harikrishna Nakshatri, *Indiana Univ.
School of Medicine*

Avindra Nath,
*National Institutes of Neurological
Disorders and Stroke/NIH*

Kenneth Offit, *Memorial Sloan
Kettering Cancer Center*

Vivian W. Pinn,
Fogarty International Center/NIH

Victor G. Prieto, *The Univ. of Texas
MD Anderson Cancer Center*

Ling Qi, *Univ. of Michigan*

Rajinder S. Ranu,
Colorado State Univ.

Lewis R. Roberts, *Mayo Clinic*

Cheryl S. Rosenfeld,
Univ. of Missouri-Columbia

Peter H. Seeberger, *Max Planck
Institute of Colloids and Interfaces/
Freie Universität Berlin (Germany)*

Michael M. Shen,
*Columbia Univ. Vagelos College
of Physicians and Surgeons*

Dean Sheppard, *Univ. of California,
San Francisco*

Katherine R. Spindler,
Univ. of Michigan Medical School

Paula H. Stern, *Northwestern Univ.
Feinberg School of Medicine*

Stephan F. Taylor, *Univ. of Michigan*

Jerry Vockley, *Univ. of Pittsburgh
School of Medicine and Graduate
School of Public Health*

John J. Voorhees, *Univ. of Michigan
Medical School*

Lorraine B. Ware, *Vanderbilt Univ.*

Paula I. Watnick,
Harvard Medical School

Michael A. Weiss, *Indiana Univ.
School of Medicine*

Ann H. West, *Univ. of Oklahoma*

E. John Wherry III,
Univ. of Pennsylvania

Pamela K. Woodard, *Washington
Univ. in St. Louis*

William W. Wright,
Johns Hopkins Univ.

Jian Yang, *Pennsylvania State Univ.*

Section on Neuroscience

Katerina Akassoglou, *Gladstone
Institutes/Univ. of California,
San Francisco*

Mark S. Blumberg, *Univ. of Iowa*

Emanuel M. DiCicco-Bloom,
*Rutgers Robert Wood Johnson
Medical School*

Guoping Feng,
*Massachusetts Institute
of Technology*

Viviana Gradinaru,
California Institute of Technology

Anne Church Hart, *Brown Univ.*

Christine F. Hohmann,
Morgan State Univ.

Alexandra Leigh Joyner,
*Memorial Sloan Kettering
Cancer Center*

Sharlene D. Newman,
Univ. of Alabama

Samuel Pfaff, *Salk Institute
for Biological Studies*

Susan Shore, *Univ. of Michigan*

David R. Sibley,
*National Institute of Neurological
Disorders and Stroke/NIH*

Nathan Anthony Smith,
*Children's National Hospital/ George
Washington Univ. School of Medicine
and Health Sciences*

Hongjun Song,
Univ. of Pennsylvania

Catherine Woolley,
Northwestern Univ.

Huaxi Xu, *Chongqing Medical Univ.
(China)*

Bing Ye, *Univ. of Michigan*

Karen Zito, *Univ. of California, Davis*

Section on Pharmaceutical Sciences

Namandjé N. Bumpus,
*Johns Hopkins Univ. School
of Medicine*

Stephen V. Frye, *Univ. of North
Carolina at Chapel Hill, Eshelman
School of Pharmacy*

Beth A. Habecker, *Oregon Health &
Science Univ.*

Alexander Victorovich Kabanov,
*Univ. of North Carolina
at Chapel Hill, Eshelman School
of Pharmacy*

James W. Lillard Jr.,
Morehouse School of Medicine

Gary W. Miller, *Columbia Univ.*

Yashwant V. Pathak,
Univ. of South Florida

Aliasger K. Salem, *Univ. of Iowa*

Bonnie Sloane, *Wayne State Univ.*

Jian-Ting Zhang, *Univ. of Toledo
College of Medicine and Life Sciences*

Section on Physics

Leon Balents, *Univ. of California, Santa Barbara*

Robert Howard Bernstein, *Fermi National Accelerator Laboratory*

Chandrashekhara Bhat, *Fermi National Accelerator Laboratory*

Nicholas P. Bigelow, *Univ. of Rochester*

Edward Charles Blucher, *Univ. of Chicago*

Philip Bucksbaum, *Stanford Univ.*

Roberto Car, *Princeton Univ.*

Paul Curmi, *Univ. of New South Wales (Australia)*

Karen E. Daniels, *North Carolina State Univ.*

J.C. Séamus Davis, *Univ. of Oxford (UK)/Univ. College Cork (IE)/Cornell Univ.*

Abhay Deshpande, *Stony Brook Univ./Brookhaven National Laboratory*

Persis S. Drell, *Stanford Univ.*

Douglas J. Durian, *Univ. of Pennsylvania*

Aida X. El-Khadra, *Univ. of Illinois Urbana-Champaign*

Henriette Elvang, *Univ. of Michigan*

Sarah Eno, *Univ. of Maryland, College Park*

Matthew P. A. Fisher, *Univ. California, Santa Barbara*

Eduardo Fradkin, *Univ. of Illinois Urbana-Champaign*

Cecilia E. Gerber, *Univ. of Illinois Chicago*

John F. Gunion, *Univ. of California, Davis*

Tony F. Heinz, *Stanford Univ.*

Thomas Charles Irving, *Illinois Institute of Technology*

Changqing Jin, *Institute of Physics, Chinese of Academy of Sciences (IOPCAS)(China)*

Aharon Kapitulnik, *Stanford Univ.*

John Kogut, *US Department of Energy/Univ. of Maryland, College Park*

I. Joseph Kroll, *Univ. of Pennsylvania*

Michael Annan Lisa, *The Ohio State Univ.*

Mark D. Lumsden, *Oak Ridge National Laboratory*

Hitoshi Murayama, *Univ. of California, Berkeley*

Filomena Nunes, *Michigan State Univ.*

Leo Piilonen, *Virginia Polytechnic Institute and State Univ.*

Carlos A. R. Sa de Melo, *Georgia Institute of Technology*

Jing Shi, *Univ. of California, Riverside*

David H. Shoemaker, *Massachusetts Institute of Technology*

James P. Vary, *Iowa State Univ.*

Hanno Weitering, *Univ. of Tennessee, Knoxville*

Xiaoxing Xi, *Temple Univ.*

Section on Psychology

Jerome Busemeyer, *Indiana Univ. - Bloomington*

Fernanda Ferreira, *Univ. of California, Davis*

Leonard Green, *Washington Univ. in St. Louis*

James J. Gross, *Stanford Univ.*

Mary Hegarty, *Univ. of California, Santa Barbara*

Ann M. Kring, *Univ. of California, Berkeley*

Ping Li, *The Hong Kong Polytechnic Univ. (China)*

Susan Kerri Lutgendorf, *Univ. of Iowa*

Mark A. McDaniel, *Washington Univ. in St. Louis*

Darcia Narvaez, *Univ. of Notre Dame*

James R. Pomerantz, *Rice Univ.*

C. Cybele Raver, *New York Univ.*

Patricia Ann Reuter-Lorenz, *Univ. of Michigan*

Marilyn Stern, *Univ. of South Florida*

Anne Tsui, *Arizona State Univ.*

Edward A. Wasserman, *Univ. of Iowa*

Section on Social, Economic, and Political Sciences

Bear Braumoeller, *The Ohio State Univ.*

Marcia Castro, *Harvard TH Chan School of Public Health*

Rachel T. A. Croson, *Univ. of Minnesota*

David E. Ervin, *Portland State Univ.*

Bridget J. Goosby, *The Univ. of Texas at Austin*

Michael Hout, *New York Univ.*

Jeanne C. Marsh, *Univ. of Chicago*

Margaret Marsh, *Rutgers Univ.-Camden and New Brunswick*

Jill J. McCluskey, *Washington State Univ.*

Julia McQuillan, *Univ. of Nebraska-Lincoln*

Alondra Nelson, *White House Office of Science and Technology Policy/Institute for Advanced Study*

Paul M. Romer, *New York Univ.*

Duncan Watts, *Univ. of Pennsylvania*

Amanda Woodward, *Univ. of Chicago*

Section on Societal Impacts of Science and Engineering

David Edward Blockstein, *Bard College*

Sara Brownell, *Arizona State Univ.*

Junji Cao, *Institute of Atmospheric Physics, Chinese Academy of Sciences (IAP) (China)*

Jason A. Delborne, *North Carolina State Univ.*

Baruch Fischhoff, *Carnegie Mellon Univ.*

Jerlando F. L. Jackson, *Univ. of Wisconsin-Madison*

Mae C. Jemison, *The Dorothy Jemison Foundation for Excellence*

Susan D. Renoe, *Univ. of Missouri*

Donald Siegel, *Arizona State Univ.*

Tania Simoncelli, *Chan Zuckerberg Initiative*

Section on Statistics

Veerabhadran Baladandayuthapani, *Univ. of Michigan*

Valen Earl Johnson, *Texas A&M Univ.*

Mingyao Li, *Univ. of Pennsylvania*

Tapabrata (Taps) Maiti, *Michigan State Univ.*

Sarah Nusser, *Iowa State Univ.*

Annie Qu, *Univ. of California, Irvine*

Nalini Ravishanker, *Univ. of Connecticut*

Luke Tierney, *Univ. of Iowa*

Call for nomination of 2022 Fellows

Fellows who are current members of AAAS are invited to nominate members for election as Fellows. A member whose efforts on behalf of the advancement of science or its applications are scientifically or socially distinguished, and who has been a continuous member for the 4-year period leading up to the year of nomination, may by virtue of such meritorious contribution be elected a Fellow by the AAAS Council.

A nomination must be sponsored by three previously elected AAAS Fellows (who are current in their membership), two of whom must have no affiliation with the nominee's institution. Nominations undergo review by the steering groups of the Association's sections (the chair, chair-elect, retiring chair, secretary, and four members-at-large of each section). Each steering group reviews only those nominations designated for its section. Names of Fellow nominees who are approved by the steering groups are presented to the Council in the fall for election.

REMINDER FOR 2022

The AAAS Executive Office is using a submission portal to accept all nominations this cycle, which means we will no longer be accepting nomination packets via email. Nominations with complete documentation must be received by 20 April 2022 at 11:59 p.m. EDT. Nominations received after that date or nominations that are incomplete as of the deadline will not move forward.

Complete instructions are available at <https://www.aaas.org/programs/fellows/current-nomination-cycle>. Questions may be directed to fellownomination@aaas.org.

RESEARCH

IN SCIENCE JOURNALS

Edited by Michael Funk

ANIMAL MIGRATION

Where to stop

Many migratory species undertake incredibly long migrations throughout a year. Much research has focused on understanding how these animals know where to go and how to return, and most work has focused on understanding how animals know—or learn—routes and directions. Equally important, however, is how they know when and where to stop migrating. Wynn *et al.* looked at a century of leg ringing and banding data in Eurasian reed warblers and found that the birds rely on the magnetic inclination as a “stop sign” to return to within meters of their breeding site. —SNV

Science, abj4210, this issue p. 446

Eurasian reed warblers perceive Earth's magnetic field to know where to stop in their migrations.



STRUCTURAL BIOLOGY

Nonhallucinogenic psychedelic analogs

Psychedelic drugs such as lysergic acid diethylamide (LSD) and mushroom-derived psilocybin exert their effects by binding the serotonin 2A receptor (5-HT_{2A}R). These drugs also have antidepressant effects, but the hallucinations they cause complicate their use as therapeutics. Cao *et al.* present structures of 5-HT_{2A}R bound to psychedelic drugs, the endogenous ligand serotonin, and the nonhallucinogenic drug lisuride. The structures reveal ligand-receptor interactions that cause a bias toward arrestin recruitment. Based on these insights, the authors designed arrestin-biased ligands that

displayed antidepressant-like activity in mice without hallucination effects. Arrestin recruitment alone is insufficient for antidepressant effects, but the low G-protein signaling of the arrestin-biased ligands appears to allow antidepressant effects without causing hallucination. —VV

Science, abl8615, this issue p. 403

NEUROSCIENCE

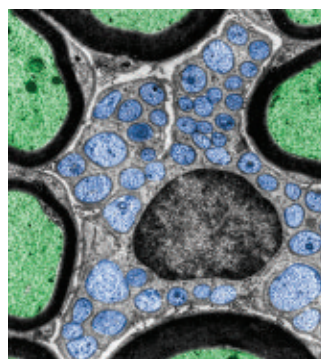
Phosphorylation dynamics for myelination

Myelin sheaths produced by Schwann cells protect and insulate the axons of peripheral neurons, enabling more rapid neurotransmission. Miyamoto *et al.* found that the production of Schwann cell myelin in mice

is regulated by phosphorylation dynamics at a tyrosine residue in cytohesin-2. In cultured cells, the adaptor protein SH2B1 maintained and the phosphatase PTP4A1 reversed the phosphorylation of this residue. Myelination

in sciatic nerve tissue was increased in mice in which cytohesin-2 phosphorylation was maintained and decreased in mice in which phosphorylation was suppressed. —LKF

Sci. Signal. **15**, eabi5276 (2022).



False-color electron microscopy image of a Schwann cell (center) within a nerve fiber

PROTEOMICS

Getting to know our proteoform

Over the past few years, large-scale proteomics efforts have allowed us to begin to understand phenotype at a protein level. These research efforts have included studies that map tissue- and cell-specific protein compositions. However, proteins function in the context of modifications that include alternative splicing and posttranscriptional

and posttranslational processing. Melani *et al.* compiled an atlas of proteoforms found in 21 cell types in human blood and bone marrow and show that proteoforms have higher cell-type specificity than proteins and so provide better indicators of cell type. These data are accessible in the Blood Proteoform Atlas, and as an example of potential applications, the authors show that the proteome signatures can distinguish normal graft function from graft rejection in liver transplants. —VV

Science, aaz5284, this issue p. 411

QUANTUM CRITICALITY Unexpected benefits of the sign problem

Solving challenging problems in quantum many-body physics often involves using numerical Monte Carlo methods. However, in the most interesting regime of strong interactions and low temperatures, the so-called sign problem can make calculations intractable. Mondaini *et al.* studied the severity of the sign problem quantitatively in several representative models. The researchers found that quantum critical behavior in these models correlated with the regions in the phase diagram where the sign problem was most pronounced. Viewed as a diagnostic for quantum criticality, the sign problem then becomes a tool (in addition to being a nuisance). —JS

Science, abg9299, this issue p. 418

2D MATERIALS Control through spin-orbit coupling

Twisting two graphene layers with respect to each other by a small, “magic” angle enhances electronic correlations in this two-dimensional (2D) material, leading to superconductivity and correlated insulating phases. These phases can be tuned by external factors such as pressure. Lin *et al.* add another control knob to this system by placing a layer of tungsten diselenide in the proximity

of the graphene bilayer. This arrangement results in spin-orbit coupling at the interface, causing the appearance of ferromagnetism at specific carrier concentrations. —JS

Science, abh2889, this issue p. 437

MOLECULAR BIOLOGY Dominant association

Intuitively, strong binding between two biological macromolecules means that at any given time, it is unlikely that they detach. However, Marklund *et al.* show that when the *lac* repressor interacts with DNA, it is primarily the probability of the repressor recognizing its target sequence that dictates the binding strength; the time spent in the bound conformation is subordinate. Dissociation will appear slow because the molecules can undergo many rebinding events after leaving the bound conformation but before separating in space. These results shed new light on the speed-stability paradox of DNA search kinetics. —DJ

Science, abg7427, this issue p. 442

CORONAVIRUS Reopening without COVID resurgence

After reopenings in May 2020, not all US states experienced a summer COVID resurgence. Wilke *et al.* combined 11 streams of age-structured public health and mobility data to show that during these reopenings, mobility increased but population mixing remained low, which limited transmission. This analysis also revealed that limiting population mixing was uneven across age groups, with the oldest and most vulnerable having the least flexibility. These findings illustrate the potential of multiple clinical data streams to support more accurate epidemic transmission models and explain how certain states managed their May 2020 reopenings to avoid a resurgence of COVID transmission later in the summer. —AJC

Sci. Adv. 10.1126/sciadv.abf9868 (2022).

IN OTHER JOURNALS

Edited by **Caroline Ash**
and **Jesse Smith**



Sunflowers rearrange their carbon metabolism to cope with drought conditions.

PLANT SCIENCE

Drought shifts carbon metabolism

Photosynthetic cells harness the sun's power by assimilating carbon through the Calvin-Benson cycle. This cycle is usually self-sufficient and regenerates its own substrate, ribulose 1,5-bisphosphate. After analyzing hydrogen isotopes in sunflower leaf starch, Wieloch *et al.* found evidence for an additional substrate supply with carbon diverted from the oxidative pentose phosphate pathway. These inputs increased as carbon dioxide concentrations inside the leaves decreased, a condition seen under drought. Rearrangement of carbon metabolism is likely to affect plant performance and biosphere-atmosphere carbon dioxide exchange in response to drought. —PJH

New Phytol. 10.1111/nph.17957 (2022).

VASCULAR DISEASE

Systemic cardiovascular disease

In the bone marrow, hematopoietic stem cell proliferation and leukocyte transit are controlled by the endothelial cells of blood vessels. Abnormal proliferation of inflammatory cells is a hallmark of cardiovascular disease. However, hypertension,

atherosclerosis, and myocardial infarction, which are prevalent in cardiovascular disease, negatively affect the vasculature systemically. Rohde *et al.* found that cardiovascular disease affected the microvascular anatomy of the bone marrow of mice. The authors observed that the endothelial-derived cytokine, interleukin (IL)-6, and an extracellular matrix



Humpback whale entangled in tackle used by the US Pacific Dungeness crab fishing industry

HUMAN-WILDLIFE CONFLICT

Crabs versus whales

Many conservation management plans are built on a narrow set of conditions that aim to both protect species and allow exploitation of natural resources. Climate change is likely to disrupt many of these given that it shifts the ways in which all species use their environment. Interactions between the lucrative Dungeness crab fishery and blue and humpback whale populations have long been managed through temporal and spatial displacement. Samhouri *et al.* found that an extended marine heat wave during 2014–2016 in the Northeast Pacific burned a hole in usual management practices that reduce conflict between the crab fishery and whale migration. During the heat wave, whales shifted their movement patterns, which led to significant increases in whale entanglement in crab fishing gear when the (already delayed) crab fishery began. —SNV *Proc. R. Soc. London Ser. B* 10.1098/rspb.2021.1607 (2021).

component called versican promoted myelopoiesis and leukocytosis. By deleting the gene for vascular endothelial growth factor (Vegfr2), angiogenesis was reduced, and when IL-6 or versican was eliminated, hematopoiesis slowed and myeloid cells declined. These insights indicate potential therapeutic targets. —BAP

Nat. Cardiovasc. Res. 1, 28 (2022).

MASS SPECTROMETRY

Focusing nanoparticles in air

Intact viruses and nanoparticles with masses beyond 10 megadaltons, too large to be detectable using conventional mass spectrometry, can be detected with chip-based nanomechanical resonators.

However, only a tiny fraction of nanoparticles hit the detector, and ion-focusing optics that can improve their efficiency require additional large vacuum systems. Erdogan *et al.* show that a large polymer sheet around the chip itself can act as a focusing lens. Nanoparticle ions generated at ambient pressure through electrospray ionization landed on the polymer. The charged region focused the central ion plume into the detector, leading to a greater than 100-fold increase in efficiency. Mass spectra of gold and polystyrene nanoparticles, as well as of severe acute respiratory syndrome coronavirus 2 (SARS-CoV-2) and bovine herpes virus viral particles, were obtained in this way. —PDS

ACS Nano 10.1021/acsnano.1c08423 (2022).

SUPERNOVAE

The final months of a dying star

When a sufficiently massive star runs out of fuel, the core collapses, leading to a supernova explosion. Theory predicts that the progenitor star can evolve substantially in the months before the supernova. Jacobson-Galán *et al.* analyzed photometry and spectroscopy of the supernova SN 2020tlf, which occurred in September 2020. They found a brightening of the progenitor for about 130 days before the explosion and an interaction of the expanding supernova with dense material close to the star. The authors infer a sudden release of energy in the star's core due to changing fusion reactions, which caused the ejection of substantial material

a few months before the star exploded. —KTS

Astrophys. J. 924, 15 (2022).

BIOMATERIALS

Feeling out the healing

Hydrogels have been used to release drugs or growth factors to help tissue repair, and the release of different agents and concentrations over time can accelerate the healing. However, the rate of release is usually preprogrammed into the host matrix. Li *et al.* developed a double-network hydrogel consisting of phenylboronic acid–cross-linked polyvinyl alcohol (PVA) and gelatin nanoparticles to aid in the repair of diabetic bone defects. The PVA network will reversibly degrade upon exposure to reactive oxygen species or high glucose, whereas the gelatin particles were designed to respond to certain proteinases. Therefore, the hydrogel is able to sense and respond to the local environment at the wound site so that the delivery of drugs is targeted to each stage of the healing process. —MSL

Adv. Mater. 10.1002/adma.202108430 (2021).

SYSTEMS BIOLOGY

Nitrogen stress patterns

Bacterial communities within an extracellular matrix, called biofilms, can exhibit a pattern-forming process that resembles the repeated patterns found in the segmentation of animals and plants. In such a colony, nitrogen is more available at the edges as the colony grows. However, Chou *et al.* detected cell-autonomous oscillations in the nitrogen stress response that result in ring-like patterns of cellular differentiation in a colony. Because the nitrogen stress response is linked to sporulation, this resulted in patterns of sporulation within the community. Whether the bacteria gain advantages from such multicellular behavior is unclear, but this work provides an example of clock-driven pattern formation previously only ascribed to higher organisms. —LBR

Cell 185, 145 (2022).

ALSO IN *SCIENCE* JOURNALS

Edited by Michael Funk

BRAIN DEVELOPMENT

Physiopathology in the human brain

Development of the human brain involves processes not seen in most animals. Eichmüller *et al.* identified CLIP cells, a human progenitor cell type responsible for tuberous sclerosis, a rare form of epilepsy triggered by excessive mechanistic target of rapamycin (mTOR) signaling, and recapitulated the disease in human cerebral organoids (see the Perspective by Ihrie and Henske). Excessive CLIP cell proliferation causes tumorigenesis and brain abnormalities. The researchers found that the sensitivity of these cells for mTOR signaling, not loss of healthy alleles, is responsible for the disease. This work changes our understanding of neurodevelopmental disease and reveals crucial aspects of human brain development. —BAP

Science, abf5546, this issue p. 401;
see also abn6158, p. 382

NEURODEVELOPMENT

Nests of interneuron proliferation

A transient structure in brain development, the medial ganglionic eminence is the birthplace of brain interneurons. These cells will migrate tangentially through the brain to contribute their inhibitory regulation to neuronal circuits. Looking closely at how the fetal human medial ganglionic eminence is structured, Paredes *et al.* found clusters of proliferative cells (see the Perspective by Kessaris). When cells from these clusters were transplanted into the neonatal mouse brain, the human-derived cells migrated and differentiated throughout. The nests of proliferative cells that characterize the developing human brain may support the greater need for interneurons in the larger

human brain compared with the smaller mouse brain. —PJH

Science, abk2346, this issue p. 402;
see also abn6333, p. 383

PALEOBOTANY

The origin of the dipterocarps

The Dipterocarpaceae are a prominent family of mainly tropical trees, reaching particularly high diversity and dominance in present-day Southeast Asian rainforests, where several species regularly reach heights of 50 meters or more. Bansal *et al.* used fossil pollen, molecular data, and paleobiogeographic analysis to study the origin and dispersal of the family (see the Perspective by Hoorn and Lim). The authors trace the origin of the dipterocarps to the mid-Cretaceous of tropical Africa, and postulate subsequent dispersal eastward across an Indian Ocean island arc to the then-isolated Indian subcontinent. The collision of the subcontinent with the Asian landmass then facilitated further dispersal toward Southeast Asia. —AMS

Science, abk2177, this issue p. 455;
see also abn6191, p. 380

HIBERNATION

While they sleep

Hibernation has evolved to remove animals from seasonal periods that are especially challenging for survival. Despite this protective feature, hibernation poses its own challenges because of the extensive fasting period. One particularly challenging aspect is the lack of dietary nitrogen, which can lead to protein imbalance. Regan *et al.* looked at gut microbiome activity in hibernating thirteen-lined ground squirrels and found that symbionts recycled nitrogen from urea into their own metabolites, which were then incorporated by the squirrels, allowing them to maintain protein balance (see the Perspective

by Sommer and Bäckhed). These results reveal the importance of the gut microbiome to hibernation and suggest that gut microbes could play such a role in other species. —SNV

Science, abh2950, this issue p. 460;
see also abn6187, p. 376

CORONAVIRUS

A site of vulnerability in SARS-CoV-2

Neutralizing antibodies are a key defense against severe acute respiratory syndrome coronavirus 2 (SARS-CoV-2). Many neutralizing antibodies target the region of the viral spike protein that is involved in binding to the human ACE2 receptor, known as the receptor binding motif (RBM). This region of the protein is divergent between SARS-CoV-2 variants, leading to failure of existing monoclonal antibody treatments and evasion of antibodies elicited by previous infection or vaccination. Park *et al.* describe a monoclonal antibody that neutralizes a broad range of sarbecoviruses, including both the 2003 SARS-CoV and SARS-CoV-2. This antibody also binds in the RBM but targets residues that are more conserved because they are involved in ACE2 binding. The antibody protects against the SARS-CoV-2 Beta variant, and none of the individual mutations in the Omicron variant affected antibody binding. —VV

Science, abm8143, this issue p. 449

TUMOR IMMUNOLOGY

Hematopoietic tumors SLAM macrophages

SLAM family receptors (SFRs) are widely expressed on hematopoietic cells and have been implicated in various innate immune functions. Li *et al.* used various cell lines and mice with gene deletions to show that SFR deficiency, specifically SLAMF3 and SLAMF4, increases the

ability of macrophages to phagocytose hematopoietic cells. Mice with SFR deletion exhibited hematopoietic tumor rejection, and SFR deletion was able to enhance the efficacy of chimeric antigen receptor macrophage therapy against hematopoietic cancer. These data show that SFR expression on hematopoietic cells can inhibit the function of macrophages, pointing to a potential therapeutic target for hematopoietic cancers. —DAE

Sci. Immunol. **6**, eabj5501 (2022).

HIV

PD-1 blockade for HIV

Strategies to target and reverse the latent HIV reservoir are required to cure HIV. Because CD4⁺ T cells expressing programmed cell death protein 1 (PD-1) are preferentially infected with HIV in individuals on antiretroviral therapy, PD-1 is an attractive target to manipulate the latent reservoir. To this end, Uldrick *et al.* measured the impact of anti-PD-1 treatment with pembrolizumab on the HIV reservoir in 32 individuals living with HIV and diagnosed with cancer. They observed evidence of increased unspliced HIV RNA and an increased ratio of unspliced RNA:DNA, consistent with anti-PD-1 treatment having the potential to reverse HIV latency. Further studies are needed to evaluate the dose and frequency of anti-PD-1 treatment required for latency reversal. —CSM

Sci. Transl. Med. **14**, eabl3836 (2022).

PLANT SCIENCE

Genomic handoff to the next generation

Haploid plant pollen grains are not simply passive carriers of genomes but rather serve as a developmentally and physiologically active bridge between the diploid parental plant and the diploid offspring plant. Nelms and Walbot sequenced the RNA content of single maize

pollen precursor cells and grains through the 26 days from the beginning of meiosis to pollen shed. These data reveal that about halfway through pollen development, the pollen grain's haploid genome wrests control from the going-away supplies left by the parental, diploid genome. With this sporophyte-to-gametophyte transition, the foundations are set for the next generation. —PJH

Science, abI7392, this issue p. 424

SOLAR CELLS

Inverted solar cells' surface sulfidation

Perovskite solar cells (PSCs) with high power conversion efficiency (PCE) and stability have been reported in regular n-i-p devices, but inverted p-i-n PSCs that could be easier to use in tandem solar cells usually have lower PCEs (22 to 23%). Li *et al.* sulfurized a lead-rich layer with hexamethyldisilathiane, and the lead-sulfur bonds shifted the Fermi level of perovskite-transporter layer interface to create an electric field that enhanced electron extraction. The inverted PSCs had PCEs >24%, and the strong lead-sulfur bonds helped to maintain >90% of this efficiency during illuminated operation for 1000 hours at 55°C and after dark aging at 85°C for 2200 hours. —PDS

Science, abI5676, this issue p. 434

2D MATERIALS

Displacing the Fermi surface

Electrons that contribute to electrical conduction in a metal typically occupy high energy levels near the Fermi level. To get electrons from lower bands to join the flow, extremely large electric fields would be needed. In graphene and its superlattices, Berdyugin *et al.* show that small, experimentally accessible fields are sufficient to achieve this regime. The researchers discerned the signatures of this highly nonequilibrium state in transport data. —JS

Science, abI8627, this issue p. 430

RESEARCH ARTICLE SUMMARY

BRAIN DEVELOPMENT

Amplification of human interneuron progenitors promotes brain tumors and neurological defects

Oliver L. Eichmüller, Nina S. Corsini*, Ábel Vértesy, Ilaria Morassut, Theresa Scholl, Victoria-Elisabeth Gruber, Angela M. Peer, Julia Chu, Maria Novatchkova, Johannes A. Hainfellner, Mercedes F. Paredes, Martha Feucht, Jürgen A. Knoblich*

INTRODUCTION: Development of the human brain is protracted and involves distinct processes that have contributed to its large size and complexity. However, these changes might have also increased the vulnerability of the human brain to genetic disorders. Tuberous sclerosis complex (TSC) is a neurodevelopmental disorder characterized by debilitating neuropsychiatric symptoms, including epilepsy, autism, and intellectual disabilities. It involves distinct morphological aberrations in the brain such as the formation of benign subependymal tumors and dysplastic cortical lesions, which are commonly referred to as cortical tubers. TSC arises from mutations in the mechanistic target of rapamycin (mTOR) inhibitors TSC1 and TSC2 and is thought to be caused by elevated mTOR signaling activity.

RATIONALE: TSC is thought to originate from heterozygous TSC1/2 germline mutations fol-

lowed by loss-of-function mutations that disrupt the second allele and cause somatic loss of heterozygosity (LOH). This hypothesis is generally supported by mouse models, but analysis of patient tissues revealed LOH only in tumors and rarely in the dysplastic regions. In addition, the animal models failed to recapitulate the full spectrum of pathognomonic lesions. We hypothesized that aspects of specifically human brain development rather than LOH could initiate the disease.

RESULTS: We generated a human model for TSC by growing cerebral organoids from patients who carried mutations in TSC2. The organoid model recapitulates the emergence of both brain tumors and dysplastic cortical regions. Using single-cell RNA-sequencing (scRNA-seq) and extensive histological validation, we identified a specific interneuron progenitor population that gives rise to both

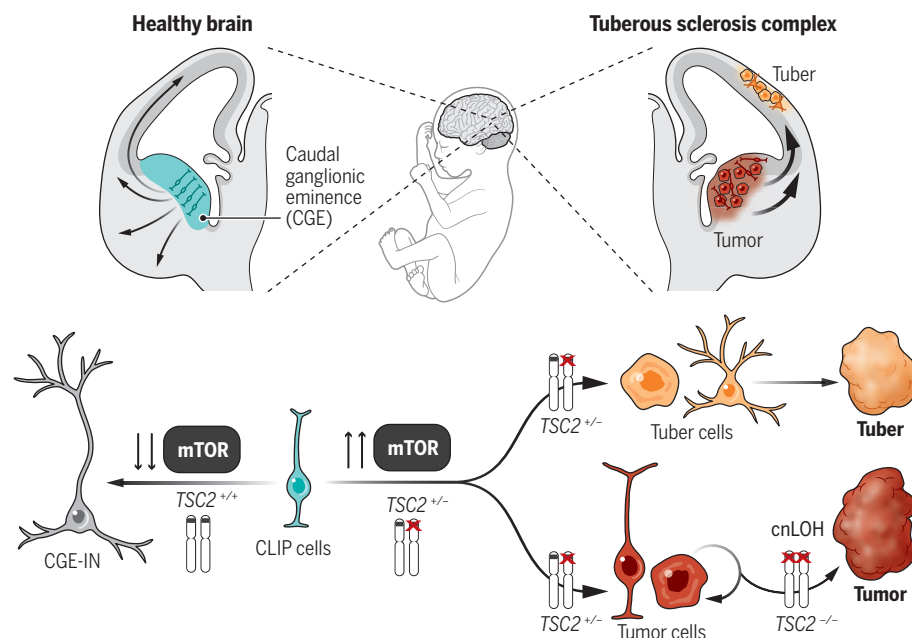
tumor and cortical tuber lesions. Comparisons of expression signatures with fetal brain scRNA-seq data revealed the origin of this cell type in the caudal ganglionic eminence (CGE) during mid-gestation. We therefore refer to this cell type as caudal late interneuron progenitor (CLIP) cells.

Our analysis uncovered particularly low amounts of TSC1/2 complex proteins in CLIP cells, making them susceptible to TSC1/2 levels. CLIP cells overproliferate and initiate both tumor and cortical tuber formation even when just one copy of TSC2 is lost. The second TSC2 allele can be mutated during tumor progression, but this does not occur through a second somatic mutation. Instead, it is caused by copy-neutral LOH (cnLOH), the exchange of large genomic regions between homologous chromosomes. CLIP cells depend on epidermal growth factor receptor (EGFR) signaling, and EGFR inhibition can revert the TSC phenotype, suggesting an alternative inroad to therapeutic intervention.

The sequence of events leading to TSC was validated in postmortem patient tissues. The seemingly confusing histological appearance of TSC brain lesions can be explained by the initiation of cortical lesions by CLIP cells and their derivatives, whereas other cell types contribute only at later stages. Thus, our analysis can explain the different mutational status of brain tumors and cortical tubers in TSC patients in the context of a common cell of origin.

CONCLUSION: This work shows that the analysis of neurodevelopmental genetic disorders can lead to fundamental mechanistic insights into human brain development. CLIP cells are identified as the shared cell of origin for brain lesions in TSC. The contribution of different lineages over time then generates the complex neurological defects observed in TSC. Although cnLOH occurs during TSC tumor progression, it is dispensable for disease initiation, demonstrating that the disease relevance of mutations should always be evaluated in the context of a specific cell of origin.

Human brain expansion was accompanied by a diversification of progenitor cell types. This work showcases an example of such a human progenitor cell type responsible for a human neurodevelopmental disease and demonstrates the necessity of using human models to identify disease mechanisms that involve processes not conserved in all mammals. ■



During mid-gestation, CLIP cells residing in the CGE generate interneurons that migrate into the cortex.

(Top right) In TSC, CLIP cells generate brain tumors and cortical tubers. Heterozygous mutations in TSC2 result in excessive proliferation of CLIP cells, generating cell types of cortical tubers (orange) as well as brain tumors (red). During progression, the healthy allele is lost because of cnLOH, increasing tumor proliferation.

The list of author affiliations is available in the full article online.

*Corresponding author. Email: nina.corsini@imba.oew.ac.at (N.S.C.); juergen.knoblich@imba.oew.ac.at (J.A.K.)
Cite this article as O. L. Eichmüller et al., *Science* 375, eabf5546 (2022). DOI: 10.1126/science.abf5546

READ THE FULL ARTICLE AT
<https://doi.org/10.1126/science.abf5546>

RESEARCH ARTICLE

BRAIN DEVELOPMENT

Amplification of human interneuron progenitors promotes brain tumors and neurological defects

Oliver L. Eichmüller^{1,2}, Nina S. Corsini^{1*}, Ábel Vértesy¹, Ilaria Morassut¹, Theresa Scholl³, Victoria-Elisabeth Gruber³, Angela M. Peer¹, Julia Chu⁴, Maria Novatchkova¹, Johannes A. Hainfellner⁵, Mercedes F. Paredes⁴, Martha Feucht³, Jürgen A. Knoblich^{1,5*}

Evolutionary development of the human brain is characterized by the expansion of various brain regions. Here, we show that developmental processes specific to humans are responsible for malformations of cortical development (MCDs), which result in developmental delay and epilepsy in children. We generated a human cerebral organoid model for tuberous sclerosis complex (TSC) and identified a specific neural stem cell type, caudal late interneuron progenitor (CLIP) cells. In TSC, CLIP cells over-proliferate, generating excessive interneurons, brain tumors, and cortical malformations. Epidermal growth factor receptor inhibition reduces tumor burden, identifying potential treatment options for TSC and related disorders. The identification of CLIP cells reveals the extended interneuron generation in the human brain as a vulnerability for disease. In addition, this work demonstrates that analyzing MCDs can reveal fundamental insights into human-specific aspects of brain development.

Malformations of cortical development (MCDs) comprise varied neurodevelopmental disorders that cause more than 40% of medically refractory childhood seizures (1). Several MCDs—including hemimegalencephaly, focal cortical dysplasia IIb, and tuberous sclerosis complex (TSC)—are caused by mutations in mechanistic target of rapamycin (mTOR) pathway members, but their disease mechanisms remain elusive. TSC is a rare autosomal dominant disorder caused by mutation of either *TSC1* (hamartin) or *TSC2* (tuberin), which form a complex and inhibit the mTOR kinase. Patients suffer from debilitating, often drug-resistant neuropsychiatric symptoms, including intractable epileptic seizures, autism spectrum disorder (ASD), and intellectual disability (ID) (2). Most patients have focal dysplastic regions (cortical tubers) in the cortex, which consist of dysmorphic neurons, giant cells (GCs), and dysmorphic astrocytes (3, 4). In addition, 80% of patients display subependymal nodules (SEN), benign tumors that form along the proliferative niches at the lateral ventricle and can develop into subependymal giant cell astrocytomas (SEGAs) (5). Analysis of human primary tissues suggested a common cell-of-origin for cortical tubers and SEN/SEGAs on the basis of shared transcrip-

tomic alterations (6); however, the nature of this cell remains unclear. In mice, TSC pathogenesis is initiated through inactivation of the second allele of either *TSC1* or *TSC2* (7–12), and similar results have been obtained in spheroids (13). Genetic analysis in patients, however, revealed loss of the second allele in most SEN/SEGAs, but only few cortical tubers (6, 14–16), challenging the previously suggested two-hit model (7, 17). We hypothesized that these inconsistencies arise because cell types and processes specific to the human brain are critical for disease initiation. To identify those human-specific features, we generated human cerebral organoids (18) from patient-derived induced pluripotent stem cells (iPSCs) and compared our results with human primary material.

Cerebral organoids recapitulate TSC

To model the brain pathology of TSC, we derived iPSCs from patients with known *TSC2* mutations who suffer from drug-resistant epilepsy and show cortical tubers and subependymal tumors (Fig. 1A and fig. S1, A to C). Isogenic *TSC2*^{+/+} lines were acquired directly from the germline mosaic first patient and generated by means of scarless CRISPR-based genome editing for the second patient (fig. S1, D, E, and H). Both patient mutations resulted in an early stop codon in regions commonly mutated in TSC (fig. S1, F and G). To study subependymal tumors, we cultured organoids in a high-nutrient (H) medium that promotes proliferation (Fig. 1B and indicated in all figures with an “H” by the staining panels). To examine the formation of cortical tubers, which emerge in less proliferative cortical regions, we transferred organoids to a low-nutrient (L)

medium adapted from a published formulation (19) to three-dimensional culture (Fig. 1B and indicated in all figures with an “L” by the staining panels, and materials and methods).

We found no obvious differences between genotypes within the first 90 days of culture (fig. S2) corresponding to early phases of neurodevelopment, which is consistent with previous results (13); 110 days after embryoid body (EB) formation, however, nodular aggregates of cells expressing the proliferative marker Ki67 and the mTOR activation marker phospho-S6 (pS6) formed in *TSC2*^{+/+} organoids cultured in H-medium (*TSC2*^{+/+} H-organoids) (Fig. 1, D, G, and H; and fig. S3, A to F). These structures morphologically resembled SENs (Fig. 1C) (20–22). We validated the emergence of SEN-like tumors in organoids derived from a third TSC patient (Fig. 1, G and H, and fig. S3, C and D). SEN/SEGAs have been proposed to originate from an uncharacterized population of neural stem cells (NSCs) (23, 24). To test for an NSC origin of SEN-like tumors in organoids, we stained for NSC markers. Expression of Nestin, ASCL1, and SOX2 (fig. S3, B, G, and H) demonstrated the NSC identity of SEN-like tumors in organoids.

To determine whether we could recapitulate the pathological cell types found in cortical tubers, we analyzed organoids cultured for 120 to 150 days in L-medium. In organoids derived from *TSC2*^{+/+} cells, we found neurons with an enlarged soma and thickened processes similar to those of dysmorphic neurons in cortical tubers (Fig. 1, E and I, and fig. S4, A to D). After prolonged maturation in L-medium (~230 days), clusters of enlarged pS6-positive cells appeared (Fig. 1, F and J, and fig. S4, E to I). The morphology and expression of markers such as glial fibrillary acidic protein (GFAP) and Vimentin were reminiscent of GCs (3, 5), which had characteristically low proliferation rates (Fig. 1F).

Dysmorphic astrocytes, a cell type previously identified in patient tubers, share marker expression with GCs but are morphologically distinct (4). In organoids, we identified individual enlarged GFAP-expressing cells morphologically similar to dysmorphic astrocytes with characteristic thickened and prolonged processes (fig. S4J). GCs expressed the neural progenitor marker Nestin (fig. S4F) (24), and almost all enlarged GFAP cells (GCs and dysmorphic astrocytes) in organoids expressed SOX2, suggesting a neural progenitor identity (patient 1, 99.7%; patient 2, 96%) (fig. S4, J and K).

Both cortical and tumor lesions were detected in H- and L-medium organoids (figs. S3I and S4L); however, the use of two different culturing conditions favored the emergence of the two specific phenotypes. Thus, organoids derived from *TSC2*^{+/+} hiPSCs recapitulate the major histopathological features found in the brain of TSC patients.

¹Institute of Molecular Biotechnology (IMBA), Austrian Academy of Sciences, Vienna Biocenter (VBC), Vienna, Austria.

²University of Heidelberg, Heidelberg, Germany. ³Department of Pediatric and Adolescent Medicine, Medical University of Vienna, Vienna, Austria. ⁴Department of Neurology, University of California, San Francisco, San Francisco, CA, USA. ⁵Department of Neurology, Medical University of Vienna, Vienna, Austria.

*Corresponding author. Email: nina.corsini@imba.oew.ac.at (N.S.C.); juergen.knoblich@imba.oew.ac.at (J.A.K.)

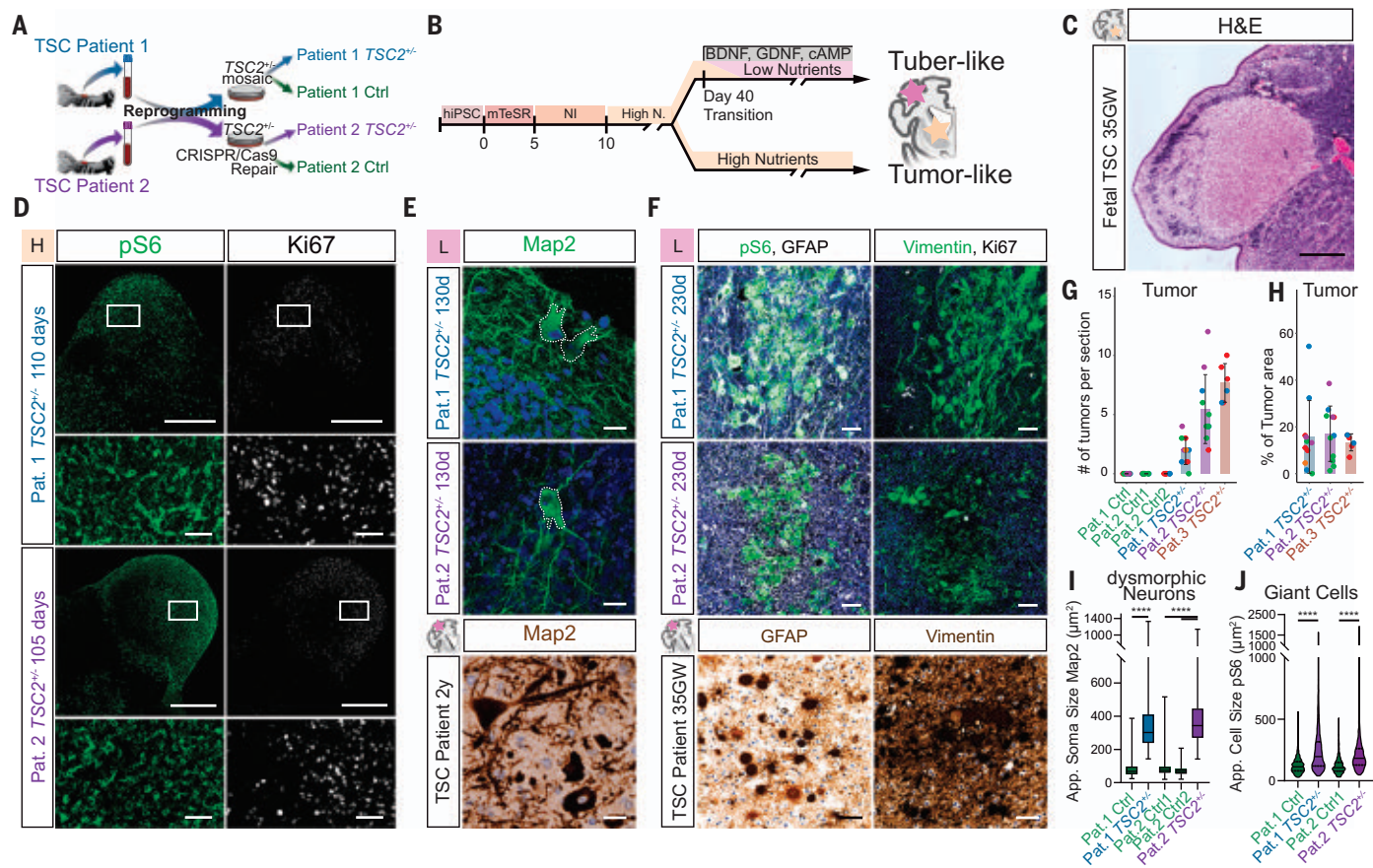


Fig. 1. TSC2^{+/−}-derived organoids recapitulate histopathology of TSC.

(A) Control (Ctrl) and TSC2^{+/−} cell lines derived from two patients (supplementary materials, materials and methods). (B) High- and low-nutrient organoid protocols used to model distinct TSC phenotypes. (C) Hematoxylin and eosin (H&E) staining of 35GW fetal brain depicts histopathology of a fetal SEN. (D) pS6 and Ki67 staining on 110- and 105-day-old TSC2^{+/−}-derived organoids in high-nutrient medium identifies SEN-like structures. (Bottom) Higher magnification of inset. (E) (Top) Map2 staining on 130-day-old organoids in L-medium shows dysmorphic neurons, with morphology comparable to those in (bottom) a resected tuber of a 2-year-old patient. Nuclear counterstain was performed with 4',6-diamidino-2-phenylindole (DAPI) or hematoxylin. (F) pS6 and GFAP identifies GCs in 230-day-old organoids comparable with GCs in patient tubers. GCs in organoids express Vimentin, as shown in patients. GCs can be distinguished from tumors by their lower expression of Ki67. Nuclear counterstain was performed with DAPI or hematoxylin. (G) Tumors identified as pS6- and Ki67-positive areas are found in TSC2^{+/−}-derived organoids of all three patients. Control organoids of patient 1 and two clones of repaired

patient 2 showed no tumors. Color of dots indicate independent batches of experiments (a summary of replicates is available in fig. S3E). (H) Percentage of tumor area of the total organoid area reveals similar tumor burden for organoids derived from three TSC2^{+/−} patients. Color of dots indicate independent batches of experiments (a summary of replicates is available in fig. S3F). (I) Area of the soma in Map2⁺ neurons shows that dysmorphic neurons in TSC2^{+/−}-derived organoids are roughly fourfold larger than Map2⁺ neurons in control organoids [patient 1 control versus TSC2^{+/−} $P < 0.0001$; patient 2 control 1 versus TSC2^{+/−} and patient 2 control 2 versus TSC2^{+/−} both $P < 0.0001$; ordinary one-way analysis of variance (ANOVA)] a summary of replicates is available in fig. S4D). (J) Cell area of pS6-positive cells shows enlarged pS6 cells in TSC2^{+/−}-derived organoids. (patient 1 control versus TSC2^{+/−} $P < 0.0001$, patient 2 control versus TSC2^{+/−} $P < 0.0001$, patient 1 control versus patient 2 control $P > 0.9999$, patient 1 TSC2^{+/−} versus patient 2 TSC2^{+/−} $P > 0.9999$; Kruskal-Wallis test with Dunn's multiple comparisons test) (a summary of replicates is available in fig. S4E) Scale bars, (C) and (D) 500 μ m; (E) 20 μ m; and (D), inset, and (F), inset, 50 μ m.

Interneuron progenitors in TSC tumors

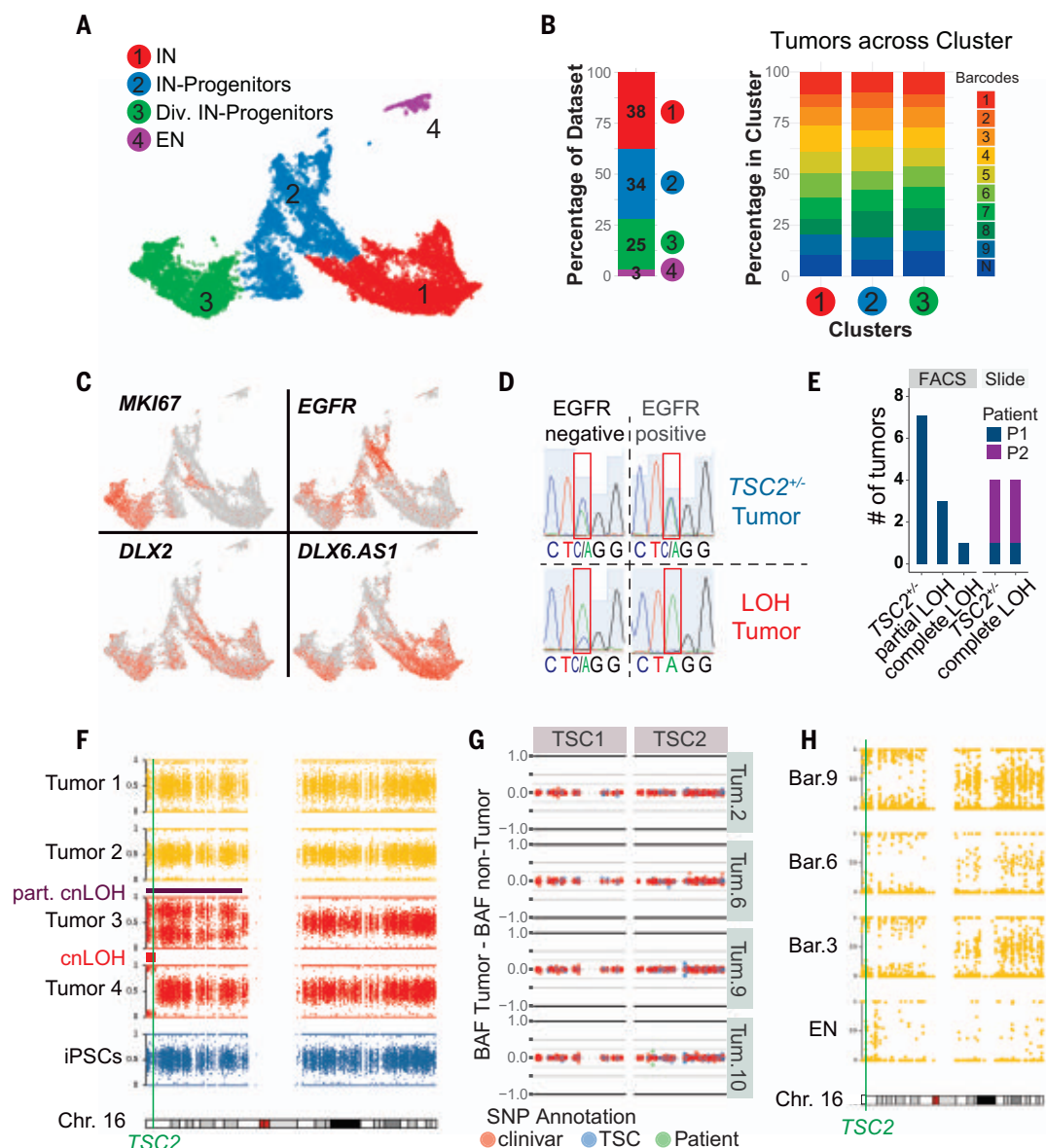
To characterize the cellular composition of tumors in TSC organoids, we performed single-cell transcriptomic analysis on 220-day-old organoids grown in H-medium. At this age, organoids consist almost exclusively of tumor tissues (fig. S5A). To compare intertumoral heterogeneity, three organoids were dissected into three tumor regions each and barcoded separately (25). Unsupervised clustering in UMAP projection identified four main clusters: interneurons (cluster 1), interneuron progenitors (cluster 2), dividing interneuron progenitors

(cluster 3), and excitatory neurons (cluster 4) (Fig. 2A). Interneurons were characterized by the expression of canonical regulators of interneuron development such as *DLX2*, *DLX5*, and *DLX6-AS1* (Fig. 2C and fig. S5B). Interneuron progenitors expressed *DLX2*; *EGFR*; and progenitor markers such as *HES1*, *SLC1A3*, or *VIM* (Fig. 2C and fig. S5B). Dividing progenitors of the interneuron lineage were characterized by additionally expressing markers such as *MKI67* and *TOP2A* (Fig. 2C and fig. S5B). Only a very small number of excitatory lineage cells (cluster 4) were detected (3%) (Fig.

2B), marked by the expression of *NEUROD2* and *NEUROD6* (fig. S5B). Thus, tumors in TSC2^{+/−} H-organoids consist mainly of progenitors and interneurons of ventral origin (Fig. 2C).

To investigate intertumoral heterogeneity, we compared the barcoded tumor regions. The cell type composition was highly consistent among the ventral lineage clusters, with all barcodes being evenly distributed (Fig. 2B and fig. S5, C and D). Whereas in the traditional view of tumorigenesis, in which TSC inactivation of the second allele is thought to be a

Fig. 2. TSC tumors consist of interneuron progenitors and acquire cnLOH during progression. (A) UMAP projection of cells isolated from 220-day-old TSC tumor organoids identified four main clusters: interneurons (cluster 1), interneuron progenitors (cluster 2), dividing interneuron progenitors (cluster 3), and excitatory neurons (cluster 4). (B) Data-set composition and contribution of different tumor regions. Of cells in tumors, 97% were ventral cells, and all nine tumor regions of three organoids were similarly distributed across ventral clusters (clusters 1, 2, and 3). (C) Expression of genes specific for dividing cells (*MKI67*) and interneurons (*DLX2* and *DLX6.AS1*) in 220-day-old TSC tumors. *EGFR* was specifically expressed in TSC tumor progenitors. (D) Genotyping example of FACS-sorted tumor (*EGFR*⁺) and nontumor (*EGFR*⁻) population, showing a heterozygous tumor and a LOH tumor that lost the wild-type (WT) allele (C) within the tumor. (E) Genotyping of tumors of patient 1 in FACS-sorted samples showing that 7 out of 11 TSC tumors were heterozygous, three showed a partial LOH, and one tumor showed a full LOH. Genotyping tumors from stained slides confirmed the presence of heterozygous and LOH tumors (patient 1, one *TSC2*^{+/-} tumor and one LOH tumor; patient 2, three *TSC2*^{+/-} tumors and three LOH tumors). (F) B-allele frequency (BAF) of chromosome 16 for four tumors of patient 1 *TSC2*^{+/-}-derived organoids. Whereas tumors 1 and 2 remain heterozygous, a shift in BAF is seen in tumors 3 and 4 compared with iPSCs. BAF and log R ratio (LRR) are provided in fig. S6L. Tumor 2 showed a partial cnLOH of a large section, whereas tumor 4 had a small complete cnLOH at the beginning of chromosome 16. Both cnLOH regions included the *TSC2* gene. (G) Targeted amplification of *TSC1* and *TSC2* in four tumors and matched nontumor samples of patient 1. Detected SNPs are colored as annotation of clinivar database (red), Leiden Open Variation Database (LOVD) TSC database (blue), or disease-causing



SNP of patient 1 (green). The difference between BAF of the tumor and matched nontumor sample is shown. No disease-causing SNPs increased in the tumor samples could be detected. In tumor 10, there was a small shift of the patient SNP, which was confirmed as partial cnLOH (fig. S6I). (H) SNP mapping of scRNA-seq data shown in (A). Cells from tumors with sufficient reads (barcodes 3, 6, and 9) and excitatory neurons were aggregated per group, and allelic frequencies were determined. All tumors showed cnLOH, whereas excitatory neurons [(A), cluster 4] remained heterozygous.

prerequisite for causing the disease (7), our data suggest that a specific cell type that is sensitive to levels of mTOR signaling gives rise to TSC tumors.

Copy-neutral loss of heterozygosity in TSC tumors

To determine whether biallelic inactivation is required for the initiation of tumor lesions, we tested the mutational status of *TSC2*^{+/-}-derived organoids grown in H-medium at earlier

stages (135 to 160 days). Tumor cells were isolated from patient 1 mutant organoids by means of fluorescence-activated cell sorting (FACS) for epidermal growth factor receptor (*EGFR*) (fig. S6, A to D and F to H), which was highly expressed on the interneuron progenitor cells in dissected tumors (Fig. 2C and fig. S6E). Genotyping of the *TSC2* locus indicated that many tumors remained heterozygous (Fig. 2, D and E, and fig. S6, I to K). In organoids

from patient 1, we identified complete loss of heterozygosity (LOH) in one tumor and partial LOH in three tumors (Fig. 2E and fig. S6I). Additionally, we genotyped tumor sections and confirmed LOH in a subset of tumors of patients 1 and 2 (Fig. 2E and fig. S6, J and K).

To analyze recombination events in TSC tumors, we performed whole-genome sequencing (WGS) on two heterozygous and two LOH tumor samples (Fig. 2F and fig. S6, L and M).

WGS revealed no major genomic rearrangements in heterozygous tumors (Fig. 2F and fig. S6, L and M). By contrast, in LOH tumors extensive regions of chromosome 16, ranging from the telomere to and beyond the *TSC2* locus, had become homozygous through copy-neutral LOH (cnLOH) (Fig. 2F and fig. S6, L and M), the same genomic event resulting in LOH in TSC patients (6).

To test whether heterozygous tumors acquired second-hit mutations, we performed targeted amplification of *TSC1* and *TSC2* on four tumors and matched controls of patient 1 (Fig. 2G). No other pathogenic single-nucleotide polymorphisms (SNPs) were increased in tumor samples (Fig. 2G). Thus, a second hit at the *TSC1* or *TSC2* locus is not required for tumor initiation.

To probe whether cnLOH occurred at later stages during tumor progression, we investigated allelic frequencies in the 220-day-old single-cell RNA-sequencing (scRNA-seq) data (Fig. 2H). Tumor cells aggregated per barcode showed cnLOH in all tumors (Fig. 2H). Excitatory neurons (Fig. 2A, cluster 4) did not show cnLOH, further supporting an interneuron origin of TSC tumors (Fig. 2H). Thus, tumors in TSC organoids initiated from a heterozygous interneuron progenitor and acquired cnLOH only during progression.

To investigate whether cnLOH was required for the formation of cortical tuber-like structures, we analyzed GCs in 230-day-old *TSC2*^{+/-} organoids. *TSC2* protein expression was detected in more than 98% of GCs by using an antibody that recognizes only the wild-type *TSC2* variant (patient 1, 98.4%; patient 2, 98.7%) (fig. S7, A to C). *TSC2* protein was also expressed in GCs in fetal cortical tubers (fig. S7D), which is consistent with previous data (26, 27). This suggests that second-hit events are not a prerequisite for tuber formation. Thus, although previous studies in mice have defined LOH in *Tsc1* (8, 9, 11, 12, 28) or *Tsc2* (10) as a requirement for TSC-like phenotypes, our data demonstrate that in human tissues, biallelic inactivation is dispensable for disease initiation. Our observations are consistent with reports that identify biallelic inactivation in subependymal tumors but rarely in cortical tubers (6, 14–16, 29, 30).

Given that tumorigenesis in TSC organoids did not require cnLOH, we hypothesized that low amounts of *TSC1/2* complex could sensitize interneuron progenitors to further reduction of *TSC1* or *TSC2*. We observed reduced *TSC2* in EGFR-positive interneuron progenitors in both control and in *TSC2*^{+/-}-derived organoids from both patients grown in H-medium (fig. S7, E to H) by using immunofluorescence. To quantitate *TSC1* and *TSC2* protein amounts, we performed targeted parallel reaction monitoring mass spectrometry (tPRM-MS) on FACS-sorted samples from patient 1 in H-medium.

Both in control and *TSC2*^{+/-}-derived organoids, *TSC1* and *TSC2* were lower in EGFR-positive samples than in EGFR-negative samples (fig. S7J). Comparing EGFR-positive populations, we observed that whereas *TSC1* was expressed at similar levels, *TSC2* was significantly more down-regulated in EGFR-positive cells in the *TSC2* mutant as compared with the control population (fig. S7K). Thus, although in control organoids both components of the TSC complex were equally reduced, in TSC tumor cells, loss of one functional *TSC2* allele led to disproportional reduction of *TSC2*. These data suggest that interneuron progenitors have low levels of TSC proteins, which could sensitize them to heterozygous mutations in TSC genes.

The developmental trajectories of tumors and tubers

To determine whether tumors and tubers have a common cell of origin, we investigated H- and L-organoids at 110 days, when the TSC phenotypes were beginning to emerge (fig. S8, E to G). We integrated these data with the 220-day-old TSC tumor dataset (Fig. 3A). Unsupervised clustering in UMAP projection identified dorsal progenitor cells (clusters 3, 10, and 12), excitatory neurons (clusters 1, 2, 4, and 14), interneuron progenitor cells, and interneurons (clusters 5 to 9, 11, 13, 16, and 17), and cells resembling pre-oligodendrocyte-progenitor (OPC)-like cells (cluster 15) (Fig. 3A and fig. S8, B and C) (31). The 220-day-old TSC tumors contributed almost exclusively to the clusters that contained interneuron progenitor cells and interneurons (clusters 5 to 9, 11, and 13) (Fig. 3B). The same clusters were more abundant in 110-day-old *TSC2*^{+/-} H- and L-organoids compared with control organoids: *TSC2*^{+/-} H-organoids had more progenitor cells (clusters 5, 7, 11, and 13) (Fig. 3B), whereas in *TSC2*^{+/-} L-organoids, mature interneurons were substantially increased (clusters 9 and 16) (Fig. 3B). Pre-OPC-like cells (Cl. 15) were slightly increased in 110-day-old TSC organoids. However, this cell type did not show morphological changes (fig. S9F). Thus, OPC lineages did not seem to contribute to TSC lesions in organoids.

To confirm that cnLOH was not required for the initiation of TSC phenotypes, we tested allelic frequencies in the d110 scRNA-seq datasets. Interneuron progenitors in *TSC2*^{+/-} datasets did not show cnLOH, which is consistent with a disease initiation from a heterozygous progenitor (fig. S8H). This suggests that expansion of a common interneuron progenitor rather than cnLOH initiates tumor and tuber phenotypes.

To characterize the common cell of origin, we analyzed the gene expression signatures of the cells overrepresented in TSC organoids. Expression of markers such as *DLX2*, *DLX5*, *SP8*,

COUP-TFII (*NR2F2*), and *SCGN* (fig. S8, B and D) revealed that this lineage originated from the caudal ganglionic eminence (CGE), a region in the ventral forebrain. The quiescent CGE progenitors (cluster 7) also expressed markers previously not found in interneuron progenitors, such as *EDNRB* and *PTGDS* (fig. S8D).

To investigate the developmental trajectories of these populations, we performed RNA velocity and pseudotime analysis (Fig. 3C and fig. S9, A to E). RNA velocity revealed a major trajectory toward CGE interneurons and a small bifurcation of CGE progenitors toward pre-OPC cells (Fig. 3C). Along the CGE lineage, we found expression of markers for quiescent (*GFAP*, *HOPX* together with *EDNRB* and *PTGDS*) and activated progenitors (*EGFR* and *DLX2*) and CGE interneurons (*DLX6-AS1* and *SCGN*) in both control and *TSC2*^{+/-} organoids (Fig. 3D and fig. S9C). The small trajectory toward pre-OPC cells showed markers recently described for human pre-OPC lineages (fig. S9, D and E) (31).

Both tumor and tuber organoids shared the trajectory from CGE progenitors to CGE interneurons (Fig. 3C). To test whether lesion-specific cell types emerge, we investigated the trajectories within interneurons as determined from RNA velocity (Fig. 3C). We found that mature interneurons were separated into tumor- and tuber-enriched interneurons (fig. S10, A to F). Tumor interneurons were enriched in Gene Ontology (GO) terms related to ribosomal proteins and translation, whereas tuber interneurons showed specific up-regulation related to synapse formation and activity (fig. S10, G to O).

Although the descriptive nature of our scRNA-seq experiments limits their generalizability, these data indicate that interneuron progenitors that are increased in TSC follow defined developmental trajectories and diverge into lesion-specific interneuron subtypes.

Therefore, to determine whether the common developmental trajectory is present in the human fetal brain, we integrated our data with published scRNA-seq data from different fetal ages (fig. S11A) (32). Coclustering revealed similar cell types in the fetal brain (fig. S11, A and B), and pseudotime analysis confirmed trajectories toward interneurons and OPC cells (fig. S11, B and C). We found similar gene expression cascades along the neurogenic trajectory, with markers of quiescent progenitors expressed together with *EDNRB* and *PTGDS*, followed by activated progenitors and interneurons (fig. S11, D to F). Thus, developmental trajectories that are increased in TSC patient organoids are present in the human fetal brain.

Because phenotypes in TSC organoids arose at later stages of organoid development, we hypothesized that the expanded CGE progenitors might correspond to specific progenitors in the fetal brain (Fig. 3E, red circle).

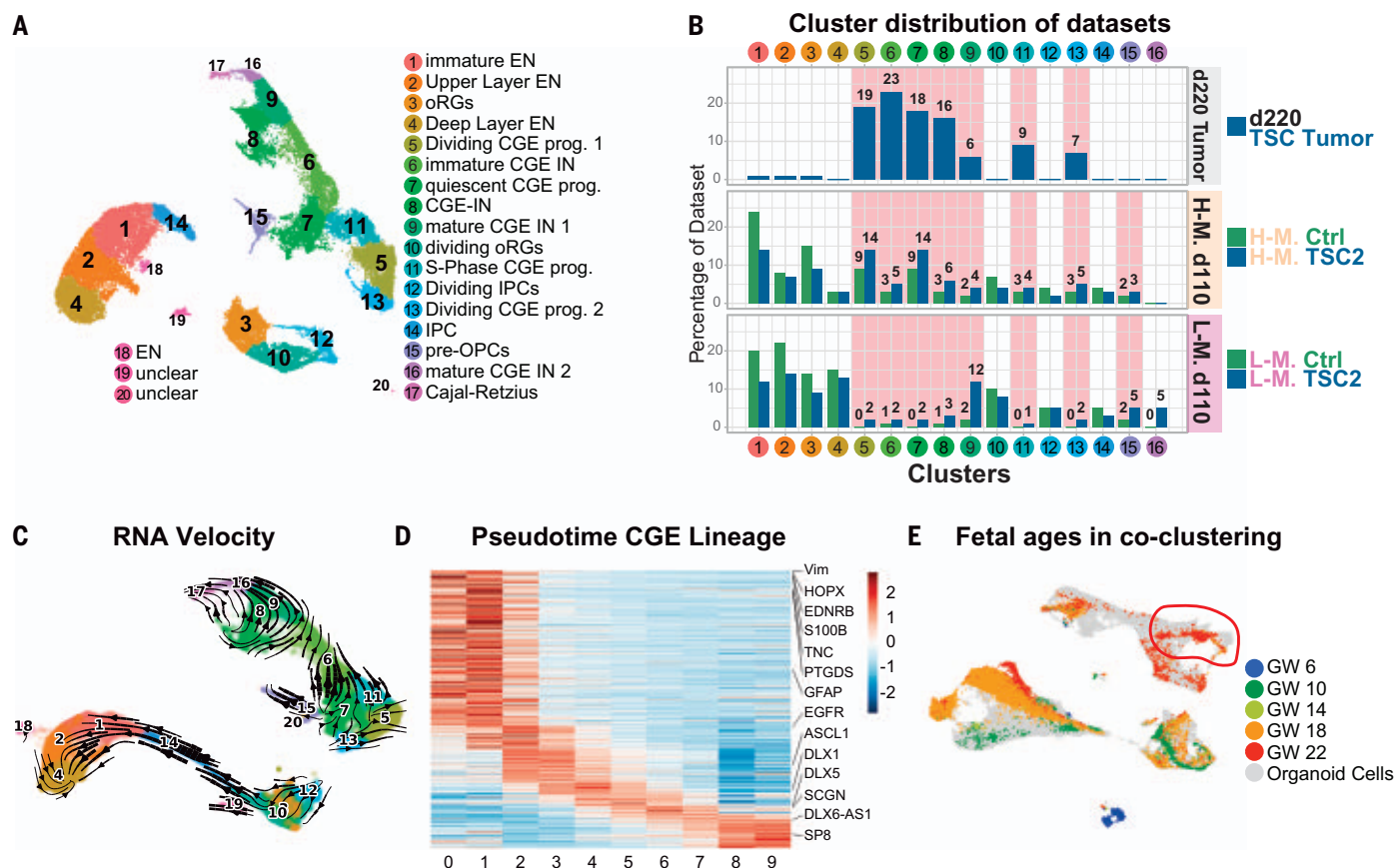


Fig. 3. Late CGE progenitors give rise to TSC phenotypes. (A) UMAP projection of 220-day-old TSC tumor organoids with 110-day-old control and $TSC2^{+/-}$ -derived organoids in H- and L-medium. All cell types of the dorsal lineage were present, with radial glia (RG; clusters 3 and 10), intermediate progenitors (IPCs; clusters 12 and 14), and excitatory neurons (EN; clusters 1, 2, 4, and 18). A separate lineage of CGE-derived cells was identified with quiescent CGE progenitors (cluster 7), dividing CGE progenitor cells (clusters 5, 11, and 13), and CGE interneurons (IN; clusters 6, 8, 9, 16, and 17). Pre-OPC-like cells (cluster 15) cluster close to quiescent CGE progenitors. (B) Contribution of different datasets to clusters shown in (A). TSC tumors 220 days old only contributed to CGE progenitors and their progeny (clusters 5, 6, 7, 8, 9, 11, and 13). These clusters were also increased in 110-day-old $TSC2^{+/-}$ -derived organoids. H-medium enriched

for progenitors. L-medium organoids had more mature CGE-INs (clusters 9 and 16). (C) RNA velocity projected in two dimensions. The cluster annotation corresponds to (A). From the increased CGE progenitor population, two trajectories emerge: a small trajectory toward pre-OPC cells (cluster 15) and a larger trajectory toward interneurons (clusters 6 and 9). (D) Expression of genes along pseudotime in CGE lineage. Genes enriched along pseudotime were calculated, and cells were binned into 10 groups (x axis) (fig. S9B). All genes with enriched expression along the trajectory were ordered by using a sliding average. (Top left) Genes enriched in progenitors. (Bottom right) Genes in mature interneurons. Selected genes are highlighted. (E) UMAP of integration of organoid and fetal cells color-coded for gestational ages shows that GW22 cells coclustered with (top right) quiescent CGE progenitor cluster.

To test this, we subclustered all progenitors (fig. S11, G and H) and found that 98% of fetal cells coclustering with the expanded CGE progenitors originated from gestational week 22 (GW22) (fig. S11, G, H, and I). We calculated gene modules (33) in progenitors (fig. S11J) and compared organoid and fetal progenitors of various stages. Quiescent CGE progenitor cells showed the highest correlation with fetal progenitors from GW22 (+0.74) (fig. S11, K and L). These data suggest that the expanded CGE progenitors emerge around late mid-gestation, a time when cortical tubers and subependymal tumors are first detected in TSC patients (20). On the basis of their CGE origin and late emergence, we named the expanded cell type caudal late interneuron progenitor (CLIP) cells.

CLIP cells and their progeny are abundant in tumors

To independently validate our observations in the scRNA-seq experiments, we investigated expression of markers for CGE, medial ganglionic eminence (MGE), and excitatory cells through immunostaining of patient tumor primary tissue and organoids.

We confirmed expression of EGFR in tumors in organoids and in surgically resected SEGAs (Fig. 4A and fig. S12). Consistent with the scRNA-seq results, the CGE interneuron progenitor markers DLX2, COUP-TFII, and SP8 were found in tumors in organoids from three TSC patients (Fig. 4, B and D, and figs. S12 and S13). By contrast, NKX2.1, a marker for MGE progenitors or SATB2, specific for excitatory neurons, was not expressed (Fig. 4D and fig. S14, A and B).

To investigate the origin of TSC tumors in patients, we stained 35GW SENs. Fetal tumors such as their organoid counterparts were enriched in CGE cells, whereas NKX2.1-expressing cells were rare (Fig. 4, E and F, and fig. S14, C and D). By contrast, NKX2.1 has been shown to be expressed in postnatal SEGAs (34). We confirmed expression of NKX2.1 (fig. S14E) but found that postnatal tumor cells also expressed CGE markers (fig. S14, E to G). Thus, although fetal SENs consisted mostly of CGE cells, co-expression of NKX2.1 and CGE markers in postnatal SEGAs could suggest aberrant differentiation at later stages or the involvement of other lineages.

To test which lineages can generate tumors in TSC organoids, we used patterning protocols to generate dorsal and ventral forebrain

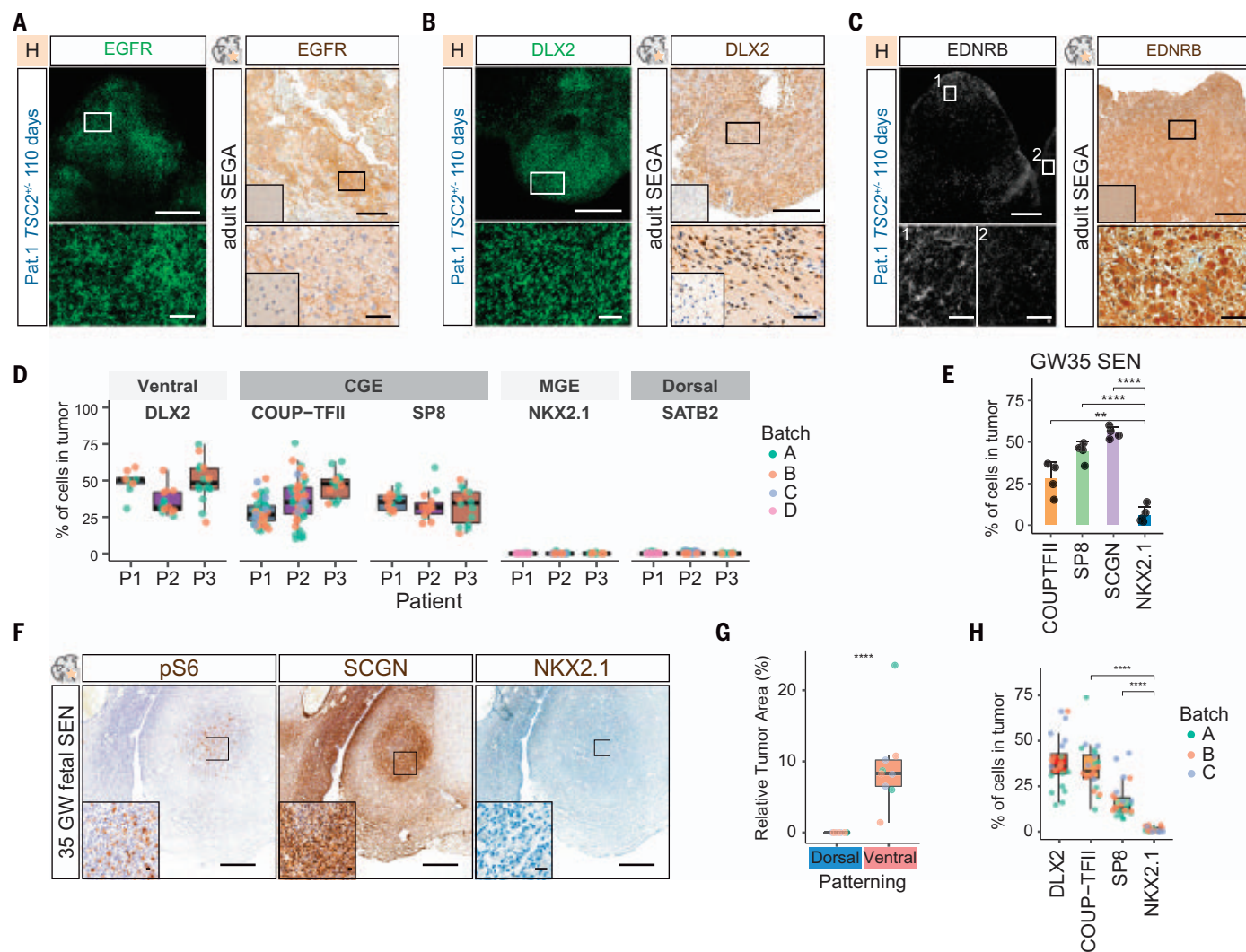


Fig. 4. CGE progenitors initiate TSC tumors. (A) Immunostaining for EGFR identified tumors in 110-day-old TSC2^{+/-}-derived organoids grown in H-medium. EGFR expression was present in adult SEGAs. (Inset) In primary tissue, staining shows healthy control cortex negative for EGFR (costaining with COUP-TFII in organoids is provided in fig. S12C). (B) DLX2 was expressed in tumors in 110-day-old TSC2^{+/-}-derived organoids and resected SEGA tissue. (Inset) In primary tissue, staining shows healthy control cortex negative for DLX2 (fig. S13) (EGFR and SP8 in organoid and patient tumors are provided in fig. S13). (C) EDNRB was expressed in tumors in 110-day-old TSC2^{+/-}-derived organoids. Zoom-ins 1 and 2 are of tumor regions expressing EDNRB and negative region (costaining with PROX1 and pS6 in two patients is provided in fig. S16A). EDNRB expression was found in adult SEGAs. (Inset) In primary tissue, staining shows healthy control cortex negative for EDNRB. (D) Quantification of ventral (DLX2), CGE (COUP-TFII and SP8), MGE (NKX2.1), and dorsal markers (SATB2) in tumors of three patients. Tumors of at least two independent batches were quantified,

indicated with different colors. Ventral and CGE markers are found in all tumors; MGE and dorsal markers are not found (statistical comparison is provided in fig. S14B). (E) Quantification of CGE markers COUP-TFII, SCGN, SP8, and MGE marker NKX2.1 in 35GW fetal SENs (mean and standard deviation) (statistical comparison is provided in fig. S14D). (F) Immunostaining on fetal SENs. Fetal tumors characteristically expressed Vimentin (fig. S14C) and pS6 in enlarged cells. Tumor were enriched in SCGN-expressing CGE interneurons. Only a few MGE cells were found. (G) Dorsal and ventral patterning of tumors of patient 1. In 120-day-old TSC2^{+/-}-derived organoids, tumors only appear in ventral patterned organoids that contain interneuron progenitors (Student's *t* test) (an overview of samples is available in fig. S15B). (H) Tumors in ventral patterned organoids expressed the ventral marker DLX2 and the CGE markers COUP-TFII and SP8, whereas NKX2.1 is almost absent (ordinary one-way ANOVA with Tukey's multiple comparison test) (statistical comparison is provided in fig. S15H). Scale bars, (A), (B), and (C) overview images, 500 μ m; (A), (B), and (C) zoom-ins, 50 μ m; (F) overview, 500 μ m; (F) inset, 20 μ m.

separately (fig. S15A) (35, 36). Dorsal patterning produced excitatory cells, whereas ventral patterned organoids contained both CGE and MGE lineages (fig. S15, C and D). Tumors were only observed in ventral patterned organoids (Fig. 4G and fig. S15B), supporting an origin in the ventral forebrain. All tumors in ventral patterned organoids expressed abun-

dantly the CGE markers COUP-TFII and SP8, whereas only a few cells were positive for NKX2.1 (Fig. 4H and fig. S15, D to H). This further supports the hypothesis that CGE progenitors initiate TSC tumors.

To test whether CGE progenitors in TSC tumors were CLIP cells, we stained for EDNRB and PTGDS. Both patient primary tumor sam-

ples and organoid tumors contained cells that expressed these CLIP cell markers together with ventral neural stem cell (NSC) (SOX2 and GAD1) and CGE markers (PROX1 and COUP-TFII) (organoids, EDNRB in Fig. 4C and PTGDS in fig. S16I, with PROX1, COUP-TFII, GAD1, and SOX2 in fig. S16, A, F, and I; surgically removed SEGA, EDNRB in Fig. 4C, with GAD1 in fig. S16,

E and G). These data suggest that CLIP cells are the neural progenitors found in TSC tumors.

Besides CLIP cells, TSC tumors also contained interneurons (Fig. 2, A and B) (24). Expression of the CGE interneuron marker SCGN (secretagogin) (fig. S17, A and B) in fetal SENs (Fig. 4F and fig. S17D) and in tumors in organoids (fig. S17C) supported a CGE origin for these interneurons. The lineage relationship between CLIP cells and CGE interneurons was further confirmed with EdU labeling (fig. S17, E and F). After 24 hours, EdU-labeled cells coexpressed either EGFR and SCGN or both, confirming that CLIP cells produce SCGN-positive interneurons (fig. S17, E and F).

Our data indicating that CLIP cells that originate from the CGE generate TSC tumors could provide an explanation for why SEN/SEGAs are typically found in the caudothalamic groove, the region where the CGE is located during fetal development.

CLIP cells initiate cortical tuber development

To determine whether CLIP cells also give rise to GCs that make up cortical tubers, we stained tuber-like structures in L-organoids and tubers in patient-derived brain tissue. GCs in organoids and in fetal cortical tubers expressed markers of ventral NSCs [GAD1] (Fig. 5, A to C, and fig. S19A) and EGFR (figs. S18A and S19D)]. Expression of CLIP cell markers [EDNRB (Fig. 5, D and F) and PTGDS (fig. S18D)] together with CGE markers [PROX1 and COUP-TFII (fig. S18, B to D)] in GCs in organoids underlined their CLIP cell origin. Similarly, expression of EDNRB (Fig. 5E and fig. S19, A and B) and PTGDS with CGE-markers (PROX1 and COUP-TFII) (fig. S19C) further suggested that CLIP cells are also the cell of origin for GCs in TSC patients.

Dysmorphic neurons in cortical tubers have been shown to express excitatory and inhibitory neuron markers (4). In addition, early TSC lesions are populated by a high density of migrating neurons of unknown origin (4). To determine whether CGE interneurons produced by CLIP cells contribute to cortical tubers, we evaluated expression of CGE (SCGN and COUP-TFII), MGE [Parvalbumin (PV)], and excitatory neuron markers (SATB2) in organoids and patients. We found that at early stages, most dysmorphic neurons in organoids were CGE interneurons (Fig. 5H and fig. S20, A to E). At later stages, the contribution of excitatory neurons increased, whereas only few MGE interneurons are found (Fig. 5, G and H, and fig. S20, F and G).

To test whether CGE interneurons are involved in early tuber lesions in patients, we tested expression of SCGN and PV in a 25GW TSC case. At this stage, tuber pathogenesis initiates with white matter lesions (WMLs). Similar to the organoid model, we found that WMLs were highly enriched in CGE inter-

neurons, whereas no MGE cells were detected (Fig. 5, I and J, and fig. S21, A to D). This suggests that CGE interneurons are the migrating neurons previously described in TSC lesions.

Because excitatory dysmorphic neurons increased over time in organoids, we evaluated the contribution of different lineages during the development of TSC tubers. Around 35GW, CGE interneurons were still increased (Fig. 5, K and L). At the same time, the first dysmorphic neurons (DNs) appeared, with CGE-DNs being more abundant in WMLs (Fig. 5M and fig. S21E). With progression of tuber lesions at postnatal stages, however, numbers of both excitatory and MGE neurons increased (fig. S22, A to E).

MGE and CGE markers identify distinct populations during normal brain development. In TSC patient organoids, we detected a subpopulation of dysmorphic interneurons expressing the MGE marker PV together with the CGE marker SCGN (fig. S20, G and H). To test whether this misdifferentiated population is present in cortical tubers, we tested expression of PV with the CGE markers SCGN and SP8. In a matched control case, no cells coexpressing these markers were found, whereas in a cortical tuber, several triple-positive cells were detected (fig. S22F). Taken together, our data suggest that CGE lineages initiate cortical lesion development in TSC. Excitatory and MGE dysmorphic neurons appear over time and are frequent in postnatal lesions. Furthermore, our data show that a comprehensive analysis of different markers is necessary to study the contribution of different lineages to cortical tubers because misdifferentiated cells can be observed.

EGFR inhibition reduces tumor burden

mTOR inhibition has been clinically used to treat SEN/SEGAs in TSC patients. However, known side effects and limitations, such as tumor regrowth after drug discontinuation, necessitate exploring alternative therapeutic strategies (37–39). Both CLIP cells and proliferating cells in TSC tumors express EGFR. To assess the role of the EGFR pathway in tumor growth, we performed a drug testing assay in *TSC2*^{+/-} H-organoids at 110 days, when tumors were already apparent. We used the EGFR receptor tyrosine kinase inhibitor (RTKI) Afatinib and Everolimus, an mTOR Complex 1 inhibitor. Organoids were treated for 30 days with Everolimus, Afatinib, or dimethyl sulfoxide (DMSO) (fig. S23A). Tumor reduction was determined by measuring areas coexpressing pS6 and EGFR. Everolimus treatment almost completely abolished tumors in 140-day-old organoids (Fig. 6, A and B, and fig. S23B). After Afatinib treatment, both tumor load and mean tumor size were significantly reduced when compared with those of untreated organoids (Fig. 6, A and B, and fig. S23, B to D).

Thus, targeting the EGFR pathway could be an alternative strategy for the treatment of TSC brain lesions.

We have shown that the neurodevelopmental disorder TSC is initiated by a caudal late interneuron progenitor, the CLIP cells (fig. S24). Early lesions consisted almost exclusively of CLIP cell lineages, whereas other cell types appeared during disease progression. Although our scRNA-seq analysis is descriptive and we only analyzed organoids from one patient, our extensive validation in organoids from three TSC patients plus tissues from more than 10 additional TSC cases demonstrates that the TSC organoid model recapitulated fetal disease dynamics. However, the organoid model was limited in modeling postnatal processes, possibly because of the absence of environmental factors that are present in vivo.

The cell of origin for many human brain tumors remains elusive; however, the idea that cancer stems from the reactivation of a remnant of developmental tissue was proposed more than a century ago (40, 41). Studies in mice have revealed sensitivity of adult neural stem cells to cancer-initiating mutations, resulting in the formation of glioblastoma, a high-grade brain tumor. Transcriptional similarities between CLIP cells and mouse adult neural stem cells suggest that CLIP cells could be involved more generally in brain cancers. Our data suggest that a sensitivity to increased mTOR signaling makes CLIP cells vulnerable to mutations in *TSC2*. We hypothesize that a similar mechanism could explain other malformations of cortical development caused by mTOR dysregulation, such as FCD type II.

Extensive migration of interneurons into the cortex continues in humans even after birth (42). Because these late migrating neurons also arise from the CGE and share markers with CLIP cells, we speculate that CLIP cells give rise to late migrating interneurons in the healthy human brain. This is consistent with previous results showing that CGE-derived interneurons contribute to the human brain in much higher percentages (43, 44) and with the observation that late-migrating SCGN interneurons from the CGE are found in humans but not in mice (45). The protracted brain development seen in large, gyrated cortices was accompanied by the generation or expansion of cell types. These are not or less present in small lissencephalic brains such as the mouse brain, necessitating human disease models. Our data suggest that CLIP cells are among the cell types specific for or amplified in the human brain, which would make TSC a disease specific to large, gyrated brains.

Materials and methods summary

Detailed information on all materials and methods performed are provided in the supplementary materials.

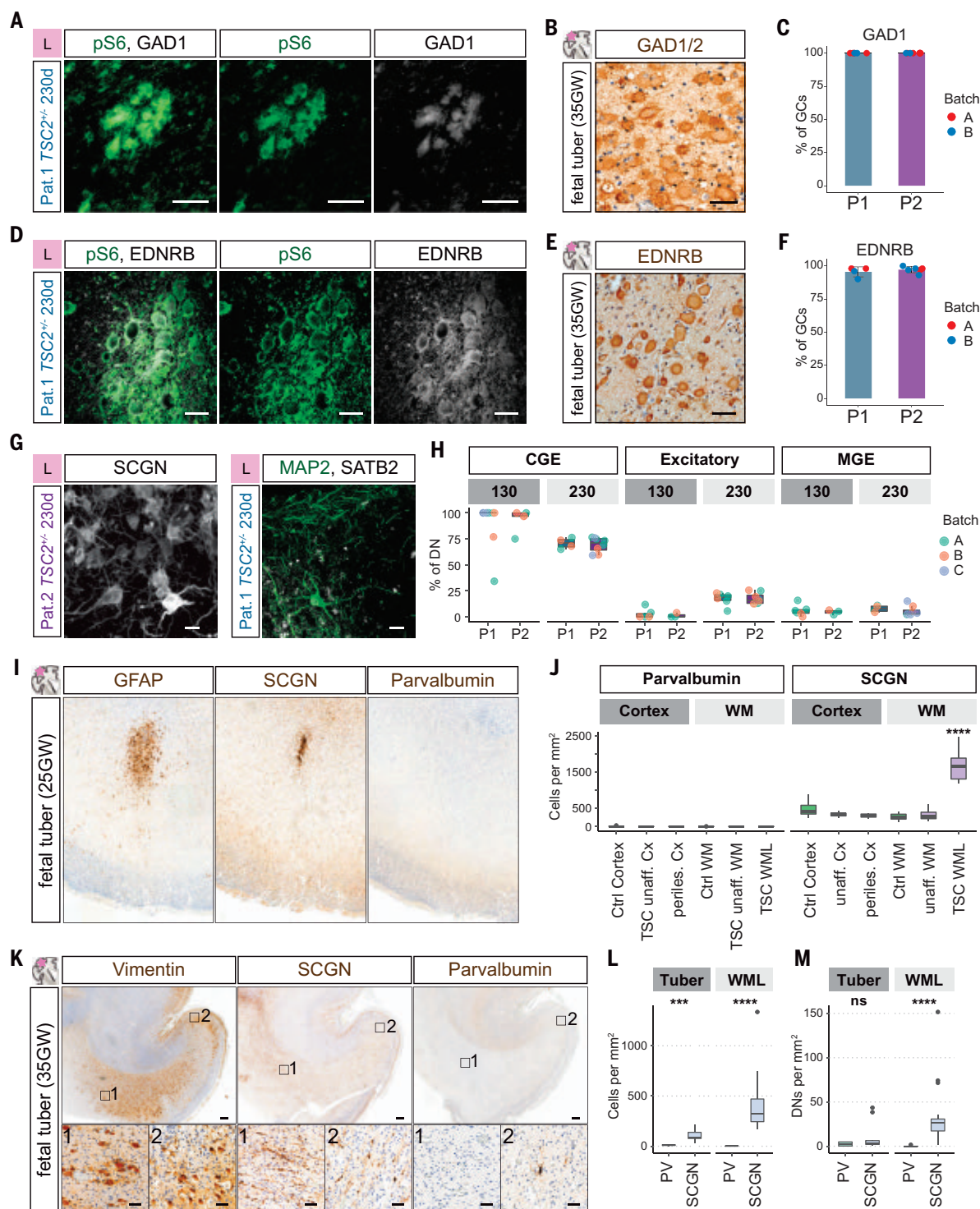


Fig. 5. CLIP cells initiate cortical tuber pathogenesis. (A and B) GCs in (A) organoids and (B) fetal tubers expressed the interneuron lineage marker GAD1. (C) Quantification of coexpression of GAD1 and pS6 in GCs in organoids (patient 1, $N = 2$ independent batches $n = 6$ organoids mean = 100%; patient 2: $N = 2$ independent batches $n = 8$ organoids mean = 100%). (D and E) EDNRB was expressed in GCs in organoids and in fetal tubers. (F) Quantification of coexpression of EDNRB and pS6 in GCs in organoids (patient 1, $N = 2$ independent batches $n = 4$ organoids mean = 95.5%; patient 2: $N = 2$ independent batches $n = 6$ organoids mean = 97.2%). (G) Dysmorphic neurons at 230 days expressed the CGE marker SCGN. Individual dysmorphic neurons expressed the excitatory marker

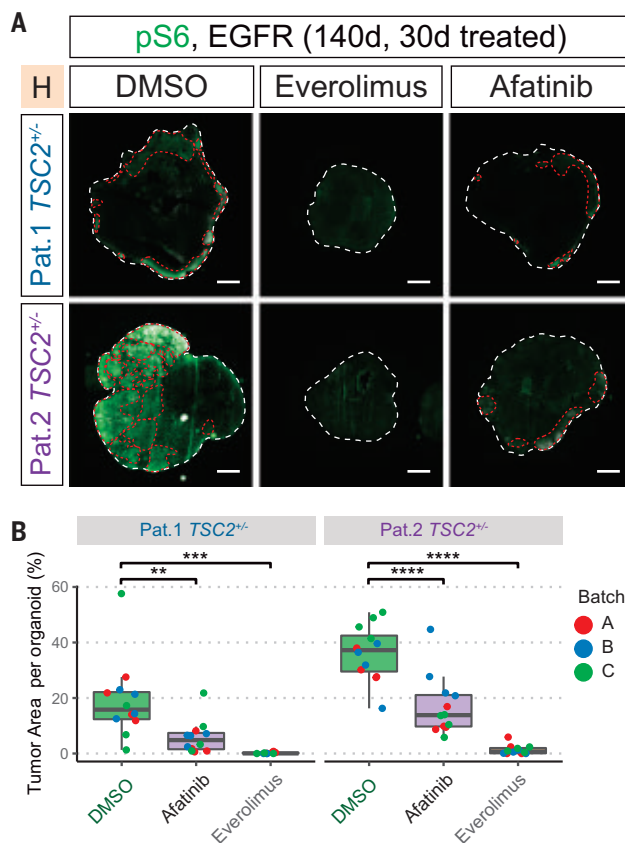
SATB2 (stainings at different time points are available in fig. S20, C to G). (H) Quantification of expression of CGE (SCGN and COUP-TFII), excitatory (SATB2), and MGE markers (PV) in dysmorphic neurons (DNs) at early and late stages in organoids of two patients. CGE DN were enriched at 130 days and decreased over time. Excitatory DN increased over time. Statistical analysis is provided in fig. S20, I and J. (I) GFAP identified early dysplastic regions at 25GW located in the white matter below the cortex. There was a focal enrichment of SCGN-expressing CGE interneurons, whereas PV expressing MGE interneurons were rare (fig. S21, A and B). (J) Quantification of MGE marker PV and CGE marker SCGN in ~25GW fetal brain. Unaffected cortical areas, unaffected white matter, as well as white matter lesions

(WMLs) and adjacent cortex (perilesional cortex) quantified for density of cells expressing PV or SCGN (fig. S21, A and B). WMLs were significantly enriched in CGE interneurons compared with all other regions (one-way ANOVA) (statistical analysis is provided in fig. S12, C and D). **(K)** At 35GW, Vimentin staining identified streams of cells in WMLs and affected cortex. SCGN-expressing cells were abundant in the WMLs and cortex, whereas PV-expressing cells were mainly found in cortical regions. **(L and M)** Quantification of MGE marker PV and CGE marker SCGN in

35GW TSC case. Density of all cells is shown in (L), with increase of SCGN cells in tuber and WML areas. In (M), the density of DNs expressing PV and SCGN in tuber and WML areas is shown. SCGN DNs were significantly enriched in WMLs, whereas tubers contained similar density of PV and SCGN cells (all neurons, Tuber $P = 0.0002$, WML $P \leq 0.0001$; DNs, Tuber $P = 0.248$, WML $P \leq 0.0001$; pairwise Wilcoxon test) (an overview of samples is available in fig. S21E). Scale bars, (A), (B), (D), (E), and (K) inset, 50 μm ; (G) 20 μm ; (I) and (K) overview, 500 μm .

Fig. 6. EGFR inhibition reduces tumor burden.

(A) Thirty days of treatment started at 110 days after EB formation (fig. S23A). Immunostaining for pS6 and EGFR identified tumors (red lines) in the control group (DMSO) in both patients. Tumors were reduced through Afatinib and Everolimus treatment. **(B)** Quantification of tumor area per organoid. All sections of each organoid stained on one slide were used for quantification. Tumors were identified as regions of overlapping pS6 and EGFR staining. Although tumors were detected in DMSO-control for both patients, Afatinib or Everolimus treatment both reduce tumor burden (two-way ANOVA for treatment condition controlling for batches, Tukey's multiple comparison test) (fig. S23B). Scale bars, (A) 1 mm.



iPS cell generation and culture

Patients were selected from the TSC data registry of the Medical University of Vienna (MUV). Blood was collected from patients, and peripheral blood mononuclear cells (PBMCs) were isolated. Reprogramming was performed by using Sendai Vectors. iPSCs cells were cultured by using the Cellartis DEF-CS 500 culture system (Takara). Isogenic control cell lines were directly isolated (mosaic patient 1) or generated by using scarless CRISPR repair (patient 2).

Organoid generation

Organoids were generated by using either a high-nutrient (H-organoids) or low-nutrient (L-organoids) medium to favor proliferation or neuronal maturation, respectively. In addition, organoids were patterned toward dorsal or ventral brain regions as described (35, 36).

Single-cell transcriptomics and analysis

Organoids were dissociated. Library preparation was performed with the Chromium Single Cell 3' Library and Gel Bead Kit v.3 (10x Genomics, PN-1000075). Libraries were sequenced on a NextSeq 550 (Illumina) or on a NovaSeq SP lane (Illumina). Quality control and preprocessing were performed by use of Seurat R package v.3. Visualization and pseudotime analysis were performed by use of monocle3.

Immunohistochemistry

Immunohistochemistry on frozen organoid samples was performed as described with slight modifications (18, 35). Human brain tissue samples were collected in strict observance of the local legal and institutional ethical regulations. Tissue was processed for cryosections or paraffin sections. Antigen retrieval was performed

followed by immunohistochemistry as described in table S6.

REFERENCES AND NOTES

- R. I. Kuzniecky, MRI in cerebral developmental malformations and epilepsy. *Magn. Reson. Imaging* **13**, 1137–1145 (1995). doi: 10.1016/0730-725X(95)02024-N; pmid: 8750328
- E. A. Thiele, Managing and understanding epilepsy in tuberous sclerosis complex. *Epilepsia* **51** (Suppl 1), 90–91 (2010). doi: 10.1111/j.1528-1167.2009.02458.x; pmid: 20331728
- V. Ruppé et al., Developmental brain abnormalities in tuberous sclerosis complex: A comparative tissue analysis of cortical tubers and peritubular cortex. *Epilepsia* **55**, 539–550 (2014). doi: 10.1111/epi.12545; pmid: 24512506
- A. B. Gelot, A. Represa, Progression of fetal brain lesions in tuberous sclerosis complex. *Front. Neurosci.* **14**, 899 (2020). doi: 10.3389/fnins.2020.00899; pmid: 32973442
- E. P. Henske, S. Jóźwiak, J. C. Kingswood, J. R. Sampson, E. A. Thiele, Tuberous sclerosis complex. *Nat. Rev. Dis. Primers* **2**, 16035 (2016). doi: 10.1038/nrdp.2016.35; pmid: 27226234
- K. R. Martin et al., The genomic landscape of tuberous sclerosis complex. *Nat. Commun.* **8**, 15816 (2017). doi: 10.1038/ncomms15816; pmid: 28643795
- P. B. Crino, Evolving neurobiology of tuberous sclerosis complex. *Acta Neuropathol.* **125**, 317–332 (2013). doi: 10.1007/s00401-013-1085-x; pmid: 23386324
- D. M. Feliciano, T. Su, J. Lopez, J. C. Platel, A. Bordey, Single-cell Tsc1 knockout during corticogenesis generates tuber-like lesions and reduces seizure threshold in mice. *J. Clin. Invest.* **121**, 1596–1607 (2011). doi: 10.1172/JCI44909; pmid: 21403402
- D. M. Feliciano, J. L. Quon, T. Su, M. M. Taylor, A. Bordey, Postnatal neurogenesis generates heterotopias, olfactory micronodules and cortical infiltration following single-cell Tsc1 deletion. *Hum. Mol. Genet.* **21**, 799–810 (2012). doi: 10.1093/hmg/ddr511; pmid: 22068588
- S. W. Way et al., Loss of Tsc2 in radial glia models the brain pathology of tuberous sclerosis complex in the mouse. *Hum. Mol. Genet.* **18**, 1252–1265 (2009). doi: 10.1093/hmg/ddp025; pmid: 19150975
- R. P. Carson, D. L. Van Nielsen, P. A. Winzenburger, K. C. Ess, Neuronal and glia abnormalities in Tsc1-deficient forebrain and partial rescue by rapamycin. *Neurobiol. Dis.* **45**, 369–380 (2012). doi: 10.1016/j.nbd.2011.08.024; pmid: 21907282
- J. Goto et al., Regulable neural progenitor-specific Tsc1 loss yields giant cells with organellar dysfunction in a model of tuberous sclerosis complex. *Proc. Natl. Acad. Sci. U.S.A.* **108**, E1070–E1079 (2011). doi: 10.1073/pnas.1106454108; pmid: 22025691
- J. D. Blair, D. Hockemeyer, H. S. Bateup, Genetically engineered human cortical spheroid models of tuberous sclerosis. *Nat. Med.* **24**, 1568–1578 (2018). doi: 10.1038/s41591-018-0139-y; pmid: 30127391
- W. Qin et al., Analysis of TSC cortical tubers by deep sequencing of TSC1, TSC2 and KRAS demonstrates that small second-hit mutations in these genes are rare events. *Brain Pathol.* **20**, 1096–1105 (2010). doi: 10.1111/j.1750-3639.2010.00416.x; pmid: 20633017
- E. P. Henske et al., Allelic loss is frequent in tuberous sclerosis kidney lesions but rare in brain lesions. *Am. J. Hum. Genet.* **59**, 400–406 (1996). pmid: 8755927
- J. A. Chan et al., Pathogenesis of tuberous sclerosis subependymal giant cell astrocytomas: Biallelic inactivation of TSC1 or TSC2 leads to mTOR activation. *J. Neuropathol. Exp. Neurol.* **63**, 1236–1242 (2004). doi: 10.1093/jnen/63.12.1236; pmid: 15624760

17. A. G. Knudson Jr., Mutation and cancer: Statistical study of retinoblastoma. *Proc. Natl. Acad. Sci. U.S.A.* **68**, 820–823 (1971). doi: [10.1073/pnas.68.4.820](https://doi.org/10.1073/pnas.68.4.820); pmid: 5279523
18. M. A. Lancaster *et al.*, Cerebral organoids model human brain development and microcephaly. *Nature* **501**, 373–379 (2013). doi: [10.1038/nature12517](https://doi.org/10.1038/nature12517); pmid: 23995685
19. C. Bardy *et al.*, Neuronal medium that supports basic synaptic functions and activity of human neurons in vitro. *Proc. Natl. Acad. Sci. U.S.A.* **112**, E2725–E2734 (2015). doi: [10.1073/pnas.1504393112](https://doi.org/10.1073/pnas.1504393112); pmid: 25870293
20. S. H. Park *et al.*, Tuberous sclerosis in a 20-week gestation fetus: Immunohistochemical study. *Acta Neuropathol.* **94**, 180–186 (1997). doi: [10.1007/s004010050691](https://doi.org/10.1007/s004010050691); pmid: 9255394
21. M. Mizuguchi, S. Takashima, Neuropathology of tuberous sclerosis. *Brain Dev.* **23**, 508–515 (2001). doi: [10.1016/S0387-7604\(01\)00304-7](https://doi.org/10.1016/S0387-7604(01)00304-7); pmid: 11701246
22. A. M. Buccoliero *et al.*, Subependymal giant cell astrocytoma: A lesion with activated mTOR pathway and constant expression of glutamine synthetase. *Clin. Neuropathol.* **35**, 295–301 (2016). doi: [10.5414/NP300936](https://doi.org/10.5414/NP300936); pmid: 27390104
23. A. M. Buccoliero *et al.*, Subependymal giant cell astrocytoma (SEGA): Is it an astrocytoma? Morphological, immunohistochemical and ultrastructural study. *Neuropathology* **29**, 25–30 (2009). doi: [10.1111/j.1440-1789.2008.00934.x](https://doi.org/10.1111/j.1440-1789.2008.00934.x); pmid: 18564101
24. J. A. Cotter, An update on the central nervous system manifestations of tuberous sclerosis complex. *Acta Neuropathol.* **139**, 613–624 (2020). doi: [10.1007/s00401-019-02003-1](https://doi.org/10.1007/s00401-019-02003-1); pmid: 30976976
25. C. S. McGinnis *et al.*, MULTI-seq: Sample multiplexing for single-cell RNA sequencing using lipid-tagged indices. *Nat. Methods* **16**, 619–626 (2019). doi: [10.1038/s41592-019-0433-8](https://doi.org/10.1038/s41592-019-0433-8); pmid: 31209384
26. H. V. Vinters *et al.*, Tuberous sclerosis-related gene expression in normal and dysplastic brain. *Epilepsy Res.* **32**, 12–23 (1993). doi: [10.1016/S0920-1211\(98\)00036-9](https://doi.org/10.1016/S0920-1211(98)00036-9); pmid: 9761305
27. M. W. Johnson, J. K. Emelin, S. H. Park, H. V. Vinters, Co-localization of TSC1 and TSC2 gene products in tubers of patients with tuberous sclerosis. *Brain Pathol.* **9**, 45–54 (1999). doi: [10.1111/j.1750-3639.1999.tb00209.x](https://doi.org/10.1111/j.1750-3639.1999.tb00209.x); pmid: 9989450
28. J. Zhou *et al.*, Tsc1 mutant neural stem/progenitor cells exhibit migration deficits and give rise to subependymal lesions in the lateral ventricle. *Genes Dev.* **25**, 1595–1600 (2011). doi: [10.1101/gad.16750211](https://doi.org/10.1101/gad.16750211); pmid: 21828270
29. J. S. Lim *et al.*, Somatic mutations in TSC1 and TSC2 cause focal cortical dysplasia. *Am. J. Hum. Genet.* **100**, 454–472 (2017). doi: [10.1016/j.ajhg.2017.01.030](https://doi.org/10.1016/j.ajhg.2017.01.030); pmid: 28215400
30. C. Kerfoot *et al.*, Localization of tuberous sclerosis 2 mRNA and its protein product tuber in normal human brain and in cerebral lesions of patients with tuberous sclerosis. *Brain Pathol.* **6**, 367–375 (1996). doi: [10.1111/j.1750-3639.1996.tb00866.x](https://doi.org/10.1111/j.1750-3639.1996.tb00866.x); pmid: 8944308
31. W. Huang *et al.*, Origins and proliferative states of human oligodendrocyte precursor cells. *Cell* **182**, 594–608.e11 (2020). doi: [10.1016/j.cell.2020.06.027](https://doi.org/10.1016/j.cell.2020.06.027); pmid: 32679030
32. A. Bhaduri *et al.*, Cell stress in cortical organoids impairs molecular subtype specification. *Nature* **578**, 142–148 (2020). doi: [10.1038/s41586-020-1962-0](https://doi.org/10.1038/s41586-020-1962-0); pmid: 31996853
33. C. Trapnell *et al.*, The dynamics and regulators of cell fate decisions are revealed by pseudotemporal ordering of single cells. *Nat. Biotechnol.* **32**, 381–386 (2014). doi: [10.1038/nbt.2859](https://doi.org/10.1038/nbt.2859); pmid: 24658644
34. J. F. Hang *et al.*, Thyroid transcription factor-1 distinguishes subependymal giant cell astrocytoma from its mimics and supports its cell origin from the progenitor cells in the medial ganglionic eminence. *Mod. Pathol.* **30**, 318–328 (2017). doi: [10.1038/modpathol.2016.205](https://doi.org/10.1038/modpathol.2016.205); pmid: 27910945
35. M. A. Lancaster *et al.*, Guided self-organization and cortical plate formation in human brain organoids. *Nat. Biotechnol.* **35**, 659–666 (2017). doi: [10.1038/nbt.3906](https://doi.org/10.1038/nbt.3906); pmid: 28562594
36. J. A. Bagley, D. Reumann, S. Bian, J. Lévi-Strauss, J. A. Knoblich, Fused cerebral organoids model interactions between brain regions. *Nat. Methods* **14**, 743–751 (2017). doi: [10.1038/nmeth.4304](https://doi.org/10.1038/nmeth.4304); pmid: 28504681
37. D. N. Franz *et al.*, Everolimus for subependymal giant cell astrocytoma in patients with tuberous sclerosis complex: 2-year open-label extension of the randomised EXIST-1 study. *Lancet Oncol.* **15**, 1513–1520 (2014). doi: [10.1016/S1470-2045\(14\)70489-9](https://doi.org/10.1016/S1470-2045(14)70489-9); pmid: 25456370
38. D. A. Krueger *et al.*, Long-term treatment of epilepsy with everolimus in tuberous sclerosis. *Neurology* **87**, 2408–2415 (2016). doi: [10.1212/WNL.0000000000003400](https://doi.org/10.1212/WNL.0000000000003400); pmid: 27815402
39. F. Martins *et al.*, A review of oral toxicity associated with mTOR inhibitor therapy in cancer patients. *Oral Oncol.* **49**, 293–298 (2013). doi: [10.1016/j.oraloncology.2012.11.008](https://doi.org/10.1016/j.oraloncology.2012.11.008); pmid: 23312237
40. A. Bhaduri *et al.*, Outer radial glia-like cancer stem cells contribute to heterogeneity of glioblastoma. *Cell Stem Cell* **26**, 48–63.e6 (2020). doi: [10.1016/j.stem.2019.11.015](https://doi.org/10.1016/j.stem.2019.11.015); pmid: 31901251
41. S. Sell, Stem cell origin of cancer and differentiation therapy. *Crit. Rev. Oncol. Hematol.* **51**, 1–28 (2004). doi: [10.1016/j.critrevonc.2004.04.007](https://doi.org/10.1016/j.critrevonc.2004.04.007); pmid: 15207251
42. M. F. Paredes *et al.*, Extensive migration of young neurons into the infant human frontal lobe. *Science* **354**, eaaf7073 (2016). doi: [10.1126/science.aaf7073](https://doi.org/10.1126/science.aaf7073); pmid: 27846470
43. D. V. Hansen *et al.*, Non-epithelial stem cells and cortical interneuron production in the human ganglionic eminences. *Nat. Neurosci.* **16**, 1576–1587 (2013). doi: [10.1038/nn.3541](https://doi.org/10.1038/nn.3541); pmid: 24097039
44. R. D. Hodge *et al.*, Conserved cell types with divergent features in human versus mouse cortex. *Nature* **573**, 61–68 (2019). doi: [10.1038/s41586-019-1506-7](https://doi.org/10.1038/s41586-019-1506-7); pmid: 31435019
45. C. S. Raju *et al.*, Secretagogin is expressed by developing neocortical GABAergic neurons in humans but not mice and increases neurite arbor size and complexity. *Cereb. Cortex* **28**, 1946–1958 (2018). doi: [10.1093/cercor/bhx101](https://doi.org/10.1093/cercor/bhx101); pmid: 28449024
46. O. Eichmüller, OliverEichmueller/TSC_Science2021: Reference scripts. Zenodo (2021); doi: [10.5281/zenodo.5741170](https://doi.org/10.5281/zenodo.5741170)

ACKNOWLEDGMENTS

We thank C. da Cunha E. Silva Martins Costa, P. Möseneder, H. Eleanor Gustafson, and S. Wolfinger for help with experiments and analyses; the IMBA Stem Cell Core Facility and C. Allison Agu for generation of IPS Cell Lines; B. Gebarski and A. Vogt for

library preparation and sequencing performed at the VBCF NGS Unit (www.viennabiocenter.org/facilities/next-generation-sequencing); the Genome Engineering Unit of VBCF ProTech facility (<http://www.viennabiocenter.org/facilities/protein-technologies>) for assistance with isogenic control line preparation; K. Stejskal and E. Roitinger for mass spectrometry performed at the IMBA/IMP mass spectrometry facility; the IMBA/IMP Biooptics facility; A. Mancebo Gimenez and M. Zeba of the VBCF HistoPathology facility for immunohistochemistry; A. Meixner for coordinating ethical approvals; R. Diehm; G. Kasprian for providing MRIs; the KIN Biobank of the Medical University of Vienna (MUV); K. Auguste and the UCSF Brain Tumor SPORE Biorepository (NIH/NCI 5P50CA097257) for their coordination for surgical tissue collection; V. Elorriaga Benavides for work on primary material; and O. Wöseke for establishing contact with the MUV. We thank G. Riddihough/Life Science Editors for help with editing the initial version of the manuscript. We especially thank all patients and their families for participating in this study or donating tissue. **Funding:** A.V. was supported by an EMBO Fellowship (ALTF-1112-2019). Work in J.A.K.'s laboratory is supported by the Austrian Federal Ministry of Education, Science and Research, the Austrian Academy of Sciences, the City of Vienna, and the SFB F78 Stem Cell (F 7803-B). This project has received funding from the European Research Council (ERC) under the European Union's Horizon 2020 research and innovation (695642). **Author contributions:** O.L.E., N.S.C., M.F., and J.A.K. designed the study and analysis. Experiments were performed by O.L.E., I.M., N.S.C., T.S., V.-E.G., A.M.P., and J.C. Data analysis was performed by O.L.E., N.S.C., J.A.H., A.V., M.N., and M.F.P. The study was supervised by N.S.C. and J.A.K. The manuscript was prepared by O.L.E., N.S.C., and J.A.K., with input from all authors. **Competing interests:** J.A.K. is on the supervisory and scientific advisory board of ahead bio AG (<https://aheadbio.com>) and is an inventor on several patents relating to cerebral organoids. **Data and materials availability:** WGS and scRNA-seq data are available through controlled access at the European genome-phenome Archive (EGA). Study number, EGAS00001004586. Datasets: single cell RNA-seq, EGAD00001006332; whole genome sequencing, EGAD00001006333. All code used in this study is available on GitHub (https://github.com/OliverEichmueller/TSC_Science2021), Zenodo (46), and upon request. TSC patient IPS cell lines will be made available upon request after obtaining ethical approval from the Ethics Committee of MUV under a materials transfer agreement with the Institute of Molecular Biotechnology of the Austrian Academy of Sciences. This study was approved by the local ethics committee of MUV.

SUPPLEMENTARY MATERIALS

science.org/doi/10.1126/science.abf5546

Materials and Methods

Figs. S1 to S24

References (47–59)

Tables S1 to S7

MDAR Reproducibility Checklist

3 November 2020; resubmitted 14 June 2021

Accepted 6 December 2021

[10.1126/science.abf5546](https://doi.org/10.1126/science.abf5546)

RESEARCH ARTICLE SUMMARY

NEURODEVELOPMENT

Nests of dividing neuroblasts sustain interneuron production for the developing human brain

Mercedes F. Paredes^{*†}, Cristina Mora[‡], Quetzal Flores-Ramirez[‡], Arantxa Cebrian-Silla[‡], Ashley Del Dosso, Phil Larimer, Jiawei Chen, Eugene Kang, Susana Gonzalez Granero, Eric Garcia, Julia Chu, Ryan Delgado, Jennifer A. Cotter, Vivian Tang, Julien Spatazza, Kirsten Obernier, Jaime Ferrer Lozano, Maximo Vento, Julia Scott, Colin Studholme, Tomasz J. Nowakowski, Arnold R. Kriegstein, Michael C. Oldham, Andrea Hasenstaub, Jose Manuel Garcia-Verdugo, Arturo Alvarez-Buylla^{*}, Eric J. Huang^{*}

INTRODUCTION: Balance between excitatory and inhibitory neuron (interneuron) populations in the cortex promotes normal brain function. Interneurons are primarily generated in the medial, caudal, and lateral ganglionic eminences (MGE, CGE, and LGE) of the ventral embryonic forebrain; these subregions give rise to distinct interneuron subpopulations. In rodents, the MGE generates cortical interneurons, the parvalbumin⁺ (PV⁺) and somatostatin⁺ (SST⁺) subtypes that connect with excitatory neurons to regulate their activity. Defects in interneuron production have been implicated in neurodevelopmental and psychiatric disorders including autism, epilepsy, and schizophrenia.

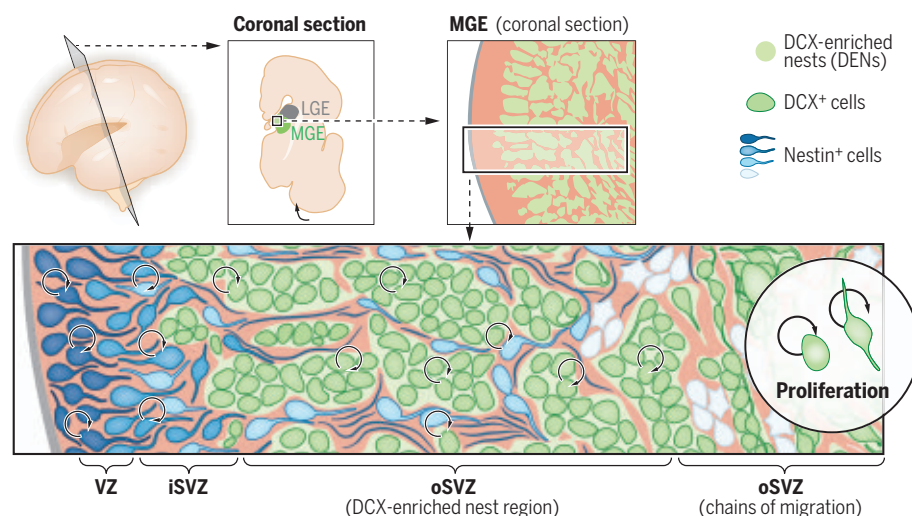
RATIONALE: How does the human MGE (hMGE) produce the number of interneurons required to populate the forebrain? The hMGE contains

progenitor clusters distinct from what has been observed in the rodent MGE and other germinal zones of the human brain. This cytoarchitecture could be the key to understanding interneuron neurogenesis. We investigated the cellular and molecular properties of different compartments within the developing hMGE, from 14 gestational weeks (GW) to 39 GW (term), to study their contribution to the production of inhibitory interneurons. We developed a xenotransplantation assay to follow the migration and maturation of the human interneurons derived from this germinal region.

RESULTS: Within the hMGE, densely packed aggregates (nests) of doublecortin⁺ (DCX⁺) and LHX6⁺ cells were surrounded by nestin⁺ progenitor cells and their processes. These DCX⁺ cell-enriched nests (DENs) were ob-

served in the hMGE but not in the adjacent LGE. We found that cells within DENs expressed molecular markers associated with young neurons, such as DCX, and polysialylated neural cell adhesion molecule (PSA-NCAM). A subpopulation also expressed Ki-67, a marker of proliferation; therefore, we refer to these cells as neuroblasts. A fraction of DCX⁺ cells inside DENs expressed SOX2 and E2F1, transcription factors associated with progenitor and proliferative properties. More than 20% of DCX⁺ cells in the hMGE were dividing, specifically within DENs. Proliferating neuroblasts in DENs persisted in the hMGE throughout prenatal human brain development. The division of DCX⁺ cells was confirmed by transmission electron microscopy and time-lapse microscopy. Electron microscopy revealed adhesion contacts between cells within DENs, providing multiple sites to anchor DEN cells together. Neuroblasts within DENs express PCDH19, and nestin⁺ progenitors surrounding DENs express PCDH10; these findings suggest a role for differential cell adhesion in DEN formation and maintenance. When transplanted into the neonatal mouse brain, dissociated hMGE cells reformed DENs containing proliferative DCX⁺ cells, similar to DENs observed in the prenatal human brain. This suggests that DENs are generated by cell-autonomous mechanisms. In addition to forming DENs, transplanted hMGE-derived neuroblasts generated young neurons that migrated extensively into cortical and subcortical regions in the host mouse brain. One year after transplantation, these neuroblasts had differentiated into distinct γ -aminobutyric acid-expressing (GABAergic) interneuron subtypes, including SST⁺ and PV⁺ cells, that showed morphological and functional maturation.

CONCLUSION: The hMGE harbors DENs, where cells expressing early neuronal markers continue to divide and produce GABAergic interneurons. This MGE-specific arrangement of neuroblasts in the human brain is present until birth, supporting expanded neurogenesis for inhibitory neurons. Given the robust neurogenic output from this region, knowledge of the mechanisms underlying cortical interneuron production in the hMGE will provide insights into the cell types and developmental periods that are most vulnerable to genetic or environmental insults. ■



Nests of DCX⁺ cells in the ventral prenatal brain. Schematic of a coronal view of the embryonic human forebrain showing the medial ganglionic eminence (MGE, green), with nests of DCX⁺ cells (DENs, green). Nestin⁺ progenitor cells (blue) are present within the VZ and iSVZ and are intercalated in the oSVZ (where DENs reside). The initial segment of the oSVZ contains palisades of nestin⁺ progenitors referred to as type I clusters (light blue cells) around DENs. In the outer part of the oSVZ, DENs transition to chains of migrating DCX⁺ cells; surrounding nestin⁺ progenitors are arranged into groups of cells referred to as type II clusters (white cells). In addition to proliferation of nestin⁺ progenitors, cell division is present among DCX⁺ cells within DENs, suggesting multiple progenitor states for the generation of MGE-derived interneurons in the human forebrain.

The list of author affiliations is available in the full article online.

^{*}Corresponding author. Email: mercedes.paredes@ucsf.edu (M.F.P.); alvarezbuylla@ucsf.edu (A.A.-B.); eric.huang2@ucsf.edu (E.J.H.)

[†]These authors contributed equally to this work.

Cite this article as M. F. Paredes et al., *Science* 375, eabk2346 (2022). DOI: 10.1126/science.abk2346

S READ THE FULL ARTICLE AT
https://doi.org/10.1126/science.abk2346

RESEARCH ARTICLE

NEURODEVELOPMENT

Nests of dividing neuroblasts sustain interneuron production for the developing human brain

Mercedes F. Paredes^{1,2,3,4,*†}, Cristina Mora^{5†}, Quetzal Flores-Ramirez^{1†}, Arantxa Cebrian-Silla^{2,6†}, Ashley Del Dosso⁵, Phil Larimer¹, Jiawei Chen^{3,5}, Eugene Kang^{4,6}, Susana Gonzalez Granero⁷, Eric Garcia¹, Julia Chu¹, Ryan Delgado², Jennifer A. Cotter⁸, Vivian Tang⁵, Julien Spatazza⁶, Kirsten Obner⁶, Jaime Ferrer Lozano⁹, Maximo Vento^{10,11}, Julia Scott¹², Colin Studholme^{13,14,15}, Tomasz J. Nowakowski^{2,16}, Arnold R. Kriegstein^{1,2,3,4}, Michael C. Oldham^{4,5,6}, Andrea Hasenstaub¹⁷, Jose Manuel Garcia-Verdugo⁷, Arturo Alvarez-Buylla^{2,3,4,6,*}, Eric J. Huang^{2,3,4,5,*}

The human cortex contains inhibitory interneurons derived from the medial ganglionic eminence (MGE), a germinal zone in the embryonic ventral forebrain. How this germinal zone generates sufficient interneurons for the human brain remains unclear. We found that the human MGE (hMGE) contains nests of proliferative neuroblasts with ultrastructural and transcriptomic features that distinguish them from other progenitors in the hMGE. When dissociated hMGE cells are transplanted into the neonatal mouse brain, they reform into nests containing proliferating neuroblasts that generate young neurons that migrate extensively into the mouse forebrain and mature into different subtypes of functional interneurons. Together, these results indicate that the nest organization and sustained proliferation of neuroblasts in the hMGE provide a mechanism for the extended production of interneurons for the human forebrain.

A proper balance between glutamatergic excitatory neurons and γ -aminobutyric acid (GABA)-expressing inhibitory neurons (GABAergic interneurons) is central to brain function. Deficits in GABAergic interneurons have been implicated in neurodevelopmental and psychiatric disorders

including autism, epilepsy, and schizophrenia (1–3). GABAergic cortical interneurons are primarily born in germinal zones of the embryonic ventral forebrain, including the medial and caudal ganglionic eminences (MGE and CGE) (4). Young interneurons born in the ganglionic eminences then undertake an extensive migration to reach the cortex and many other forebrain regions (5–7). After completing their migration, young neurons mature into different subtypes, including MGE-derived PV⁺ (parvalbumin-positive) and SST⁺ (somatostatin-positive) interneurons, that are required for normal cortical rhythms and cognitive function (8, 9). It remains unclear how the human MGE (hMGE) generates sufficient interneurons to meet the demand of the larger gyrencephalic cortex.

The hMGE can be delineated by the expression of transcription factor NKX2-1 (NK2 homeobox 1) (10, 11). An initial analysis of the hMGE described two types of nestin⁺ progenitor clusters around DCX⁺ (doublecortin-positive) and LHX6⁺ (LIM homeobox 6-positive) cells. Type I clusters contain nestin⁺ progenitor cell bodies and fibers located in the inner part of the outer subventricular zone (oSVZ), whereas type II progenitor clusters in the outer part of the oSVZ surround streams of DCX⁺/LHX6⁺ migrating young neurons (10). Here, we show that these aggregates of DCX⁺/LHX6⁺ cells in the hMGE, which we refer to as DCX⁺ cell-enriched nests (DENs), contain actively proliferating neuroblasts that persist until birth. Our data further suggest that hMGE cells can reform DENs in a xenograft

model and are a source of GABAergic neurons in the developing human brain.

Nests of DCX⁺ cells in the human MGE

We analyzed the hMGE between 14 and 39 gestational weeks (GW) (Fig. 1A and table S1). Using NKX2-1 staining to delineate the hMGE, we found that the size of hMGE increased between 14 and 22 GW (Fig. 1B). By 34 and 39 GW, the MGE became smaller but was still discernible as a wedge-shaped NKX2-1⁺ structure next to the ventricular wall (Fig. 1B). By cross-referencing NKX2-1 expression patterns and magnetic resonance imaging (MRI) of the human GE (12, 13), we found that the volume of the hMGE increased from 18 to 22 GW and decreased at 33 GW (Fig. 1, D and E). Next, we evaluated the expression of LHX6, a transcription factor activated by NKX2-1 that is necessary for subtype specification and migration of hMGE-derived interneurons (14, 15). Similar to NKX2-1, LHX6 expression was detected in the hMGE from 14 to 39 GW (fig. S1A). LHX6⁺ cells were organized into tight cellular aggregates, or nests (fig. S1, B and C). The majority of LHX6⁺ cells expressed DCX and PSA-NCAM (polysialylated neural cell adhesion molecule), another marker found in young migratory neurons (figs. S1C and S2C). Confocal imaging showed that radial glia fibers stained with nestin or vimentin encased DCX⁺ cells within the hMGE, a relationship that persisted from 14 to 39 GW (Fig. 1C and fig. S2, A and B). To better understand the configuration of these DCX⁺ nests (DENs), we performed serial coronal and axial (horizontal) mapping of the hMGE at 22 GW. Quantification of DEN size showed no change along the rostral-caudal (coronal) axis but a progressive increase in DEN size along the dorsal to ventral (axial) planes (Fig. 1, F and G). The average area of a DEN in coronal sections decreased by 53% between 14 and 39 GW (Fig. 1E).

A second germinal zone of the ventral telencephalon is the lateral ganglionic eminence (LGE) that sits immediately dorsal to the MGE. Work in rodents has shown that the LGE is a source of GABAergic projection neurons for the striatum and of interneurons for the olfactory bulb (16). In contrast to the hMGE, DCX⁺ cells in the hLGE were homogeneously distributed and showed no evidence of DEN formation (fig. S2B). The above results indicate that during a period of hMGE expansion and heightened neurogenesis, young DCX⁺/LHX6⁺ neurons become tightly packed into DENs surrounded by bundles of nestin⁺ and vimentin⁺ cells and fibers (type I clusters) in the first and early second trimester of hMGE development (10). DENs decreased in area with age, although they were still present at 39 GW. The persistent presence of DENs in

¹Department of Neurology, University of California, San Francisco, CA 94143, USA. ²Eli and Edythe Broad Institute for Stem Cell Research and Regeneration Medicine, University of California, San Francisco, CA 94143, USA. ³Biomedical Sciences Graduate Program, University of California, San Francisco, CA 94143, USA. ⁴Developmental and Stem Cell Graduate Program, University of California, San Francisco, CA 94143, USA. ⁵Department of Pathology, University of California, San Francisco, CA 94143, USA. ⁶Department of Neurological Surgery, University of California, San Francisco, CA 94143, USA. ⁷Laboratorio de Neurobiología Comparada, Instituto Cavanilles de Biodiversidad y Biología Evolutiva, Universitat de València—Centro de Investigación Biomédica en Red sobre Enfermedades Neurodegenerativas (CIBERNED), Valencia, Spain. ⁸Department of Pathology, Children's Hospital Los Angeles, and Keck School of Medicine of University of Southern California, Los Angeles, CA 90027, USA. ⁹Department of Pathology, Hospital Universitari i Politècnic La Fe, Valencia, Spain. ¹⁰Neonatal Research Group, Health Research Institute La Fe, Valencia, Spain. ¹¹Division of Neonatology, University and Polytechnic Hospital La Fe, Valencia, Spain. ¹²Department of Bioengineering, Santa Clara University, Santa Clara, CA 95053, USA. ¹³Biomedical Image Computing Group, Departments of Pediatrics, Bioengineering, and Radiology, University of Washington, Seattle, WA 98195, USA. ¹⁴Department of Bioengineering, University of Washington, Seattle, WA 98195, USA. ¹⁵Department of Radiology, University of Washington, Seattle, WA 98195, USA. ¹⁶Department of Anatomy and Department of Psychiatry and Behavioral Sciences, University of California, San Francisco, CA 94143, USA. ¹⁷Department of Otolaryngology, University of California, San Francisco, CA 94143, USA.

*Corresponding author. Email: mercedes.paredes@ucsf.edu (M.F.P.); alvarezbuylla@ucsf.edu (A.A.-B.); eric.huang@ucsf.edu (E.J.H.)

†These authors contributed equally to this work.

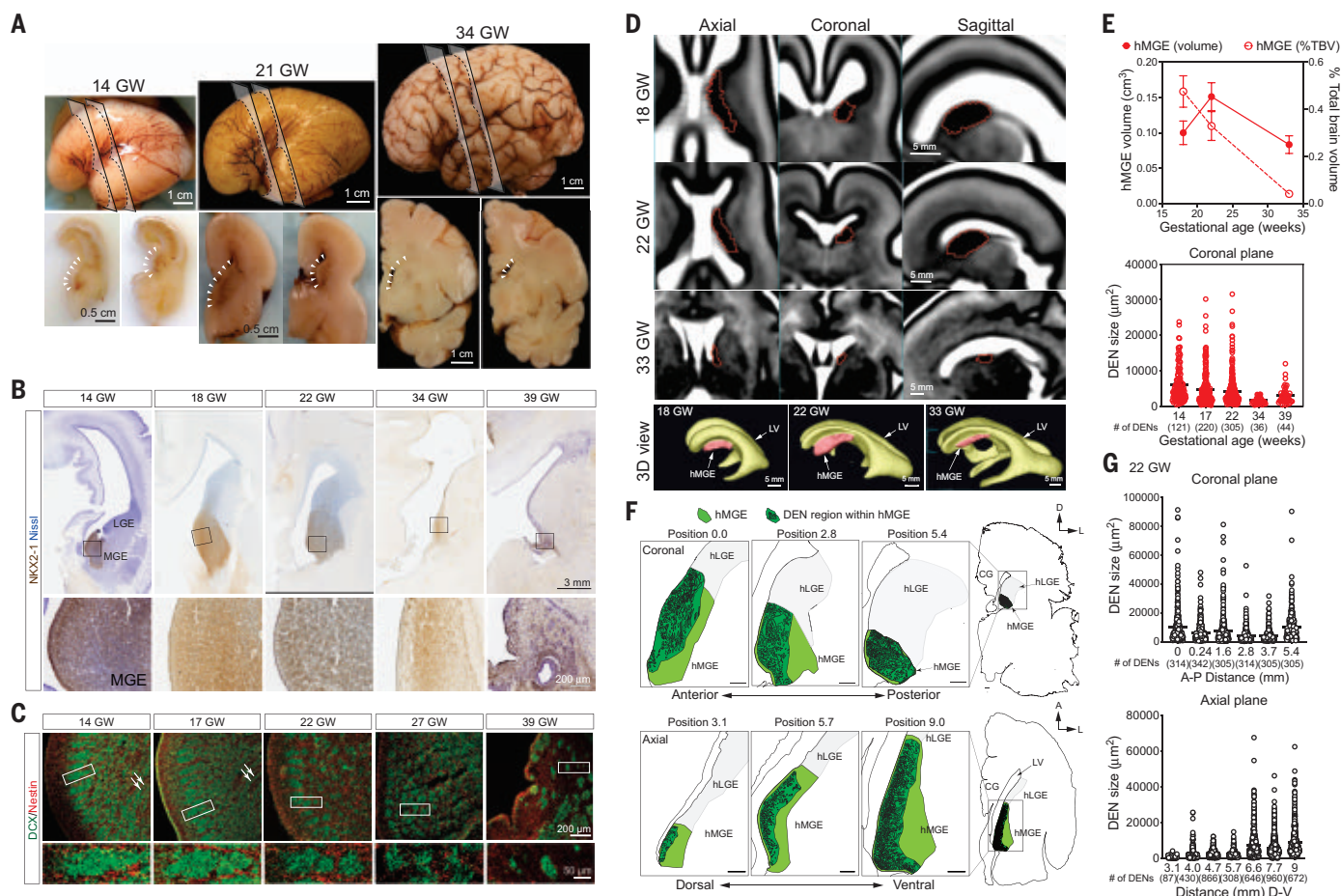


Fig. 1. hMGE organization in the prenatal and perinatal brain. (A) Lateral views (top) and coronal cross sections (bottom) of the prenatal human brain at 14, 21, and 33 GW. Dashed lines indicate the locations where the coronal sections are made; arrowheads indicate the location of human ganglionic eminences located next to the lateral walls of the lateral ventricles. **(B)** Immunohistochemical stains for NKX2-1 in the hMGE at 14, 18, 22, 34, and 39 GW. NKX2-1 shows a robust expression from 14 to 22 GW. Despite the decrease in hMGE size at 34 GW, NKX2-1 expression remains high. At 39 GW, NKX2-1 expression in the hMGE is reduced to a thin slit along the subventricular zone. **(C)** Confocal images of the hMGE from 14 to 39 GW reveal the unique organization of dense DCX⁺ nests that intermix with nestin⁺ fibers. **(D)** MRI images of prenatal hMGE (highlighted in red) on the axial, coronal, and sagittal planes at 18, 22, and 33 GW. Three-dimensional (3D) reconstruction highlights the position of the hMGE in relationship to the lateral ventricle (LV) at the respective ages. **(E)** Top: Quantification of hMGE volume relative to total brain volume by MRI images at 18, 22, and 33 GW. By cross-referencing NKX2-1 expression patterns and MRI images of human GE, we

found that hMGE volume increased from $115 \pm 15 \text{ mm}^3$ at 18 GW to $158 \pm 13 \text{ mm}^3$ at 22 GW, then decreased to $88 \pm 3 \text{ mm}^3$ at 33 GW. Data are means \pm SD; $n = 10$ for each gestational age. Bottom: Quantification of the size of DEN in hMGE on the coronal planes shows the progressive reduction in size from 14 to 39 GW. The average area of a DEN in coronal sections decreased from $6053 \pm 452 \mu\text{m}^2$ at 14 GW to $4052 \pm 242 \mu\text{m}^2$ at 22 GW, and dropped further to $2870 \pm 360 \mu\text{m}^2$ at 39 GW. The number of DENs for each gestational age is included in parentheses. **(F)** Schematic diagrams highlighting DENs (dark green) in hMGE (light green) in 22 GW prenatal brain at the coronal plane (top) and axial plane (bottom) reveal relatively similar sizes of DCX⁺ nests. The adjacent hLGE is shaded light gray. The positions of the hMGE indicated on the coronal plane are from anterior (position 0.0) to posterior (position 5.4). On the axial plane, the positions of the hMGE are from top (position 3.1) to bottom (position 9.0). Scale bars, 500 μm . **(G)** Top: Quantification of DEN size in the hMGE at 22 GW shows similar sizes from anterior to posterior on the coronal plane. Bottom: DEN size appears to become progressively larger from top to bottom on the axial plane.

the hMGE during an extended period of prenatal development suggests that this organization is fundamental to the production of inhibitory neurons in the human brain.

The majority of DCX⁺ cells within DENs appear destined to become GABAergic interneurons, as analysis at 14 and 39 GW showed that these cells expressed DLX2 (distal-less homeobox 2) (17, 18) (fig. S3A). In contrast to DLX2, ASCL1 (achaete-scute family BHLH transcription factor 1), frequently found in intermediate progenitors, was detected in

SOX2⁺ progenitors outside DENs (fig. S3B). Consistently, DEN cells also expressed GABA protein and glutamate decarboxylase (*GAD1*) transcripts (fig. S3, C and D). These results further suggest that DCX⁺ cells within DENs are early GABAergic interneurons.

Ultrastructural and transcriptomic features define DENs

We next used transmission electron microscopy (TEM) to analyze the hMGE at 14, 17, and 23 GW. DENs were identified as nests of cells

separated by bundles of radial glia fibers (Fig. 2, A and C). Cells within the DENs had a small nucleus with dark nucleoplasm, heterochromatin clumps, scarce cytoplasm with many free ribosomes, and frequent small adherens junctions (<200 nm in length) (Fig. 2, D to G), features seen in young neurons (19, 20). Immunogold TEM staining confirmed that cells in DENs were DCX⁺ (Fig. 2, H and I). In addition to the DEN cells, we identified ventricle-contacting radial glia (vRG) and other progenitor cells in the iSVZ and oSVZ

Fig. 2. Ultrastructural characteristics of DENs in the hMGE.

(A to C) Schematics of 14, 17, and 23 GW hMGE in coronal sections used to map identified cell types in TEM ultrathin section micrographs. Ventricular radial glia (vRG) (dark blue), intermediate progenitors (cyan), mitoses (orange), DEN cells (green), outer subventricular zone (oSVZ) progenitors (purple), and blood vessels (gray) were identified by ultrastructural characteristics (table S2 and fig. S4). (D) DEN cells close to the lateral ventricle in (C) showed scarce cytoplasm and thin interdigitated expansions oriented in all directions (DEN cell cytoplasm outlined in green). (E) High magnification of DEN cell expansions showing frequent small adherens junctions (white arrows). (F and G) DEN cells deep into the hMGE showing long cell expansions rich in mitochondria and microtubules (black arrows). Note that contacts through small adherens junctions were frequent (white arrows). (H to J) Immunogold TEM of DCX⁺ cells within DENs in 22 GW hMGE. Note that DCX-Au⁺ cells show scarce cytoplasm and small adherens junctions (white arrows). DCX-Au⁺ mitotic figures inside DENs were also observed. (K) Mitotic figure within DEN in (C). Scale bars, 0.5 mm [(A) to (C)], 2 μ m [(D), (F), and (H)], 500 nm [(E), (G), and (I)], 1 μ m [(J) and (K)].

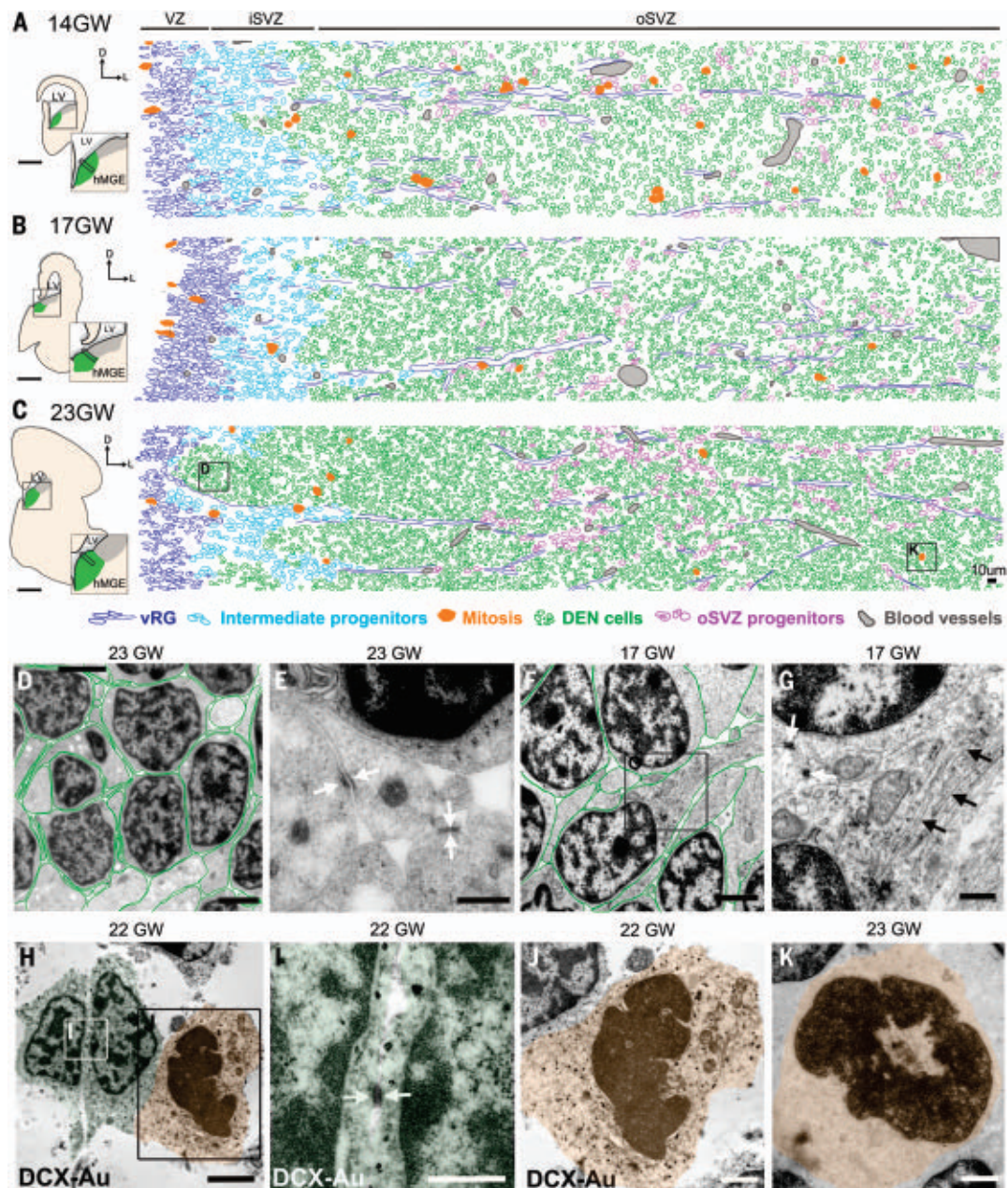


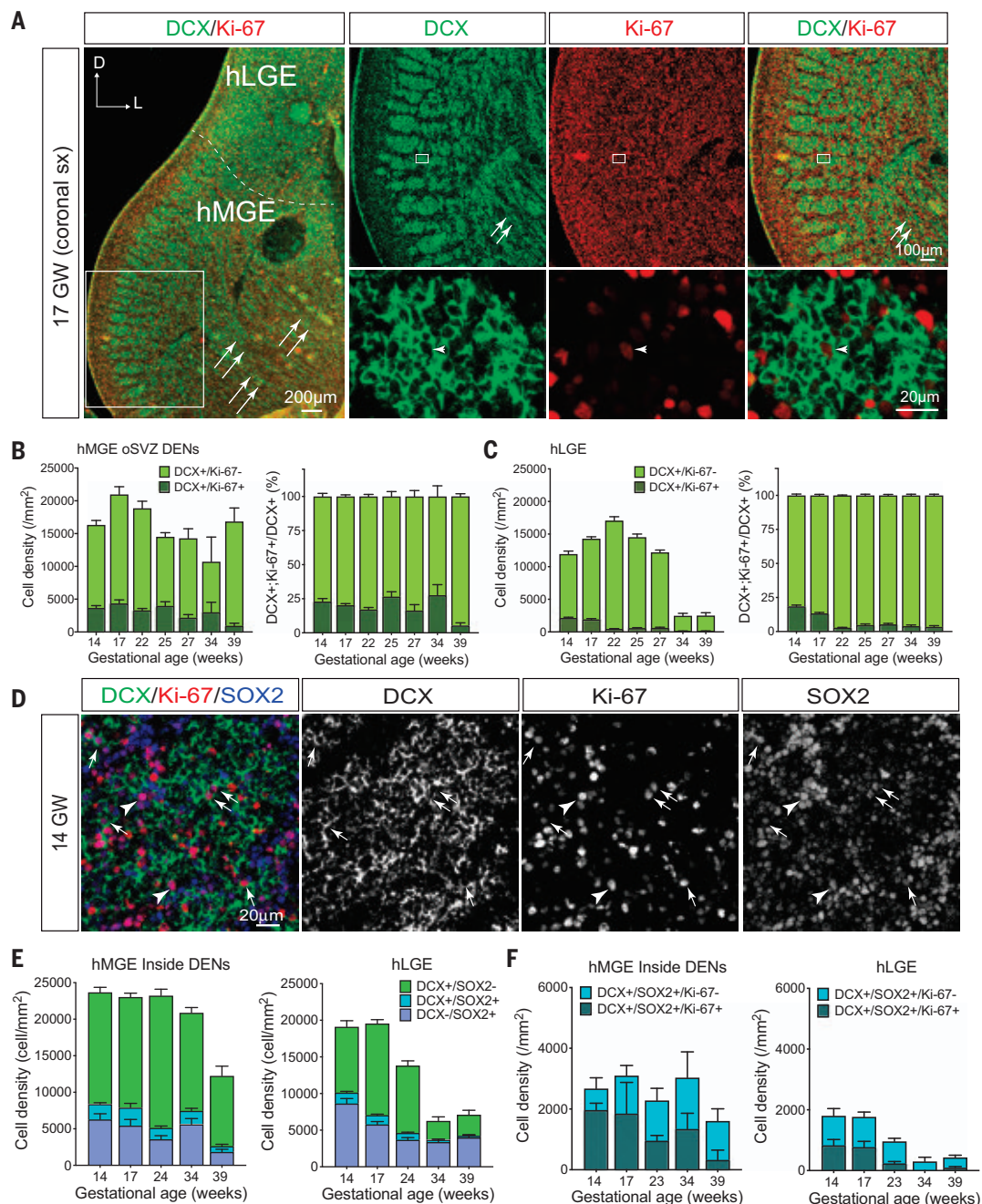
(table S2). vRG contacted the ventricle through thin apical expansions that had apical junctions and a primary cilium. Their nuclei were elongated and irregular and frequently had nuclear envelope chromatin sheets (21, 22) (fig. S4, A to D). In the iSVZ, progenitor cells had more rounded nuclei than vRG and a higher number of heterochromatin clumps. iSVZ progenitors lacked apical junctions, indicating that they were not part of the ventricular epithelium (fig. S4, E and F). Prominent bundles of stacked radial glia expansions rich in intermediate filaments and microtubules were noted in oSVZ at all ages studied (Fig. 2, A to C, and fig. S4, L to O). These bundles correspond to type I clusters of radial glia fibers previously described

(10) and contain an interspersed third type of progenitor cell with fewer intermediate filaments and a morphology that resembles outer-radial glia-like cells (fig. S4, H to K). MGE cells, including cells within DENs, at all ages studied had a cytoplasmic cylindrical structure that we refer to as ribosomal barrels, containing membrane lamellae with ribosomes lining the inner side (fig. S4, P and Q). The function of ribosomal barrels, or lamellae, is unknown.

On the basis of this cell classification scheme, we used tiled high-resolution TEM images to reconstruct the cellular composition of the hMGE at 14, 17, and 23 GW (Fig. 2, A to C). These reconstructions revealed the location of DENs and their consolidation with age.

Mitoses were frequent in the VZ and iSVZ, and within and around DENs, at the three gestational ages studied (Fig. 2, A to C, and fig. S4, R to T). At 14 GW, we noted that the majority of mitoses were associated with radial glia bundles, but by 17 and 23 GW, mitotic figures were among DEN cells (Fig. 2 and fig. S4, fuchsia). Using immunogold staining at 22 GW, we confirmed that mitoses within DENs were DCX⁺ (Fig. 2, H to J). These results suggested that a subpopulation of DEN cells were proliferative between 14 and 23 GW (Fig. 2, J and K). By 23 GW, cells in DENs closer to the VZ had thin interdigitated expansions oriented in all directions (Fig. 2, D and E). In contrast, DEN cells located farther away from the ventricle (~900 μ m) had more polyribosomes

Fig. 3. DCX⁺ cells proliferate in the human ganglionic eminences. (A) Left: Confocal image of a coronal section of 17 GW hMGE and hLGE immunostained with DCX (green) and Ki-67 (red). Dashed line highlights the boundary that separates the hLGE and hMGE; arrows indicate streams of DCX⁺ cells migrating away from DENs at the edge of the hMGE. Right: Higher magnifications of DENs in the boxed area in the left panel (top row) where many DCX⁺ cells show positive staining for Ki-67 (bottom row); arrowhead points to a DCX⁺/Ki-67⁺ cell in the DENs. **(B and C)** Quantification of DCX⁺/Ki-67⁺ cells and DCX⁺/Ki-67⁻ cells in hMGE (B) and hLGE (C) at 14, 17, 22, 25, 27, 34, and 39 GW. DCX⁺/Ki-67⁺ cells and DCX⁺/Ki-67⁻ cells are presented as cell density (number of cells per mm²) (left panels); in addition, DCX⁺/Ki-67⁺ cells are presented as the percentage of DCX⁺ cells (right panels). Data are means ± SEM. **(D)** Confocal images of hMGE at 14 GW immunostained with DCX, Ki-67, and SOX2 antibodies. Arrows in the merged panel and individual channels highlight DCX⁺/SOX2⁺/Ki-67⁺ cells; arrowhead indicates a DCX⁺/SOX2⁺/Ki-67⁺ cell within DENs. **(E and F)** Quantifications of DCX⁺/SOX2⁺, DCX⁺/SOX2⁻, and DCX⁺/SOX2⁺ progenitors (E) and DCX⁺/SOX2⁺ progenitors that are still in the cell cycle (Ki-67⁺) or already exited cell cycle (Ki-67⁻) (F) in hMGE and hLGE at 14, 17, 24, 34, and 39 GW. Data are means ± SEM and are presented as cell density (number of cells per mm²).



and mitochondria, and their expansions were thicker and longer; this may reflect a higher degree of differentiation and activation of the migratory stage away from the MGE (Fig. 2, F and G, and table S2).

The organization of progenitor cells in the hMGE, which differs from that of neighboring hLGE, suggests that the pattern of gene expression responsible for DEN formation may be specific to the MGE. Using public microdissected hLGE and hMGE transcriptomic data (23), we performed gene coexpression analysis (24) from 17, 18, 23, and 23.5 GW samples (fig. S5A). This analysis revealed a group of genes highly correlated in their

expression in the hMGE at all ages studied (the sienna3 module; fig. S5B). This module included genes implicated in neuronal stem cell population maintenance, regulation of cell-substrate adhesion, homophilic cell adhesion, and extracellular matrix organization. The expression of all these genes decreased with gestational age. Among the top genes in the sienna3 module, there were several cell adhesion-related nonclustered protocadherin genes (*PCDH17*, *PCDH10*). Immunostaining at 22 GW showed that *PCDH10*⁺ cells were located almost exclusively outside DENs. In the 22 GW hLGE, *PCDH10*⁺ was widely distributed, interspersed between DCX⁺ cells (fig. S5C).

Another protocadherin gene found in this module, *PCDH19*, showed robust and extensive expression in the 22 GW hMGE that colocalized with DCX⁺ cells within DENs (fig. S5D); *PCDH19*⁺ cells were not detected in the hLGE (fig. S5D).

In addition to the sienna3 module, a second module (greenyellow) enriched in the hMGE contained genes implicated in regulating the cell cycle, DNA replication, and mitotic nuclear division (fig. S5E). The gene expression differences within this module between the hMGE and hLGE increased with age. Immunostains showed that E2F1 (E2F transcription factor 1), a top gene in this module, was

enriched as punctate staining in the 22 GW hMGE, but not in hLGE. E2F1 staining frequently overlapped with DCX staining. Unlike DCX⁺ cells in the hMGE that frequently expressed E2F1, DCX⁺ cells in hLGE were E2F1⁻ (fig. S5F). Together with the presence of mitosis in DCX⁺ cells (Fig. 2, H to J), these results suggest that a subpopulation of DCX⁺ neuroblasts in DENs have proliferative capacity.

Proliferating DCX⁺ cells within DENs

To further characterize the proliferation of cells within DENs, we performed immunostains for Ki-67, a protein expressed in dividing cells. Proliferating neuroblasts (DCX⁺/Ki-67⁺ cells) were detected in both the hMGE and hLGE from 14 to 39 GW (Fig. 3A). In the hMGE, DCX⁺ cells were primarily located within DENs (Fig. 3B and fig. S6B) and a substantial fraction of all dividing (Ki-67⁺) cells in the hMGE were DCX⁺ (31% at 14 GW, 21% at 17 GW, and 24% at 23 GW). The proportion of DCX⁺ cells in DENs that were Ki-67⁺ remained at 20 to 25% from 14 to 34 GW and dropped to ~5% at 39 GW (Fig. 3B). Ki-67⁺ cells were observed both in the center and close to the edge of DENs. Similarly, ~20% of the DCX⁺ cells in the hLGE were Ki-67⁺ at 14 and 17 GW, but these proportions in the LGE decreased to ~3% between 17 and 22 GW; by 22 GW, DCX⁺/Ki-67⁺ cells were rare in the hLGE (Fig. 3C).

Using SOX2 as a marker for undifferentiated progenitor cells (25, 26), we found that the majority of SOX2⁺ cells were located outside DENs (fig. S6, A and C), consistent with previous observations (10). However, a subpopulation of DCX⁺ cells in DENs also expressed SOX2, and more than 50% of these DCX⁺/SOX2⁺ cells were Ki-67⁺ (Fig. 3D, arrows). DCX⁺/SOX2⁺/Ki-67⁺ or DCX⁺/SOX2⁺/Ki-67⁻ cells could still be detected in the hMGE at 39 GW (Fig. 3, E and F, and fig. S6B), but these cells were rarely observed outside DENs from 14 to 34 GW (fig. S6A). The hLGE contained fewer DCX⁺/SOX2⁺ cells than the hMGE. Consistent with the above data, DCX⁺/SOX2⁺ cells in the hLGE could be observed at 14 and 17 GW (Fig. 3, E and F), but their numbers dropped between 17 and 23 GW and there were very few at 34 and 39 GW (Fig. 3, E and F). Like the DCX⁺/SOX2⁺ cells, a number of SOX2⁺ progenitors were Ki-67⁺ in both the hMGE and hLGE. The number of SOX2⁺/Ki-67⁺ progenitors decreased earlier in the hLGE (by 23 GW) than in the hMGE (34 GW) (fig. S6C). To validate the proliferative properties of DCX⁺ cells, we infected 18 GW hMGE slice cultures with CMV-GFP adenovirus (adenovirus expressing green fluorescent protein under a CMV promoter) to label cells and used time-lapse confocal imaging to follow proliferative behavior during 72 hours (fig. S7A). Dividing cells displaying interkinetic migration in the VZ (movie S1), but more than half (56%) of the

observed mitoses ($n = 122$) occurred deeper in the hMGE in the iSVZ and oSVZ. Among these divisions, we noted cells that showed mitotic somatic translocation typical of outer radial glia progenitor cells (27). We also observed cells with processes after division that corresponded to DCX⁺ cells in post hoc immunostaining (fig. S7, B and C, and movie S2). Quantification of the cellular populations in the slices showed that 27% of DCX⁺ cells in hMGE cultures expressed Ki-67, similar to what was observed in the postmortem quantifications (Fig. 3B). Taken together, our results indicate that a subpopulation of DCX⁺ neuroblasts in the hMGE continues to proliferate within DENs.

Transplanted hMGE cells recapitulate DEN features

We next investigated whether hMGE development could be recapitulated by xenotransplantation (7, 28). We dissected the hMGE from 14 to 16 GW samples and transplanted the dissociated hMGE cells into the cortex of immunosuppressed recipient animals. Transplanted cells, identified by the expression of human nuclear antigen (HNA), were analyzed at 45, 90, and 365 days after transplant (DAT). At 45 and 90 DAT (corresponding to hMGE cells at ~21 GW and 26 GW, respectively), transplanted cells formed large masses of densely packed HNA⁺ cells around the injection site (Fig. 4B); HNA⁺ cells expressed NKX2-1 at 45 DAT (86%) and 90 DAT (94%) (Fig. 4C and fig. S8D), but not SP8 or COUP transcription factor 2 (COUPTFII), associated with LGE and CGE, respectively (fig. S8, A to C). These results supported the ability of the transplanted hMGE cells to maintain their regional identity. At 45 DAT, HNA⁺ cells became organized into nests of DCX⁺ cells encased by vimentin⁺ radial glial fibers and cells, similar to the DEN architecture found in the intact hMGE in vivo (Fig. 4D). HNA⁺/DCX⁺ DENs were also identified at 90 DAT, but these were smaller and had fewer cells (Fig. 4E and fig. S9A).

The ability of the transplanted hMGE progenitors to organize as DENs (Fig. 4D and fig. S9A) raised the possibility that the transplant-derived DCX⁺ nests retain proliferative activity as observed in vivo. We quantified the proportion of all HNA⁺ transplant-derived cells that were Ki-67⁺. Within the transplant mass, we found that 23% of all HNA⁺ cells were Ki-67⁺ at 45 DAT, dropping to 3.5% by 90 DAT (fig. S10, A to C). By 365 DAT, no HNA⁺/Ki-67⁺ cells were present (fig. S10B). Of all HNA⁺/DCX⁺ cells in the transplant mass at 45 DAT, 19% were Ki-67⁺, similar to the 20 to 25% of DCX⁺ cells that were in the cell cycle in the post mortem DENs at 17 to 22 GW (fig. S10D). Among the Ki-67⁺/HNA⁺ cells, about half (58%) were DCX⁺ at 45 DAT. However, HNA⁺/DCX⁺ cells that

migrated outside the transplant were Ki-67⁻, which suggests that as hMGE-derived young neurons become migratory, they stop dividing.

To further characterize the cellular composition close to the transplant site, we performed immunostains for DCX and SOX2. At 45 DAT, ~35% of HNA⁺ cells were DCX⁺/SOX2⁺, ~45% were DCX⁺/SOX2⁻, and ~20% were DCX⁻/SOX2⁺ ($n = 4$) (Fig. 4, E and F). By 90 DAT, the majority of SOX2⁺ cells were no longer DCX⁺ ($n = 2$). DCX⁺/SOX2⁺ cells made up 36.6% of the HNA⁺/Ki-67⁺ population at 45 DAT and 13.2% at 90 DAT (Fig. 4, G and H). As observed in vivo, a fraction of the Ki-67⁺ cells within the transplant mass were DCX⁺/SOX2⁺ (~10%) at 45 and 90 DAT. By 365 DAT, most of the transplant mass disappeared, and the remaining HNA⁺ cells did not express DCX or Ki-67 (Fig. 4H). Taken together, these results indicate that hMGE progenitor cells transplanted into the mouse brain grew into a mass of cells that mimicked the composition and self-organization of the hMGE, including the formation of DENs.

Transplanted hMGE cells display properties of interneurons

We noted that at 45 DAT, HNA⁺/DCX⁺ cells were dispersing away from DENs and the transplant site (Fig. 5A); the majority of these cells had a migratory morphology. More than 99% of the dispersing hMGE cells at 45 and 90 DAT were DCX⁺ (99.1% and 99.4%, respectively), but at both these ages, the majority of HNA⁺/DCX⁺ cells were NKX2-1⁻, consistent with the down-regulation of this transcription factor in migrating GABAergic interneurons (29). HNA⁺/DCX⁺ cells were observed as far as 3 mm from the transplant site at 45 and 90 DAT, respectively (fig. S9B). From these results, we infer that hMGE-derived transplanted cells are migratory in the brain of juvenile mice. To study this migratory behavior, we infected 14 GW hMGE-dissociated cells with lentiviruses that expressed GFP under the control of *DLX1/2* (distal-less homeobox 1/2) enhancer (i12b-GFP lentivirus) and transplanted these cells into the neonatal mouse cortex. GFP⁺ hMGE cells were recorded at 21 DAT in organotypic slices prepared for time-lapse microscopy (Fig. 5C). Individual GFP⁺ cells had a migratory behavior similar to that observed in mouse cortical interneurons (30), including extension of a leading process (frequently bifurcated) and nucleokinesis. Cells outside the transplant moved at an average speed of 21 $\mu\text{m}/\text{hour}$ (Fig. 5C). We also noted movements of cells within the transplant (movie S3), but the high cell density prevented us from precisely following the movement of individual cells and determining their migratory behavior.

By 90 DAT, HNA⁺ cells were observed leaving the injection site as DCX⁺ chains (Fig. 5, D and E), and individual DCX⁺ cells

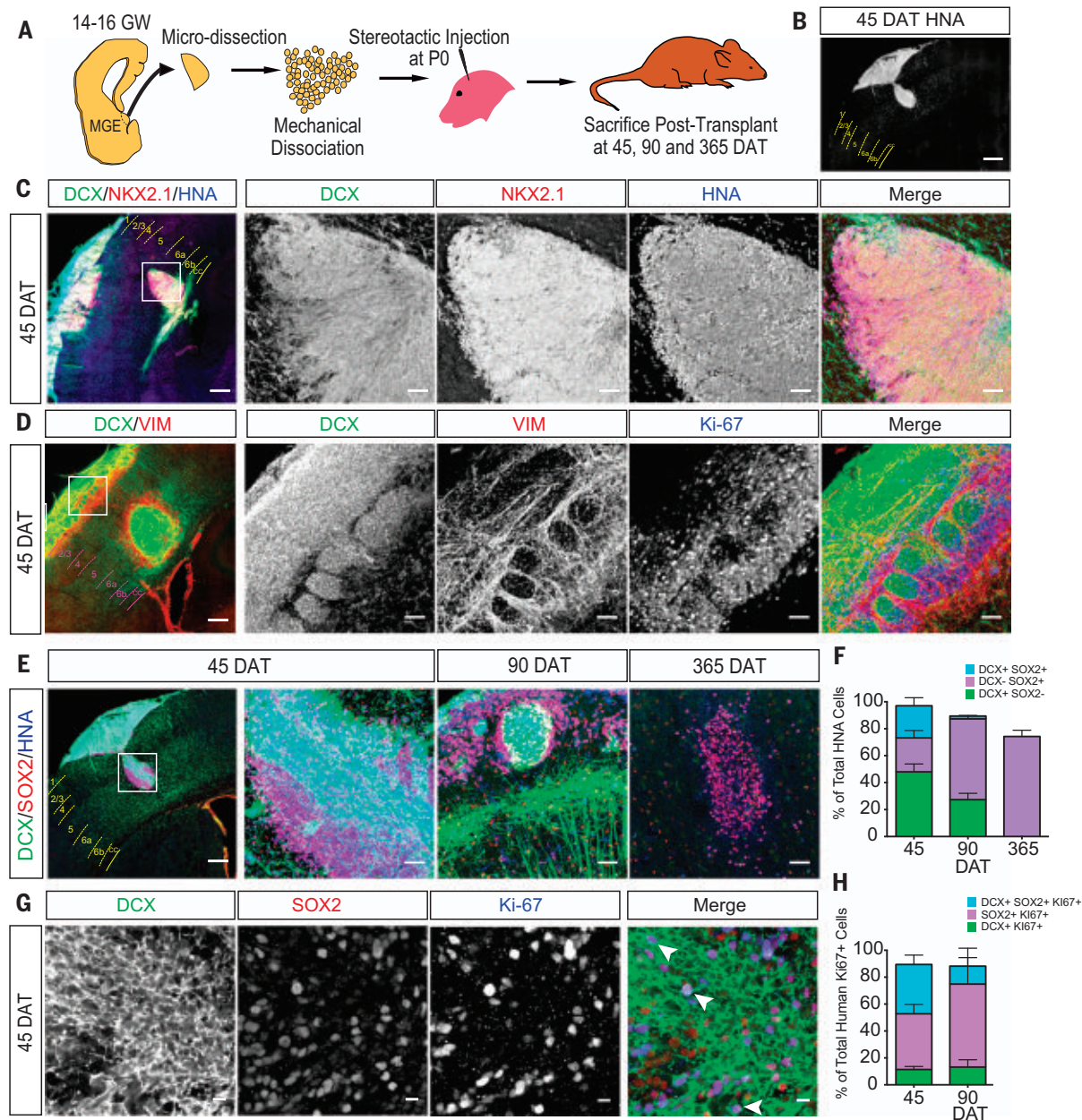


Fig. 4. Transplanted hMGE cells recapitulate DEN organization and proliferation. (A) Schematic of hMGE transplantation surgery. (B) Coronal section indicating injection site of HNA⁺ cells (white) at 45 DAT. Dashed lines delimit cortical layers; cc, corpus callosum. (C) HNA⁺ cells at the injection site at 45 DAT express DCX and NKX2.1. The transplant (boxed area of the leftmost panel) is shown at higher magnification. (D) Transplanted hMGE cells form dense DCX⁺ nests encased by VIM⁺ radial glia fibers at the site of injection at 45 DAT. The transplant (boxed area of the leftmost panel) is shown at higher magnification. Many VIM⁺ and DCX⁺ cells are Ki-67⁺. (E) HNA⁺ (blue) cells at injection sites

express DCX and SOX2 at 45, 90, and 365 DAT. (F) Quantification of proportion of total HNA⁺ cells at the injection site (45 DAT, $n = 4$; 90 DAT, $n = 2$; 365 DAT, $n = 3$) that are DCX⁺ (green), SOX2⁺ (purple), or DCX⁺/SOX2⁺ (cyan). Data are means \pm SEM. (G) High magnification of DCX⁺, SOX2⁺, and Ki-67⁺ cells in DENs at 45 DAT. (H) Quantification of proportion of HNA⁺/Ki-67⁺ cells at the injection site (45 DAT, $n = 4$; 90 DAT, $n = 2$; 365 DAT, $n = 3$) that are DCX⁺ (green), SOX2⁺ (purple), or DCX⁺/SOX2⁺ (cyan). Data are means \pm SEM. Scale bars, 500 μ m [(B) and leftmost panel in (C) to (E)], 50 μ m [other panels in (C) to (E)], 10 μ m (G).

were found dispersed into many regions of the mouse brain including the hippocampus, amygdala, corpus callosum, striatum, septum, olfactory bulb, and piriform cortex (fig. S11). Relative to 45 DAT, most of the hMGE-derived cells at 90 DAT exhibited a more complex neuronal morphology with

increased branch number and length (Fig. 5, A and B, and fig. S11). At 90 DAT, a subpopulation of the DCX⁺/HNA⁺ cells expressed GABA (Fig. 5E), but these cells were negative for the mature neuronal marker NeuN. By 210 DAT, the expression of DCX was reduced (fig. S12, A and B); a fraction of hMGE-derived cells

were NeuN⁺ and several expressed the interneuron subtype marker SST (fig. S12C), which suggested that these cells had begun their differentiation (fig. S12C). By 365 DAT, most HNA⁺/NeuN⁺ cells expressed GABA, with many expressing SST and some rare cells expressing PV⁺, calbindin⁺, or calretinin⁺ (Fig. 5,

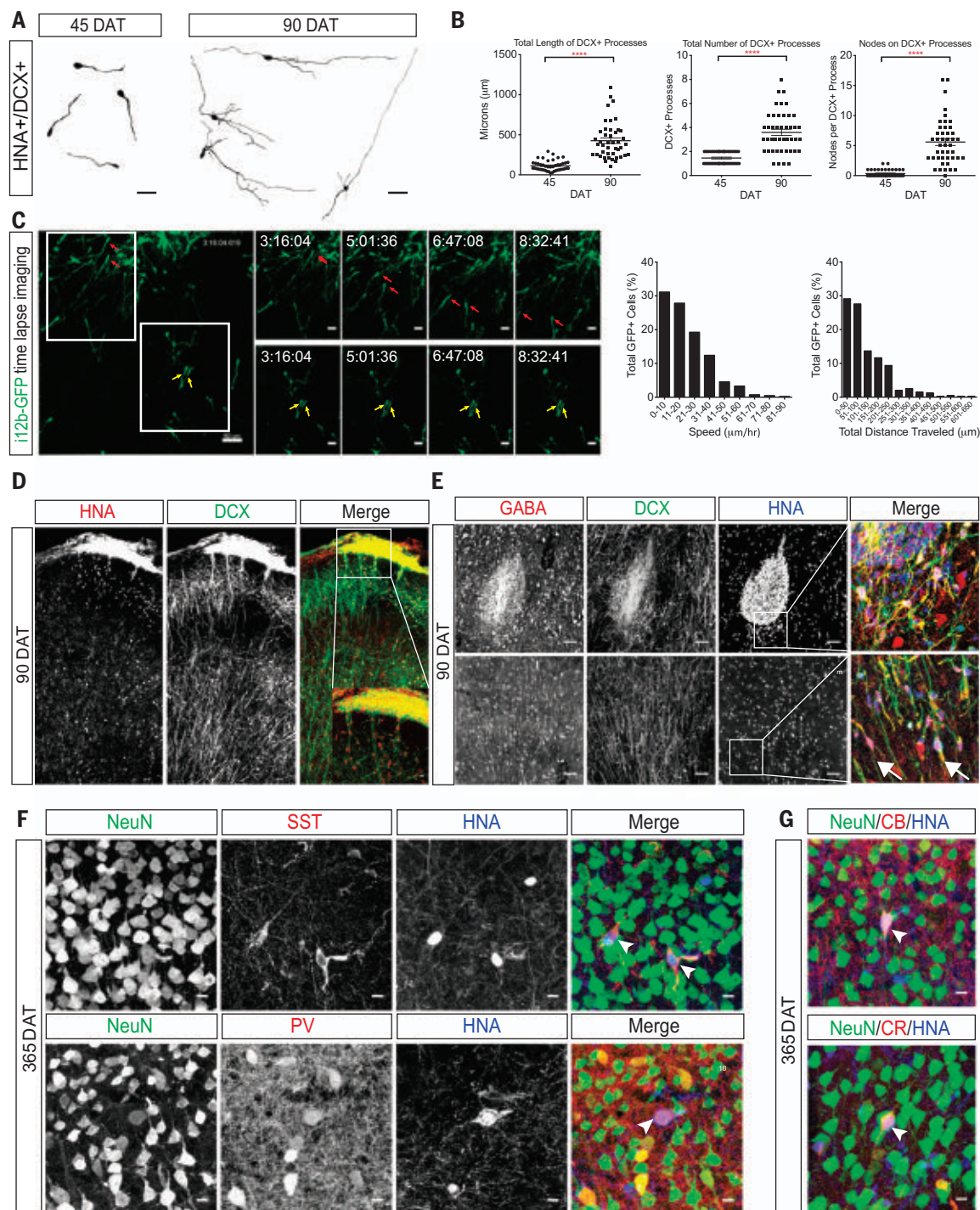


Fig. 5. Transplanted hMGE cells display migratory and functional inter-neuronal features. (A) Neurolucida tracings of DCX⁺ transplanted hMGE at 45 and 90 DAT (four cells shown per time point). (B) Quantification of the length (left) and total number (center) of DCX-positive processes at 45 and 90 DAT. Right graph shows quantification of the number of DCX⁺ branching nodes per transplanted cell analyzed at 45 or 90 DAT. For all graphs, $n = 22$ cells per animal for both 45 and 90 DAT; **** $P < 0.0001$. (C) Left: Sequential images of time-lapse confocal microscopy showing two example sets (red and yellow arrows) of GFP⁺ transplanted hMGE cells at 21 DAT. Right: Proportion of GFP-positive transplanted hMGE cells (total 395 cells) analyzed for speed (left) and total distance traveled (right).

(D) Confocal image of transplanted mouse cortex at 90 DAT showing dispersal of HNA⁺DCX⁺ cells. Inset shows boxed area at higher magnification. (E) Top: Injection site at 90 DAT contains cells that coexpress DCX, GABA, and HNA. Bottom: Transplanted hMGE cells away from the injection site also coexpress DCX and GABA (arrows). (F) Examples of transplanted hMGE cells at 365 DAT that express NeuN (green) and HNA (blue) either with SST (red, arrowheads in top panel) or PV (red, arrowhead in bottom panel). (G) Examples of transplanted hMGE cells at 365 DAT that express NeuN, calbindin (CB⁺, arrowhead in top), and calretinin (CR⁺, arrowhead in bottom). Scale bars, 50 µm [(A), (C) (leftmost panel), (E)], 25 µm [(C) (upper and lower rows)], 10 µm [(D) (inset), (F), (G)].

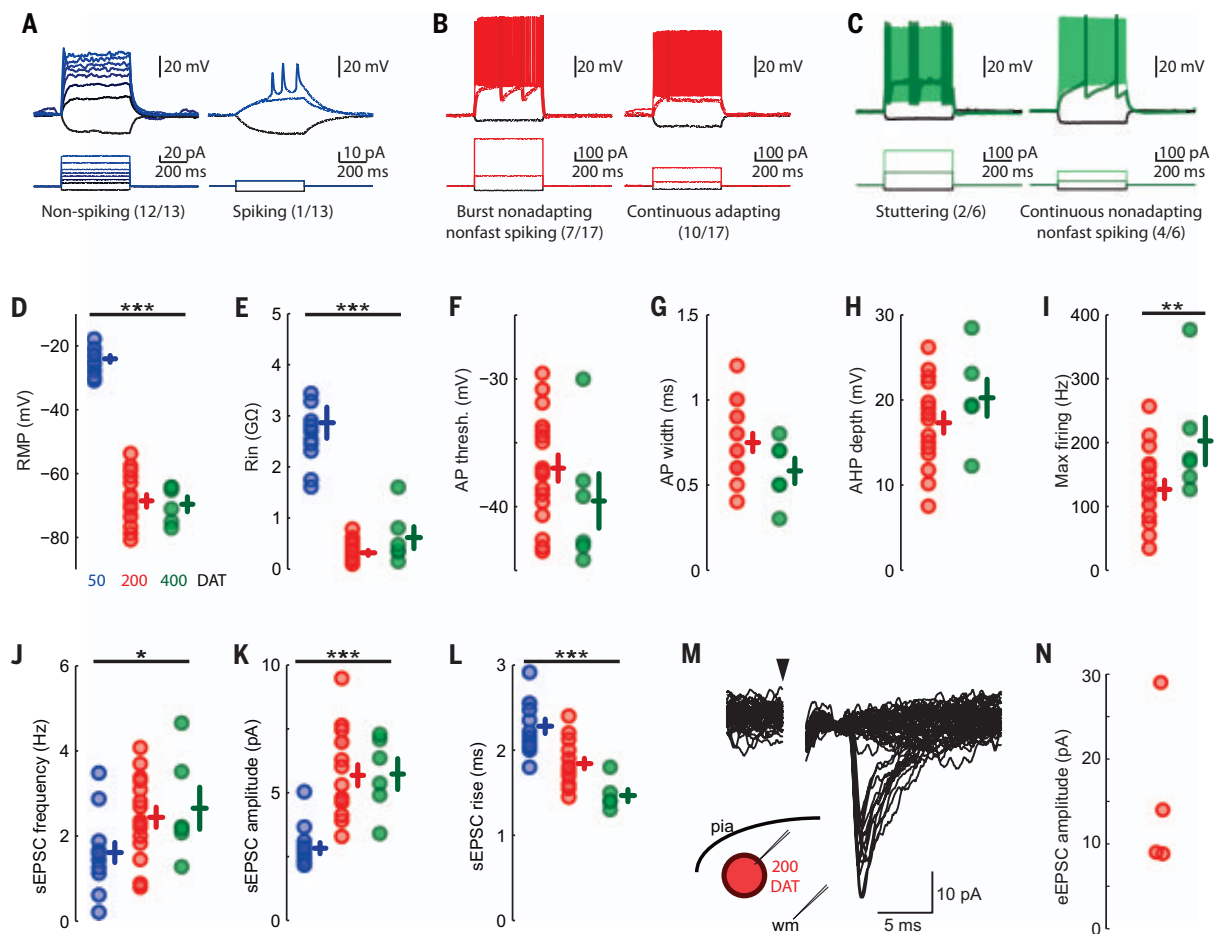


Fig. 6. Physiological parameters of hMGE cells after transplantation.

(A) hMGE cells at 50 DAT demonstrate immature action potentials with either minimal regenerative current (left) or a few short/broad action potentials (right). (B) hMGE cells at 200 DAT have regenerative action potentials (17/17 tested) that occur in one of two distinct temporal patterns, either burst nonadapting nonfast spiking (left) or continuous adapting (right). (C) hMGE cells at 400 DAT have action potentials in either a stuttering pattern (left) characteristic of fast-spiking interneurons or a continuous nonadapting phenotype (right). (D and E) Passive physiological properties changed over maturation with a significant hyperpolarization of resting membrane potential [(D), $P < 10^{-18}$ by one-way analysis of variance (ANOVA)] and a significant decrease in input resistance [(E), $P < 10^{-10}$ by one-way ANOVA]. (F to I) Active membrane

properties were not assessed in 50 DAT transplant-derived cells because they almost uniformly did not fire action potentials. There were no significant changes to the action potential threshold (F) or width (G), the action potential after hyperpolarization (AHP) depth (H), or the maximal firing rate [(I), by two-sample Kolmogorov-Smirnov test]. (J) All cells recorded had clearly identifiable EPSCs at 50 DAT, but sEPSC frequency increased significantly at 200 and 400 DAT ($P = 0.038$ by one-way ANOVA). (K and L) sEPSC amplitude also increased upon maturation ($P < 10^{-5}$ by one-way ANOVA) (K), whereas rise time decreased (L) ($P < 10^{-6}$ by one-way ANOVA). (M and N) EPSCs evoked by deep white matter stimulation $>500 \mu\text{m}$ from the recorded soma (M) demonstrate small eEPSCs (20 sequential traces at minimal stimulation amplitude) in all cells in which extracellular stimulation was attempted (N). * $P < 0.05$, ** $P < 0.01$, *** $P < 0.001$.

F and G). Patch-clamp recording in slices prepared at 50 DAT showed that the majority (12/13) of GFP⁺ hMGE-derived cells had immature action potential with minimal regenerative currents. Only one recorded cell at 50 DAT showed spiking in response to current injections (Fig. 6A, right). At 200 DAT, all hMGE-derived neurons (17 GFP⁺ cells) had mature action potentials and could be classified by their firing patterns into continuous adapting or burst nonadapting (Fig. 6B). By 400 DAT, recorded GFP⁺ cells exhibited action potentials with stuttering patterns characteristic of fast-spiking GABAergic interneurons (2/6 GFP⁺ cells) or a continuous nonadapting phenotype (Fig. 6C). Synaptic input in the

hMGE-derived cells was detected as early as 50 DAT. By 200 DAT, white matter stimulation elicited excitatory postsynaptic currents (eEPSCs) in all recorded cells (Fig. 6, M and N) indicating that hMGE-derived neurons were integrated into the host mouse brain. These results demonstrate that a subpopulation of hMGE-derived cells transplanted into the mouse brain migrates widely and matures into functional interneuron subtypes that receive synaptic input.

Discussion

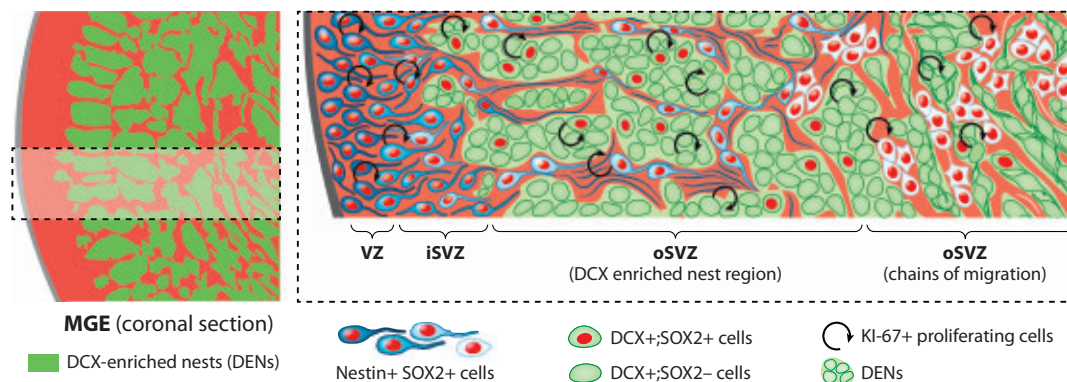
Our results reveal that the hMGE is organized into nests of DCX⁺ cells (DENs) containing proliferative neuroblasts (Fig. 7). DENs are

surrounded by nestin⁺ progenitors, an arrangement not observed in the rodent MGE (5, 31, 32) or in other germinal zones of the human forebrain, including the LGE or the pallium (10). DENs are also not apparent in the human CGE (10), another major source of cortical interneurons (11, 33, 34). Furthermore, transplantation of hMGE cells into the rodent brain formed DENs containing proliferative DCX⁺ cells and gave rise to GABAergic interneuron subtypes. These results suggest that DENs are formed by cell-autonomous mechanisms and give rise to highly migratory cells that differentiate into GABAergic interneurons.

Do DCX⁺/SOX2⁺ cells represent an intermediate or transient amplifying progenitor state?

Fig. 7. The developing hMGE contains multiple layers of proliferating nestin⁺ progenitors and DCX⁺ neuroblasts.

Left: Schematic overview of hMGE showing organization of progenitor regions (red) surrounding DCX⁺ cells (green regions). Right: Higher magnification of the boxed area at left. DCX⁺ cells (green) are organized into DENs surrounded by nestin⁺/SOX2⁺ progenitors (illustrated in different shades of blue to white).



Cell proliferation was observed among DCX⁺ cells in DENs until the end of gestation (see text). Nestin⁺/SOX2⁺ progenitors are also proliferative and are found within the VZ, the inner SVZ (iSVZ), and around DENs in the outer SVZ (oSVZ). Nestin⁺ progenitors and fibers surround DENs and are organized into tight bundles, previously identified as type I clusters (10) (light blue cells) in the initial segment of the oSVZ. In the outer part of the oSVZ, DENs transition to chains of migrating cells, and nestin⁺ progenitor cells are arranged as type II clusters (10). [Illustration by Noel Sirivansanti]

SOX2 is a transcription factor present in stem cells and is necessary for their progression to neural fates. Yet SOX2 also functions to maintain proliferation (35–37). Therefore, the presence of SOX2 could maintain a proliferative state in a subpopulation of DCX⁺ cells that are already committed to become inhibitory interneurons expressing GABA (DLX2⁺). It remains unknown how SOX2 expression is maintained in a subset of DCX⁺ cells within the hMGE. Nor is it known whether these cells divide symmetrically to amplify their population, or divide asymmetrically to retain a population of less differentiated progenitors. Proliferation in the hMGE was also highlighted by the expression of E2F1 among DCX⁺ cells within the DENs (fig. S3). The E2F family is involved in regulating the cell cycle (38–40) and could also function in maintaining the proliferative properties of DCX⁺ cells in DENs.

Work in the rodent brain has shown that the MGE is also an important source of oligodendrocytes (41, 42). We found large numbers of OLIG2⁺ cells in the hMGE, but these cells were found outside the DENs from 15 to 39 GW (fig. S3, E and F). We also observed a pronounced expansion of oligodendrocyte progenitors from hMGE transplants at 210 and 365 DAT (fig. S9C). Oligodendrocyte progenitor cells continue to divide after they leave the MGE (43); this suggests that unlike interneuron precursor proliferation, which seems to be closely linked to DENs, oligodendrocyte amplification can occur outside the MGE.

How are DENs formed? Electron microscopy revealed frequent adhesion contacts between cells within DENs, providing multiple sites to anchor DEN cells together. Our data also showed that cells within DENs express PCDH19, whereas nestin⁺ progenitors surrounding DENs express PCDH10, suggesting a role for differential cell adhesion in the

formation and maintenance of DENs. Mutations in *PCDH19* have been causally linked to epilepsy in females with mental retardation (EFMR), whereas variants of human *PCDH10* have been associated with autism (44).

The diversity of interneurons has evolved across species, including the presence of unique interneuron subtypes in humans and a reallocation of interneuron subtypes in primate brains (45, 46). Previous work has suggested that distinct ventrodorsal levels of the mouse MGE generate different subtypes of cortical interneurons (47). We found that the size of DENs within the MGE, and the proportion of the MGE occupied by DENs, varies depending on the dorsoventral level (Fig. 1). DENs in different regions of the hMGE may represent expansion of different subtypes of interneurons. The presence of a distinctive neurogenic niche with spatially discrete nests of proliferating DCX⁺ cells could contribute to differences in interneuron populations across organisms. Discovering the mechanisms underlying cortical interneuron production in the hMGE will also provide insight into the cell types and developmental periods that are vulnerable to genetic or environmental insults.

Methods summary

We studied human MGE samples from 14 to 39 gestational weeks. Tissues were collected with previous patient consent according to institutional ethical regulations of the University of California San Francisco Committee on Human Research. Histological sections were generated from human MGE tissues for immunohistochemistry and in situ hybridization to identify young neurons, progenitor cells, and molecular markers for proliferation, intermediate progenitor states, and transcription factors associated with the ganglionic eminences. To determine the MGE volume and changes through gestational stages, we performed volumetric measurements of hMGE

in MRI and combined them with immunohistochemical and immunofluorescence staining. We used transmission electron microscopy to perform an ultrastructural analysis of the cellular composition of the hMGE and identification of DEN cells at 14, 17, and 23 GW. To identify DCX⁺ cells and nestin radial glial fibers under TEM, we performed immunogold staining against these markers. To identify the MGE pattern of gene expression compared to LGE, we performed transcriptomic analysis on publicly available gene expression data of the human ganglionic eminences from the Allen Institute. Analyses were on laser-microdissected CNS bulk tissue from four prenatal human brains at 17 to 23 GW. (23). Unsupervised gene coexpression module detection and identification of region-specific modules revealed genes associated with the MGE that were validated in the human tissue sections. To determine the proliferative capacity of the human MGE ex vivo, we generated organotypic slice cultures from the human MGE that were infected with CMV-GFP adenovirus and imaged for 3 days using time-lapse confocal imaging. We performed xenograft experiments transplanting human MGE cells into immunocompromised neonatal mice and analyzed brains at 45, 90, 210, and 400 days after transplantation. Transplanted brains were used for histological analysis and to generate live tissue sections for migration assays and electrophysiology experiments.

REFERENCES AND NOTES

1. R. Canitano, M. Pallagrosi, Autism Spectrum Disorders and Schizophrenia Spectrum Disorders: Excitation/Inhibition Imbalance and Developmental Trajectories. *Front. Psychiatry* **8**, 69 (2017). doi: 10.3389/fpsy.2017.00069; pmid: 28507523
2. B. Chattopadhyaya, G. D. Cristo, GABAergic circuit dysfunctions in neurodevelopmental disorders. *Front. Psychiatry* **3**, 51 (2012). doi: 10.3389/fpsy.2012.00051; pmid: 22666213
3. O. Marin, Interneuron dysfunction in psychiatric disorders. *Nat. Rev. Neurosci.* **13**, 107–120 (2012). doi: 10.1038/nrn3155; pmid: 22251963

4. C. P. Wonders, S. A. Anderson, The origin and specification of cortical interneurons. *Nat. Rev. Neurosci.* **7**, 687–696 (2006). doi: [10.1038/nrn1954](#); pmid: [16883309](#)
5. S. A. Anderson, O. Marin, C. Horn, K. Jennings, J. L. Rubenstein, Distinct cortical migrations from the medial and lateral ganglionic eminences. *Development* **128**, 353–363 (2001). doi: [10.1242/dev.128.3.353](#); pmid: [11152634](#)
6. O. Marin, Cellular and molecular mechanisms controlling the migration of neocortical interneurons. *Eur. J. Neurosci.* **38**, 2019–2029 (2013). doi: [10.1111/ejn.12225](#); pmid: [23651101](#)
7. H. Wichterle, J. M. Garcia-Verdugo, D. G. Herrera, A. Alvarez-Buylla, Young neurons from medial ganglionic eminence disperse in adult and embryonic brain. *Nat. Neurosci.* **2**, 461–466 (1999). doi: [10.1038/8131](#); pmid: [10321251](#)
8. V. S. Sohal, F. Zhang, O. Yizhar, K. Deisseroth, Parvalbumin neurons and gamma rhythms enhance cortical circuit performance. *Nature* **459**, 698–702 (2009). doi: [10.1038/nature07991](#); pmid: [19396159](#)
9. B. R. Ferguson, W.-J. Gao, Thalamic Control of Cognition and Social Behavior Via Regulation of γ -Aminobutyric Acidergic Signaling and Excitation/Inhibition Balance in the Medial Prefrontal Cortex. *Biol. Psychiatry* **83**, 657–669 (2018). doi: [10.1016/j.biopsych.2017.11.033](#); pmid: [29373121](#)
10. D. V. Hansen et al., Non-epithelial stem cells and cortical interneuron production in the human ganglionic eminences. *Nat. Neurosci.* **16**, 1576–1587 (2013). doi: [10.1038/nn.3541](#); pmid: [24097039](#)
11. T. Ma et al., Subcortical origins of human and monkey neocortical interneurons. *Nat. Neurosci.* **16**, 1588–1597 (2013). doi: [10.1038/nn.3536](#); pmid: [24097041](#)
12. C. Studholme, Mapping the developing human brain in utero using quantitative MR imaging techniques. *Semin. Perinatol.* **39**, 105–112 (2015). doi: [10.1053/j.semper.2015.01.003](#); pmid: [25813665](#)
13. J. A. Scott et al., Growth trajectories of the human fetal brain tissues estimated from 3D reconstructed in utero MRI. *Int. J. Dev. Neurosci.* **29**, 529–536 (2011). doi: [10.1016/j.jidvneu.2011.04.001](#); pmid: [21530634](#)
14. D. Vogt et al., Lhx6 directly regulates Arx and CXCR7 to determine cortical interneuron fate and laminar position. *Neuron* **82**, 350–364 (2014). doi: [10.1016/j.neuron.2014.02.030](#); pmid: [24742460](#)
15. P. Liodis et al., Lhx6 activity is required for the normal migration and specification of cortical interneuron subtypes. *J. Neurosci.* **27**, 3078–3089 (2007). doi: [10.1523/JNEUROSCI.3055-06.2007](#); pmid: [17376969](#)
16. J. Stenman, H. Toresson, K. Campbell, Identification of two distinct progenitor populations in the lateral ganglionic eminence: Implications for striatal and olfactory bulb neurogenesis. *J. Neurosci.* **23**, 167–174 (2003). doi: [10.1523/JNEUROSCI.23-01-00167.2003](#); pmid: [12514213](#)
17. M. A. Petryniak, G. B. Potter, D. H. Rowitch, J. L. R. Rubenstein, Dlx1 and Dlx2 control neuronal versus oligodendroglial cell fate acquisition in the developing forebrain. *Neuron* **55**, 417–433 (2007). doi: [10.1016/j.neuron.2007.06.036](#); pmid: [17678855](#)
18. J. E. Long, I. Cobos, G. B. Potter, J. L. R. Rubenstein, Dlx1&2 and Mash1 transcription factors control MGE and CGE patterning and differentiation through parallel and overlapping pathways. *Cereb. Cortex* **19** (suppl. 1), i96–i106 (2009). doi: [10.1093/cercor/bhp045](#); pmid: [19386638](#)
19. C. Lois, J. M. Garcia-Verdugo, A. Alvarez-Buylla, Chain migration of neuronal precursors. *Science* **271**, 978–981 (1996). doi: [10.1126/science.271.5251.978](#); pmid: [8584933](#)
20. M. F. Paredes et al., Extensive migration of young neurons into the infant human frontal lobe. *Science* **354**, aaf7073 (2016). doi: [10.1126/science.aaf7073](#); pmid: [27846470](#)
21. H. Guerrero-Cázares et al., Cytoarchitecture of the lateral ganglionic eminence and rostral extension of the lateral ventricle in the human fetal brain. *J. Comp. Neurol.* **519**, 1165–1180 (2011). doi: [10.1002/cne.22566](#); pmid: [21344407](#)
22. A. Cebrián-Silla et al., Unique Organization of the Nuclear Envelope in the Post-natal Quiescent Neural Stem Cells. *Stem Cell Rep.* **9**, 203–216 (2017). doi: [10.1016/j.stemcr.2017.05.024](#); pmid: [28648897](#)
23. J. A. Miller et al., Transcriptional landscape of the prenatal human brain. *Nature* **508**, 199–206 (2014). doi: [10.1038/nature13185](#); pmid: [24695229](#)
24. K. W. Kelley, H. Nakao-Inoue, A. V. Molofsky, M. C. Oldham, Variation among intact tissue samples reveals the core transcriptional features of human CNS cell classes. *Nat. Neurosci.* **21**, 1171–1184 (2018). doi: [10.1038/s41593-018-0216-z](#); pmid: [30154505](#)
25. M. Götz, S. Sirkko, J. Beckers, M. Imrlir, Reactive astrocytes as neural stem or progenitor cells: In vivo lineage, In vitro potential, and Genome-wide expression analysis. *Glia* **63**, 1452–1468 (2015). doi: [10.1002/glia.22850](#); pmid: [25965557](#)
26. M. Komitova, P. S. Eriksson, Sox-2 is expressed by neural progenitors and astroglia in the adult rat brain. *Neurosci. Lett.* **369**, 24–27 (2004). doi: [10.1016/j.neulet.2004.07.035](#); pmid: [15380301](#)
27. D. V. Hansen, J. H. Lui, P. R. L. Parker, A. R. Kriegstein, Neurogenic radial glia in the outer subventricular zone of human neocortex. *Nature* **464**, 554–561 (2010). doi: [10.1038/nature08845](#); pmid: [20154730](#)
28. D. G. Southwell et al., Interneurons from embryonic development to cell-based therapy. *Science* **344**, 1240622 (2014). doi: [10.1126/science.1240622](#); pmid: [24723614](#)
29. S. Nóbrega-Pereira et al., Postmitotic Nkx2-1 controls the migration of telencephalic interneurons by direct repression of guidance receptors. *Neuron* **59**, 733–745 (2008). doi: [10.1016/j.neuron.2008.07.024](#); pmid: [18786357](#)
30. O. Marin et al., Directional guidance of interneuron migration to the cerebral cortex relies on subcortical Slit1/2-independent repulsion and cortical attraction. *Development* **130**, 1889–1901 (2003). doi: [10.1242/dev.00417](#); pmid: [12642493](#)
31. J. S. Hu, D. Vogt, M. Sandberg, J. L. Rubenstein, Cortical interneuron development: A tale of time and space. *Development* **144**, 3867–3878 (2017). doi: [10.1242/dev.132852](#); pmid: [29089360](#)
32. G. Paxinos, G. Halliday, C. Watson, M. S. Kassem, *Atlas of the Developing Mouse Brain* (Academic Press, 2020).
33. S. Nery, G. Fishell, J. G. Corbin, The caudal ganglionic eminence is a source of distinct cortical and subcortical cell populations. *Nat. Neurosci.* **5**, 1279–1287 (2002). doi: [10.1038/nn971](#); pmid: [12411960](#)
34. L. Lim, D. Mi, A. Llorca, O. Marin, Development and Functional Diversification of Cortical Interneurons. *Neuron* **100**, 294–313 (2018). doi: [10.1016/j.neuron.2018.10.009](#); pmid: [30359598](#)
35. V. Graham, J. Khudyakov, P. Ellis, L. Pevny, SOX2 functions to maintain neural progenitor identity. *Neuron* **39**, 749–765 (2003). doi: [10.1016/S0896-6273\(03\)00497-5](#); pmid: [12948443](#)
36. S. Gómez-López et al., Sox2 and Pax6 maintain the proliferative and developmental potential of gliogenic neural stem cells In vitro. *Glia* **59**, 1588–1599 (2011). doi: [10.1002/glia.21201](#); pmid: [21766338](#)
37. D. W. Hagey et al., SOX2 regulates common and specific stem cell features in the CNS and endoderm derived organs. *PLOS Genet.* **14**, e1007224 (2018). doi: [10.1371/journal.pgen.1007224](#); pmid: [29432416](#)
38. L. Magri et al., E2F1 coregulates cell cycle genes and chromatin components during the transition of oligodendrocyte progenitors from proliferation to differentiation. *J. Neurosci.* **34**, 1481–1493 (2014). doi: [10.1523/JNEUROSCI.2840-13.2014](#); pmid: [24453336](#)
39. K. Ohtani, J. DeGregori, J. R. Nevins, Regulation of the cyclin E gene by transcription factor E2F1. *Proc. Natl. Acad. Sci. U.S.A.* **92**, 12146–12150 (1995). doi: [10.1073/pnas.92.26.12146](#); pmid: [8618861](#)
40. P.-D. Denechaud, L. Fajas, A. Giralt, E2F1, a Novel Regulator of Metabolism. *Front. Endocrinol.* **8**, 311 (2017). doi: [10.3389/fendo.2017.00311](#); pmid: [29176962](#)
41. N. Kassarlis et al., Competing waves of oligodendrocytes in the forebrain and postnatal elimination of an embryonic lineage. *Nat. Neurosci.* **9**, 173–179 (2006). doi: [10.1038/nn1620](#); pmid: [16388308](#)
42. S. A. Goldman, N. J. Kuypers, How to make an oligodendrocyte. *Development* **142**, 3983–3995 (2015). doi: [10.1242/dev.126409](#); pmid: [26628089](#)
43. W. Huang et al., Origins and Proliferative States of Human Oligodendrocyte Precursor Cells. *Cell* **182**, 594–608.e11 (2020). doi: [10.1016/j.cell.2020.06.027](#); pmid: [32679030](#)
44. E. M. Morrow et al., Identifying autism loci and genes by tracing recent shared ancestry. *Science* **321**, 218–223 (2008). doi: [10.1126/science.1157657](#); pmid: [18621663](#)
45. F. M. Krienen et al., Innovations present in the primate interneuron repertoire. *Nature* **586**, 262–269 (2020). doi: [10.1038/s41586-020-2781-z](#); pmid: [32999462](#)
46. E. Boldog et al., Transcriptomic and morphophysiological evidence for a specialized human cortical GABAergic cell type. *Nat. Neurosci.* **21**, 1185–1195 (2018). doi: [10.1038/s41593-018-0205-2](#); pmid: [30150662](#)
47. N. Flames et al., Delineation of multiple subpallial progenitor domains by the combinatorial expression of transcriptional codes. *J. Neurosci.* **27**, 9682–9695 (2007). doi: [10.1523/JNEUROSCI.2750-07.2007](#); pmid: [17804629](#)

ACKNOWLEDGMENTS

We thank and honor the families who generously donated the tissue samples used in this study, A. Paredes for editing comments, and E. Marsan for data analysis discussion. **Funding:** R25 NS070680 (P.L. and J.A.C.); R01 MH113896 (M.C.O.); R01 EB017133, R01 NS055064, and NSF CRCNS 2011088 (C.S.); P01 NS083513 (A.A.-B., M.F.P., A.R.K., and E.J.H.); K08 NS091537 (M.F.P.); R01 NS028478 (A.A.-B.); AHA Predoctoral Fellowship 19PRE3480616 (J.Chen); Roberta and Oscar Gregory Endowment in Stroke and Brain Research (M.F.P.); Valencian Council for Innovation, Universities, Sciences and Digital Society (PROMETEO/2019/075) and Red de Terapia Celular (TerCel-RD16/0011/0026) (J.M.G.-V.); Spanish Generalitat Valenciana and European Social Fund Postdoctoral Fellowship (APOSTD2018/A113) (A.C.-S.); and CIRIM Bridges (EDUC2-126-93) (C.M.). **Author contributions:** M.F.P., A.A.-B., and E.J.H. designed the study with assistance from J.A.C., C.M., and Q.F.-R.; C.M., Q.F.-R., A.D.D., J. Chen, J. Chu, E.G., J.A.C., V.T., and J.S. performed the histological work with the postmortem samples and analyzed the data; J.S. and C.S. performed the analysis on the prenatal MRI datasets; A.C.-S. and S.G.G. performed the ultrastructural analysis under the supervision of J.M.G.-V.; R.D. and T.J.N. performed live imaging analysis; P.L. and A.H. performed and led the electrophysiological studies; G.K. and M.C.O. performed the bioinformatics analysis of hMGE and hLGE RNA datasets; A.R.K., J.F.L., and M.V. contributed tissue resources and data interpretation; and M.F.P., C.M., Q.F.-R., A.C.-S., A.A.-B., and E.J.H. wrote the manuscript with feedback from all authors. **Competing interests:** P.L. is currently an employee of Vertex Pharmaceuticals and owns shares in the company. A.A.-B. is co-founder and on the scientific advisory board of Neurena Therapeutics. **Data and materials availability:** All data are available in the main text or the supplementary materials.

SUPPLEMENTARY MATERIALS

science.org/doi/10.1126/science.abk2346

Materials and Methods

Figs. S1 to S12

Tables S1 to S3

References (48–57)

Movies S1 to S3

10 July 2021; accepted 1 December 2021

10.1126/science.abk2346

RESEARCH ARTICLES

STRUCTURAL BIOLOGY

Structure-based discovery of nonhallucinogenic psychedelic analogs

Dongmei Cao^{1†}, Jing Yu^{1†}, Huan Wang^{2†}, Zhipu Luo^{3†}, Xinyu Liu^{4†}, Licong He¹, Jianzhong Qi¹, Luyu Fan¹, Lingjie Tang¹, Zhangcheng Chen¹, Jinsong Li⁴, Jianjun Cheng^{2*}, Sheng Wang^{1*}

Drugs that target the human serotonin 2A receptor (5-HT_{2A}R) are used to treat neuropsychiatric diseases; however, many have hallucinogenic effects, hampering their use. Here, we present structures of 5-HT_{2A}R complexed with the psychedelic drugs psilocin (the active metabolite of psilocybin) and D-lysergic acid diethylamide (LSD), as well as the endogenous neurotransmitter serotonin and the nonhallucinogenic psychedelic analog lisuride. Serotonin and psilocin display a second binding mode in addition to the canonical mode, which enabled the design of the psychedelic IHCH-7113 (a substructure of antipsychotic lumateperone) and several 5-HT_{2A}R β -arrestin-biased agonists that displayed antidepressant-like activity in mice but without hallucinogenic effects. The 5-HT_{2A}R complex structures presented herein and the resulting insights provide a solid foundation for the structure-based design of safe and effective nonhallucinogenic psychedelic analogs with therapeutic effects.

Serotonin, or 5-hydroxytryptamine (5-HT), is a neurotransmitter that modulates most human behavioral processes (1), and drugs that target serotonin receptors are widely used in psychiatry and neurology (1). Among these drugs, the serotonergic hallucinogens (psychedelics) alter consciousness and may have potential for drug development (2–5). For example, D-lysergic acid diethylamide (LSD) and psilocybin have shown promise for addressing many neuropsychiatric diseases (2). Preliminary open-label trials have shown their potential for symptom alleviation in mood disorders and anxiety in the terminally ill (2, 6), and recently completed phase 2 clinical trials showed that psilocybin is a viable alternative to current antidepressant medications (7). The therapeutic effects of LSD and psilocybin appear to be both rapid and enduring (6, 8–10).

Previous studies have identified oleamide (an endogenous fatty acid amide) in the cerebrospinal fluid of sleep-deprived cats and rats and demonstrated that it was able to potentiate human serotonin 2A receptor (5-HT_{2A}R)-mediated signaling (11–14). This result sug-

gested that abnormal sensitivity of 5-HT_{2A}R to oleamide and other endogenous fatty acids could be responsible for some aspects of psychiatric disorders, such as anxiety and depression. A lack of structural information of 5-HT_{2A}R with fatty acids limits our ability to undertake the structure-based design of safe and effective antidepressants. Additionally, although two recent studies have reported nonhallucinogenic psychedelic analogs with antidepressant-like behavior (15, 16), it remains unclear how to rationally design such compounds, even with the 25 serotonin receptor structures in hand (17–24), and it is unclear whether the hallucinogenic effects of psychedelics are necessary for therapeutic effects (2, 7–10).

Lipid activation of 5-HT_{2A}R

Based on modeling and site-directed mutagenesis studies, tryptamine ligands, such as serotonin and psilocin, are predicted to bind to serotonin receptors in a similar manner to ergoline ligands (3, 19, 23). To investigate this, we compared the conformations of two ergoline-bound 5-HT_{2A}R structures (LSD and lisuride) with the serotonin- and psilocin-bound 5-HT_{2A}R complex structures (Fig. 1A and table S1). Recent structures of serotonin bound to 5-HT_{1A}R and 5-HT_{1D}R are reminiscent of structures of ergolines bound to serotonin receptors (17–21, 23, 24). In our structures with 5-HT_{2A}R, the ergoline moieties of LSD and lisuride are bound similarly to previous structures at the bottom of the orthosteric binding pocket (OBP) (17–21, 23), but in contrast, the indole serotonin-psilocin core is located higher in the orthosteric pocket, closer to extracellular loop 2 (EL2) and the extracellular space, where they engage the extended binding pocket (EBP) of the receptor, which is

occupied by the diethyl moiety of LSD and lisuride (19, 20).

All of our 5-HT_{2A}R complex structures showed clear density maps occupying the previously identified side-extended pocket (SEP) (22) that could be best fit with monoolein, the lipid used in crystallization, which is structurally similar to oleamide (Fig. 1B and figs. S1A and S2A). In the serotonin-, psilocin-, LSD-, and lisuride-bound structures, the Fo-Fc omit maps allowed us to unambiguously define the binding pose of the monoolein glycerol group (Fig. 1B). Because of its high flexibility, the exact position of the alkyl chain could only be partially assigned (Fig. 1B and fig. S1A). However, all the glycerol groups of monoolein are inserted into the SEP in the serotonin-, psilocin-, LSD-, and lisuride-bound 5-HT_{2A}R structures. Compared with the LSD- and lisuride-bound complexes, the glycerol groups of monoolein are driven deep into the OBP in the structures of the serotonin- and psilocin-bound complexes (fig. S1B). Here, the deep insertion of monoolein may partially explain why serotonin and psilocin engage the EBP and not the OBP of the receptor (fig. S1B).

Our serotonin- and psilocin-bound structures show monoolein directly interacting with S239^{5,43} and S242^{5,46} (S, serine), which have been proposed as key residues in serotonin, dopamine, and adrenergic receptor activation (23, 25, 26) (fig. S1B). This suggested that binding of monoolein at the SEP might activate 5-HT_{2A}R. Based on calcium flux and β -arrestin2 recruitment assays (see methods), we found monoolein to be a modest G protein partial agonist without detectable β -arrestin2 activity and found that the 5-HT_{2A}R selective antagonist MDL100907 can block monoolein's G protein partial agonism (Fig. 1C and fig. S1C). We also tested monoolein in orthogonal β -arrestin2 association and G_{q- γ} , G_{11- γ} , G_{12- γ} , G_{13- γ} , G_{15- γ} , and G_{2- γ} dissociation assays by bioluminescence resonance energy transfer (BRET) (23, 27), which confirmed G protein partial agonism and no agonist activity in β -arrestin2 association (fig. S1, D and E). Among the different G protein signaling pathways, monoolein most robustly induced G_{q- γ} , G_{11- γ} , and G_{15- γ} dissociation assays (fig. S1E).

We found that oleamide, oleyethanolamide (OEA), and 2-oleoyl glycerol (2OG) also activated 5-HT_{2A}R-mediated G protein signaling and not β -arrestin2 activity (Fig. 1D and fig. S2, A and B). Conversely, oleic acid and oleoyl-L- α -lysophosphatidic acid (LPA) did not activate 5-HT_{2A}R-mediated signaling (fig. S2A). The 5-HT_{2A}R selective antagonist MDL100907 blocked the G protein partial agonism of these lipids (fig. S2C).

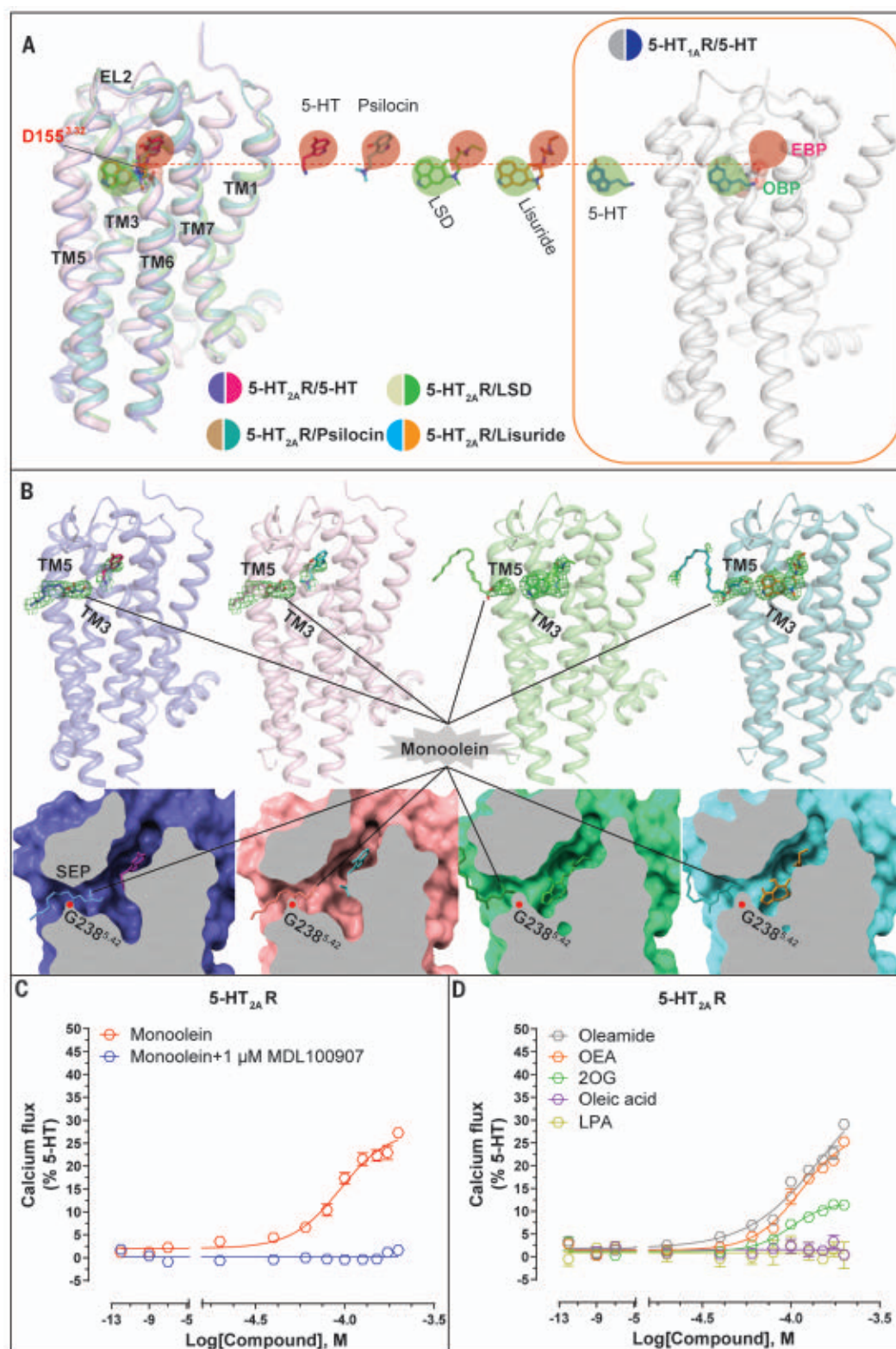
At position 5.42 (the key residue of OBP), a glycine residue is conserved only in the 5-HT₂ family among aminergic receptors (fig. S2D). This glycine allows the SEP to extend from

¹State Key Laboratory of Molecular Biology, Shanghai Institute of Biochemistry and Cell Biology, Center for Excellence in Molecular Cell Science, Chinese Academy of Sciences, University of Chinese Academy of Sciences, 320 Yueyang Road, Shanghai 200031, China. ²Human Institute, ShanghaiTech University, 393 Middle Huaxia Road, Shanghai 201210, China. ³Institute of Molecular Enzymology, School of Biology and Basic Medical Sciences, Soochow University, Suzhou, Jiangsu 215123, China. ⁴State Key Laboratory of Cell Biology, Shanghai Institute of Biochemistry and Cell Biology, Center for Excellence in Molecular Cell Science, Chinese Academy of Sciences, University of Chinese Academy of Sciences, 320 Yueyang Road, Shanghai 200031, China.

*Corresponding author. Email: chengji@shanghaitech.edu.cn (J.C.) and wangsheng@sibcb.ac.cn (S.W.)

†These authors contributed equally to this work.

Fig. 1. Lipid regulation of 5-HT_{2A}R. (A) Overall view of 5-HT_{2A}R in complex with 5-HT, psilocin, LSD, and lisuride structures. (B) The bound monoolein in the SEP of 5-HT_{2A}R. Monoolein and the ligands are shown as sticks with omit electron density maps (Fo-Fc omit map) at the contour level of 3.0 σ . (C) Monoolein is a G protein-mediated calcium flux partial agonist in 5-HT_{2A}R. (D) 5-HT_{2A}R G protein calcium flux activity by oleamide, OEA, and 2OG. In all panels, the Ballesteros-Weinstein numbering is shown as superscript. In (C) and (D), error bars represent SEM ($n = 3$).



the OBP (Fig. 1B). Other aminergic receptors have an alanine, serine, cysteine, or threonine at this position and the side chain blocks the cavity (22). Introducing a G238^{S42}S (G, glycine) substitution in 5-HT_{2A}R to mimic other 5-HT receptors abolished the agonist activity of the

lipids but not of serotonin (fig. S2E). 5-HT_{2B}R and 5-HT_{2C}R have the conserved glycine, but structures show that the side chain of F^{5.38} (F, phenylalanine) disrupts the SEP (21, 22) (fig. S2F). As expected, lipids did not induce robust G protein signaling at 5-HT_{2B}R or

5-HT_{2C}R, or at other 5-HT receptors, such as 5-HT₆R and 5-HT₇R, where the glycine is not conserved (fig. S2G). These results provide a structural basis for the long-standing observation that 5-HT_{2A}R signaling is modulated by lipids (11–14).

Serotonin and psilocin have a second binding mode at 5-HT_{2A}R

Unlike previous docking results (23), our crystal structures showed that the indole core of serotonin or psilocin fits into a narrow cleft previously described as the EBP (20, 28) that is lined mainly by hydrophobic side chains from residues in EL2 and transmembrane helices TM3, TM6, and TM7 (Fig. 2, A and B). Both ligands form a salt bridge between D155^{3.32} (D, aspartic acid) and the terminal basic nitrogen of the molecules as well as an extra hydrogen bond between N352^{6.55} (N, asparagine) and the hydroxyl group on the indole core. Mutagenesis of many of these contact residues to alanine reduced the affinity of serotonin and psilocin binding to 5-HT_{2A}R (table S2). We observed strong electron density at the top of OBP but no electron density at the bottom, which was previously shown to be the pocket of serotonin in 5-HT_{1A}R and 5-HT_{1D}R (24) (Fig. 1B and fig. S1A). However, alanine mutagenesis of residues at the bottom of the OBP that are implicated in serotonin binding in the 5-HT_{1A}R and 5-HT_{1D}R complex structures (24) also greatly affected serotonin and psilocin binding to 5-HT_{2A}R (table S2). A comparison of the previous published active 5-HT_{2A}R with our serotonin- and psilocin-bound 5-HT_{2A}R (23) shows that there is no obvious difference in the area of the actual ligand binding site (fig. S3, A and B). Thus, it appears that the alternative poses of serotonin and psilocin are compatible with the active state.

These findings suggested that serotonin and psilocin might adopt two different positions (OBP versus EBP) that could differentially affect receptor function. Accordingly, we mutated the key residues S239^{5.43} and S242^{5.46} for OBP, respectively, and W151^{3.28} and L362^{7.35} for EBP, respectively (W, tryptophan; L, leucine). Consistent with previous findings (22, 23), S239^{5.43}A and S242^{5.46}A (A, alanine) substitutions substantially diminished serotonin and psilocin's agonism (fig. S3, C and D) and binding affinity (table S2), indicating that both agonists occupy the bottom of the OBP. The substitution of W151^{3.28} or L362^{7.35} with phenylalanine or alanine, which we predicted would dampen hydrophobic contacts with the indole core of serotonin and psilocin in the second pose, also substantially decreased or abolished agonist activity. Because lisuride and LSD occupy the EBP and OBP, all mutants also dampened the efficacy of lisuride and LSD. Importantly, the L362^{7.35}F substitution did not affect the potency of the ligands' G_q agonism, but it abolished psilocin's and lisuride's β -arrestin association (fig. S3, C and D). In all mutants, 5-HT_{2A}R expression levels were comparable to that of the wild type (fig. S3E). These results indicate that ligand recognition in the EBP, specifically at L362^{7.35}, affects ligand bias.

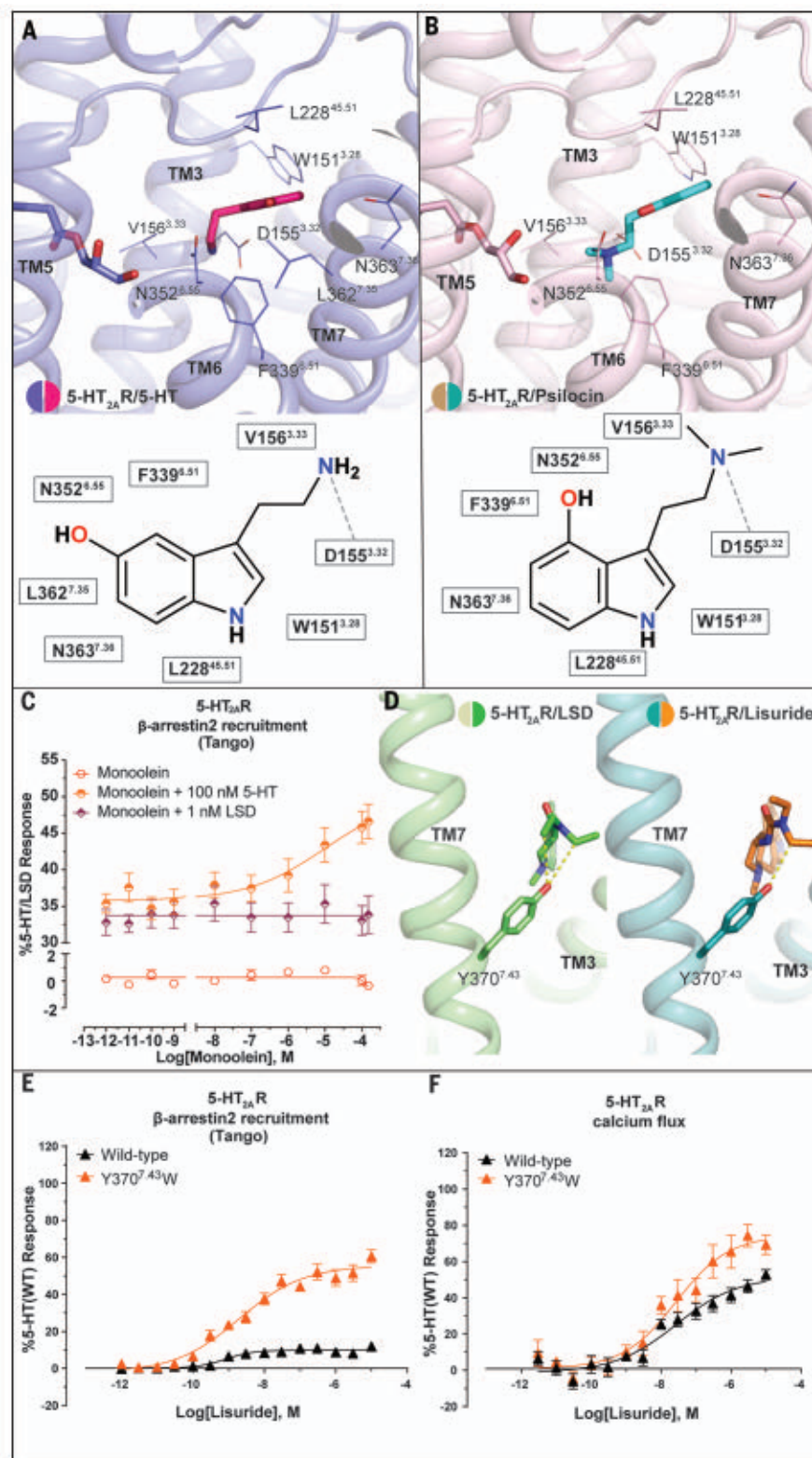
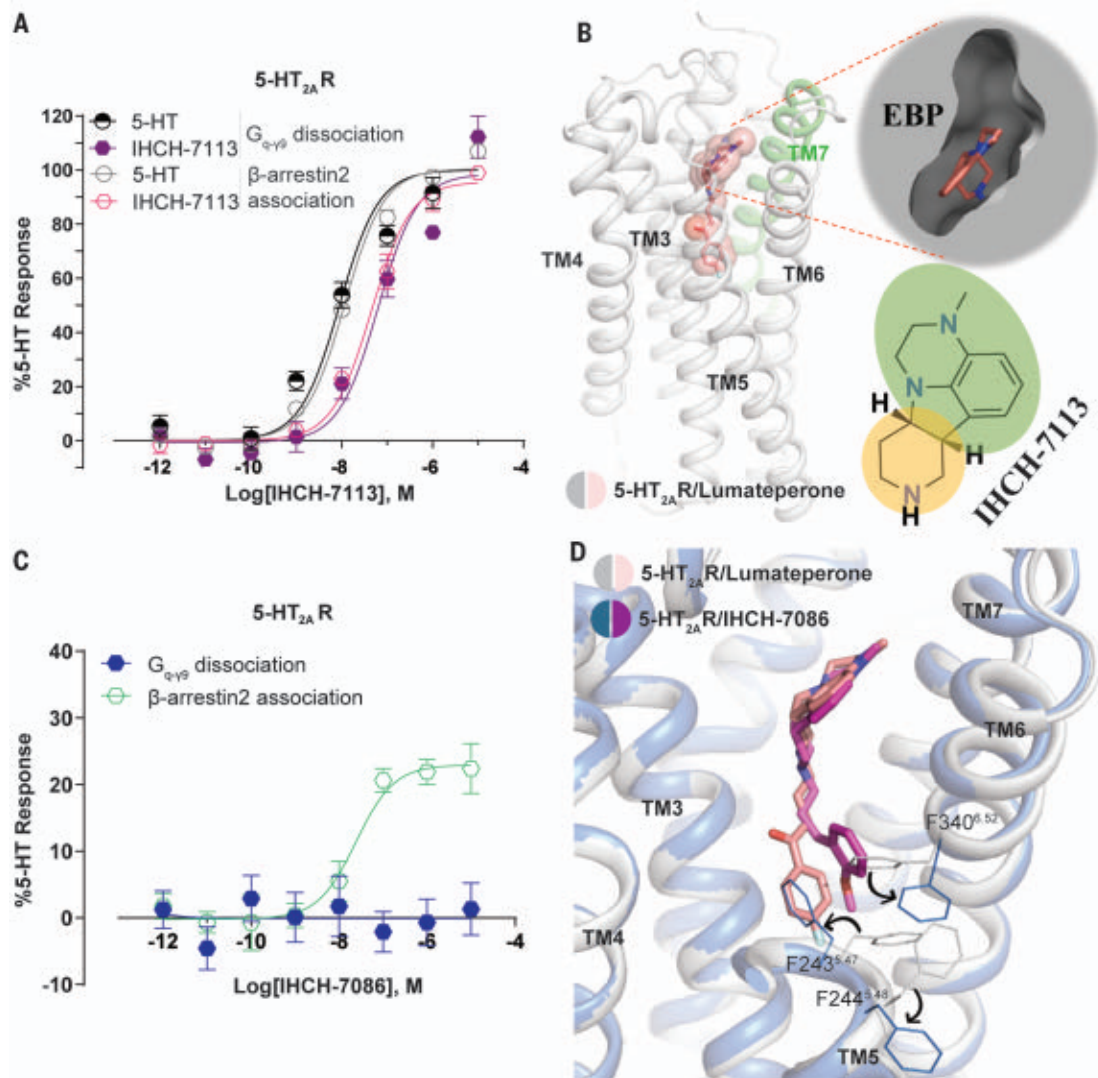


Fig. 2. EBP of 5-HT_{2A}R. (A and B) The second binding mode of 5-HT (A) and psilocin (B) with interaction residues at a 4.0-Å cut-off. Hydrogen bonds between D155^{3.32} and the 5-HT or psilocin basic nitrogen are shown by a dashed line. V, valine. (C) Monoolein is a positive allosteric modulator of 5-HT_{2A}R-mediated β -arrestin2 recruitment (as measured by the Tango assay). (D) Comparison of the binding poses between LSD and lisuride at 5-HT_{2A}R. The specific contacts between Y370^{7.43} and lisuride or LSD are shown with dashed lines. (E and F) Lisuride β -arrestin2 recruitment (E) and calcium flux (F) activity of the Y370^{7.43}W mutant (yellow) compared with wild-type 5-HT_{2A}R (black). In (C), (E), and (F), error bars represent SEM ($n = 3$).

Fig. 3. Structure-guided design of 5-HT_{2A}R β -arrestin-biased agonists.

(A) Normalized concentration-response studies for IHCH-7113 in 5-HT_{2A}R-mediated activation of G_{q-19} dissociation and β -arrestin2 association as measured by BRET. (B) The lumateperone-bound 5-HT_{2A}R complex structure highlights the potential binding pose of IHCH-7113 at the EBP. (C) Profiling of IHCH-7086 for ligand bias showing β -arrestin2 association partial agonist activity but no G_{q-19} dissociation activity (BRET assay). (D) Comparison of the binding poses between lumateperone and IHCH-7086 at 5-HT_{2A}R, showing IHCH-7086's 2-methoxyphenyl moiety wedged between TM5 and TM6. In (A) and (C), error bars represent SEM ($n = 3$).



We previously reported that differences in ligand recognition in the EBP, specifically at TM7, result in divergent effects on ligand bias at 5-HT_{2B}R, especially for β -arrestin signaling (19, 20). We hypothesized that the serotonin and psilocin binding pose that occupies the EBP in 5-HT_{2A}R would modulate β -arrestin signaling. We measured the β -arrestin2 recruitment activity caused by monoolein in the presence or absence of serotonin and found that monoolein can dose-dependently activate 5-HT_{2A}R-mediated β -arrestin signaling in the presence of serotonin in wild-type 5-HT_{2A}R but not in the G238^S mutant where binding of serotonin to the bottom of the OBP is inhibited (Fig. 2C and fig. S3F). In the absence of serotonin, monoolein only shows modest G protein partial agonism, without detectable β -arrestin activity (Fig. 1C and fig. S1C). By contrast, monoolein did not activate the 5-HT_{2A}R-mediated β -arrestin activity in the presence of LSD (Fig. 2C). These results are consistent with serotonin and psilocin adopting

a second binding pose in 5-HT_{2A}R and suggest that their interaction with EBP appears essential for monoolein-induced β -arrestin signaling.

To obtain further insight into the roles of the EBP in 5-HT_{2A}R-mediated β -arrestin2 recruitment, we solved the x-ray structures of the 5-HT_{2A}R-lisuride and 5-HT_{2A}R-LSD complexes to a resolution of 2.6 Å for both (table S1). The relatively high-resolution density maps of the two complexes allowed us to unambiguously assign the bound compounds and residues (Fig. 1B and fig. S1A). The overall structure of LSD-bound 5-HT_{2A}R is similar to the recently reported 3.4-Å structure (23), with root mean square deviation values of 0.81 Å for the C α atoms of the receptor (fig. S4, A and B). A ~1- to 2-Å shift in the binding mode of LSD in our structure compared with the previous structure (fig. S4, A and B) may be attributed to the structures' different resolutions. A comparison of the LSD- or lisuride-bound 5-HT_{2A}R with the same ligand-bound 5-HT_{2B}R structures also shows that the overall orientation is similar

(fig. S4, C to F). However, the binding mode of lisuride in 5-HT_{2A}R revealed a subtly different positioning of the (S)-diethylurea at the EBP of the receptor (fig. S4F).

We have previously shown that LSD's diethylamide, which is the key to LSD's potent hallucinogenic effects, contacts TM3 and TM7 within the EBP (19). Furthermore, we found that recognition of LSD in this region is stereoselective, because LSD's potent agonism was recapitulated only by the conformationally restricted (S,S)-azetidine stereoisomer. Surprisingly, in our 5-HT_{2A}R structure, the (S)-diethylurea of lisuride recapitulated the conformation of the diethylamide of LSD in the LSD-5-HT_{2A}R and LSD-5-HT_{2B}R complexes rather than the conformation of the (S)-diethylurea observed in the lisuride-5-HT_{2B}R complex (fig. S4, B, D, and F). This likely explains why lisuride is not an agonist of 5-HT_{2B}R but is an agonist of 5-HT_{2A}R (20).

Alignment of the 5-HT_{2A}R-LSD and 5-HT_{2A}R-lisuride structures further shows

that the two ethyl groups of LSD contact residue Y370^{7,43} (Y, tyrosine), which only interacts with one ethyl group of lisuride (Fig. 2D and fig. S4G). Consistent with the idea that the steric extrusion of Y370^{7,43} may cause a slight rotation of the diethyl group of lisuride in the EBP versus that of LSD (Fig. 2D and fig. S4G), we found that Y370^{7,43}W substitution strongly increases the efficacy of lisuride's β -arrestin2 recruitment agonism (Fig. 2E), despite similar surface expression levels relative to the wild-type receptor (fig. S3E). By contrast, it only slightly increases lisuride's G_q -mediated signaling efficacy (Fig. 2F). The Y370^{7,43}W mutation likely reduces LSD's efficacy in G_q -mediated signaling and β -arrestin2 recruitment because the Y370^{7,43} directly interacts with the two ethyl groups of LSD (fig. S4, H and I). Similar results were obtained by the orthogonal β -arrestin2 association and G_q - $\gamma 9$ dissociation BRET assays (fig. S4, J and K). We observed no substantial affinity changes of lisuride and LSD at the Y370^{7,43}W mutant relative to wild-type 5-HT_{2A}R (table S3). Taken together, our results show that LSD and lisuride occupy the OBP in a similar fashion yet exhibit different poses in the EBP. It appears that ligand engagement with TM7, especially with Y370^{7,43} in the EBP, leads to an auxiliary mechanism of 5-HT_{2A}R-mediated β -arrestin signaling activation.

Structure-oriented synthesis of arrestin-biased compounds

We posited that targeting the EBP may enhance β -arrestin recruitment at 5-HT_{2A}R, facilitating identification of β -arrestin-biased ligands. The recently solved 5-HT_{2A}R-risperidone and 5-HT_{2C}R-ritanserin crystal structures provide a starting point for identifying suitable chemotypes that engage the EBP (21, 22) (fig. S5A). The two 5-HT_{2A}R antagonists, risperidone and ritanserin, share the same deep binding pose at 5-HT₂ receptors, which is characterized by the fluorobenzisoxazol ring and 4-fluorophenyl group, respectively, occupying the hydrophobic deep binding pocket (21, 22, 28) (fig. S5A). The top site moiety of risperidone and ritanserin is located in the EBP and adopts a similar pose to the second binding pose of serotonin and psilocin (fig. S5, A and B). Our design strategy, therefore, was to identify rigid substructures that can target the EBP and mimic the second binding pose of serotonin and psilocin, without engaging the bottom hydrophobic deep binding pocket that is responsible for antagonist activity. Because atypical antipsychotics are also 5-HT_{2A}R antagonists and share a similar embedded 4-fluorophenyl group, we suspected that they may adopt the same deep binding pose at 5-HT_{2A}R. After analyzing all available 5-HT_{2A}R 4-fluorophenyl antipsychotics, we identified three rigid moieties that are possibly suit-

able for binding the EBP: IHCH-7113 (moiety from lumateperone), IHCH-7117 (moiety from spiperone), and IHCH-7125 (moiety from pimozide and benperidol), which we synthesized (fig. S5A). Of the three molecules tested, IHCH-7113 was a 5-HT_{2A}R agonist [inhibition constant (K_i) = 758.58 nM; Fig. 3A and table S5]. Interestingly, IHCH-7113 showed a weak preference for β -arrestin2 association over G_q signaling (bias factor = 1.52) relative to serotonin (Fig. 3A and table S5).

To explore whether the tetracyclic scaffold of IHCH-7113 occupied the EBP, we crystallized lumateperone in 5-HT_{2A}R and solved the 5-HT_{2A}R-lumateperone structure at 2.45-Å resolution (fig. S5, C and D, and table S1). Analysis of lumateperone's binding pose revealed that the tetracyclic core is oriented in the EBP and adopts a similar pose to the second binding pose of serotonin and psilocin (Fig. 3B and fig. S5, E and F). We validated lumateperone's binding pose by alanine mutagenesis of the contacting residues, most of which decreased lumateperone's affinity (table S4). Like the previously solved risperidone and ritanserin poses, lumateperone places the 4-fluorophenyl group in the deep hydrophobic binding pocket defined by the side chains of TM3, TM5, and TM7 (fig. S5D). The close contacts between the lumateperone's 4-fluorophenyl group and I163^{3,40} and F332^{6,44} (I, isoleucine) in the PIF (proline-isoleucine-phenylalanine) motif and the "toggle switch" W336^{6,48} (fig. S5D) apparently prevent the rearrangements required for receptor activation and potentially explain the antagonist activity of lumateperone at 5-HT_{2A}R.

To further test the hypothesis that the contact between the 4-fluorophenyl group of lumateperone determines its antagonist activity at 5-HT_{2A}R (29), we synthesized two analogs of lumateperone: IHCH-7112 and IHCH-7120, with the linker group shortened by one carbon in both cases and additional removal of the fluorine atom for IHCH-7120 to potentially attenuate the contact with the 4-fluorophenyl group. As expected, IHCH-7112 and IHCH-7120 were modest 5-HT_{2A}R agonists and were arrestin-biased by factors of 6.70 and 12.76, respectively (fig. S5G and table S5). In the previously solved 5-HT_{2A}R-25CN-NBOH structure, the 2-hydroxyphenyl moiety of the 25CN-NBOH agonist engages with TM3, TM6, and TM7 and avoids the conserved TM5 serine (S239^{5,43} and S242^{5,46}) in the SEP (fig. S6A). Inspired by this, we further modified the structure of IHCH-7112 by introducing 2-methoxy or 2-hydroxy substitutions on the terminal phenyl group and adjusting the length of the linker (fig. S6B). These analogs retain the major interactions of the tetracyclic scaffold with the EBP that determine arrestin bias, but their increased flexibility limits binding to the conserved TM5 serine in the SEP. With

respect to serotonin, all six hybrid analogs displayed a bias for β -arrestin-mediated signaling at 5-HT_{2A}R (Fig. 3C, fig. S6C, and table S5), with the most potent analogs being IHCH-7079 and IHCH-7086 (K_i = 16.98 and 12.59 nM, respectively) (Fig. 3C and fig. S6C). Unlike the nonselective agonists serotonin, psilocin, LSD, and lisuride, IHCH-7079 and IHCH-7086 prefer to bind 5-HT₂ receptors among the serotonin and dopamine receptors (table S6).

To obtain a better understanding of the ligand bias at 5-HT_{2A}R, we solved the crystal structures of 5-HT_{2A}R in complex with IHCH-7086, which showed β -arrestin-mediated signaling without detectable G_q activity (Fig. 3C and table S5). The structures were obtained at 2.5 Å (table S1). The electron density map for IHCH-7086 was well resolved (fig. S6D). The overall differences between the IHCH-7086- and lumateperone-bound 5-HT_{2A}R structures are relatively subtle, as predicted (Fig. 3D). The major difference is a rightward shift of the 2-methoxyphenyl moiety of IHCH-7086 versus the 4-fluorophenyl moiety of lumateperone (Fig. 3D). The 2-methoxyphenyl moiety of IHCH-7086, avoiding the PIF motif, drives close to F243^{5,47}, F244^{5,48}, and F340^{6,52}, consequently relocating three phenylalanines, which may explain the agonist activity of IHCH-7086 (Fig. 3D and figs. S5F and S6E). We also validated IHCH-7086's binding pose by alanine mutagenesis of contacting residues, most of which decreased IHCH-7086's affinity (table S4 and fig. S6F). As mentioned above, monoonleuin, which contacts the conserved TM5 serine (S239^{5,43} and S242^{5,46}) related to the SEP, only shows modest G protein partial agonism, without detectable β -arrestin activity (Fig. 1C and fig. S1C). Finally, the 2-methoxyphenyl moiety does not interact with the conserved TM5 serine, which potentially explains the nondetectable G protein activity of IHCH-7086 at 5-HT_{2A}R (fig. S6F).

Effects of 5HT_{2A}R-mediated signaling on hallucination and antidepressant-like behavior

A century of research has demonstrated that the affinities of psychedelics for 5-HT_{2A}R strongly correlate with their psychoactive potencies (30, 31). Animal behavioral models cannot precisely capture the perturbations of perception, cognition, and mood produced by psychedelics in humans. However, studies have demonstrated that the mouse head twitch response (HTR) strongly correlates with the production of psychedelic-induced hallucinations in humans (3). Lisuride lacks comparable psychoactive properties in humans and also fails to induce the HTR in mice (32, 33). Previously, genetic deletion of β -arrestin2 was found to decrease responsiveness to L-5-hydroxytryptophan and LSD-induced HTR (34, 35). However, 2,5-dimethoxy-4-iodoamphetamine hydrochloride

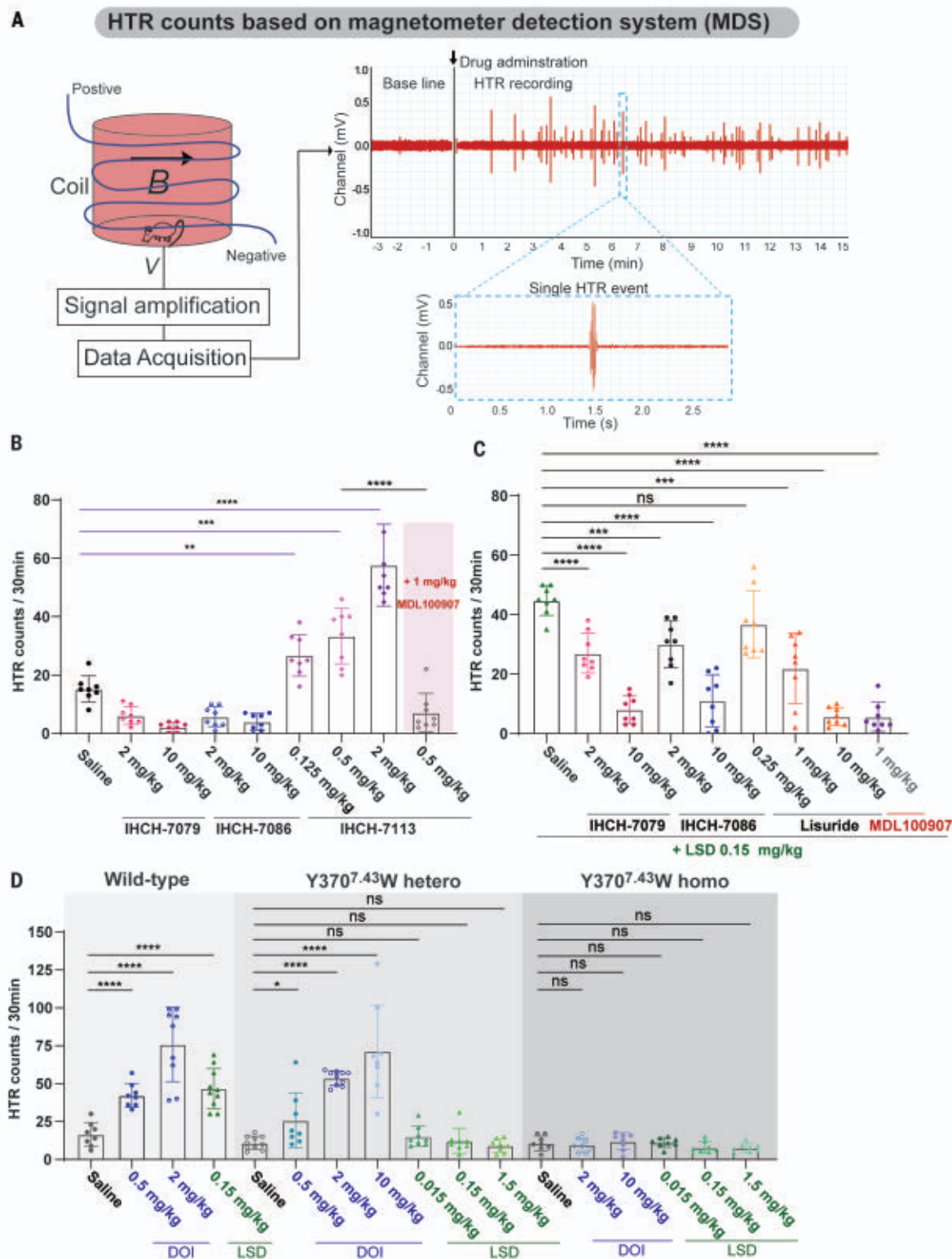


Fig. 4. Effects of the designed 5-HT_{2A}R agonists on animal behavior relevant to hallucination. (A) Scheme of the automated HTR detection system. A small magnet, surgically implanted on the mouse skull surface, produces an electrical signal of greater amplitude than background noise when the mouse displays an HTR. The signal is amplified and transduced by a data acquisition system. (B) IHCH-7113, not IHCH-7079 or IHCH-7086, induces a dose-dependent HTR in mice that is blocked by 5-HT_{2A}R selective antagonist MDL100907 (30- to 60-min

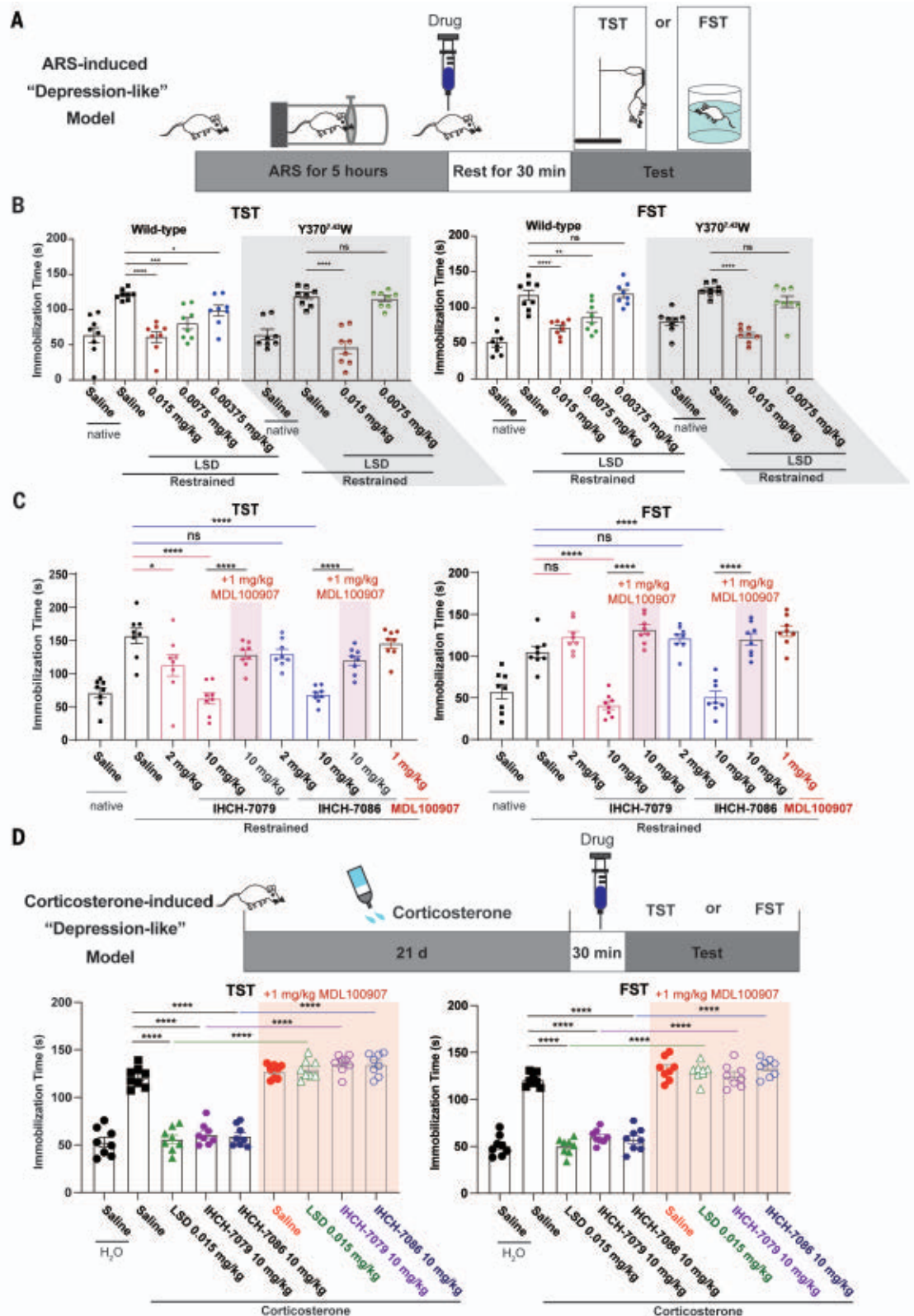
time interval; see related fig. S8, E to G). (C) LSD-induced HTR is blocked by IHCH-7079, IHCH-7086, Lisuride, and MDL100907 (60- to 90-min time interval; see related fig. S8H). (D) Effect of LSD and DOI on HTR behavior in 5-HT_{2A}R wild-type, Y370^{7.43}W-heterozygous, and Y370^{7.43}W-homozygous mice (0- to 30-min time interval; see related fig. S9). In (B) to (D), error bars represent SEM ($n = 8$ to 10 C57/BL6J or B6D2F1 mice). ns is not significant, * $P < 0.05$, ** $P < 0.01$, *** $P < 0.001$, and **** $P < 0.0001$ (two-tailed unpaired Student's t test).

Fig. 5. The antidepressant effects of the designed 5-HT_{2A}R agonists on animal behavior relevant to depression. (A) Scheme of the ARS-induced depression-like model.

(B) Effects of LSD on freezing behavior in ARS-induced depression-like mice in 5-HT_{2A}R wild-type and Y370^{Δ3W}-homozygous mice.

(C) Effects of IHCH-7086 and IHCH-7079 on freezing behavior in ARS-induced depression-like mice that are blocked by MDL100907.

(D) Scheme of corticosterone-induced depression-like model. Effects of LSD, IHCH-7079, and IHCH-7086 on freezing behavior in corticosterone-induced depression-like mice that are blocked by MDL100907. The freezing behavior of mice was tested by the TST and FST. In (B) to (D), error bars represent SEM ($n = 8$ C57/BL6J or B6D2F1 mice). ns is not significant, * $P < 0.05$, ** $P < 0.01$, *** $P < 0.001$, and **** $P < 0.0001$ (two-tailed unpaired Student's t test).



(DOI), another commonly used psychedelic that shows greatly attenuated HTR in G_q knock-out mice (36), produced an HTR of equal magnitude in wild-type and β -arrestin2 knockout mice (37).

To test what intracellular signaling is required for the effects of psychedelics, we studied psychedelics (LSD, DOI, and psilocin), the nonhallucinogenic psychedelic analog (lisuride), and 5-HT_{2A}R arrestin-bias ligands (IHCH-

7113, IHCH-7079, and IHCH-7086) for their ability to induce HTR in mice as detected by a fully automated magnetometer-based detection system (MDS) (Fig. 4A). As expected, the psychedelics (LSD, DOI, and psilocin), but not

lisuride, induced a significant HTR in mice (figs. S7A and S8, A to D). To our surprise, IHCH-7079 and IHCH-7086 failed to produce any HTR, even at doses as high as 10 mg/kg, unlike IHCH-7113, which produced HTR at doses as low as 0.125 mg/kg (Fig. 4B and fig. S8, E to G). However, the IHCH-7113-induced HTR was abolished by the 5-HT_{2A}R selective antagonist MDL100907. In mouse pharmacokinetic studies, IHCH-7113, IHCH-7079, and IHCH-7086 showed a reasonable half-life and excellent brain penetration properties (fig. S7B). Furthermore, LSD-induced HTR was not only abolished by the 5-HT_{2A}R selective antagonist MDL100907 but was also abolished by the nonhallucinogenic psychedelic analogs lisuride, IHCH-7079, and IHCH-7086 (Fig. 4C and fig. S8H).

Next, we analyzed the transduction efficiency of hallucinogenic psychedelics (DOI, LSD, psilocin, and IHCH-7113) and their nonhallucinogenic analogs (lisuride, IHCH-7079, and IHCH-7086) in G protein signaling and β -arrestin association at 5-HT_{2A}R by summarizing their relative $\log(\tau/K_A)$ values in a heat map (figs. S7C and S9) (τ , the efficacy of the agonist in the given pathway; K_A , the functional dissociation constant for the agonist). All tested psychedelics exhibited higher relative $\log(\tau/K_A)$ values than nonhallucinogenic analogs (fig. S7C). The above-mentioned data showed that the Y370^{7.43}W mutation significantly reduced LSD's transduction efficiency for both β -arrestin recruitment and G protein signaling (fig. S4, H to J). Similar effects were observed for LSD and DOI activity on the mouse wild-type 5-HT_{2A}R and its Y370^{7.43}W mutation (fig. S7D). In Y370^{7.43}W mutant heterozygous mice, DOI induced HTR but LSD did not, whereas in homozygous mice, neither induced HTR (Fig. 4D and fig. S10). No significant differences were observed for 5-HT_{2A}R expression between wild-type and Y370^{7.43}W littermates (fig. S7E). These data suggest that the psychoactive effects of psychedelics require a high transduction efficiency in 5-HT_{2A}R-mediated signaling.

Hallucinogens like psilocybin and LSD have been described to have potential therapeutic effects for depression (2). As shown in fig. S7F, acute administration of LSD [0.0075 and 0.015 mg/kg intraperitoneally (ip)] significantly attenuated acute restraint stress (ARS)-induced "depression-like" freezing behavior in the forced swimming test (FST) and tail suspension test (TST) (Fig. 5A). We further validated that acute administration of LSD (0.015 mg/kg ip) had antidepressant effects on 5-HT_{2A}R Y370^{7.43}W mutant mice in the ARS-induced depression-like model (Fig. 5B). Given that there is no HTR activity induced by 0.015 mg/kg LSD in wild-type mice (fig. S7A) or 5-HT_{2A}R Y370^{7.43}W mutant mice (Fig. 4D), it seems that the hallucinogenic effect may not be required for the antidepressant-like effect of LSD, consistent

with a clinical trial of its microdose usage as an antidepressant (2). Because lisuride, IHCH-7079, and IHCH-7086 are not predicted to produce hallucinations (Fig. 4A and fig. S7A), we were interested in assessing their antidepressant potential in vivo. As shown in Fig. 5C and fig. S7F, acute administration of lisuride, IHCH-7079, and IHCH-7086 also significantly attenuated ARS-induced depression-like freezing behavior in the FST and TST, and the antidepressant-like effect of IHCH-7079 and IHCH-7086 was abolished by the 5-HT_{2A}R selective antagonist MDL100907 (Fig. 5C). To further validate the antidepressant-like effect of IHCH-7079 and IHCH-7086, C57BL/6J mice were subjected to the corticosterone-induced animal model of depression (38) and then tested in the FST and TST. As expected, mice treated with corticosterone for 21 days showed an increase in immobility compared with vehicle treatment (Fig. 5D). Similar to LSD, IHCH-7079 and IHCH-7086 also reduced immobility in corticosterone-treated mice, and the effects were abolished by MDL100907 (Fig. 5D). These data suggest that the low efficacy of 5-HT_{2A}R arrestin-biased agonists such as IHCH-7079 and IHCH-7086 may be sufficient for antidepressant effects.

Discussion

By leveraging six new 5-HT_{2A}R crystal structures, we have been able to reveal the structural basis of the lipid activation on 5-HT_{2A}R and also uncover a second binding mode for serotonin and psilocin, thereby enabling structure-based design of β -arrestin-biased ligands. Although the precise mechanisms of action of psychedelics remain largely unclear, 5-HT_{2A}R agonism is essential for their psychedelic effects in humans (2, 3). We find that although the β -arrestin activity of 5-HT_{2A}R agonists plays a key role in their antidepressant effects and that the activity correlates with the agonists contacting TM7 residues of the EBP, this β -arrestin activity is insufficient for inducing psychoactive actions. Previous studies in humans reported that a 50 to 70% 5-HT_{2A}R occupancy level was required for an intense psilocybin-induced psychological experience (39). Indeed, it seems that the hallucinogenic effect requires high transduction efficiency of 5-HT_{2A}R agonists at both G protein-mediated signaling and β -arrestin recruitment. By contrast, the low transduction efficiency of 5-HT_{2A}R β -arrestin-biased agonists with no hallucinogenic effects may be sufficient to achieve the antidepressant effects. Finally, given recent successes in leveraging crystal structures of G protein-coupled receptors for ligand discovery, we anticipate that the reported structures herein will accelerate the search for new psychedelics and nonhallucinogenic psychedelic analogs for treatment of neuropsychiatric diseases.

REFERENCES AND NOTES

1. M. Berger, J. A. Gray, B. L. Roth, *Annu. Rev. Med.* **60**, 355–366 (2009).
2. D. Nutt, D. Erritzoe, R. Carhart-Harris, *Cell* **181**, 24–28 (2020).
3. D. E. Nichols, *Pharmacol. Rev.* **68**, 264–355 (2016).
4. A. S. A. T. Shulgin, *PIHKAL: A Chemical Love Story* (Transform Press 1991).
5. A. S. A. T. Shulgin, *TIHKAL: The Continuation* (Transform Press 1997).
6. C. M. Reiff et al., *Am. J. Psychiatry* **177**, 391–410 (2020).
7. R. Carhart-Harris et al., *N. Engl. J. Med.* **384**, 1402–1411 (2021).
8. S. Ross et al., *J. Psychopharmacol.* **30**, 1165–1180 (2016).
9. R. L. Carhart-Harris et al., *Psychopharmacology* **235**, 399–408 (2018).
10. R. R. Griffiths et al., *J. Psychopharmacol.* **30**, 1181–1197 (2016).
11. J. P. Huidobro-Toro, R. A. Harris, *Proc. Natl. Acad. Sci. U.S.A.* **93**, 8078–8082 (1996).
12. E. A. Thomas, M. J. Carson, M. J. Neal, J. G. Sutcliffe, *Proc. Natl. Acad. Sci. U.S.A.* **94**, 14115–14119 (1997).
13. D. L. Boger, J. E. Patterson, Q. Jin, *Proc. Natl. Acad. Sci. U.S.A.* **95**, 4102–4107 (1998).
14. W. B. Mendelson, A. S. Basile, *Neuropsychopharmacology* **25**, S36–S39 (2001).
15. L. P. Cameron et al., *Nature* **589**, 474–479 (2021).
16. C. Dong et al., *Cell* **184**, 2779–2792.e18 (2021).
17. C. Wang et al., *Science* **340**, 610–614 (2013).
18. D. Wacker et al., *Science* **340**, 615–619 (2013).
19. D. Wacker et al., *Cell* **168**, 377–389.e12 (2017).
20. J. D. McCorry et al., *Nat. Struct. Mol. Biol.* **25**, 787–796 (2018).
21. Y. Peng et al., *Cell* **172**, 719–730.e14 (2018).
22. K. T. Kimura et al., *Nat. Struct. Mol. Biol.* **26**, 121–128 (2019).
23. K. Kim et al., *Cell* **182**, 1574–1588.e19 (2020).
24. P. Xu et al., *Nature* **592**, 469–473 (2021).
25. Y. Zhuang et al., *Cell* **184**, 931–942.e18 (2021).
26. R. O. Dror et al., *Proc. Natl. Acad. Sci. U.S.A.* **108**, 18684–18689 (2011).
27. R. H. J. Olsen et al., *Nat. Chem. Biol.* **16**, 841–849 (2020).
28. S. Wang et al., *Nature* **555**, 269–273 (2018).
29. K. E. Vanover et al., *Neuropsychopharmacology* **44**, 598–605 (2019).
30. R. A. Glennon, M. Titeler, J. D. McKenney, *Life Sci.* **35**, 2505–2511 (1984).
31. B. Sadzot et al., *Psychopharmacology* **98**, 495–499 (1989).
32. J. González-Maeso et al., *Neuron* **53**, 439–452 (2007).
33. J. González-Maeso et al., *J. Neurosci.* **23**, 8836–8843 (2003).
34. C. L. Schmid, L. M. Bohn, *J. Neurosci.* **30**, 13513–13524 (2010).
35. R. M. Rodríguez, V. Nadkarni, C. R. Means, Y.-T. Chiu, B. L. Roth, W. C. Wetsel, *bioRxiv* 2021.02.04.429772 [Preprint] (2021); <https://doi.org/10.1101/2021.02.04.429772>.
36. E. E. Garcia, R. L. Smith, E. Sanders-Bush, *Neuropharmacology* **52**, 1671–1677 (2007).
37. C. L. Schmid, K. M. Raehal, L. M. Bohn, *Proc. Natl. Acad. Sci. U.S.A.* **105**, 1079–1084 (2008).
38. S. L. Gourley, J. R. Taylor, *Curr. Protoc. Neurosci.* **49**, 9.32.1–9.32.11 (2009).
39. M. K. Madsen et al., *Neuropsychopharmacology* **44**, 1328–1334 (2019).

ACKNOWLEDGMENTS

The diffraction data were collected at the BL45XU of SPring-8 (JASRI proposals 2021A2746 and 2020A2605). We thank K. Hirata, Y. Nakamura, and K. Hasegawa for their help with data collection. The psilocin and LSD involved in this paper were provided by the drug reference materials laboratory of the Third Research Institute of the Ministry of Public Security (China). **Funding:** This work was funded by Ministry of Science and Technology of China grant 2020YFA0509102 (S.W.); National Natural Science Foundation of China grant 32071197 (S.W.); Strategic Priority Research Program of the Chinese Academy of Sciences grant XDB19020111 (S.W.); Shanghai Science and Technology Committee grant 19ZR1466200 (S.W.); Thousand Talents Plan-Youth (S.W.); Shanghai Rising-Star Program grant 20QA140600 (S.W.); National Natural Science Foundation of China grants 22177074 and 81703361 (J.C.); Shanghai Science and Technology Committee grant 20S11901200 (J.C.); and Shanghai Municipal Government and ShanghaiTech University (J.C.). **Author contributions:** Conceptualization: S.W., J.C., D.C.; Methodology: D.C., J.Y., H.W., Z.L., X.L., L.H., J.Q., L.F., L.T., Z.C.; Investigation: D.C., J.Y., H.W., Z.L., S.W.; Funding acquisition: S.W., J.C.; Project administration: S.W., J.C., J.L.; Supervision: S.W., J.C.; Writing – original draft: S.W.; Writing – review and editing: S.W., J.C., J.L., D.C. **Competing interests:** The authors declare that they have no competing interests. **Data and materials availability:** The data presented in this paper are

tabulated in the main paper and in the supplementary materials. Coordinates and structure factors for the 5-HT_{2A}R complexes with serotonin, psilocin, LSD, lisuride, lumateperone, and IHCH-7086 ligands are deposited in the Protein Data Bank under accession codes 7WC4, 7WC5, 7WC6, 7WC7, 7WC8, and 7WC9, respectively. All materials are available upon request.

SUPPLEMENTARY MATERIALS

science.org/doi/10.1126/science.abl8615
Materials and Methods
Supplementary Text
Figs. S1 to S10
Tables S1 to S7

References (40–49)
MDAR Reproducibility Checklist

10 August 2021; accepted 21 December 2021
10.1126/science.abl8615

PROTEOMICS

The Blood Proteoform Atlas: A reference map of proteoforms in human hematopoietic cells

Rafael D. Melani^{1†}, Vincent R. Gerbasi^{1†}, Lissa C. Anderson^{2†}, Jacek W. Sikora¹, Timothy K. Toby¹, Josiah E. Hutton¹, David S. Butcher², Fernanda Negrão¹, Henrique S. Seckler¹, Kristina Szrentic¹, Luca Fornelli¹, Jeannie M. Camarillo¹, Richard D. LeDuc¹, Anthony J. Cesnik^{3,4}, Emma Lundberg^{3,4}, Joseph B. Greer¹, Ryan T. Fellers¹, Matthew T. Robey¹, Caroline J. DeHart¹, Eleonora Forte^{5,6}, Christopher L. Hendrickson², Susan E. Abbatiello⁷, Paul M. Thomas¹, Andy I. Kokaji⁸, Josh Levitsky^{9*}, Neil L. Kelleher^{1,10*}

Human biology is tightly linked to proteins, yet most measurements do not precisely determine alternatively spliced sequences or posttranslational modifications. Here, we present the primary structures of ~30,000 unique proteoforms, nearly 10 times more than in previous studies, expressed from 1690 human genes across 21 cell types and plasma from human blood and bone marrow. The results, compiled in the Blood Proteoform Atlas (BPA), indicate that proteoforms better describe protein-level biology and are more specific indicators of differentiation than their corresponding proteins, which are more broadly expressed across cell types. We demonstrate the potential for clinical application, by interrogating the BPA in the context of liver transplantation and identifying cell and proteoform signatures that distinguish normal graft function from acute rejection and other causes of graft dysfunction.

Human biology is tightly linked to proteins, and mass spectrometry-based proteomics has established a strong linkage between phenotype and protein-level biology (1, 2). Notable efforts for the compositional mapping of proteins include two drafts of the human proteome in 2014 (3, 4); the Human Protein Atlas, with various tissue- and cell-specific resources available (5, 6); and the recent release of the Human Blood Atlas (HBA), with transcriptomic data from 18 cell types (7). However, these datasets do not capture posttranscriptional and post-translational processing or how mRNA splicing combines with modifications to create protein-level diversity. Measurement of proteoforms (8) can close these gaps by capturing the complete molecular composition of proteins, refining phenotypic correlations. Furthermore, a reference map of experimentally identified proteoforms would serve as a reference for next-generation technologies, including single-cell proteomics (9, 10).

Protein isoforms vary by cell type (11, 12). With the growth in cell atlas projects, includ-

ing the Human Biomolecular Atlas Program (HuBMAP) (13), the Human Cell Atlas (5), and others (6, 7), conditions are set for cell-based proteomics. Determination of protein composition in specific cell types using bottom-up proteomics has been accomplished in different studies (3, 14, 15). In this study, we used top-down proteomics (TDP) (16), which avoids the problem of inferring proteins using peptide data from shotgun proteomics analysis (17), to obtain cell- and proteoform-specific information (18) from the major cell types present in the blood and bone marrow. In the past decade, TDP has gained momentum, but limitations in protein separation and coverage of large proteoforms (>30 kDa) are still present (19). In this work, we employed negative or positive cell selection using specific antibodies to cell surface markers and fluorescence-activated cell sorting (FACS) to isolate cells of interest that were then analyzed for their proteoform content (table S1). In characterizing proteoforms across hematopoietic cell ontogeny, we took a three-pronged approach to protein fractionation, depending on cell numbers available (Fig. 1A).

Proteins and proteoforms

Table 1 captures a total of 29,620 nonredundant proteoforms and 1690 proteins (i.e., specific genes assigned from proteoform spectral matches) across 21 different human hematopoietic cell types and plasma. Many proteoforms discovered have posttranslational modifications; lysine acetylation (32.9%) and C- and N-terminal cleavage (30.6%) are the two most common, with coding polymorphisms (7.6%) or alternative splicing (3.8%) being minority occurrences (fig. S1 and table S2). The number of experimentally determined proteoforms exceeded that of previous reports by ~10-fold (16) and were identified in a dataset comprising 1553 liquid chromatography tandem mass spectrometry (LC-MS/MS) runs performed on Fourier transform (FT) mass spectrometers. In total, 4,042,173 database searches required ~9 days to complete, with a consistent proportion (34%) of them yielding a hit using a conservative 1% global false discovery rate (FDR) at the protein and proteoform levels (20) (see materials and methods section of the supplementary materials). Sample preparation required a total of ~1600 hours for all studies, and acquisition of mass spectra required ~3660 hours. Total proteoforms discovered from each category of cells throughout hematopoiesis are indicated in Fig. 1B and are interactively viewable at <http://blood-proteoform-atlas.org/>. Proteoform identifiers (PFRs) are cross-referenced to gene-specific accessions in UniProtKB/Swiss-Prot and linked to 19,670 transcripts in the HBA (7). For the BPA, the average number of proteoforms arising from each “protein” (i.e., proteoform hits mapped back to their corresponding human gene) was 17.5. Despite the accelerating pace of development for TDP, most identified proteoforms (~93%) are <20 kDa, even analyzing GELFrEE fractions containing proteins up to 50 kDa.

Confident assignment of isoforms from RNA splicing

From the HBA, we generated a proteogenomic database with 50,177 protein sequences, corresponding to 95,979 transcripts reconstructed

¹Department of Molecular Biosciences, Department of Chemistry, and the Feinberg School of Medicine, Northwestern University, Evanston, IL, USA. ²National High Magnetic Field Laboratory, Florida State University, Tallahassee, FL, USA. ³Department of Genetics, Stanford University, Stanford, CA, USA. ⁴Science for Life Laboratory, School of Engineering Sciences in Chemistry, Biotechnology and Health, KTH—Royal Institute of Technology, Stockholm, Sweden. ⁵Proteomics Center of Excellence, Northwestern University, Evanston, IL, USA. ⁶Department of Surgery, Feinberg School of Medicine, Northwestern University, Chicago, IL, USA. ⁷Thermo Fisher Scientific, Cambridge, MA, USA. ⁸STEMCELL Technologies Inc., Vancouver, BC, Canada. ⁹Comprehensive Transplant Center, Feinberg School of Medicine, Northwestern University, Chicago, IL, USA. ¹⁰Department of Biochemistry and Molecular Genetics, Feinberg School of Medicine, Northwestern University, Chicago, IL, USA.

*Corresponding author. Email: n-kelleher@northwestern.edu (N.L.K.); j-levitsky@northwestern.edu (J.L.)

†These authors contributed equally to this work.

from RNA sequencing (RNA-seq) data for 19 cell types (table S3) (7). Searching 12 cell types shared between the BPA and the HBA, we identified slightly fewer proteins and proteoforms using the HBA database search (801 proteins and 4344 proteoforms; table S4) than with the human UniProtKB/Swiss-Prot database (887 proteins and 4993 proteoforms; table S5). Most proteoforms observed with the HBA database were shared with the UniProtKB/Swiss-Prot database (82.7%), while 2.2% (114)

of proteoforms were only in the HBA database (fig. S2), and of these, 49 (0.96%) represented newly identified proteoforms that are confidently assigned to being derived from transcript isoform or sequence variation (table S6). These results indicate that RNA splicing produces only a handful of new detectable proteoforms <30 kDa, which are expressed from an average of just four introns. However, a few abundant isoforms are missed without cell type-specific RNA splicing information.

Protein-resolved versus proteoform-resolved maps of hematopoietic cell types

Deep TDP of cell populations results in high-dimensional data containing cell type and proteoform identifications (e.g., PFR1033, which maps to the gene-specific accession P62805 in UniProtKB/Swiss-Prot for histone H4). We compared protein- versus proteoform-level data in t-distributed stochastic neighbor embedding (t-SNE) plots (Fig. 2, A and B), accumulation curves (Fig. 2, C and D), and

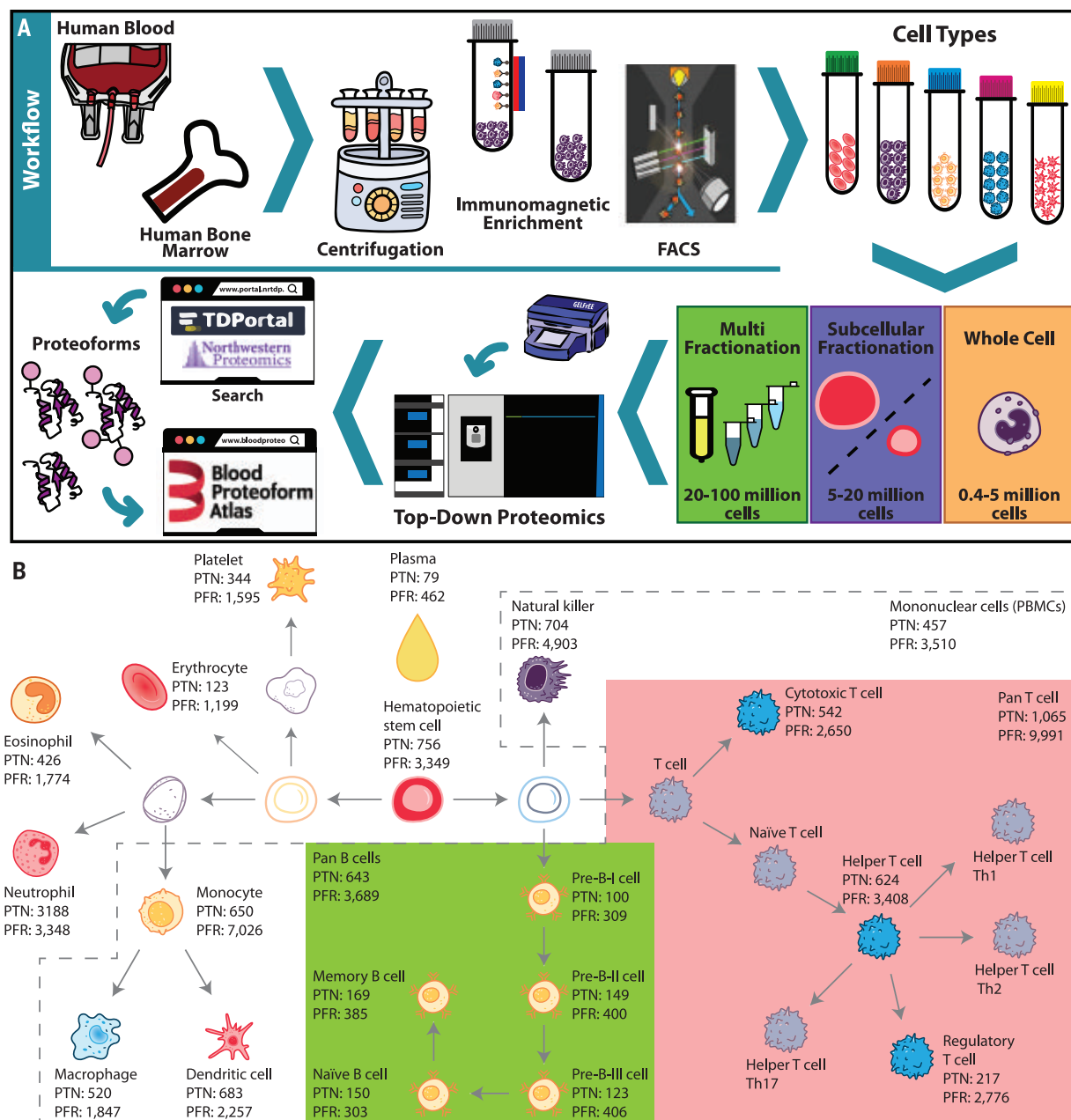


Fig. 1. Workflow and number of identified proteoforms in the Blood Proteoform Atlas. (A) Human blood or bone marrow samples were subjected to centrifugation, immunomagnetic enrichment, and/or FACS. Cell types were submitted to whole-cell, subcellular, and/or protein fractionation on the basis of the obtained cell amounts, followed by systematic proteoform discovery.

Proteoforms were identified using a database search against the human proteome and deposited in the Blood Proteoform Atlas (BPA) website. **(B)** A map of hematopoiesis shows the number of proteoforms identified in each cell type. Certain cell groups (pan B cells, green; pan T cells, pink; and PBMCs, dashed gray lines) were also analyzed in pools. PTN, proteins; PFR, proteoforms.

heatmaps after hierarchical clustering (Fig. 2E). Both protein and proteoform data clustered differentiated cell types along primary branches of hematopoiesis at the same level of confidence upon t-SNE analysis. The cluster of antigen-presenting cells (monocytes, macrophages, and dendritic cells) was separated from lymphoid lineage cells [T cells, B cells, and natural killer (NK) cells]. Additionally, the lymphoid lineage clustered together, and the three pre-B cell types from bone marrow formed a distinct cluster (Fig. 2, A and B).

Cell relatedness at the protein versus proteoform levels

To probe the specificity of proteins versus proteoforms, we compared their incidence frequency across all cell types studied. The

histogram in Fig. 2C shows that most proteins are shared between two or more cell types (81%). In contrast, the majority of proteoforms (58%) were identified in only one cell type (Fig. 2D), which shows that uniqueness is significantly more pronounced with proteoform-level information [$\chi^2(21) = 0.519$, $P = 4.73 \times 10^{-14}$]. Figure 2E shows the heatmap for all proteins and proteoforms identified. The high number of unique proteoforms per cell type is evident, and the clustering distance for proteoforms is one order of magnitude higher than for proteins. The average number of cell types in which a proteoform was found was 2.19, whereas for proteins it was 6.51. The mean number of identified nonredundant proteoforms per cell type was 1346, compared with only 76 for proteins (more statistical measures

are presented in table S7). These results indicate that proteoforms are better markers of a cell type than monitoring gene expression using just protein-level assignments.

Depth of proteome coverage

The BPA currently provides 8.3% coverage (fig. S3) of the total human proteome (20,395 genes) and 16% of the predicted proteome <30 kDa in UniProtKB/Swiss-Prot. However, the accumulation curve for proteins shows that ~80% of possible protein identifications (fig. S3) were made from the analyzed cell types using current workflows. In contrast, the collector's curve for proteoforms did not reach a plateau (fig. S3), with just ~37% of projected proteoforms identified. This modeling indicates that saturation of primary hematopoietic cells

Table 1. Proteins and proteoforms identified across 21 human cell types and plasma, aggregated in redundant and nonredundant fashion. Analysis methods used: Nuc/Cyt, nuclear and cytosolic fractions were analyzed individually; WC, whole-cell lysate; IEX, ion exchange used before the GELFrEE-LC-MS/MS; PM, ProteoMiner equalized cell lysates.

| Cell type | Analysis method | LC-MS/MS runs | Proteins 1% FDR | Unique proteins 1% FDR | Proteoforms 1% FDR (C-score > 30) | Unique proteoforms 1% FDR |
|--------------------------|-----------------|---------------|--------------------|---------------------------|--------------------------------------|------------------------------|
| Hematopoietic stem cell* | Nuc/Cyt | 57 | 756 | 16 | 3,349 (2,520) | 596 |
| PBMC | WC | 112 | 457 | 27 | 3,510 (2,618) | 1,507 |
| | IEX | | | | | |
| Pan T cell | IEX | 367 | 1,065 | 116 | 9,991 (5,839) | 4,163 |
| | WC | | | | | |
| Cytotoxic T cell | Nuc/Cyt | 68 | 542 | 2 | 2,650 (963) | 436 |
| | WC | | | | | |
| Helper T cell | Nuc/Cyt | 89 | 624 | 2 | 3,408 (1,319) | 617 |
| | WC | | | | | |
| Regulatory T cell | Nuc/Cyt | 58 | 217 | 0 | 2,776 (477) | 899 |
| | WC | | | | | |
| Pan B cell | Nuc/Cyt | 118 | 643 | 8 | 3,689 (1,653) | 745 |
| | WC | | | | | |
| Pan B cell* | WC | 12 | 334 | 1 | 1,225 (602) | 111 |
| Pre-B-I cell* | WC | 4 | 100 | 0 | 309 (253) | 13 |
| Pre-B-II cell* | WC | 4 | 149 | 0 | 400 (323) | 26 |
| Pre-B-III immature cell* | WC | 4 | 123 | 3 | 406 (334) | 33 |
| Naïve B cell | WC | 5 | 150 | 0 | 303 (176) | 19 |
| Memory B cell | WC | 5 | 169 | 0 | 385 (208) | 20 |
| Natural killer cell | Nuc/Cyt | 98 | 704 | 25 | 4,903 (1,859) | 1,123 |
| Monocyte | Nuc/Cyt | 128 | 650 | 8 | 7,026 (3,029) | 2,391 |
| Immature dendritic cell | Nuc/Cyt | 52 | 683 | 20 | 2,257 (1,343) | 376 |
| Macrophage | Nuc/Cyt | 46 | 520 | 15 | 1,847 (1,082) | 472 |
| Eosinophil | Nuc/Cyt | 52 | 426 | 10 | 1,774 (1,427) | 391 |
| Neutrophil | WC | 104 | 318 | 27 | 3,348 (2,784) | 1,728 |
| | Nuc/Cyt | | | | | |
| Erythrocyte (RBC) | WC | 41 | 123 | 6 | 1,199 (555) | 477 |
| | PM | | | | | |
| Platelet | WC | 78 | 344 | 14 | 1,595 (1,122) | 728 |
| | PM | | | | | |
| Plasma | PM | 50 | 79 | 17 | 462 (326) | 232 |
| Total | – | 1,553 | 9,239 | 317 | 56,813 (30,812) | 17,103 |
| Total (nonredundant) | – | 1,553 | 1,690 | 317 | 29,620 (17,630) | 17,103 |

*Cell types isolated from human bone marrow.

would uncover >50,000 additional proteoforms in this size regime. We expect that larger proteins that act as hubs of cellular decision-making could have more proteoforms per protein [e.g., tumor suppressor protein p53 (27)]. Further, to estimate the number of human proteoforms, we multiplied the theoretical number of proteins by three times the standard deviation of the mean number of proteoforms observed per protein. From this, we estimated the number of proteoforms to be ~1.1 million in a human cell type, close to a previous estimation (22).

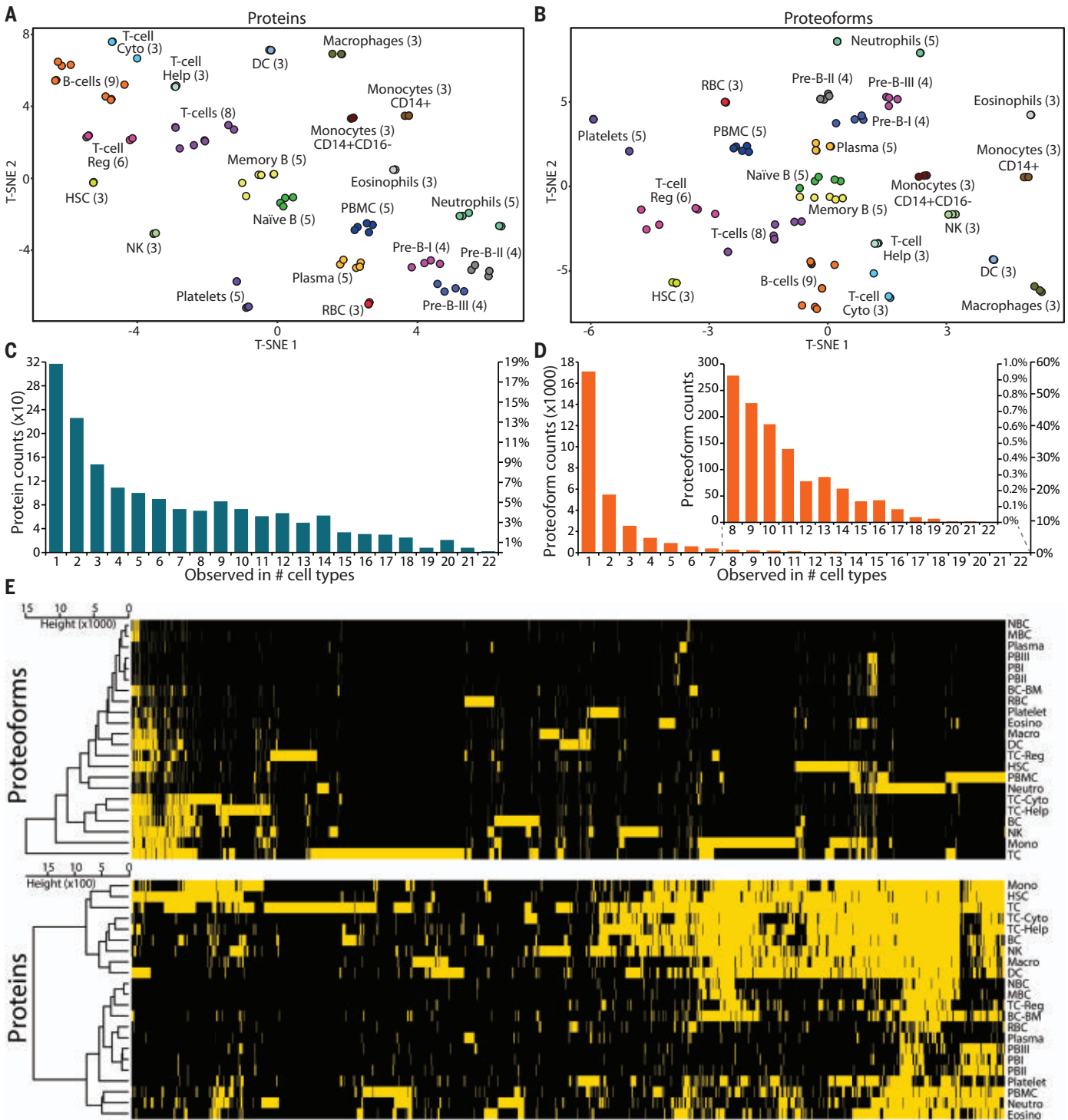


Fig. 2. Display of protein and proteoform analysis for entries in the Blood Proteome Atlas. t-SNE plots display cell types grouped by presence or absence of (A) proteins and (B) proteoforms. T-cell Cyto, cytotoxic T cells; T-cell Help, helper T cells; T-cell Reg, regulatory T cells; HSC, hematopoietic stem cells; DC, dendritic cells; RBC, red blood cells. Histograms of (C) proteins and (D) proteoforms shared by different cell types. (E) Heatmaps and cell

type hierarchical clustering of identified (yellow) or not-identified (black) proteins (1690) and proteoforms (29,620) at 1% FDR, with proteoforms exhibiting higher specificity for distinct cell types. NBC, naive B cells; MBC, memory B cells; PBI, pre-B-I cells; BC-BM, B cells from bone marrow; Eosino, eosinophils; Macro, macrophages; Neutro, neutrophils; BC, B cells from blood; Mono, monocytes; TC, T cells.

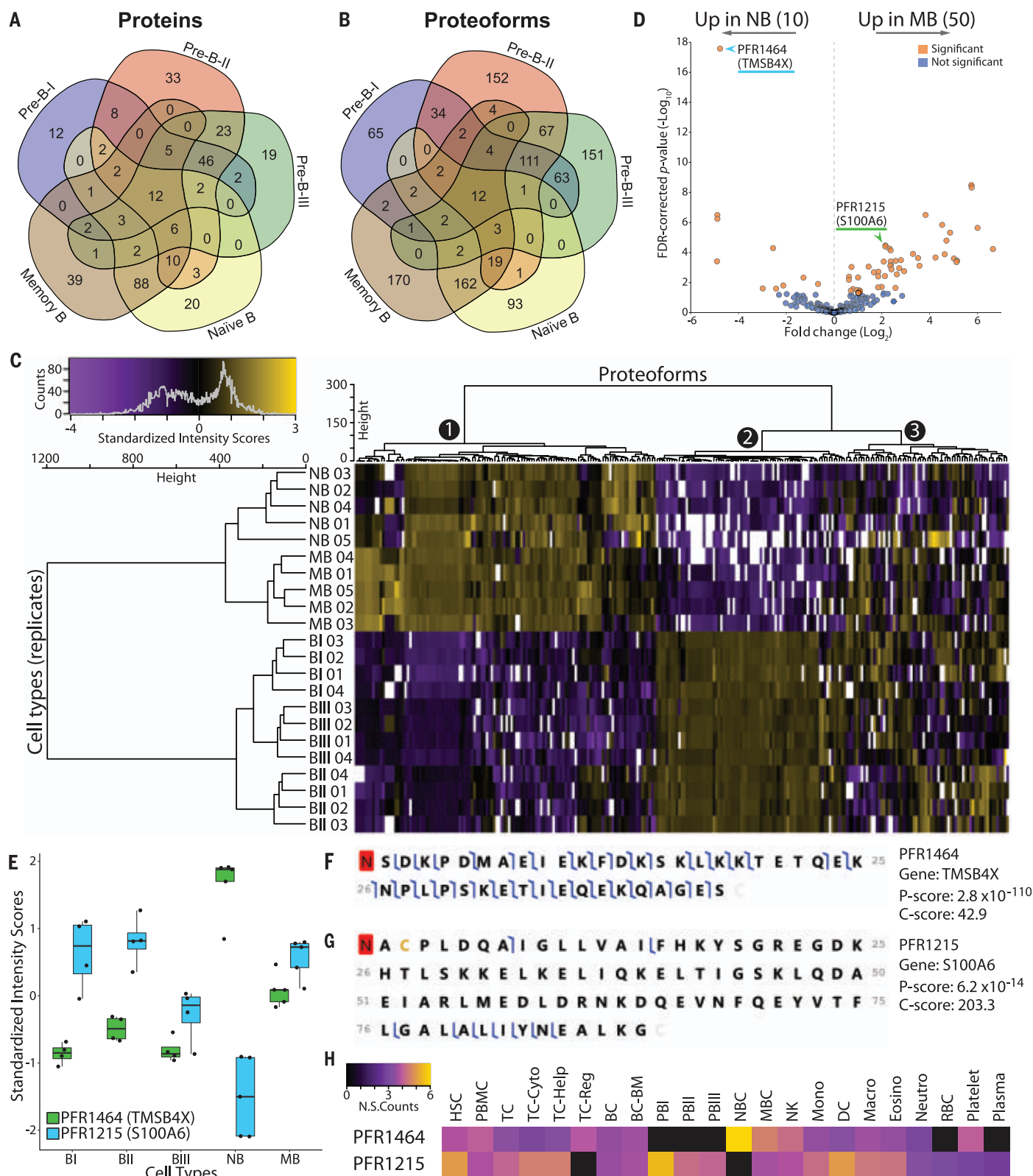


Fig. 3. Comparison of B cell subtypes using quantitative top-down proteomics.

Venn diagram analysis of (A) proteins and (B) proteoforms observed in pre-B-I, pre-B-II, and pre-B-III cells; naïve B cells; and memory B cells. (C) Heatmap and hierarchical clustering of quantified proteoforms from B cell subtypes. Numbers 1 to 3 represent the three major clusters of proteoforms found. (D) Volcano plot of up- and down-regulated proteoforms from naïve B cells (NB) relative to memory B cells (MB). (E) Box-and-whisker

plots of proteoforms PFR1464 (TMSB4X) and PFR1215 (S100A6) levels show their variance among the five B cell subtypes. Fragmentation maps of (F) PFR1464 and (G) PFR1215. Red box indicates N-terminal acetylation. Single-letter abbreviations for the amino acid residues are as follows: A, Ala; C, Cys; D, Asp; E, Glu; F, Phe; G, Gly; H, His; I, Ile; K, Lys; L, Leu; M, Met; N, Asn; P, Pro; Q, Gln; R, Arg; S, Ser; T, Thr; V, Val; W, Trp; and Y, Tyr. (H) Distributions of proteoforms PFR1464 and PFR1215 in blood cell types of the BPA.

Hence, this study likely accounts for at most ~3% of human proteoforms distributed from 1 to 59 kDa (fig. S3), demonstrating a clear need to improve technologies for systematic proteoform discovery (23).

Quantitative TDP of hematopoietic cell types

Quantitative comparison of proteoforms using label-free TDP (24) was applied to compare pools of B cells (CD19⁺) against T cells (CD3⁺) from the same donor (fig. S4 and supplementary text in the supplementary materials). We also compared five B cell subtypes from a single donor sorted by FACS, including pre-B-I, pre-B-II, and pre-B-III from bone marrow and memory and naïve B cells from blood (table S1 and Fig. 3). Many proteins or proteoforms are shared by cells from the bone marrow or between their mature forms in the blood, indicating that these cell types are distinct (Fig. 3, A and B). The same pattern is observed in the expression heatmap generated from the standardized intensities scores (Fig. 3C), separating the two cell groups by >66% of the total clustering distance. Three clusters of proteoforms were observed: (i) those up-regulated in naïve and memory B cells, (ii) those up-regulated in pre-B cells, and (iii) those with a random regulation pattern.

A closer look into the differentially regulated proteoforms from the mature B cells showed 10 proteoforms with increased relative abundance in naïve B cells, with 50 elevated in memory B cells (Fig. 3D). The proteoform PFR1464 from thymosin beta-4 (Fig. 3F) was elevated by ~10-fold in naïve B cells relative to memory cells, whereas proteoform PFR1215 from the protein S100A (Fig. 3G) was increased in memory relative to naïve B cells. Exploring the presence of these two proteoforms in the five B cell subtypes showed that PFR1215 is present at low levels in naïve B cells and at high levels in pre-B cells and memory B cells (Fig. 3E). PFR1464 is present mainly in naïve B cells and has low levels in pre-B cells (Fig. 3E). Expanding this comparison to all cell types in the BPA, we observe that PFR1464 is more abundant in naïve B cells, whereas PFR1215 is more widely observed in different cell types (Fig. 3H). Quantitative results were consistent using spectral counting and intact proteoform quantification methods in both cases.

BPA and peripheral blood mononuclear cells from liver transplant recipients

With a reference set of proteoforms, the BPA can inform clinical research and care with more precise protein information, for example, the prostate-specific antigen isoform test in prostate cancer (25). One area of unmet need is organ transplantation, in particular liver transplantation (LT), where episodes of acute rejection (AR) limit survival (26). AR

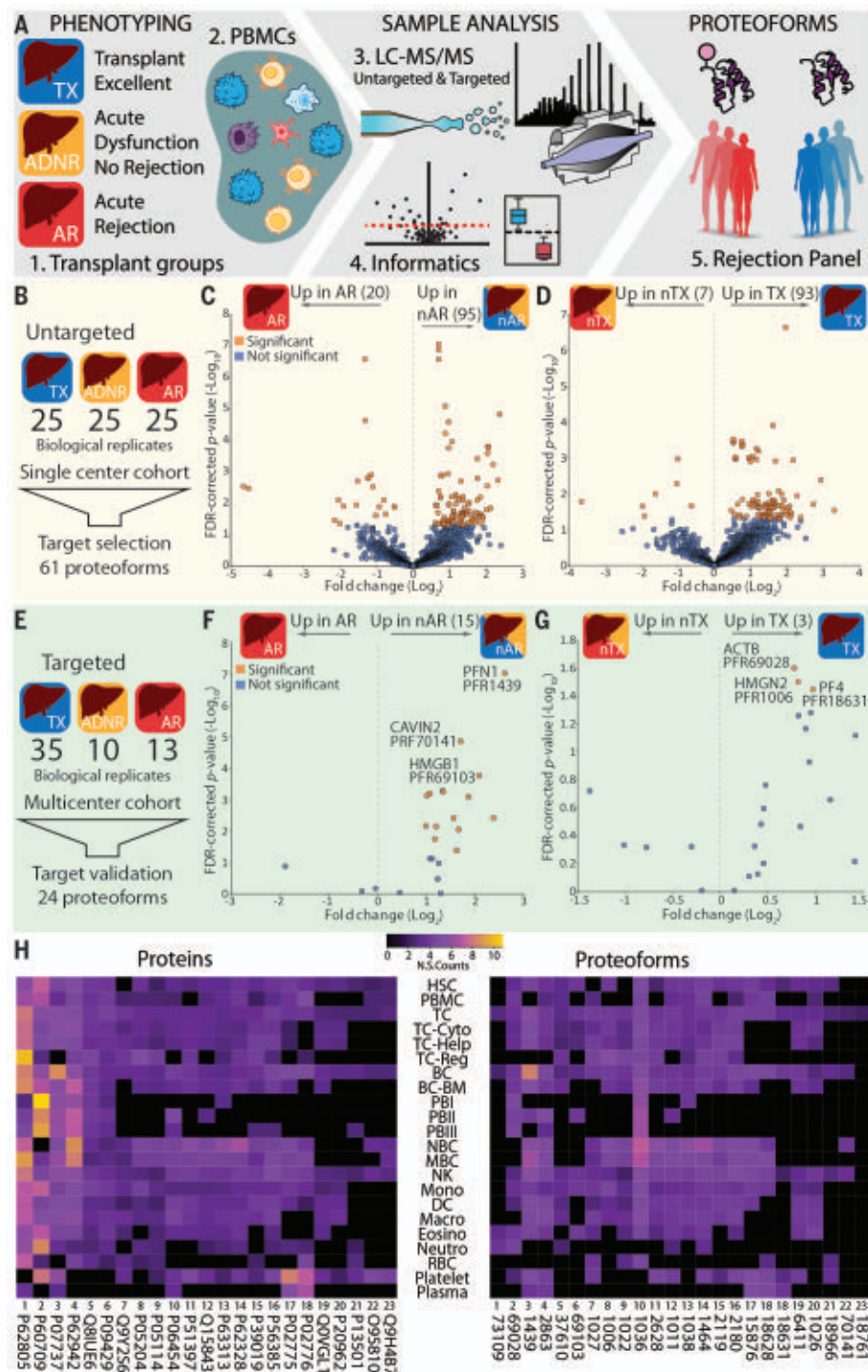


Fig. 4. Quantitative top-down proteomics analysis of PBMC proteoforms from liver transplant recipients. (A) Workflow used to compare patients with transplant excellent (TX); with acute dysfunction, no rejection (ADNR); and with acute rejection (AR). (B) The number of patients whose PBMCs were analyzed in an untargeted fashion. Volcano plot showing differentially expressed proteoforms in (C) AR patients relative to non-AR (TX+ADNR) and (D) TX patients relative to non-TX (ADNR+AR). (E) The number of patients whose PBMCs were analyzed for targeted proteoforms. Volcano plot with the relative levels of the 24 targeted proteoforms in (F) AR versus non-AR and (G) TX versus non-TX. (H) Distributions of the normalized spectral (N.S.) counts of proteins (left) and proteoforms (right) observed in BPA cell types.

arises from an imbalance of immune activation (IA) related to cellular and humoral anti-donor responses (e.g., effector CD4⁺, cytotoxic CD8⁺ T cells, and donor-specific antibodies) over immune quiescence (IQ) suppressor countermechanisms (e.g., regulatory T cells) (27–30). This key balance of IA versus IQ relating to AR risk is, however, difficult to determine without available objective markers in LT recipients (LTRs). Given this critical clinical scenario, we sought to discover and validate cell-based proteoforms as indicators of LTR immune status for future clinical applications.

We first conducted an untargeted quantitative TDP analysis of peripheral blood mononuclear cells (PBMCs) using the 0 to 30 kDa GELFrEE fractions of whole PBMC lysates from a cohort of 75 LTRs (Fig. 4, A and B). Patients were initially divided into three groups: transplant excellent (TX representing IQ and healthy graft function; $n = 25$), acute dysfunction no rejection (ADNR, representing nonrejection causes of graft injury; $n = 25$), and AR ($n = 25$). The AR and ADNR phenotypes were diagnosed by needle biopsy, and TX by clinical and laboratory criteria, as previously described (31–34). The absence of biopsies in TX was a limitation; however, transplant centers do not generally perform surveillance biopsies in LTR with healthy graft function. Figure 4 shows the results for AR versus non-AR (TX+ADNR) and TX versus non-TX (AR+ADNR), grouped for simplification and alignment with clinical utility. We identified a total of 198 differentially expressed proteoforms (DEPs) from 99 proteins (Fig. 4, C and D), many of which were detected in our small exploratory study (31). Pathway and process analysis was performed on the identified proteins from each group using Metascape (35) (fig. S5 and table S8). Between the groups, we found some commonly enriched pathways involved in T cell activation and graft migration, including RHO GTPase effectors (36). TX-specific pathways include regulated exocytosis, platelet degranulation, and cytoskeletal organization. These pathways could be related to exocytosis of granules from cytotoxic T cells, platelet-mediated thrombosis, and remodeling of the actin cytoskeleton (37).

Next, we performed a targeted validation study using some of the most significant proteoforms from discovery (table S9). A panel with 24 proteoforms from 23 proteins (table S10) was deployed on a new cohort of 59 patient PBMCs (TX = 36, ADNR = 10, and AR = 13) (Fig. 4E) from a multicenter LT study (NIAID CTOT-14; NCT01672164) (32). We note that the number of AR subjects is small but reflects the ~20% prevalence of AR in LTR (26, 38–40). Statistical analysis comparing AR and non-AR or TX and non-TX populations confirmed significantly up-regulated proteo-

forms from the TX or non-AR groups (Fig. 4, F and G, and table S10). The proteoforms differentially regulated in TX were platelet factor 4 (PF4) N-terminally truncated with five extra amino acids, PFR18631; nonhistone chromosomal protein HMG-17 (HMGN2) canonical sequence, PFR1006; and a C terminus part of cytoplasmic actin 1 (ACTB) from amino acid positions 330 to 375, PFR69028. On the other hand, 15 proteoforms were significantly increased in non-AR (table S10). The three proteoforms with the higher q values were a piece of serum deprivation-response protein (CAVIN2) from amino acid positions 297 to 343, PFR70141; a C-terminal portion of high mobility group protein B1 (HMGB1) from amino acid positions 107 to 214, PFR69103; and the canonical sequence of profilin-1 (PFN1) N-terminally acetylated, PFR1439.

With a cell-based expression atlas in hand, we could identify the cell types in which these 24 proteoform targets are typically present. Figure 4H shows the heatmaps of proteins (left) and their proteoforms (right). Most proteoforms are found in a narrower range of cell types; for example, PFR70141 from the CAVIN2 gene was only identified in NK cells, naïve B cells, B cells, and T cells, while at the protein level (O95810) it was additionally observed in platelets, PBMCs, and hematopoietic stem cells (HSCs). Moreover, transcriptome data from the HBA point to the CAVIN2 gene as highly expressed in PBMCs, supporting the results. All proteoforms from the panel were identified in T cells, 23 in B cells, and 22 in NK cells—collectively the most abundant PBMC types (41). Five were identified in red blood cells (RBCs), neutrophils, and plasma, suggesting nonspecific cell proteoforms. On the basis of the protein and proteoform hits in Fig. 4H, we performed a cell enrichment test against all BPA identifications (fig. S6). Consistent with a narrower distribution of proteoforms, one proteoform of PF4, PFR18631, was observed in six cell types (platelets, plasma, B cells, T cells, and HSCs). A second proteoform, PFR18628, was identified in 11 cell types, and the corresponding protein (P02776) in 15 different cell types. In this case, platelets showed the highest normalized spectral counts for the protein that is an archetype of the chemokine family essential in platelet aggregation and inflammation (42).

Some of the identified proteoforms derive from proteins with immune functions, including PF4 and PFN1. PF4 expression is reduced in humans and mice with acute liver injury and inhibits ischemia-reperfusion injury in LT mouse models (43, 44). PFN1 is involved in actin organization, which inhibits CD8⁺ cytotoxicity by reducing migration and degranulation (45). Box-and-whisker plots showing the prominent striation in individual patient responses are presented in fig. S7. Proteoforms related to ACTB, PFN1, and PF4 were statisti-

cally significant in TX and non-AR groups, supporting the discovery-stage experiments. Notably, the protein PF4 had two proteoforms in the 24 proteoform panel, and only PFR18631 was 1.9-fold up-regulated in the TX group compared with the non-TX group. This proteoform has four extra amino acids (FASA) on the N terminus compared with PFR18628, which maps to the canonical isoform in UniProtKB/Swiss-Prot (42) and was not differentially expressed. The N-terminal processing of PFR18631 may represent an essential mechanism for modulating PF4 activity similar to the one described to inhibit endothelial cell growth (42). Additional studies are underway to monitor proteoform changes over time and in specific cell types in LTR patients (32).

The results from this small cohort suggest that in the clinical context of liver transplantation (i) leukocyte proteoform levels might have diagnostic value for IA versus IQ, and (ii) clinically relevant immunoproteoforms are present in select blood cell populations. The novelty of direct proteoform measurement versus less specific epitope- or peptide-based methods could advance care by identifying early specific signs of IA versus IQ to personalize LTR immunosuppressive therapy monitoring and modulation.

Summary

By mapping ~57,000 redundant proteoforms present in human blood, bone marrow, plasma, and within main hematopoietic cell types, we have advanced fundamental knowledge of protein components present in the human body. At the transcript level, the field is advancing single-cell RNA-seq from a compositional tool to connect with spatial localization (46). A reference map of human proteoforms can serve a similar function at the protein level as we seek to understand the spatial and temporal dynamics of proteins operative in human tissue (13). Here, both cell- and proteoform-specific information in the context of organ transplantation were provided as a potential clinical application. This cellular and molecular specificity can help advance the future of protein-level diagnostics and broader goals for understanding human biology.

REFERENCES AND NOTES

- P. Picotti et al., *Nature* **494**, 266–270 (2013).
- A. Battle et al., *Science* **347**, 664–667 (2015).
- M. S. Kim et al., *Nature* **509**, 575–581 (2014).
- M. Wilhelm et al., *Nature* **509**, 582–587 (2014).
- P. J. Thul et al., *Science* **356**, eaal3321 (2017).
- M. Uhlen et al., *Science* **347**, 1260419 (2015).
- M. Uhlen et al., *Science* **366**, eaax9198 (2019).
- L. M. Smith, N. L. Kelleher; Consortium for Top Down Proteomics, *Nat. Methods* **10**, 186–187 (2013).
- V. Marx, *Nat. Methods* **16**, 809–812 (2019).
- A. Doerr, *Nat. Methods* **16**, 20 (2019).
- X. Yang et al., *Cell* **164**, 805–817 (2016).
- M. A. Ghadie, L. Lambourne, M. Vidal, Y. Xia, *PLOS Comput. Biol.* **13**, e1005717 (2017).
- HuBMAP Consortium, *Nature* **574**, 187–192 (2019).
- S. Doll et al., *Nat. Commun.* **8**, 1469 (2017).

15. S. Di Palma *et al.*, *J. Proteome Res.* **10**, 3814–3819 (2011).
16. J. C. Tran *et al.*, *Nature* **480**, 254–258 (2011).
17. A. I. Nesvizhskii, R. Aebersold, *Mol. Cell. Proteomics* **4**, 1419–1440 (2005).
18. L. M. Smith, N. L. Kelleher, *Science* **359**, 1106–1107 (2018).
19. K. A. Brown, J. A. Melby, D. S. Roberts, Y. Ge, *Expert Rev. Proteomics* **17**, 719–733 (2020).
20. R. D. LeDuc *et al.*, *Mol. Cell. Proteomics* **18**, 796–805 (2019).
21. V. N. Uversky, *Int. J. Mol. Sci.* **17**, 1874 (2016).
22. R. Aebersold *et al.*, *Nat. Chem. Biol.* **14**, 206–214 (2018).
23. L. M. Smith *et al.*, *Sci. Adv.* **7**, eabk0734 (2021).
24. I. Ntai *et al.*, *Mol. Cell. Proteomics* **15**, 45–56 (2016).
25. M. Stovsky *et al.*, *J. Urol.* **201**, 1115–1120 (2019).
26. J. Levitsky *et al.*, *Clin. Gastroenterol. Hepatol.* **15**, 584–593.e2 (2017).
27. A. Moreau, E. Vairey, I. Anegón, M. C. Cuturi, *Cold Spring Harb. Perspect. Med.* **3**, a015461 (2013).
28. V. Ronca, G. Wootton, C. Milani, O. Cain, *Front. Immunol.* **11**, 2155 (2020).
29. J. A. Pons *et al.*, *Transplantation* **86**, 1370–1378 (2008).
30. M. Romano, G. Fanelli, C. J. Albany, G. Giganti, G. Lombardi, *Front. Immunol.* **10**, 43 (2019).
31. T. K. Toby *et al.*, *Am. J. Transplant.* **17**, 2458–2467 (2017).
32. J. Levitsky *et al.*, *Am. J. Transplant.* **20**, 2173–2183 (2020).
33. J. Levitsky *et al.*, *Transplantation* 10.1097/TP.0000000000003895 (2021).
34. J. Levitsky *et al.*, *Am. J. Transplant.* **21**, 16835 (2021).
35. Y. Zhou *et al.*, *Nat. Commun.* **10**, 1523 (2019).
36. R. El Masri, J. Delon, *Nat. Rev. Immunol.* **21**, 499–513 (2021).
37. W. Witke *et al.*, *EMBO J.* **17**, 967–976 (1998).
38. A. Ramji *et al.*, *Liver Transpl.* **8**, 945–951 (2002).
39. T. Uemura *et al.*, *Clin. Transplant.* **22**, 316–323 (2008).
40. P. H. Thuraiajah *et al.*, *Transplantation* **95**, 955–959 (2013).
41. C. R. Kleiveland, in *The Impact of Food Bioactives on Health: In Vitro and Ex Vivo Models*, K. Verhoeckx *et al.*, Eds. (Springer, 2015), pp. 161–167.
42. S. K. Gupta, T. Hassel, J. P. Singh, *Proc. Natl. Acad. Sci. U.S.A.* **92**, 7799–7803 (1995).
43. H. Guo, Y. Wang, Z. Zhao, X. Shao, *Scand. J. Immunol.* **81**, 129–134 (2015).
44. H. K. Drescher *et al.*, *Front. Physiol.* **10**, 326 (2019).
45. R. Schoppmeyer *et al.*, *Eur. J. Immunol.* **47**, 1562–1572 (2017).
46. T. Stuart *et al.*, *Cell* **177**, 1888–1902.e21 (2019).

ACKNOWLEDGMENTS

The authors thank N. Haverland and the following members of the Robert H. Lurie Comprehensive Cancer Center Flow Cytometry Core Facility for helpful discussions and experimental assistance with FACS methodology: S. Swaminathan, P. Mehl, and C. Ostigau. We thank P. Oksvold for discussions and assistance with making the HPA Blood Cell Atlas data available. Analysis of these transcriptomic data was performed on resources provided by the Swedish National Infrastructure for Computing (SNIC) through Uppsala Multidisciplinary Center for Advanced Computational Science (UPPMAX) under project sens2019032. We also thank L. M. Smith for additional computational resources for proteomic analysis with MetaMorpheus. **Funding:** Funding was provided by Paul G. Allen Frontiers Program award 11715 (N.L.K.); HuBMAP grant UH3 CA246635-02 (N.L.K.); the National Institute of General Medical Sciences of the National Institutes of Health under grants P41 GM108569 (N.L.K.), R21LM013097 (P.M.T.), T32 GM105538 (T.K.T.), and R21 AI135827 (J.L.); Knut and Alice Wallenberg Foundation grant 2016.0204 (A.J.C. and E.L.); and Swedish Research Council grant 2017-05327 (E.L.). A portion of this work was performed at the Ion Cyclotron Resonance User Facility at the National High Magnetic Field Laboratory, which is supported by the National Science Foundation Division of Materials Research and Division of Chemistry through DMR-1644779, and the State of Florida. **Author contributions:** Conceptualization: N.L.K., P.M.T., and J.L. Methodology: R.D.M., V.R.G., T.K.T., K.S., J.E.H., N.L.K., P.M.T., and J.L. Investigation: R.D.M., V.R.G., J.W.S., T.K.T., J.E.H., F.N., H.S.S., K.S., L.F., J.M.C., C.J.D., E.F., S.E.A., L.C.A., D.S.B., C.L.H., and A.J.C. Visualization: R.D.M., V.R.G., T.K.T., K.S., J.E.H., and F.N. Data curation: R.D.M., R.D.L., A.J.C., J.B.G., R.T.F., M.T.R., and P.M.T. Formal analysis: R.D.M., V.R.G., F.N., H.S.S., R.D.L., A.J.C., J.B.G., R.T.F., M.T.R., and P.M.T. Software: R.D.M., V.R.G., H.S.S., R.D.L., A.J.C., J.B.G., R.T.F., M.T.R., and P.M.T. Resources: N.L.K., J.L., E.L., C.L.H., and A.I.K. Funding acquisition: N.L.K.,

P.M.T., E.L., and J.L. Writing – original draft: R.D.M., V.R.G., N.L.K., P.M.T., R.D.L., L.C.A., E.F., and J.L. Writing – review & editing: R.D.M., V.R.G., N.L.K., P.M.T., R.D.L., L.C.A., and J.L. **Competing interests:** N.L.K. is involved in entrepreneurial activities in top-down proteomics and consults for Thermo Fisher Scientific. A.I.K. is an employee of Stem Cell Technologies. **Data and materials availability:** All cell types and cell enrichment kits used are commercially available and listed in the material and methods section of the supplementary materials. All .raw files are available at the Proteomics Identifications Database (PRIDE; www.ebi.ac.uk/pride/) under accession numbers PXD026123 to PXD026178. Proteoform information is available in the Blood Proteoform Atlas (<https://blood-proteoform-atlas.org>).

SUPPLEMENTARY MATERIALS

science.org/doi/10.1126/science.aaz5284
Materials and Methods
Supplementary Text
Figs. S1 to S7
Tables S1 to S12
References (47–76)
MDAR Reproducibility Checklist

12 June 2021; accepted 17 December 2021
10.1126/science.aaz5284

QUANTUM CRITICALITY

Quantum critical points and the sign problem

R. Mondaini¹, S. Tarat¹, R. T. Scalettar²

The “sign problem” (SP) is a fundamental limitation to simulations of strongly correlated matter. It is often argued that the SP is not intrinsic to the physics of particular Hamiltonians because its behavior can be influenced by the choice of algorithm. By contrast, we show that the SP in determinant quantum Monte Carlo (QMC) is quantitatively linked to quantum critical behavior. We demonstrate this through simulations of several models with critical properties that are relatively well understood. We propose a reinterpretation of the low average sign for the Hubbard model on the square lattice away from half filling in terms of the onset of pseudogap behavior and exotic superconductivity. Our study charts a path for exploiting the average sign in QMC simulations to understand quantum critical behavior.

Over the past several decades, quantum Monte Carlo (QMC) simulations have provided great insight into challenging strong correlation problems in chemistry (1, 2), condensed-matter physics (3, 4), nuclear physics (5), and high-energy physics (6). In all of these areas, however, the sign problem (SP), which occurs when the probability for specific quantum configurations in the importance sampling becomes negative, substantially constrains their application. Solving, or at least mitigating, the SP is one of the central endeavors of computational physics. The extent and importance of the effort is indicated by the many proposed solutions and their continued development over the past three decades [for an overview, see the supplementary materials (7) and references therein].

Despite enormous effort, the SP remains unsolved. In fact, the lack of progress is one of the main driving forces behind a number of large-scale research efforts, including the quest for quantum emulators (8–10) and quantum computing itself (11, 12). One of the most fundamental mysteries concerns the possible link between the SP and the underlying physics of the Hamiltonian being investigated.

Here, instead of challenging this non-deterministic polynomial hard problem (13) or proposing solutions that can partially ameliorate its behavior (14, 15), we show that there is a clear connection between the behavior of the average sign $\langle S \rangle$ in the widely used determinant quantum Monte Carlo (DQMC) method and several quantum phase transitions (QPTs): that of the semimetal to antiferromagnetic Mott insulator (MI) of Dirac fermions in the spinful [SU(2)] honeycomb-Hubbard Hamiltonian (16, 17), the band to correlated insulator transition (18–20), and charge density wave (CDW) transitions of spinless [U(1)] fermions on a honeycomb lattice (21, 22). In the first example, simulations at half-filling, where the quantum critical point (QCP) occurs, are SP-free. We introduce a small doping μ and show, in the limit $\mu \rightarrow 0^+$ at temperature $T \rightarrow 0$, that $\langle S \rangle$ evolves rapidly as we tune through the QCP.

Our second illustration, the ionic Hubbard model, has an SP even at half-filling. Here, the average sign undergoes an abrupt drop at the band insulator (BI) to correlated metal (CM) transition. The third example, spinless fermions on a honeycomb lattice, also features a semimetal to (charge) insulator transition but allows for an SP-free approach. Studying it with a method that contains an “unnecessary” SP lends insight into the key question of the influence of different algorithms on the connection between the SP and the physics of model Hamiltonians.

¹Beijing Computational Science Research Center, Beijing 100193, China. ²Department of Physics, University of California, Davis, CA 95616, USA.

Correspondence: rmondaini@csrc.ac.cn (R.M.); tarats@csrc.ac.cn (S.T.); scalettar@physics.ucdavis.edu (R.T.S.)

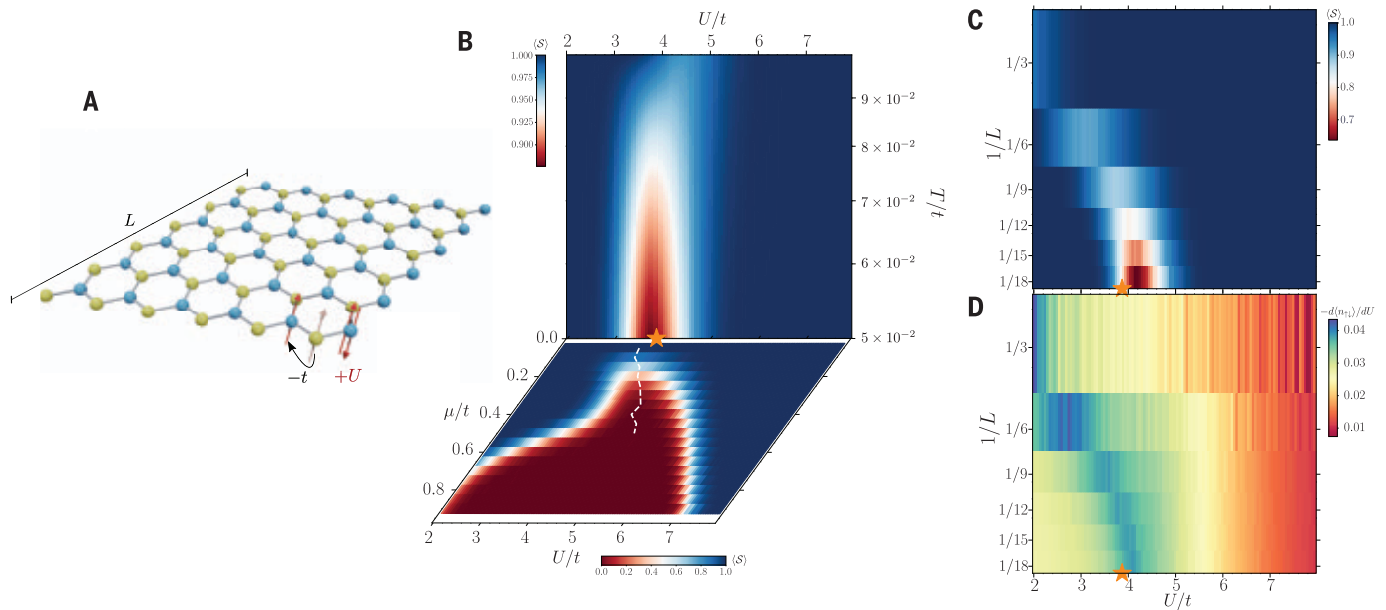


Fig. 1. The SU(2) Hubbard model on the honeycomb lattice. (A) Diagram depicting a honeycomb lattice with $N = 2L^2$ sites ($L = 6$ here), accompanied by the relevant terms in \hat{H} . (B) Contour plot of the average $\langle S \rangle$ in the T/t (μ/t) versus U/t in the upper (lower) panel. Here $L = 9$ and $\mu/t = 0.1$ ($T/t = 1/20$) in the upper (lower) panel. (C) Average sign extrapolated with the linear system size L using $T/t = 1/20$ and $\mu/t = 0.1$. (D) Similar extrapolation as in

(C) but displaying a local quantity (the derivative of the double occupancy), which is an indicator of the QCP. In all panels with data, the prediction for the ground-state phase transition occurring at $U_c/t = 3.869$ (17) is depicted by a star marker. In all data, Trotter discretization is chosen as $t\Delta\tau = 0.1$. See fig. S1 for additional observables and fig. S2 for the fermionic flavor-dependent average sign.

These three discussions establish a link between known physics of the models and the fermion sign. Having made that connection, we turn to the iconic square lattice Hubbard model, the physics of which has not been conclusively established. We find that the onset of the SP occurs in a dome-shaped region of the filling-temperature phase space under that of the pseudogap physics. The SP is sufficiently well controlled in the pseudogap phase to obtain reliable results for various observables, including the pairing correlations in various channels, exhibiting dominant enhancement for d -wave symmetry. Because it behaves exponentially in inverse temperature, the SP provides a rather sharp demarcation of the regime, mimicking the superconducting dome of the cuprates (23). Although the SP prevents DQMC from resolving a signal of a d -wave transition, the groundwork established for the honeycomb lattice and BI-CM models suggests that this SP dome might be linked to the onset of a superconducting phase.

The SP: Model and methodology

The origin of the SP can be understood in two related classes of algorithms, world-line QMC (WLQMC) (24) and Green's function QMC (GFQMC) (25, 26), by considering Feynman's path integral approach, which provides a mapping of quantum statistical mechanics in D dimensions to classical statistical mechanics

in $D + 1$ dimensions. Paralleling Feynman's original exposition for the real-time evolution operator $e^{-i\hat{H}\tau/\hbar}$, the imaginary time evolution operator $e^{-\beta\hat{H}}$ is subdivided into L_τ incremental pieces $\hat{U}_{\Delta\tau} = e^{-\Delta\tau\hat{H}}$, where \hbar is the reduced Planck's constant, \hat{H} is the Hamiltonian, and $L_\tau\Delta\tau = \beta$ is the inverse temperature. Complete sets of states $I_\tau = \sum_{S_\tau} |S_\tau\rangle\langle S_\tau|$ are introduced between each $\hat{U}_{\Delta\tau}$ so that the partition function $Z = \text{Tr} e^{-\beta\hat{H}}$ becomes a sum over the classical degrees of freedom associated with the spatial labels of each I_τ and also an additional imaginary time index denoting the location $\tau = 1, 2, \dots, L_\tau$ of I_τ in the string of operators $\hat{U}_{\Delta\tau}$. The quantity being summed in the calculation of Z is the product of matrix elements $\langle S_\tau | \hat{U}_{\Delta\tau} | S_{\tau+1} \rangle$.

In such WLQMC/GFQMC methods, the SP arises when $\Pi_\tau \langle S_\tau | \hat{U}_{\Delta\tau} | S_{\tau+1} \rangle < 0$. Negative matrix elements are unavoidable for itinerant fermionic models in $D > 1$ because their sign depends on the number of fermions intervening between two particles undergoing exchange, and thus changes as the particle positions are updated. The basis dependence of the SP is apparent by considering intermediate states $|S_\tau\rangle$ chosen to be eigenstates $|\phi_\alpha\rangle$ of \hat{H} , with eigenvalues E_α . In that case, the matrix elements are just $e^{-\Delta\tau E_\alpha}$ and thus are trivially positive definite. Of course, because the eigenstates of \hat{H} are unknown, this is not a practical choice in any nontrivial situation. Moreover, the SP can generally be avoided for bosonic or spin

models as long as the lattice is bipartite. Nonetheless, even bosonic and spin Hamiltonians can have negative matrix elements on frustrated geometries (27), especially for antiferromagnetic models, emphasizing that the SP is not solely a consequence of Fermi statistics.

Auxiliary field QMC (AFQMC) algorithms (28–30) typically have a much less severe SP than WLQMC (7, 31). They are based on the observation that the trace of an exponential of a quadratic form of fermionic operators can be done analytically, resulting in the determinant of a matrix of dimension set by the cardinality of fermionic operators. The determinant is the product $\prod_j (1 + e^{-\beta\epsilon_j})$, where ϵ_j is the noninteracting energy level and is always positive.

If interactions are present, quartic terms in \hat{H} are reduced to quadratic ones with a Hubbard-Stratonovich transformation. The trace of the resulting product of exponentials of quadratic forms can be performed, but now they each depend on a different, i.e., imaginary-time dependent, auxiliary field. The resulting determinant is no longer guaranteed to be positive; the consequence is the SP given that the Hubbard-Stratonovich field needs to be sampled stochastically to compute operator expectation values.

In AFQMC, the trace over fermionic degrees of freedom is done for all species (i.e., all spin and orbital indices α). If there is no hybridization between different α 's, each trace gives an

individual determinant. In some situations, particle-hole, time-reversal, or other symmetries (32–34) impose a relation between the determinants for different α 's, and as a consequence the negative determinants always come in pairs. Low-temperature (ground-state) properties can be accessed in such “SP-free”

cases, and a host of interesting quantum phase transitions has been explored (35–38).

If such a partnering does not occur, then a reasonable rule of thumb is that the average sign $\langle S \rangle$ is sufficiently bounded away from zero with measurements that exhibit sufficiently small error bars for $T \gtrsim W/20 - W/40$,

at intermediate interaction strengths (of the same order as the bandwidth W) (39).

The DQMC methodology (28, 29) that we used is a specific implementation of AFQMC. We used the discrete Hubbard-Stratonovich transformation introduced by Hirsch (40) and chose the Trotter discretization $\Delta\tau$ such that systematic errors in $\langle S \rangle$ and other observables are of the same order as statistical sampling errors [for additional details, see the materials and methods (7)].

We mainly consider models in which two (spin) species of itinerant electrons hop on a lattice with an on-site repulsion, i.e., variants of the Hubbard Hamiltonian,

$$\hat{H} = -\sum_{ij\sigma} t_{ij} (\hat{c}_{i\sigma}^\dagger \hat{c}_{j\sigma}) + \left(\hat{c}_{j\sigma}^\dagger \hat{c}_{i\sigma} \right) - \sum_{i\sigma} \mu_i \hat{n}_{i\sigma} + U \sum_i \left(\hat{n}_{i\uparrow} - \frac{1}{2} \right) \left(\hat{n}_{i\downarrow} - \frac{1}{2} \right) \quad (1)$$

Here, $\hat{c}_{j\sigma}^\dagger$ ($\hat{c}_{j\sigma}$) are creation (destruction) operators at site i with spin σ and $\hat{n}_{i\sigma} = \hat{c}_{i\sigma}^\dagger \hat{c}_{i\sigma}$ is the number operator. In the first model, i and j are near-neighbor (NN) sites on a honeycomb lattice, with $t_{ij} = t$. As a consequence of particle hole symmetry, $\mu_i = 0$ corresponds to half-filling and $\rho = \langle \hat{n}_{i\sigma} \rangle = 1/2$, for arbitrary U and temperature T . For the second model, we consider a $t_{ij} = t$ square lattice with $\mu_i = +\Delta$ on one sublattice and $\mu_i = -\Delta$ on the other, a situation that has an SP even at half-filling, but which is mild enough to allow its phase diagram to be established with reasonable reliability. The third model concerns a single species model with interactions between fermions on neighboring sites, notable because an SP-free QMC formulation exists (22, 41).

All of these models have QCPs that have been located to fairly high precision and so serve as testbeds for demonstrating that the average sign can be used as an alternative means to study the onset of quantum criticality. In our final investigation, we consider the doped, spinful, square lattice Hubbard model, much of the low-temperature physics of which remains shrouded in mystery. We correlate the behavior of the SP with some of the model's properties at intermediate temperature and then describe what might be inferred concerning the presence of a low-temperature superconducting dome.

Semimetal to antiferromagnetic MI on a honeycomb lattice

On a honeycomb lattice (Fig. 1A), the $U = 0$ Hubbard Hamiltonian has a semimetallic density of states that vanishes linearly at $E = 0$. Its dispersion relation $E(k)$ has Dirac points in the vicinity of which the kinetic energy varies linearly with momentum. Unlike the square lattice that displays AF order for all $U \neq 0$, the honeycomb Hubbard model at $T \rightarrow 0$ remains a semimetal for small nonzero U , turning to an

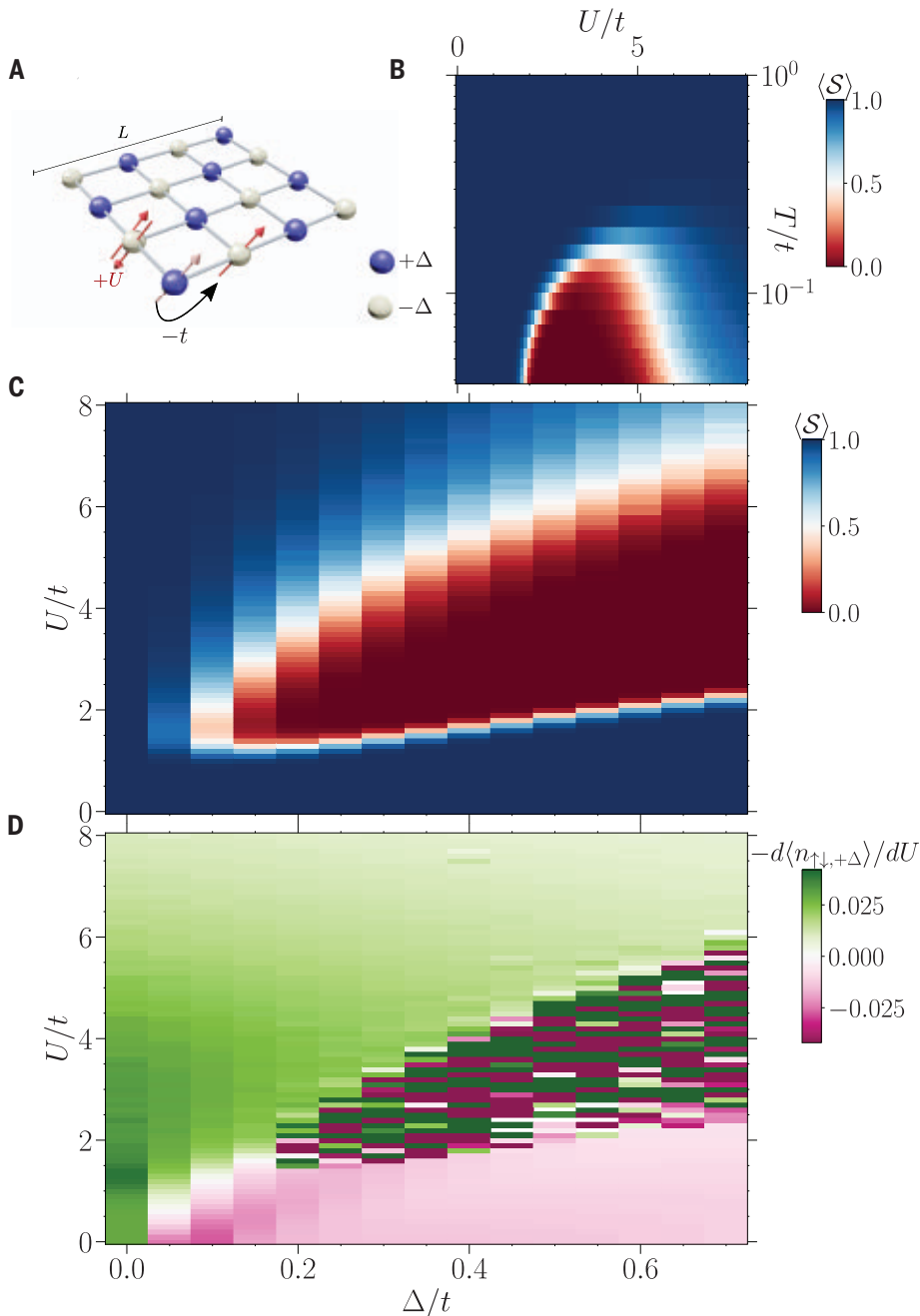


Fig. 2. The SU(2) ionic Hubbard model on the square lattice. (A) Diagram depicting a square lattice with $N = L^2$ sites ($L = 4$ here), accompanied by the relevant terms in \hat{H} . (B) Contour plot of the average $\langle S \rangle$ in the U/t versus T/t plane, with staggered potential $\Delta/t = 0.5$. (C) Contour plot of $\langle S \rangle$ as a function of the competing parameters U/t and Δ/t at a temperature $T/t = 1/24$. (D) The corresponding derivative of the double occupancy on the $+\Delta$ sites at the same parameters as in (C). In all data, Trotter discretization is chosen as $t\Delta\tau = 0.1$ and the lattice size is $L = 12$. Finite-size analyses are shown in figs. S3 and S4.

AF insulator only for U exceeding a critical U_c . Early DQMC and series expansion calculations estimated $U_c \sim 4t$ (42), with subsequent studies (16, 17) yielding the more precise value $U_c/t = 3.869$.

The upper panel of Fig. 1B gives $\langle S \rangle$ in the U - T plane. By introducing a small, nonzero $\mu = 0.1$, we can induce a SP that begins to develop at $T/t \sim 0.1$. As T is lowered further, the average sign deviates from $\langle S \rangle = 1$ in a relatively narrow window of U/t close to the known U_c . In turn, we show the $\langle S \rangle$ on the U - μ plane at fixed $T/t = 0.05$ in the lower panel of Fig. 1B. For large μ , the sign is small for a broad swath of interaction values. As μ decreases, this region pinches down until it terminates close to U_c ; the dashed white line displays the minimum $\langle S \rangle$ in the relevant range. In both panels, the behavior of the average sign outlines the quantum critical fan that extends above the QCP.

Figure 1C shows a finite size extrapolation of $\langle S \rangle$ in the $1/L$ - U plane, where L is the linear lattice size. Just as $\langle S \rangle$ worsens with increasing β , it is also known to deviate increasingly from $\langle S \rangle = 1$ with growing L (29). The extrapolation $L \rightarrow \infty$ clearly reveals U_c in the presence of a small chemical potential. So far, we have exclusively used $\langle S \rangle$ in locating U_c . Original investigations used more “traditional” (and more physical) correlation functions such as the AF structure factor and conductivity. For comparison with the evolution of $\langle S \rangle$, Fig. 1D shows one example, the rate of change of the double occupancy $\langle n_{\uparrow\downarrow} \rangle$, again in the $1/L$ - U plane. A peak in $-d\langle n_{\uparrow\downarrow} \rangle/dU$ indicates where local moments $\langle m^2 \rangle$ are growing most rapidly. The similarity between Fig. 1, C and D, emphasizes how $\langle S \rangle$ is tracking the physics of the model in a way markedly similar to $\langle m^2 \rangle$. The combination of the three limits, μ , β , and L , unequivocally points out the QCP location; the supplementary materials (7) contain further discussion and other observables. Two of these limits can be simultaneously approached by fixing the ratio L_c/L^z with z , the dynamical critical exponent (43).

Ionic Hubbard BI to AF transition

Among the different types of nonconducting states are BIs, in which the chemical potential lies in a gap in the noninteracting density of states, and MIs, in which strong repulsive interactions prevent hopping at commensurate filling. The evolution from BI to MI is a fascinating issue in condensed-matter physics (18–20, 44–46). In the ionic Hubbard model that we investigated here, a staggered site energy $\mu_i = \pm\Delta$ on the two sublattices of a square lattice (Fig. 2A) leads to a dispersion relation $E(k) = \pm\sqrt{\varepsilon(k)^2 + \Delta^2}$ with $\varepsilon(k) = -2t(\cos k_x + \cos k_y)$. The resulting density of states vanishes in the range $-\Delta < E < +\Delta$ in which the lattice is half-filled, resulting in a BI.

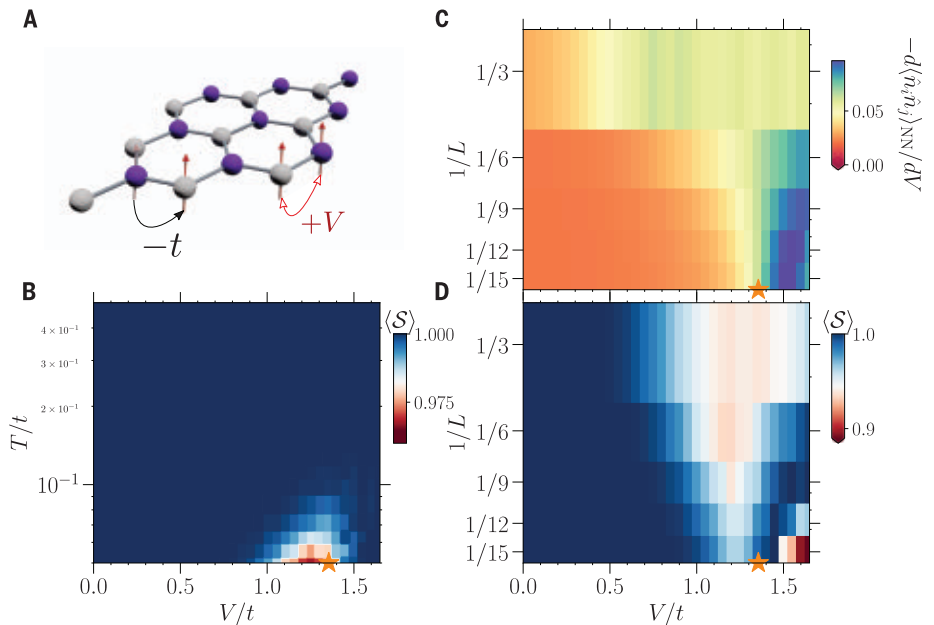


Fig. 3. The $U(1)$ Hubbard model on the honeycomb lattice. (A) Schematics of the spinless fermion Hamiltonian (Eq. 2) with NN interaction on a lattice with $L = 3$. (B) Temperature extrapolation of the average $\langle S \rangle$ as a function of the NN interaction V/t for a lattice with $L = 9$. (C) Extrapolation of the derivative of the NN correlation with respect to V , with the inverse of the linear size L for a range of interactions at a temperature T that scales with the system size $T/t = 0.0375/L\Delta\tau$. (D) Same as (C) but showing the average sign. Here, $\langle S \rangle$ marginally increases when tackling larger sizes, indicating that the dynamical critical exponent z in the scaling with L_c/L^z is > 1 (7, 43); we used $z = 1$ above. In all data, Trotter discretization is chosen as $t\Delta\tau = 0.1$. As for the $SU(2)$ case, the star marker depicts the best known value of the interactions that trigger the Mott insulating phase, here with CDW order at the ground state (41). Figure S5 reports a finite-temperature analysis of physical quantities, and fig. S6 analyzes the $\Delta\tau$ influence on $\langle S \rangle$.

The occupation of the “low-energy” sites $\mu_i = -\Delta$ is greater than that of the “high-energy” sites $\mu_i = +\Delta$, so that there is a trivial CDW order associated with an explicit breaking of the sublattice symmetry in the Hamiltonian.

An onsite repulsion U disfavors this density modulation: The potential energy $U\langle n_{\uparrow\downarrow} \rangle$ is higher than that for a uniform occupation. Thus, the driving physics of the BI, the staggered site energy Δ , and that of the MI, the repulsion U , are in competition. Although the simplest scenario is a direct BI to MI transition with increasing U , one of the more exotic possible outcomes is the emergence of a metallic phase when these two energy scales are in balance and neither type of insulator can dominate the behavior. Past DQMC simulations suggest that this less trivial case occurs and have used the temperature dependence of the DC conductivity to bound the metallic phase (46, 47).

Here, we investigated how this physics might be reflected in the average sign. Figure 2B shows $\langle S \rangle$ in the U/t - T/t plane at $\Delta = 0.5t$. As T is lowered, $\langle S \rangle$ deviates from unity for a range of intermediate U values. Figure 2C gives the behavior in the U/t - Δ/t plane at fixed low $T = t/24$. The central result is that $\langle S \rangle$ is small in a region that maps well with

the previously determined boundaries of the metallic phase (46, 47). This is emphasized by comparison with Fig. 2D, which uses one of the “traditional” methods for phase boundary location, namely the behavior of the double occupancy. The BI has a low occupancy and thus very low double occupancy on the $+\Delta$ sites. Increasing U smooths out the density so that the double occupancy on the $+\Delta$ sites increases: $d\langle \hat{n}_{\uparrow\downarrow,+\Delta} \rangle/dU > 0$. By contrast, in the MI region, $U \gtrsim \Delta$, the physics is that of the usual Hubbard Hamiltonian and double occupancy decreases as U grows: $d\langle \hat{n}_{\uparrow\downarrow,+\Delta} \rangle/dU < 0$.

In the CM region between BI and MI, however, obtaining a relevant signal-to-noise ratio for the traditional observables is exponentially challenging precisely because the average sign vanishes in this region. The “phase diagram” obtained by using $\langle S \rangle$ (Fig. 2C) is very similar to that given by the physical observable, the rate of change of double occupancy with U (Fig. 2D).

As in the determination of the QCP for the spinful Hubbard model on a honeycomb lattice, $\langle S \rangle$ emerges as more than a mere nuisance, but also as a harbinger of the physics. An in-depth similarity between these two situations is discussed in the supplementary materials

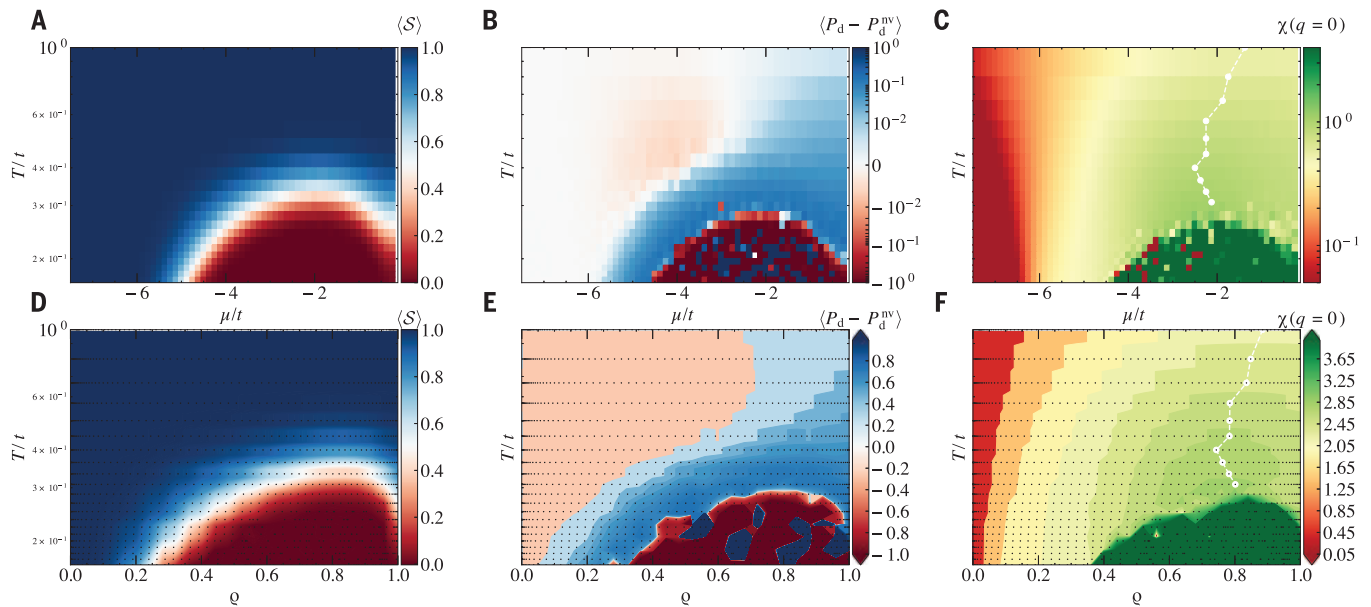


Fig. 4. Square lattice Hubbard model. (A) Temperature dependence of the average $\langle S \rangle$ as a function of the chemical potential μ/t for a lattice with $L = 16$, $U/t = 6$, and next-NN hopping $t'/t = -0.2$, values chosen to be close to those in cuprate materials. (B) d -wave pair susceptibility (with the non-vertex contribution subtracted) for the same parameters. (C) Corresponding static spin susceptibility $\chi(q = 0)$. The white markers describe its peak for values at which the average sign is large enough to allow a reliable calculation, which encompasses the pseudogap regime. See the supplementary materials (7)

for a perspective on the onset of this regime. (D to F) Corresponding diagrams when converting to the calculated average density. The black markers depict the actual average density extracted from the regular mesh of μ used in the upper panels and where an interpolation of the data is performed. In all data, Trotter discretization is chosen as $t\Delta\tau = 0.0625$. A finite-size analysis (fig. S7), different pairing channels (fig. S8), and the behavior of the spectral weight (figs. S9 and S10) is given in the supplementary materials (7). Equivalent results for $t' = 0$ are reported in fig. S11.

(7), where we show that the BI-metal QCP is again uniquely identified by the $1/L$ scaling of $\langle S \rangle$, in precise analogy with the honeycomb case. These results suggest the existence of a quantum critical region associated with the CM phase and the vanishing $\langle S \rangle$.

An “unnecessary” SP

We now consider spinless fermions, in which the on-site Hubbard interaction U , made irrelevant by the Pauli principle, is replaced by an intersite repulsion V ,

$$\hat{H} = -t \sum_{\langle ij \rangle} (\hat{c}_i^\dagger \hat{c}_j + \hat{c}_j^\dagger \hat{c}_i) + V \sum_{\langle ij \rangle} \hat{n}_i \hat{n}_j \quad (2)$$

Equation 2 provides an example of a model in which the SP can be completely solved by using special techniques such as the fermion bag in the continuous time QMC approach (35) or by going to a different basis using a Majorana representation of the fermions in the AFQMC method (41), as long as the system is on a bipartite lattice and $V > 0$. The standard Blankenbecler, Scalapino, and Sugar approach (28), on the other hand, manifestly displays a SP in the low-temperature regime. Nevertheless, to study the sign and its connection with the underlying physics, we used a Blankenbecler, Scalapino, and Sugar-based algorithm to investigate the system on a

honeycomb lattice (Fig. 3A). Consideration of this “unnecessary” SP allows us to address fundamental issues related to the influence of different algorithms on the connection between the SP and the physics of model Hamiltonians.

At $T = 0$, the model displays a QPT between a Dirac semimetal and an insulating staggered CDW state as the interaction is tuned through a critical value V_c (22). At large V , the repulsive interaction favors a CDW state, distinguished from that of the ionic Hubbard model by the fact that there is no staggered external field here; the CDW phase is a result of spontaneous symmetry breaking. As V is reduced, increasing quantum fluctuations caused by hopping finally destroy the CDW state, resulting in a Dirac semimetal for $V < V_c$. Accurate estimates based on SP-free methods yield $V_c \sim 1.35t$ (41).

In Fig. 3B, we show a map of the temperature extrapolation of $\langle S \rangle$ as a function of V . The sign shows a clear reduction around the known V_c (denoted by the star). Figure 3D shows the spatial lattice size dependence of the sign, and Fig. 3C, once again, a more “traditional” local variable, the derivative of the nearest-neighbor (NN) density-density correlation $\langle \hat{n}_i \hat{n}_j \rangle_{NN}$ with respect to V . In the CDW phase, increasing V strengthens the staggered order, reducing the NN density correlations,

and thus $-d\langle \hat{n}_i \hat{n}_j \rangle_{NN}/dV$ is positive. Conversely, the effect is much smaller in the semimetal state, where the derivative is close to zero. The transition V_c is characterized by a clear downturn in this quantity, which becomes progressively sharper as L increases, as Fig. 3C shows. This variable thus serves as a physical indicator of the QPT, allowing a comparison of Fig. 3, C and D, to demonstrate the connection between the QCP and the behavior of $\langle S \rangle$. In this model, $\langle S \rangle$ is sufficiently well behaved that a study of the finite-temperature CDW transition with DQMC is feasible (7) without having to resort to SP-free approaches (48).

Square lattice Hubbard model

The essential elements of the physics of the cuprate superconductors include antiferromagnetic order at and near one hole per CuO_2 cell, a superconducting dome upon doping, which typically extends to densities $0.6 \leq \rho \leq 0.9$, and a “pseudogap”/“strange metal” phase above the dome (23, 49). There are many quantitative, experimentally based phase diagrams of different materials that determine the regions occupied by these phases (50). Likewise, there are computational studies of individual (ρ, T, U) points establishing magnetic/charge order (51), linear resistivity (52), a reduction in the spectral weight for spin excitations (53, 54), and d -wave pairing (55, 56).

Here, we reveal an “SP phase diagram” that bears notable resemblance to the experimental phase diagram. As is well known, the severity of the SP itself precludes determination of d -wave order in DQMC through “traditional” observables such as the associated correlation functions. However, Fig. 4, which is based on the behavior of the sign itself, is suggestive. We report the average sign (Fig. 4A), the enhancement of the d -wave pairing susceptibility over its value in the absence of the pairing vertex (57) (Fig. 4B), and the uniform, static spin susceptibility $\chi(q = 0)$ (Fig. 4C) in the T/t - μ/t plane. Figure 4, D to F, shows analogous plots for the T/t - ρ plane (7).

The most salient features of this “sign phase diagram” are (i) the “dome” of vanishing $\langle S \rangle$ that occurs in a range of densities $0.4 \leq \rho \leq 1$ as T is lowered (Fig. 4D), (ii) the enhancement of d -wave pairing (Fig. 4E) surrounding the sign dome, and (iii) the magnetic properties being also linked to the $\langle S \rangle$ dome: The trajectory tracing the peak value of $\chi(q = 0)$ as T is decreased terminates precisely at the top of the dome (Fig. 4F). In isolation, the comparisons of the behavior of the sign and the pairing and magnetic responses in the square lattice Hubbard model appear likely to be coincidental. Indeed, the fact that the sign is worse precisely for optimal dopings has been previously discussed, but thought to be just “bad luck” (32, 57–59). However, that the known QCPs of the three models discussed in the preceding three sections can be quantitatively linked to the behavior of $\langle S \rangle$ suggests that the sign dome might actually be indicative of the presence of d -wave superconductivity.

Discussion and outlook

Early in the history of the study of the SP, a simple connection was noted between the fermionic physics and negative weights in AFQMC: If one artificially constructs two Hubbard-Stratonovich field configurations, one associated with two particle exchanging as they propagate in imaginary time and another with no exchange, one finds that the associated fermion determinants are negative in the former case and positive in the latter. This interesting observation, however, pertains to low density, that is, to the propagation of just two electrons. Another key observation is that the SP can be viewed as being proportional to the exponential of the difference of free energy densities of the original fermionic problem and the one used with the weights in the Monte Carlo sampling taken to be positive, akin to a bosonic formulation of the problem (13, 32). It highlights how intrinsic the SP is in QMC methods. A last important remark is that ordered phases are often associated with a reduction in the importance of configurations that scramble the sign. This is graphically illustrated in the snap-

shots of (24). Although less crisp, similar effects are seen in AFQMC, for example, in considering the evolution from the attractive Hubbard model to the Holstein model with decreasing phonon frequency ω_0 . Reducing ω_0 acts to increase the effect of the phonon potential energy term \hat{P}^2 in \hat{H} , thereby straightening the auxiliary field in imaginary time.

Here, we have shown that the behavior of the average sign $\langle S \rangle$ in DQMC simulations holds information concerning finite density thermodynamic phases and transitions between them: the QCPs in the semimetal to antiferromagnetic MI transition of Dirac fermions, the BI to CM to correlated insulator evolution of the ionic Hubbard Hamiltonian, and the QCP of spinless fermions (even though a sign-problem free formulation exists). Specifically, a rapid evolution of $\langle S \rangle$ marks the positions of QCPs. We have chosen these models as representative examples of QCP physics of itinerant electrons that have been extensively studied in the condensed-matter physics community but speculate that the result is general. In fact, in a model for frustrated spins in a ladder using a completely different QMC method (stochastic series expansion), similar conclusions can be inferred (60), further corroborating this generality. Likewise, in the square lattice version of the $U(1)$ Hubbard model that we studied here, with an added π flux, it can be shown that in the sign-problem free formulation, the QMC weights, when expressed in terms of the square of Pfaffians (Pf), holds similar information, namely that $\langle \text{sgn}(Pf) \rangle$ departs from 1 close to the QCP for this model (61). These results provide further evidence that the average sign of the QMC weights is inherently connected to the physics of the model in many mutually unrelated models and methods, but an even broader study is necessary to establish this conclusively.

Having established this connection in Hamiltonians with known physics, we have also presented a careful study of the SP for the Hubbard model on a 2D square lattice, which is of central interest to cuprate d -wave superconductivity. The intriguing “coincidence” that the SP is the worst at a density $\rho \sim 0.87$, which corresponds to the highest values of the superconducting transition temperature, has been noted previously (32, 57–59). It is worth emphasizing that we have not here presented any solution to the SP. However, our work does establish the surprising fact that $\langle S \rangle$ can be used as an “observable” that can quite accurately locate QCPs in models such as the spinful and spinless Hubbard Hamiltonians on a honeycomb lattice and the ionic Hubbard model and also provides a clearer connection between the evolution of the fermion sign and the strange metal/pseudogap and supercon-

ducting phases of the iconic square lattice Hubbard model.

REFERENCES AND NOTES

- B. Hammond, W. Lester, P. Reynolds, *Monte Carlo Methods in Ab Initio Quantum Chemistry, Lecture and Course Notes in Chemistry* (World Scientific, 1994), vol. 1.
- R. J. Needs, M. D. Towler, N. D. Drummond, P. López Ríos, J. R. Trail, *J. Chem. Phys.* **152**, 154106 (2020).
- D. Ceperley, *Rev. Mod. Phys.* **67**, 279–355 (1995).
- W. Foulkes, L. Mitás, R. Needs, G. Rajagopal, *Rev. Mod. Phys.* **73**, 33–83 (2001).
- J. Carlson et al., *Rev. Mod. Phys.* **87**, 1067–1118 (2015).
- T. Degrand, C. DeTar, *Lattice Methods for Quantum Chromodynamics* (World Scientific, 2006).
- See the supplementary materials and references therein.
- T. Esslinger, *Annu. Rev. Condens. Matter Phys.* **1**, 129–152 (2010).
- I. Bloch, J. Dalibard, S. Nascimbène, *Nat. Phys.* **8**, 267–276 (2012).
- F. Schäfer, T. Fukuhara, S. Sugawa, Y. Takasu, Y. Takahashi, *Nat. Rev. Phys.* **2**, 411–425 (2020).
- J. Preskill, *Quantum* **2**, 79 (2018).
- G. Clemente et al., *Phys. Rev. D* **101**, 074510 (2020).
- M. Troyer, U.-J. Wiese, *Phys. Rev. Lett.* **94**, 170201 (2005).
- D. Hangleiter, I. Roth, D. Nagaj, J. Eisert, *Sci. Adv.* **6**, eabb8341 (2020).
- Z.-Q. Wan, S.-X. Zhang, H. Yao, Mitigating sign problem by automatic differentiation. arXiv:2010.01141 [cond-mat.str-el] (2020).
- Z. Y. Meng, T. C. Lang, S. Wessel, F. F. Assaad, A. Muramatsu, *Nature* **464**, 847–851 (2010).
- S. Sorella, Y. Otsuka, S. Yunoki, *Sci. Rep.* **2**, 992 (2012).
- M. Fabrizio, A. O. Gogolin, A. A. Nersisyan, *Phys. Rev. Lett.* **83**, 2014–2017 (1999).
- L. Craco, P. Lombardo, R. Hayn, G. Japaridze, E. Müller-Hartmann, *Phys. Rev. B* **78**, 075121 (2008).
- A. Garg, H. R. Krishnamurthy, M. Randeria, *Phys. Rev. Lett.* **112**, 106406 (2014).
- E. F. Huffman, S. Chandrasekharan, *Phys. Rev. B* **89**, 111101 (2014).
- L. Wang, P. Corboz, M. Troyer, *New J. Phys.* **16**, 103008 (2014).
- B. Keimer, S. A. Kivelson, M. R. Norman, S. Uchida, J. Zaanen, *Nature* **518**, 179–186 (2015).
- J. Hirsch, R. Sugar, D. Scalapino, R. Blankenbecler, *Phys. Rev. B* **26**, 5033–5055 (1982).
- D. Ceperley, B. Alder, *J. Chem. Phys.* **81**, 5833–5844 (1984).
- M. A. Lee, K. E. Schmidt, *Comput. Phys.* **6**, 192 (1992).
- P. Henelius, A. W. Sandvik, *Phys. Rev. B* **62**, 1102–1113 (2000).
- R. Blankenbecler, D. Scalapino, R. Sugar, *Phys. Rev. D Part. Fields* **24**, 2278–2286 (1981).
- S. R. White et al., *Phys. Rev. B* **40**, 506–516 (1989).
- S. Zhang, J. Carlson, J. E. Gubernatis, *Phys. Rev. B* **55**, 7464–7477 (1997).
- M. Iazzi, A. A. Soluyanov, M. Troyer, *Phys. Rev. B* **93**, 115102 (2016).
- E. Y. Loh Jr. et al., *Phys. Rev. B* **41**, 9301–9307 (1990).
- C. Wu, S.-C. Zhang, *Phys. Rev. B* **71**, 155115 (2005).
- Z.-X. Li, Y.-F. Jiang, H. Yao, *Phys. Rev. Lett.* **117**, 267002 (2016).
- S. Chandrasekharan, *Phys. Rev. D Part. Fields Gravit. Cosmol.* **82**, 025007 (2010).
- E. Berg, M. A. Metlitski, S. Sachdev, *Science* **338**, 1606–1609 (2012).
- L. Wang, Y.-H. Liu, M. Iazzi, M. Troyer, G. Harcos, *Phys. Rev. Lett.* **115**, 250601 (2015).
- Z.-X. Li, H. Yao, *Annu. Rev. Condens. Matter Phys.* **10**, 337–356 (2019).
- This is just a rough guideline: the precise onset of the SP is determined by lattice geometry, doping (chemical potential), and interaction strength. A catalog of the SP in DQMC for the single-band Hubbard model in different situations is given in (59).
- J. Hirsch, *Phys. Rev. B* **28**, 4059–4061 (1983).
- Z.-X. Li, Y.-F. Jiang, H. Yao, *Phys. Rev. B* **91**, 241117 (2015).
- T. Paiva, R. Scalettar, W. Zheng, R. Singh, J. Oitmaa, *Phys. Rev. B* **72**, 085123 (2005).
- H. Rieger, A. P. Young, *Phys. Rev. Lett.* **72**, 4141–4144 (1994).
- A. Kampf, M. Sekania, G. Japaridze, P. Brune, *J. Phys. Condens. Matter* **15**, 5895–5907 (2003).

45. A. Garg, H. R. Krishnamurthy, M. Randeria, *Phys. Rev. Lett.* **97**, 046403 (2006).
46. N. Paris, K. Bouadim, F. Hebert, G. G. Batrouni, R. T. Scalettar, *Phys. Rev. Lett.* **98**, 046403 (2007).
47. A. Chattopadhyay, S. Bag, H. R. Krishnamurthy, A. Garg, *Phys. Rev. B* **99**, 155127 (2019).
48. S. Hesselmann, S. Wessel, *Phys. Rev. B* **93**, 155157 (2016).
49. A. Damascelli, Z. Hussain, Z.-X. Shen, *Rev. Mod. Phys.* **75**, 473–541 (2003).
50. P. A. Lee, N. Nagaosa, X.-G. Wen, *Rev. Mod. Phys.* **78**, 17–85 (2006).
51. H.-C. Jiang, T. P. Devereaux, *Science* **365**, 1424–1428 (2019).
52. E. W. Huang, R. Sheppard, B. Moritz, T. P. Devereaux, *Science* **366**, 987–990 (2019).
53. M. Randeria, N. Trivedi, A. Moreo, R. T. Scalettar, *Phys. Rev. Lett.* **69**, 2001–2004 (1992).
54. A.-M. S. Tremblay, B. Kyung, D. Sénéchal, *Low Temp. Phys.* **32**, 424–451 (2006).
55. T. A. Maier, M. Jarrell, T. C. Schulthess, P. R. C. Kent, J. B. White, *Phys. Rev. Lett.* **95**, 237001 (2005).
56. T. A. Maier et al., *Nat. Commun.* **7**, 11875 (2016).
57. S. R. White, D. J. Scalapino, R. L. Sugar, N. E. Bickers, R. T. Scalettar, *Phys. Rev. B* **39**, 839–842 (1989).
58. D. Scalapino, “Does the Hubbard model have the right stuff?,” in *Proceedings of the International School of Physics*, R. A. Broglia, J. R. Schrieffer, eds. (North-Holland, 1994); pp. 95–122.
59. V. Iglavik, E. Khatami, R. Scalettar, *Phys. Rev. B* **92**, 045110 (2015).
60. S. Wessel, B. Normand, F. Mila, A. Honecker, *SciPost Phys.* **3**, 005 (2017).
61. A. Goetz, S. Beyl, M. Hohenadler, F. F. Assaad, Langevin dynamics simulations of the two-dimensional Su-Schrieffer-Heeger model. [arXiv:2102.08899](https://arxiv.org/abs/2102.08899) [cond-mat.str-el] (2021).
62. R. Mondaini, S. Tarat, R. T. Scalettar, Data for: Quantum critical points and the sign problem, Zenodo (2021); <https://doi.org/10.5281/zenodo.5575501>.
63. “QUEST: Quantum Electron Simulation Toolbox” (UC Davis, 2009); https://www.cs.ucdavis.edu/~bai/QUEST_public/.

ACKNOWLEDGMENTS

We acknowledge insightful discussions with S.-J. Hu and H.-Q. Lin. **Funding:** R.T.S. was supported by grant DE-SC0014671 funded by the US Department of Energy, Office of Science. R.M. acknowledges support from the National Natural Science

Foundation of China (NSFC grants NSAF-U1930402, 11974039, 12050410263, and 12111530010). Computations were performed on the Tianhe-2JK at the Beijing Computational Science Research Center. **Author contributions:** R.T.S. proposed the original idea for the honeycomb lattice; R.M. suggested its extension to the ionic and spinless fermion cases. All authors considered the square lattice Hubbard model, performed numerical simulations, analyzed data, and cowrote the manuscript. **Competing interests:** The authors declare no competing interests. **Data and materials availability:** All data needed to reproduce the conclusions in this study are present in the main text or the supplementary materials. Data presented in the figures are deposited at Zenodo (62), and input files for QUEST codes, which can be used to reproduce the results, are available at (63).

SUPPLEMENTARY MATERIALS

science.org/doi/10.1126/science.abg9299
Supplementary Text
Figs. S1 to S11
References (64–167)

4 February 2021; accepted 15 December 2021
10.1126/science.abg9299

PLANT SCIENCE

Gametophyte genome activation occurs at pollen mitosis I in maize

Brad Nelms^{1*} and Virginia Walbot²

Flowering plants alternate between multicellular haploid (gametophyte) and diploid (sporophyte) generations. Pollen actively transcribes its haploid genome, providing phenotypic diversity even among pollen grains from a single plant. In this study, we used allele-specific RNA sequencing of single pollen precursors to follow the shift to haploid expression in maize pollen. We observed widespread biallelic expression for 11 days after meiosis, indicating that transcripts synthesized by the diploid sporophyte persist long into the haploid phase. Subsequently, there was a rapid and global conversion to monoallelic expression at pollen mitosis I, driven by active new transcription from the haploid genome. Genes showed evidence of increased purifying selection if they were expressed after (but not before) pollen mitosis I. This work establishes the timing during which haploid selection may act in pollen.

Plants do not make gametes directly after meiosis; instead, they form a multicellular haploid organism called the gametophyte. Although the size of the gametophyte is reduced in flowering plants (2 or 3 cells for male pollen and 4 to 15 cells for the female embryo sac), the haploid generation retains a high degree of independence. Gametophytes actively transcribe genes, with more than 60% of the genome expressed postmeiotically in pollen (1). Many genes are required during the haploid phase, as even modest chromosome deletions are not transmitted (2, 3) and gametophytic mutants are routinely isolated in plant genetic screens (4). This widespread haploid expression exposes a large portion of the genome to natural selection

in the gametophyte. Pollen, in particular, has a high capacity for selection because of large population sizes and intense competition during dispersal, pollen tube growth, and fertilization. Unsurprisingly, pollen selection has diverse consequences (5, 6): It reduces inbreeding depression (7), increases offspring fitness (8), and contributes to sex chromosome evolution (9) and sex-specific differences in recombination rates (10). Pollen selection has further been employed in breeding programs to derive cold-tolerant crop varieties (11) and has been proposed as a key factor that drove the origin of flowering plants (12).

When does the haploid gametophyte genome take control from the genome of its diploid sporophyte parent? The haploid phase of pollen development is a complex and dynamic process that, in maize, lasts 20 days (13) (Fig. 1A)—roughly one-third of the time from seed to anthesis. There is no guarantee that gene products will be derived from the haploid genome immediately after meiosis. By comparison,

the maternal genome controls most early events in animal postfertilization development, followed by a maternal-to-zygotic transition in which degradation of maternal products is coordinated with zygotic genome activation (14). Does an analogous parent-to-offspring transition occur in pollen? If plants provision some portion of pollen development with diploid-derived gene products, the timing and intensity of haploid selection would be constrained. We obtained allele-specific RNA sequencing (RNA-seq) data from single pollen precursors across 26 days of development, from the beginning of meiosis through pollen shed. These data allowed us to identify when expression from the haploid genome began and to follow its progress throughout time and on a gene-by-gene basis.

Allele-specific RNA-seq of single pollen precursors

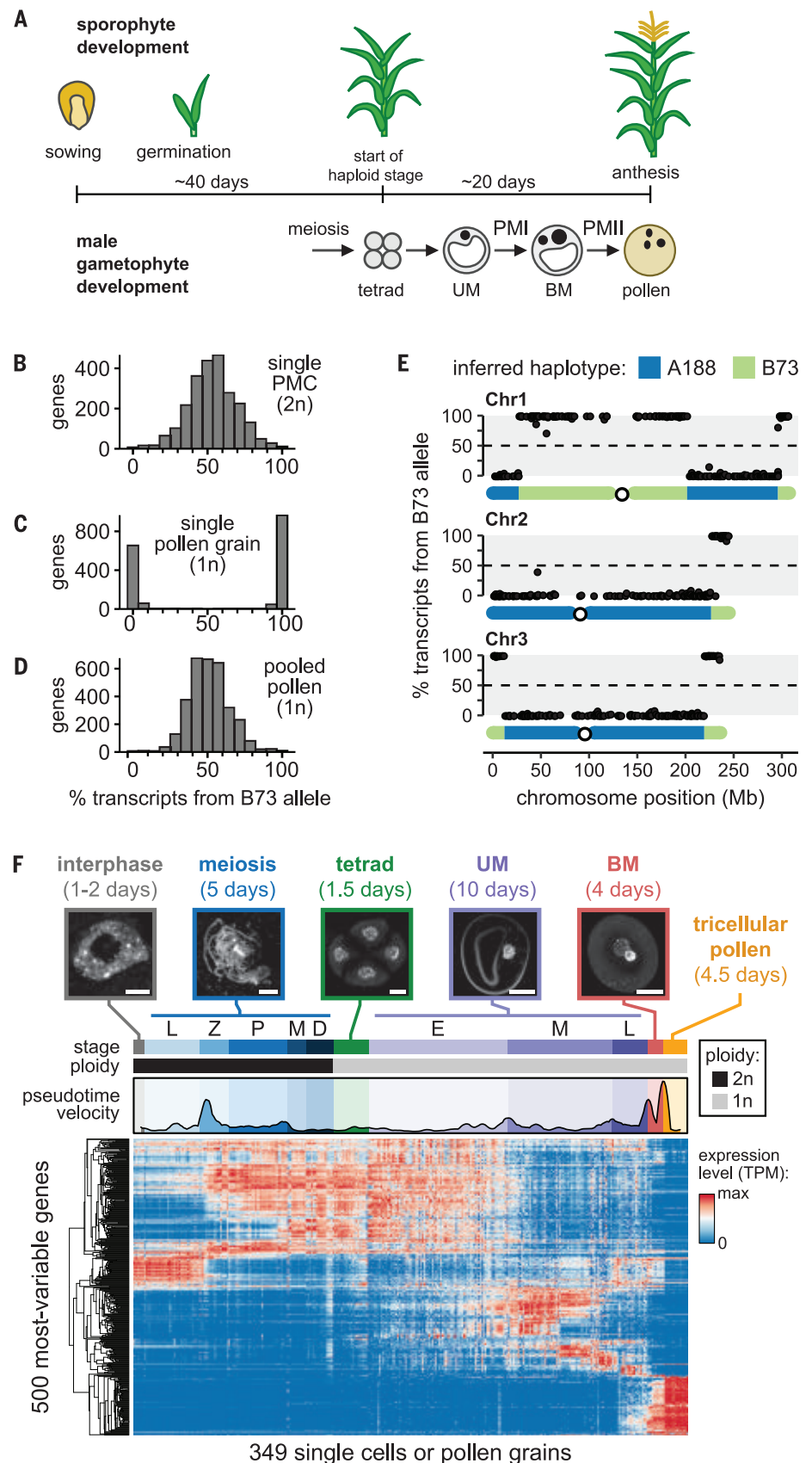
To test our ability to separate the contributions of parent (sporophyte) and offspring (gametophyte) to the transcriptome of single pollen precursors, we first isolated single diploid pollen mother cells (PMCs; i.e., cells poised to initiate meiosis) and haploid pollen grains from an F₁ hybrid between the A188 and B73 inbred maize lines. The PMC and mature pollen stages are separated by 26 days. We detected a mean of 364,003 transcripts per sample (unique molecular identifiers; see materials and methods). On average, 32.4% of transcripts could be unambiguously mapped to either the A188 or B73 parental alleles, hereafter referred to as genoinformative transcripts. At least one genoinformative transcript was detected for 16,730 genes (table S1).

In single PMCs, most genes were expressed from both alleles (Fig. 1B), as expected for diploid genome expression. By contrast, in

¹Department of Plant Biology, University of Georgia, Athens, GA 30606, USA. ²Department of Biology, Stanford University, Stanford, CA 94305, USA.

*Corresponding author. Email: nelms@uga.edu

Fig. 1. Allele-specific RNA-seq of single pollen precursors. (A) Timeline of sporophyte and (male) gametophyte development. (B to D) Histogram of the fraction of transcripts matching the B73 allele for genes in (B) a single diploid PMC or (C) a single pollen grain, as well as (D) the average across pollen grains (computationally pooled data; $N = 15$ pollen grains). n, number of chromosomes. (E) Allelic bias of genes is correlated with their genomic location in a single pollen grain. The inferred haplotypes are shown below each graph. It is unclear whether the rare genes with apparent biallelic expression (non-0% or non-100% on the y axis) are the result of biological factors or technical noise; no genes were consistently biallelically expressed in multiple pollen grains (fig. S1 and 2C). In (B) to (E), all genes with at least 10 genoinformative transcripts are shown. (F) Single pollen precursors and pollen grains were isolated from maize anthers for RNA-seq. (Top) Exemplar microscopy images of DAPI (4',6-diamidino-2-phenylindole)-stained material used for sample staging. (Middle) Pseudotime velocity, which quantifies the rate of expression change over time (17); peaks indicate periods of rapid gene expression change. (Bottom) Heatmap of gene expression for the 500 most-variable genes. Scale bars are 5 μm for interphase and meiosis and 20 μm for later stages. Substages of meiosis: L, leptotene; Z, zygotene; P, pachytene; M, meiosis I division; D, dyad. UM substages: E, early; M, middle; L, late.



mature pollen grains, genes were expressed almost exclusively from one allele (Fig. 1C). Although multiple biological mechanisms can produce monoallelic expression, two pieces of evidence confirm that pollen monoallelic expression reflects expression from the haploid genome. First, there was no bias toward either the A188 or B73 alleles (Fig. 1D), as would be predicted by parental imprinting or inbred-specific effects such as presence-absence variation. Second, extensive blocks of linked genes on chromosome arms were expressed from the same parental allele, with infrequent shifts to the alternate parental allele, as is characteristic of meiotic recombination (Fig. 1E and fig. S1). Using the allele-specific expression data, we infer an average of 1.36 crossovers per chromosome (fig. S2A), with more-frequent crossovers toward the telomeres (fig. S2B and table S2), in agreement with the established crossover frequency (15) and distribution (16) in maize. Thus, RNA-seq of single cells and pollen grains can distinguish expression originating from the diploid and haploid genomes.

Gene expression during pollen development

We next profiled 349 single pollen precursors collected from 67 staged anthers, with dense sampling from premeiotic interphase through mature pollen (Fig. 1F and table S2). To facilitate sample staging, precursors were collected from one anther for RNA-seq while the remaining two anthers from the same floret were fixed for microscopy. Reproducible correspondence was observed between gene expression and the microscopic stage (Fig. 1F). Because we will be comparing bi- and tricellular stages of pollen development with earlier unicellular stages, we collectively refer to these samples as single pollen precursors rather than single cells.

Gene expression did not change uniformly during development but rather showed periods of rapid change interspersed with periods of relative stasis. There was a large shift in gene expression during early meiotic prophase I (Fig. 1F and fig. S3), consistent with our previous description of an early prophase transcriptome rearrangement (17). This was followed by several smaller expression changes during the rest of prophase I, a comparably static transcriptome from metaphase I through the early unicellular microspore (UM) stage, and another large shift in expression between UMs and bicellular microspores (BMs). We found distinct temporal expression patterns for many gene categories (tables S4 and S5), including transcription factors, genes involved in meiotic recombination and synapsis (fig. S4), and phased small RNA precursors (fig. S5). This dataset provides a time course of gene expression throughout meiosis and pollen development.

Timing and extent of haploid expression

To follow the shift from diploid to haploid expression, we first compared the proportion of genes with biallelic and monoallelic expression in single precursors at each stage (Fig. 2A). Gene expression was categorized as monoallelic if >80% of transcripts were from a single allele and as biallelic otherwise. We observed biallelic expression for the majority of genes during meiosis I (median of 83.5% biallelic genes per cell; Fig. 2A) while the cells were still diploid. Cells at the haploid tetrad and UM stages displayed a similar level of biallelic expression, with a median of 82.5% of genes with biallelic expression per cell (interquartile range: 79.6 to 84.5%). Thus, premeiotic (biallelic) transcripts persist until the end of the UM stage, 11 days after meiosis. Subsequently, a rapid conversion to monoallelic expression occurred around the time of pollen mitosis I (PMI), with a median of 99.1 and 99.5% of genes with monoallelic expression in BMs and pollen grains, respectively. Linked genes were consistently expressed from the same allele in BMs and pollen but not in earlier stages (Fig. 2A, right, and fig. S6), a characteristic sign of haploid genome expression. Thus, the haploid microspore is provisioned with sporophytic transcripts, followed by a sharp transition to gametophytic expression around PMI.

Most genes had biallelic expression through PMI, but does a gene cohort exist with earlier expression from the haploid genome? To answer this, we needed to distinguish haploid expression from other causes of monoallelic expression for individual genes. One distinctive characteristic of haploid expression is that it does not produce any bias toward a specific allele; haploid-expressed transcripts will match the A188 allele in some precursors but the B73 allele in others, depending on the precursor haplotype (Fig. 2B and fig. S7). By contrast, most other causes of monoallelic expression result in a consistent skew toward one allele. For instance, in diploid meiotic cells 5.5% of genes were expressed monoallelically (>80% of transcripts from the most-abundant allele); however, such genes were consistently biased toward either the B73 or the A188 allele, so their expression can be distinguished from haploid expression (Fig. 2C). In UMs, 90.0% of genes had biallelic expression and only 0.1% had monoallelic expression (Fig. 2D and fig. S8; the remaining 9.9% were B73- or A188-biased). In the following stage (BMs), the reverse was true: 0.3% of genes had biallelic expression and 93.3% of genes had monoallelic expression. Thus, the shift to haploid expression is largely all-or-none: We found no evidence for genes that are expressed from the haploid genome before PMI or, conversely, that persist as biallelically expressed

transcripts beyond PMI. There may be early haploid-expressed genes that we did not sample in this study, as only 1068 genes had a sufficient number of genoinformative transcripts in the UM stage to infer haploid expression; however, any such genes would be rare exceptions or genes with a consistently low level of expression.

Conservation of gametophyte-expressed genes

In many species, genes expressed in mature pollen show evidence for increased selection (both purifying and adaptive) compared with those in the genomic background (18, 19). One proposed explanation is that selection may be more efficient on the haploid generation (18, 19). Because our data show that the haploid genome becomes active primarily after PMI—midway through pollen development—we asked whether there were differences in the average rate of nonsynonymous to synonymous substitutions (d_n/d_s) in genes expressed at different times in pollen development. We focused on genes with moderate or greater expression at each stage [≥ 100 transcripts per million (TPM)] because there was a nonmonotonic relationship between expression level and d_n/d_s at low levels of expression (fig. S9), complicating the interpretation for low-abundance transcripts. Genes expressed at ≥ 100 TPM after meiosis but not after PMI (i.e., genes expressed in the tetrad or UM stages but not later) showed a similar distribution of d_n/d_s compared with those in the genomic background (Fig. 3A and fig. S9). By contrast, genes expressed after PMI had a 30.7% lower median d_n/d_s , consistent with purifying selection acting in the haploid gametophyte. This stage-dependent change in d_n/d_s may be explained by the provisioning of haploid pollen precursors with diploid transcripts, eliminating heritable phenotypic variation until after PMI.

We next estimated the fraction of genes expressed in the diploid sporophyte that might be subject to haploid selection in pollen. To identify sporophyte-expressed genes, we obtained expression data from whole seedlings (roots and shoots), defining sporophytic genes as those expressed in either seedlings or diploid pollen precursors. Consistent with prior results (1, 20), we found that a large fraction of the genome is expressed during both diploid and haploid stages: 87.3% of genes had detectable transcripts in both the sporophyte and gametophyte (Fig. 3B), and 54.0% were expressed at ≥ 100 TPM in both (Fig. 3C). Of these, a substantial portion were expressed after PMI and thus potentially subject to haploid selection (Fig. 3, B and C); this subset had a significantly lower median d_n/d_s (Fig. 3D). The haploid expression of these genes likely contributes to lowering the genetic load in diploid plants.

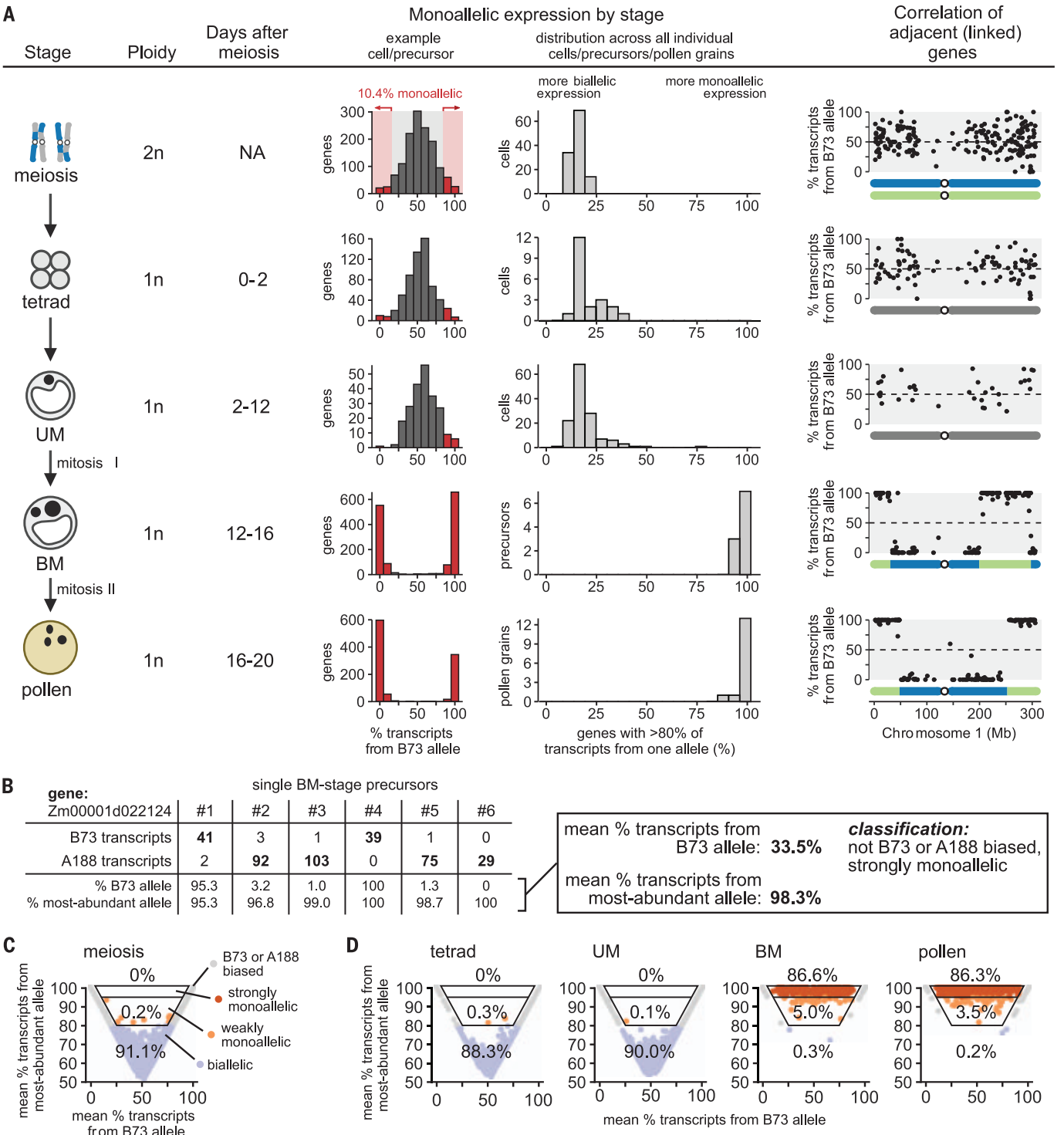


Fig. 2. Timing of haploid expression during pollen development. (A) Table showing the proportion of monoallelic expression for each stage in pollen development. Column three: mean number of days after meiosis when each stage begins and ends (13). NA, not applicable. Column four: histogram of genes, showing the fraction of transcripts matching the B73 allele in a representative precursor. Column five: histogram of precursors, showing the percentage of monoallelic genes in all precursors at a given stage. Column six: percentage of transcripts matching the B73 allele for each gene, by location on chromosome 1. **(B)** Expression data from individual BMs for *Zm00001d022124*, a representative haploid-expressed gene. This gene

falls in the “strongly monoallelic” category in (C). Only BMs with at least 10 genoinformative transcripts are shown; see fig. S7 for the complete data for this and other example genes. **(C and D)** Scatter plots showing the mean percentage of transcripts matching the B73 allele versus the mean percentage matching the most-abundant allele within a precursor for each gene, by stage. The two boxed regions near the top of the plot highlight genes with strong monoallelic expression (red dots; >95% from the most-abundant allele) and weak monoallelic expression (orange dots; 80 to 95% from the most-abundant allele), excluding genes with a consistent bias toward a specific parental allele (gray dots).

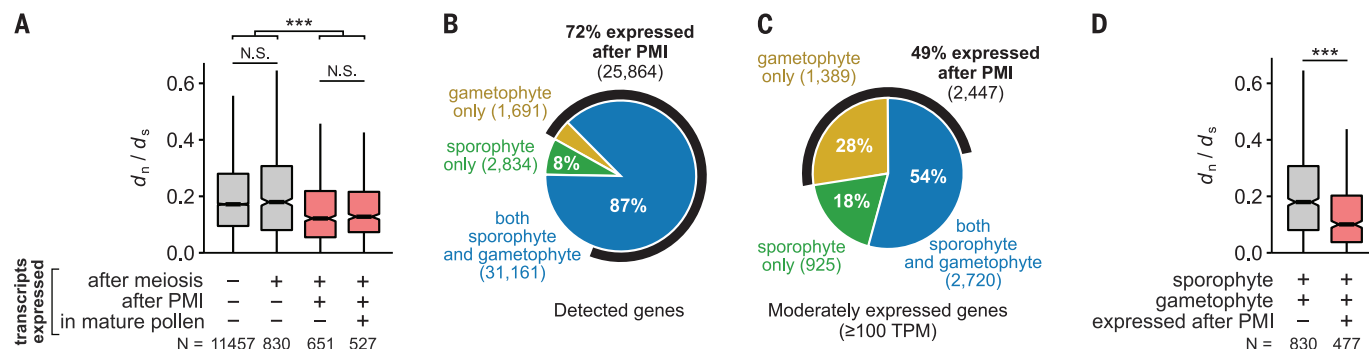


Fig. 3. Conservation of gametophyte-expressed genes. (A) Ratio of the number of nonsynonymous substitutions per nonsynonymous site (d_n) to the number of synonymous substitutions per synonymous site (d_s) for genes expressed at different times in pollen development. Categories of genes expressed after PMI are shaded red. N, number of genes. (B and C) Proportion of genes detected (B) or expressed at ≥ 100 TPM (C) in the sporophyte, gametophyte, or both. The number of genes expressed after PMI is also indicated. (D) d_n/d_s

for genes expressed in both the gametophyte and sporophyte stages, separated on the basis of whether they were expressed after PMI. For (A) and (D), only genes expressed at ≥ 100 TPM were considered. Box plots show the median (horizontal line), interquartile range (IQR; shaded area), and whiskers extending up to 1.5 times the IQR. Gene categories expressed after PMI are shaded red. *** $P < 0.001$; Wilcoxon test adjusted for multiple hypothesis testing with Holm's method. N.S., not significant.

Widespread gametophyte genome activation at PMI

What is the contribution of new transcription versus transcript turnover to the shift to haploid expression? RNA dynamics usually cannot be inferred from steady-state transcript levels alone, because opposing changes in the rates of RNA synthesis and degradation can produce similar effects on transcript abundance. However, our data provide a way to separate synthesis from degradation, because during the haploid phase any new transcription can come from only one allele. We find that the mean number of transcripts per precursor changed substantially during pollen development (Fig. 4A), suggesting large differences in the relative rate of new synthesis versus that of degradation between stages. The number of transcripts per cell decreased steadily from the peak during early meiosis to the minimum at the UM stage. This was followed by a sharp, 7.5-fold increase in the total number of transcripts per precursor between late UMs and BMs (95% confidence interval = 3.0- to 14.2-fold; bootstrap test), indicating that substantial new transcription activity may drive the shift to monoallelic expression during this period. Indeed, 7361 genes had at least a twofold increase in absolute transcript abundance between late UMs and BMs (Fig. 4B), and this increase was attributable to the more-abundant (haploid) allele (Fig. 4C). By contrast, the less-abundant allele remained relatively constant between UMs and BMs (median fold change of 0.02; Fig. 4D). This suggests that premeiotic (biallelic) transcripts persist into the BM stage for many genes but that a large increase in new transcription overtakes preexisting transcript levels to produce a net shift toward monoallelic expression. Thus, the transition to haploid expression is driven by

new transcription and gametophyte genome activation, with degradation of sporophytic transcripts playing a relatively minor role at the transition.

De novo motif analysis identified the RY repeat (CATGCA[TG]) as significantly enriched in the promoters of the 200 most up-regulated genes during PMI, with 35 of 200 promoters (17.5%) having a perfect match to the full RY repeat (6.1-fold enrichment; $P = 7.1 \times 10^{-15}$, Fisher's exact test) and 72 promoters (36%) containing the minimal CATGCA motif (2.4-fold enrichment; $P = 6.2 \times 10^{-9}$, Fisher's exact test). The RY repeat is the binding site for three paralogous transcription factors (ABI3, FUS3, and LEC2) that regulate embryogenesis in *Arabidopsis* (21). Although the RY repeat has no known function in pollen development, conserved RY repeats have been observed in the pollen-specific β -expansin genes (22). This sequence may serve as the binding site for a transcription factor that contributes to gametophyte genome activation.

Gene regulation before PMI

Before PMI, there appeared to be very little new transcription from the haploid genome, as evident in the continued biallelic status of most transcripts (Fig. 2). There were, however, clear changes in relative transcript abundance entering the mid- and late-UM stages (Fig. 1F and tables S4 and S5). To understand how the transcriptome might change in the absence of new transcription, we examined the absolute transcript abundance attributable to each allele for UM-expressed genes. Most genes showed biallelic transcript loss in UMs, ranging from rapid loss (fig. S11A) to slower degradation over time (fig. S11B). Thus, differences in mRNA half-life explain some expression changes during the UM stage. Many

genes also had a biallelic increase in transcripts within UMs (fig. S11, C and D). What could cause a biallelic transcript increase in a haploid cell? One possibility is that these transcripts were synthesized premeiotically but then stored and not processed until later. Our sequencing libraries enrich for polyadenylated RNA and consequently do not detect stored RNAs with a short or missing polyadenylate tail. The storage of unprocessed RNAs has been described in other pathways, such as seed development (23), and would provide a mechanism for regulation of gene expression during the UM stage without transcription from the haploid genome. Collectively, our data show that the UM transcriptome is not static despite the lack of new transcription.

Discussion

Our study shows that diploid-derived transcripts persist long into the haploid phase of maize pollen development, followed by a rapid transition to monoallelic expression around PMI. We propose to call this the sporophyte-to-gametophyte transition (SGT), in analogy to the maternal-to-zygote transition (MZT), as both represent a shift from parent to offspring expression between generations. The widespread provisioning of the UM with sporophytic transcripts indicates a substantial parental investment in the developing gametophyte and implies that most cellular processes are under sporophytic control for the first half of pollen development.

Why might the SGT be delayed until PMI? One explanation is that PMI sets up the gametophyte germline (generative cell) and soma (vegetative cell). Active transcription is associated with an increased mutation rate (24); therefore, limiting transcription during the UM

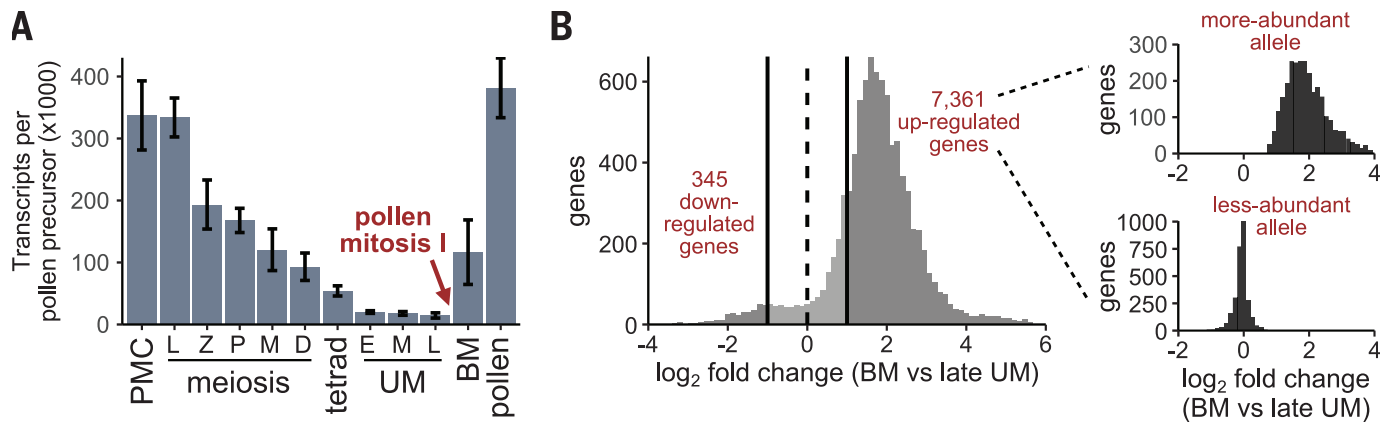


Fig. 4. Widespread gametophyte genome activation at PMI. (A) Total transcripts detected per pollen precursor, by stage. Shown are trimmed means (trim = 0.2) \pm SE, estimated by bootstrapping. (B) (Left) \log_2 fold change in absolute transcript abundance between the late UM and BM stages for genes with a mean expression level of at least one transcript per precursor. Solid black lines separate genes up- or down-regulated by twofold or more. (Right) \log_2 fold change in transcript abundance for transcripts mapping to the more- and less-abundant alleles (top and bottom, respectively), showing only genes with a twofold or greater increase in overall transcript abundance. Up-regulated genes show an increase in transcript levels for the more-abundant (haploid) allele only.

stage might reduce transcription-coupled DNA damage and accessibility of the genome to transposons. After PMI, the somatic vegetative cell is far more transcriptionally active than the generative cell (25) and could accommodate transcription without an associated risk to the germline. It will be important to establish whether SGT timing varies between species and between male and female gametophytes. Is PMI a conserved moment of gametophyte genome activation? Or does the SGT occur at different times in distinct plant lineages?

The substantial increase in new transcripts around PMI suggests that the SGT is driven by gametophyte genome activation resulting in new transcription, although the mechanisms of this activation are unknown. It is unlikely that the mitotic division itself is required to activate transcription, as vegetative cell-like development continues even when PMI is blocked (26–28), and several gametophytic mutants have been isolated that disrupt PMI (4). Our working hypothesis is that the SGT begins immediately before PMI rather than during this stage. Many substantial changes have been observed around PMI, including broad shifts in protein and RNA composition (29), transposon activity [in *Arabidopsis* (30)], and histone modifications (31). There is much to learn about how these pathways are coordinated to establish the independence of the gametophyte generation.

The scope of haploid selection in predominantly diploid organisms has long been debated (6). Plants are generally accepted to experience greater haploid selection than animals, in part because they require many genes to complete the haploid phase (2–4). By contrast, fully enucleate animal sperm are viable and can

fertilize an egg (6). This distinction between kingdoms may be more nuanced than previously thought: Many genes have haploid-biased expression in mammalian sperm (32), which suggests that animal sperm may have a greater amount of heritable phenotypic variation than often assumed. Our results demonstrate an absence of haploid transcript accumulation for half of the haploid phase in maize pollen, limiting the time period that haploid selection may act in the male plant gametophyte. The ability to measure allele-specific expression directly in haploid gametes and gametophytes will provide needed clarity on this short but important life-cycle stage.

REFERENCES AND NOTES

- S. D. Tanksley, D. Zamir, C. M. Rick, *Science* **213**, 453–455 (1981).
- G. S. Khush, C. M. Rick, *Genetica* **38**, 74–94 (1967).
- B. Kindiger, J. B. Beckett, E. H. Coe Jr., *Genome* **34**, 579–594 (1991).
- L. C. Boavida *et al.*, *Genetics* **181**, 1369–1385 (2009).
- F. E. G. Beaudry, J. L. Rifkin, S. C. H. Barrett, S. I. Wright, *Plant Commun.* **1**, 100115 (2020).
- S. Immler, *Annu. Rev. Ecol. Evol. Syst.* **50**, 219–236 (2019).
- W. S. Armbruster, D. Gobeille Rogers, *Am. J. Bot.* **91**, 1939–1943 (2004).
- D. L. Mulcahy, *Nature* **249**, 491–493 (1974).
- G. Sandler, F. E. G. Beaudry, S. C. H. Barrett, S. I. Wright, *Evol. Lett.* **2**, 368–377 (2018).
- T. Lenormand, J. Duthiel, *PLOS Biol.* **3**, e63 (2005).
- H. J. Clarke, T. N. Khan, K. H. M. Siddique, *Euphytica* **139**, 65–74 (2004).
- D. L. Mulcahy, *Science* **206**, 20–23 (1979).
- S. Hsu, Y. Huang, P. Peterson, *Maydica* **33**, 77–98 (1988).
- K. N. Schulz, M. M. Harrison, *Nat. Rev. Genet.* **20**, 221–234 (2019).
- K. K. Sidhu *et al.*, *Proc. Natl. Acad. Sci. U.S.A.* **112**, 15982–15987 (2015).
- P. M. A. Kianian *et al.*, *Nat. Commun.* **9**, 2370 (2018).
- B. Nelms, V. Walbot, *Science* **364**, 52–56 (2019).
- T. I. Gossmann, M. W. Schmid, U. Grossniklaus, K. J. Schmid, *Mol. Biol. Evol.* **31**, 574–583 (2014).

- R. Arunkumar, E. B. Josephs, R. J. Williamson, S. I. Wright, *Mol. Biol. Evol.* **30**, 2475–2486 (2013).
- A. M. Chettoor *et al.*, *Genome Biol.* **15**, 414 (2014).
- H. Jia, M. Suzuki, D. R. McCarty, *Wires Dev. Biol.* **3**, 135–145 (2014).
- E. R. Valdivia, J. Sampedro, J. C. Lamb, S. Chopra, D. J. Cosgrove, *Plant Physiol.* **143**, 1269–1281 (2007).
- B. Harris, L. Dure 3rd, *Biochemistry* **17**, 3250–3256 (1978).
- N. Kim, S. Jinks-Robertson, *Nat. Rev. Genet.* **13**, 204–214 (2012).
- S. McCormick, *Plant Cell* **5**, 1265–1275 (1993).
- C. Eady, K. Lindsey, D. Twell, *Plant Cell* **7**, 65–74 (1995).
- J. Zhang *et al.*, *Nat. Plants* **3**, 17079 (2017).
- B. Glöckle *et al.*, *Development* **145**, dev152645 (2018).
- P. A. Bedinger, M. D. Edgerton, *Plant Physiol.* **92**, 474–479 (1990).
- R. K. Slotkin *et al.*, *Cell* **136**, 461–472 (2009).
- M. Borg, F. Berger, *Plant J.* **83**, 177–188 (2015).
- K. Bhutani *et al.*, *Science* **371**, eabb1723 (2021).

ACKNOWLEDGMENTS

We thank J. Ross-Ibarra and E. Josephs for helpful discussions, J. Dinnery for use of the SP8 confocal microscope, and S. Liu for providing the A188 genome sequence ahead of publication. **Funding:** This work was supported by National Science Foundation award 17540974. B.N. was supported by an NSF PGPR postdoctoral fellowship. **Author contributions:** B.N. and V.W. designed experiments, discussed results, and wrote the manuscript. B.N. conceived the project, performed experiments, and conducted data analysis. **Competing interests:** The authors declare no competing interests. **Data and materials availability:** Sequencing data and mapped allele-specific transcript counts are available at the NCBI Gene Expression Omnibus (accession no. GSE175916). All other data required to evaluate the conclusions are in the main paper or the supplementary materials.

SUPPLEMENTARY MATERIALS

science.org/doi/10.1126/science.abl7392
Materials and Methods
Figs. S1 to S12
Tables S1 to S6
References (33–49)
MDAR Reproducibility Checklist

5 August 2021; accepted 9 December 2021
10.1126/science.abl7392

REPORTS

2D MATERIALS

Out-of-equilibrium criticalities in graphene superlattices

Alexey I. Berdyugin^{1,2,*}, Na Xin^{1,2,†}, Haoyang Gao³, Sergey Slizovskiy^{1,2}, Zhiyu Dong³, Shubhadeep Bhattacharjee^{1,2}, P. Kumaravadeivel^{1,2}, Shuigang Xu^{1,2}, L. A. Ponomarenko^{1,4}, Matthew Holwill^{1,2}, D. A. Bandurin^{1,2}, Minsoo Kim^{1,2,‡}, Yang Cao^{1,2}, M. T. Greenaway^{5,6}, K. S. Novoselov², I. V. Grigorieva¹, K. Watanabe⁷, T. Taniguchi⁸, V. I. Fal'ko^{1,2,9}, L. S. Levitov³, Roshan Krishna Kumar^{1,2,10,*}, A. K. Geim^{1,2,*}

In thermodynamic equilibrium, current in metallic systems is carried by electronic states near the Fermi energy, whereas the filled bands underneath contribute little to conduction. Here, we describe a very different regime in which carrier distribution in graphene and its superlattices is shifted so far from equilibrium that the filled bands start playing an essential role, leading to a critical-current behavior. The criticalities develop upon the velocity of electron flow reaching the Fermi velocity. Key signatures of the out-of-equilibrium state are current-voltage characteristics that resemble those of superconductors, sharp peaks in differential resistance, sign reversal of the Hall effect, and a marked anomaly caused by the Schwinger-like production of hot electron-hole plasma. The observed behavior is expected to be common to all graphene-based superlattices.

The electric response of metallic systems is routinely described by a Fermi surface displacement in momentum space, established through a balance between acceleration of charge carriers and their relaxation caused by scattering (1). The displacement is usually small, so that the drift velocity v_d is minute compared with the Fermi velocity v_F . In theory, if inelastic scattering is sufficiently weak, it should be possible to shift the Fermi surface so far from equilibrium that all charge carriers within the topmost, partially filled bands start streaming along the applied electric field E . The field would then start producing extra carriers through interband transitions (2), allowing electronic bands under the Fermi energy to contribute to the charge flow. Such an extreme out-of-equilibrium regime has never been achieved in metallic systems because Ohmic heating, phonon emission, and other mechanisms greatly limit v_d (3–5).

A rare exception is semimetallic graphene. At high carrier densities n , the drift velocity in graphene is limited by phonon emission (6, 7), similar to other metallic systems. However, at low n , thermal excitations can create a relativistic plasma of massless electrons and holes, the “Dirac fluid.” Its properties in thermodynamic equilibrium were in the focus of recent research (8–12), but the behavior at high biases represents an uncharted territory. Yet close to the Dirac point, even a small E can shift the entire Fermi surface and tap into a supply of carriers from another band (13, 14). This can trigger processes analogous to the vacuum breakdown and Schwinger particle-antiparticle production in quantum electrodynamics, in which they are predicted to occur at enormous fields of $\sim 10^{18}$ V m^{−1} (15). Because such E are inaccessible, it is enticing to mimic the Schwinger effect and access the resulting out-of-equilibrium plasma in a condensed matter experiment (13, 14, 16). Certain nonlinearities observed near graphene’s neutrality point (NP) were previously attributed to the creation of electron-hole (e-h) pairs by means of a Schwinger-like mechanism (13, 14), but the expected intrinsic behavior was obscured by low mobility, charge inhomogeneity, and self-gating effects (6, 17).

We used graphene-based superlattices to identify an out-of-equilibrium state that sharply develops above a well-defined critical current j_c . The current marks an onset of the Schwinger pair production and a transition from a weakly dissipative fluid-like flow to a strongly dissipative e-h plasma regime. The out-of-equilibrium Dirac fluid is realized at surprisingly small E , thanks to the narrow electronic bands and low v_F characteristic of graphene superlattices (18, 19). The resulting dual-band transport

leads to striking anomalies in longitudinal and Hall resistivities. Counterintuitively, an apparent drift velocity in this regime exceeds v_F . With hindsight, we show that the current-induced critical state can be reached even in standard graphene, by using extra-high currents allowed by the point contact geometry.

The studied superlattices were of two types: graphene crystallographically aligned on top of hexagonal boron nitride (G/hBN) (20–23) and small-angle twisted bilayer graphene (TBG) (24–28). The superlattices were encapsulated in hBN, to ensure high electronic quality, and shaped into multiterminal Hall bar devices by using the standard fabrication procedures (29). The devices were first characterized by measuring their longitudinal resistivity ρ as a function of n as shown in Fig. 1, A to C, for three representative devices. The twist angles θ were determined from measurements of Brown-Zak oscillations (30); for TBG, θ was intentionally chosen away from the magic angle to avoid many-body states (27, 28). Aside from the familiar peak in ρ at zero doping, satellite peaks indicating secondary NPs were observed at n that agreed well with the θ values (20–22, 26). For G/hBN superlattices, the low-energy electronic spectrum is practically identical to that of monolayer graphene (18), and the spectral reconstruction occurs only near and above the edge of the first miniband (Fig. 1D, top). By contrast, all minibands in TBG are strongly reconstructed (Fig. 1D, bottom) (19). At low biases (Fig. 1, A to C, and fig. S1), our devices exhibited transport characteristics similar to those reported previously for G/hBN and TBG superlattices (20–22, 26).

Next, we studied high-bias transport using current densities j up to 0.1 mA μm^{-1} , limited only to avoid device damage. Unless stated otherwise, all the reported measurements were carried out at the bath temperature $T = 2$ K. The superlattices exhibited qualitatively similar current-voltage (I - V) characteristics (Fig. 1, E to G), which were nearly linear at $j < 0.01$ mA μm^{-1} and then rapidly switched into a high-resistance state so that the differential resistivity dV/dI showed a pronounced peak at a certain critical current j_c . The behavior was universal, found in all our devices (more than 10) (figs. S3 and S6), if the Fermi energy was tuned inside narrow minibands (that is, away from the main NP in the case of G/hBN). The I - V characteristics in Fig. 1, E to G, strongly resemble the superconducting response, despite electron transport being ballistic at low j and viscous at moderate currents (31); ρ always remained finite, although could be as low as < 0.01 kilohms, a few orders of magnitude smaller than dV/dI above j_c . Further details are provided in Fig. 2 by showing dV/dI as a function of n , where the narrow white arcs indicate peaks in dV/dI . Considerable similarities

¹School of Physics and Astronomy, University of Manchester, Manchester M13 9PL, UK. ²National Graphene Institute, University of Manchester, Manchester M13 9PL, UK.

³Massachusetts Institute of Technology, Cambridge, MA 02139, USA. ⁴Department of Physics, University of Lancaster, Lancaster LA1 4YW, UK. ⁵Department of Physics, Loughborough University, Loughborough LE11 3TU, UK.

⁶School of Physics and Astronomy, University of Nottingham, Nottingham NG7 2RD, UK. ⁷Research Center for Functional Materials, National Institute for Materials Science, 1-1 Namiki, Tsukuba 305-0044, Japan. ⁸International Center for Materials Nanoarchitectonics, National Institute for Materials Science, 1-1 Namiki, Tsukuba 305-0044, Japan. ⁹Henry Royce Institute for Advanced Materials, Manchester M13 9PL, UK. ¹⁰Institut de Ciències Fotòniques (ICFO), Barcelona Institute of Science and Technology, 08860 Castelldefels, Barcelona, Spain.

*Corresponding author. Email: alexey.berdyugin@manchester.ac.uk (A.I.B.); roshankrishnakumar90@gmail.com (R.K.K.); geim@manchester.ac.uk (A.K.G.)

†These authors contributed equally to this work.

‡Present address: Department of Applied Physics, Kyung Hee University, Yong-In 17104, South Korea.

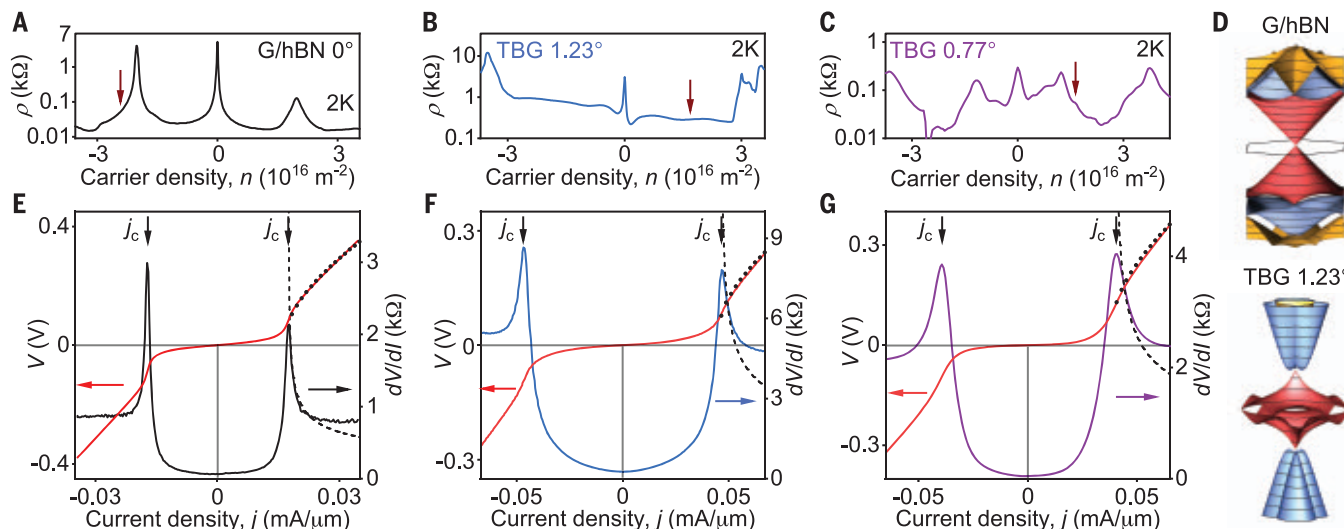


Fig. 1. Linear and nonlinear transport in graphene superlattices.

(A to C) $\rho(n)$ in the linear regime ($j = 50 \text{ nA } \mu\text{m}^{-1}$) for (A) G/hBN with $\theta \approx 0^\circ$ and for TBG with (B) $\theta \approx 1.23^\circ$ and (C) $\theta \approx 0.77^\circ$. Micrographs of the studied devices are provided in (29). (D) Band structures of G/hBN and TBG 1.23° superlattices (29). Colors indicate different energy bands. The bands are shown for the energy range of ± 340 and $\pm 80 \text{ meV}$ for G/hBN and TBG 1.23°, respectively.

(E to G) I - V characteristics for the devices in panels (A) to (C), respectively. The doping levels for the curves are indicated with the arrows in (A) to (C). The dependence $(j - j_c) \propto V^{3/2}$ expected above j_c is indicated by the dotted curves and the corresponding $dV/dI \propto (j - j_c)^{-1/3}$ is indicated by the dashed curves. All V and dV/dI are normalized according to devices' aspect ratios.

are clearly seen across different superlattice types. One feature shared by all the maps was the rapidly decreasing j_c as n approached NPs (Fig. 2, A to C, and figs. S2 and S6). The only exception was the main NP in G/hBN superlattices, where the resistivity in its vicinity increased monotonically for all accessible j (fig. S2).

To gain more insight, we studied the Hall effect in small (nonquantizing) magnetic fields B . An example of such measurements for G/hBN near the hole-side NP is shown in Fig. 2D. At small j , the Hall voltage V_{xy} increased linearly with j , and dV_{xy}/dI was positive, reflecting the hole doping. However, dV_{xy}/dI abruptly turned negative above j_c , revealing a change in the dominant-carrier type. dV_{xy}/dI maps for the G/hBN and TBG superlattices are shown in Fig. 2, E to G. There are clear correlations between the longitudinal and Hall maps so that the peaks in dV/dI and the Hall effect's reversal occurred at same j_c . The observed nonlinearities were robust against T up to $\sim 50 \text{ K}$, above which the peaks in dV/dI became gradually smeared (fig. S4). This shows that Ohmic heating—which is generally expected at high j (14, 31, 32)—was not the reason for the critical-current behavior (29).

The rapid decrease in j_c near all secondary NPs prompts the question why such a critical-current behavior was not observed in graphene (13, 14) or near the main NP of G/hBN (Fig. 2A) and whether it can be achieved at some higher j . With this in mind, we used a point contact geometry that funneled the current through a short constriction, whereas wide adjacent regions provided a thermal bath for electron cooling. This allowed us to reach j an order

of magnitude greater than those achievable in the standard geometry. At these j , I - V characteristics near the main NP of G/hBN superlattices became similar to those near its secondary NPs (fig. S3), although they were more smeared because of Ohmic heating and, possibly, edge irregularities in the superlattice periodicity within narrow constrictions. To circumvent the latter problems and demonstrate the universality of the critical behavior at all NPs, we made constrictions from nonsuperlatticed graphene (monolayer graphene encapsulated in hBN but nonaligned). These devices also displayed a clear critical behavior, although peaks at j_c were notably broader because of heating (Fig. 3A).

To understand the criticalities, we first discuss the conceptually simplest case of the Dirac spectrum, such as in nonsuperlatticed graphene. We consistently observed that the transition between the low- and high-resistance states occurred at $j_c \approx nev_F$ (e is the electron charge)—that is, at $v_d \approx v_F$, independently of n (Fig. 3B). This condition means that the Fermi surface is shifted from equilibrium by the entire Fermi momentum, and all electrons in the conduction band move along E with a drift velocity of about v_F (Fig. 3C). If the spectrum were fully gapped, j could not increase any further because all available carriers already move at maximum speed. This should result in saturation of j as a function of V , which is in agreement with the observations at $j \lesssim j_c$. Simulations of this intraband-only transport corroborate our conclusions (Fig. 3A, dashed curves). To explain the supercritical behavior at $j > j_c$ for a gapless spectrum E can move

electrons up in energy from the valence band into the conduction band, leaving empty states (holes) behind (Fig. 3C, bottom). The extra electrons and holes created by the interband transitions allow the current to exceed j_c . Accordingly, the apparent $v_d = j/ne$ seemingly exceeds the maximum possible group velocity, v_F (because n is fixed by gate voltage, but the actual concentration of carriers increases by Δn). Quantitatively, the e-h production at $j > j_c$ can be described by the Schwinger (or Zener-Klein tunneling) mechanism. It can generate interband carriers at a rate $\propto E^{3/2}$ (13, 16), but at small biases, the production is forbidden by the Pauli exclusion principle. Above j_c , the Fermi distribution is shifted sufficiently far from equilibrium so that E depletes the states near the NP, which eliminates the Pauli blocking and enables the e-h pair production (Fig. 3C). Accounting for e-h annihilation (recombination processes bring the electronic system back into the equilibrium), we found the stationary concentration of extra carriers Δn to be $\propto E^{3/2} \propto V^{3/2}$, if $\Delta n \ll n$ (29). This translates into extra current $\Delta nev_F \propto V^{3/2}$ and $dV/dI \propto j^{-1/3}$. Because dV/dI decreases for $j > j_c$ but increases for $j < j_c$, a peak is expected at j_c , which is in agreement with Fig. 3A.

The above analysis can also be applied to graphene superlattices. Their narrow minibands display low v_F , and therefore, the onset of interband transitions is expected at small j . The switching transition in our superlattices occurred at v_d typically > 10 times smaller than in nonsuperlatticed graphene (fig. S5). This yields a characteristic v_F of several 10^4 m s^{-1} , which translates into minibands' widths

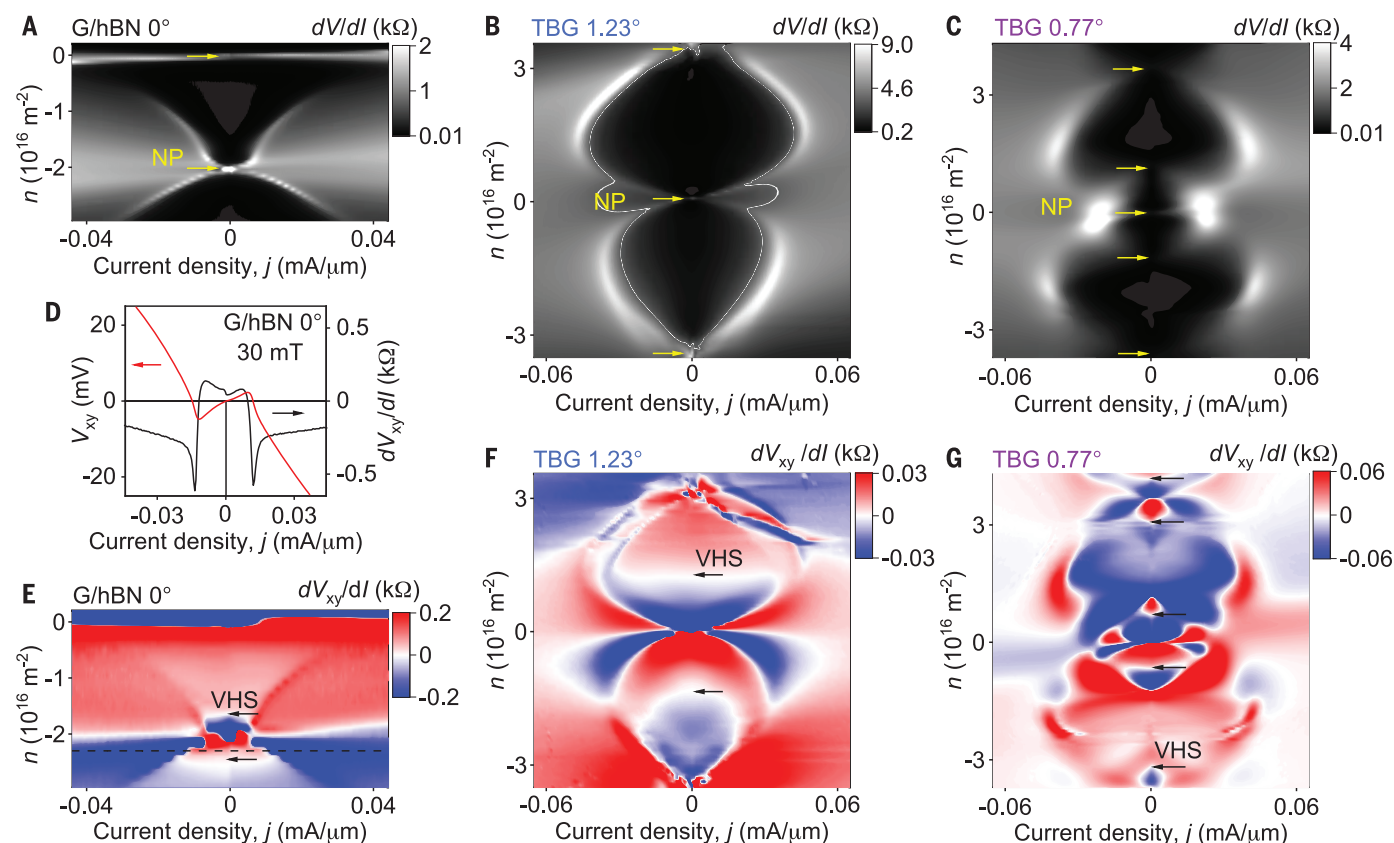


Fig. 2. Switching into the high-bias regime. (A to C) dV/dI as a function of j and n for the superlattices in Fig. 1, A, to C, respectively. Bright arcs appear at the critical current. Yellow arrows indicate NPs as found with low-bias measurements (29). (D) Hall voltage (red curve) and the corresponding differential resistivity (black curve) measured at n indicated by the dashed line in (E). (E to G) Maps of dV_{xy}/dI for the superlattices in (A) to (C), respectively. $B = 30$ mT; $T = 2$ K. The black arrows indicate positions of van Hove singularities.

of ~ 10 meV, as expected from band structure calculations (19). For the relatively small j_c , superlattices were much less affected by heating than graphene and, accordingly, exhibited sharper transitions (Figs. 2 and 3A). The experimental I - V curves are compared with the above predictions for Schwinger-like carrier generation in Fig. 1, E to G. Good agreement was found for $j \gtrsim j_c$. Notable deviations seen at highest j are expected because Δn is no longer small compared with n , the assumption used to derive the plotted dependences (29). Furthermore, j_c in graphene evolved $\propto n$ as expected for the Dirac spectrum (Fig. 3B). By contrast, superlattices exhibited clear deviations from the linear dependence (Figs. 2, A to C). This is attributed to the group velocity of charge carriers rapidly decreasing away from secondary NPs, dropping to zero at van Hove singularities (VHSs). If non-equilibrium carriers reside near VHSs, they move at low speed and contribute little to the current (fig. S5C), leading to the sub-linear $j_c(n)$, as observed experimentally.

Extending the described physics onto the Hall effect, it is straightforward to understand the sign changes in Fig. 2, D to G. With reference to Fig. 3C, interband transitions result

in extra holes near the NP plus extra electrons that effectively appear at higher energies in the out-of-equilibrium Fermi distribution (Fig. 3C). For superlattices, contributions of these e-h pairs into V_{xy} do not cancel each other because of the broken e-h symmetry, which results in different masses and mobilities of the extra carriers. The effect is particularly strong upon approaching a VHS. For example, if the dominant carriers are electrons, their distribution would be shifted by E upward toward a VHS (fig. S5C), and they should have heavy masses. By contrast, the reciprocal holes generated near the NP should be light (fig. S5C). These higher-mobility holes are expected to provide a dominant contribution into the Hall signal, and therefore, dV_{xy}/dI should change its sign from electron to hole near $j \approx j_c$, as observed experimentally. If the asymmetry is sufficiently strong, even V_{xy} can reverse its sign (Fig. 2D). The observed changes in the Hall effect can qualitatively be described by using the two-carrier model with different mobilities of out-of-equilibrium electrons and holes (fig. S7).

Last, we discuss the interband carrier generation at the main NP in graphene (Fig. 3), which closely mimics the Schwinger effect in

quantum electrodynamics. Consequences of the Schwinger-like effect at the Dirac point are qualitatively different from those described by Zener-Klein tunneling at finite doping (29). In contrast to the latter case, there is no low-to-high resistance switching at $n = 0$, and dV/dI rapidly drops with increasing j , reaches a minimum, and then gradually increases (Fig. 3D). This behavior was highly reproducible for all graphene constrictions (fig. S8) but, because of self-gating and heating effects, could not be observed in the standard geometry, where I - V curves were similar to those in the literature (6). The initial drop is attributed to e-h puddles present at NPs, in which small E starts generating interband carriers along puddles' boundaries and enhances conductivity (13). Minima in dV/dI typically occurred at $j_m \approx 0.05$ mA μm^{-1} (Fig. 3D), which translates into $\Delta n = j_m / ev_F \approx 3 \times 10^{10}$ cm $^{-2}$, which is in agreement with the charge inhomogeneity δ found in our devices. In principle, the initial dV/dI drop could be fitted again by $\propto j^{-1/3}$, but such fits were inconclusive because of the involved inhomogeneity. For higher j so that $\Delta n \gg \delta$, the Schwinger production fills graphene with a plasma of electrons and holes in equal concentrations, $n_e \approx n_h = \Delta n$. Because

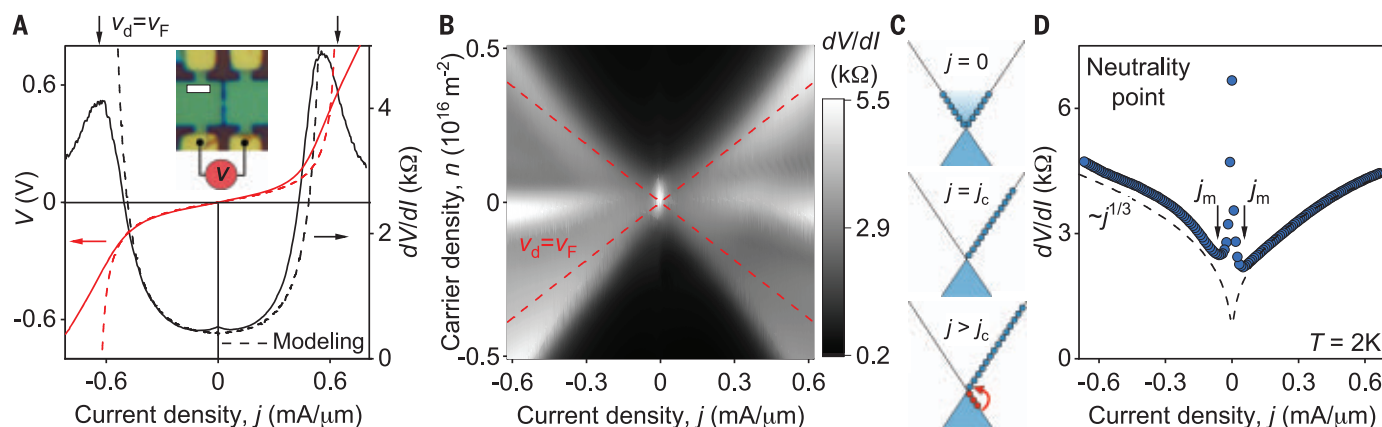


Fig. 3. Nonlinear transport in nonsuperlatticed graphene near the Dirac point.

(A) Voltage and differential resistance (red and black curves, respectively) for a constriction of 0.4 μm in width; $n = 0.4 \times 10^{16} \text{ m}^{-2}$. (Inset) Optical micrograph of the graphene device and its measurement geometry. Scale bar, 2 μm . The small bump at zero bias is caused by electron-electron scattering (34). Dashed curves indicate I - V characteristics calculated for the Dirac spectrum at $j < j_c$ (29).

The vertical arrows indicate j with $v_d = v_F = 1 \times 10^6 \text{ m s}^{-1}$. (B) Example of dV/dI maps for graphene constrictions. Red lines indicate $j = nev_F$. (C) Schematic of graphene's spectrum and its occupancy in (top) equilibrium and in out-of-equilibrium for (middle) $j = j_c = nev_F$ and (bottom) $j > j_c$. Blue and red circles indicate electrons and holes, respectively. The red arrow illustrates e-h pair production. (D) dV/dI at the NP for a 0.6- μm -wide constriction. The arrows indicate minima.

the annihilation rate of e-h pairs scales with $n_e n_h = \Delta n^2$, theory predicts (29) that the Schwinger production rate ($\propto E^{3/2}$) leads to $\Delta n \propto E^{3/4}$, resulting in $dV/dI \propto j^{1/3}$. This contrasts the reported Zener-Klein behavior at graphene's NP (13) but is in quantitative agreement with our experiment (Fig. 3D and fig. S8). For highest j , the hot e-h plasma inside graphene constrictions is expected to approach the quantum critical limit (8–12), in which e-h scattering is governed by the uncertainty principle and ρ is predicted to become rather universal, $\sim 1.3\alpha^2(h/e^2)$, where α is the interaction constant and h/e^2 is the resistance quantum (8, 9). For encapsulated graphene, $\alpha \approx 0.3$, whereas the constriction geometry results in resistance of $\sim 1.8\rho$ (29). Accordingly, the quantum-critical resistance for our constrictions is expected to be ~ 5 kilohms, which is in qualitative agreement with Fig. 3D and fig. S8, where the curves approach this value. We do not expect better agreement because E strongly disturbs the e-h plasma, making it anisotropic, which is rather different from the Dirac fluids in thermal equilibrium, which were discussed previously (8–12). This anisotropic regime requires further theoretical analysis and would be interesting to probe through other experimental techniques.

At high biases, Fermi liquids in graphene-based systems can be turned into Dirac-like fluids characterized by intense interband carrier generation. The transition between the weakly and strongly dissipative electronic states is marked by peculiar superconducting-like dV/dI . Such I - V characteristics, although of interest on their own right as a signature of out-of-equilibrium criticalities, also serve as a warning that they alone—without other essential attributes (such as zero resistance)—do not

constitute a proof of “emerging/fragile” superconductivity. It is possible that the nonlinear response reported in some graphene-based flat-band systems [for example, (33)] was governed by the out-of-equilibrium physics rather than superconductivity. Other attributes of nonequilibrium behavior such as Bloch oscillations and associated terahertz radiation are likely to accompany the reported criticalities, which is an appealing opportunity for further investigation.

REFERENCES AND NOTES

- C. Kittel, *Introduction to Solid State Physics* (Wiley, ed. 8, 2005).
- C. Zener, *Proc. R. Soc. A Math. Phys. Eng. Sci.* **145**, 523–529 (1934).
- W. Shockley, *Bell Syst. Tech. J.* **30**, 1035–1037 (1951).
- E. J. Ryder, *Phys. Rev.* **90**, 766–769 (1953).
- S. M. Sze, K. K. Ng, *Physics of Semiconductor Devices* (Wiley-Interscience, 2007).
- I. Meric et al., *Nat. Nanotechnol.* **3**, 654–659 (2008).
- M. A. Yamoah, W. Yang, E. Pop, D. Goldhaber-Gordon, *ACS Nano* **11**, 9914–9919 (2017).
- L. Fritz, J. Schmalian, M. Müller, S. Sachdev, *Phys. Rev. B Condens. Matter Mater. Phys.* **78**, 085416 (2008).
- A. B. Kashuba, *Phys. Rev. B Condens. Matter Mater. Phys.* **78**, 085415 (2008).
- J. Cossentino et al., *Science* **351**, 1058–1061 (2016).
- P. Gallagher et al., *Science* **364**, 158–162 (2019).
- M. J. H. Ku et al., *Nature* **583**, 537–541 (2020).
- N. Vandecasteele, A. Barreiro, M. Lazzeri, A. Bachtold, F. Mauri, *Phys. Rev. B Condens. Matter Mater. Phys.* **82**, 045416 (2010).
- W. Yang et al., *Nat. Nanotechnol.* **13**, 47–52 (2018).
- J. Schwinger, *Phys. Rev.* **82**, 664–679 (1951).
- D. Allor, T. D. Cohen, D. A. McGady, *Phys. Rev. D Part. Fields Gravit. Cosmol.* **78**, 096009 (2008).
- Y. Wu et al., *ACS Nano* **6**, 2610–2616 (2012).
- J. R. Wallbank, A. A. Patel, M. Mucha-Kruczynski, A. K. Geim, V. I. Fal'ko, *Phys. Rev. B Condens. Matter Mater. Phys.* **87**, 245408 (2013).
- R. Bistritzer, A. H. MacDonald, *Proc. Natl. Acad. Sci. U.S.A.* **108**, 12233–12237 (2011).
- L. A. Ponomarenko et al., *Nature* **497**, 594–597 (2013).
- C. R. Dean et al., *Nature* **497**, 598–602 (2013).
- B. Hunt et al., *Science* **340**, 1427–1430 (2013).
- M. Yankowitz, Q. Ma, P. Jarillo-Herrero, B. J. LeRoy, *Nat. Rev. Phys.* **1**, 112–125 (2019).
- Y. Cao et al., *Phys. Rev. Lett.* **117**, 116804 (2016).
- K. Kim et al., *Proc. Natl. Acad. Sci. U.S.A.* **114**, 3364–3369 (2017).
- Y. Cao et al., *Nature* **556**, 80–84 (2018).

- L. Balents, C. R. Dean, D. K. Efetov, A. F. Young, *Nat. Phys.* **16**, 725–733 (2020).
- E. Y. Andrei, A. H. MacDonald, *Nat. Mater.* **19**, 1265–1275 (2020).
- Materials and methods are available in the supplementary materials.
- R. Krishna Kumar et al., *Science* **357**, 181–184 (2017).
- D. A. Bandurin et al., *Science* **351**, 1055–1058 (2016).
- M. Freitag et al., *Nano Lett.* **9**, 1883–1888 (2009).
- S. Xu et al., *Nat. Phys.* **17**, 619–626 (2021).
- E. S. Tikhonov et al., *Phys. Rev. B Condens. Matter Mater. Phys.* **90**, 161405 (2014).
- A. I. Berdyugin et al., Out-of-equilibrium criticalities in graphene superlattices. *Zenodo* (2021); doi:10.5281/zenodo.5639021.

ACKNOWLEDGMENTS

Funding: We acknowledge financial support from the European Research Agency (grants ARTIMATTER and VANDER), Lloyd's Register Foundation, Graphene Flagship Core3 Project, and the Royal Society. M.T.G. acknowledges the support from EPSRC grant EP/V008110/1, and A.I.B. acknowledges the support from NOWNANO Doctoral Training Centre. R.K.K. acknowledges a EPSRC doctoral-prize fellowship award and the EU Horizon 2020 program under the Marie Skłodowska-Curie grants 754510 and 893030. V.I.F. was also supported by EU Quantum Flagship Project 2D-SIPC and EPSRC grants EP/V007033 and EP/S030719. L.L. acknowledges support from the Science and Technology Center for Integrated Quantum Materials, NSF grant DMR-1231319, and Army Research Office grant W911NF-18-1-0116. K.W. and T.T. acknowledge support from Elemental Strategy Initiative of Japan (grant JPMXP0112101001) and JSPS KAKENHI (19H05790, 20H00354, and 21H05233). L.S.L. acknowledges support by the Science and Technology Center for Integrated Quantum Materials, NSF grant DMR-1231319, and Army Research Office grant W911NF-18-1-0116. **Author contributions:** A.I.B., R.K.K., and A.K.G. conceived and led the project; N.X., P.K., S.X., M.H., and Y.C. made the studied devices; A.I.B., S.B., L.A.P., D.A.B., M.K., and R.K.K. carried out the measurements and analyzed their results, with help from N.X., S.S., P.K., K.S.N., I.V.G., L.S.L., V.I.F., and A.K.G.; H.G., S.S., Z.D., M.T.G., A.I.B., V.I.F., and L.S.L. provided theory; K.W. and T.T. supplied hBN crystals. A.I.B., R.K.K., and A.K.G. wrote the manuscript, with contributions from L.S.L., N.X., H.G., S.S., and I.V.G. All authors discussed the results and commented on the manuscript. **Competing interests:** The authors declare no competing interests. **Data and materials availability:** All data discussed in the main text and the supplementary materials are available at Zenodo (35).

SUPPLEMENTARY MATERIALS

science.org/doi/10.1126/science.abi8627
Supplementary Text
Figs. S1 to S8
References (36–46)

7 April 2021; accepted 16 December 2021
10.1126/science.abi8627

SOLAR CELLS

Constructing heterojunctions by surface sulfidation for efficient inverted perovskite solar cells

Xiaodong Li¹, Wenxiao Zhang¹, Xuemin Guo¹, Chunyan Lu¹, Jiyao Wei¹, Junfeng Fang^{1,2*}

A stable perovskite heterojunction was constructed for inverted solar cells through surface sulfidation of lead (Pb)-rich perovskite films. The formed lead-sulfur (Pb-S) bonds upshifted the Fermi level at the perovskite interface and induced an extra back-surface field for electron extraction. The resulting inverted devices exhibited a power conversion efficiency (PCE) >24% with a high open-circuit voltage of 1.19 volts, corresponding to a low voltage loss of 0.36 volts. The strong Pb-S bonds could stabilize perovskite heterojunctions and strengthen underlying perovskite structures that have a similar crystal lattice. Devices with surface sulfidation retained more than 90% of the initial PCE after aging at 85°C for 2200 hours or operating at the maximum power point under continuous illumination for 1000 hours at 55° ± 5°C.

Perovskite solar cells (PSCs) have reached power conversion efficiencies (PCEs) >25% in regular (n-i-p) PSCs (1–5), but for inverted (p-i-n) PSCs, PCEs are between 22 and 23% (6, 7). The origin of this inferior performance is unclear, but different heterojunction contacts could be the underlying cause (8). Nonradiative recombination occurs at the contacts with the carrier transporting layer (9, 10), so it is the contact heterojunction, rather than the perovskite or transporting layer itself, that limits PSC performance. In regular PSCs, perovskite within the mesoporous scaffold tends to be more n-type in nature than bulk perovskite, which induces

an extra field to promote electron extraction through band bending at this contact interface (11). In inverted PSCs, the p-type nature of the perovskite film in direct contact with the n-type electron transporting layer induces efficiency (6, 12, 13). Thus, in inverted PSCs, it is necessary to control the semiconductor nature at the perovskite interface.

The contact properties at the perovskite heterojunction also influence device stability. At the contact interface, perovskite components are assembled with weak chemical bonds, such as ionic bonds, hydrogen bonds, and van der Waals interactions (14–16). The resulting soft nature of the perovskite interface makes it susceptible to attack from ambient air and water (17, 18). Perovskite components will also diffuse and penetrate the transporting layer, degrade the heterojunction (19, 20) and the transporting layer (21, 22), and even corrode the electrode (23). Many organic molecules can passivate the perovskite interface with

secondary bonds, such as hydrogen bonds, coordination interactions, or ionic bonds (24–27), but these weak secondary bonds still lead to stability issues (28).

Motivated by the n-type and stable inorganic nature of PbS, we proposed a surface sulfidation treatment (SST) to construct stable heterojunctions for inverted PSCs. After SST, perovskites exhibited a shallow Fermi level (became more n-type), which induced an extra back-surface field at the perovskite interface through band bending. This field was in the same direction as the built-in potential (V_{bi}) of inverted PSCs. PSCs with SST had PCEs >24% with a high open-circuit voltage (V_{oc}) of 1.19 V, corresponding to a low voltage loss of 0.36 V in a formamidinium (FA)-based perovskite system (bandgap of 1.55 eV). The Pb-S bond was much stronger than the Pb-I bond; the solubility product constant of PbS (K_{sp} of 1.0×10^{-28}) was 19 orders of magnitude smaller than that of PbI₂ (7.1×10^{-9}). The S²⁻ anions would strongly bond with Pb ions at the perovskite interface and inhibit degradation reactions. The similar crystal lattice between PbS and the perovskite should also stabilize the crystal structure of FA-based perovskite (29) (30). The resulting SST PSCs retained 91.8% of initial efficiency after aging at 85°C for 2200 hours. Notably, the operational stability was also greatly improved, and >90% of the initial PCE was retained after maximum power point (MPP) tracking under continuous illumination for 1000 hours at 55° ± 5°C.

In the SST method (Fig. 1A), a Pb-rich perovskite surface was formed by spin-coating pyridine-2-carboxylic lead (PbPyA₂), and it was sulfurized with hexamethyldisilathiane (TMS) (31), which can react with solid-phase PbPyA₂ (fig. S1). We used PbPyA₂ because of

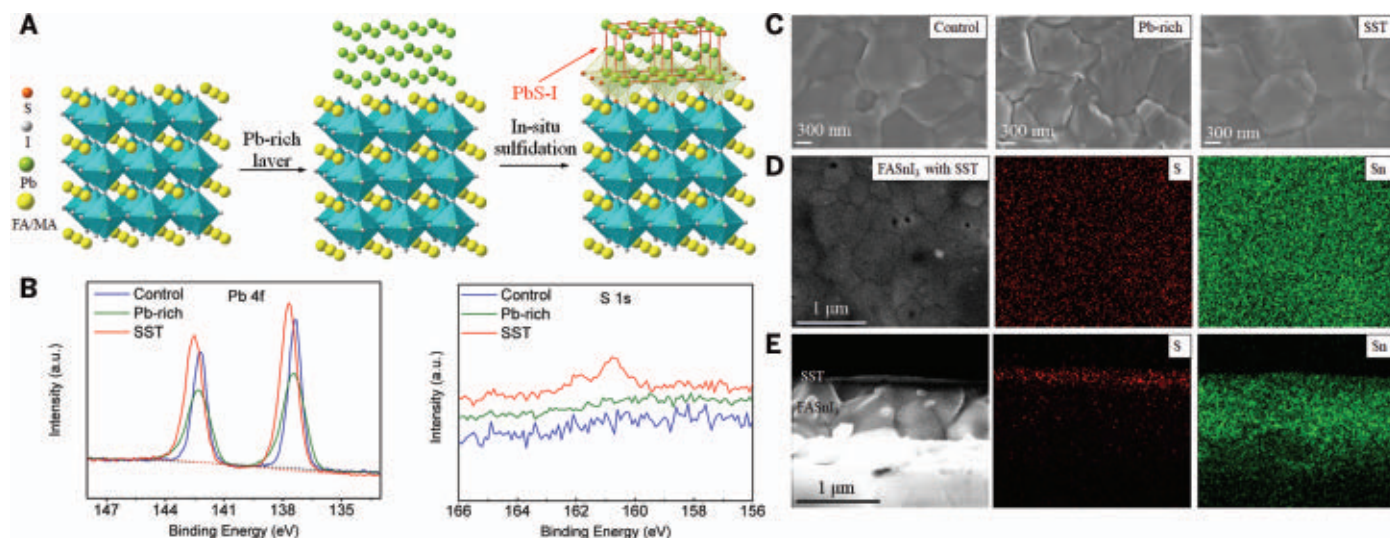


Fig. 1. SST and perovskite morphology. (A) Schematic diagram of SST. (B) XPS spectra of Pb 4f and S 1s in control, Pb-rich, and SST-based perovskite films. a.u., arbitrary units. (C) SEM images of control, Pb-rich, and SST perovskite films. (D) SEM-EDX mapping of perovskite film with SST. Because of the overlap of S and Pb elements under the SEM-EDX mode, lead-free FASnI₃ perovskite is used instead. (E) Cross-sectional SEM-EDX mapping of perovskite film with SST.

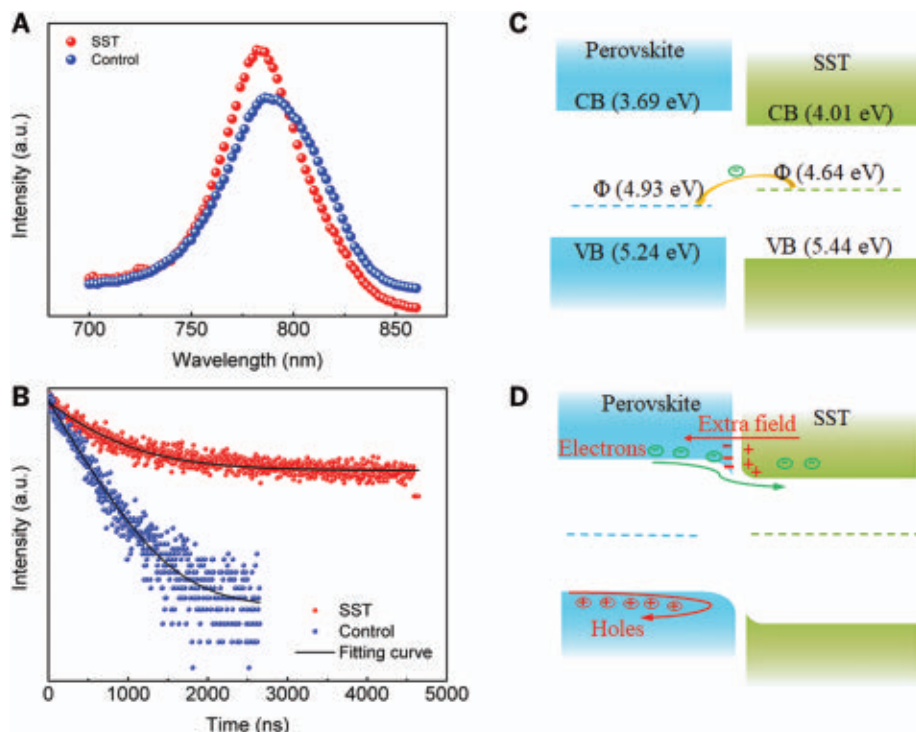


Fig. 2. Photoelectric properties of perovskite films. (A and B) PL (A) and TRPL (B) spectra of control and SST perovskite films. (C) Energy level of perovskite films. Φ represents the Fermi level. The yellow arrow indicates the spontaneous electron flow to bulk perovskite created by the shallow Fermi level of the perovskite surface with SST. (D) Back-surface field formation at the perovskite surface with SST. Because of the difference in Fermi levels, positive charges accumulate at the perovskite interface, inducing band bending and the formation of a back-surface field.

its defect passivation function (32) and its high solubility in nonaqueous solvent, which preserved the underlying perovskite layer. X-ray photoelectron spectroscopy (XPS; Fig. 1B) showed a broadening peak and increasing peak area in Pb 4f after PbPyA₂ deposition (table S1), whereas the I 3d peak decreased (fig. S2). After depositing TMS, the S 1s peak appeared at 162.0 and 160.8 eV (Fig. 1B). This result confirmed perovskite sulfidation because TMS volatilized during thermal annealing. The Pb 4f peak shifted by 0.3 eV to a higher binding energy in perovskite with SST (Fig. 1B), which should be caused by the strong bonding between S and Pb.

The control perovskite exhibited uniform morphology with obvious grains and boundaries under scanning electron microscopy (SEM; Fig. 1C). In Pb-rich perovskite, some bright signal appeared, which we attributed to the Pb-rich sites, given the poor conductivity of PbPyA₂. When further treated with TMS, the bright signal disappeared and some new species appeared, indicating sulfidation of Pb-rich perovskite (fig. S3). In SEM-energy-dispersive x-ray spectroscopy (EDX), the signal from the Pb element overlapped with that from S, so we used Sn-based perovskite (FASnI₃) instead. In SEM-EDX mapping, the S element represented the sulfidation area and the Sn

element represented the perovskite phase. The S element signal at ~2.4 keV (total element spectra in fig. S4A) covered the entire SEM images (Fig. 1D), indicating uniform sulfidation. An extra intact layer was observed in cross-sectional SEM images, and EDX mapping showed that this layer was S-rich (Fig. 1E; see total element spectra in fig. S4B).

The SST strategy also passivated defects at the perovskite interface. Previous studies confirmed that surface defects would red-shift photoluminescence (PL) (33). The control perovskite exhibited a PL peak at 789 versus 783 nm in SST perovskite (Fig. 2A); this blue shift was evidence of defect passivation (traps density shown in fig. S5), which should be caused by the Pb-S bonds. Time-resolved PL (TRPL; Fig. 2B) indicated that the control perovskite exhibited a decay lifetime of 462 versus 706 ns for SST perovskite, which was indicative of a lower recombination rate. However, the improved lifetime of 706 ns was insufficient to ensure the high V_{oc} of PSCs with SST (1.19 V; see below) according to previous reports. (34, 35)

Introducing an extra back-surface field is an effective method to improve device V_{oc} and has been widely applied in Si-based solar cells. The energy level of the control perovskite (or bulk perovskite) and the perovskite surface

with SST (Fig. 2C) was obtained from ultraviolet photoelectron spectroscopy (fig. S6) and the Tauc plot of ultraviolet-visible absorption spectra (fig. S7). The control perovskite (perovskite bulk) was p-type and had a Fermi level of 4.93 eV, a conduction band (CB) of 3.69 eV, and a valence band (VB) of 5.24 eV, in agreement with previous reports. (8, 12) The SST perovskite was a weak n-type surface with a shallow Fermi level of 4.64 eV, CB of 4.01 eV, and VB of 5.44 eV. Electrons will spontaneously flow from surface to bulk because of the shallow Fermi level of the SST perovskite surface. Positive charge that accumulated at the perovskite surface would form a back-surface field pointing toward the indium tin oxide (ITO) (Fig. 2D) aligned with V_{bi} in inverted PSCs. The improved electron transport and inhibited hole transport would then increase the device's V_{oc} .

We verified the V_{bi} improvement of PSCs with SST using Mott-Schottky plot analysis (testing details in figs. S8 and S9) (35, 36). As shown in Fig. 3A, PSCs with SST had a V_{bi} of 1.21 versus 1.07 V in control devices. We fabricated inverted PSCs with a configuration of ITO/P3CT-N/(FAPbI₃)_{0.95}(MAPbBr₃)_{0.05}/PCBM/C60/TPBi/Cu {where P3CT-N is poly [3-(methylamine-5-pentanoate)thiophene-2,5-diyl] (37, 38); PCBM is [6,6]-phenyl-C₆₁-butyric acid methyl ester; and TPBi is 1,3,5-tris(1-phenyl-1H-benzimidazol-2-yl)benzene}. Inverted PSCs with SST exhibited a PCE of 24.3% with V_{oc} up to 1.19 V in agreement with the V_{bi} from Mott-Schottky plots (Fig. 3B; see certified PCE of 23.5% in fig. S10, PCE dependence on SST thickness in fig. S11, and device hysteresis in fig. S12). The stabilized PCE under MPP reached 24.2% (fig. S13A). Control PSCs had lower PCEs of 21.8% (stabilized PCE of 21.0%; fig. S13A) mainly because of the lower V_{oc} of 1.09 V. In addition, the device fill factor (FF) was also increased from 80.0 to 82.9% in PSCs with SST. Both control and SST-based devices exhibited high external quantum efficiency values (fig. S13B), in agreement with their similar short-circuit current density from current density-voltage ($J-V$) curves. PSCs with the commonly used phenethylammonium iodide (PEAI) passivator were also fabricated, and limited improvement was observed (PCE of 22.4%; fig. S14). Statistical analysis indicated good reproducibility in PSCs with SST, with an average efficiency of $23.3 \pm 0.5\%$ among 50 separate devices (figs. S15 and S16). SST PSCs with an area of 1 cm² showed a PCE of 20.7% with a high V_{oc} of 1.17 V (fig. S17). In methylammonium (MA)-free Cs_{0.05}FA_{0.95}PbI₃ PSCs, SST also worked well and increased PCE from 21.1 to 23.5% (fig. S18 and certified PCE of 23.4% in fig. S19).

Device stability under MPP tracking is important for PSCs because illumination and external field (load) can degrade the soft perovskite interface. As shown in the inset of

Fig. 3. Photovoltaic performance of PSCs.

(A) Mott-Schottky plots of control and SST-based PSCs at 10 kHz. (B) *J*-*V* curves of control and SST-based PSCs. (C) Operational stability of PSCs under MPP tracking with continuous illumination at $55^\circ \pm 5^\circ\text{C}$. The inset shows photographs of PSCs after MPP tracking. (D) Thermal stability of PSCs under 85°C aging in a glovebox without encapsulation.

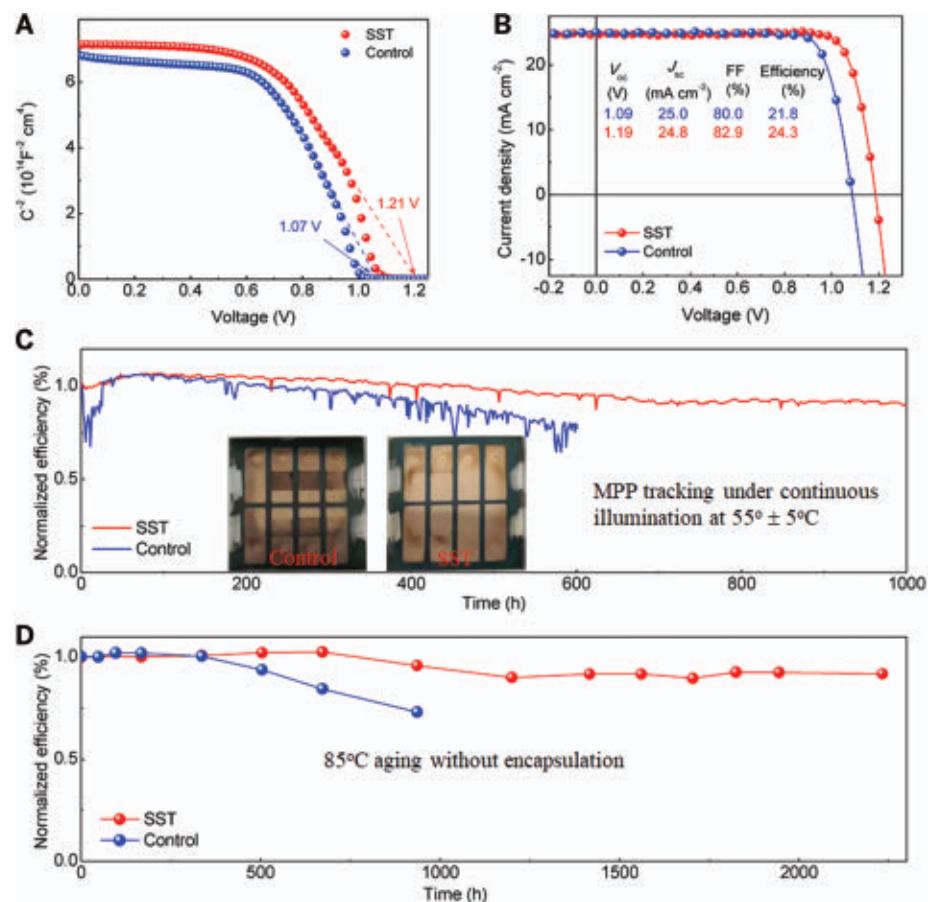


Fig. 4. Stabilization of the perovskite heterojunction. (A and B) SEM-EDX mapping in the PCBM layer of control (A) and SST-based (B) PSCs after MPP tracking. The samples are prepared by removing the top Cu electrode of the PSCs (movie S1). The I elements indicate the ion penetration from perovskite to PCBM. The C elements represent the PCBM. (C) Surface potential mapping of the PCBM layer in PSCs using KPFM.

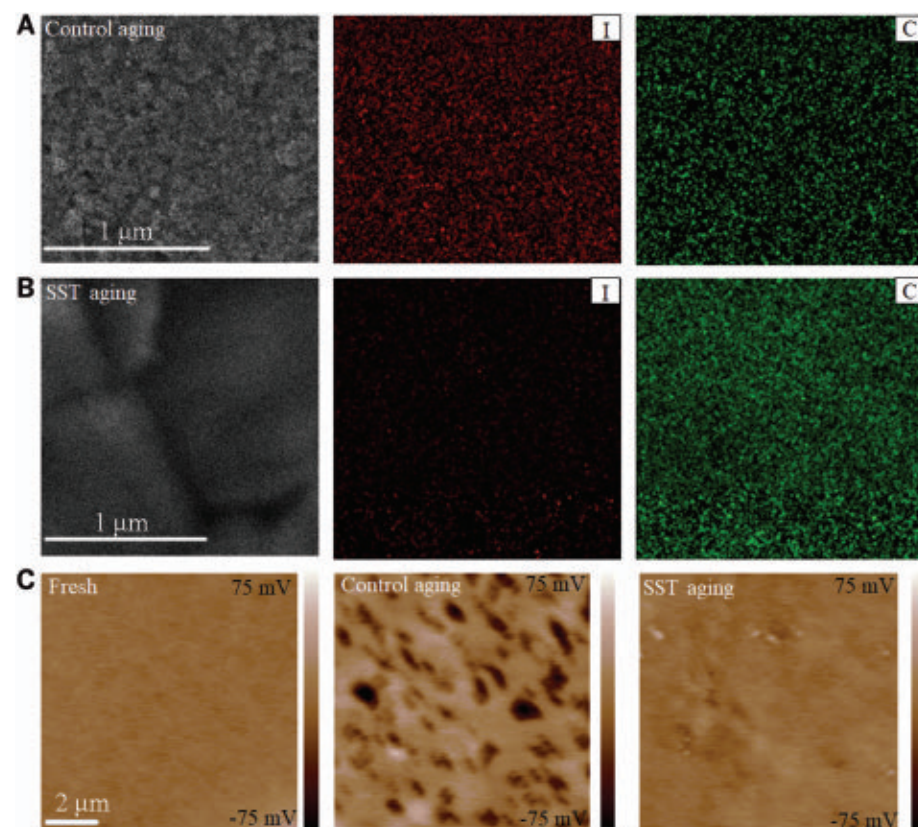


Fig. 3C, the Cu electrode of PSCs became black after MPP tracking, indicating severe degradation (23). Only 77.6% of the initial PCE was retained in control PSCs after MPP tracking for 600 hours. In PSCs with SST, no obvious change in the Cu electrode was observed. PSCs with SST retained 90.5% of their initial PCE after continuous MPP tracking for 1000 hours under illumination at $55^\circ \pm 5^\circ\text{C}$ (Fig. 3C, with non-normalized data in fig. S20A). Thermal stability was also greatly improved in PSCs with SST, and 91.8% of the initial PCE was retained after aging at 85°C for 2200 hours (Fig. 3D), whereas control PSCs retained only 73.2% of the initial PCE after 1000 hours (non-normalized data in fig. S20B).

In PSCs, ion migration or diffusion is a major cause for device degradation that cannot be avoided by encapsulation. Ion diffusion in PSCs induced degradation of perovskite and perovskite/PCBM heterojunctions (22) and also corroded metal electrodes (23). The color variations of the Cu electrode in control PSCs confirmed the electrode corrosion, which should be caused by I^- ion diffusion during MPP tracking (inset of Fig. 3C). To verify this point, we removed the Cu electrode of PSCs after MPP tracking (fig. S21 and movie S1) and measured the exposed PCBM with SEM-EDX. In control PSCs, almost no perovskite morphology was distinguished and a strong I signal appeared in the PCBM layer (Fig. 4A, with total element spectra in fig. S22A), indicating the degradation of the perovskite interface and severe ion diffusion. In PSCs with SST, perovskite grains were still distinguished and the I signal was very weak (Fig. 4B, with total element spectra in fig. S22B), indicative of a well-protected perovskite interface. We also used Kelvin probe force microscopy (KPFM) to investigate the electrical properties of the exposed PCBM layer. In PSCs with SST, the PCBM layer after MPP tracking showed a surface potential similar to that of the PCBM layer in fresh devices (Fig. 4C), whereas in control PSCs, the surface potential showed large fluctuations and low potential areas (dark regions in Fig. 4C) appeared randomly after MPP tracking.

We therefore conclude that besides improving device efficiency, SST also effectively inhibits ion migration and protects the PCBM layer in inverted PSCs, thus increasing device stability.

REFERENCES AND NOTES

- National Renewable Energy Laboratory, Best research-cell efficiency chart; www.nrel.gov/pv/cell-efficiency.html.
- Q. Jiang et al., *Nat. Photonics* **13**, 460–466 (2019).
- W. Hui et al., *Science* **371**, 1359–1364 (2021).
- J. J. Yoo et al., *Nature* **590**, 587–593 (2021).
- H. Lu et al., *Science* **370**, eabb8985 (2020).
- S. Bai et al., *Nature* **571**, 245–250 (2019).
- X. Zheng et al., *Nat. Energy* **5**, 131–140 (2020).
- D. Luo et al., *Science* **360**, 1442–1446 (2018).
- G. E. Eperon, D. Moerman, D. S. Ginger, *ACS Nano* **10**, 10258–10266 (2016).
- F. Deschler et al., *J. Phys. Chem. Lett.* **5**, 1421–1426 (2014).
- T. Leijtens et al., *ACS Nano* **8**, 7147–7155 (2014).
- S. Xiong et al., *Joule* **5**, 467–480 (2021).
- J. Qing et al., *Adv. Energy Mater.* **8**, 1800185 (2018).
- A. Amat et al., *Nano Lett.* **14**, 3608–3616 (2014).
- C. Motta et al., *Nat. Commun.* **6**, 7026 (2015).
- F. El-Mellouhi et al., *ChemSusChem* **9**, 2648–2655 (2016).
- Y. Wang et al., *Science* **365**, 687–691 (2019).
- X. Li et al., *Nat. Commun.* **9**, 3806 (2018).
- J. Carrillo et al., *Adv. Energy Mater.* **6**, 1502246 (2016).
- A. Guerrero et al., *ACS Nano* **10**, 218–224 (2016).
- Y. Zhao et al., *J. Phys. Chem. C* **121**, 14517–14523 (2017).
- X. Li et al., *Nano Energy* **64**, 103962 (2019).
- X. Li et al., *Sci. Adv.* **6**, eabd1580 (2020).
- X. Li, W. Zhang, W. Zhang, H.-Q. Wang, J. Fang, *Nano Energy* **58**, 825–833 (2019).
- X. Li et al., *J. Mater. Chem. A* **9**, 12684–12689 (2021).
- N. Li et al., *Nat. Energy* **4**, 408–415 (2019).
- F. Wang, S. Bai, W. Tress, A. Hagfeldt, F. Gao, *NPJ Flex. Electron.* **2**, 22 (2018).
- S. Yang et al., *Science* **365**, 473–478 (2019).
- Z. Ning et al., *Nature* **523**, 324–328 (2015).
- M. Liu et al., *Nature* **570**, 96–101 (2019).
- M. A. Hines, G. D. Scholes, *Adv. Mater.* **15**, 1844–1849 (2003).
- S. Fu et al., *Adv. Energy Mater.* **9**, 1901852 (2019).
- Y. Shao, Z. Xiao, C. Bi, Y. Yuan, J. Huang, *Nat. Commun.* **5**, 5784 (2014).
- W. Tress, *Adv. Energy Mater.* **7**, 1602358 (2017).
- Y.-W. Jang et al., *Nat. Energy* **6**, 63–71 (2021).
- O. Almora, C. Aranda, E. Mas-Marzá, G. García-Belmonte, *Appl. Phys. Lett.* **109**, 173903 (2016).
- X. Li et al., *J. Mater. Chem. A* **3**, 15024–15029 (2015).
- X. Li et al., *ACS Appl. Mater. Interfaces* **9**, 31357–31361 (2017).

ACKNOWLEDGMENTS

Funding: This work was supported by the National Natural Science Foundation of China (51903242, 52173161, 61974150, and 62104070), the Key Research Program of Frontier Sciences, the Chinese Academy of Sciences (CAS) (QY2DB-SSW-JSC047), and the Fundamental Research Funds for the Central Universities.

Author contributions: J.F. supervised the whole project. J.F. and X.L. conceived the idea. X.L. designed the experiment and characterized the devices. W.Z. and X.G. helped fabricate the perovskite solar cells. C.L. and J.W. helped conduct the SEM and EDX mapping characterization. X.L. and J.F. discussed and co-wrote the paper. **Competing interests:** J.F. and X.L. are inventors on patent (202110941804.1, China) submitted by East China Normal University. **Data and materials availability:** All data are available in the main text or the supplementary materials.

SUPPLEMENTARY MATERIALS

science.org/doi/10.1126/science.abl5676
Materials and Methods
Supplementary Text
Fig. S1 to S22
Table S1
Movie S1

22 July 2021; accepted 17 December 2021
10.1126/science.abl5676

2D MATERIALS

Spin-orbit-driven ferromagnetism at half moiré filling in magic-angle twisted bilayer graphene

Jiang-Xiazi Lin¹, Ya-Hui Zhang², Erin Morissette¹, Zhi Wang¹, Song Liu³, Daniel Rhodes³, K. Watanabe⁴, T. Taniguchi⁴, James Hone³, J. I. A. Li^{1*}

Strong electron correlation and spin-orbit coupling (SOC) can have a profound influence on the electronic properties of materials. We examined their combined influence on a two-dimensional electronic system at the atomic interface between magic-angle twisted bilayer graphene and a tungsten diselenide crystal. We found that strong electron correlation within the moiré flatband stabilizes correlated insulating states at both quarter and half filling, and that SOC transforms these Mott-like insulators into ferromagnets, as evidenced by a robust anomalous Hall effect with hysteretic switching behavior. The coupling between spin and valley degrees of freedom could be demonstrated through control of the magnetic order with an in-plane magnetic field or a perpendicular electric field. Our findings establish an experimental knob to engineer topological properties of moiré bands in twisted bilayer graphene and related systems.

The van der Waals (vdW) moiré structures are an intriguing platform for exploring the interplay of correlation, topology, and broken symmetry in two-dimensional (2D) electronic systems. The rotational alignment between two sheets of vdW crystal gives rise to a flat moiré energy band where strong Coulomb correlation plays a dominating role in a rich landscape of emergent quantum phenomena (1–7). In a graphene moiré struc-

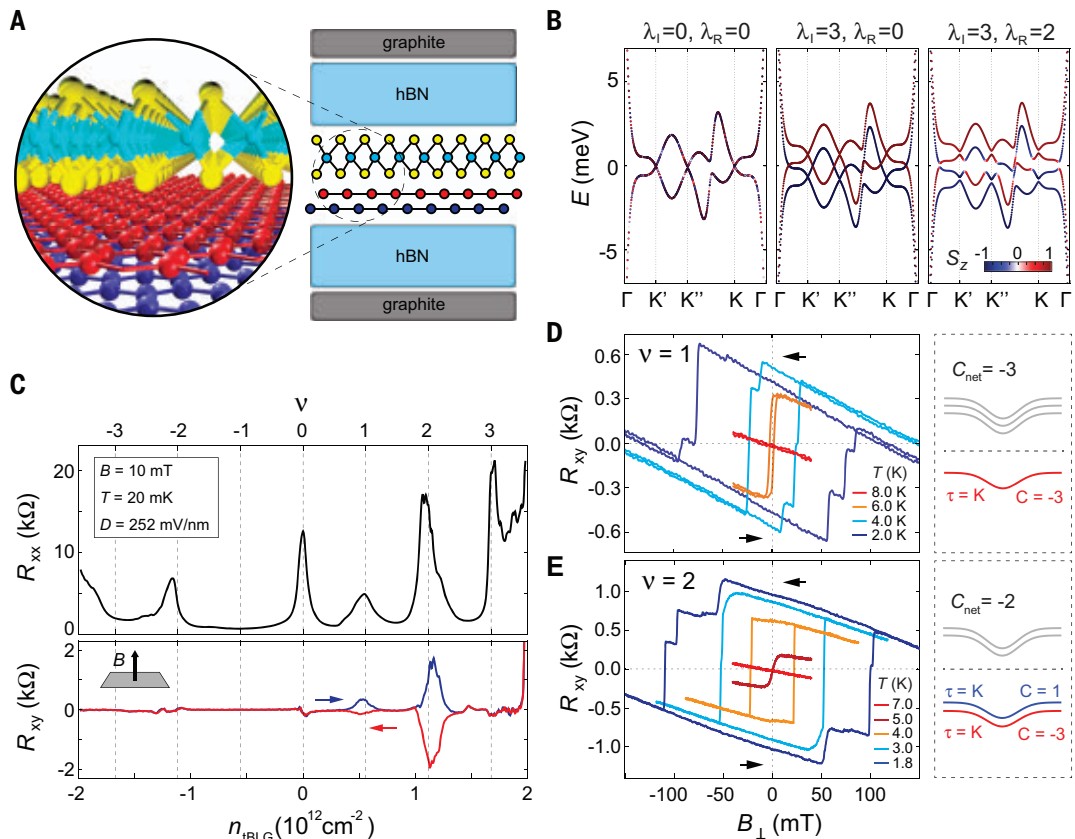
ture, breaking the C_2T symmetry was shown to stabilize spontaneous orbital ferromagnetism at quarter and three-quarter filling, which is manifested in a robust anomalous Hall effect (AHE) with hysteretic switching transitions (8–11). Unlike one- and three-quarter filling, a potential orbital ferromagnetic state at a half-filled moiré band would feature a spin-unpolarized edge mode that is able to approximate superconducting pairing along a ferromagnet/superconductor interface (12). Such a construction has been proposed to be the key to realization of the Majorana mode. However, an orbital ferromagnet is predicted to be energetically unfavorable in twisted graphene structures, owing to the intervalley Hund's coupling (13–16).

¹Department of Physics, Brown University, Providence, RI 02912, USA. ²Department of Physics, Harvard University, Cambridge, MA 02138, USA. ³Department of Mechanical Engineering, Columbia University, New York, NY 10027, USA. ⁴National Institute for Materials Science, 1-1 Namiki, Tsukuba 305-0044, Japan.

*Corresponding author. Email: jia_li@brown.edu

Fig. 1. Emerging ferromagnetic order from the tBLG/WSe₂ interface.

(A) Schematic of the heterostructure, consisting of a tBLG/WSe₂ interface that is doubly encapsulated with hBN and graphite. **(B)** Calculated dispersion of moiré bands for a single valley. λ_I and λ_R indicate the strength of Ising and Rashba SOC, respectively, in units of meV. Red and blue colors denote the out-of-plane component of the spin moment of each band. The Chern number is expected to be zero for all energy bands in the absence of λ_R (left and center panels). The combination of strong Ising and Rashba SOC gives rise to a nonzero valley Chern number. Values of λ_I and λ_R are taken from previous measurements of proximity-induced SOC (27, 44). **(C)** Longitudinal and transverse resistance, R_{xx} and R_{xy} , as carrier density n_{tBLG} is swept back and forth. Carrier density n_{tBLG} and moiré filling ν are denoted as the bottom and top axis, respectively. The measurement is performed at $B = 10$ mT, $T = 20$ mK, and $D = 252$ mV/nm. **(D and E)** R_{xy} measured at $n_{\text{tBLG}} = 0.55 \times 10^{12} \text{ cm}^{-2}$ near $\nu = 1$ (D) and $n_{\text{tBLG}} = 1.22 \times 10^{12} \text{ cm}^{-2}$ near $\nu = 2$ (E) as B_{\perp} is swept back and forth. These measurements are performed at $D = 0$. The hysteresis loop disappears at high temperature. Right: Schematic band structure at $\nu = +1$ (D) and $\nu = +2$ (E). In (E), the two lowest bands feature the same valley index and have nonzero Chern numbers of $C = -3$ and $+1$. As a result, the ground state at $\nu = 2$ is valley-polarized with net Chern number $C_{\text{net}} = -2$.



As an essential ingredient in forming certain topological phases, spin-orbit coupling (SOC) provides an additional experimental knob to engineer the topological properties of moiré structures (17–19). It was recently proposed that SOC endows the moiré energy band with nonzero Berry curvature, making ferromagnetic order at half moiré filling a possibility without alignment with the hexagonal boron nitride (hBN) substrate (16, 20). Unlike bulk materials, where tuning the chemical composition is required to produce spin-orbit locking, an alternative route through the proximity effect exists in vdW structures. Close proximity between graphene and transition metal dichalcogenide crystals, such as tungsten diselenide (WSe₂), allows the electron wave functions from both crystals to overlap and hybridize, endowing graphene with strong SOC (21–28). In this work, we use transport measurement to examine the effect of proximity-induced SOC on properties of the moiré band and its associated quantum phases.

The geometry of the twisted bilayer graphene (tBLG)/WSe₂ heterostructure is shown in Fig. 1A. An atomic interface is created by stacking a few-layer WSe₂ crystal on top of magic-

angle tBLG, which is further encapsulated with dual hBN and graphite crystals above and below to achieve optimal sample quality (29). Transport measurement indicated excellent sample quality with low charge fluctuation $\delta n \sim 0.08 \times 10^{12} \text{ cm}^{-2}$ (fig. S10). Longitudinal resistance R_{xx} (measured from tBLG) exhibited a series of well-defined resistance peaks emerging at partial filling of the moiré band, $\nu = -2, +1, +2$, and $+3$, which are associated with the correlated insulator states. The positions of these peaks were consistent with a twist angle of $\theta \approx 0.98^\circ$. The tBLG and the hBN substrate were maximally misaligned, according to the optical image of the heterostructure (fig. S2) (16), which is consistent with the gapless appearance of the sample at the charge neutrality point (CNP) [see (16) for more discussion of the coupling between tBLG and hBN] (8, 9). Transverse resistance measurements revealed large Hall resistance R_{xy} at $\nu = +1$ and $+2$; the Hall resistance exhibited hysteretic switching behavior as the field effect-induced doping in tBLG, n_{tBLG} , was swept back and forth (Fig. 1C). Hysteresis in magnetization reversal was also observed while sweeping an external magnetic field aligned

perpendicular to the 2D interface, B_{\perp} (Fig. 1, D and E). We note that the resistance peak at $\nu = +2$ vanishes at large in-plane B field (fig. S9) (16), indicating a spin-unpolarized isospin configuration. As such, the ground state is likely valley-polarized and the ferromagnetic order is orbital. This is further illustrated by a schematic representation of the band structure (Fig. 1, D and E, right panels), where the two lowest conduction bands feature the same valley index with nonzero Chern numbers $C = -3$ and $+1$.

A valley-polarized state at $\nu = 2$ is unfavorable in the absence of SOC because of the influence of intervalley Hund's coupling (13–16). As a result, observations of orbital ferromagnetism at the half-filled moiré band have remained elusive (8, 9, 30). To this end, the AHE at $\nu = +2$ in our sample provides strong evidence that the moiré band structure is transformed by proximity-induced SOC, which is more dominant than intervalley Hund's coupling (20). Although the presence of SOC endows the moiré flatband with a nonzero Chern number (Fig. 1, D and E), the observed Hall resistance is much smaller than the expected value of the quantum AHE. We ascribe

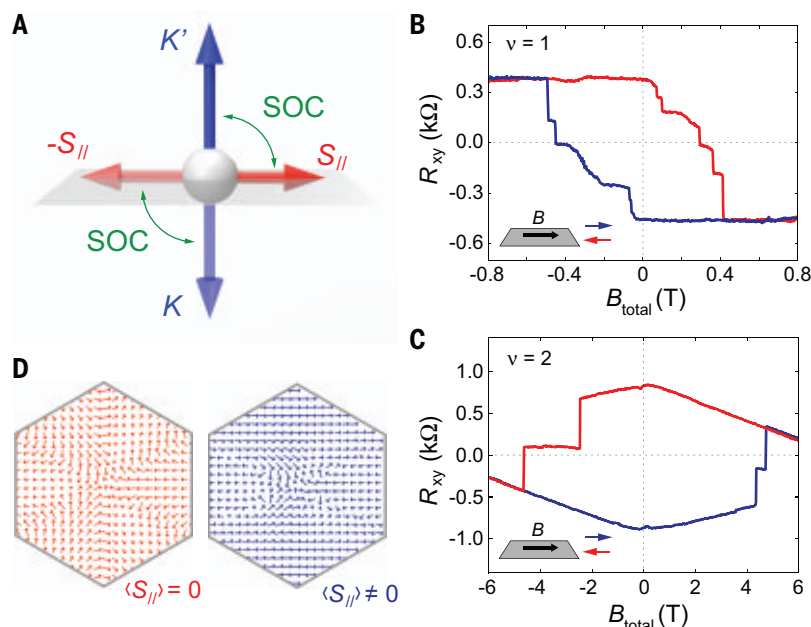


Fig. 2. Control of magnetic order using an in-plane magnetic field. (A) Schematic showing the effect of SOC, which couples the in-plane component of spin, $\pm S_{||}$, with the out-of-plane component of valley, $\tau_z = K$ and K' . (B and C) R_{xy} as a function of in-plane B field, which is aligned within 0.5° of the tBLG/WSe₂ interface. Traces and retraces are shown as blue and red solid lines, respectively. The measurement is performed at $v = +1$ and $D = -167$ mV/nm (B) and at $v = +2$ and $D = 0$ (C). (D) The orientation of in-plane spin momentum over the MBZ for valley K , which is obtained by diagonalizing the single-particle Hamiltonian (Fig. 1B) (16). Here we show the first conduction band with valley index K above the neutrality. In the presence of C_3 symmetry, $\langle S_{||}^K \rangle$ averages to zero (left), whereas a uniaxial strain breaks C_3 , resulting in nonzero $\langle S_{||}^K \rangle$ (right).

this behavior to the presence of bulk conduction channels parallel to the chiral edge conduction, which could result from the presence of magnetic domain walls (8) or sample disorder. A fully developed Chern insulator state could be realized in a sample with lower disorder or stronger SOC, hence a larger energy gap.

To better understand the influence of proximity-induced SOC, we note that the introduction of SOC adds an extra term to the Hamiltonian:

$$h_{\text{SOC}}(\mathbf{k}) = \frac{1}{2} \lambda_I \tau_z s_z + \frac{1}{2} \lambda_R (\tau_x \sigma_x s_y - \sigma_y s_x) \quad (1)$$

where τ , σ , and s denote the Pauli matrix for valley, sublattice, and spin at each momentum \mathbf{k} , and λ_I and λ_R represent the Ising and Rashba SOC coefficients, respectively (eqs. S3 to S7) (16). The Ising SOC locks the valley moment τ_z with the spin moment s_z , whereas the Rashba term λ_R locks the in-plane spin s_x, s_y with the sublattice σ_x, σ_y (the locking depends on the valley τ_z). For tBLG without SOC, there is a C_2 symmetry defined as $C_2: \tau_x \sigma_x$ and time-reversal symmetry defined as $T: i \tau_x s_y K$, where K is the complex conjugation. Both the Ising and Rashba SOC break the C_2 symmetry while preserving

the time reversal. Therefore, $C_2 T$ is broken in the presence of proximity-induced SOC.

The combination of Rashba SOC and time-reversal symmetry gives rise to a valley-contrasting spin texture within the mini-Brillouin zone (MBZ) for each band: For any momentum k , spin for the two valleys points in opposite directions, $\mathbf{s}_K(\mathbf{k}) = -\mathbf{s}_{K'}(-\mathbf{k})$. The average value of the in-plane spin moment of each band is obtained by integrating over the MBZ for valley K (K'),

$$\langle S_{||,K}^K \rangle = \frac{1}{N} \sum_{\mathbf{k} \in \text{MBZ}} \langle s_{||,K}^K(\mathbf{k}) \rangle \quad (2)$$

where N is the system size. We note that a broken C_3 rotation symmetry could lead to nonzero $\langle S_{||}^K \rangle$ and $\langle S_{||}^{K'} \rangle$. In this scenario, time-reversal symmetry is preserved by the valley-contrasting spin texture $\langle S_{||}^K \rangle = -\langle S_{||}^{K'} \rangle$. On the other hand, an orbital ferromagnetic state emerges because valley-polarized Chern bands are occupied, spontaneously breaking time-reversal symmetry. Most remarkably, the combination of SOC, valley polarization, and a broken C_3 rotation symmetry allows an in-plane magnetic field to couple to the orbital magnetic order through the in-plane Zeeman energy.

This control of the out-of-plane magnetic order using an in-plane magnetic field, $B_{||}$, is demonstrated in Fig. 2, B and C: As $B_{||}$ is swept back and forth, R_{xy} exhibits hysteretic switching behavior at both $v = +1$ and $+2$. Using Hall resistance measurements, we show that the out-of-plane component of the B field is negligible relative to the out-of-plane coercive field, confirming that the magnetic order is indeed controlled by the in-plane component of the B field, $B_{||}$ (fig. S4). At the same time, direct coupling between the valley order and $B_{||}$ is shown to be absent in tBLG samples without SOC (31), which rules out the orbital effect as a possible origin for the observed $B_{||}$ dependence. These results suggest that B_{\perp} and $B_{||}$ couple to the magnetic order through different mechanisms: B_{\perp} directly controls the magnetic ground state through valley Zeeman coupling, $E_Z^v = -\gamma_v B_{\perp} \tau_z$, whereas the influence of $B_{||}$ arises from the combination of SOC and spin Zeeman coupling, $E_Z^s = -\gamma_s \tau_z \mathbf{B}_{||} \cdot \langle \mathbf{S}_{||} \rangle$. Here, τ_z corresponds to the valley polarization, and γ_v and γ_s are the valley and spin gyromagnetic ratio, respectively.

We note a few intriguing properties of the B -induced hysteresis behavior in Figs. 1 and 2: (i) A large value of $B_{||}$ stabilizes opposite magnetic orders at $v = +1$ and $+2$, as is evidenced by R_{xy} with opposite signs (Fig. 2, B and C). This indicates that $\langle S_{||} \rangle$ points in opposite directions for $v = +1$ and $+2$. On the other hand, an out-of-plane B field stabilizes the same magnetic order at different fillings (Fig. 1, D and E), providing further confirmation that $v = +1$ and $+2$ feature the same valley index and the ground state at half-filling is valley-polarized. (ii) Although the out-of-plane coercive fields are similar, the in-plane coercive field at $v = 2$ is much bigger than at $v = 1$. This suggests that the average in-plane spin moment $\langle S_{||} \rangle$ is much smaller at $v = 2$, which is consistent with a predominantly spin-unpolarized ground state (fig. S9) (16). It is noteworthy that the observed behavior at $v = +2$ does not rule out alternative isospin configurations. Our results provide important constraints for future theoretical work to examine such possibilities. The effective control of in-plane B field on the magnetic order not only provides further validation that the orbital ferromagnetic order is stabilized by proximity-induced SOC, it also reveals that a broken C_3 rotational symmetry gives rise to a nonzero $\langle S_{||} \rangle$. A spontaneously broken C_3 symmetry naturally derives from the combination of strong SOC and nematic charge order (32–34). Alternatively, a preferred in-plane direction for spin could result from a small amount of uniaxial strain in the moiré lattice (Fig. 2D), which is known to be common for tBLG samples (35, 36).

The proximity-induced SOC arises from wave function overlap across the interface (22). The role of wave function overlap was

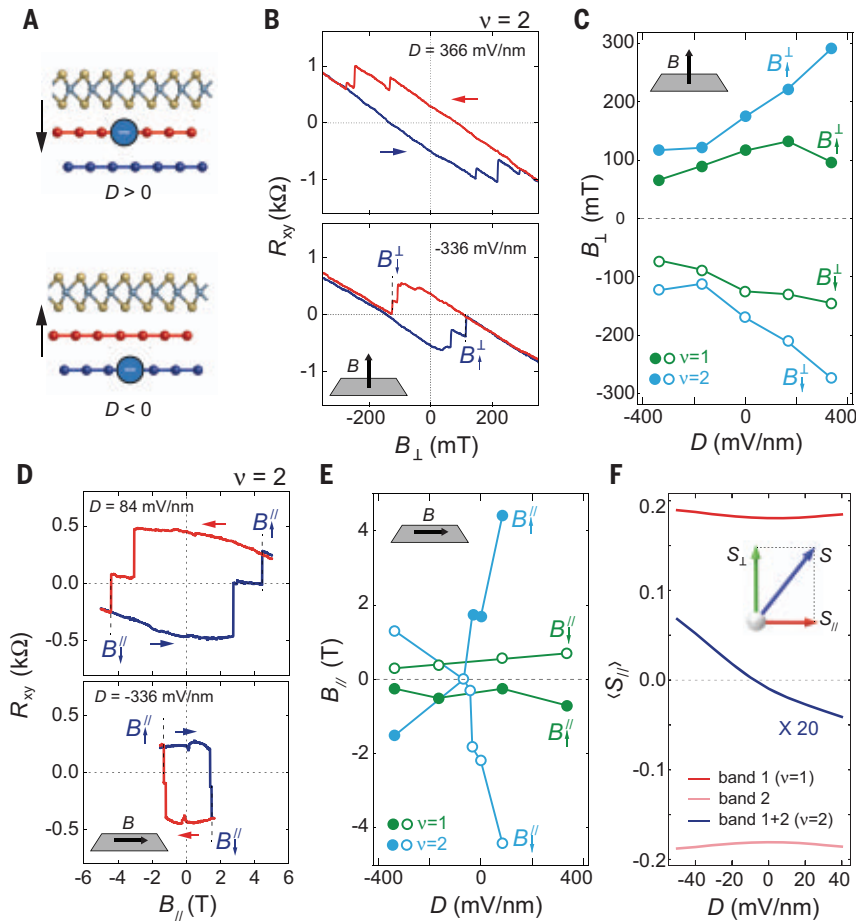


Fig. 3. Displacement-field dependence. (A) Schematic demonstrating the effect of electric displacement D on layer polarization. (B) B -induced hysteresis loops of R_{xy} measured at different values of D , with B field aligned perpendicular to the 2D layers. (C) Out-of-plane coercive fields B_{\perp}^+ and B_{\perp}^- for both $\nu = +1$ and $+2$ as a function of D . (D) Same as (B), but for B field parallel to the 2D layers. (E) Same as (C), but for in-plane coercive fields B_{\parallel}^+ and B_{\parallel}^- . B_{\perp} and B_{\parallel} are defined as the value of B where the sign of R_{xy} switches from negative to positive and from positive to negative, respectively; the superscript denotes the orientation of the B field (fig. S11) (16). Both in-plane and out-of-plane magnetic hysteresis behaviors for $\nu = +1$ are measured at $T = 20$ mK. At $\nu = +2$, out-of-plane magnetic hysteresis is measured at $T = 20$ mK, whereas in-plane hysteresis is measured at $T \leq 3$ K (fig. S11) (16). (F) $\langle S_{\parallel} \rangle$ calculated from the four-band model as a function of D for the two lowest-energy bands 1 and 2 for the valley K. Both bands feature large $\langle S_{\parallel} \rangle$ that are mostly independent of D , shown as red and pink traces, respectively. The combination of bands 1 and 2 yields a nonzero, albeit small, $\langle S_{\parallel} \rangle$, which changes sign around $D = 0$.

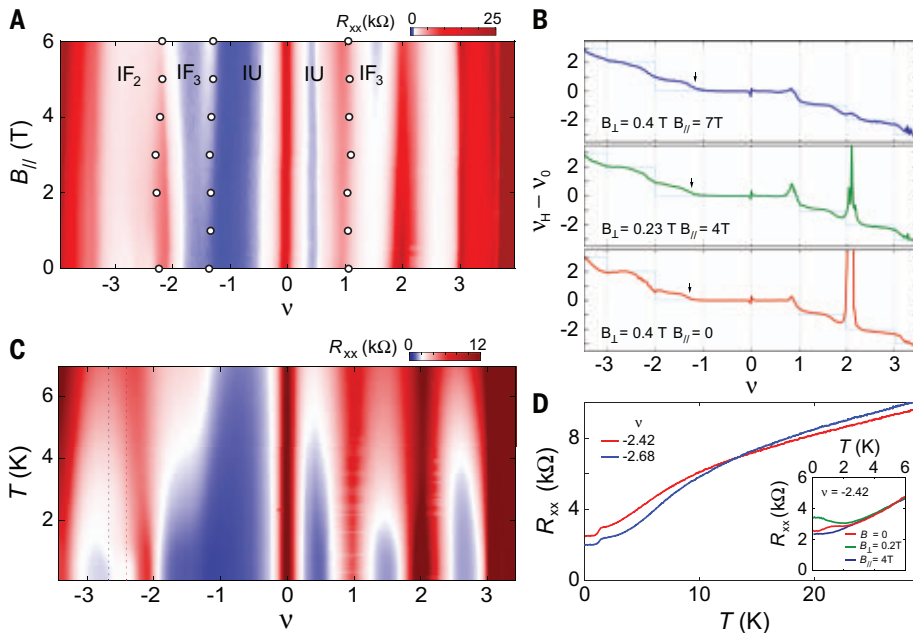


Fig. 4. Isospin order and the absence of superconductivity. (A) R_{xx} as a function of moiré filling ν and in-plane magnetic field B_{\parallel} measured at $T = 20$ mK. Carrier density is controlled by sweeping bottom-gate voltage while top-gate voltage is kept at zero. Circles denote the phase boundary between symmetry-breaking isospin ferromagnets (IF₂ and IF₃) and an isospin-unpolarized state (IU), which is defined as the peak position in $d(\nu_H - \nu_0)/d\nu$. (B) Renormalized Hall density, $\nu_H - \nu_0$, expressed in electrons per superlattice unit cell, measured at different values of B_{\parallel} and B_{\perp} for $D = 252$ mV/nm. The expected Hall density steps of tBLG without SOC are shown in light blue for each condition (38). (C) Longitudinal resistance R_{xx} as a function of temperature and moiré filling measured at $B = 0$ and $D = 252$ mV/nm. (D) R - T line trace extracted from (C) along the vertical dashed lines. Inset: R_{xx} increases slightly with increasing B_{\perp} but decreases with B_{\parallel} , displaying no clear indication of Zeeman-induced Cooper pair breaking.

recently demonstrated experimentally, as SOC strength has been shown to depend on inter-layer separation, which is tunable with hydrostatic pressure (37). In the same vein, we show that SOC strength can be controlled with a

perpendicular electric field D : Under a positive D , charge carriers are polarized toward the WSe₂ crystal, resulting in increased wave function overlap and stronger SOC; contrari-

polarized away from the WSe₂ crystal, resulting in decreased wave function overlap and weaker SOC (Fig. 3A) (22, 37). Figure 3 demonstrates the effect of D by plotting the evolution of B -induced hysteresis loops: With increasing

D , hysteresis loops exhibit larger coercive fields (B_{\uparrow}^{\parallel} and $B_{\downarrow}^{\parallel}$) for both $\nu = +1$ and $+2$ (Fig. 3, B and C). Transport measurements near the CNP show that the width of the disorder regime remains the same over a wide range of D field (fig. S10B), which suggests that changes in the coercive field are not caused by the influence of disorder across two graphene layers. Because the value of the coercive field reflects the robustness of magnetic order, the D dependence shown in Fig. 3C provides another indication that the orbital ferromagnetism is stabilized by proximity-induced SOC.

The effect of varying D at $\nu = +2$ is drastically different in the presence of an in-plane magnetic field B_{\parallel} : Changing D induces a magnetization reversal, as evidenced by hysteresis loops with opposite signs in R_{xy} (Fig. 3D and fig. S12A) (16). The D -induced reversal is also manifested in the sign change of coercive fields B_{\uparrow}^{\parallel} and $B_{\downarrow}^{\parallel}$ at $D \sim -100$ mV/nm (Fig. 3E). A possible explanation for this unique D dependence is obtained by examining the average in-plane spin moment for valley K , $\langle S_K^{\parallel} \rangle$. Calculations using the four-band model show that $\langle S_K^{\parallel} \rangle$ changes sign with varying D at $\nu = 2$ (Fig. 3F), indicating that an in-plane B field favors opposite valley polarizations at different values of D . By comparison, Fig. 3F shows that no sign change in $\langle S_K^{\parallel} \rangle$ is expected at $\nu = 1$, which is consistent with our experimental observation (Fig. 3E). Because carrier density remains the same when changing D , the D -controlled magnetization reversal represents electric field control of the magnetic order, which is made possible by proximity-induced SOC.

Next, we consider the effect of SOC on iso-spin polarization and superconductivity. In the absence of SOC, the ground state at $\nu = -1$ was shown to be isospin-unpolarized at $B = 0$ (38, 39). The application of a large in-plane magnetic field lifts the isospin degeneracy, stabilizing an isospin ferromagnetic state (IF_3) near $\nu = -1$, which is separated from the unpolarized state (IU) by a resistance peak in R_{xx} and a step in the Hall density (38, 39). Figure 4, A and B, shows that this phase boundary between IF_3 and IU extends to $B_{\parallel} = 0$ in the presence of proximity-induced SOC. These studies show that the influence of SOC on the iso-spin degeneracy is comparable to that of a large in-plane magnetic field (fig. S7) (16).

Our findings show that the superconducting phase is unstable against proximity-induced SOC in our sample. As shown in Fig. 4C, no zero-resistance state is observed over the full density range of the moiré band. In addition, R_{xx} - T traces exhibit no clear downturn with decreasing T at moiré filling $\nu = -2 - \delta$, where a robust superconducting phase usually emerges in magic-angle tBLG (Fig. 4D). Because strong Ising and Rashba SOC break C_2T symmetry, the absence of superconductivity, combined

with the emergence of AHE, is potentially consistent with a recent theoretical proposal that C_2T symmetry is essential for stabilizing the superconducting phase in tBLG (40). Our results are distinct from another experimental report showing robust superconductivity stabilized by SOC in tBLG away from the magic angle (28). Apart from the difference in twist angle range, these distinct observations could result from other factors discussed below. The D dependence shown in Fig. 3 suggests that a dual-gated geometry, which allows independent control on D and n_{tBLG} , is key to investigating the influence of proximity-induced SOC in WSe_2/tBLG samples. When carrier density is controlled with only the bottom-gate electrode (28), doping tBLG with electrons also gives rise to a D field that pulls electrons away from the WSe_2 crystal (fig. S1) (16). This results in weaker SOC strength, which could contribute to the observation of superconductivity in singly gated tBLG/ WSe_2 samples (28).

In addition, it has been proposed that the strength of proximity-induced SOC is sensitive to the rotational alignment between graphene and WSe_2 : Strong SOC is expected when graphene is rotationally misaligned with WSe_2 by 10° to 20° , whereas perfect alignment produces weak proximity-induced SOC (41). If confirmed, this rotational degree of freedom could provide an additional experimental knob to engineer moiré band structure (42). Our sample features a twist angle of $\sim 16^\circ$ (fig. S1F) between tBLG and WSe_2 , falling in the range that is predicted to induce the strongest SOC strength. We investigated the effect of rotational misalignment between tBLG and WSe_2 in two additional samples near the magic angle: AHE and hysteresis loops were observed at $\nu = +2$ in sample A1, where tBLG and WSe_2 were misaligned at $\sim 10^\circ$ (fig. S14). On the other hand, tBLG and WSe_2 were perfectly aligned in sample A2, where AHE was absent (fig. S15) (16). The superconducting phase was absent or suppressed in all samples. These observations provide experimental support for the notion that the rotational misalignment between tBLG and WSe_2 , and thus the SOC strength, plays a key role in determining the stability of the ferromagnetic and superconducting states. Although transport measurement alone cannot definitively confirm the influence of SOC on the superconducting phase near the magic angle, our results could motivate future efforts, both theoretical and experimental, to investigate the influence of SOC on moiré structures as a function of graphene twist angle and graphene/ WSe_2 misalignment (42).

REFERENCES AND NOTES

1. Y. Cao *et al.*, *Nature* **556**, 80–84 (2018).
2. Y. Cao *et al.*, *Nature* **556**, 43–50 (2018).
3. X. Lu *et al.*, *Nature* **574**, 653–657 (2019).
4. M. Yankowitz *et al.*, *Science* **363**, 1059–1064 (2019).
5. G. Chen *et al.*, *Nature* **579**, 56–61 (2020).

6. X. Liu *et al.*, *Nature* **583**, 221–225 (2020).
7. Y. Cao *et al.*, *Nature* **583**, 215–220 (2020).
8. A. L. Sharpe *et al.*, *Science* **365**, 605–608 (2019).
9. M. Serlin *et al.*, *Science* **367**, 900–903 (2020).
10. H. Polshyn *et al.*, *Nature* **588**, 66–70 (2020).
11. S. Chen *et al.*, *Nat. Phys.* **17**, 374–380 (2021).
12. X.-L. Qi, T. L. Hughes, S.-C. Zhang, *Phys. Rev. B* **82**, 184516 (2010).
13. Y.-H. Zhang, D. Mao, Y. Cao, P. Jarillo-Herrero, T. Senthil, *Phys. Rev. B* **99**, 075127 (2019).
14. C. Repellin, Z. Dong, Y.-H. Zhang, T. Senthil, *Phys. Rev. Lett.* **124**, 187601 (2020).
15. N. Bultinck, S. Chatterjee, M. P. Zaletel, *Phys. Rev. Lett.* **124**, 166601 (2020).
16. See supplementary materials.
17. H. Zhang *et al.*, *Nat. Phys.* **5**, 438–442 (2009).
18. M. Z. Hasan, C. L. Kane, *Rev. Mod. Phys.* **82**, 3045–3067 (2010).
19. X.-L. Qi, S.-C. Zhang, *Rev. Mod. Phys.* **83**, 1057–1110 (2011).
20. T. Wang, N. Bultinck, M. P. Zaletel, *Phys. Rev. B* **102**, 235146 (2020).
21. M. Gmitra, J. Fabian, *Phys. Rev. B* **92**, 155403 (2015).
22. M. Gmitra, J. Fabian, *Phys. Rev. Lett.* **119**, 146401 (2017).
23. Z. Wang *et al.*, *Nat. Commun.* **6**, 8339 (2015).
24. Z. Wang *et al.*, *Phys. Rev. X* **6**, 041020 (2016).
25. B. Yang *et al.*, *Phys. Rev. B* **96**, 041409 (2017).
26. A. Avsar *et al.*, *Nat. Commun.* **5**, 4875 (2014).
27. J. O. Island *et al.*, *Nature* **571**, 85–89 (2019).
28. H. S. Arora *et al.*, *Nature* **583**, 379–384 (2020).
29. A. Zibrov *et al.*, *Nat. Phys.* **14**, 930–935 (2018).
30. P. Stepanov *et al.*, *Phys. Rev. Lett.* **127**, 197701 (2021).
31. A. L. Sharpe *et al.*, *Nano Lett.* **21**, 4299–4304 (2021).
32. Y. Cao *et al.*, *Science* **372**, 264–271 (2021).
33. C.-C. Liu, L.-D. Zhang, W.-Q. Chen, F. Yang, *Phys. Rev. Lett.* **121**, 217001 (2018).
34. A. O. Sboychakov, A. V. Rozhkov, A. L. Rakhmanov, F. Nori, *Phys. Rev. B* **100**, 045111 (2019).
35. L. J. McGilly *et al.*, *Nat. Nanotechnol.* **15**, 580–584 (2020).
36. A. Uri *et al.*, *Nature* **581**, 47–52 (2020).
37. B. Fülöp *et al.*, *npj 2D Mater.* **5**, 82 (2021).
38. Y. Saito *et al.*, *Nature* **592**, 220–224 (2021).
39. A. Rozen *et al.*, *Nature* **592**, 214–219 (2021).
40. E. Khalaf, S. Chatterjee, N. Bultinck, M. P. Zaletel, A. Vishwanath, *Sci. Adv.* **7**, eabf5299 (2021).
41. Y. Li, M. Koshino, *Phys. Rev. B* **99**, 075438 (2019).
42. D. M. Kennes *et al.*, *Nat. Phys.* **17**, 155–163 (2021).
43. J.-X. Lin *et al.*, Data repository for “Spin-orbit-driven ferromagnetism at half moiré filling in magic-angle twisted bilayer graphene”; doi: 10.17605/OSF.IO/UGNAV (2021).

ACKNOWLEDGMENTS

We thank A. F. Young, M. Yankowitz, and A. Vishwanath for helpful discussions and A. Mounce and M. Lilly for experimental assistance. **Funding:** This work was primarily supported by Brown University. Device fabrication was performed in the Institute for Molecular and Nanoscale Innovation at Brown University. This work was performed, in part, at the Center for Integrated Nanotechnologies, an Office of Science User Facility operated for the US Department of Energy (DOE) Office of Science. J.-X.L., E.M., and J.I.A.L. acknowledge the use of equipment funded by MRI award DMR-1827453. Synthesis of WSe_2 (S.L., D.R., J.H.) at Columbia was supported by the NSF MRSEC program through the Center for Precision-Assembled Quantum Materials (DMR-2011738). K.W. and T.T. acknowledge support from the EMEXT Element Strategy Initiative to Form Core Research Center, grant JPMXP0112101001, and CREST (JPMJCR15F3). **Author contributions:** J.-X.L., E.M., and Z.W. fabricated the devices and performed the measurements. J.-X.L., E.M., Z.W., and J.I.A.L. analyzed the data. Y.-H.Z. constructed the theoretical model. K.W. and T.T. provided the hBN crystals. S.L., D.R., and J.H. provided the WSe_2 crystals. The manuscript was written with input from all authors. **Competing interests:** The authors declare no competing financial interests. **Data and materials availability:** Experimental data files are available at the Open Science Framework (43).

SUPPLEMENTARY MATERIALS

science.org/doi/10.1126/science.abh2889
Materials and Methods
Supplementary Text
Figs. S1 to S19
References (44–46)

26 February 2021; accepted 15 December 2021
Published online 6 January 2022
10.1126/science.abh2889

MOLECULAR BIOLOGY

Sequence specificity in DNA binding is mainly governed by association

Emil Marklund¹, Guanzhong Mao^{1†}, Jinwen Yuan^{1†}, Spartak Zikrin¹, Eldar Abdurakhmanov², Sebastian Deindl^{1*}, Johan Elf^{1*}

Sequence-specific binding of proteins to DNA is essential for accessing genetic information. We derive a model that predicts an anticorrelation between the macroscopic association and dissociation rates of DNA binding proteins. We tested the model for thousands of different *lac* operator sequences with a protein binding microarray and by observing kinetics for individual *lac* repressor molecules in single-molecule experiments. We found that sequence specificity is mainly governed by the efficiency with which the protein recognizes different targets. The variation in probability of recognizing different targets is at least 1.7 times as large as the variation in microscopic dissociation rates. Modulating the rate of binding instead of the rate of dissociation effectively reduces the risk of the protein being retained on nontarget sequences while searching.

Sequence-specific recognition and binding of DNA target sites by proteins such as polymerases, DNA-modifying enzymes, and transcription factors are essential for gene expression and regulation across all kingdoms of life (1). The textbook explanation for this sequence dependence of binding posits that favorable hydrogen bonding interactions between the protein and particular DNA sequences result in prolonged binding times (2). Consequently, the rate of protein dissociation would depend on the DNA sequence, whereas the association rate would be invariant with respect to sequence. Indeed, the rate of protein association with DNA has often been assumed to be sequence independent (3–6). However, single-molecule measurements have shown that when a protein scans the DNA for binding sites, the association rate does depend on the sequence (7), and that different target sequences can be bypassed with distinct probabilities (8). These variations have been ascribed to differences in the probability of recognition when the protein is centered on the target sequence (7). It is, however, unknown whether the specific retention of a given sequence is chiefly caused by differences in the probability of recognition or in the rate of dissociation. The physical constraints on the rate constants are unknown beyond the fact that the ratio of association and dissociation rates is necessarily dictated by the free-energy difference between the free and bound states.

To explore what limits the association and dissociation rates, we considered the theoretical standard model (9), according to which a protein has a nonspecific testing mode where it is

bound nonspecifically to DNA (Fig. 1A). In the testing state, where the protein can slide into the target sequence through nonspecific interactions, the protein can either specifically bind the target with probability p_{tot} or dissociate into solution with probability $1 - p_{\text{tot}}$. When the association process is modeled as a three-state (specifically bound, nonspecifically bound, and dissociated) continuous-time Markov chain, the effective macroscopic target association and dissociation rate constants (k_a and k_d) relate to each other according to

$$k_a = k_{\text{on,max}} - \frac{k_{\text{on,max}}}{k_{\text{off},\mu}} k_d \quad (1)$$

where $k_{\text{on,max}}$ is the association rate constant given by a searching protein that binds the target upon every nonspecific encounter ($p_{\text{tot}} = 1$), and $k_{\text{off},\mu}$ is the rate of microscopic dissociation from the bound state into the nonspecifically-bound searching mode (see supplementary text for derivation of Eq. 1). This equation implies that the macroscopic association and dissociation rates are inherently coupled, and linearly anticorrelated if binding sites exhibit identical microscopic dissociation rates, because $k_{\text{on,max}}$ does not depend on the specific sequence. The linear relationship between k_a and k_d described by Eq. 1 is implicitly parameterized by the probability p_{tot} of binding rather than dissociating from the nonspecifically bound state, such that an increase in p_{tot} causes an increase in k_a and a corresponding decrease in k_d (Fig. 1B). The anticorrelation can be intuitively understood by acknowledging that a decrease in the number of target site encounters required for successful binding must in turn result in a corresponding increase in the number of dissociation attempts needed for the macroscopic dissociation from the target (Fig. 1C). Notably, Eq. 1 makes it possible to access the microscopic parameters $k_{\text{off},\mu}$ and p_{tot} from

macroscopically measurable parameters, such as k_a and k_d . In Fig. 1D, we show predictions for the distributions of k_a and k_d that would be observed experimentally for different binding sequences when $k_{\text{off},\mu}$ and p_{tot} are varied in different ways (see also materials and methods). Three scenarios that yield the same range of $K_D = k_d/k_a$ are simulated by (i) varying mainly $k_{\text{off},\mu}$, (ii) varying $k_{\text{off},\mu}$ and p_{tot} to the same extent, or (iii) by varying mainly p_{tot} . Notably, all three scenarios give distinct distributions in (k_a, k_d) -space (Fig. 1D). The linear anticorrelation between k_a and k_d is observed only in the scenario when p_{tot} varies to a larger extent than $k_{\text{off},\mu}$.

To experimentally test whether there is anticorrelation between association and dissociation rates, we measured the kinetics by which a prototypical DNA-binding protein—the *lac* repressor (LacI)—binds to different operator sequences. To directly compare the rates for the association to and dissociation from different operators under identical experimental conditions, we used a protein binding microarray (PBM) (10) with 2479 different operator sequences that are mutated versions of the natural O_1 and O_2 , as well as the artificially strong O_{sym} sequences. PBMs are normally used to study equilibrium binding, but by mounting the array in a flow cell on the microscope (fig. S1A), we were able to monitor the binding and unbinding kinetics of fluorescent LacI-Cy3 in real time (Fig. 2, A and B). The Cy3 label at a site distal to the DNA binding domain has previously been shown to affect neither the specific nor the nonspecific DNA binding (8) (labeling efficiency: 84.5%; see also supplementary text and table S1). Because it is impossible to measure a dissociation rate when the fluorescence signal at equilibrium is not substantially higher than the background, weak target sequences showed poor reproducibility for individual sequences in repeat experiments (gray points in Fig. 2, C and D). In the remainder of our analysis we therefore focused on operators where the fluorescence signal at equilibrium was >3% of the signal for O_{sym} . For these operators the measurements of both association and dissociation rates were reproducible in repeat experiments (cyan points in Fig. 2C; see also fig. S1B). Moreover, equilibrium dissociation constants K_D estimated by $K_D = k_d/k_a$, versus K_D estimated from the fluorescence values at equilibrium (see methods), show excellent agreement (fig. S1C). In a plot of the association versus dissociation rates for all operators we observed an anticorrelation (Fig. 2D), which implies that the microscopic rate of binding p_{tot} is different for different operators. To quantify the relative importance of p_{tot} and $k_{\text{off},\mu}$ for binding strength, we computed which range of p_{tot} and $k_{\text{off},\mu}$ values would give rise to the observed spread in (k_a, k_d) -space. According to this analysis, the ratio of variation in p_{tot} to

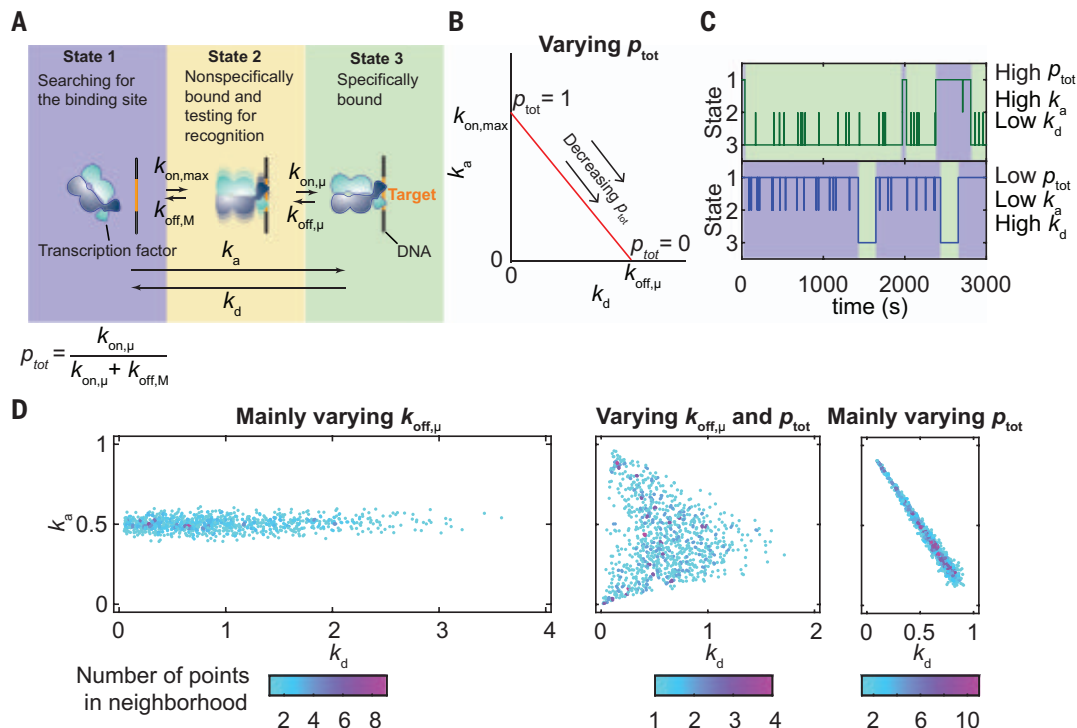
¹Department of Cell and Molecular Biology, Science for Life Laboratory, Uppsala University, Box 596, 75124, Uppsala, Sweden. ²Drug Discovery and Development Platform, Science for Life Laboratory, Department of Chemistry, BMC, Uppsala University, Box 576, 751 23 Uppsala, Sweden.

*Corresponding author. Email: sebastian.deindl@icm.uu.se (S.D.); johan.elf@icm.uu.se (J.E.)

†These authors contributed equally to this work.

Fig. 1. Bimolecular association and dissociation rates are inherently coupled as a result of target site probing. (A) Schematic of the kinetic model describing protein-DNA binding.

(B) The effective rate constants for the association (k_a) and dissociation (k_d) from the target site are coupled according to Eq. 1. This relationship becomes anticorrelated and linear when $k_{off,\mu}$ is constant and p_{tot} changes (red line). (C) Example traces from stochastic simulations sampling the association, dissociation, and nonspecific binding with target site probing. When p_{tot} is high (top), the search time becomes short ($1/k_a$, blue areas) and the binding time becomes long ($1/k_d$, green areas). When p_{tot} is low (bottom), the search time becomes long and the binding time becomes short. (D) Effect on k_a and k_d when varying: $k_{off,\mu}$ 10 times more than p_{tot} (left), $k_{off,\mu}$ and p_{tot} to the same extent (center), and p_{tot} 10 times more than $k_{off,\mu}$ (right), in simulations of the model. Each plot contains 1000 points, where each point represents one target site with a randomly sampled ($k_{off,\mu}$, p_{tot}).



variation in $k_{off,\mu}$ was 1.70 ± 0.20 , depending on the noise floor reached in different experiments (Fig. 2D and fig. S1B). A larger measurement noise limits the range of p_{tot} and at the same time increases the estimated variation in $k_{off,\mu}$. For this reason, the measured ratio represents a lower limit, implying that variation in binding probability is the major source of variation in binding strength.

Although PBMs have been shown to enable accurate measurements of relative binding kinetics, the absolute rates are not expected to be identical to those measured by other methods (11). We therefore also calculated $k_{off,\mu}$ for the different O_{sym} , O_1 , O_2 , and O_3 operators (Fig. 3A) from in vivo estimates of k_a and k_d (7, 12–14) (Fig. 3B). $k_{on,max}$ has been measured in vivo (7) (see methods), and $k_{off,\mu}$ can therefore be calculated as the only unknown in Eq. 1 for each operator. The large error in the k_d estimate for O_3 [68% confidence interval (CI): $(-0.08$ to $0.24) \text{ s}^{-1}$] renders it impossible to determine how similar the $k_{off,\mu}$ for O_3 [68% CI: $(-0.08$ to $0.29) \text{ s}^{-1}$] actually is in relation to the other operators. However, consistent with our in vitro PBM experiments, the $k_{off,\mu}$ estimates obtained from in vivo data are similar for the rest of the operators (Fig. 3C). For example, even though the K_D value of O_2 exceeds that of O_1 by more than a factor of 4 and that of O_{sym} by a factor of 20, these operators exhibit a similar $k_{off,\mu} \approx 0.006 \text{ s}^{-1}$ in vivo as they all fall on the same

k_a versus k_d line in Fig. 3B. In terms of a binding energy diagram, similar $k_{off,\mu}$ for different operators suggests that LacI binding dynamics can be described with one kinetic barrier, the height of which differs for different operators; i.e., it is more favorable for LacI to bind to certain operators than to others when sliding by, but the rate of escaping from the specifically bound state does not change much with sequence (Fig. 3D). For the in vivo data, the ratio of variation in p_{tot} to variation in $k_{off,\mu}$ is $(0.67$ to 3.01 ; 68% CI), where the large error in the estimate comes from the inaccuracies in the single molecule in vivo measurements. This also means that we cannot statistically exclude the possibility that $k_{off,\mu}$ and p_{tot} have a similar contribution to binding on the basis of these data alone.

To change association and dissociation rates in a manner that is orthogonal to changing the operator sequence, we next performed single-molecule measurements where we varied the salt concentration in experiments with a single operator (Fig. 4A). Changes in salt concentration are expected to affect the time that LacI spends nonspecifically bound to DNA while sliding along it (9, 15). This in turn would change the number of operator encounters per nonspecific association, such that p_{tot} is expected to increase with decreasing salt concentrations. To investigate this, we surface-immobilized a Cy5-labeled DNA construct containing a natural *lacO* operator site (O_1)

and used total internal reflection fluorescence microscopy to monitor individual DNA molecules (Fig. 4; see also fig. S2). Upon addition of fluorescent LacI, we monitored the appearance and disappearance of well-defined spots with colocalized fluorescence emission from both Cy3 and Cy5 (Fig. 4B). Few DNA molecules featured colocalized LacI-Cy3 spots in control experiments with Cy5-labeled DNA constructs lacking an operator site (11 and 3% at 1 and 100 mM NaCl, respectively, in contrast to >65, >60, and >20% at 1, 100, and 200 mM NaCl, respectively, for DNA with an O_1 operator; fig. S2A), indicating that the Cy3 spots represent complexes of LacI-Cy3 specifically bound to the operator with only a minor contribution from nonspecific binding of LacI-Cy3 to DNA or to the surface. The measured k_a values should be interpreted as being merely proportional to the true bimolecular association rate constants, as the exact concentration of active LacI needed for normalization can vary between salt titration repeats as a result of differences in the extent of protein surface adsorption, protein stability, and other factors. Nevertheless, we obtain an anticorrelated relationship between the measured k_a and k_d , with an estimated ratio of variation in p_{tot} to variation in $k_{off,\mu}$ of 1.65 ± 0.19 (Fig. 4, C and D). To independently corroborate the dependence on salt concentration, we used surface plasmon resonance (SPR) to measure k_a and k_d for surface-immobilized O_1 operators. We

Fig. 2. Kinetic measurements with LacI on a protein binding microarray. (A) Example images taken during association (left) and dissociation (right) of LacI-Cy3 to spots on the DNA microarray. Orange circle, O_{sym} operator; red circle, O_1 operator; green circle, O_2 operator. O_3 is not present on the array, because initial experiments with this operator showed no binding over background. (B) Association and dissociation curves for the O_{sym} , O_1 , and O_2 operators (thick lines), and 100 examples of their mutants (faint colors). The dissociation curves for each operator were normalized to the fluorescence count for the first frame of the corresponding dissociation movie (C) Reproducibility of k_a (top) and k_d (bottom) for individual operators (cyan points) between replicates. The k_a values are all normalized to the k_a value of O_{sym} in that replicate. Sequences associated with weak binding (fluorescence signal at equilibrium <3% of signal for O_{sym} ; gray points). (D) Measured association and dissociation rates for wild-type operators (circles) and their single and double mutants [points are colored by operator density in that (k_a, k_d) neighborhood; gray points are the same as in (C)]. The value for each operator is a mean from two PBM replicate experiments; see fig. S1B for data from individual replicates.

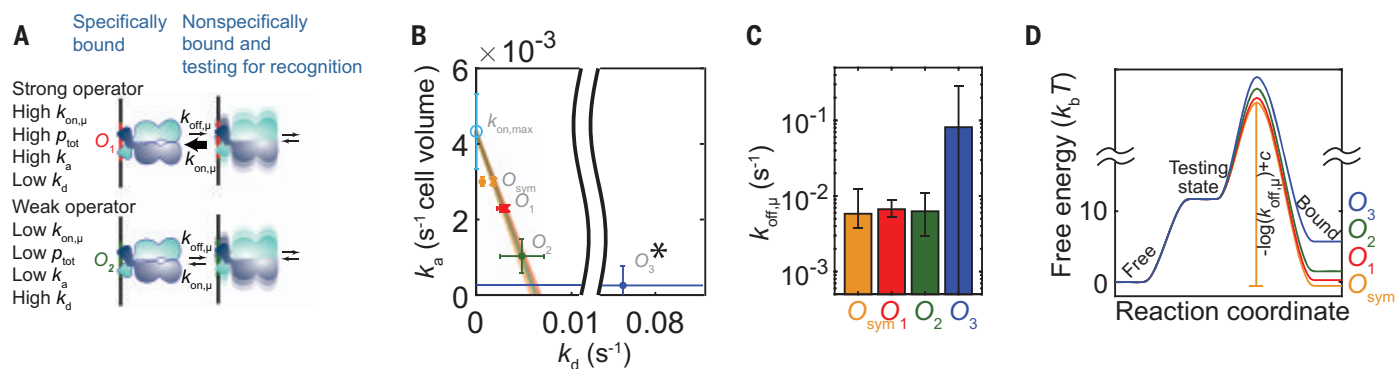
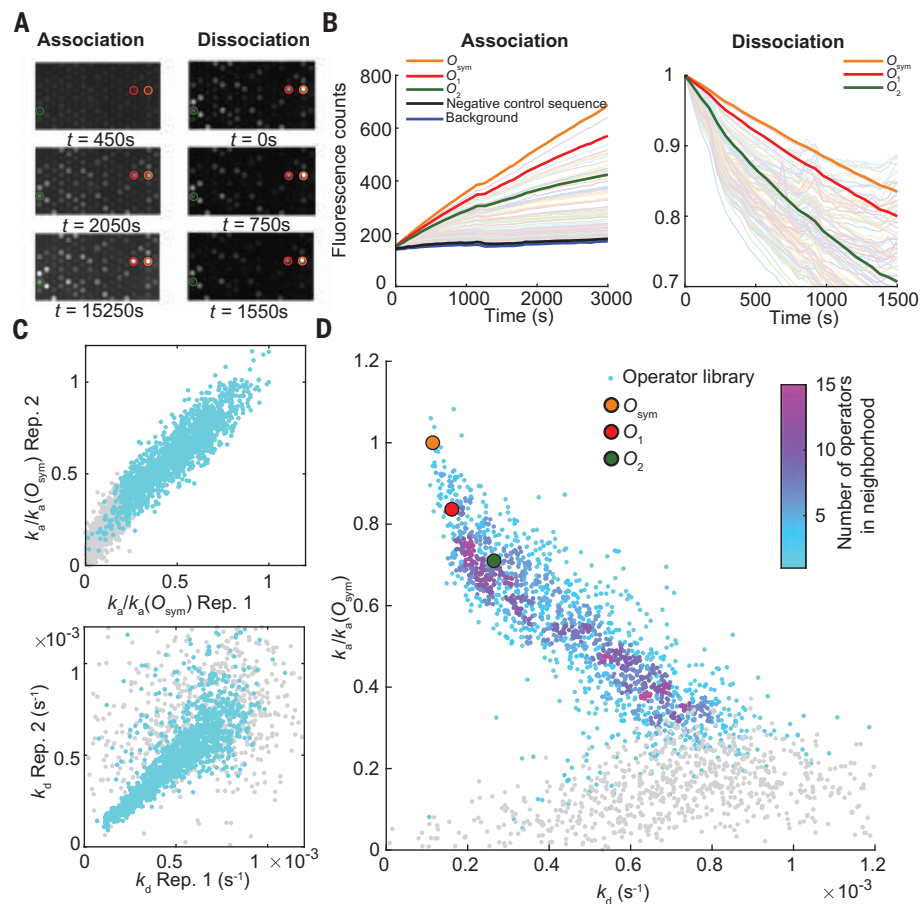


Fig. 3. Analysis of in vivo binding kinetics. (A) Predicted effect on the association and dissociation rates if the $k_{\text{on},\mu}$ values were different but $k_{\text{off},\mu}$ was identical for the different operators. (B) Experimental single-molecule target-site association rate constants k_a (7) plotted against the dissociation rate constants k_d for the different *lac* operators. For the crosses, k_d was directly measured by single-molecule imaging (14). For the dots, k_d was calculated as $K_D \times k_a$, where the equilibrium constant K_D was measured through the repression ratio of gene expression (12, 13). Cyan circle, measured $k_{\text{on},\text{max}}$ (see methods). Colored lines, $k_{\text{off},\mu}$ -lines, found by evaluating Eq. 1, for individual operators. *Due to the large error in the k_d estimate for O_3 [68% CI: $(-0.08 \text{ to } 0.24) \text{ s}^{-1}$], the $k_{\text{off},\mu}$ -line for O_3 is not shown. Error bars are

standard errors, obtained by propagating experimental errors. (C) Microscopic dissociation rates $k_{\text{off},\mu}$ for the different operators, estimated from the in vivo data with Eq. 1. Error bars are 68% CI, obtained by propagating experimental errors. (D) Energy landscapes (a putative rather than a true reaction coordinate is shown) for the transition from free to bound states (state 1 and state 3, respectively) for the different operators, as determined by the measured K_D and $k_{\text{off},\mu}$ values. The activation energy on the transition path between the testing state and bound state is not uniquely determined, but the differences in activation energies between the different operators are. The activation energy is equal to $-\log(k_{\text{off},\mu}) + c$, where c is the same constant for all operators (see supplementary text).

found an anticorrelation between k_a and k_d with this measurement technique as well, with an estimated ratio of variation in p_{tot} to variation in $k_{\text{off},\mu}$ of 1.97 ± 0.07 (fig. S3).

As an extension, our theoretical framework can be used to dissect the binding path for

proteins with more complex, sequential binding mechanisms, considering that mutations along the binding pathway can be seen as energetic barriers for binding. Accordingly, one would first mutate a binding sequence in several different ways, measure the resulting

macroscopic rates k_a and k_d , and then determine which sector of the (k_a, k_d) -space the different mutations fall into (fig. S4, A and B). Assuming that the native sequence has the highest k_a value and that mutations introduce a rate-limiting step, the sectors will be ordered

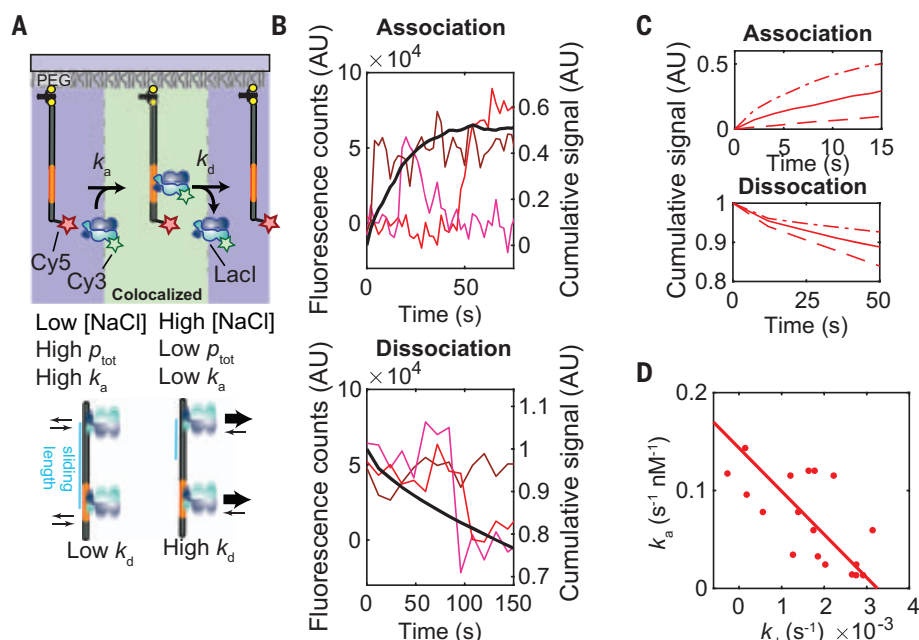


Fig. 4. Effect of changing the salt concentration. (A) Single-molecule colocalization measurements detect association and dissociation for LacI binding to its operators (top) and the predicted effect on association and dissociation rates of changing the salt concentration (bottom). (B) Example single-molecule traces showing binding to and unbinding from the O_1 operator at 100 mM NaCl (colored lines), and the normalized association and dissociation curves (black lines) obtained after summing 649 and 777 traces for the association and dissociation experiment, respectively. AU, arbitrary units. (C) Normalized association and dissociation curves for O_1 binding at 1 mM (dashed dotted lines), 100 mM (solid lines), and 200 mM NaCl (dashed lines). (D) Measured k_a and k_d values for O_1 binding at different salt concentrations, and a fit to Eq. 1 (red line). The salt concentrations used for the different experiments are in the range of 1 to 250 mM supplemented NaCl (fig. S2, A to D).

according to the position of the mutations along the reaction pathway. Thus, rate-limiting steps closer to the bound state will result in fewer rebinding events, leading to an increase in k_d for the same value of k_a . In the case of LacI (Figs. 2 and 3), the mutations fall on one line corresponding to one common rate-limiting step. In the supplementary materials, we apply this method to high-throughput association and dissociation data available for dCas9 binding to off-target, mismatched mutants (16) (fig. S4 and S5). As expected, mutations related to the same step in the reaction pathway fall into sectors of the $(k_a k_d)$ -space, and the order of the sectors corresponds to the previously known reaction path.

In conclusion, the efficiency of target-site recognition is not only crucial for determining protein-DNA association rates, but also plays an equally important role in determining how long proteins remain bound to their targets. In the case of the *lac* repressor, we have shown that the efficiency of target-site recognition (p_{tot})—and not how long the protein remains in the bound state—is the main determinant for binding strength observed for different sequences. This behavior may represent an evolutionary adaptation to facilitate fast search by minimizing the risk of the protein being retained on sequences that resemble bona

fide operators. We note that the measurements and models for LacI in this work all consider the noninduced, allolactose analog-free repressor, which is the conformation of LacI that is capable of binding to DNA with sequence specificity and high affinity (17, 18). Addition of an inducer pushes the system into a new steady state where the k_d/k_a -ratio is very high. Moreover, earlier work (19) indicates that the induced repressor spends some amount of time in a nonspecific testing state before binding the inducer. What this implies on the microscopic level—i.e., if the inducer exerts its effect mainly through a change in $k_{on,\mu}$ or $k_{off,\mu}$ —is not clear from the current study. However, considering that dissociation is very fast at high concentrations of inducer (14), changes in $k_{off,\mu}$ are expected.

The coupling between association and dissociation rates proposed in this work holds for all bimolecular association-dissociation processes adhering to detailed balance, where a step of rapid testing for molecular recognition precedes the strong binding of a target. Indeed, the anticorrelated relationship between association and dissociation has been observed previously for numerous other systems when perturbing the sequence or salt conditions (16, 20–22). We therefore believe that our

theoretical result is very likely to be generally applicable to a wide range of kinetic systems in addition to the ones investigated here, including processes that do not involve protein-DNA interactions.

REFERENCES AND NOTES

- W. Gilbert, B. Müller-Hill, *Proc. Natl. Acad. Sci. U.S.A.* **58**, 2415–2421 (1967).
- R. Milo, R. Phillips, *Cell Biology by the Numbers* (Garland Science, 2015).
- A. Grönlund, P. Lötstedt, J. Elf, *Nat. Commun.* **4**, 1864 (2013).
- D. L. Jones, R. C. Brewster, R. Phillips, *Science* **346**, 1533–1536 (2014).
- M. Z. Ali, V. Paritham, S. Choubey, R. C. Brewster, *eLife* **9**, e56517 (2020).
- M. Morrison, M. Razo-Mejia, R. Phillips, *PLOS Comput. Biol.* **17**, e1008572 (2021).
- P. Hammar *et al.*, *Science* **336**, 1595–1598 (2012).
- E. Marklund *et al.*, *Nature* **583**, 858–861 (2020).
- O. G. Berg, R. B. Winter, P. H. von Hippel, *Biochemistry* **20**, 6929–6948 (1981).
- M. F. Berger, M. L. Bulyk, *Nat. Protoc.* **4**, 393–411 (2009).
- T. Siggers, M. H. Duyzend, J. Reddy, S. Khan, M. L. Bulyk, *Mol. Syst. Biol.* **7**, 555 (2011).
- H. G. Garcia, R. Phillips, *Proc. Natl. Acad. Sci. U.S.A.* **108**, 12173–12178 (2011).
- R. C. Brewster *et al.*, *Cell* **156**, 1312–1323 (2014).
- P. Hammar *et al.*, *Nat. Genet.* **46**, 405–408 (2014).
- P. C. Blainey, A. M. van Oijen, A. Banerjee, G. L. Verdine, X. S. Xie, *Proc. Natl. Acad. Sci. U.S.A.* **103**, 5752–5757 (2006).
- E. A. Boyle *et al.*, *Proc. Natl. Acad. Sci. U.S.A.* **114**, 5461–5466 (2017).
- M. Lewis *et al.*, *Science* **271**, 1247–1254 (1996).
- J. Chen, S. Alberti, K. S. Matthews, *J. Biol. Chem.* **269**, 12482–12487 (1994).
- S. L. Laiken, C. A. Gross, P. H. Von Hippel, *J. Mol. Biol.* **66**, 143–155 (1972).
- A. Poddar *et al.*, *Nat. Commun.* **12**, 874 (2021).
- N. F. Dupuis, E. D. Holmstrom, D. J. Nesbitt, *Biophys. J.* **105**, 756–766 (2013).
- S. Bonilla *et al.*, *J. Am. Chem. Soc.* **139**, 18576–18589 (2017).
- E. Marklund, G. Mao, J. Yuan, S. Zikrin, E. Abdurakhmanov, S. Deindl, J. Elf, Data and code for: Sequence specificity in DNA binding is mainly governed by association (Version 1.0). SciLifeLab (2021); doi:10.17044/scilifelab.17099687.

ACKNOWLEDGMENTS

We thank O. Berg, M. Ehrenberg, H. Danielson, J. Wiktor, M. Löking, D. Fange, I. Barkefors, and D. Jones for discussions. **Funding:** This research was supported by the Knut and Alice Wallenberg Foundation (2016.0077 and 2019.0439 to J.E.; 2019.0306 to S.D.), the Swedish Research Council (2016-06213 to J.E.; 2020-06459 to E.M.), the European Research Council (Starting Grant, 714068 to S.D.; Advanced Grant, 885360 to J.E.), the eSSSENCE e-science initiative and the Swedish National Infrastructure for Computing (SNIC) at UPPMAX. **Author contributions:** J.E. and E.M. conceived the study; E.M. derived models and equations; S.D., E.M., and M.G. designed the single-molecule experiments; M.G. performed the single-molecule experiments; E.M. analyzed the single-molecule data; J.Y., E.M., and J.E. designed the PBM experiments; J.Y. performed the PBM experiments; J.Y. and S.Z. analyzed the PBM experiments; E.M. and EA designed, EA performed, and E.M. analyzed the SPR experiments; E.M., J.E., and S.D. interpreted the results and wrote the paper, with input from all authors. **Competing interests:** The authors declare no competing interests. **Data and materials availability:** All raw data and analysis codes are available at the SciLifeLab Repository (23).

SUPPLEMENTARY MATERIALS

science.org/doi/10.1126/science.abg7427
Materials and Methods
Supplementary Text
Figs. S1 to S5
Table S1
References (24–38)
MDAR Reproducibility Checklist

25 January 2021; resubmitted 13 September 2021
Accepted 21 December 2021
10.1126/science.abg7427

ANIMAL MIGRATION

Magnetic stop signs signal a European songbird's arrival at the breeding site after migration

Joe Wynn^{1*}, Oliver Padget¹, Henrik Mouritsen^{2,3}, Joe Morford¹, Paris Jagers¹, Tim Guilford^{1*}

Although it is known that birds can return to their breeding grounds with exceptional precision, it has remained a mystery how they know when and where to stop migrating. Using nearly a century's worth of Eurasian reed warbler (*Acrocephalus scirpaceus*) ringing recoveries, we investigated whether fluctuations in Earth's magnetic field predict variation in the sites to which birds return. Ringing recoveries suggest that magnetic inclination is learned before departure and is subsequently used as a uni-coordinate "stop sign" when relocating the natal or breeding site. However, many locations have the same inclination angle. Data from populations with different migratory directions indicate that birds solve this ambiguity by stopping at the first place where the right inclination is encountered on an inherited return vector.

Although first outbound migration in songbirds is typically, though not universally (1), thought to use an inherited clock and compass (vector) navigation program (2–5), additional or alternative mechanisms must be required to account for the accuracy with which birds return to the natal or breeding site (philopatry) (6, 7). Experienced birds could use learnt bicoordinate maps comprising two or more cue gradients during philopatry, with cues derived from Earth's magnetic field suggested to be prime candidates for accurate natal or breeding site return (3, 4). Such cues include magnetic inclination, or the dip angle between Earth's magnetic field and Earth's surface; magnetic declination, or the angle between magnetic and true north; and magnetic intensity, or the overall strength of Earth's magnetic field (7). Maps comprising these components have been suggested to underlie navigation in sea turtles (8), fish (9), and songbirds (10, 11). Previous studies have suggested that songbirds could

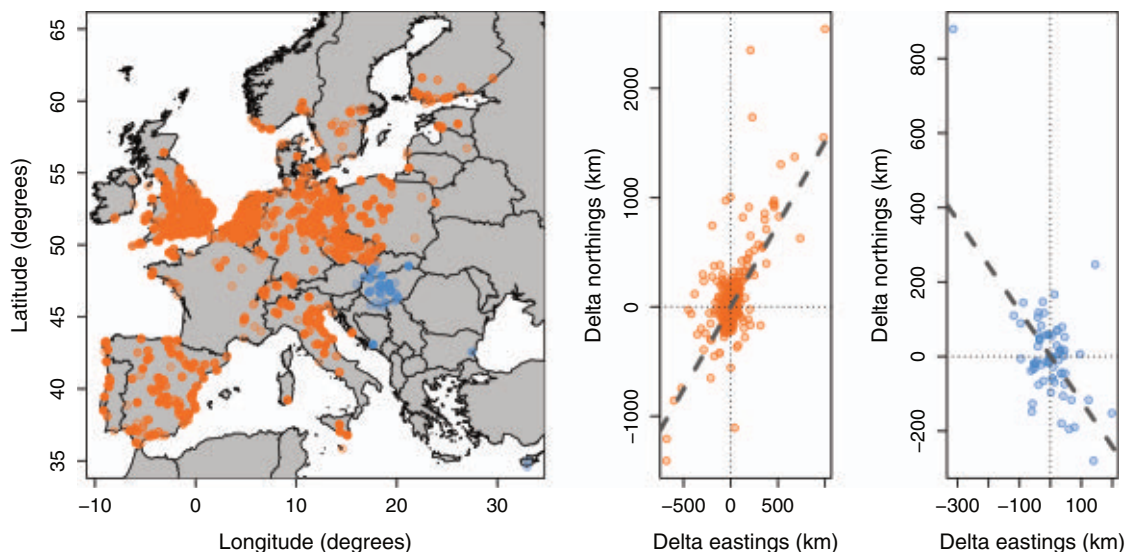
use declination alongside inclination and/or intensity as a bicoordinate map when compensating for long-distance displacement (10, 11), although magnetic gradient cues (alongside other cues) might also allow songbirds to locate the natal or breeding site during philopatry.

Here, we used 17,799 ringing recoveries (from 1940 to 2018) made in consecutive years to investigate whether the Eurasian reed warbler (*Acrocephalus scirpaceus*), a trans-Saharan migratory songbird (12), used magnetic information during philopatry and, if so, how. Because Earth's magnetic field shifts slightly year by year, the magnetic parameter values characteristic of an individual's natal or breeding site will exist in a different location the following year. Hence, if birds used magnetic parameters to determine the location of their natal or breeding site, we would expect that positional changes between years would reflect year-on-year changes in the location of specific magnetic parameters.

First, we investigated whether changes in specific magnetic parameters (inclination, declination, and intensity) between ringing and recovery were smaller than would be expected by chance. This, we reasoned, would test whether birds were attentive to specific magnetic cues. Using randomization analyses, we compared the changes in magnetic field parameters experienced by ringed and recovered reed warblers with those that would be expected if movements were equivalent but random, parameterizing our null reed warbler movements using the observed movements. We found that the median observed change in inclination (randomization; $P < 0.001$) (fig. S3), but not in declination ($P > 0.99$) or intensity ($P = 0.18$), was smaller than would be expected under our null model of philopatry. We found, however, that the mean changes in inclination, declination, and intensity were not significantly smaller than those expected under our null distribution (randomization; inclination, $P > 0.99$; declination, $P = 0.4$; intensity, $P = 0.38$). Because the distribution of between-year movements is necessarily long-tailed and nonnormal (13), it is perhaps unsurprising that the mean and median changes in a given magnetic parameter yield different results. Further, this disparity could imply that the processes driving long-distance dispersal are not closely linked to magnetic secular variation. To test this, we reran our randomization analysis with birds from the first percentile for ringing to recovery distance removed. This was done for adults and chicks separately, ensuring that the proportion of adults to chicks

¹Oxford Navigation Group, Department of Zoology, Oxford OX1 3SZ, UK. ²AG "Neurosensory/(Animal Navigation)," Carl-von-Ossietzky Universität Oldenburg, 26111 Oldenburg, Germany. ³Research Centre for Neurosensory Sciences, University of Oldenburg, 26111 Oldenburg, Germany.
*Corresponding author. Email: joseph.wynn@zoo.ox.ac.uk (J.W.); tim.guilford@zoo.ox.ac.uk (T.G.)

Fig. 1. Changes in position between ringing and recovery for Eurasian reed warblers. (Left) Reed warbler ringing sites, colored orange for west-migrating birds and blue for east-migrating birds. **(Middle)** Changes in longitude (eastings in kilometers) plotted against changes in latitude (northings in kilometers) for birds breeding in northern and western Europe. **(Right)** Changes in longitude plotted against changes in latitude for birds breeding in south-eastern Europe. In all panels, opacity indicates multiple overlapping data points.



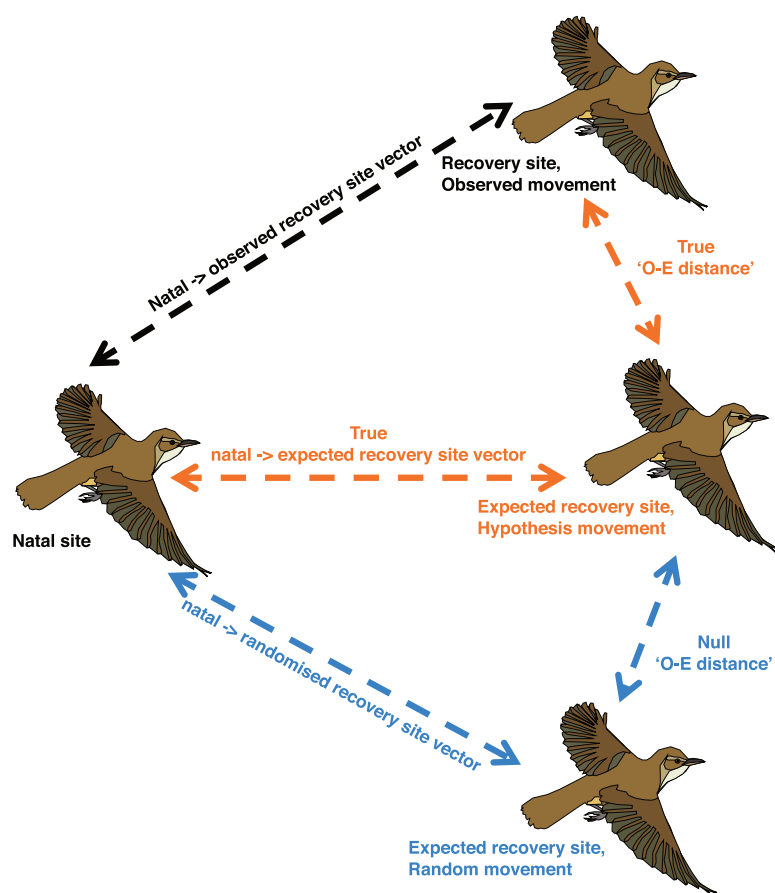


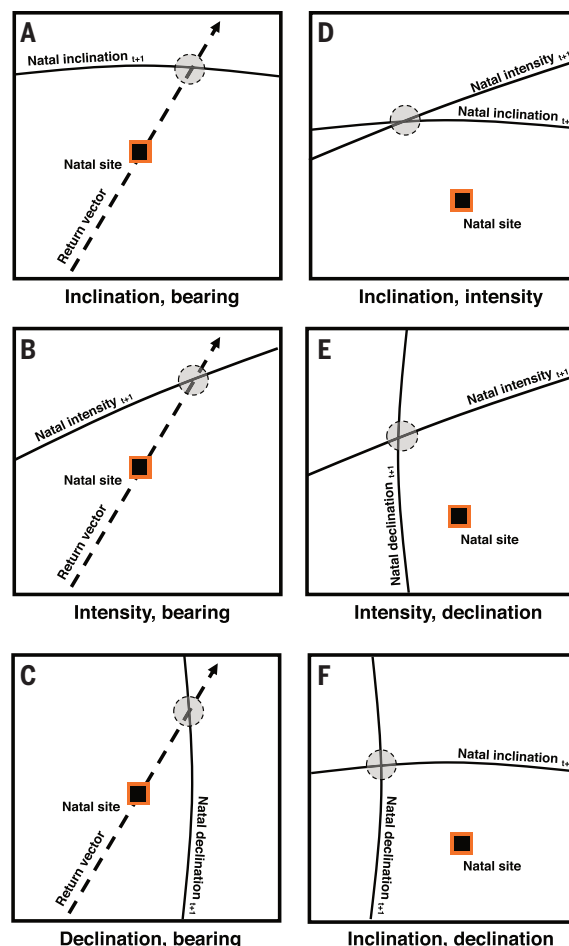
Fig. 2. Using the observed-versus-expected distance to test navigational hypotheses. (Left) The observed-versus-expected distance between the hypothesized and observed recovery sites (true O-E distance) can be calculated and compared with the distance between the hypothesized recovery site and the

was maintained. Using this subset, we found that the observed mean change in inclination was smaller than would be expected by chance (randomization; $P < 0.001$) but that changes in intensity (randomization; $P = 0.96$) and declination (randomization; $P = 0.69$) were not, which suggests that our initial result is primarily driven by birds moving shorter distances between ringing and recovery.

Taken together, these results imply that birds on average target the area denoted by the inclination value encountered at the natal or breeding site a year prior. However, because we find no evidence for attention to other magnetic cues, this result is inconsistent with the use of inclination as part of a learnt bicoordinate magnetic map during philopatry. Instead, we hypothesize that this is consistent with inclination acting as a uni-coordinate stop sign: Birds could recall their natal or breeding location using only one coordinate dimension, if used alongside a compass bearing linking the wintering and breeding sites (14, 15).

This would predict that errors in the sites to which birds return should distribute along an inherited return migratory bearing linking the natal or breeding site to the site at which birds crossed the Mediterranean Sea. We reasoned that linking the natal or breeding site to this crossing point was a reasonable estimate for a putative inherited compass bearing because outbound migration in European passerines is thought to involve a series of migratory bearings, with the most-northern bearing thought to connect the breeding site with the Mediterranean crossing point (12, 16, 17). Reed warblers breeding in northern and western Europe cross the Mediterranean in southwestern Europe, whereas birds breeding southeast of the Austrian Alps are known to cross the Mediterranean in southeast Europe (12, 18, 19). Therefore, we predict that if reed warblers use magnetic stop signs during philopatry, changes in longitude and latitude between consecutive breeding seasons should distribute along a southwest-to-northeast

recovery site expected under equal but random movements (null O-E distance). Through this comparison, we can calculate the likelihood of a hypothesis outperforming chance. (A to F) Diagrams showing how expected recovery positions under each hypothesis are calculated.



axis for northern and western birds and along a southeast-to-northwest axis for southeastern birds.

When changes in latitude were regressed against changes in longitude, we found a significant change in latitude with longitude [linear model (LM); $F = 143,445$, $P < 0.0001$] and, further, found a significant difference in the direction of this effect between migratory populations (LM; $F = 1579$, $P < 0.0001$; Fig. 1). We found that the northern and western populations showed significant eastward movement with northern movement (gradient = 1.51 ± 0.0480), whereas the southeastern population showed significant westward movement with northward movement (gradient = -1.21 ± 0.0675 ; Fig. 1). This is consistent with birds using magnetic inclination as a stop sign, but it is also consistent with ineffective exclusion of nonbreeding birds still currently migrating. Therefore, we sought to ensure that the result was robust to our selection criteria by rerunning our analyses with three more stringent

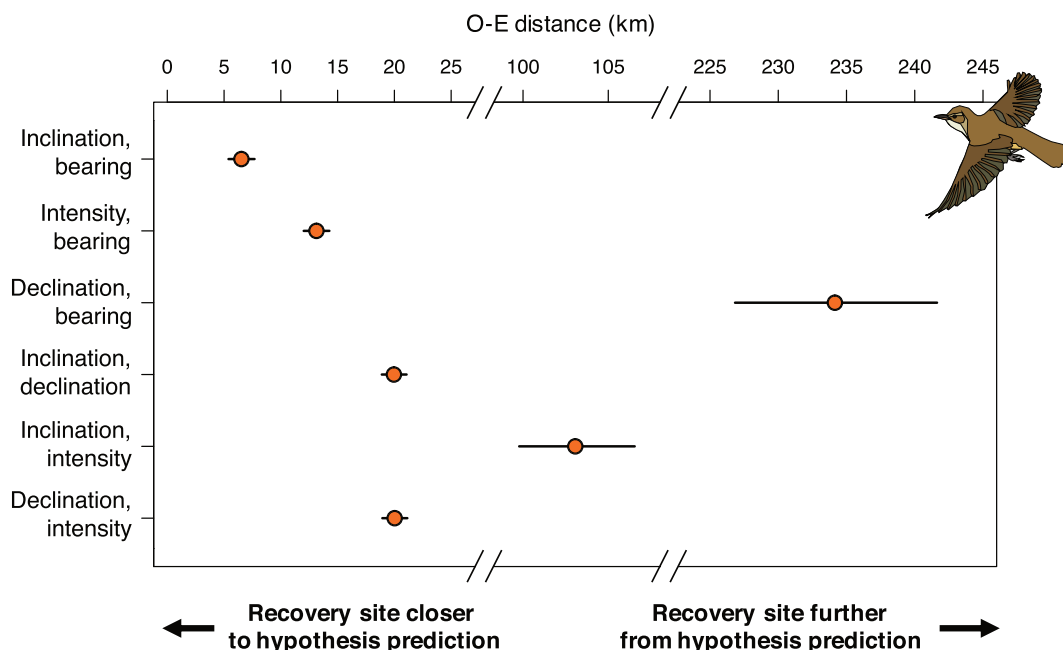


Fig. 3. How closely do different navigational hypotheses fit the observed ringing data? A comparison of the mean observed-versus-expected distances (Fig. 2) for all hypotheses tested, with smaller values representing a better fit between the hypothesis and the observed data. Error bars represent bootstrapped 99% confidence intervals. There are breaks in the scale on the horizontal axis.

subsets: birds ringed in a restricted core breeding window (15 June to 15 July); birds ringed as chicks and recovered at or north of their natal site; and birds sexed at capture, which requires identification through breeding phenotype (20) (figs. S4 to S7).

Under a magnetic stop sign hypothesis, we might expect birds to be recovered at the intersect between the natal or breeding inclination isoline and the return compass bearing. A similarly precise predicted recovery location exists for any magnetic navigation hypothesis, including both stop sign and bicoordinate models (Fig. 2). Because for each bird there is a unique location where it would be expected to be recovered under a given model of navigation, we can measure how close a given ringing recovery is to this position (the observed-versus-expected distance) (Fig. 2 and materials and methods). The smaller this observed-versus-expected distance is, the better the hypothesis fits the observed data. We can test the likelihood of different models of navigation in a randomization by comparing observed-versus-expected distances for a given hypothesis with the observed-versus-expected distances of null birds making equivalent but random between-year movements (fig. S9).

We found that the only hypothesis that significantly outperformed the null model was inclination acting as a stop sign (randomization; $P < 0.001$) (Fig. 3 and figs. S1 and S2), with the observed-versus-expected distance of all other models no smaller than that which

would be expected if birds moved randomly. Notably, we also found that birds were recovered closer to the site predicted by the inclination stop sign model than they were to their natal or breeding site (Mann-Whitney U test; $P < 0.0001$), which implies that birds showed a preference for the site predicted by the inclination stop sign over even their own breeding or natal site.

Because this is a correlative analysis, it is, necessarily, possible that our findings are the result of a confound between movements of the magnetic field and some other parameter. However, given that we found no substantial confound with environmental phenology (table S1), that we found no difference in our results when analyzing different subsets of the data (supplementary text), and that there are no long-term temporal trends in longitudinal or latitudinal shift between ringing and recovery (latitude LM; $F = 1.69$, $P = 0.190$; longitude LM; $F = 0.99$, $P = 0.590$), we believe that the most parsimonious interpretation of our result is that magnetic inclination is used as a stop sign during philopatry. This might make sense because magnetic inclination has been repeatedly implicated in avian navigation (7). Additionally, other magnetic gradient-derived positions move further with secular variation, which makes the proposed mechanism relatively robust. The position of the natal site as estimated using inclination and declination as a bicoordinate map would move, on average, 18.5 km (± 0.0760 km) between years; as estimated using intensity and declination,

20.4 km (± 0.0510 km); and as estimated using intensity and inclination, 98.2 km (± 2.60 km). By contrast, the location of the breeding site denoted using inclination as a stop sign moves only 1.22 km (± 0.0133 km) between years. We suggest that, by remembering breeding location relative to the most stable cue and referencing it alongside a compass bearing, the proposed strategy minimizes the impact of secular variation. Nevertheless, an inclination stop sign cannot be the only system used, because even slight secular variation would inhibit philopatry. Therefore, other cues must complement magnetic inclination when locating the natal or breeding site (7).

Although our results shed light on the sensory and developmental underpinnings of philopatry, they may also imply that magnetic secular variation is of some importance when considering the drivers of range shift in migratory taxa (21, 22). As with any correlative contrasts drawn using environmental variance, experimental verification of our suggested mechanism is essential. Nonetheless, we believe our findings provide evidence for an unconventional mechanism of long-distance navigation, both within birds and migratory animals more generally.

REFERENCES AND NOTES

1. K. Thorup et al., *Sci. Rep.* **10**, 7698 (2020).
2. A. J. Helbig, *Behav. Ecol. Sociobiol.* **28**, 9–12 (1991).
3. A. C. Perdeck, *Ardea* **55**, 1–2 (1958).
4. K. Thorup et al., *Proc. Natl. Acad. Sci. U.S.A.* **104**, 18115–18119 (2007).
5. H. Mouritsen, O. Mouritsen, *J. Theor. Biol.* **207**, 283–291 (2000).
6. R. R. Baker, *The Evolutionary Ecology of Animal Migration* (Hodder and Stoughton, 1978).
7. H. Mouritsen, *Nature* **558**, 50–59 (2018).

8. J. R. Brothers, K. J. Lohmann, *Curr. Biol.* **25**, 392–396 (2015).
9. N. F. Putman *et al.*, *Curr. Biol.* **23**, 312–316 (2013).
10. N. Chernetsov *et al.*, *Curr. Biol.* **27**, 2647–2651.e2 (2017).
11. N. Chernetsov, A. Pakhomov, A. Davydov, F. Cellarius, H. Mouritsen, *PLOS ONE* **15**, e0232136 (2020).
12. K. Schulze-Hagen, B. Leisler, *The Reed Warblers: Diversity in a Uniform Bird Family* (KNNV, 2011).
13. R. Tittler, M. A. Villard, L. Fahrig, *Ecography* **32**, 1051–1061 (2009).
14. R. A. Holland, *J. Zool.* **293**, 1–15 (2014).
15. H. Mouritsen, in *Avian Migration*, P. Berthold, E. Gwinner, E. Sonnenschein, Eds. (Springer, 2003), pp. 493–513.
16. N. Chernetsov, D. Kishinev, S. Gashkov, V. Kosarev, C. V. Bolshakov, *Anim. Behav.* **75**, 539–545 (2008).
17. E. Gwinner, W. Witschko, *J. Comp. Physiol.* **125**, 267–273 (1978).
18. P. Procházka *et al.*, *J. Avian Biol.* **49**, jav-012516 (2018).
19. L. Zwarts, R. G. Bijlsma, J. Van der Kamp, E. Wymenga, *Living on the Edge: Wetlands and Birds in a Changing Sahel* (BRILL, 2012).
20. L. Svensson, *Identification Guide to European Passerines* (Naturhistoriska Riksmuseet, 1970).
21. J. R. Brothers, K. J. Lohmann, *Curr. Biol.* **28**, 1325–1329.e2 (2018).
22. J. Wynn, O. Padgett, H. Mouritsen, C. Perrins, T. Guilford, *Curr. Biol.* **30**, 2869–2873.e2 (2020).

ACKNOWLEDGMENTS

We thank both the EURING scheme and everyone across Europe who has contributed to this dataset over the years; this study would not be possible without their input. We also thank the members of the Oxnab research group for their insightful contributions, and we thank A. Holguin, C. Randall, and T. Malpas for their comments on a draft manuscript. The data used in this manuscript are available in the online supplementary materials as data S1. **Funding:** J.W. and J.M. were funded by a UKRI BBSRC scholarship (grant no. BB/M011224/1); P.J. was funded by a UKRI NERC scholarship (grant no. NE/S007474/1); O.P. was funded by a Junior Research Fellowship at St John's College, University of Oxford; H.M. received funding from the European Research Council [under the European Union's Horizon 2020 research and innovation program, grant agreement no. 810002 (synergy grant: "QuantumBirds")] and the Deutsche Forschungsgemeinschaft (SFB 1372, "Magnetoreception and navigation in vertebrates," and GRK 1885, "Molecular basis of sensory biology"); and T.G.'s research was supported by Merton College, Oxford, and by the Mary Griffiths award.

Author contributions: Conceptualization: J.W., O.P., and T.G. Methodology: J.W. and O.P. Investigation: J.W., O.P., T.G., H.M., J.M., and P.J. Writing – original draft: J.W. Writing – review and editing: J.W., O.P., T.G., H.M., J.M., and P.J. **Competing interests:** The authors declare no competing interests. **Data and materials availability:** The data used in this study are available in the supplementary materials.

SUPPLEMENTARY MATERIALS

science.org/doi/10.1126/science.abj4210
Materials and Methods
Supplementary Text
Figs. S1 to S10
Table S1
References (23–27)
MDAR Reproducibility Checklist
Data S1

12 May 2021; accepted 14 December 2021
10.1126/science.abj4210

CORONAVIRUS

Antibody-mediated broad sarbecovirus neutralization through ACE2 molecular mimicry

Young-Jun Park^{1,2†}, Anna De Marco^{3†}, Tyler N. Starr^{4†}, Zhuoming Liu^{5†}, Dora Pinto³, Alexandra C. Walls^{1,2}, Fabrizia Zatta³, Samantha K. Zepeda¹, John E. Bowen¹, Kaitlin R. Sprouse¹, Anshu Joshi¹, Martina Giuridanella³, Barbara Guarino³, Julia Noack⁶, Rana Abdelnabi⁷, Shi-Yan Caroline Foo⁷, Laura E. Rosen⁶, Florian A. Lempp⁶, Fabio Benigni³, Gyorgy Snell⁶, Johan Neyts⁷, Sean P. J. Whelan⁵, Herbert W. Virgin^{6,8,9}, Jesse D. Bloom^{2,4}, Davide Corti^{3*}, Matteo Samuele Pizzuto^{3*}, David Veesler^{1,2*}

Understanding broadly neutralizing sarbecovirus antibody responses is key to developing countermeasures against severe acute respiratory syndrome coronavirus 2 (SARS-CoV-2) variants and future zoonotic sarbecoviruses. We describe the isolation and characterization of a human monoclonal antibody, designated S2K146, that broadly neutralizes viruses belonging to SARS-CoV- and SARS-CoV-2-related sarbecovirus clades, which use angiotensin-converting enzyme 2 (ACE2) as an entry receptor. Structural and functional studies show that most of the virus residues that directly bind S2K146 are also involved in binding to ACE2. This allows the antibody to potently inhibit receptor attachment. S2K146 protects against SARS-CoV-2 Beta variant challenge in hamsters, and viral passaging experiments reveal a high barrier for emergence of escape mutants, making it a good candidate for clinical development. The conserved ACE2-binding residues present a site of vulnerability that might be leveraged for developing vaccines eliciting broad sarbecovirus immunity.

The zoonotic spillover of severe acute respiratory syndrome coronavirus 2 (SARS-CoV-2) has resulted in a global pandemic causing more than 266 million infections and more than 5.2 million fatalities as of December 2021. Continued SARS-CoV-2 evolution leads to the emergence of variants of concern (VOCs) that are characterized by higher transmissibility, immune evasion, and/or disease severity. For pandemic preparedness, we need pan-sarbecovirus countermeasures,

such as vaccines and therapeutics that are effective against all SARS-CoV-2 variants and divergent zoonotic sarbecoviruses (1).

The coronavirus spike (S) glycoprotein promotes viral entry into host cells and is the main target of neutralizing antibodies elicited by infection or vaccination (2–7). The S protein comprises an S₁ subunit, which recognizes host cell receptors, and an S₂ subunit that drives viral cell membrane fusion. The S₁ subunit includes the N-terminal domain and the receptor

binding domain (RBD) and two additional domains designated C and D (6). For SARS-CoV and SARS-CoV-2, the RBD interacts with angiotensin-converting enzyme 2 (ACE2) to allow virus entry into host cells (4, 8–16). The RBD is also the main target of serum neutralizing activity elicited by infection (17) and vaccination (7, 18) and exposes multiple antigenic sites that are recognized by broadly neutralizing sarbecovirus antibodies (Abs) (19–25) (fig. S1). However, a large fraction of Abs in polyclonal sera (17) and most monoclonal Abs (mAbs) selected for therapeutic development (26) target a subset of epitopes that overlap the ACE2-contact surface [designated the receptor binding motif (RBM)]. The marked genetic divergence and plasticity of the RBM among SARS-CoV-2 variants and sarbecoviruses have thus far limited the breadth of Abs recognizing this region, and they are readily escaped by mutations (20, 27–32).

To identify broadly neutralizing sarbecovirus Abs, we isolated SARS-CoV-2 S-specific [immunoglobulin G (IgG)] memory B cells from one symptomatic COVID-19 convalescent individual (who was not hospitalized) 35 days after symptoms onset. We identified one mAb, designated S2K146 [immunoglobulin heavy and light variable genes 3-43 and 1-44, respectively (IGHV3-43; IGL1-44)], which did not compete with S309 (site IV) (21) or S2X259 (site II) (19) but competed with S2E12 (site I), a potent RBM mAb with neutralization breadth against SARS-CoV-2-related sarbecoviruses (33) (Fig. 1A and fig. S1). Like S2E12, S2K146 bound to all SARS-CoV-2 VOC RBDs as well as all clade 1b sarbecovirus RBDs tested by

¹Department of Biochemistry, University of Washington, Seattle, WA 98195, USA. ²Howard Hughes Medical Institute, University of Washington, Seattle, WA 98195, USA. ³Humabs Biomed SA, a subsidiary of Vir Biotechnology, 6500 Bellinzona, Switzerland. ⁴Basic Sciences Division, Fred Hutchinson Cancer Research Center, Seattle, WA 98109, USA. ⁵Department of Molecular Microbiology, Washington University School of Medicine, St. Louis, MO 63110, USA. ⁶Vir Biotechnology, San Francisco, CA 94158, USA. ⁷Laboratory of Virology and Chemotherapy, Rega Institute for Medical Research, KU Leuven, 3000 Leuven, Belgium. ⁸Department of Pathology and Immunology, Washington University School of Medicine, St. Louis, MO 63110, USA. ⁹Department of Internal Medicine, University of Texas Southwestern Medical Center, Dallas, TX 75390, USA.

*Corresponding author. Email: dveesler@uw.edu (D.V.); mpizzuto@vir.bio (M.S.P.); dcorti@vir.bio (D.C.)

†These authors contributed equally to this work.

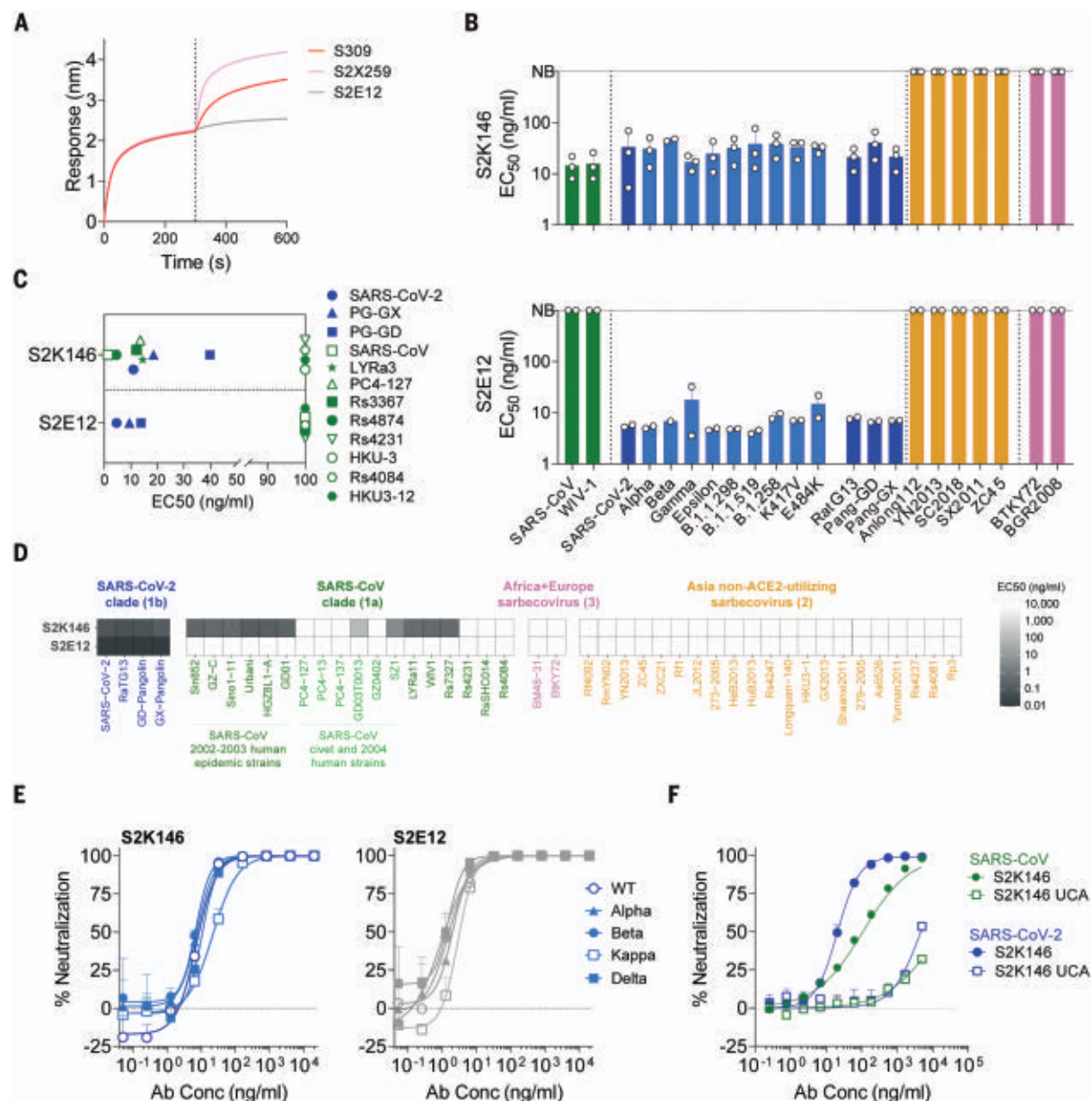


Fig. 1. Identification of the S2K146 cross-reactive and broadly neutralizing sarbecovirus mAb. (A) Binding of site I-targeting S2E12 (33), site IV-targeting S309 (19), and site II-targeting S2X259 (19) recombinant IgG1 (second phase) after association of S2K146 mAb (first phase) to His-tagged SARS-CoV-2 RBD immobilized on anti-His sensors, as measured by biolayer interferometry. (B) Cross-reactivity of S2K146 (upper panel) and S2E12 (lower panel) with 22 sarbecovirus RBDs from four sarbecovirus clades and SARS-CoV-2 variants analyzed by ELISA. Median effective concentration (EC₅₀) of at least two independent experiments is shown. Error bars indicate standard deviation

between experimental repeats. (C) Flow cytometry analysis of S2K146 cross-reactivity with a panel of 12 S glycoproteins representative of sarbecovirus clades 1a and 1b transiently expressed on the surface of mammalian cells. (D) S2K146 cross-reactivity with sarbecovirus RBDs displayed at the surface of yeast. (E) S2K146- and S2E12-mediated neutralization of replication-competent SARS-CoV-2 (USA-WA1/2020) and SARS-CoV-2 VOC viruses. WT; wild type; Ab Conc, antibody concentration. (F) S2K146- and S2K146 UCA-mediated neutralization of VSV pseudotypes harboring SARS-CoV-2 S or SARS-CoV S. Error bars indicating standard deviation between replicates are represented only in one direction.

enzyme-linked immunosorbent assay (ELISA) (Fig. 1B and fig. S2A). In contrast to S2E12 and other site I-targeting Abs described so far, however, S2K146 also cross-reacted with the SARS-CoV and WIV-1 RBDs (clade 1a), which share 73 and 76% sequence identity with the SARS-CoV-2 RBD, respectively (Fig. 1B and fig. S2A). S2K146 did not bind to clades 2 and 3

sarbecovirus RBDs, similarly to the broadly neutralizing sarbecovirus S309 mAb but in contrast to the S2X259 and S2H97 (site V) mAbs (19, 20). We observed S2K146 cross-reactivity with clades 1a and 1b sarbecoviruses using native S trimers transiently expressed on the surface of mammalian cells (Fig. 1C) and yeast surface-displayed RBDs (Fig. 1D),

consistent with the ELISA results. On the basis of these results, we hypothesized that S2K146 recognizes a previously uncharacterized RBM epitope that is conserved among sarbecovirus clades 1a and 1b.

To evaluate the neutralization potency of the S2K146 mAb, we carried out dose-response inhibition assays using a vesicular stomatitis

virus (VSV) pseudotyping platform. S2K146 efficiently blocked SARS-CoV and SARS-CoV-2 S-mediated entry into cells with median inhibitory concentration (IC_{50}) of 108 and 16 ng/ml, respectively (fig. S2B). Moreover, S2K146 potentially neutralized VSV pseudotypes harboring SARS-CoV-2 S glycoproteins from VOCs including Alpha, Beta, Gamma, Delta plus (AY.1/AY.2), Epsilon, and Lambda (fig. S2B). S2K146 also weakly neutralized VSV pseudotyped with BtKY72 S (clade 3) harboring the K493Y/T498W mutations (SARS-CoV-2 numbering) (fig. S2C), which enable human ACE2-mediated entry (34), whereas S2E12 did not recognize the wild-type or double-mutant BtKY72 RBD (fig. S3). Finally, S2K146 neutralized authentic SARS-CoV-2 (isolate USA-WA1/2020, lineage A, IC_{50} = 10 ng/ml) and SARS-CoV-2 VOCs (Alpha, IC_{50} = 9 ng/ml; Beta, IC_{50} = 9 ng/ml; Delta, IC_{50} = 8 ng/ml; Kappa, IC_{50} = 30 ng/ml) with a potency approaching that observed with the ultrapotent S2E12 mAb (33) (Wuhan-1, IC_{50} = 3.5 ng/ml; Alpha, IC_{50} = 2.5 ng/ml; Beta, IC_{50} = 2 ng/ml; Delta, IC_{50} = 1.5 ng/ml; Kappa, IC_{50} = 4.5 ng/ml) in a side-by-side comparison (Fig. 1E).

To assess the role of somatic mutations for S2K146 binding and neutralization, we generated its inferred unmutated common ancestor (S2K146 UCA). Alignment with the UCA amino acid sequence reveals that S2K146 harbors seven and two somatic hypermutations in the heavy- and light-chain complementarity determining regions (CDR), respectively [V_H (variable region of immunoglobulin heavy chain) identity: 94.4%; V_L (variable region of immunoglobulin light chain) identity: 98.9%] (fig. S2D). Except for WIV-1, S2K146 and S2K146 UCA showed no major cross-reactivity differences with a panel of RBDs representative of clade 1 sarbecoviruses, as determined by ELISA (fig. S2E). Nevertheless, biolayer interferometry revealed that S2K146 bound to prefusion-stabilized SARS-CoV and SARS-CoV-2 S ectodomain trimers with enhanced avidities compared with S2K146 UCA (fig. S2F). Accordingly, S2K146 UCA showed a marked loss in neutralizing activity against both SARS-CoV S and SARS-CoV-2 S VSV pseudotypes (Fig. 1F). Our results suggest that somatic hypermutations associated with S2K146 affinity maturation are especially important for enhancing mAb avidity and potency.

To understand the sarbecovirus cross-reactivity of the RBM-specific S2K146 mAb, we determined a cryo-electron microscopy (cryo-EM) structure of the S2K146 Fab fragment in complex with the SARS-CoV-2 S ectodomain trimer at 3.2-Å resolution (Fig. 2A, fig. S4, and table S1). Three-dimensional (3D) classification of the data led to the determination of a structure with three open RBDs, each bound to a S2K146 Fab, as well as a structure with two open RBDs and one closed RBD, with a Fab

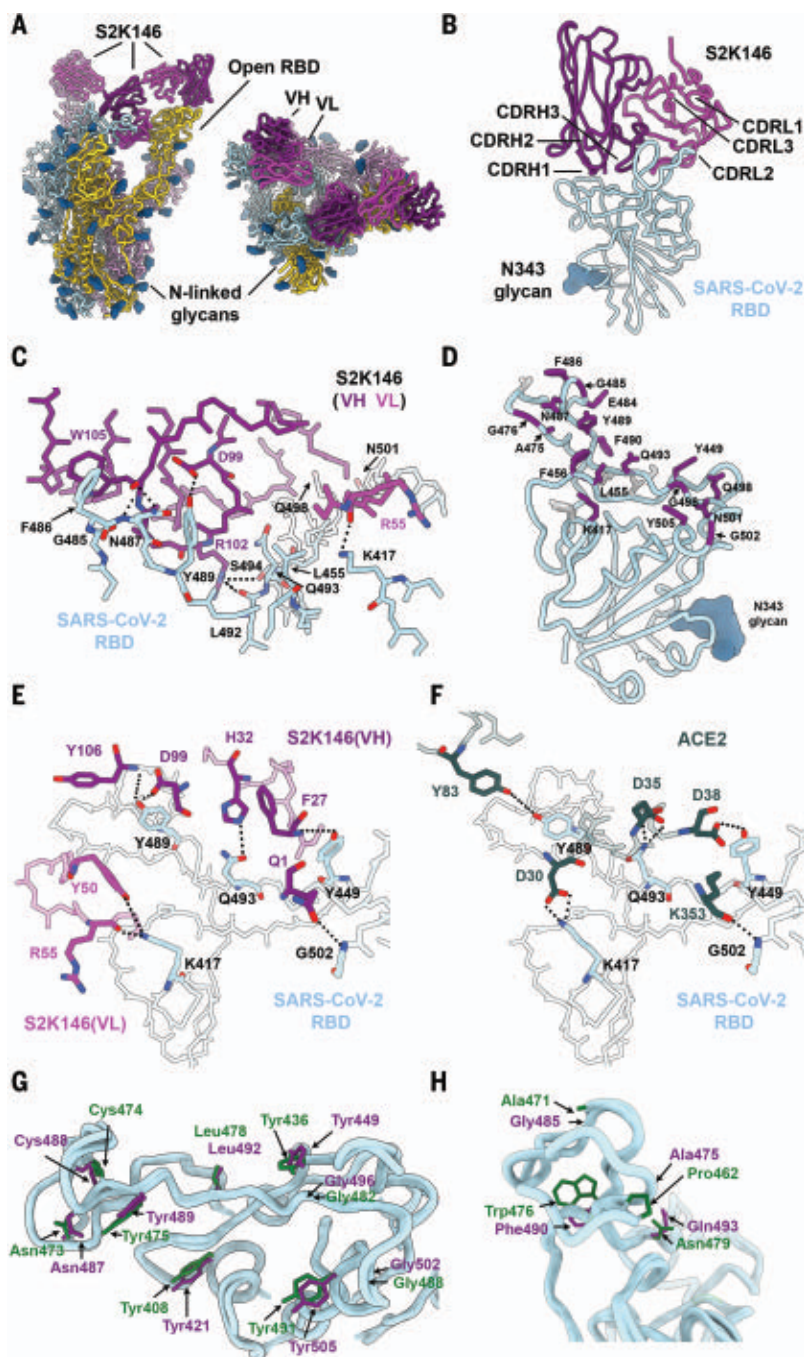


Fig. 2. The S2K146 broadly neutralizing mAb recognizes RBD antigenic site I. (A) Cryo-EM structure viewed along two orthogonal orientations of the prefusion SARS-CoV-2 S ectodomain trimer with three S2K146 Fab fragments bound to two open RBDs and one partially closed RBD. SARS-CoV-2 S protomers are colored cyan, pink, and gold. S2K146 heavy chain and light chain variable domains are colored purple and magenta, respectively. Glycans are rendered as blue spheres. (B) Ribbon diagram of the S2K146-bound SARS-CoV-2 RBD. (C) Zoomed-in view of the contacts formed between S2K146 and the SARS-CoV-2 RBD. Selected epitope residues are shown as sticks, and electrostatic interactions are indicated with dotted lines. S2K146 heavy chain and light chain variable domains are colored as in (A). Single-letter abbreviations for the amino acid residues are as follows: A, Ala; C, Cys; D, Asp; E, Glu; F, Phe; G, Gly; H, His; I, Ile; K, Lys; L, Leu; M, Met; N, Asn; P, Pro; Q, Gln; R, Arg; S, Ser; T, Thr; V, Val; W, Trp; and Y, Tyr. (D) S2K146 epitope residues shown as sticks and colored purple (labeled) if they are involved in ACE2 binding or colored gray if not (unlabeled). (E and F) Similar electrostatic interactions (dotted lines) formed between S2K146 (E) or ACE2 (F) and the SARS-CoV-2 RBD. (G) The side chains of the nine S2K146 epitope residues conserved between the SARS-CoV-2 (purple) and SARS-CoV [green, Protein Data Bank (PDB) ID 2AJF (12)] RBDs are shown as sticks. (H) The side chains of the four S2K146 epitope residues conservatively substituted between the SARS-CoV-2 (purple) and SARS-CoV (green) RBDs are shown as sticks.

bound to each of them (fig. S4). Our cryo-EM data show that the opening of two RBDs is enough to allow three Fabs to bind to an S trimer, as the remaining closed RBD can engage an S2K146 Fab owing to its angle of approach.

To overcome the conformational heterogeneity of the S2K146-bound RBDs relative to the rest of the S trimer, we used focused 3D classification and local refinement of the S2K146 variable domains and RBD to obtain a reconstruction at 3.2-Å resolution enabling unambiguous model building and providing a detailed view of the binding interface (Fig. 2B, fig. S4, and table S1). S2K146 recognizes an epitope in antigenic site I (17), which overlaps with the RBM and is partially masked when the three RBDs adopt a closed state leading to clashes between the mAb and a neighboring RBD (Fig. 2, A

and B, and fig. S1). The S2K146 paratope includes the heavy chain N terminus and CDRH1, CDRH2, and CDRH3, accounting for three-quarters of the surface buried upon binding, with light chain CDRL1, CDRL2, and CDRL3 making up the rest of the interface. A total of 1000 Å² of the paratope surface is buried at the interface with the RBM through electrostatic interactions and shape complementarity.

The S2K146 footprint on the SARS-CoV-2 RBD highly resembles that of the ACE2 receptor, with 18 of 24 epitope residues shared with the ACE2 binding site, including key ACE2 contact positions L455, F486, Q493, Q498, and N501 (Fig. 2, C and D). Moreover, electrostatic interactions formed between S2K146 and the SARS-CoV-2 RBD recapitulate some of the contacts involved in ACE2

binding, such as with residues K417, Y449, Y489, Q493, and G502 (Fig. 2, E and F). Although some S2K146 contact residues are mutated in several variants, such as K417 (Beta and Gamma), L452 (Delta, Epsilon, and Kappa), E484 (Beta, Gamma, and Kappa), and N501 (Alpha, Beta, and Gamma), the retention of neutralization of these variants suggests that the binding interface is resilient to these residue substitutions (Fig. 1E and fig. S2B). The cross-reactivity with and broad neutralization of SARS-CoV by S2K146 may be partially explained by the strict conservation or conservative substitution of nine and four epitope residues relative to SARS-CoV-2, respectively (Fig. 2, G and H, and fig. S5A), consistent with the ability of both RBDs to bind human ACE2.

S2K146 therefore overcomes the mutational plasticity of the RBM, which is implicated in immune evasion, by targeting residues required for binding to the ACE2 receptor. This is supported by S2K146 recognition of the reconstructed RBD ancestor of SARS-CoV and SARS-CoV-2 (fig. S5, A and B), where human ACE2 binding first arose during sarbecovirus evolution (34), in line with the hypothesis that human ACE2 binding participates in conferring S2K146 susceptibility. As S2K146 does not compete with broadly neutralizing sarbecovirus mAbs targeting other antigenic sites, such as S309 (21) and S2X259 (19) (figs. S1 and S6), they could be combined in a cocktail to enhance breadth further and set an even higher barrier for emergence of escape mutants.

To prospectively evaluate the impact of antigenic drift on S2K146 neutralization, we mapped RBD mutations that affect mAb binding using deep mutational scanning (DMS) of a yeast-displayed RBD mutant library covering all possible single residue substitutions in the Wuhan-Hu-1 RBD background (30). S2K146 binding was reduced by only a restricted number of amino acid substitutions compared to S2E12, which binds an overlapping but distinct epitope (Fig. 3, A to D, and fig. S7, A and B). All these mutations correspond to RBD residues buried upon ACE2 recognition (F456, A475, E484, F486, N487, and Y489) (Fig. 3B). Only one of these residue substitutions (Y489H) is accessible through a single-nucleotide change and could escape S2K146 recognition with a penalty on ACE2 binding affinity smaller than an order of magnitude, as determined by DMS data (30). None of the individual mutations present in the recently identified SARS-CoV-2 Omicron VOC affected S2K146 binding (Fig. 3B), although the effect of the full constellation of mutations remains to be evaluated. Conversely, DMS profiling of the S2K146 UCA revealed a greater number of binding-escape mutations, including some residue substitutions present in Omicron (e.g., Q493R or Q498R) (Fig. 3B). Therefore, the hotspot targeting of S2K146 on residues

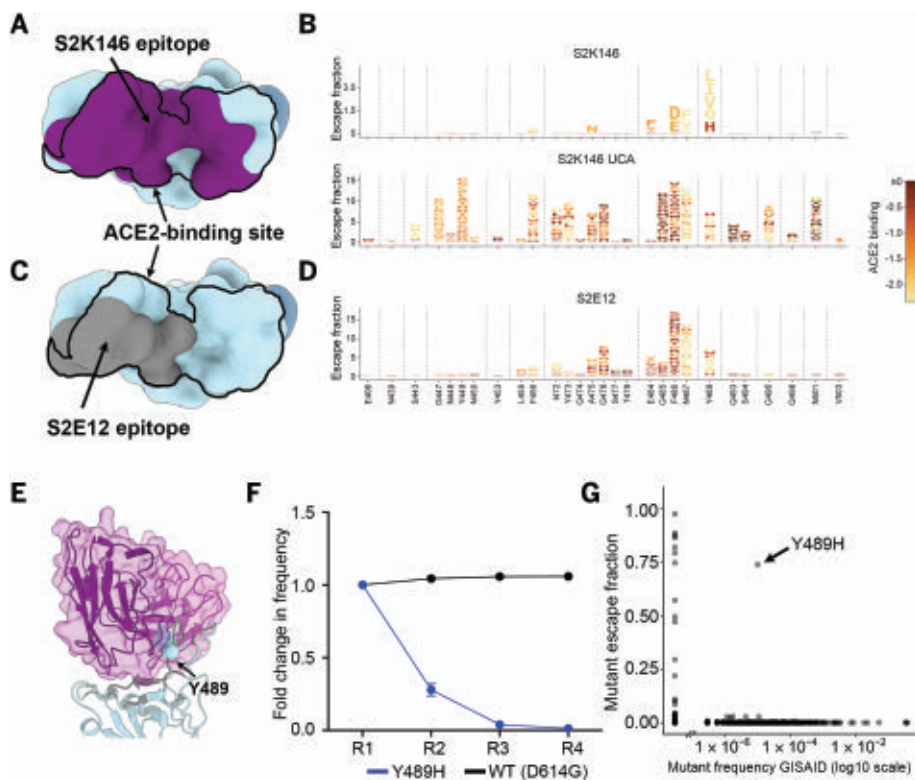


Fig. 3. S2K146 is resilient to a broad spectrum of escape mutations. (A) Molecular surface representation of the SARS-CoV-2 RBD with the S2K146 epitope colored purple and the ACE2 footprint indicated as a black outline. (B) Mapping of RBD mutations reducing S2K146 (top) or S2K146 UCA (bottom) binding using DMS of the yeast-displayed SARS-CoV-2 RBD. Sites of strong escape (pink underlines in fig. S7A) are shown in logo plot. Letters are colored according to how mutations affect the ACE2 binding affinity of the SARS-CoV-2 RBD, as measured via yeast display by Starr *et al.* (30). (C) Molecular surface representation of the SARS-CoV-2 RBD with the S2E12 epitope colored gray and the ACE2 footprint indicated as a black outline. The N343 glycan is rendered as blue spheres in (A) and (C). (D) Mapping of RBD mutations reducing S2E12 binding using DMS of the yeast-displayed SARS-CoV-2 RBD. Sites of strong escape (purple underlines in fig. S7A) are shown in logo plot, as measured previously by Starr *et al.* (20). (E) Zoomed-in view of the S2K146-bound SARS-CoV-2 RBD (blue) highlighting the Y489H neutralization escape mutation. The S2K146 heavy and light chain variable domains are shown as ribbons within transparent purple and magenta surfaces, respectively. (F) Viral replication competition between VSV chimeras harboring the SARS-CoV-2 Wuhan-Hu-1/D614G S with or without the Y489H substitution using VeroE6 cells. (G) Mutations reducing binding of S2K146 to the RBD on the basis of DMS (escape score) are plotted versus their frequencies among the human-derived SARS-CoV-2 sequences on GISAID as of 27 September 2021. The large escape mutant (>5× global median escape fraction) with nonzero frequency is indicated.

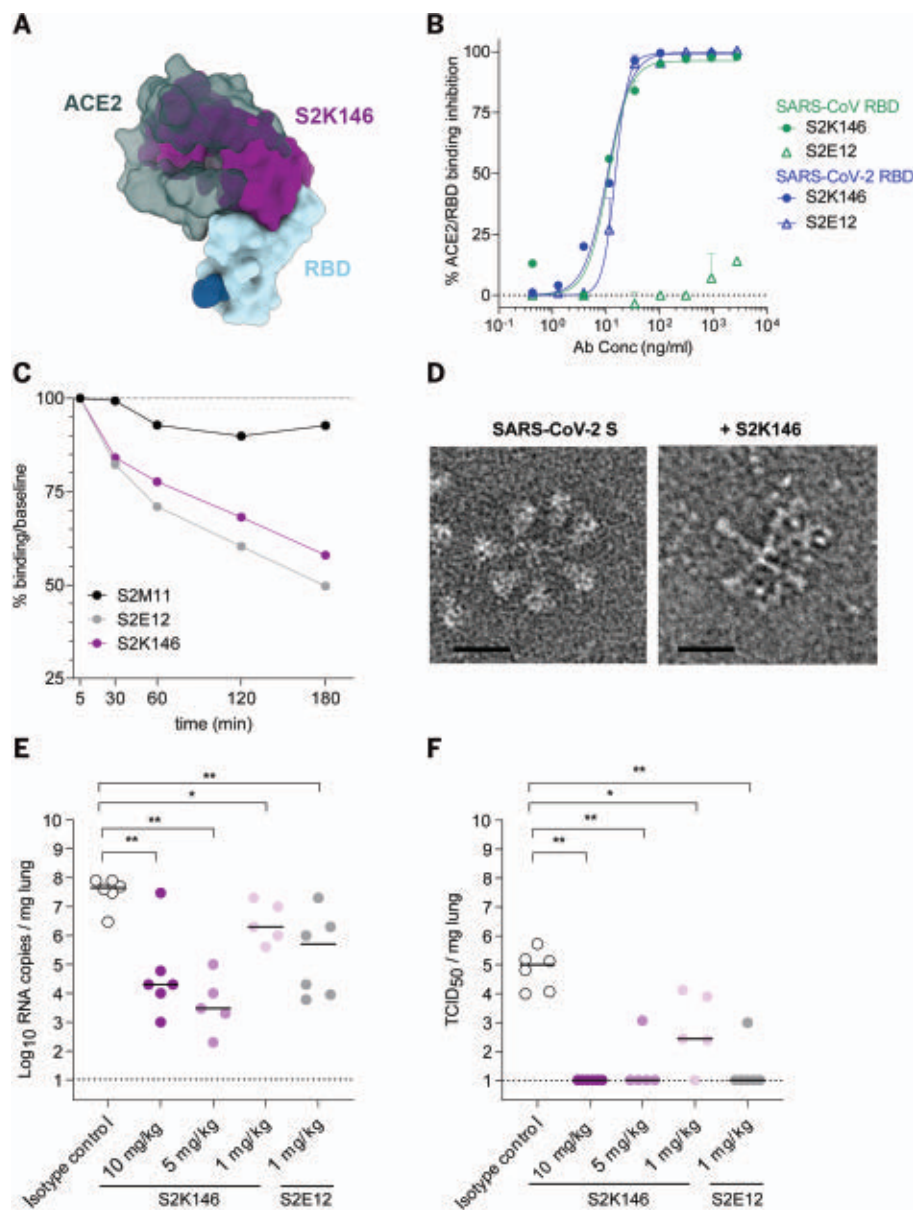


Fig. 4. S2K146 blocks receptor attachment, triggers premature S refolding, and protects against SARS-CoV-2 challenge therapeutically. (A) Superimposition of the S2K146-bound (purple) and ACE2-bound [dark gray, PDB ID 6MOJ (16)] SARS-CoV-2 RBD (light blue) structures showing steric overlap. The N343 glycan is rendered as blue spheres. (B) Preincubation of serial dilutions of S2K146 with the SARS-CoV-2 RBD prevents binding to immobilized human ACE2 (hACE2) ectodomain in ELISA. Error bars indicate standard deviation between replicates. (C) S2K146-mediated S_1 -shedding from cell surface-expressed SARS-CoV-2 S as determined by flow cytometry. S2E12 mAb was used as positive control, whereas S2M11 was used as a negative control. (D) Cropped electron micrographs of negatively stained SARS-CoV-2 S trimer before (left, prefusion state) or after (right, postfusion state) incubation with S2K146. One representative micrograph for each dataset is shown out of 93 (SARS-CoV-2 S alone) and 225 (SARS-CoV-2 S with S2K146) micrographs. Scale bars, 200 Å. (E and F) Quantification of viral RNA (E) and replicating virus titers [50% tissue culture infectious dose (TCID₅₀)] (F) in the lung of Syrian hamster 4 days after intranasal infection with SARS-CoV-2 Beta VOC followed by therapeutic administration of S2K146 mAb at three different doses: 10, 5, or 1 mg/kg of body weight ($n = 5$ or 6 animals per group). S2E12 mAb was administered as control ($n = 6$ animals). Isotype control was administered at 10 mg/kg ($n = 6$ animals). * $P < 0.05$, ** $P < 0.01$, as determined by Mann Whitney two-tailed test.

that are constrained in SARS-CoV-2 evolution appears to be a direct consequence of mAb affinity maturation.

To explore whether our escape map was consistent with in vitro viral evolution under

mAb pressure, a replication competent VSV-SARS-CoV-2 S Wuhan-Hu-1/D614G chimera (35) was passaged in cell culture in the presence of the S2K146 mAb. Consistent with the DMS data, Y489H was the sole mutation re-

sulting from a single nucleotide substitution that was detected in all the 36 neutralization-resistant plaques sampled (Fig. 3E, fig. S8A, and table S2). SARS-CoV-2 residue Y489 forms multiple interactions with S2K146 CDRH3 and accounts for ~10% of the total epitope buried surface area (Fig. 3E), in line with the major impact of the Y489H substitution on mAb neutralization. Of all the mutations at position 489 identified by DMS to reduce S2K146 binding (Fig. 3B), the Y-to-H substitution had the lowest impact on ACE2 binding, which might explain why it was the sole neutralization escape mutant selected upon passaging.

To evaluate the fitness of the Y489H mutant, we carried out a competition assay in which replicating VSV chimeras harboring the Wuhan-Hu-1/D614G S with or without the Y489H substitution were mixed at equal titers and passaged together without mAb. Because of the fitness cost associated with the mutation, which dampens ~4.5-fold the 1:1 ACE2-binding affinity to the SARS-CoV-2 RBD (fig. S8B), the Y489H S chimera was out-competed by the Wuhan-Hu-1/D614G S chimera after only four rounds of passaging (Fig. 3F). Accordingly, only 29 out of 2.9 million genomes were found to harbor the S Y489H mutation, underscoring the rarity of and the fitness cost imposed by this residue substitution (Fig. 3G). Collectively, these data illustrate the high barrier for emergence of escape mutants imposed by the S2K146 mAb, making it a good candidate for clinical development.

S2K146 targets antigenic site Ia, which overlaps with the RBM, indicating that mAb binding would compete with ACE2 attachment to the RBD via steric hindrance (Fig. 4A). Indeed, S2K146 inhibited binding of the SARS-CoV-2 and SARS-CoV RBDs to human ACE2 in a concentration-dependent manner, as measured by competition ELISA (Fig. 4B). As S2K146 conformationally selects for open RBDs, we assessed whether the mAb could promote shedding of the S_1 subunit from cell surface-expressed full-length SARS-CoV-2 S, similar to some other RBD-specific mAbs (17, 19, 24, 33). S2K146 induced shedding of the S_1 subunit as efficiently as the RBM-targeting S2E12 mAb, whereas the control mAb S2M11, which locks S in the prefusion closed state, did not (19) (Fig. 4C). Furthermore, S2K146 Fab triggered fusogenic rearrangement of a wild-type-like S ectodomain trimer, as previously described for several SARS-CoV and SARS-CoV-2 neutralizing mAbs (20, 36–38) (Fig. 4D). Thus S2K146-mediated sarbecovirus neutralization relies on competitively blocking viral attachment to the ACE2 receptor and putative inactivation of S trimers at the surface of virions before encountering host cells.

The efficient S2K146-induced S_1 shedding could explain the lack of FcγRIIIa and FcγRIIIa

activation, which we used as a proxy for Ab-dependent cellular phagocytosis and Ab-dependent cellular cytotoxicity, respectively (fig. S9, A and B). However, S2K146 also did not activate FcγRIIa and triggered FcγRIIIa only weakly when target cells expressed an uncleavable prefusion-stabilized SARS-CoV-2 S protein (fig. S9, C and D). The greater efficiency of S2E12 for activating FcγRIIIa, relative to S2K146, might be explained by the different angles of approach at which these two mAbs bind to the RBD (fig. S9, E and F).

Next, we evaluated the therapeutic activity of S2K146 against challenge with the SARS-CoV-2 Beta VOC in a Syrian hamster model of infection (39, 40). S2K146 was administered in doses of 1, 5, and 10 mg/kg of body weight via intraperitoneal injection 24 hours after intranasal challenge with SARS-CoV-2, and the lungs of the animals were collected 3 days later for the quantification of viral RNA and replicating virus. In parallel, six animals were administered 1 mg/kg of the ultrapotent S2E12 mAb for benchmarking (33). Viral RNA loads in the lungs were reduced by ~1, 4, and 3 orders of magnitude after receiving 1, 5, and 10 mg/kg of S2K146, respectively (Fig. 4E). Viral replication in the lungs was completely abrogated for the 5 and 10 mg/kg groups and reduced by greater than 2.5 orders of magnitude for the 1 mg/kg group (Fig. 4F). Overall serum mAb concentrations measured at day 4 after infection inversely correlated with viral RNA loads and infectious virus in the lungs (fig. S10, A and B). S2K146 therefore effectively protects against SARS-CoV-2 challenge in vivo in a stringent therapeutic setting.

The SARS-CoV-2 RBD accounts for most serum neutralizing activity in both COVID-19 convalescent (17, 41) and vaccinated individuals (7, 18), and a subset of antigenic sites are targeted by broadly neutralizing sarbecovirus Abs (19–25). RBD-based subunit vaccines and mRNA vaccines based on chimeric S glycoproteins elicit broadly neutralizing sarbecovirus Abs and heterotypic protection in vivo (42–46). Most of the Abs with broad neutralizing activity are expected to target conserved RBD epitopes, owing to their much greater potency and protection efficacy compared to Abs that target the conserved fusion machinery (47–52). The discovery of a functionally constrained and conserved RBM epitope associated with broad sarbecovirus neutralization is consistent with the strong cross-reactivity with the SARS-CoV RBM observed with polyclonal Abs elicited by a clinical stage SARS-CoV-2 vaccine in nonhuman primates (44) and will guide the development of next-generation pan-sarbecovirus vaccines to protect from future zoonotic transmission events.

The broadly neutralizing sarbecovirus mAb S309 was isolated from a survivor of a 2003 SARS-CoV infection, and its derivative

(sotrovimab) has received emergency use authorizations in several countries around the world for the early treatment of mild-to-moderate COVID-19 in adults and some pediatric patients who test positive for SARS-CoV-2 by direct viral testing and who are at high risk for progression to severe COVID-19, including hospitalization or death (19, 27, 29, 53). S309 has proven resilient to the emergence of SARS-CoV-2 variants in preclinical studies, possibly owing to targeting of a conserved RBD epitope with very limited mutational tolerance (20, 53). The mechanism of S2K146-mediated ACE2 molecular mimicry also provides a high barrier for emergence of escape mutants in spite of the known mutational plasticity of the SARS-CoV-2 RBM (30). Therefore, the discovery of the S2K146 mAb might be a milestone for future treatment of COVID-19 patients and for pandemic preparedness against divergent sarbecoviruses.

REFERENCES AND NOTES

- C. A. Sánchez *et al.*, medRxiv 2021.09.09.21263359 [Preprint] (2021). <https://doi.org/10.1101/2021.09.09.21263359>.
- A. C. Walls *et al.*, *Nature* **531**, 114–117 (2016).
- A. C. Walls *et al.*, *Proc. Natl. Acad. Sci. U.S.A.* **114**, 11157–11162 (2017).
- A. C. Walls *et al.*, *Cell* **181**, 281–292.e6 (2020).
- D. Wrapp *et al.*, *Science* **367**, 1260–1263 (2020).
- M. A. Tortorici, D. Veerles, *Adv. Virus Res.* **105**, 93–116 (2019).
- L. Stamatatos *et al.*, *Science* **372**, 1413–1418 (2021).
- P. Zhou *et al.*, *Nature* **579**, 270–273 (2020).
- M. Letko, A. Marzi, V. Munster, *Nat. Microbiol.* **5**, 562–569 (2020).
- M. Hoffmann *et al.*, *Cell* **181**, 271–280.e8 (2020).
- W. Li *et al.*, *Nature* **426**, 450–454 (2003).
- F. Li, W. Li, M. Farzan, S. C. Harrison, *Science* **309**, 1864–1868 (2005).
- Q. Wang *et al.*, *Cell* **181**, 894–904.e9 (2020).
- R. Yan *et al.*, *Science* **367**, 1444–1448 (2020).
- J. Shang *et al.*, *Nature* **581**, 221–224 (2020).
- J. Lan *et al.*, *Nature* **581**, 215–220 (2020).
- L. Piccoli *et al.*, *Cell* **183**, 1024–1042.e21 (2020).
- A. J. Greaney *et al.*, *Sci. Transl. Med.* **13**, eabi9915 (2021).
- M. A. Tortorici *et al.*, *Nature* **597**, 103–108 (2021).
- T. N. Starr *et al.*, *Nature* **597**, 97–102 (2021).
- D. Pinto *et al.*, *Nature* **583**, 290–295 (2020).
- C. A. Jette *et al.*, *Cell Rep.* **36**, 109760 (2021).
- D. R. Martinez *et al.*, bioRxiv 2021.04.27.441655 [Preprint] (2021). <https://doi.org/10.1101/2021.04.27.441655>.
- A. Z. Wee *et al.*, *Science* **369**, 731–736 (2020).
- C. G. Rappazzo *et al.*, *Science* **371**, 823–829 (2021).
- D. Corti, L. A. Purcell, G. Snell, D. Veerles, *Cell* **184**, 3086–3108 (2021).
- M. McCallum *et al.*, *Science* **373**, 648–654 (2021).
- M. McCallum *et al.*, *Science* **374**, 1621–1626 (2021).
- P. Micochova *et al.*, *Nature* **599**, 114–119 (2021).
- T. N. Starr *et al.*, *Cell* **182**, 1295–1310.e20 (2020).
- T. N. Starr, A. J. Greaney, A. S. Dingens, J. D. Bloom, *Cell Rep. Med.* **2**, 100255 (2021).
- T. N. Starr *et al.*, *Science* **371**, 850–854 (2021).
- M. A. Tortorici *et al.*, *Science* **370**, 950–957 (2020).
- T. N. Starr *et al.*, bioRxiv 2021.07.17.452804 [Preprint] (2021). <https://doi.org/10.1101/2021.07.17.452804>.
- J. B. Case *et al.*, *Cell Host Microbe* **28**, 475–485.e5 (2020).
- A. C. Walls *et al.*, *Cell* **176**, 1026–1039.e15 (2019).
- F. A. Lempp *et al.*, *Nature* **598**, 342–347 (2021).
- J. Huo *et al.*, *Cell Host Microbe* **28**, 445–454.e6 (2020).
- R. Abdelnabi *et al.*, *EBioMedicine* **68**, 103403 (2021).
- R. Boudewijns *et al.*, *Nat. Commun.* **11**, 5838 (2020).
- W. Dejnirattai *et al.*, *Cell* **184**, 2183–2200.e22 (2021).
- P. S. Arunachalam *et al.*, *Nature* **594**, 253–258 (2021).
- A. C. Walls *et al.*, *Cell* **183**, 1367–1382.e17 (2020).
- A. C. Walls *et al.*, *Cell* **184**, 5432–5447.e16 (2021).
- K. O. Saunders *et al.*, *Nature* **594**, 553–559 (2021).
- D. R. Martinez *et al.*, *Science* **373**, 991–998 (2021).

- D. Pinto *et al.*, *Science* **373**, 1109–1116 (2021).
- M. M. Sauer *et al.*, *Nat. Struct. Mol. Biol.* **28**, 478–486 (2021).
- G. Song *et al.*, *Nat. Commun.* **12**, 2938 (2021).
- P. Zhou *et al.*, bioRxiv 2021.03.30.437769 [Preprint] (2021). <https://doi.org/10.1101/2021.03.30.437769>.
- C. Wang *et al.*, *Nat. Commun.* **12**, 1715 (2021).
- C.-L. Hsieh *et al.*, *Cell Rep.* **37**, 109929 (2021).
- A. L. Cathcart *et al.*, bioRxiv 2021.03.09.434607 [Preprint] (2021). <https://doi.org/10.1101/2021.03.09.434607>.

ACKNOWLEDGMENTS

The authors thank C. Castedo and N. Blais (GSK Vaccines) for their help in the selection of the genetically divergent sarbecoviruses used in this study and H. Tani (University of Toyama) for providing the reagents necessary for preparing VSV pseudotyped viruses.

Funding: This study was supported by the National Institute of Allergy and Infectious Diseases (DPIA158186 and HHSN272201700059C to D.V.), the National Institute of General Medical Sciences (5T32GM008268 to S.K.Z.), a Pew Biomedical Scholars Award (D.V.), an Investigators in the Pathogenesis of Infectious Disease Award from the Burroughs Wellcome Fund (D.V.), Fast Grants (D.V.), the University of Washington Arnold and Mabel Beckman cryo-EM center and the National Institutes of Health grant S100D032290 (to D.V.). J.D.B. and D.V. are investigators of the Howard Hughes Medical Institute.

Author contributions: Y.-J.P., A.D.M., T.N.S., Z.L., D.P., J.D.B., D.C., M.S.P., and D.V. designed the experiments. A.D.M., D.P., A.C.W., S.K.Z., K.R.S., F.Z., M.G., J.No., L.E.R., and F.A.L. isolated mAb and performed binding, neutralization assays, biolayer interferometry, and SPR measurements. A.D.M. and D.P. performed ACE2 binding inhibition and S₁ shedding assays. B.G. evaluated effector functions. T.N.S. and J.D.B. performed deep-mutational scanning. Z.L. and S.P.J.W. performed mutant selection and fitness assays. R.A., S.-Y.C.F., F.B., J.Ne., D.C., and M.S.P. performed hamster model experiments and data analysis. Y.-J.P. carried out cryo-EM specimen preparation, data collection, and processing. Y.-J.P. and D.V. built and refined the atomic models. S.K.Z., A.J., and J.E.B. purified recombinant glycoproteins. Y.-J.P., A.D.M., T.N.S., Z.L., D.P., J.D.B., D.C., M.S.P., and D.V. analyzed the data. Y.-J.P., A.D.M., D.C., M.S.P., and D.V. wrote the manuscript, with input from all authors. F.A.L., F.B., G.S., J.Ne., S.P.J.W., H.W.V., J.D.B., D.C., M.S.P., and D.V. supervised the project. **Competing interests:** A.D.M., D.P., F.Z., M.G., B.G., J.No., L.E.R., F.A.L., F.B., G.S., H.W.V., D.C., and M.S.P. are employees of Vir Biotechnology Inc. and may hold shares in Vir Biotechnology Inc. D.C. is currently listed as an inventor on multiple patent applications, which disclose the subject material described in this manuscript. J.D.B. is an inventor on patents licensed by Fred Hutchinson Cancer Research Center related to deep mutational scanning of viral proteins. The Veerles and Neyts laboratories have received sponsored research agreements from Vir Biotechnology Inc. H.W.V. is a founder of PierianDx and Casma Therapeutics; neither company provided funding for this work or is performing related work. J.D.B. consults for Moderna, Oncorus, and Flagship Labs 77. **Data and materials availability:** The cryo-EM map and coordinates have been deposited to the Electron Microscopy Data Bank and Protein Data Bank with the following accession numbers: SARS-CoV-2 S/S2K146 (3RBDs open), EMD-25785; SARS-CoV-2 S/S2K146 (2RBDs open), PDB 7TAT and EMD-25784; SARS-CoV-2 S RBD/S2K146 (local refinement), PDB 7TAS and EMD-25783. Materials generated in this study will be made available on request, but we may require a completed materials transfer agreement signed with Vir Biotechnology or the University of Washington. This work is licensed under a Creative Commons Attribution 4.0 International (CC BY 4.0) license, which permits unrestricted use, distribution, and reproduction in any medium, provided the original work is properly cited. To view a copy of this license, visit <https://creativecommons.org/licenses/by/4.0/>. This license does not apply to figures/photos/artwork or other content included in the article that is credited to a third party; obtain authorization from the rights holder before using such material.

SUPPLEMENTARY MATERIALS

science.org/doi/10.1126/science.abm8143
Materials and Methods
Figs. S1 to S10
Tables S1 and S2
References (54–76)
MDAR Reproducibility Checklist

13 October 2021; accepted 22 December 2021
Published online 6 January 2022
10.1126/science.abm8143

PALEOBOTANY

Southeast Asian Dipterocarp origin and diversification driven by Africa-India floristic interchange

Mahi Bansal^{1†}, Robert J. Morley^{2,3†}, Shivaprakash K. Nagaraju^{4†}, Suryendu Dutta⁵, Ashish Kumar Mishra¹, Jeyakumar Selveraj¹, Sumit Kumar⁵, Deepti Niyolia⁵, Sachin Medigeshe Harish^{6,7}, Omer Babiker Abdelrahim⁸, Shaa eldin Hasan⁸, Bramasamdura Rangana Ramesh⁹, Selvadurai Dayanandan^{6,7}, Harsanti P. Morley², Peter S. Ashton¹⁰, Vandana Prasad^{1*†}

The evolution and diversification of ancient megathermal angiosperm lineages with Africa-India origins in Asian tropical forests is poorly understood because of the lack of reliable fossils. Our palaeobiogeographical analysis of pollen fossils from Africa and India combined with molecular data and fossil amber records suggest a tropical-African origin of Dipterocarpaceae during the mid-Cretaceous and its dispersal to India during the Late Maastrichtian and Paleocene, leading to range expansion of aseasonal dipterocarps on the Indian Plate. The India-Asia collision further facilitated the dispersal of dipterocarps from India to similar climatic zones in Southeast Asia, which supports their out-of-India migration. The dispersal pathway suggested for Dipterocarpaceae may provide a framework for an alternative biogeographic hypothesis for several megathermal angiosperm families that are presently widely distributed in Southeast Asia.

Many of the megathermal angiosperm families that constitute major components of today's tropical rainforest, such as Annonaceae, Combretaceae, Ebenaceae, Myristicaceae, etc., show disjunct pantropical distributions. The colonization and diversification of megathermal angiosperms in Southeast Asian tropical forests is believed to be influenced by their ancient origin in Africa and out-of-India dispersal (1–4). However, the limited number of molecular studies and the sparse fossil record of megathermal angiosperms from the Cretaceous of Africa (1) and the Paleogene of India (4, 5) provide insufficient information to conclude their ancient African origin or that India aided their dispersal and diversification in Asian tropical forests. Here, we present fossil pollen data from the family Dipterocarpaceae that suggest their African origin during the mid-Cretaceous and subsequent dispersal to Southeast Asia.

Dipterocarpaceae are a pantropical, obligate megathermal angiosperm family comprising more than 500 species grouped into three

subfamilies with an intercontinental disjunct distribution: Monotoideae in Africa, Madagascar, and South America; Pakaraimaeoideae in South America; and Dipterocarpoideae in the Seychelles, India, and Southeast Asia (6). A specific combination of morphological and ecological characteristics determined the ecological success of Dipterocarpoideae and enabled them to out-shade the canopy of other tree families, which led to their dominance in the mature forests of Southeast Asia (6). These characteristics include ectotrophic mycorrhizal association, specific pollinators, mast fruiting overcoming seed predation, protective resin in multicellular secretory ducts, poorly nutritious and resinous unpalatable leaves for many herbivores, and plagiotropic followed by orthotropic branching patterns in trees. Dipterocarps have been the major source for timber extraction across Southeast Asia over the past 50 years, which has led to their overexploitation and has left many formerly superabundant species critically endangered.

We present eight fossil pollen types, extracted using the standard palynological techniques (7), referable to five living genera of the subfamily Dipterocarpoideae (*Dipterocarpus*, *Dryobalanops*, *Shorea*, *Vateriopsis*, and *Vatica*) and one genus of the subfamily Monotoideae (*Monotes*) (Fig. 1 and figs. S1 to S4) from the Maastrichtian of Sudan and the Paleocene and early Eocene of India (Fig. 2, appendix S1, and table S1). These are combined with the secobiscadinane biomarkers of dipterocarps retrieved from the Late Cretaceous sediments from central India (fig. S5), phylogenetic analysis (8–13) of pollen (fossil and extant) morphology, and DNA sequence data of 54% of the known Dipterocarpaceae species to do the following: (i) trace

the origin and evolution of the family; (ii) define the role of climate and dispersal pathways, including movement of the Indian Plate during the Late Cretaceous–early Paleogene in the diversification of the family; and (iii) resolve the paleobiogeographic history of lowland dipterocarp rainforests in Southeast Asia.

The pollen of the subfamily Dipterocarpoideae is distinctive in being tricolpate, with very long colpi reaching almost to the poles, and with exine consisting of a thin basal layer, except in *Vateriopsis* and allied genera, with a much thicker outer, sculptured layer. The columellae and frequently grooved or crenelated ridge-bearing tectum of the outer layer fuses into a tilioid structure, except in the tribe Shoreae (14). Pollen of most species of Dipterocarpoideae are smaller than 35 μm , whereas *Dipterocarpus* pollen ranges from ~50 to 100 μm . The diagnostic characteristics of *Dipterocarpus* pollen can mostly be seen in light microscopy (LM), whereas the identification of other genera also requires scanning electron microscopy (SEM) examination. No other plant family exhibits the combination of tricolpate configuration, absence or reduced endexine, and tilioid exine structure (table S2). By contrast, the subfamily Monotoideae pollen is tricolporate with the ectexine forming a fairly coarse tilioid structure (14). Phylogenetic analyses based on pollen morphological characters confirm the placement of seven of the eight fossil taxa within five extant genera of Dipterocarpoideae, namely *Vateriopsis*, *Dipterocarpus*, *Dryobalanops*, *Vatica*, and the three different *Shorea* sections—Anthoshorea, Parashorea, and Rubroshorea (figs. S6 to S8)—and the remaining one fossil taxon was placed within the genus *Monotes*, belonging to subfamily Monotoideae (figs. S6 to S8). The fossil pollen types represent five clades of Dipterocarpaceae based on our molecular phylogenetic analyses and previously published phylogenetic literature (15) (Fig. 3B, table S1, and appendix S2).

The discovery of fossil pollen with clear affinity to the subfamilies Dipterocarpoideae and Monotoideae from the Maastrichtian of Sudan and the Paleocene of India refutes frequent references to the unreliability in determination of fossil dipterocarp pollen (16). The previous skepticism largely stems from the fact that there are abundant records of Dipterocarpoideae leaves and woods from the Indian Neogene (17) but very few from the Late Cretaceous and Paleogene. This disparity most likely relates to many factors, including differences in the depositional setting. Other factors to bear in mind are (i) the possibility that the earliest phase of evolution of the family may have involved a long period of mosaic evolution and (ii) early macrofossils may not have borne anatomical features recognizable as Dipterocarpaceae.

The presence of pollen comparable to that of *Monotes* in the late Paleocene and early

¹Birbal Sahni Institute of Palaeosciences, Lucknow 226007, India. ²Palynova Ltd., Littleport, Cambridgeshire CB6 1PY, UK. ³Earth Sciences Department, Royal Holloway, University of London, Egham, Surrey TW20 0EX, UK. ⁴The Nature Conservancy Centre, New Delhi 110024, India. ⁵Department of Earth Sciences, Indian Institute of Technology Bombay, Mumbai 400076, India. ⁶Department of Biology and Centre for Structural and Functional Genomics, Concordia University, Montreal, Quebec H4B 1R6, Canada. ⁷Quebec Centre for Biodiversity Science, Montreal, Quebec H3A 1B1, Canada. ⁸Petroleum Laboratories, Research & Studies (PLRS), Ministry of Petroleum and Gas, Khartoum, Republic of Sudan. ⁹Institut Français de Pondichéry, UMIFRE 21 CNRS-MAEE, Puducherry 605001, India. ¹⁰Organismic and Evolutionary Biology, Harvard University, Cambridge, MA, USA.

*Corresponding author. Email: prasad.van@gmail.com

†These authors contributed equally to this work.

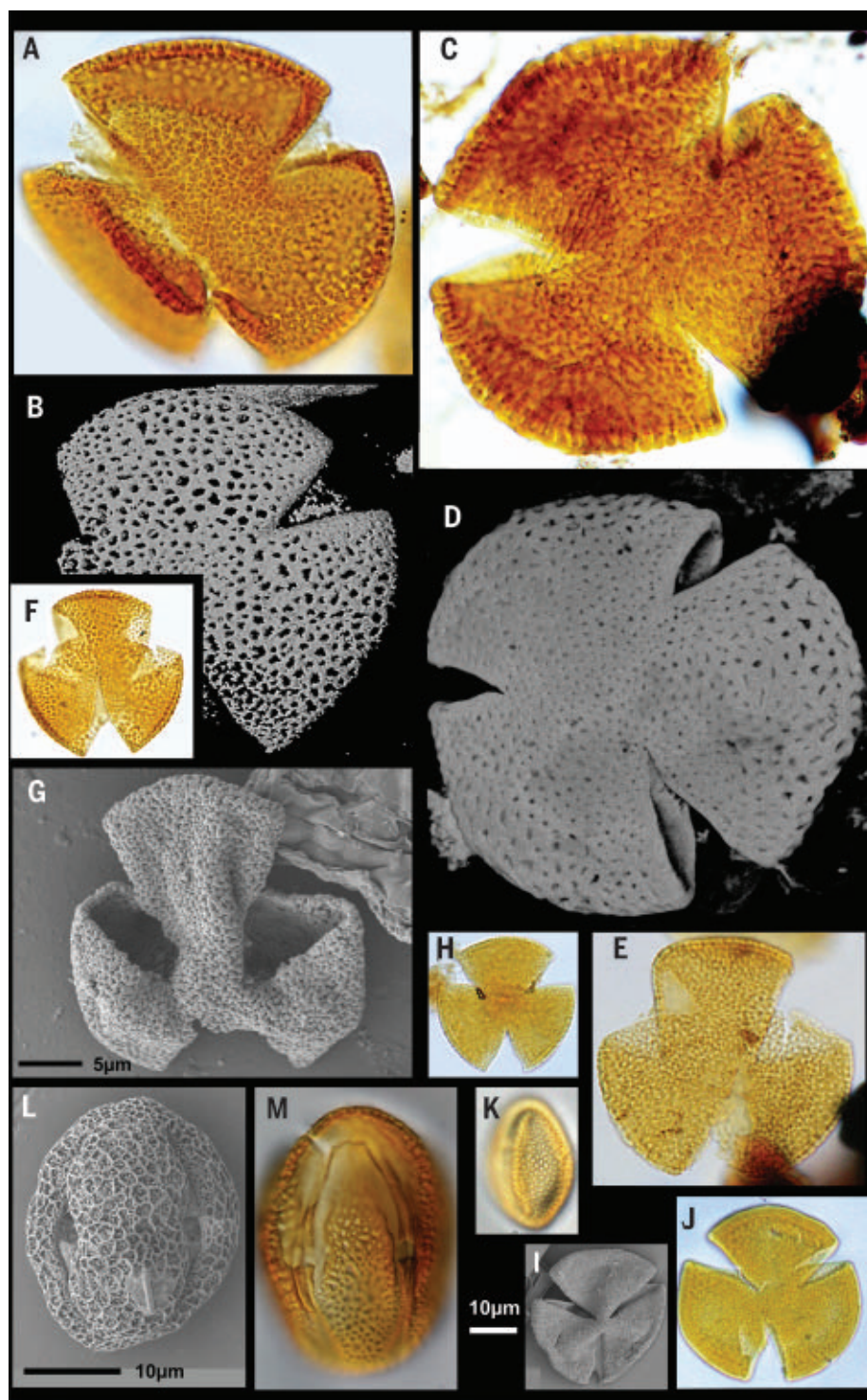


Fig. 1. Pollen of Dipterocarpaceae from India and Sudan. (A and B) *Dipterocarpus* type-a light microscopy (LM) image (A) and confocal laser scanning microscopy (CLSM) image (B) from the Matasukh Lignite Mine. (C and D) *Dipterocarpus* type-a LM image (C) and CLSM image (D) from the Baraka Formation, Sudan. (E) *Dipterocarpus* type-b LM image from the Sonari Lignite Mine. (F and G) *Dryobalanops* type LM image (F) and SEM image (G) from the Vastan Lignite Mine. (H) *Shorea* type LM image from the Vastan Lignite Mine. (I) *Vatica* type LM image from the Vastan Lignite Mine. (J and K) *Vateriopsis* type LM image (J) and SEM image (K) from the Sonari Lignite Mine. (L and M) *Monotes* type LM image (L) and SEM image (M) from the Sonari Lignite Mine. All images are scaled to the 10-μm bar at base of the plate except for (G) and (L), which are scaled as indicated.

Eocene of northwest India testifies to a much wider geographical range of Monotoideae during the early Paleogene. The Monotoideae, which also extends to the Neotropics, is estimated to have a stem molecular age of ~102 million years (Myr) (Fig. 3B and table S3), and it is likely that its distribution from Africa to South America was established at a very early age, as has been suggested by Moyersoen (18). Our results suggest the evolution of Dipterocarpaceae during the mid-Cretaceous [~102.9 million years ago (Ma); 93.5 to 112.2 Ma] and its diversification across tropical Africa as the climate changed from semi-arid to wet seasonal and perhumid during the Late Cretaceous (Fig. 3B, fig. S9, and table S3). Thus, the estimated mid-Cretaceous molecular age of origin and fossil records dating back to the late Cretaceous to the early Eocene (table S3) from Africa and India indicate a longer evolutionary history of Dipterocarpaceae than that suggested previously (6, 15) and ranks the family as one of the first obligate megathermal eudicot clades to originate in the mid-Cretaceous of Africa.

The family diverged into two main lineages, Monotoideae with an approximate crown age of 72.1 Myr (63 to 84.5 Myr) and Dipterocarpoideae at ~94.6 Ma (85 to 104.3 Ma), and their adaptation to tropical dry seasonal and wet seasonal habitats, respectively, could be attributable to phylogenetic niche conservatism of habitat specialization in the family. We further suggest a subsequent climatic adaptation of Dipterocarpoideae to wet seasonal settings for the genus *Dipterocarpus* (clade I) and to perhumid settings for the divergence of the near-basal genera *Stemonoporus*, *Vateriopsis*, and *Cotylelobium* (clade IV). Subsequent divergences followed the same pattern, with *Dipterocarpus* (clade I) (wet seasonal) diverging into *Dryobalanops* (clade II) (perhumid) and *Shorea* diverging into perhumid (IIIA) and seasonal (IIIB) clades (Fig. 3B and table S3). As noted above, diversification in Dipterocarpoideae corresponded with the development of more wet seasonal and perhumid climates across tropical Africa since the Santonian-Coniacian, and they may have contributed to the first multistoried rainforests (1) (Fig. 4). In India too, the diversification pattern of dipterocarps follows the same trend, with the association of *Dipterocarpus*-type pollen (clade I) with pollen floras of seasonally wet climates during the Paleocene (19) and of pollen of clade IV (*Vatica*- and *Vateriopsis*-type pollen) with a perhumid climate during the late Paleocene–early Eocene (Fig. 4). The presence of *Shorea* fossil pollen (20) and possible wood in the Vastan lignites (21) and Myanmar red-beds (22), respectively, suggests the association of *Shorea* with perhumid and seasonal climates during the Eocene.

The dispersal of Dipterocarpaceae from Africa to India is most likely to have taken place when

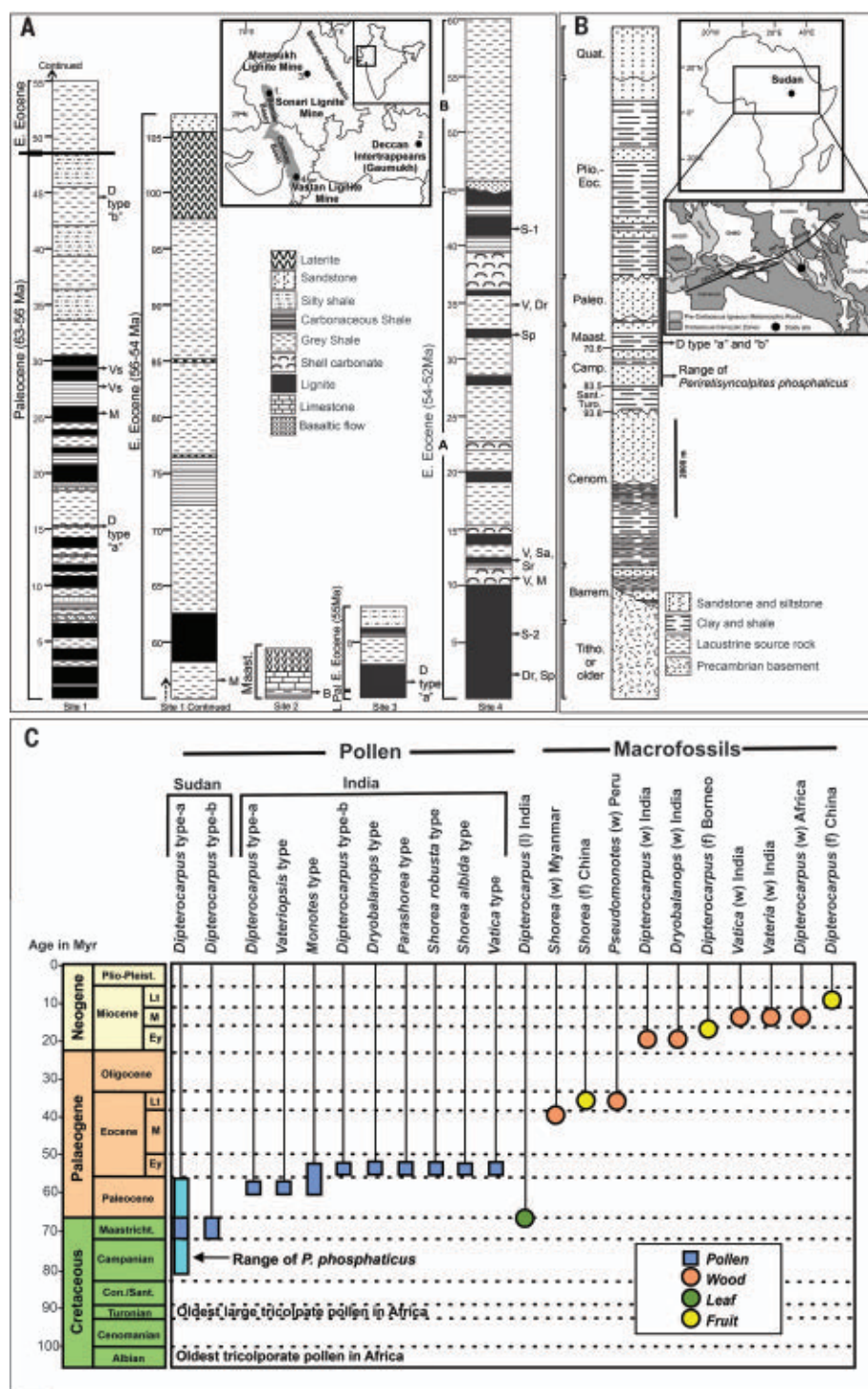


Fig. 2. Stratigraphy, location, and distribution of Dipterocarpaceae pollen in Sudan and India.

(A) Location and stratigraphy of Indian localities: the Sonari Lignite Mine (site 1), the Gaumukh section (site 2), the Matasukh Lignite Mine (site 3), and the Vastan Lignite Mine (site 4). (B) Location and stratigraphy of the Baraka Formation in Sudan. (C) Stratigraphic distribution of Dipterocarpaceae pollen in Sudan and India and the oldest records of dipterocarp macrofossils from Africa, South America, and tropical Asia (6, 16, 24, 35–37). E. Eocene, early Eocene; Maast., Maastrichtian; L. Pal., late Paleocene; Quat., Quaternary; Plio.-Eoc., Pliocene-Eocene; Paleo., Paleocene; Camp., Campanian; Sant.-Turo., Santonian-Turonian; Cenom., Cenomanian; Barrem., Barremian; Titho., Tithonian; Myr., million years; B., geochemical biomarker; Vs, *Veteriopsis* type; M, *Monotes* type; D, *Dipterocarpaceae* type-a and *Dipterocarpaceae* type-b; V, *Vatica* type; Dr, *Dryobalanops* type; Sp, *Parashorea* type; Sa, *Shorea albidula* type; Sr, *Shorea robusta* type.

the same climatic conditions prevailed on adjacent landmasses (23). For the seasonal *Dipterocarpus* and *Monotes*, appropriate habitats may have been available in Africa from ~75 Ma onward, but for the perhumid *Dryobalanops* and clade IV genera, habitats were unlikely to have been in place until the Late Maastrichtian (Fig. 4A). At this time, the African and Indian plates were separated by a wide ocean, which would have hampered the dispersal of large-seeded taxa, such as dipterocarps. The presence of Dipterocarpaceae in the geologically very young islands of Sulawesi (24) and New Guinea (25) testifies to their ability to disperse across substantial water bodies within the same climatic zone. The taxa present on these islands are all winged, which raises the possibility of their dispersal by wind, suggesting that a similar mechanism may have enabled the dispersal of dipterocarps from Africa to India. The wingless configuration seen in *Stemonoporus* and *Vateriopsis* may appear to conflict with this suggestion, but these genera may have lost wings after their arrival on their respective islands, as reflected by their fruit wing evolution patterns (fig. S10). This finding is congruent with a well-established pattern of loss of dispersal mechanism in plants arriving on islands (26, 27).

At the time of dispersal of dipterocarps from Africa to India, the Indian Plate was in collision with a series of Tethyan island arcs termed the Kohistan-Ladakh Island Arc (KLIA) (28), which was aligned with the Burma Plate (29) and the Horn of Africa, all within the equatorial zone. It has been suggested that this island arc could have provided stepping-stones between Africa and the Indian Plate along which both fauna (30) and flora (6, 23) were able to disperse. This series of islands may have been sufficiently closely spaced to permit the land or airborne dispersal of dipterocarps into India from Africa.

The early Maastrichtian Indian sediments are characterized by gymnosperm-dominated pollen floras (31), with the widespread occurrence of calcareous lithologies suggesting a strongly water-deficient climate (32) unsuitable for the tropical angiosperm flora to flourish. We suggest that the presence of a surprising diversity of modern tropical plant families' fossils in the form of woods, leaves, fruits, and pollen in the Late Maastrichtian Intertrappean sediments may reflect their dispersal from Africa via the KLIA along with members of Dipterocarpaceae. The establishment of a dispersal corridor from Africa to India along an island arc in a setting of changing climatic conditions from semi-arid to seasonal tropical may explain this sudden diversification of tropical elements on the Indian subcontinent. This filter corridor is here referred to as the Africa-India floristic interchange (AIFI).

The isolation of *Vateriopsis* on the Seychelles also alludes to its dispersal during the Maastrichtian. The Seychelles separated from

India between 75 and 68 Ma, and the crown age of *Vateriopsis* is 68 Myr (Fig. 3B), which suggests that it originated on the Seychelles or the Seychelles-India block.

Two distinct *Vatica*-type pollen fossils are recorded in the early Eocene of the Vastan Lignite Mine. The stem and crown ages of

Vatica at 58 and 55 Ma, respectively, suggest its rapid evolution during the late Paleocene, either on the KLIA or on the Indian Plate within a perhumid climatic setting. *Shorea* clades exhibit an acceleration in divergence during the Late Maastrichtian and Paleocene—Doona at 70 Ma, Anthoshorea at 63 Ma,

Rubroshorea at 62 Ma, and Parashorea at 61 Ma. This divergence pattern is also supported by the presence of the fossil woods *Shoreoxylon panganense*, *Shoreoxylon burmense*, and *Shoreoxylon deomaliense* from the middle Eocene of the Burma Plate. These fossil woods occur in red-beds and are likely to have grown in an area of seasonally dry climate like that of *Shorea robusta* today, with which *S. panganense* has been compared (22). This suggests that ecological segregation of areas with perhumid and seasonally dry climates may have been a primary driver of *Shorea* diversification. The Dipterocarpoideae lineages are further suggested to have dispersed to Southeast Asia from India after the India-Asia collision during the middle to late Eocene (20). This implies that, despite rapid latitudinal changes, massive volcanism, and pronounced orogenic events, early dipterocarps managed to survive the Cretaceous-Paleogene (K-Pg) impact event and the Deccan Trap eruptions and eventually dispersed to Southeast Asia.

Despite the doubtful identification of an *Anisoptera* fossil from the London Clay Formation (33) as a dipterocarp, the expansion of the plant family Dipterocarpaceae into northern mid-latitudes via boreo-tropical dispersal routes (34) cannot be dismissed. The family might have dispersed from Africa or India to Eurasia during the Paleocene-Eocene hothouse periods of frost-free and humid climate in Eurasia. The validation of boreo-tropical migration of Dipterocarpaceae requires the recovery of authentically identified dipterocarps from the early Paleogene of the boreotropics.

Dipterocarpaceae maintains high endemism in Asian forests. Clades with a long evolutionary span are clearly paleoendemics, such as *Monotes*, *Upuna*, *Vateriopsis*, *Stemonoporus*, *Dipterocarpus*, and *Dryobalanops* (55.8 to 70.6 Myr) (table S3). The isolation of *Upuna* in Borneo, *Vateriopsis* in the Seychelles, *Stemonoporus* in Sri Lanka, and *Monotes* in Africa and Madagascar are extreme examples of such paleoendemism. However, most younger clades, such as *Anisoptera*, *Vateria*, and *Shorea* section Doona, with shorter evolutionary ages (18.9 to 39 Myr) are also paleoendemics because all show a clear range reduction since the Pliocene—mainly as a result of the expansion of seasonally dry climates across India (6, 23). Most neoendemism is therefore likely to be at the subclade level and is reflected in the increase in diversification after 20.4 Ma (Fig. 3C) and may account for the notable diversity of genera, such as *Shorea*, in areas like Borneo. The evolution of wingless and winged fruit in Dipterocarpaceae also explains some patterns of endemism in the family (fig. S10). The wingless species of the family are heavily represented as endemics in island habitats. Winglessness may restrict dispersal

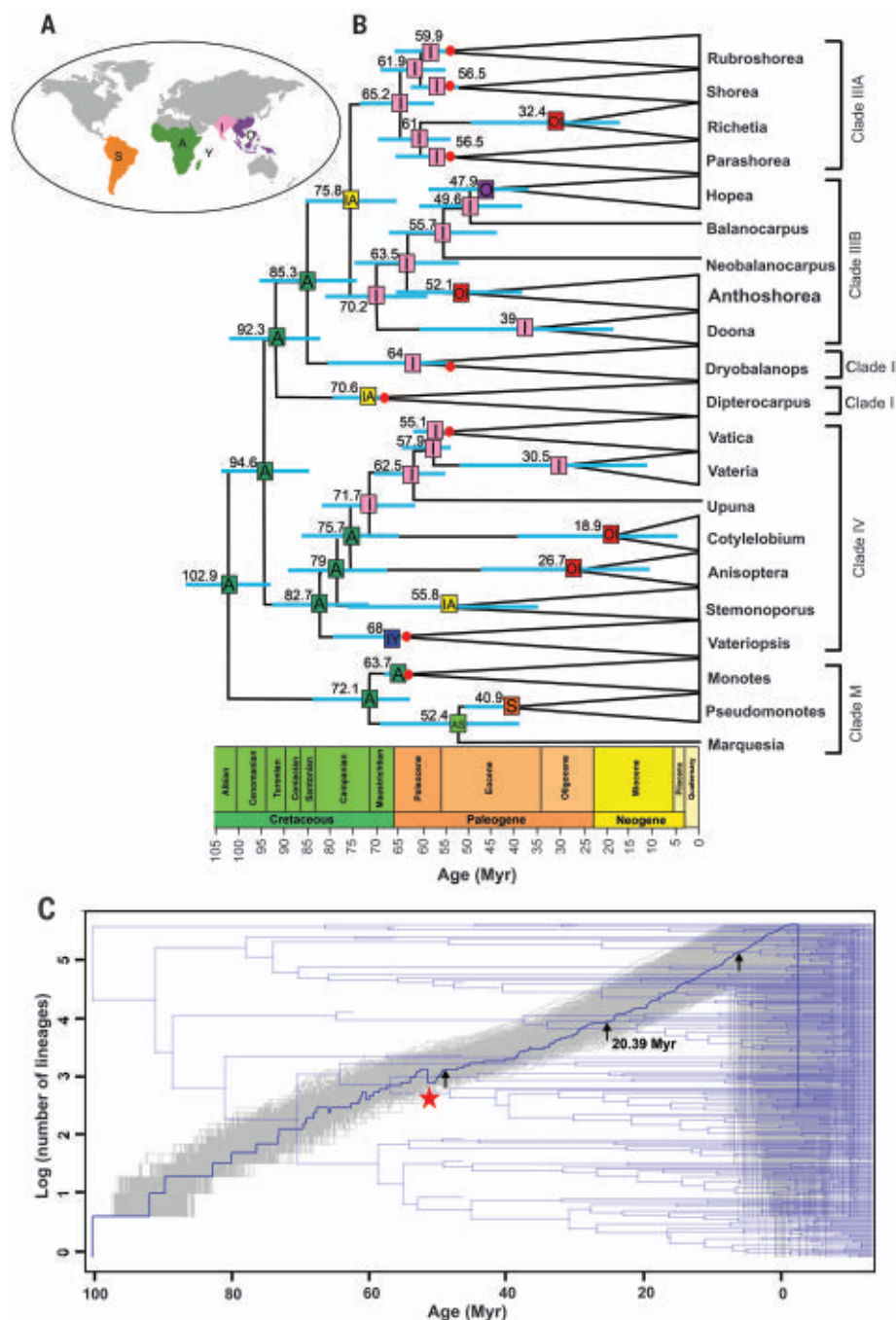


Fig. 3. Divergence dating, biogeography, and diversification pattern of Dipterocarpaceae. (A) Dipterocarpaceae geographic realms. S, South America; A, Africa; I, Peninsular India, including Bangladesh, Tibet, and Sri Lanka; Y, Seychelles; O, Southeast Asia, including Indonesia, Indochina, and China. (B) Dipterocarpaceae dated phylogram with 95% credibility intervals and ancestral area reconstruction. The clades are labeled following Heckenbauer *et al.* (14). Fossil occurrences are indicated by red dots, and reconstructed ancestral areas are shown for each internal node within rectangular boxes. (C) The LTT plot demonstrating Dipterocarpaceae diversification rates. The star symbol and arrows indicate diversification shifts over time.

distances, resulting in higher proportions of seed landing on preferred soil types, such as podsoles and humic ultisols. Such microhabitat adaptation might have led to paleo- and neo-endemism of some taxa on islands. Further, we found evidence for an increased speciation rate for the family after 20.4 Ma (Fig. 3C), coinciding with the expansion of perhumid climates across Southeast Asia (1, 23). Thus, we suggest

that after the India-Asia collision, Dipterocarpoideae species further adapted to wet climatic conditions, began to radiate and spread increasingly into the wet lowlands of the Sunda region, and became major components of Southeast Asian rainforests. By contrast, the Monotoideae went extinct from the Indian subcontinent during the mid-late Eocene and hence were unable to disperse to Southeast Asia.

The discovery of Dipterocarpoideae and Monotoideae fossils from the Maastrichtian of Sudan and the Maastrichtian, Paleocene, and early Eocene of India strengthens our understanding of tropical rainforest evolution across Asia in a deep time scale and substantially increases the recognized footprint of the AIFI in Asian tropical rainforests. However, our understanding of dispersals between Africa and India during the Late Cretaceous and the earliest Cenozoic is at a very early stage. Additional studies of fossil angiosperms from the African continent, India, and Southeast Asia will further clarify the manner in which megathermal plant taxa dispersed from Africa via India to the maritime continent of Southeast Asia, where they subsequently underwent explosive diversification within Malaysia's lowland rainforests.

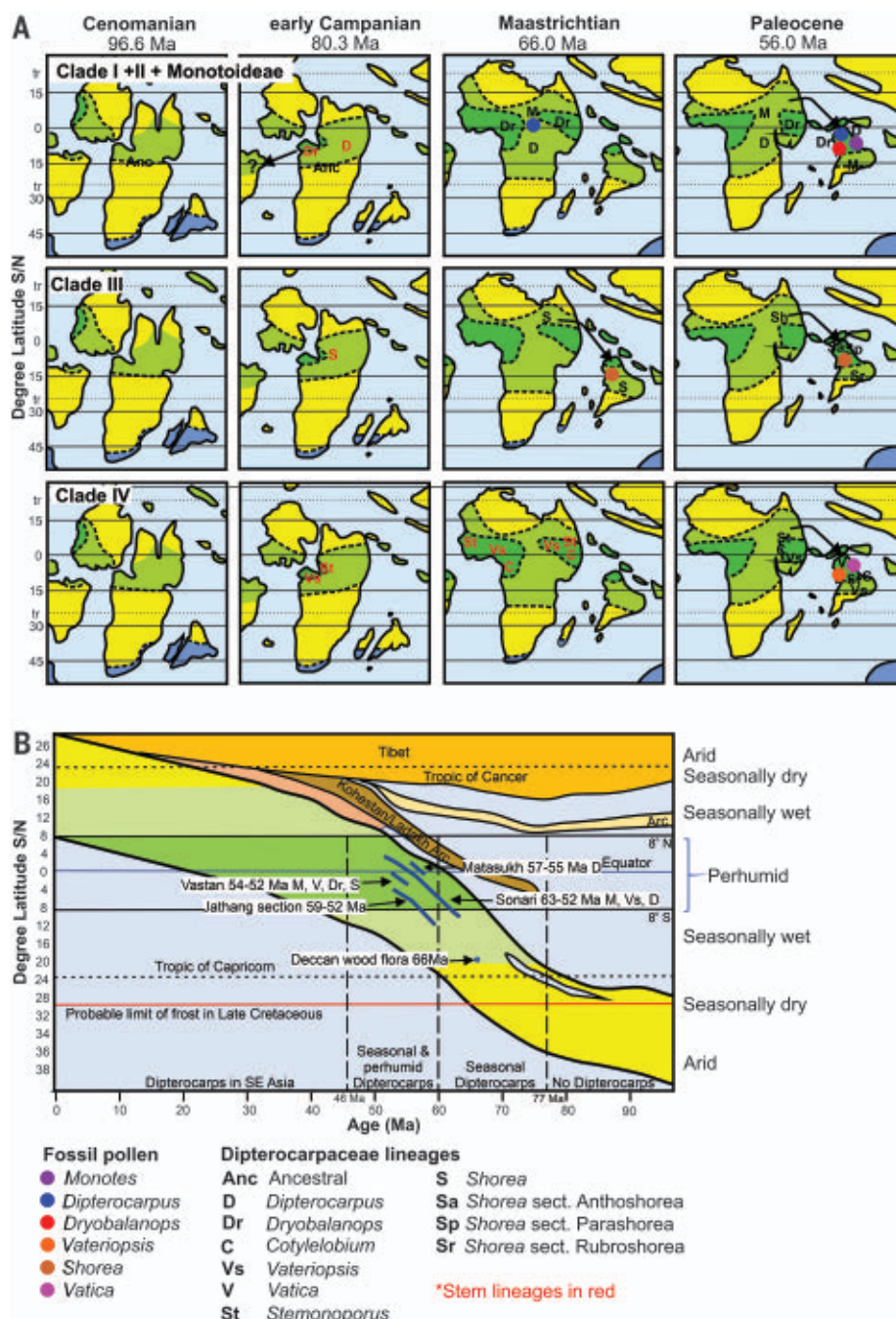


Fig. 4. Plate tectonic and paleoclimatic reconstruction and the position of the Africa and Indian plates over time. (A) Plate tectonic and paleoclimatic reconstructions for Africa and India for the Cenomanian to the Paleocene, and suggested areas of clade differentiation along with their dispersal routes. **(B)** A diagrammatic representation exhibiting the position of the Indian plate through time, from the mid-Cretaceous to the present, showing paleolatitude shift in relation to paleoclimate zones over time.

REFERENCES AND NOTES

1. R. J. Morley, *Origin and Evolution of Tropical Rain Forests* (Wiley, 2000).
2. J. A. Doyle, H. Sauquet, T. Scharaschkin, A. Le Thomas, *Int. J. Plant Sci.* **165**, S55–S67 (2004).
3. M. Grudinski, L. Wanntorp, C. M. Pannell, A. N. Muellner-Riehl, *J. Biogeogr.* **41**, 1149–1159 (2014).
4. M. Bansal et al., *Bot. J. Linn. Soc.* **197**, 147–169 (2021).
5. B. S. Venkatachala, C. Caratini, C. Tissot, R. K. Kar, *Palaeobotanist* **37**, 1–25 (1988).
6. P. S. Ashton, R. J. Morley, J. Heckenhauer, V. Prasad, *Kew Bull.* **76**, 87–125 (2021).
7. D. Phipps, G. Playford, *Pap. Dep. Geol. Univ. Qd.* **11**, 1–23 (1984).
8. R. Bouckaert et al., *PLOS Comput. Biol.* **10**, e1003537 (2014).
9. J. P. Huelsenbeck, F. Ronquist, *Bioinformatics* **17**, 754–755 (2001).
10. J. Matzke, *Front. Biogeogr.* **5**, 242–248 (2013).
11. A. Stamatakis, *Bioinformatics* **30**, 1312–1313 (2014).
12. D. L. Swofford, *PAUP: Phylogenetic Analysis Using Parsimony (*And Other Methods)* (Sinauer Associates, version 4, 2003).
13. D. J. Zwickl, “Genetic algorithm approaches for the phylogenetic analysis of large biological sequence datasets under the maximum likelihood criterion,” thesis, University of Texas at Austin (2006).
14. G. Maury, J. Muller, B. Lugardon, *Rev. Palaeobot. Palynol.* **19**, 241–289 (1975).
15. J. Heckenhauer et al., *Bot. J. Linn. Soc.* **185**, 1–26 (2017).
16. M. A. Khan et al., *Plant Syst. Evol.* **306**, 90 (2020).
17. V. Prasad, A. Farooqui, S. K. M. Tripathi, R. Garg, B. Thakur, *J. Biosci.* **34**, 777–797 (2009).
18. B. Moyersoen, *New Phytol.* **172**, 753–762 (2006).
19. V. Prasad et al., *Palaeogeogr. Palaeoclimatol. Palaeoecol.* **497**, 139–156 (2018).
20. S. Dutta et al., *Rev. Palaeobot. Palynol.* **166**, 63–68 (2011).
21. J. Rust et al., *Proc. Natl. Acad. Sci. U.S.A.* **107**, 18360–18365 (2010).
22. A. Licht et al., *Rev. Palaeobot. Palynol.* **202**, 29–46 (2014).
23. R. J. Morley, *J. Trop. Ecol.* **34**, 209–234 (2018).
24. A. M. S. Nugraha, R. Hall, *Palaeogeogr. Palaeoclimatol. Palaeoecol.* **490**, 191–209 (2018).
25. E. F. A. Toussaint et al., *Nat. Commun.* **5**, 4001 (2014).
26. B. Fresnillo, B. K. Ehlers, *Plant Syst. Evol.* **270**, 243–255 (2008).
27. H. Kudoh, K. Takayama, N. Kachi, *Pac. Sci.* **67**, 591–597 (2013).
28. S. A. Chatterjee, S. U. Bajpai, *Proc. Indian Natl. Sci. Acad.* **82**, 479–487 (2016).
29. J. Westerweel et al., *Tectonics* **39**, e2020TC006413 (2020).
30. T. Smith et al., *Geoscience Frontiers* **7**, 969–1001 (2016).
31. B. Samant, D. K. Kapgate, D. Kumar, D. M. Mohabey, A. Dhoble, *J. Geol. Soc. India* **95**, 475–482 (2020).
32. A. J. Boucot, C. Xu, C. R. Scotese, R. J. Morley, Eds., *Phanerozoic Paleoclimate: An Atlas of Lithologic Indicators of Climate*, vol. 11 of *Concepts in Sedimentology and Paleontology* (Society for Sedimentary Geology, 2013).
33. I. Poole, *Spec. Pap. Palaeontol.* **49**, 155–163 (1993).
34. D. C. Thomas et al., *Perspect. Plant Ecol. Evol. Syst.* **17**, 1–16 (2015).
35. H. Bancroft, *Am. J. Bot.* **22**, 164–183 (1935).
36. J. M. Cole, O. B. Abdelrahim, A. W. Hunter, E. Schrank, M. S. B. Ismail, *Palynology* **41**, 547–578 (2017).
37. D. W. Woodcock, H. W. Meyer, Y. Prado, *IAWA J.* **38**, 313–365 (2017).

38. M. Bansal *et al.*, Southeast Asian Dipteroecarp origin, and diversification driven by Africa-India Floristic Interchange, *Figshare*, dataset (2021); <https://doi.org/10.6084/m9.figshare.16727071.v1>.

ACKNOWLEDGMENTS

The authors extend their gratitude to BSIP for providing the infrastructural facilities to carry out this study (BSIP publication 12/ 2021-22). The authors also thank the late I. B. Singh and S. Bajpai for providing the samples from the Vastan Lignite Mine, Gujarat; A. Sharma and M. C. Manoj for their assistance during sample collection in the Barmer Basin, Rajasthan; P. Uddandam and S. Parmar for their support in the Dinoflagellate cysts study; A. Kumar, A. Ansari, and S. Mishra for providing sedimentological and chronological information of the Gaumukh section; R. K. Saxena for his help in the systematic description of the fossils; and S. Kumar and S. Srivastava for their contributions to SEM and CLSM imaging, respectively. M.B., B.R.R., and S.K.N. are thankful to T. Yamazaki for generating Dipteroecarpaceae DNA sequences. M.B. is thankful to Y. V. Dhar for providing computational facilities to

carry out the analyses for this study. **Funding:** This work is a contribution of CSIR grant no. 09/0528(11219)/2021-EMR-I, a sponsored project under MoES [MoES/P.O.(GeoSci.)/36/2014], and in-house project no. 3 at the Birbal Sahni Institute of Paleosciences and is part of a long-term evaluation of rainforest evolution supported by Palynova Ltd. A DST-sponsored project (DST/SJF/E&ASA-01/2016-17) at the Indian Institute of Technology, Bombay, has also financially supported this work.

Author contributions: Conceptualization and study design was by V.P., S.K.N., R.J.M., P.S.A., and S.Da. R.J.M. and H.P.M. enabled the study of Indian and African fossil pollen by initially identifying Dipteroecarpaceae pollen from Sudan and by bringing together the Sudanese and Birbal Sahni palynological teams. Collection of pollen material was done by V.P., O.B.A., and S.e.H. Pollen analysis and identification was performed by M.B., R.J.M., V.P., A.K.M., and J.S. Collection of data on fruit wing was done by S.M.H. DNA sequence generation, collection, and phylogenetic analysis was performed by M.B., S.K.N., and B.R.R. Biomarker analysis was by S.K., D.N., and S.Du. Plate tectonic and paleoclimate map construction was by R.J.M. R.J.M.,

M.B., S.K.N., and V.P. wrote the manuscript with inputs from all the authors. **Competing interests:** The authors declare no competing interests. **Data and materials availability:** All supporting data and analyses are available in the supplementary materials. The raw data (nexus files of phylogenetic trees, alignment files, and GenBank accession numbers) required to replicate the study are made publicly available on Figshare (38).

SUPPLEMENTARY MATERIALS

science.org/doi/10.1126/science.abk2177

Materials and Methods

Appendices S1 to S8

Figs. S1 to S12

Tables S1 to S7

References (39–61)

MDAR Reproducibility Checklist

29 June 2021; accepted 1 December 2021

10.1126/science.abk2177

HIBERNATION

Nitrogen recycling via gut symbionts increases in ground squirrels over the hibernation season

Matthew D. Regan^{1†}, Edna Chiang^{2,3}, Yunxi Liu⁴, Marco Tonelli⁵, Kristen M. Verdoorn¹, Sadie R. Gugel¹, Garret Suen², Hannah V. Carey^{1*}, Fariba M. Assadi-Porter^{1,4*}

Hibernation is a mammalian strategy that uses metabolic plasticity to reduce energy demands and enable long-term fasting. Fasting mitigates winter food scarcity but eliminates dietary nitrogen, jeopardizing body protein balance. Here, we reveal gut microbiome-mediated urea nitrogen recycling in hibernating thirteen-lined ground squirrels (*Ictidomys tridecemlineatus*). Ureolytic gut microbes incorporate urea nitrogen into metabolites that are absorbed by the host, with the nitrogen reincorporated into the squirrel's protein pool. Urea nitrogen recycling is greatest after prolonged fasting in late winter, when urea transporter abundance in gut tissue and urease gene abundance in the microbiome are highest. These results reveal a functional role for the gut microbiome during hibernation and suggest mechanisms by which urea nitrogen recycling may contribute to protein balance in other monogastric animals.

Hibernation is an adaptation to seasonal food scarcity. The hallmark of hibernation is torpor, a metabolic state that reduces rates of fuel use by up to 99% relative to active season rates. Torpor enables seasonal hibernators such as the thirteen-lined ground squirrel (*Ictidomys tridecemlineatus*) to fast for the ~6-month hibernation season, solving the problem of winter food scarcity; however, fasting deprives the squirrel of dietary nitrogen, thus jeopardizing protein balance.

Despite dietary nitrogen deficiency and prolonged inactivity, hibernators lose little muscle mass and function during winter (1).

Moreover, late in hibernation, squirrels elevate muscle protein synthesis rates to active season levels (2). It is unknown how hibernators preserve tissue protein during hibernation, but one hypothesis is that they harness the ureolytic capacities of their gut microbes to recycle urea nitrogen back into their protein pools (3). This process, termed urea nitrogen salvage, is present in ruminants and at least some nonruminant animals (4), but there is minimal evidence of its use by mammalian hibernators (5).

We hypothesized that squirrels use this mechanism to recoup urea nitrogen to facilitate tissue protein synthesis during, and particularly late in, hibernation (Fig. 1A). We tested this hypothesis with three seasonal squirrel groups: summer (active), early winter (1 month of hibernation and fasting), and late winter (3 to 4 months of hibernation and fasting) squirrels. Early and late winter squirrels were studied during induced interbout arousals at euthermic metabolic rates and body temperatures. Each seasonal group contained squirrels with intact and antibiotic-depleted gut microbiomes. For each group, we administered two intraperitoneal injections of ¹³C, ¹⁵N-urea

(~7 days apart depending on season, with unlabeled urea used as the control; fig. S1 and table S2). We then examined the critical steps of urea nitrogen salvage (Fig. 1).

This process begins with hepatic urea synthesis and transport into the blood. Urea that is not excreted by the kidneys can be transported into the gut lumen through epithelial urea transporters (UT-Bs) (6) where, in the presence of ureolytic microbes, it is hydrolyzed into ammonia and CO₂. Plasma urea concentrations in early and late winter squirrels were lower than those in summer squirrels (Fig. 2A), as observed previously (7) (fig. S2). However, UT-B abundance in the ceca of squirrels untreated with urea was about three times as high in late winter squirrels relative to summer squirrels (Fig. 2B), suggesting that lower plasma urea concentrations in winter may be partially offset through enhanced capacity for urea transport into the gut. Although this must be verified by future UT-B inhibition experiments, the observations that microbiome depletion increases UT-B expression (Fig. 2B), lowers plasma urea (Fig. 2A), and increases luminal urea concentrations (fig. S3) in summer squirrels support a role for UT-B in urea nitrogen salvage during the hibernation season. The mechanism underlying greater UT-B abundance in late winter squirrels and microbiome-depleted summer squirrels may involve luminal ammonia, which inhibits UT-B expression in ruminants (8). Commensurate with this, luminal ammonia levels were lower during hibernation in late winter squirrels than in summer squirrels (9) (fig. S4A) and in microbiome-depleted relative to microbiome-intact squirrels (Fig. 4A).

Next, we measured microbial ureolytic activity in vivo using stable isotope breath analysis where, because vertebrates lack urease, elevated ¹³CO₂:¹²CO₂ (δ¹³C) after injection of ¹³C, ¹⁵N-urea indicates microbial ureolysis. Breath δ¹³C increased after ¹³C, ¹⁵N-urea injection (Fig. 3, A to C) in microbiome-intact—but not microbiome-depleted—squirrels (Fig. 3D), thus confirming

¹Department of Comparative Biosciences, University of Wisconsin-Madison, Madison, WI 53706, USA.

²Department of Bacteriology, University of Wisconsin-Madison, Madison, WI 53706, USA.

³Microbiology Doctoral Training Program, University of Wisconsin-Madison, Madison, WI 53706, USA.

⁴Department of Integrative Biology, University of Wisconsin-Madison, Madison, WI 53706, USA.

⁵National Magnetic Resonance Facility at Madison (NMRFAM), University of Wisconsin-Madison, Madison, WI 53706, USA.

*Corresponding author. Email: hannah.carey@wisc.edu (H.V.C.); fariba@nmrfam.wisc.edu (F.M.A.-P.)

†Present address: Département de Sciences Biologiques, Université de Montréal, Montréal, QC H2B 0B3, Canada.

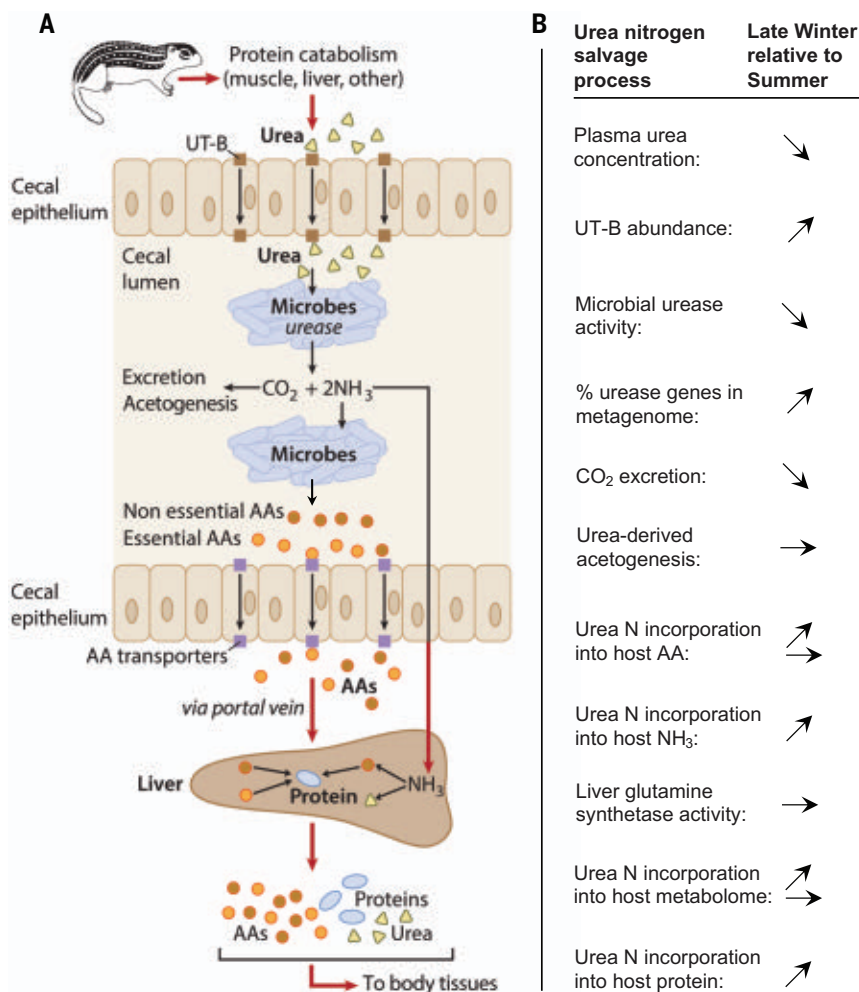


Fig. 1. Proposed mechanism for urea nitrogen salvage and relative changes during hibernation.

(A) Urea (yellow triangles), endogenously produced by the liver, is transported by epithelial urea transporters (UT-B; brown squares) from blood into the cecal lumen where it is hydrolyzed into CO₂ and NH₃ by urease-expressing gut microbes. CO₂ is excreted by the host and/or fixed by microbes. NH₃ is absorbed by the host and converted into amino acids (AAs) and/or urea in the liver, or used by microbes to synthesize AAs (circles) which are incorporated into the microbial proteome or potentially absorbed by the host through ceco-colonic amino acid transporters (purple squares) (11). Ultimately, the AAs are used to synthesize protein (blue ovals) in host tissues, recycling the urea nitrogen. (B) Arrows indicate how processes change (increase, decrease, no change) in winter versus summer as revealed by this study. All changes are based on statistically significant results except for percentage of urease genes in the metagenome ($P = 0.083$).

microbial ureolytic activity. Ureolysis was greatest in summer squirrels (Fig. 3D and fig. S4B), consistent with greater bacterial abundance in summer versus hibernating squirrels (fig. S5). Nevertheless, microbial ureolysis continued throughout hibernation.

The metagenomes of hibernating squirrels trended toward higher percentages of urease genes than those of summer squirrels (Fig. 3E) across the seven urease-related genes (Fig. 3F). This suggests that during hibernation, a higher percentage of microbes have the potential to hydrolyze urea. Indeed, *Alistipes*—the bacterial genus with the greatest detectable genomic representation of urease genes in early and late winter squirrels (Fig. 3G)—is predominant during hibernation, with a six-

fold population increase between the summer and late winter groups (9).

To benefit the host, microbial ureolytic activity would need to provide nitrogenous compounds such as amino acids and/or ammonia. Using two-dimensional ¹H-¹⁵N NMR spectroscopy, we found that more ¹⁵N was incorporated into the cecal content and liver metabolomes of microbiome-intact compared with microbiome-depleted squirrels (Fig. 4, A and B), a trend that—with a few exceptions—also held for specific metabolites such as ammonia, glutamine, and alanine (Fig. 4, A and B). ¹⁵N-metabolite levels also varied seasonally. In cecum contents, early and late winter metabolite levels were generally lower than summer levels, whereas in the liver, early and late winter

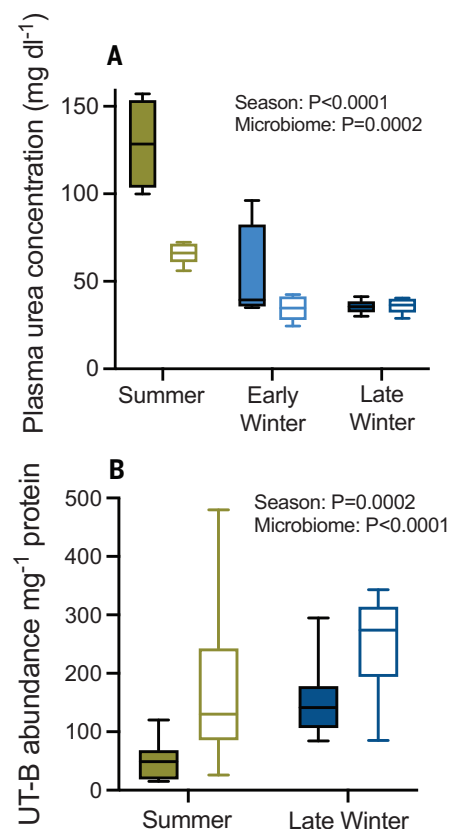


Fig. 2. Plasma urea concentration and cecal urea transporter (UT-B) expression. (A) Plasma urea concentration in urea-treated squirrels with intact (filled bars) and depleted (open bars) gut microbiomes ($n = 4$ to 5 animals). (B) UT-B protein abundance per milligram of cecal protein in cecal tissue ($n = 12$; immunoblots in fig. S8). A subset of non-urea-treated squirrels was used that lacked the early winter group. Two-way analysis of variance (ANOVA) results are shown in each panel.

metabolite levels were generally higher than summer levels and were typically highest in the late winter group (Fig. 4, A and B). For muscle, metabolite ¹⁵N incorporation was generally unaffected by the presence of a microbiome (Fig. 4C), which could be due to the timing of our ¹³C,¹⁵N-urea dosing and tissue sampling protocols. When tissues were sampled, the ¹⁵N-amino acids from the initial ¹³C,¹⁵N-urea dose may have already been incorporated into muscle protein, thus explaining the microbiome-dependent ¹⁵N-protein results (Fig. 4C), whereas the 3 hours between the second dose and tissue sampling may have been too brief for ¹⁵N-metabolites to appear in muscle. Rather, the muscle ¹⁵N-metabolite levels may represent microbiome-independent background ¹⁵N levels, which is consistent with the equivalent ¹⁵N-metabolite abundances in the muscle of squirrels treated with labeled and unlabeled urea and with intact and depleted microbiomes (table S1).

The ultimate benefit of urea nitrogen salvage is nitrogen incorporation into host protein. Using isotope ratio mass spectrometry, we found that microbiome-intact squirrels incorporated significant ¹⁵N into liver and muscle protein, but microbiome-depleted squirrels did not (Fig. 4, B and C), thereby verifying that urea nitrogen salvage is microbe-dependent and benefits the host. Moreover, ¹⁵N incorporation into liver and muscle protein was two to three times as high in the late winter group versus the summer group, indicating that urea nitrogen salvage is most beneficial late in the winter fast. We also found large amounts of ¹⁵N incorporated into cecal content protein (indicative of microbial protein; Fig. 4A) in

microbiome-intact squirrels, indicating nutritional benefits for the gut microbiome. However, unlike in muscles and the liver, microbial protein ¹⁵N incorporation was highest in the summer group (Fig. 4A), for which microbial abundance was also highest (fig. S5). Notably, ¹⁵N incorporation into host protein was highest when ureolytic activity was lowest (i.e., late winter; Fig. 3D). This can be explained by our observations at multiple steps (Fig. 1B): First, urea transport capacity into the gut likely increases during hibernation through elevated UT-B abundance (Fig. 2B). Second, the microbiome becomes proportionally (though not absolutely) more ureolytic in winter, evidenced by elevated urease gene percentages (Fig. 3E)

and bacterial urease activity levels (fig. S4B) that are higher than those predicted by the breath $\delta^{13}\text{C}$ changes (Fig. 3D). Another possible contributor is proportionally greater microbial CO_2 fixation (e.g., acetogenesis) in winter than in summer (fig. S6), thus reducing the quantity of exhaled $^{13}\text{CO}_2$. Third, higher bacterial death rates in winter (10) could liberate relatively higher amounts of bacterial contents for host absorption during hibernation, including metabolites containing urea nitrogen (Fig. 4A). Salvaged urea nitrogen can potentially be absorbed by the squirrel as amino acids or ammonia. Though ceco-colonic amino acid absorption occurs in rodents (11), our results suggest that ammonia absorption and its hepatic conversion to glutamine through glutamine synthetase may be the key step that is enhanced during hibernation. For example, tissue abundance of ¹⁵N-lysine (an essential amino acid that must be absorbed) was affected only by season and not by microbiome presence. Additionally, numerous lines of evidence support the absorption and hepatic conversion of ¹⁵N-ammonia, including elevated liver ¹⁵N-ammonia and ¹⁵N-glutamine levels in early and late winter (Fig. 4B), sustained liver glutamine synthetase activity during hibernation (fig. S7), and reduced urea cycle enzymes and intermediates (12, 13). This implies that during hibernation, the condensation of ammonia with glutamate to form glutamine is favored over its conversion to urea. Indeed, in protein-deficient rats, hepatic ammonia processing shifts from urea toward glutamine production (14), and in fasting hibernating arctic ground squirrels, ammonia from muscle protein breakdown is directed away from the urea cycle toward amino acid formation (13). Despite this implied shift in ammonia processing, urea production continues during hibernation (albeit at lower rates), with plasma concentrations lowest upon torpor reentry and highest during interbout arousal (fig. S2) (7). Much of this urea is likely transferred to the gut by urea transporters, where it becomes available for microbial ureolysis. Thus, nitrogen recycling in hibernators involves both endogenous (13) and microbe-dependent mechanisms, underscoring the importance of maintaining nitrogen balance during hibernation. Urea nitrogen salvage provides two major benefits for hibernators: First, it augments protein synthesis when dietary nitrogen is absent and appears especially important late in hibernation, just before the squirrel's emergence into its breeding season (2, 15). By facilitating protein synthesis and subsequent tissue function, this process may confer reproductive advantages. Second, as in water-deprived camels (16), urea nitrogen salvage may enhance water conservation in water-deprived hibernators by diverting urea away from the kidneys, thus requiring less water for urine production.

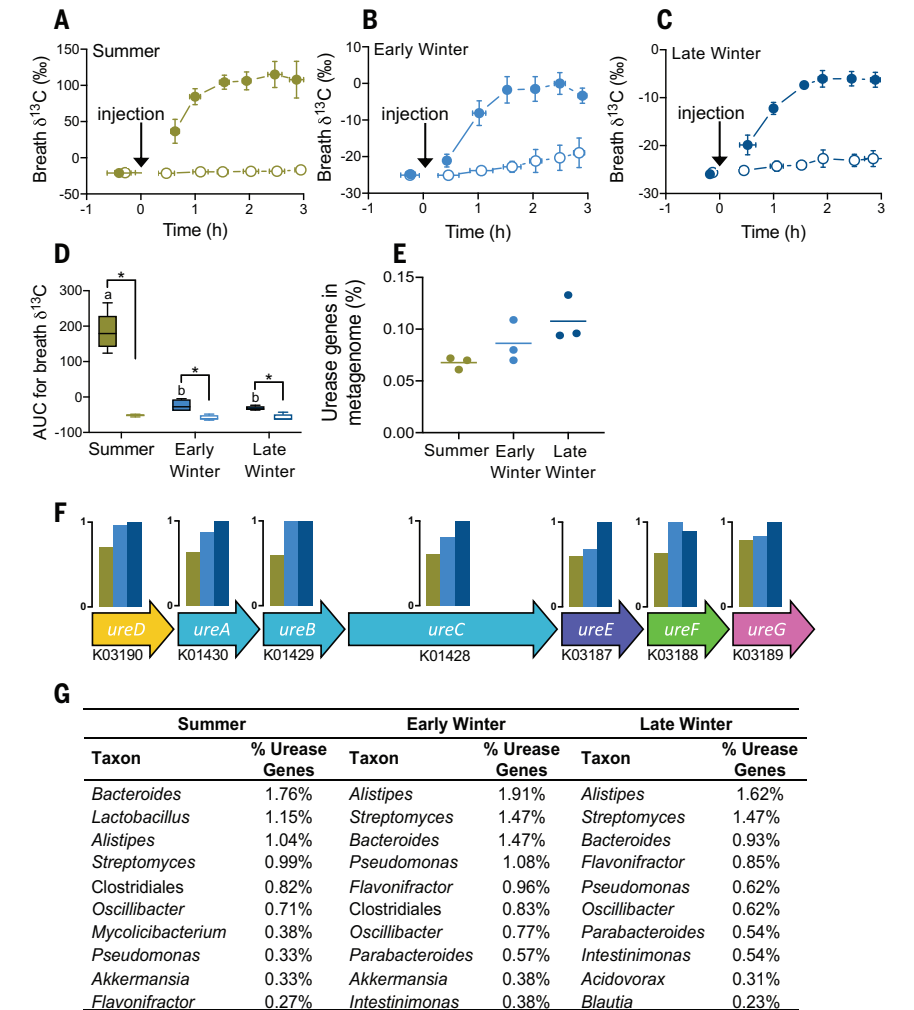


Fig. 3. Gut microbial ureolysis and metagenome. Mean breath $\delta^{13}\text{C}$ for (A) summer, (B) early winter, and (C) late winter squirrels treated with ^{13}C , ^{15}N -urea. Horizontal and vertical error bars represent SEM, and closed and open symbols represent squirrels with intact and depleted microbiomes, respectively. The arrows indicate intraperitoneal ^{13}C , ^{15}N -urea injection. (D) Mean area-under-the-curve (AUC) values for data in (A) to (C), where asterisks indicate significant differences between microbiome groups within a season, and lowercase letters indicate significant seasonal differences among microbiome-intact groups [$n = 5$, (A) to (D); $n = 4$ for early winter microbiome-depleted animals]. Seasonal effect on (E) the percentage of urease genes in the bacterial metagenome, (F) urease operons including each gene's Kyoto Encyclopedia of Genes and Genomes ontology identifier and seasonal relative abundance, and (G) the top 10 bacterial taxa from taxonomic classification of urease genes as determined by sequence abundance.

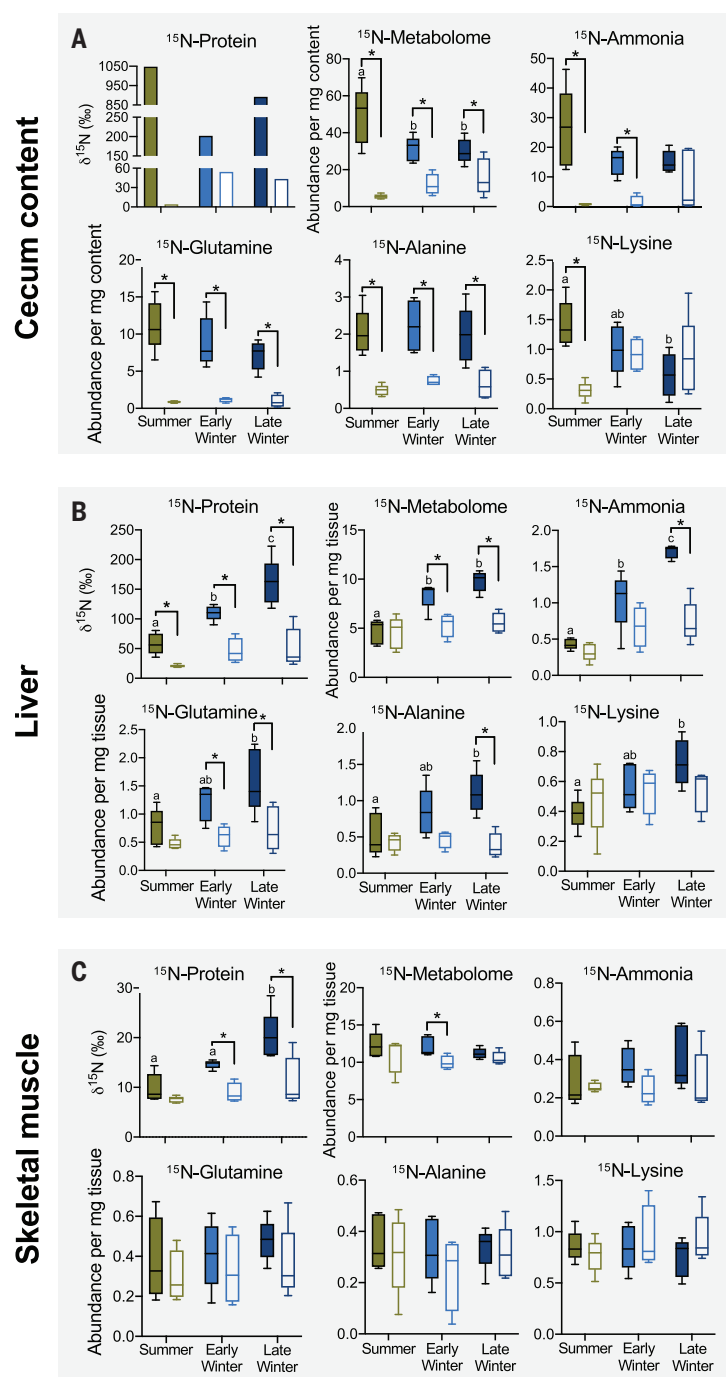


Fig. 4. ^{15}N -urea nitrogen incorporation into metabolite and protein pools of gut microbiome and host tissues. (A) Cecal content, (B) liver, and (C) muscle (quadriceps) of microbiome-intact (filled bars) and microbiome-depleted (open bars) squirrels. For each panel, ^{15}N -Protein portrays ^{15}N -incorporation into protein, ^{15}N -Metabolome portrays ^{15}N -incorporation into the total pool of metabolites (identifiable and nonidentifiable), and the remaining plots portray ^{15}N -incorporation into the metabolite named above the plot. Metabolomic data are relative abundances in arbitrary units. Asterisks indicate a significant difference between microbiome groups within a season, and different lowercase letters indicate significant seasonal difference among microbiome-intact groups. See tables S1 and S2 for statistical results. $n = 5$ for all data, except for early winter microbiome depleted ($n = 4$) and cecum content ^{15}N -protein [$n = 1$ (pooled samples)].

Our results provide evidence that the gut microbiome plays a functional role during the hibernation season, building upon earlier results that suggest a possible role for the micro-

biome in pre-hibernation fattening (17). Our demonstration of monogastric urea nitrogen salvage as a mechanism facilitating protein synthesis under nitrogen limitation has potential

implications beyond hibernation. For example, muscle wasting affects hundreds of millions of people globally as a result of nitrogen-limited diets (18) and sarcopenia (19), and there is evidence for humans possessing the necessary machinery for urea nitrogen salvage (20). Understanding the mechanisms by which hibernators maintain protein balance and mitigate muscle wasting under severe nitrogen limitation may inform strategies for muscle preservation in humans.

REFERENCES AND NOTES

- Y.-F. Gao et al., *Comp. Biochem. Physiol. A Mol. Integr. Physiol.* **161**, 296–300 (2012).
- A. G. Hindle et al., *J. Exp. Biol.* **218**, 276–284 (2015).
- M. L. Riedesel, J. M. Steffen, *Fed. Proc.* **39**, 2959–2963 (1980).
- A. K. Patra, J. R. Aschenbach, *J. Adv. Res.* **13**, 39–50 (2018).
- H. Harlow, in *Comparative Physiology of Fasting, Starvation, and Food Limitation*, M. D. McCue, Ed. (Springer, 2012) pp. 277–296. https://link.springer.com/10.1007/978-3-642-29056-5_17
- M. E. Walpole et al., *J. Dairy Sci.* **98**, 1204–1213 (2015).
- L. E. Epperson, A. Karimipour-Fard, L. E. Hunter, S. L. Martin, *Physiol. Genomics* **43**, 799–807 (2011).
- Z. Lu et al., *Am. J. Physiol. Regul. Integr. Comp. Physiol.* **308**, R283–R293 (2015).
- H. V. Carey, W. A. Walters, R. Knight, *Am. J. Physiol. Regul. Integr. Comp. Physiol.* **304**, R33–R42 (2013).
- T. J. Stevenson, K. N. Duddleston, C. L. Buck, *Appl. Environ. Microbiol.* **80**, 5611–5622 (2014).
- Y. Chen et al., *Am. J. Physiol. Gastrointest. Liver Physiol.* **318**, G189–G202 (2020).
- L. E. Epperson, J. C. Rose, H. V. Carey, S. L. Martin, *Am. J. Physiol. Regul. Integr. Comp. Physiol.* **298**, R329–R340 (2010).
- S. A. Rice et al., *Nat. Metab.* **2**, 1459–1471 (2020).
- C. Rémésy, C. Moundras, C. Morand, C. Demigné, *Am. J. Physiol.* **272**, G257–G264 (1997).
- O. J. Rongstad, *J. Mammal.* **46**, 76 (1965).
- H. M. Mousa, K. E. Ali, I. D. Hume, *Comp. Biochem. Physiol. A Comp. Physiol.* **74**, 715–720 (1983).
- F. Sommer et al., *Cell Rep.* **14**, 1655–1661 (2016).
- FAO, “The State of Food Insecurity in the World (SOFI)” (FAO, 2014) www.fao.org/publications/card/en/c/56fed1a2-0f6e-4185-8005-62170e9b27bb/.
- E. Marty, Y. Liu, A. Samuel, O. Or, J. Lane, *Bone* **105**, 276–286 (2017).
- M. Langran, B. J. Moran, J. L. Murphy, A. A. Jackson, *Clin. Sci. (Lond.)* **82**, 191–198 (1992).

ACKNOWLEDGMENTS

We thank A. Steinberg, S. Cailey, W. Porter, S. Martin, and M. T. Grahm for assistance, and the reviewers for insightful comments.

Funding: Work was supported by NSF Grant IOS-1558044 to H.V.C., F.M.A.-P., and G.S.; NIH Grants P41GM136463, P41GM103399 (NIGMS), and P41R002301 to the National Magnetic Resonance Facility at Madison; National Institute of General Medical Sciences of the NIH traineeship T32GM008349 and NSF Graduate Research Fellowship DGE-1747503 to E.C.; NSERC Canada Postdoctoral Fellowship to M.D.R. **Author contributions:** H.V.C., F.M.A.-P., G.S., M.D.R., and M.T. designed the study; M.D.R., E.C., M.T., S.G., and K.V. collected data; M.D.R., F.M.A.-P., G.S., E.C., and Y.L. conducted analyses; M.D.R. wrote the manuscript with input from all authors.

Competing interests: F.M.A.-P. is the founder of MetResponse, LLC and Isomark Health Inc. The other authors declare no competing interests. **Data and materials availability:** Metagenomic data are available at NCBI (PRJNA693524); other data are available as supplementary materials.

SUPPLEMENTARY MATERIALS

science.org/doi/10.1126/science.abh2950

Materials and Methods

Figs. S1 to S8

Tables S1 to S3

References (21–49)

MDAR Reproducibility Checklist

Data S1

1 March 2021; resubmitted 15 July 2021

Accepted 2 December 2021

10.1126/science.abh2950




**CHANGE
YOUR JOB
AND YOU
JUST MIGHT
CHANGE
THE WORLD.**



Find your next job at [ScienceCareers.org](https://www.ScienceCareers.org)

The relevance of science is at an all-time high these days. For anyone who's looking to get ahead in —or just plain get into— science, there's no better, more trusted resource or authority on the subject than *Science Careers*. Here you'll find opportunities and savvy advice across all disciplines and levels. There's no shortage of global problems today that science can't solve. Be part of the solution.

ScienceCareers

FROM THE JOURNAL SCIENCE  AAAS



TENURE-TRACK RESEARCH FELLOW IN QUANTUM TECHNOLOGIES

The Nanoscience Cooperative Research Center CIC nanoGUNE (www.nanogune.eu), created with the mission of conducting world-class nanoscience research for the competitive growth of the Basque Country, member of the Basque Research and Technology Alliance (BRTA), and recognized by the Spanish Research Agency as a "Maria de Maeztu" center of excellence for the period 2022-2025, is currently looking for a **tenure-track research fellow in quantum technologies**.

We invite applications for a tenure-track position in quantum technologies, with a focus on quantum hardware, including (but not restricted to) quantum sensors and/or solid-state devices and platforms for quantum computing and communication. Of particular interest are research areas with connection to technology and applications. The successful candidate is expected to conduct an independent research program in close collaboration with some of the existing research groups at the center.

Candidates should have an outstanding research record in Physics and/or Engineering and the potential to attract public and private funding at the highest level. Proficiency in spoken and written English is compulsory.

In addition to a start-up package, we offer an international and competitive environment, an excellently equipped state-of-the-art infrastructure, and the possibility to perform top-class research. We promote teamwork in a diverse and inclusive environment, and we welcome all kinds of applicants without regard to disability, gender, nationality, race, religion, or sexual orientation. Female candidates are particularly encouraged to apply.

Candidates should apply through the form that is available at www.nanogune.eu/careers. Preselected candidates will subsequently be contacted and asked to apply, before **March 15th 2022**, to an Ikerbasque Research Fellowship at www.ikerbasque.net

Closing date: **27 February 2022**



POSTDOCTORAL FELLOWSHIPS AVAILABLE

The Department of Pathology, Microbiology, and Immunology (PMI) at the University of South Carolina's School of Medicine invites applications for **Postdoctoral Fellowships** in any area of immunology to study epigenomic, genomic, and transcriptomic effects, and/or microbiome following environmental pollutant and dietary supplement exposure on inflammation and cancer. COVID-19 and PTSD research opportunities are also available.

A Ph.D. in biomedical sciences is required. Previous experience in -omics technology is not required. For consideration, please send C.V. and a list of three references to Dr. Mitzi Nagarkatti, Chair of Pathology, Microbiology, and Immunology, University of South Carolina School of Medicine, Columbia, SC 29208, via application link, <https://uscjobs.sc.edu/postings/109727>.

At the University of South Carolina, we strive to cultivate an inclusive environment that is open, welcoming, and supportive of individuals of all backgrounds. We recognize diversity in our workforce is essential to providing academic excellence and critical to our sustainability. The University is committed to eliminating barriers created by institutional discrimination through accountability and continuous process improvement. We celebrate the diverse voices, perspectives, and experiences of our employees.

TENURE TRACK FACULTY POSITION - HEALTH AND DISEASE IN AQUATIC ORGANISMS

The Institute of Marine and Environmental Technology (IMET) of the University System of Maryland seeks applications for the position of **Assistant Professor** (tenure-track). The successful candidate will have a track-record of outstanding research using molecular biology/genetics approaches to study health and disease in marine organisms. Candidates' research may address mechanisms of infectious disease or the impact of climate change on the health of aquatic organisms and ecosystems. Candidates with an interest in practical applications of their fundamental research are encouraged to apply. A demonstrated ability or potential to establish a well-funded research program and a commitment to diversity and inclusion is expected for the successful candidate. Primary appointment is in the Department of Marine Biotechnology (<https://marinebiotechnology.umbc.edu/>) at the University of Maryland Baltimore County, with a secondary appointment at the University of Maryland Baltimore. The primary focus of the appointee will be on research and the candidate is expected to mentor graduate students in the laboratory. Teaching at the undergraduate and graduate level is also expected.

IMET's mission is to study the biology of coastal marine biosystems and ensure their sustainable use, as well as application of marine-derived systems to improve human health (www.imet.usmd.edu). IMET brings together faculty members from three major USM research institutions - the University of Maryland Baltimore (UMB), the University of Maryland Baltimore County (UMBC), and the University of Maryland Center for Environmental Science (UMCES) - in a dedicated state-of-the-art research facility located in Baltimore's Inner Harbor.

A Ph.D. or equivalent terminal degree is required in molecular biology, marine biology, microbiology, aquatic pathology or related fields. Candidates should have postdoctoral experience and a strong publication record. Interested candidates should submit their applications electronically to <http://apply.interfolio.com/100174>, and include: 1) detailed curriculum vitae, 2) statement of research interests and goals 3) a statement demonstrating a commitment to diversity in STEM and 4) names and contact details of three to five references. To receive full consideration, application materials should be submitted by **February 28, 2022** (the position will be open until filled).

The USM is an Equal Opportunity, Affirmative Action Employer. UMBC values gender, ethnic and racial diversity; women, members of ethnic minority groups, and individuals with disabilities are strongly encouraged to apply. UMBC is the recipient of an NSF ADVANCE Institutional Transformation Award to increase the participation of women in academic careers.



ICAHN SCHOOL OF MEDICINE AT MOUNT SINAI - FACULTY OF NEUROLOGY

We are looking for an ambitious and highly motivated **postdoctoral researcher** with a strong background in biology and/or neuroscience. The successful candidate will join an international, multidisciplinary team to study Alzheimer's disease (AD) pathogenesis and develop diagnostic and therapeutic interventions for AD. Our work is highly multidisciplinary, spanning molecular and cell biology, neuroscience and bioinformatics. Using advanced wet lab technologies including human iPSC-derived culture systems and animal modeling approaches, the postdoctoral researcher will carry out research projects involved in developing novel therapies and biomarkers for Alzheimer's disease and other neurodegenerative disorders.

The postdoctoral researcher has the responsibility for the integrity of the data and the accuracy of the data analysis. Research duties include data acquisition, analysis, and interpretations; converting the results into reportable formats for presentations, publication in reputable journals, and presentation at local and international conferences. The postdoctoral researcher will be directly supervised by Dr. Cai. The postdoctoral researcher and the mentor will develop and maintain an Individual Development Plan (IDP). The applicants will be assessed on their academic performance, personal aptitude, good collaborative skills, and the ability to work across traditional disciplinary boundaries. We are looking for a candidate who is determined and has high problem-solving analysis skills. We offer a 2-year position, renewable up to 5 years, with a competitive salary and benefits package followed the NIH guidelines.

Job title: Postdoctoral Fellow

Location description: New York City, New York (US)

Salary description: We offer a 2-year position, renewable up to 5 years, with a competitive salary and benefits package.

Application email: dongming.cai@mssm.edu

By Kathleen Hupfeld

Paying it forward

When I was in high school, I typed up a letter and mailed it to the U.S. National Institutes of Health, boldly asking for “all of their research on stroke.” I was working on a yearlong project that required me to reach out to experts. Several weeks later, a thick packet arrived in the mail, along with a personalized letter thanking me for my inquiry. I was thrilled. Whoever responded could have thought, “This is just a teenager, we don’t have time for her.” Instead, they took the time to put together the information I requested. Being taken seriously boosted my confidence and reaffirmed that I belonged in STEM. Now, it’s my turn to pay it forward.

I participate in a variety of outreach activities—neuroscience demonstrations, science fairs, career panels, STEM camps. Those activities take time and energy away from my own research, as I found recently while completing my Ph.D. But they also benefit me in ways I didn’t necessarily expect, helping me grow and find satisfaction in my work as a scientist. Here are a few of the benefits.

SHARPEN COMMUNICATION. Kids are some of the best critics of science communication. They ask the hard questions and offer fresh perspectives. For instance, after a presentation to kids in which I showed MRI scans of astronaut brains, an eager kindergartner asked me how long it took to remove an astronaut’s brain from their skull, photograph it, and put it back in. His comment helped me see that I was not explaining my methods clearly.

I’ve carried this lesson with me when I’ve prepared other presentations, including those to other scientists. I now do a better job describing the big picture goals and methods and tailoring my explanations to my audience. For instance, when I presented my work on how the brain changes in outer space to spaceflight researchers from a wide range of fields, I took more time than usual to explain my methods and make it clear what information my data could, and could not, provide.

GAIN MOTIVATION. Two years into my Ph.D., I felt discouraged after several frustrating paper and grant rejections in a row. Then, a fellow graduate student convinced me to participate in our university’s Brain Awareness Week events, and my mood quickly changed. Seeing elementary schoolers’ hands shoot up—eager to answer my questions and participate in my demonstration—brightened my day and reminded me about the curiosity that got me inter-



“The future of STEM depends on those already in science reaching out to the next generation.”

ested in science in the first place.

Years later, when I was a Ph.D. student, I encountered a similarly enthusiastic middle schooler who loved black holes. When I told her to tell me all about them, her response startled me: “Do you really want to hear about black holes? Other kids tell me they’re a weird thing for a girl to like.” This led to a lengthy back and forth, during which I encouraged her to explore her scientific passions. I don’t know whether she will go on to become an astrophysicist, but I hope our conversation left her feeling that she can, and that so many of us are cheering for her.

The future of STEM depends on those already in science reaching out to the next generation. Do what you can to share your knowledge and inspire curiosity. Along the way, you just might improve your own science as well. ■

Kathleen Hupfeld is a postdoctoral fellow at the Johns Hopkins University School of Medicine. Do you have an interesting career story to share? Send it to SciCareerEditor@aaas.org.

Pushing the Boundaries of Knowledge

As AAAS's first multidisciplinary, open access journal, *Science Advances* publishes research that reflects the selectivity of high impact, innovative research you expect from the *Science* family of journals, published in an open access format to serve a vast and growing global audience. Check out the latest findings or learn how to submit your research: science.org/journal/sciadv

Science
Advances
AAAS

GOLD OPEN ACCESS, DIGITAL, AND FREE TO ALL READERS



Apply for our exciting research Prize!



\$25, 000 Grand Prize!
Get published in *Science*!

The *Science*-PINS Prize is a highly competitive international prize that honors scientists for their excellent contributions to neuromodulation research. For purposes of the Prize, neuromodulation is any form of alteration of nerve activity through the delivery of physical (electrical, magnetic, or optical) stimulation to targeted sites of the nervous system with implications for translational medicine.

For full details, judging criteria and eligibility requirements, visit:

www.science.org/pins

Submissions Open: 15 December 2021

Science
AAAS



Science
Translational
Medicine
AAAS